

NATIONAL AERONAUTICS AND SPACE ADMINISTRATION

Space Programs Summary No. 37-37, Volume IV

for the period December 1, 1965 to January 31, 1966

Supporting Research and Advanced Development

FACILITY FORM 602	N66-23526	_____
	(ACCESSION NUMBER)	(THRU)
	333	1
	(PAGES)	(CODE)
CR-74467	34	_____
(NASA CR OR TMX OR AD NUMBER)	(CATEGORY)	

GPO PRICE \$ _____

CFSTI PRICE(S) \$ _____

Hard copy (HC) 7.00

Microfiche (MF) 1.75

ff 653 July 65

pl

**JET PROPULSION LABORATORY
CALIFORNIA INSTITUTE OF TECHNOLOGY
PASADENA, CALIFORNIA**

February 28, 1966



NATIONAL AERONAUTICS AND SPACE ADMINISTRATION

Space Programs Summary No. 37-37, Volume IV

for the period December 1, 1965 to January 31, 1966

Supporting Research and Advanced Development

JET PROPULSION LABORATORY
CALIFORNIA INSTITUTE OF TECHNOLOGY
PASADENA, CALIFORNIA

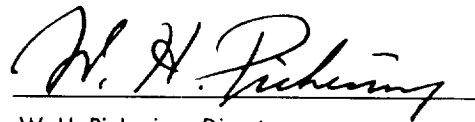
February 28, 1966

Preface

The *Space Programs Summary* is a six-volume, bimonthly publication that documents the current project activities and supporting research and advanced development efforts conducted or managed by JPL for the NASA space exploration programs. The titles of all volumes of the *Space Programs Summary* are:

- Vol. I. The Lunar Program (Confidential)
- Vol. II. The Planetary-Interplanetary Program (Confidential)
- Vol. III. The Deep Space Network (Unclassified)
- Vol. IV. Supporting Research and Advanced Development (Unclassified)
- Vol. V. Supporting Research and Advanced Development (Confidential)
- Vol. VI. Space Exploration Programs and Space Sciences (Unclassified)

The *Space Programs Summary*, Vol. VI consists of an unclassified digest of appropriate material from Vols. I, II, and III; an original presentation of technical supporting activities, including engineering development of environmental-test facilities, and quality assurance and reliability; and a reprint of the space science instrumentation studies of Vols. I and II.



W. H. Pickering, Director
Jet Propulsion Laboratory

Space Programs Summary No. 37-37, Volume IV

Copyright © 1966, Jet Propulsion Laboratory, California Institute of Technology
Prepared under Contract No. NAS 7-100, National Aeronautics & Space Administration

Contents

SYSTEMS DIVISION

I. Systems Analysis	1
A. Statistical Analysis of Three Midcourse Corrections	
<i>Task No. 388-30105-2-3120 (684-30-01-10), F. M. Sturms, Jr.</i>	1
B. Duration of Ground-Station Satellite View Periods	
<i>Task No. 388-30105-2-3120 (684-30-01-10), R. D. Bourke</i>	11
C. Periodic Comet Orbit Determination Capabilities for Spacecraft Intercept Missions from 1970 to 1973	
<i>Task No. 388-30105-2-3120 (684-30-01-10), G. E. Pease</i>	14
D. Optimum Collocation Method for Two-Point Boundary Value Problems	
<i>Task No. 329-40101-1-3120 (129-04-01-01), W. Kizner</i>	26
E. Solution of the <i>N</i> -Body Problem with Recurrent Power Series	
<i>Task No. 329-40201-1-3120 (129-04-01-02), R. Broucke</i>	27
F. On Changes of Independent Variable in Dynamical Systems	
<i>Task No. 329-40201-1-3120 (129-04-01-02), R. Broucke</i>	30
References	34
II. Deep Space Network Systems	36
A. Operational Requirements for a Remote Control Station	
<i>Task No. 327-10101-1-3192 (127-51-01-01), W. Wong and K. Heftman</i>	36

GUIDANCE AND CONTROL DIVISION

III. Spacecraft Power	39
A. Thermoelectric Performance Testing	
<i>Task No. 320-70101-2-3420 (120-27-06-01), L. Selwitz</i>	39
IV. Spacecraft Control	42
A. Solid Propellant Electrical Thruster	
<i>Task No. 384-60401-2-3440 (186-68-02-03), G. S. Perkins</i>	42
B. Sterilization of Capsule Control System	
<i>Task No. 384-80301-2-3440 (186-58-02-05), R. J. Mankovitz</i>	43
C. Horizon Scan Platform System	
<i>Task No. 384-61901-2-3440 (186-68-02-09), T. Kerner</i>	47
D. Antenna Pointing Study	
<i>Task No. 325-90401-2-3440 (125-19-03-02), G. Fleischer and J. C. Nicklas</i>	51
E. Attitude Control of Spin-Stabilized Spacecraft	
<i>Task No. 325-90501-2-3440 (125-19-04-01), B. M. Dobrotin and J. C. Nicklas</i>	54
References	60

Contents (Cont'd)

V. Guidance and Control Research	61
A. Titanium Oxide Thin Films	
<i>Task No. 329-21801-1-3450 (129-02-05-09), J. Maserjian</i>	61
B. Pure Space-Charge-Limited Electron Current in Silicon	
<i>Task No. 329-21801-1-3450 (129-02-05-09), M-A. Nicolet and S. Denda</i>	64
C. Variable-Frequency NMR Spectrometer for the 20- to 200-Mc Range	
<i>Task No. 329-21401-1-3450 (129-02-05-06), D. I. Tchernev, H. G. Vorkink, and J. E. Guisinger</i>	68
References	75
VI. Flight Computers and Sequencers	76
A. The Diagnosable Arithmetic Processor	
<i>Task No. 325-70401-2-3410 (125-17-04-02), A. Avizienis</i>	76
References	80
ENGINEERING MECHANICS DIVISION	
VII. Materials	81
A. Carbon and Graphite Research	
<i>Task No. 329-31601-1-3510 (129-03-04-02), D. B. Fischbach and W. V. Kotlensky</i>	81
B. Directional Solar Absorptance of Temperature-Control Surface Finishes	
<i>Task No. 324-90401-2-3510 (124-09-05-01), W. M. Hall</i>	82
C. Pure Oxide Ceramic Research	
<i>Task No. 329-31101-1-3510 (129-03-04-01), M. H. Leipold and T. H. Nielsen</i>	83
References	85
VIII. Lunar Spacecraft Development	86
A. High Impact Technology	
<i>Task No. 384-62801-2-3550 (186-68-04-14), J. L. Adams</i>	86
IX. Electro-Mechanical Engineering	89
A. High Voltage Insulation Using Foams in Vacuum	
<i>Task No. 325-50101-2-3570 (125-25-03-01), E. R. Bunker, Jr.</i>	89
ENVIRONMENTAL SIMULATION DIVISION	
X. Aerodynamic Facilities	91
A. Wind Tunnels	
<i>Task Nos. 324-70103-7-3730 (124-07-04-01), E. Laumann; 324-70101-7-3730 (124 07 04-01), G. Herrera and H. Enmark; 324-70109-7-3730 (124-07-04-01), H. Holway; 324 70402-7-3730 (124-07-04-02), D. Lund; 324-70107-7-3730 (124-07-04-01), R. Prislín and H. Holway</i>	91

Contents (Cont'd)

B. Hypervelocity Laboratory	
<i>Task Nos. 324-70813-2-3730 (124-07-01-04), F. Livingston, G. Stickford, and B. Riale, 324 70812-2-3730 (124-07-01-04), T. Babineaux; 324-70817-2-3730 (124-07-01-04), W. Menard and G. Thomas; 324-70806-2-3730 (124-07-01-04), T. Horton and T. Babineaux</i>	101
References	106
XI. Space Simulators and Facility Engineering	107
A. Advanced Solar Simulation Development	
<i>Task No. 384-10101-2-3750 (186-71-01-01), C. L. Youngberg</i>	107
PROPULSION DIVISION	
XII. Research and Advanced Concepts	111
A. Thermal Radiation From Ionized Argon As Determined by Application of Near-Black Cavities: Effect of Quartz Window Between Gas and Cavity	
<i>Task No. 329-10701-1-3831 (129-01-09-04), E. J. Roschke</i>	111
B. Liquid MHD Power Conversion	
<i>Task No. 320-70301-1-3830 (120-27-06-03), D. Elliott, D. Cerini, L. Hays, and E. Weinberg</i>	118
References	122
XIII. Solid Propellant Engineering	124
A. Nozzle Thrust Misalignment	
<i>Task No. 328-21101-2-3810 (128-32-06-01), L. Strand</i>	124
B. Applications Technology Satellite (ATS) Motor Development	
<i>Task No. 724-00081-7-3810 (630-01-00-00), R. G. Anderson</i>	130
Erratum	138
XIV. Polymer Research	139
A. Relationship Between Maximum Extensibility of Networks and the Degree of Crosslinking and Primary Molecular Weight	
<i>Task No. 328-20301-1-3820 (128-32-05-02), R. F. Fedors and R. F. Landel</i>	139
B. The Effect of Surface Modifications on the Burning Rate of a Composite Solid Propellant, II	
<i>Task No. 328-20301-1-3820 (128-32-05-02), B. G. Moser and R. F. Landel</i>	143
C. Polymer Degradation Mechanisms: C ¹⁴ -Labeled Adducts of Poly(Propylene Oxide)	
<i>Task No. 328-20401-1-3820 (128-32-05-03), J. D. Ingham, E. F. Kopka, and G. K. Ostrum</i>	144
D. Polymer Nuclear Magnetic Resonance Spectroscopy Studies	
<i>Task No. 328-20401-1-3820 (128-32-05-03), D. D. Lawson and J. D. Ingham</i>	145
E. Acenaphthene Radical Ion	
<i>Task No. 329-30401-1-3820 (129-03-11-03), A. Rembaum and A. M. Herman</i>	147

Contents (Cont'd)

F. Method for Calculating Outgassing Rates of Rigid Closed-Cell Foams	
<i>Task No. 384-62701-1-3820 (186-68-13-03), E. F. Cuddihy and J. Moacanin</i>	149
G. Studies on Sterilizable Elastomers	
<i>Task No. 384-62701-2-3820 (186-68-13-03), E. Cuddihy and J. Moacanin</i>	150
References	153
XV. Liquid Propulsion Systems	155
A. Advanced Liquid Propulsion Systems	
<i>Task No. 331-10101-2-3840 (731-12-03-01), L. R. Toth;</i>	
<i>Task No. 331-10201-2-3840 (731-12-03-03), R. S. Weiner;</i>	
<i>Task No. 328-11201-2-3840 (128-31-06-06), W. H. Tyler;</i>	
<i>Task No. 328-11001-2-3840 (128-31-02-03), T. A. Groudie; and</i>	
<i>Task No. 331-10301-2-3840 (731-12-03-02), R. W. Riebling</i>	155
References	170

SPACE SCIENCES DIVISION

XVI. Space Instruments	171
A. Digitizing TV Data	
<i>Task No. 325-40301-2-3230 (125-24-01-03), L. Malling</i>	171
References	173
Erratum	173
XVII. Bioscience	174
A. Soil Studies—Desert Microflora. XI. Desert Soil Algae Survival at Extremely Low Temperatures	
<i>Task No. 386-50301-1-3260 (189-55-04-01), R. E. Cameron and G. B. Blank</i>	174
References	180
XVIII. Fluid Physics	182
A. Rotational Temperature Measurements in the Low-Density Free Jet	
<i>Task No. 329-10501-1-3270 (129-01-10-01), H. Ashkenas</i>	182
B. The Neutral Point in a Plasma	
<i>Task No. 329-20701-1-3270 (129-02-03-03), A. Bratenahl</i>	185
C. Experimental Investigations of the Base-Flow Problem III. Pressure-Recovery Distribution	
<i>Task No. 329-10201-1-3270 (129-01-09-01), F. R. Hama</i>	186
D. The Inviscid Stability of the Laminar Compressible Boundary Layer for Three-Dimensional Disturbances. Part II	
<i>Task No. 329-10201-1-3270 (129-01-09-01), L. M. Mack</i>	194
References	196

Contents (Cont'd)

XIX. Physics		198
A. The Electrostatic Energy per Degree of Freedom of a Two-Temperature Plasma		
<i>Task No. 329-20901-1-3280 (129-02-07-02), E. H. Klefans and J. R. Primack</i>		198
B. Commutated Analog-to-Digital Converter		
<i>Task No. 385-60301-2-3280 (188-46-01-01), L. Lewyn</i>		201
References		204

TELECOMMUNICATIONS DIVISION

XX. Communications Elements Research		205
A. Microwave Electronics		
<i>Task No. 451-40500-1-3330 (150-22-14-05), W. H. Higo</i>		205
B. RF Techniques		
<i>Task Nos. 325-10901-1-3330 (125-21-03-04), W. V. T. Rusch and C. T. Stelzried; 451-30900-1-3330 (150-22-13-09), T. Otoshi; 350-10700-1-3330 (150-22-11-07), C. T. Stelzried and M. S. Reid</i>		206
References		218
XXI. Spacecraft Telemetry and Command		220
A. Low Capacity Dynamic Storage Devices		
<i>Task No. 384-60901-2-3340 (186-68-03-01), E. J. Bahm</i>		220
B. Magnetic Tape Recorder Sterilization		
<i>Task No. 384-85601-2-3340 (186-58-03-01), W. E. Arens</i>		236
C. A Note on the Probability Distribution of the Phase Error in a Second-Order Phase-Locked Loop		
<i>Task No. 350-70700-0-3340 (150-22-17-07), F. J. Charles</i>		246
D. Some Experimental Results on the Noise Probability Density Function Out of a Bandpass Limiter		
<i>Task No. 384-61301-2-3340 (186-68-04-04), J. C. Springett</i>		250
E. Analog-to-Digital Conversion With Integrated Circuits		
<i>Task No. 325-31601-2-3340 (125-23-02-15), J. R. Kinkel</i>		254
References		256
XXII. Spacecraft Radio		258
A. Spacecraft Power Amplifier Development Program		
<i>Task No. 384-63401-2-3360 (186-68-04-09), L. J. Derr</i>		258
B. Signal-to-Noise Ratio Monitoring: Calculation of an Important Probability Density Function		
<i>Task No. 384-63201-2-3360 (186-68-04-11), D. W. Boyd</i>		259
XXIII. Communications Systems Research: Modulation and Detection Theory		262
A. Error Bounds for M -ary Orthogonal Communication Using Stationary Stochastic Signals		
<i>Task No. 325-10601-1-3310 (125-21-02-03), A. J. Viterbi</i>		262

Contents (Cont'd)

B. A Comparison of Several Methods of Subcarrier Tracking	268
<i>Task No. 325-10601-1-3310 (125-21-02 03), J. Stiffler</i>	
References	274
XXIV. Communications Systems Research: Information Processing	276
A. Efficiency of the Floating Aperture System of Data Compression	
<i>Task No. 350-10900-1-3310 (150-22-11-09), E. C. Posner and H. C. Rumsey, Jr.</i>	276
B. The Variance of Spectral Estimates	
<i>Task No. 350-10900-2-3310 (150-22-11-09), E. Rodemich</i>	277
C. An Easily Encodable and Decodable Code of Constant Weight	
<i>Task No. 350-10900-1-3310 (150-22-11-09), H. Fredricksen and G. Solomon</i>	284
D. Simplified Decoding of the Maximal Length Shift Register Code	
<i>Task No. 350-10900-2-3310 (150-22-11-09), G. Solomon</i>	285
References	286
XXV. Communications Systems Research: Communication and Tracking	287
A. Optimum Modulation Indices for Single-Channel, One-Way and Two-Way Coherent Communication Links	
<i>Task No. 350-10800 2-3310 (150-22-11-08), W. C. Lindsey</i>	287
B. An Optimum Squaring Loop Prefilter	
<i>Task No. 350-10800-1-3310 (150-22-11-08), J. W. Layland</i>	290
C. On the Possibility of Receiving Radar Echoes From the Sun at S-Band	
<i>Task No. 350-10800-2-3310 (150-22-11-08), G. A. Morris</i>	293
References	294
XXVI. Communications Systems Research: Combinatorial Communication Research	295
A. Computation of Finite Fourier Series	
<i>Task No. 325-10701-1-3310 (125-21-01-01), L. R. Welch</i>	295
B. Two Identical Binary Erasure Channels with Feedback Are Exponentially Better Than One Channel at Low Rates	
<i>Task No. 325-10701-1-3310 (125-21-01-01), E. R. Berlekamp</i>	297
C. Coverings by Rook Domains	
<i>Task No. 325-10701-1-3310 (125-21-01-01), E. Rodemich</i>	299
References	306

SYSTEMS DIVISION

I. Systems Analysis

A. Statistical Analysis of Three Midcourse Corrections on an Earth-Venus-Mercury Trajectory

F. M. Sturms, Jr.

In Ref. 1, a trajectory analysis was presented for a 1970 mission to Mercury via a close encounter with Venus. The results showed that Earth-based radio guidance with three midcourse corrections were sufficient to obtain the required accuracy. The three corrections are performed at the following times:

- (1) Earth departure plus 6 days
- (2) Venus arrival minus 6 days
- (3) Venus arrival plus 8 days

For a typical trajectory near the middle of the launch period, the three midcourse corrections were found to have RMS velocity magnitudes of 9.7, 3.9, and 55 m/sec, respectively. This article gives the results of a subsequent study to obtain a more complete statistical description of the three midcourse correction magnitudes.

1. Guidance Analysis

A summary of the guidance analysis of Ref. 1 is useful for introducing the statistical analysis. The covariance matrix of injection errors, Λ_{r_0} , is mapped to a covariance matrix of Venus arrival errors (see Table 1 for nomenclature) by the equation

$$\Lambda_{m_0} = \left(\frac{\partial \mathbf{m}}{\partial \mathbf{x}_0} \right) \Lambda_{r_0} \left(\frac{\partial \mathbf{m}}{\partial \mathbf{x}_0} \right)^T \quad (1)$$

The covariance matrix of the first correction is then

$$\Lambda_{r_1} = \left(\frac{\partial \mathbf{m}}{\partial \mathbf{v}_1} \right)^{-1} \Lambda_{m_0} \left(\frac{\partial \mathbf{m}}{\partial \mathbf{v}_1} \right)^{-1T} \quad (2)$$

The mean squared maneuver, \bar{v}_1^2 , is given by the trace of Λ_{r_1} . The execution errors of the first correction are computed by Gates' model (Ref. 2).

$$\Lambda_{\delta r_1} = \sigma_\epsilon^2 \bar{v}_1^2 \mathbf{I} \quad (3)$$

where σ_ϵ^2 is the variance of the pointing and shutoff errors. The Venus arrival errors remaining after the first correction are described by

$$\Lambda_{m_1} = \left(\frac{\partial \mathbf{m}}{\partial \mathbf{v}_1} \right) \Lambda_{\delta r_1} \left(\frac{\partial \mathbf{m}}{\partial \mathbf{v}_1} \right)^T \quad (4)$$

Table 1. Nomenclature

Λ	= covariance matrix of subscripted vector
\mathbf{x}_0	= $[x_0, y_0, z_0, \dot{x}_0, \dot{y}_0, \dot{z}_0]^T$ = injection state matrix
$\begin{Bmatrix} x \\ z \\ y \end{Bmatrix}$	= Earth-equatorial, true-equinox-of-date, Cartesian coordinates
\mathbf{m}	= $[B \cdot T, B \cdot R, LTF]^T$ = target miss vector
$\begin{Bmatrix} B \cdot T \\ B \cdot R \end{Bmatrix}$	= B-plane miss vector components (Ref. 3)
LTF	= linearized time of flight (Ref. 4)
\mathbf{v}	= midcourse correction velocity vector
I	= identity matrix
σ^2	= variance of subscripted quantity
$E[]$	= expected value of quantity in brackets
μ	= mean value of subscripted quantity
RMS	= root-mean-square of midcourse velocity magnitude
ρ	= correlation coefficient between velocity magnitudes of subscripted maneuvers
R	= matrix of eigenvectors of Λ_{r_1}
\mathbf{e}	= vector of pointing and shutoff errors (Ref. 2)
$f(v_i)$	= probability density function of v_i
s	= parameter in half-normal distribution (Eq. 32)
a	= parameter in Rayleigh distribution (Eq. 37)

The second correction, which accounts mainly for the execution errors of the first midcourse correction, has a covariance matrix given by

$$\Lambda_{r_2} = \left(\frac{\partial \mathbf{m}}{\partial \mathbf{v}_2} \right)^{-1} \Lambda_{m_1} \left(\frac{\partial \mathbf{m}}{\partial \mathbf{v}_2} \right)^{-1T} \quad (5)$$

The Venus arrival errors remaining after the second correction are mainly due to orbit determination errors, and may be described by the covariance matrix, Λ_{m_2} . These errors are mapped into errors at Mercury by

$$\Lambda_{m_3} = \left(\frac{\partial \mathbf{m}}{\partial \mathbf{m}_2} \right) \Lambda_{m_2} \left(\frac{\partial \mathbf{m}}{\partial \mathbf{m}_2} \right)^T \quad (6)$$

Finally, the third midcourse correction is given by

$$\Lambda_{r_3} = \left(\frac{\partial \mathbf{m}}{\partial \mathbf{v}_3} \right)^{-1} \Lambda_{m_3} \left(\frac{\partial \mathbf{m}}{\partial \mathbf{v}_3} \right)^{-1T} \quad (7)$$

The values of the partials and covariance matrix elements in Eqs. (1-7) are given for the typical trajectory in Tables 2 and 3.

2. Total Midcourse Velocity Requirements

The propellant which must be available to perform the midcourse corrections is dependent on the sum of the three midcourse velocity magnitudes. An upper bound on this sum may be obtained as follows.

For any one maneuver, assume that the components, v_x, v_y, v_z are normally distributed with zero mean and variances $\sigma_{v_x}^2, \sigma_{v_y}^2, \sigma_{v_z}^2$, respectively.

$$E[v_x] = \mu_{v_x} = 0 \quad (8)$$

$$E[v_x^2] = \sigma_{v_x}^2 + \mu_{v_x}^2 = \sigma_{v_x}^2 \quad (9)$$

The magnitude of the maneuver, v , is obtained from

$$v^2 = v_x^2 + v_y^2 + v_z^2 \quad (10)$$

Then the expected value of the squared velocity is

$$\begin{aligned} E[v^2] &= E[v_x^2] + E[v_y^2] + E[v_z^2] \\ &= \sigma_v^2 + \mu_v^2 = \sigma_{v_x}^2 + \sigma_{v_y}^2 + \sigma_{v_z}^2 = (RMS)^2 \end{aligned} \quad (11)$$

A theorem in statistics states that in this case,

$$E[v] \leq (E[v^2])^{1/2} \quad (12)$$

Then an upper bound on the mean maneuver magnitude is given by

$$E[v] = \mu_r \leq (RMS) \quad (13)$$

Also, since μ_r must be positive, an upper bound on σ_r is

$$\sigma_r \leq (RMS) \quad (14)$$

Now, for a series of three maneuvers, the expected total midcourse velocity is, from Eq. (13),

$$\begin{aligned} E[v_T] = \mu_{r_T} &= E[v_1] + E[v_2] \\ &+ E[v_3] \leq \sum_{j=1}^3 (RMS_j) \end{aligned} \quad (15)$$

Table 2. Partial derivatives for guidance analysis

	x	y	z	\dot{x}	\dot{y}	\dot{z}	
$\frac{\partial m}{\partial x_0} =$	$\begin{bmatrix} -0.790484(4) \\ 0.593847(3) \\ 0.116364(4) \end{bmatrix}$	$\begin{bmatrix} 0.307434(5) \\ -0.911268(4) \\ -0.558706(4) \end{bmatrix}$	$\begin{bmatrix} -0.131856(4) \\ 0.858531(3) \\ -0.247363(3) \end{bmatrix}$	$\begin{bmatrix} -0.341510(8) \\ 0.102979(8) \\ 0.627480(7) \end{bmatrix}$	$\begin{bmatrix} 0.562454(7) \\ 0.944874(5) \\ -0.461030(6) \end{bmatrix}$	$\begin{bmatrix} -0.143995(8) \\ 0.412413(7) \\ 0.291401(7) \end{bmatrix}$	$\begin{matrix} B \cdot T \\ B \cdot R \text{ (at Venus)} \\ LTF \end{matrix}$
$\frac{\partial m}{\partial v_1} =$	$\begin{bmatrix} -0.131975(8) \\ 0.355661(7) \\ 0.168790(7) \end{bmatrix}$	$\begin{bmatrix} 0.999879(6) \\ 0.313642(7) \\ 0.720153(6) \end{bmatrix}$	$\begin{bmatrix} 0.460472(6) \\ -0.282918(7) \\ 0.486220(6) \end{bmatrix}$	$\begin{matrix} B \cdot T \\ B \cdot R \text{ (at Venus)} \\ LTF \end{matrix}$			
$\frac{\partial m}{\partial v_2} =$	$\begin{bmatrix} -0.459478(6) \\ 0.613933(5) \\ 0.291496(5) \end{bmatrix}$	$\begin{bmatrix} 0.215861(6) \\ 0.308387(6) \\ 0.455100(5) \end{bmatrix}$	$\begin{bmatrix} 0.935941(5) \\ -0.410149(6) \\ 0.379032(5) \end{bmatrix}$	$\begin{matrix} B \cdot T \\ B \cdot R \text{ (at Venus)} \\ LTF \end{matrix}$			
$\frac{\partial m}{\partial v_3} =$	$\begin{bmatrix} -0.485643(7) \\ 0.591734(7) \\ -0.694272(6) \end{bmatrix}$	$\begin{bmatrix} 0.165136(6) \\ -0.421227(7) \\ 0.551962(6) \end{bmatrix}$	$\begin{bmatrix} -0.205730(6) \\ -0.230519(7) \\ 0.133609(6) \end{bmatrix}$	$\begin{matrix} B \cdot T \\ B \cdot R \text{ (at Mercury)} \\ LTF \end{matrix}$			
$\frac{\partial m_1}{\partial m_2} =$	$\begin{matrix} B \cdot T \\ B \cdot R \\ LTF \end{matrix}$	$\begin{matrix} (at Venus) \\ B \cdot R \\ LTF \end{matrix}$	$\begin{matrix} LTF \\ B \cdot R \\ LTF \end{matrix}$	$\begin{bmatrix} 0.111975(4) \\ -0.212200(3) \\ 0.422010(1) \end{bmatrix}$	$\begin{bmatrix} -0.150872(4) \\ 0.233972(4) \\ -0.303432(3) \end{bmatrix}$	$\begin{bmatrix} -0.883427(1) \\ -0.271137(2) \\ 0.250395(1) \end{bmatrix}$	$\begin{matrix} B \cdot T \\ B \cdot R \text{ (at Mercury)} \\ LTF \end{matrix}$

The variance on the total maneuver magnitude is obtained by the following steps:

$$\begin{aligned}
 \sigma_{v_T}^2 &= E [(v_T - \mu_{v_T})^2] \\
 &= E [\{(v_1 - \mu_{v_1}) + (v_2 - \mu_{v_2}) + (v_3 - \mu_{v_3})\}^2] \\
 &= E [(v_1 - \mu_{v_1})^2] + E [(v_2 - \mu_{v_2})^2] + E [(v_3 - \mu_{v_3})^2] \\
 &\quad + 2E [(v_1 - \mu_{v_1})(v_2 - \mu_{v_2})] + 2E [(v_1 - \mu_{v_1})(v_3 - \mu_{v_3})] + 2E [(v_2 - \mu_{v_2})(v_3 - \mu_{v_3})] \\
 &= \sigma_{v_1}^2 + \sigma_{v_2}^2 + \sigma_{v_3}^2 + 2\rho_{12}\sigma_{v_1}\sigma_{v_2} + 2\rho_{13}\sigma_{v_1}\sigma_{v_3} + 2\rho_{23}\sigma_{v_2}\sigma_{v_3}
 \end{aligned} \tag{16}$$

From the nature of the corrective maneuvers as outlined in Ref. 1, it is clear that the third maneuver is independent, and hence uncorrelated from the first and second maneuvers.

$$\rho_{13} = \rho_{23} = 0 \tag{17}$$

An upper bound on σ_{v_T} may be obtained by taking ρ_{12} as unity. Eq. (16) becomes:

$$\sigma_{v_T}^2 \leq (\sigma_{v_1} + \sigma_{v_2})^2 + \sigma_{v_3}^2 \tag{18}$$

which, with Eq. (14), gives

$$\sigma_{v_T}^2 \leq [(RMS_1) + (RMS_2)]^2 + (RMS_3)^2 \tag{19}$$

From the RMS values given above and in Tables 2 and 3,

$$\mu_{v_T} \leq 68.6 \text{ m/sec}$$

$$\sigma_{v_T} \leq 56.7 \text{ m/sec}$$

A high probability of having sufficient fuel is obtained by providing for the expected (mean) total velocity plus 3 sigma above the mean:

$$\mu_{v_T} + 3\sigma_{v_T} = 239 \text{ m/sec}$$

Table 3. Covariance matrices for guidance analysis

$\Lambda_{r_0} =$	$\begin{bmatrix} x & y & z & \dot{x} & \dot{y} & \dot{z} \\ 0.417752(2) & 0.283133(2) & 0.198705(2) & 0.195943(-1) & 0.861678(-1) & 0.251724(-1) \\ 0.269811(2) & 0.179158(2) & 0.145717(-1) & 0.145717(-1) & 0.775134(-1) & 0.224823(-1) \\ (symmetrical) & 0.274477(2) & 0.108887(-1) & 0.603436(-1) & 0.218186(-1) & 0.218186(-1) \\ & & 0.100028(-4) & 0.440993(-4) & 0.131677(-4) & 0.131677(-4) \\ & & & 0.229311(-3) & 0.688711(-4) & 0.688711(-4) \\ & & & & 0.223251(-4) & 0.223251(-4) \end{bmatrix}$												
$\Lambda_{m_2} =$	<table border="0"> <tr> <td>$B \cdot T$</td> <td>$B \cdot R$</td> <td>LTF</td> <td>\dot{x}</td> <td>\dot{y}</td> <td>\dot{z}</td> </tr> <tr> <td>$\begin{bmatrix} 0.100000(5) \\ 0 \\ 0 \end{bmatrix}$</td> <td>$\begin{bmatrix} 0 \\ 0.100000(5) \\ 0 \end{bmatrix}$</td> <td>$\begin{bmatrix} 0 \\ 0 \\ 0.100000(3) \end{bmatrix}$</td> <td>$\begin{bmatrix} 0.45609291(-4) \\ 0.48503800(-5) \\ 0.36618972(-4) \end{bmatrix}$</td> <td>$\begin{bmatrix} 0.19461492(-4) \\ 0.96776720(-5) \\ 0.12339256(-4) \end{bmatrix}$</td> <td>$\begin{bmatrix} 0.19461492(-4) \\ 0.96776720(-5) \\ 0.12339256(-4) \end{bmatrix}$</td> </tr> </table>	$B \cdot T$	$B \cdot R$	LTF	\dot{x}	\dot{y}	\dot{z}	$\begin{bmatrix} 0.100000(5) \\ 0 \\ 0 \end{bmatrix}$	$\begin{bmatrix} 0 \\ 0.100000(5) \\ 0 \end{bmatrix}$	$\begin{bmatrix} 0 \\ 0 \\ 0.100000(3) \end{bmatrix}$	$\begin{bmatrix} 0.45609291(-4) \\ 0.48503800(-5) \\ 0.36618972(-4) \end{bmatrix}$	$\begin{bmatrix} 0.19461492(-4) \\ 0.96776720(-5) \\ 0.12339256(-4) \end{bmatrix}$	$\begin{bmatrix} 0.19461492(-4) \\ 0.96776720(-5) \\ 0.12339256(-4) \end{bmatrix}$
$B \cdot T$	$B \cdot R$	LTF	\dot{x}	\dot{y}	\dot{z}								
$\begin{bmatrix} 0.100000(5) \\ 0 \\ 0 \end{bmatrix}$	$\begin{bmatrix} 0 \\ 0.100000(5) \\ 0 \end{bmatrix}$	$\begin{bmatrix} 0 \\ 0 \\ 0.100000(3) \end{bmatrix}$	$\begin{bmatrix} 0.45609291(-4) \\ 0.48503800(-5) \\ 0.36618972(-4) \end{bmatrix}$	$\begin{bmatrix} 0.19461492(-4) \\ 0.96776720(-5) \\ 0.12339256(-4) \end{bmatrix}$	$\begin{bmatrix} 0.19461492(-4) \\ 0.96776720(-5) \\ 0.12339256(-4) \end{bmatrix}$								
$\Lambda_{r_2} =$	<table border="0"> <tr> <td>\dot{x}</td> <td>\dot{y}</td> <td>\dot{z}</td> <td>\ddot{x}</td> <td>\ddot{y}</td> <td>\ddot{z}</td> </tr> <tr> <td>$\begin{bmatrix} 0.11613969(-4) \\ 0.40401243(-5) \\ 0.24962705(-5) \end{bmatrix}$</td> <td>$\begin{bmatrix} 0.17684923(-5) \\ 0.87364400(-6) \\ 0.97640780(-6) \end{bmatrix}$</td> <td>$\begin{bmatrix} 0.12035990(-3) \\ 0.13323224(-2) \\ 0.16168720(-3) \end{bmatrix}$</td> <td>$\begin{bmatrix} 0.14753998(-2) \\ 0.12035990(-3) \\ 0.13323224(-2) \end{bmatrix}$</td> <td>$\begin{bmatrix} 0.31590910(-3) \\ -0.32688590(-3) \\ 0.16168720(-3) \end{bmatrix}$</td> <td>$\begin{bmatrix} 0.31590910(-3) \\ -0.32688590(-3) \\ 0.16168720(-3) \end{bmatrix}$</td> </tr> </table>	\dot{x}	\dot{y}	\dot{z}	\ddot{x}	\ddot{y}	\ddot{z}	$\begin{bmatrix} 0.11613969(-4) \\ 0.40401243(-5) \\ 0.24962705(-5) \end{bmatrix}$	$\begin{bmatrix} 0.17684923(-5) \\ 0.87364400(-6) \\ 0.97640780(-6) \end{bmatrix}$	$\begin{bmatrix} 0.12035990(-3) \\ 0.13323224(-2) \\ 0.16168720(-3) \end{bmatrix}$	$\begin{bmatrix} 0.14753998(-2) \\ 0.12035990(-3) \\ 0.13323224(-2) \end{bmatrix}$	$\begin{bmatrix} 0.31590910(-3) \\ -0.32688590(-3) \\ 0.16168720(-3) \end{bmatrix}$	$\begin{bmatrix} 0.31590910(-3) \\ -0.32688590(-3) \\ 0.16168720(-3) \end{bmatrix}$
\dot{x}	\dot{y}	\dot{z}	\ddot{x}	\ddot{y}	\ddot{z}								
$\begin{bmatrix} 0.11613969(-4) \\ 0.40401243(-5) \\ 0.24962705(-5) \end{bmatrix}$	$\begin{bmatrix} 0.17684923(-5) \\ 0.87364400(-6) \\ 0.97640780(-6) \end{bmatrix}$	$\begin{bmatrix} 0.12035990(-3) \\ 0.13323224(-2) \\ 0.16168720(-3) \end{bmatrix}$	$\begin{bmatrix} 0.14753998(-2) \\ 0.12035990(-3) \\ 0.13323224(-2) \end{bmatrix}$	$\begin{bmatrix} 0.31590910(-3) \\ -0.32688590(-3) \\ 0.16168720(-3) \end{bmatrix}$	$\begin{bmatrix} 0.31590910(-3) \\ -0.32688590(-3) \\ 0.16168720(-3) \end{bmatrix}$								

3. Monte Carlo Analysis

It is likely that the upper bound generated in the previous section is quite conservative. Considerable propellant weight reduction might be possible if a more realistic description of the total midcourse velocity statistics were available. This can be obtained numerically by computing a large number of cases, where the values of errors are generated randomly with the proper distribution. The collection of cases then represents the distribution of probable events.

The velocity components are normally distributed. A normal distribution can be obtained by sampling from a uniform distribution. In this analysis, a computer routine was used to generate values of random variable, x , where $0 \leq x \leq 1$. Random variables, y , with normal distribution having zero mean and variance σ_y^2 are then obtained (according to the central-limit theorem) by generating n values of x , from which

$$y = \left[\frac{1}{n} \sum_{j=1}^n x_j - \frac{1}{2} \right] (12n)^{1/2} \sigma_y \quad (20)$$

In this study, n was taken as 27.

The velocity components of the first midcourse correction are generated from Λ_{r_1} . In order to avoid the correlations between components, Λ_{r_1} is first diagonalized by the rotation matrix of eigenvectors, R .

$$\Lambda_{r_1}' = R^T \Lambda_{r_1} R \quad (21)$$

The variances from Λ_{r_1}' are used in Eq. (20) to generate a vector of velocity components, \mathbf{v}'_1 . Then

$$\mathbf{v}_1 = \begin{pmatrix} v_{x_1} \\ v_{y_1} \\ v_{z_1} \end{pmatrix} = R \mathbf{v}'_1 \quad (22)$$

$$v_1 = (\mathbf{v}_1 \cdot \mathbf{v}_1)^{1/2} \quad (23)$$

Next, Eq. (20) is used to generate a vector, \mathbf{e} , of shutoff and pointing error components, using $\sigma_e = 0.01$.

$$\delta \mathbf{v}_1 = v_1 \mathbf{e} \quad (24)$$

The second maneuver is then given by

$$\mathbf{v}_2 = \left(\frac{\partial \mathbf{m}}{\partial \mathbf{v}_2} \right)^{-1} \left(\frac{\partial \mathbf{m}}{\partial \mathbf{v}_1} \right) \delta \mathbf{v}_1 \quad (25)$$

$$v_2 = (\mathbf{v}_2 \cdot \mathbf{v}_2)^{1/2} \quad (26)$$

Finally, Eq. (20) is used to generate a vector of orbit determination errors, \mathbf{m} , using the covariances from Λ_{m_2} . Then

$$\mathbf{v}_3 = \left(\frac{\partial \mathbf{m}}{\partial \mathbf{v}_3} \right)^{-1} \left(\frac{\partial \mathbf{m}_1}{\partial \mathbf{m}_2} \right) \mathbf{m} \quad (27)$$

$$v_3 = (\mathbf{v}_3 \cdot \mathbf{v}_3)^{1/2} \quad (28)$$

$$v_T = v_1 + v_2 + v_3 \quad (29)$$

This process was used to generate 10,000 cases. The mean and variance of each midcourse velocity magnitude and the total velocity magnitude were accumulated after each case by the recursive formulae:

$$\mu_N = \frac{(N-1)\mu_{N-1} + v_N}{N} \quad (30)$$

$$\sigma_N^2 = \frac{(N-1)(\sigma_{N-1}^2 + \mu_{N-1}^2) + v_N^2}{N} - \mu_N^2 \quad (31)$$

where N refers to the N th case out of the sequence of 10,000.

Table 4 shows the mean, standard deviation, and RMS value of each velocity correction and also the total velocity, resulting after 50, 100, 500, 1000, 5000 and 10,000 cases. The RMS values are included as a check on the convergence of the distributions, since they must be the same as obtained from the trace of the covariance matrices. The proper RMS values are 9.7, 3.9 and 55 m/sec, respectively, for the three maneuvers. As shown in Table 4, these values are realized after about 5000 cases.

The density and distribution functions of each midcourse velocity were recorded by counting the number of cases falling in intervals 1 m/sec wide. Figs. 1 to 4 show plots of the density functions, and Figs. 5 to 8 show plots of the distribution functions obtained in this manner.

Also shown in Table 4 are the values of $\mu_{v_T} + 3\sigma_{v_T}$ and the number of cases resulting in total velocity magnitude greater than this value. The maximum value of v_T generated is also shown. The probability is 99.4% that the total velocity magnitude is less than the mean plus 3 sigma. The final tabulation in Table 4 is the value of ρ_{12} , computed from Eq. (16), assuming ρ_{13} and ρ_{23} to be zero. The values do not seem to have converged well after 10,000 cases, but ρ_{12} is probably about 0.5.

The value of 137 m/sec obtained for $\mu_{v_T} + 3\sigma_{v_T}$ indicated that the upper bound obtained previously, in Sect. 2 (239 m/sec), is conservative by about 75%.

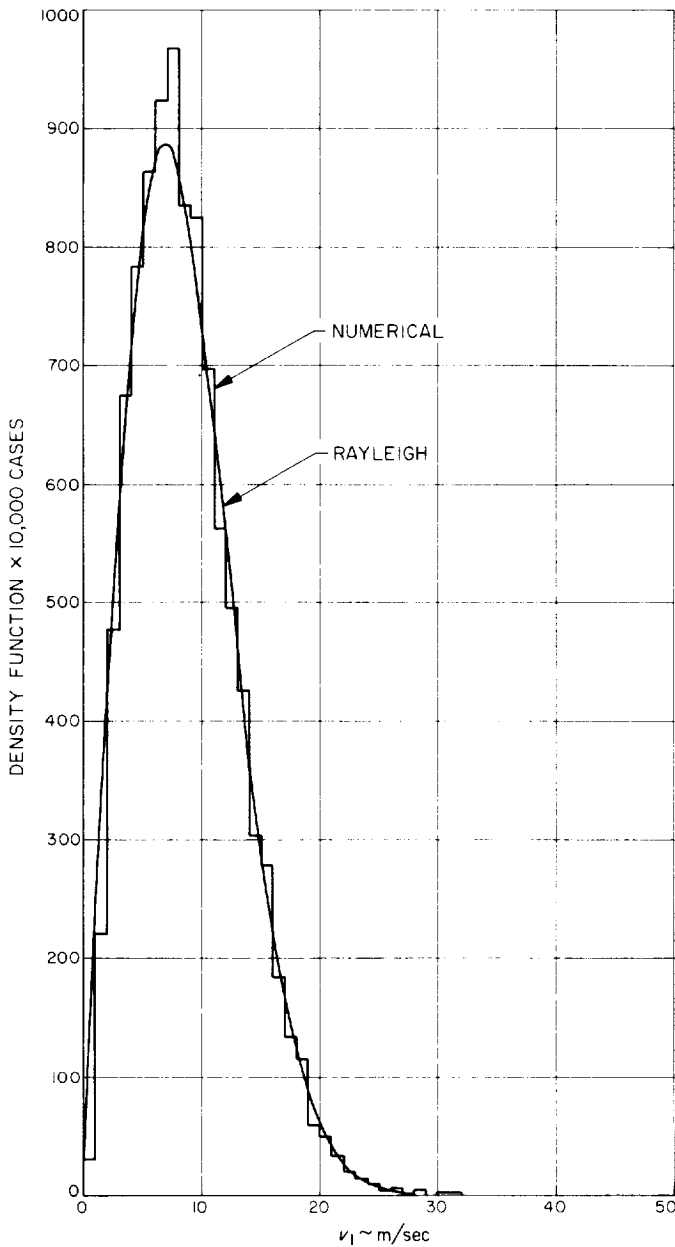


Fig. 1. Density function for first midcourse velocity magnitude

4. Analytical Distributions

It would be useful to have an analytical distribution which closely approximates the numerical results, in order to have a means for less conservative estimates of propellant requirement for missions of this type. Two analytical distributions were selected for comparison to the numerical results. Since all values of velocity magnitude are positive, the analytical distributions must reflect this characteristic. The first distribution examined is a

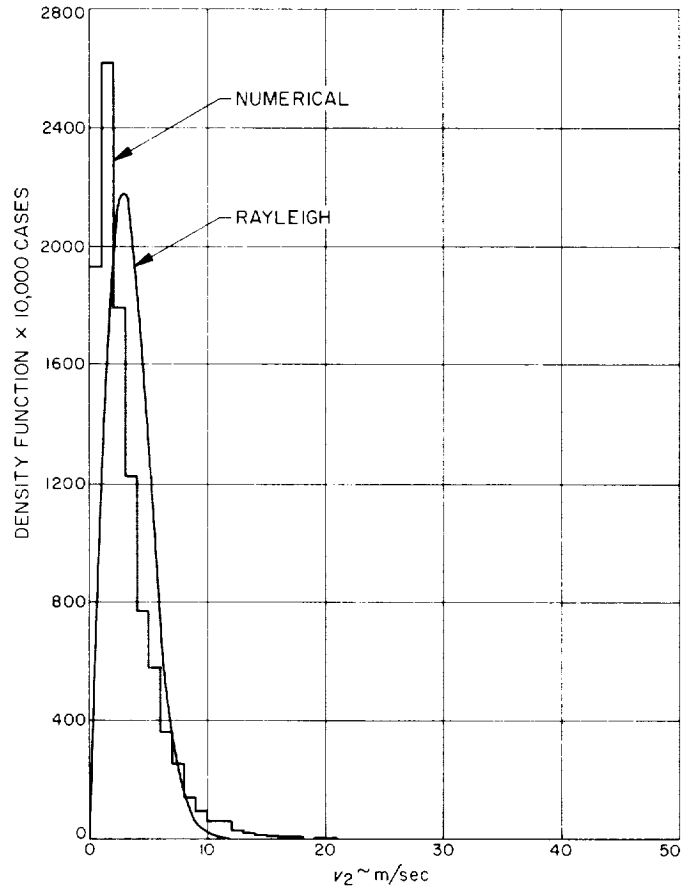


Fig. 2. Density function for second midcourse velocity magnitude

“half-normal” distribution, being the positive part of a normal distribution with zero mean. The density function is:

$$f(v_i) = \left(\frac{2}{\pi}\right)^{1/2} \frac{1}{s_i} e^{-\frac{1}{2} \left(\frac{v_i}{s_i}\right)^2} \quad \left. \begin{array}{l} 0 \leq v_i \leq \infty \\ = 0 \quad \quad \quad -\infty \leq v_i \leq 0 \end{array} \right\} \quad (32)$$

Then, for the half-normal distribution,

$$\mu_{v_i} = E[v_i] = \int_{-\infty}^{\infty} v_i f(v_i) dv = \left(\frac{2}{\pi}\right)^{1/2} s_i \quad (33)$$

$$E[v_i^2] = \int_{-\infty}^{\infty} v_i^2 f(v_i) dv = s_i^2 \quad (34)$$

From Eq. (34), s_i in the half-normal density function must be equal to the RMS value of the midcourse velocity

Table 4. Statistics from numerical results

Statistic, m/sec	Number of cases					
	50	100	500	1000	5000	10000
μ_{v_1}	8.66	8.93	8.77	8.43	8.66	8.67
σ_{v_1}	4.38	4.53	4.53	4.34	4.42	4.38
$(E[v_1^2])^{1/2}$	9.70	10.01	9.87	9.48	9.72	9.71
μ_{v_2}	2.82	2.95	2.88	2.73	2.94	2.95
σ_{v_2}	2.35	2.32	2.25	2.21	2.49	2.50
$(E[v_2^2])^{1/2}$	3.67	3.75	3.65	3.51	3.85	3.87
μ_{v_3}	52.60	51.17	49.18	49.88	48.70	48.67
σ_{v_3}	23.40	24.08	26.33	25.90	25.12	25.02
$(E[v_3^2])^{1/2}$	57.57	56.55	55.78	56.20	54.80	54.72
μ_{v_T}	64.08	63.05	60.83	61.04	60.30	60.29
σ_{v_T}	23.39	24.54	26.84	26.28	25.75	25.72
$(E[v_T^2])^{1/2}$	68.22	67.66	66.49	66.46	65.57	65.55
$\mu_{v_T} + 3\sigma_{v_T}$	134.25	136.67	141.35	139.88	137.55	137.45
Max v_T	117	142	153	153	178	178
No. $> \mu_{v_T} + 3\sigma_{v_T}$	0	1	3	6	34	58
ρ_{12} (Eq. 16)	-1.223	-0.168	+0.075	-0.203	+0.287	+0.460

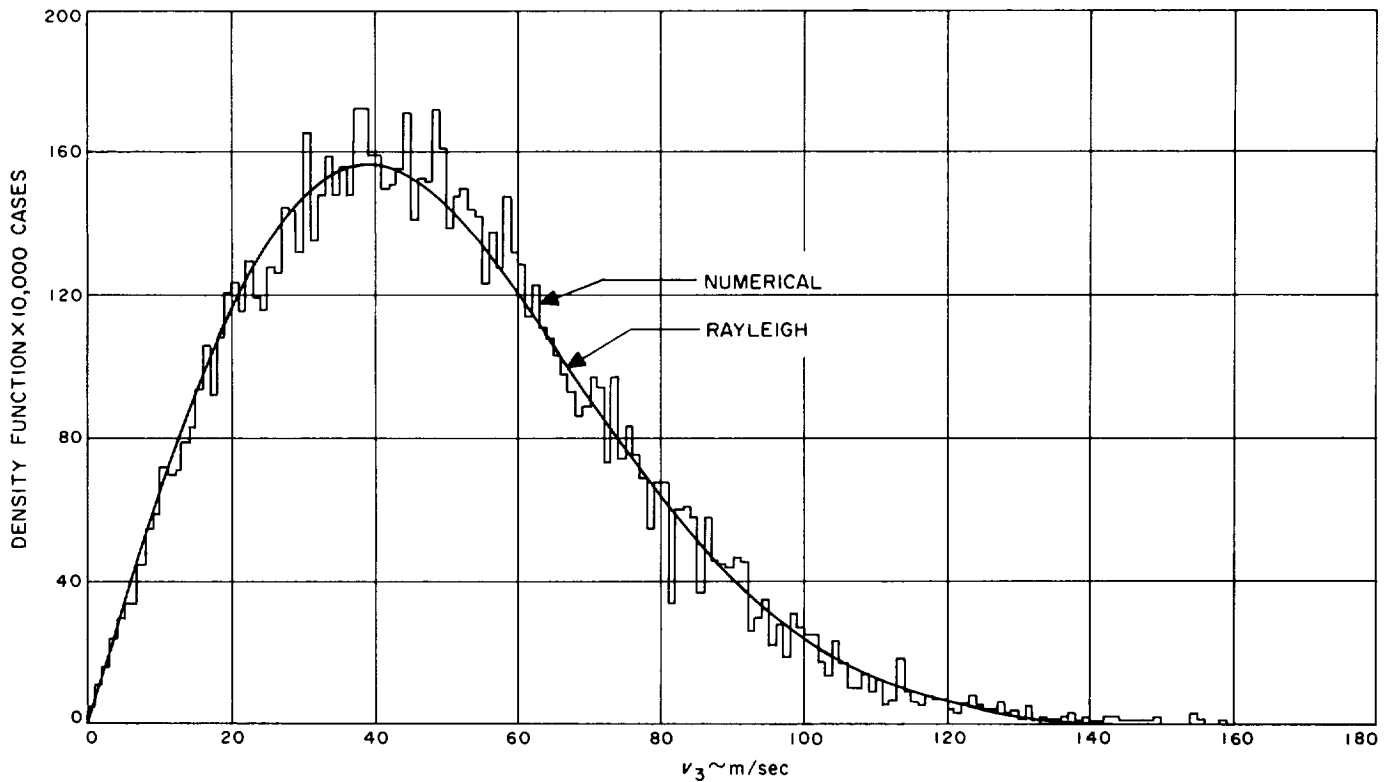


Fig. 3. Density function for third midcourse velocity magnitude

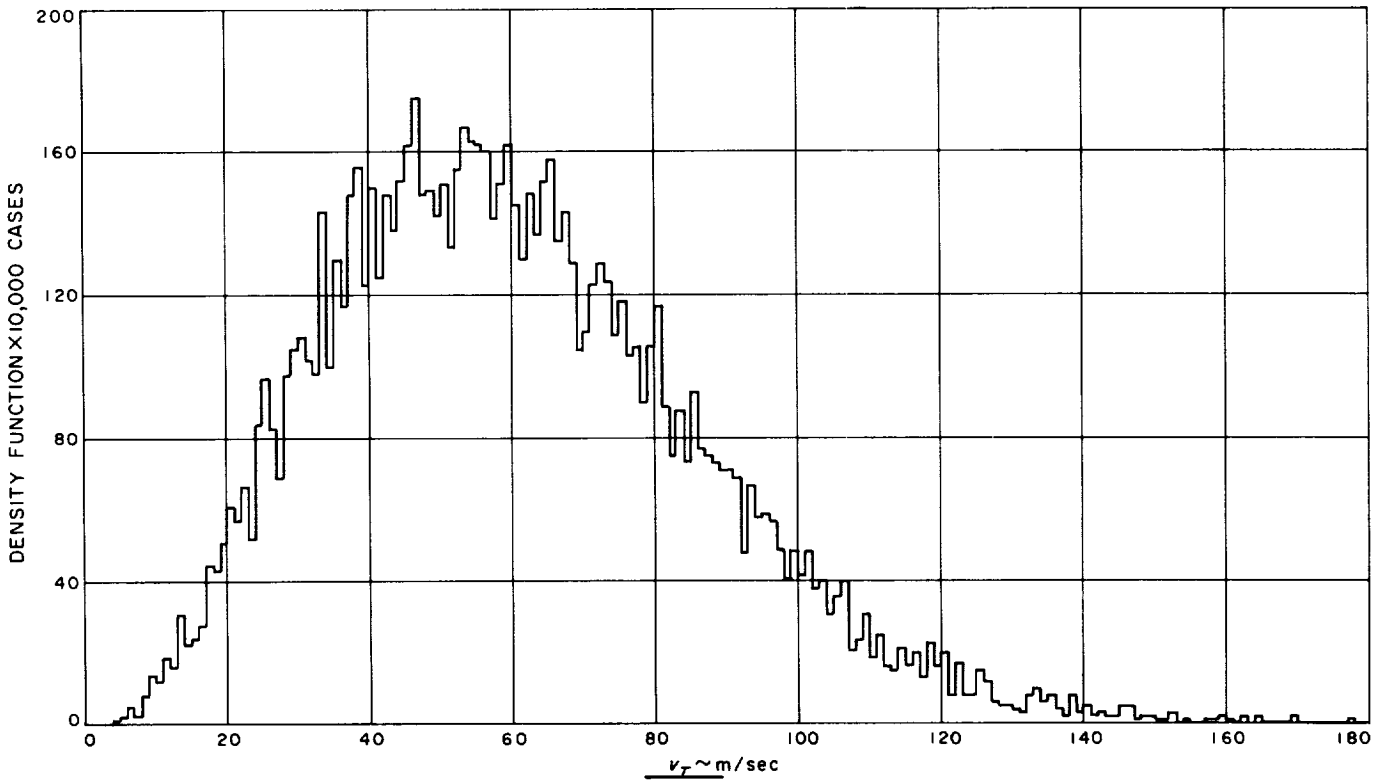


Fig. 4. Density function for total midcourse velocity magnitude

magnitude, which is obtained from the covariance matrices:

$$s_1 = RMS_1 = 9.7 \text{ m/sec}$$

$$s_2 = RMS_2 = 3.9 \text{ m/sec}$$

$$s_3 = RMS_3 = 55 \text{ m/sec}$$

For each maneuver:

$$\left. \begin{aligned} E[v_i^2] &= (RMS_i)^2 \\ \mu_{v_i} = E[v_i] &= \left(\frac{2}{\pi}\right)^{1/2} (RMS_i) \\ \sigma_{v_i}^2 &= \left(1 - \frac{2}{\pi}\right) (RMS_i)^2 \end{aligned} \right\} \quad (35)$$

For the total maneuver, Eqs. (15) and (16) give

$$\left. \begin{aligned} \mu_{v_T} &= \left(\frac{2}{\pi}\right)^{1/2} \sum_{i=1}^3 RMS_i \\ \sigma_{v_T}^2 &= \left(1 - \frac{2}{\pi}\right) \left[\sum_{i=1}^3 (RMS_i)^2 + 2\rho_{12}(RMS_1)(RMS_2) \right] \end{aligned} \right\} \quad (36)$$

Table 5 shows a comparison of the statistics for the three maneuvers as obtained from the numerical results and

Table 5. Comparison of analytical and numerical statistics

Statistic, m/sec	Numerical 10,000 cases	Half-normal		Rayleigh	
μ_{v_1}	8.7	7.7		8.6	
σ_{v_1}	4.4	5.8		4.5	
$(E[v_1^2])^{1/2}$	9.7	9.7		9.7	
μ_{v_2}	3.0	3.1		3.5	
σ_{v_2}	2.5	2.4		1.8	
$(E[v_2^2])^{1/2}$	3.9	3.9		3.9	
μ_{v_3}	48.7	43.9		48.7	
σ_{v_3}	25.0	33.2		25.5	
$(E[v_3^2])^{1/2}$	54.7	55.		55.	
	—	$\rho_{12}=0$	$\rho_{12}=1$	$\rho_{12}=0$	$\rho_{12}=1$
μ_{v_T}	60.3	54.7	54.7	60.8	60.8
σ_{v_T}	25.7	33.8	34.2	25.9	26.2
$(E[v_T^2])^{1/2}$	65.6	64.3	64.5	66.1	66.2
$\mu_{v_T} + 3\sigma_{v_T}$	137.5	156.1	157.3	138.5	139.4

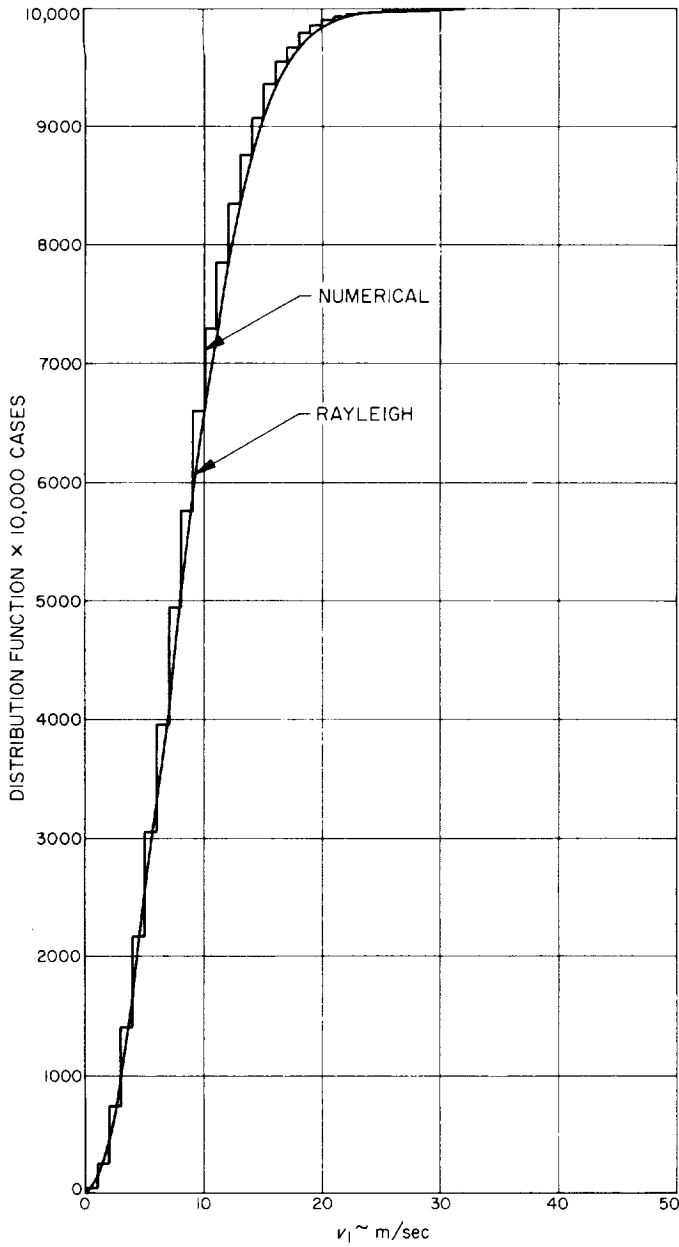


Fig. 5. Distribution function for first midcourse velocity magnitude

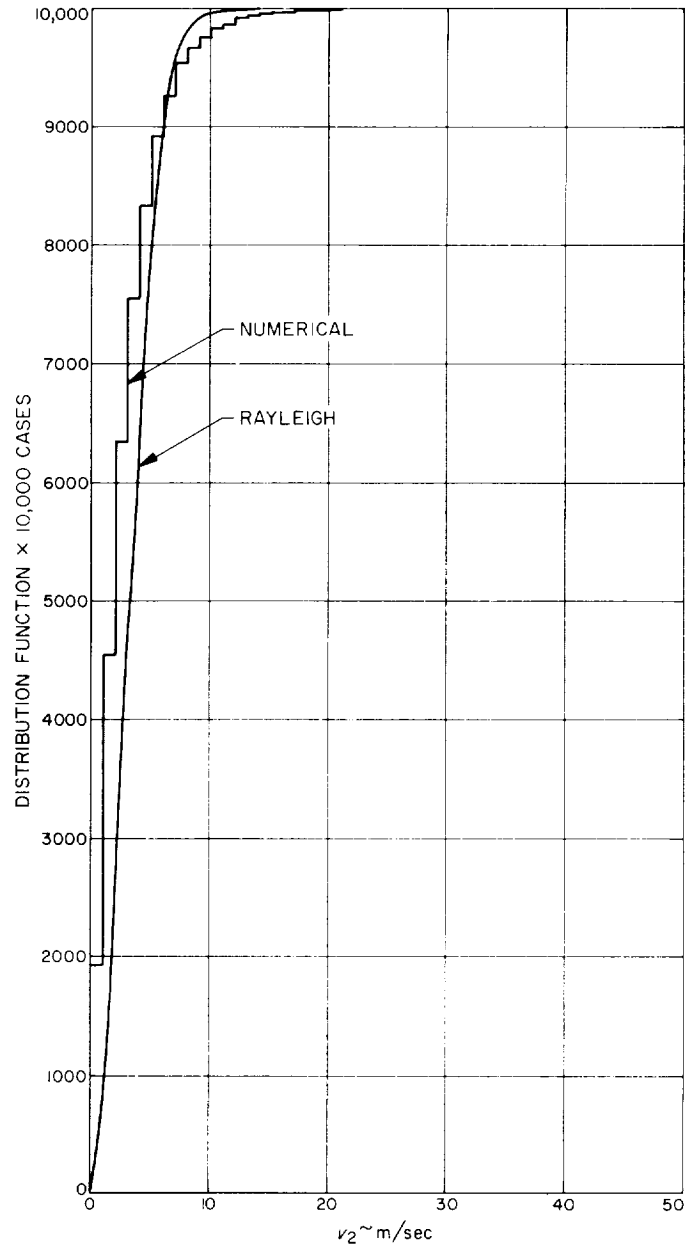


Fig. 6. Distribution function for second midcourse velocity magnitude

the analytical distributions. The value of $\mu_{v_T} + 3\sigma_{v_T}$ is conservative by about 14% for the half-normal distribution.

The second analytical distribution selected for comparison is a Rayleigh distribution. The density function is:

$$\left. \begin{aligned} f(v_i) &= \frac{v_i}{a_i^2} e^{-\frac{1}{2} \left(\frac{v_i}{a_i}\right)^2} & 0 \leq v_i \leq \infty \\ &= 0 & -\infty \leq v_i \leq 0 \end{aligned} \right\} (37)$$

Then in a manner similar to that above,

$$\mu_{v_i} = \left(\frac{\pi}{2}\right)^{1/2} a_i \tag{38}$$

$$E[v_i^2] = 2a_i^2 \tag{39}$$

$$a_i = \frac{RMS_i}{2^{1/2}} \tag{40}$$

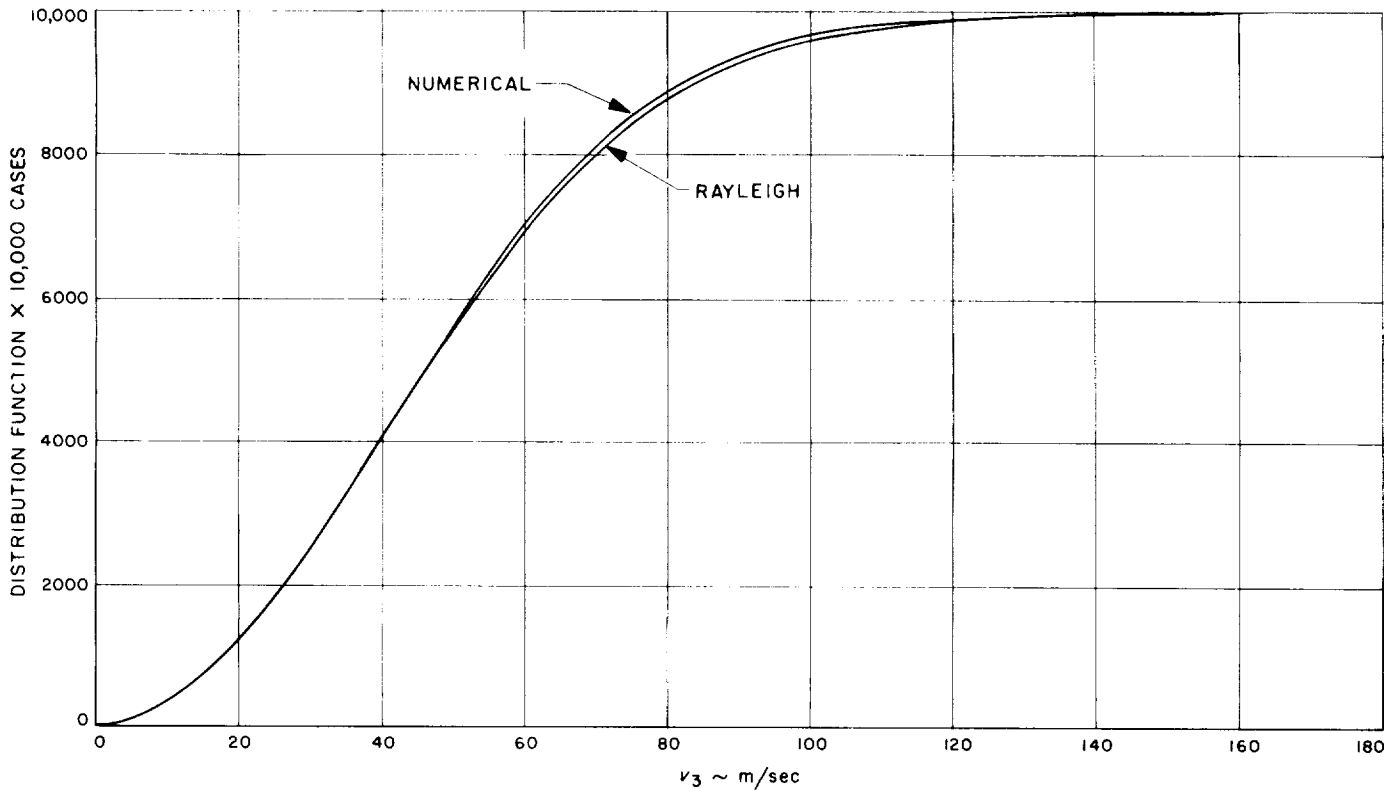


Fig. 7. Distribution function for third midcourse velocity magnitude

For each maneuver:

$$\left. \begin{aligned} E [v_i^2] &= (RMS_i)^2 \\ \mu_{v_i} &= \frac{\pi^{1/2}}{2} (RMS_i) \\ \sigma_{v_i}^2 &= \left(1 - \frac{\pi}{4}\right) (RMS_i)^2 \end{aligned} \right\} \quad (41)$$

For the total maneuver:

$$\left. \begin{aligned} \mu_{v_T} &= \frac{\pi^{1/2}}{2} \sum_{i=1}^3 (RMS_i) \\ \sigma_{v_T}^2 &= \left(1 - \frac{\pi}{4}\right) \left[\sum_{i=1}^3 (RMS_i)^2 + 2\rho_{12} (RMS_1) (RMS_2) \right] \end{aligned} \right\} \quad (42)$$

The value of $\mu_{v_T} + 3\sigma_{v_T}$ is conservative by about 1% for the Rayleigh distribution.

The Rayleigh distribution approximates the numerical results very accurately. The half-normal distribution gives a reasonable degree of safety in the estimation of the

upper bound for v_T . Out of 10,000 cases, only 12 exceed the value of 157 m/sec for $\mu_{v_T} + 3\sigma_{v_T}$ given by the half-normal distribution.

In order to compare the Rayleigh distribution to the numerical result over the whole range, Figs. 1 to 3 show the Rayleigh density function and Figs. 5 to 7 show the Rayleigh distribution function for the three midcourse maneuvers.

5. Summary

Given the RMS values of the three midcourse velocity magnitudes, an estimate of the maximum total velocity can be obtained by three methods: (1) an estimate of upper bounds on the mean and standard deviation; (2) approximation by a "half-normal" distribution; (3) approximation by a Rayleigh distribution. These methods give values of mean plus 3 sigma that are conservative by 75%, 14% and 1% respectively. The statistical standard for comparison is obtained numerically by random generation of 10,000 sample cases.

The results indicate that midcourse velocity requirements for multiple-planet missions of this type can be

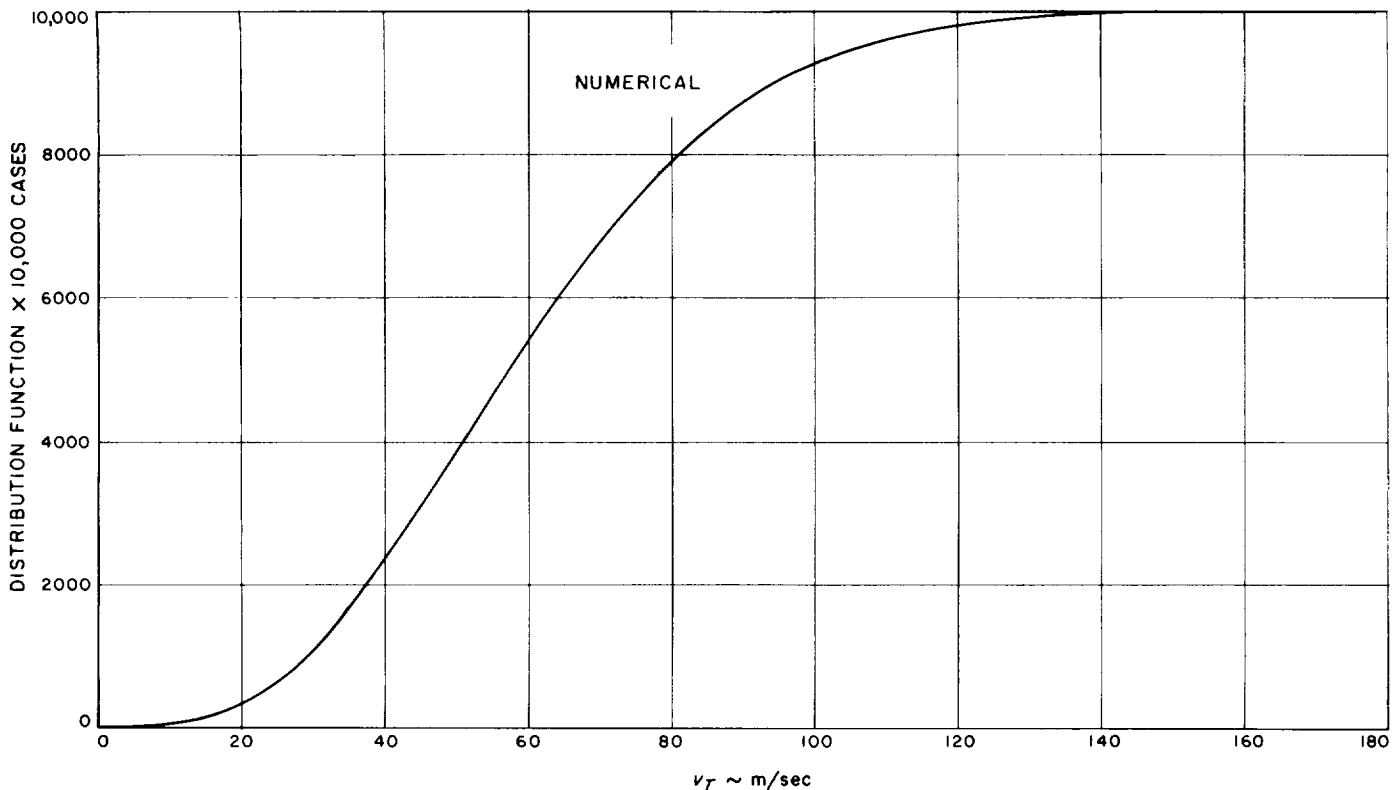


Fig. 8. Distribution function for total midcourse velocity magnitude

accurately evaluated analytically by assuming the individual maneuver magnitudes have a Rayleigh distribution with the same *RMS* value as obtained from the covariance matrices.

B. Duration of Ground-Station Satellite View Periods

R. D. Bourke

1. Introduction

This article deals with the duration of periods of possible communications between a ground station at an arbitrary location on a rotating planet and a satellite in an elliptic orbit whose line of apsides is fixed. It represents an extension of an earlier analysis (*SPS 37-34*, Vol. IV, pp. 3-9) which dealt with the long-term average fraction of time a satellite and ground station are co-visible.

The motivation for this effort stems from the *Voyager* Mars exploration project which has considered two

schemes for returning data from a capsule landed on the surface of the planet. The first is that of transmitting data from the capsule directly to a receiving station on Earth. The second involves transmitting the lander information to a Mars orbiting satellite, which then relays the information to the Earth. Analysis and design of the relay scheme requires knowledge of the expected duration of view periods so that the available time can be apportioned between lock-up and transmission.

2. Calculation of $\bar{\tau}$

The derivation of the expression for the average view period duration, $\bar{\tau}$, depends on the concept of the satellite surface developed in *SPS 37-34*, Vol. IV, pp. 3-9. As discussed in that article, the satellite surface is, in general, a toroidal body of revolution on which the satellite always lies. If now, one considers a lander viewing cone whose vertex is at the planet surface and whose axis is along the local vertical, then there is a region of the satellite surface which falls within the viewing cone, and the satellite can be seen in this area. This region is henceforth referred to as the satellite surface-viewing cone intersection. There are in general two intersections, one for the inner and one for the outer surfaces, but they may be

joined as those in Fig. 9. Fig. 10 shows a typical inner surface intersection.

If the lander is at latitude β and longitude zero, then the boundary of the intersection is related in longitude l and latitude ϕ by:

$$l(\phi) = \pm \cos^{-1} \left[\frac{\cos \alpha(\phi) - \sin \beta \sin \phi}{\cos \beta \cos \phi} \right] \quad (1)$$

where

$$\left. \begin{aligned} \cos \alpha &= \left(1 - \frac{r_{L0}^2}{r^2} \cos^2 \gamma \right)^{1/2} \\ r_{L0} &= (r^2 - r_p^2 \cos^2 \gamma)^{1/2} - r_p \sin \gamma \\ r &= \frac{a(1 - e^2)}{1 + e \cos f} \\ \sin \phi &= \sin i \sin(f + \omega) \end{aligned} \right\} \quad (2)$$

and r_p is the planet radius, a , e , i , and ω are the orbital elements, and γ is the minimum elevation angle.

Shown on the intersection of Fig. 10 is a typical satellite trace across the surface, one of a family of such trajectories. The latitude and longitude (ϕ , l) of the sub-satellite point are given by:

$$\sin \phi = \sin i \sin(f + \omega) \quad (3)$$

$$\tan(l - \Omega + \omega_p t) = \cos i \tan(f + \omega) \quad (4)$$

where ω_p is the rotation rate of the planet. Note that the term $\omega_p t$ effectively causes a recession of the node at a constant rate. The time t and true anomaly f are related through Kepler's equation. If all other parameters are constant, the trace across the intersection can be characterized by the longitude of its ascending node Ω . Other values of Ω give rise to similar parallel traces.

Associated with a typical trace are two times, t_{out} and t_{in} , corresponding to exit from an entry to the intersection respectively. Thus, for a given value of Ω , there is a view period duration of $\tau(\Omega) = t_{out} - t_{in}$. Note that this is only the first of an infinite number of view periods corresponding to this value of Ω , but attention for the moment will be directed only to this one.

Fig. 10 also shows the two traces which are tangent to the intersection boundary; these correspond to the limiting values of Ω . That is, the satellite may be viewed at some point of the inner surface if Ω is in the interval $\Omega_1 < \Omega < \Omega_2$.

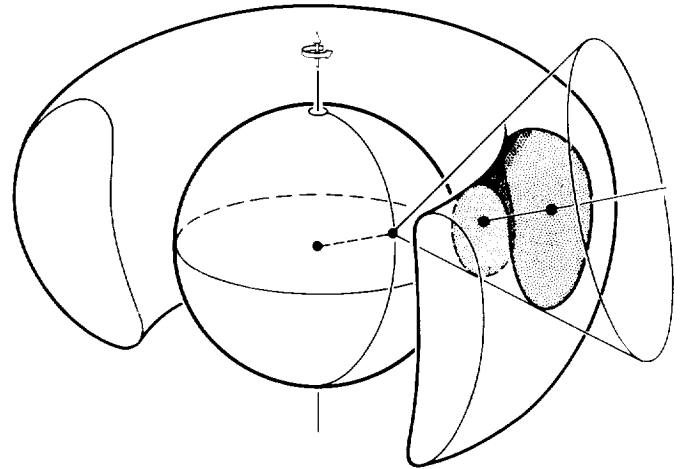


Fig. 9. Satellite surface-viewing cone intersection, inner and outer surfaces joined

For each value of Ω within this interval, there is a value of the view period duration τ ,

$$\tau(\Omega) = t_{out}(\Omega) - t_{in}(\Omega) \quad (5)$$

and $\tau = 0$ outside this interval. If the planet and satellite periods are not harmonically related (see SPS 37-34, Vol. IV, p. 9), then over a long time all values of Ω are equally likely. The mean value of τ and its variance can then be found by integration:

$$\bar{\tau} = \frac{1}{\Omega_2 - \Omega_1} \int_{\Omega_1}^{\Omega_2} \tau(\Omega) d\Omega \quad (6)$$

$$\sigma_{\tau}^2 = \frac{1}{\Omega_2 - \Omega_1} \int_{\Omega_1}^{\Omega_2} (\tau - \bar{\tau})^2 d\Omega \quad (7)$$

Similar integrals apply to the outer surface intersection.

When the intersections are joined, as are those in Fig. 9, the satellite can pass continuously from the inner to the outer while in sight of the ground station. In this case, the view periods for the two surfaces are not truly distinct and must be combined. The limits in Eqs. (6) and (7) then represent the overall extremes in Ω for both surfaces.

The perturbations of the orbital elements affect this analysis to some degree. To an observer on the planet, the effect of the regression of the nodes appears simply as a change in the planet's rotation rate. Since the derivation of the viewing fractions assumes that the satellite's longitude has been equally distributed by the rotation of the planet, the secular perturbation of the longitude of the ascending node is of no consequence in this analysis.

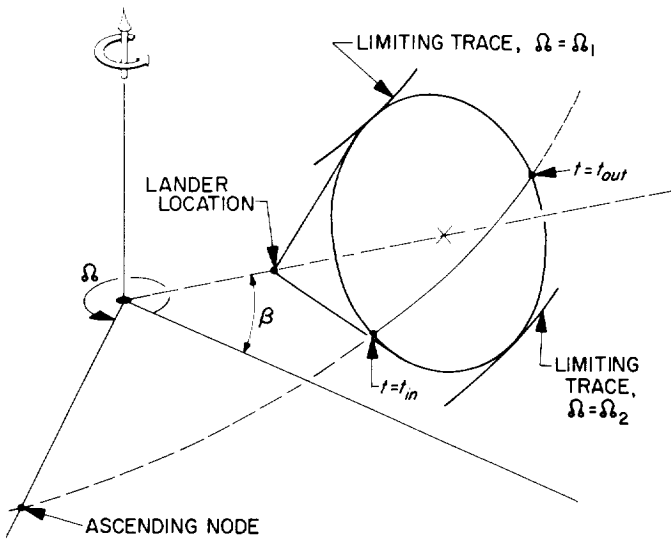


Fig. 10. Details of satellite surface-viewing cone intersection

The precession of the line of apsides is a result of the secular perturbation of the argument of periapsis, and the change of the satellite surface due to this rotation is pronounced. For long-duration missions, at inclinations for which the rate of apsidal precession is significant, the average view periods change considerably.

3. Application

The method outlined herein has been used to calculate the average view time and its standard deviation for *Telstar II*. The initial elements were:

- $a = 12,266 \text{ km}$
- $e = 0.401$
- $i = 42.74 \text{ deg}$
- $\omega = 171.8 \text{ deg}$

and the line of apsides rotated approximately 1.22 deg/day. The average view time for a station at Andover, Maine (latitude 44.6°N), is plotted as a function of time in Fig. 11 for the actual, observed, orbital elements^a (Ref. 5). Also shown are $\bar{\tau} + \sigma$ (the uppermost curve) and $\bar{\tau} - \sigma$ (the lowermost curve). The effect of the sizable precession rate is quite noticeable. In December 1963 and October 1964 perigee was at maximum latitude, i.e., directly over the station; and because of the higher linear velocity of the satellite, the view times are shortened.

Acknowledgments. The computer programing and numerical computation used to support this analysis were

^aThe intersections in this example are always joined, thus only one value of $\bar{\tau}$ is shown.

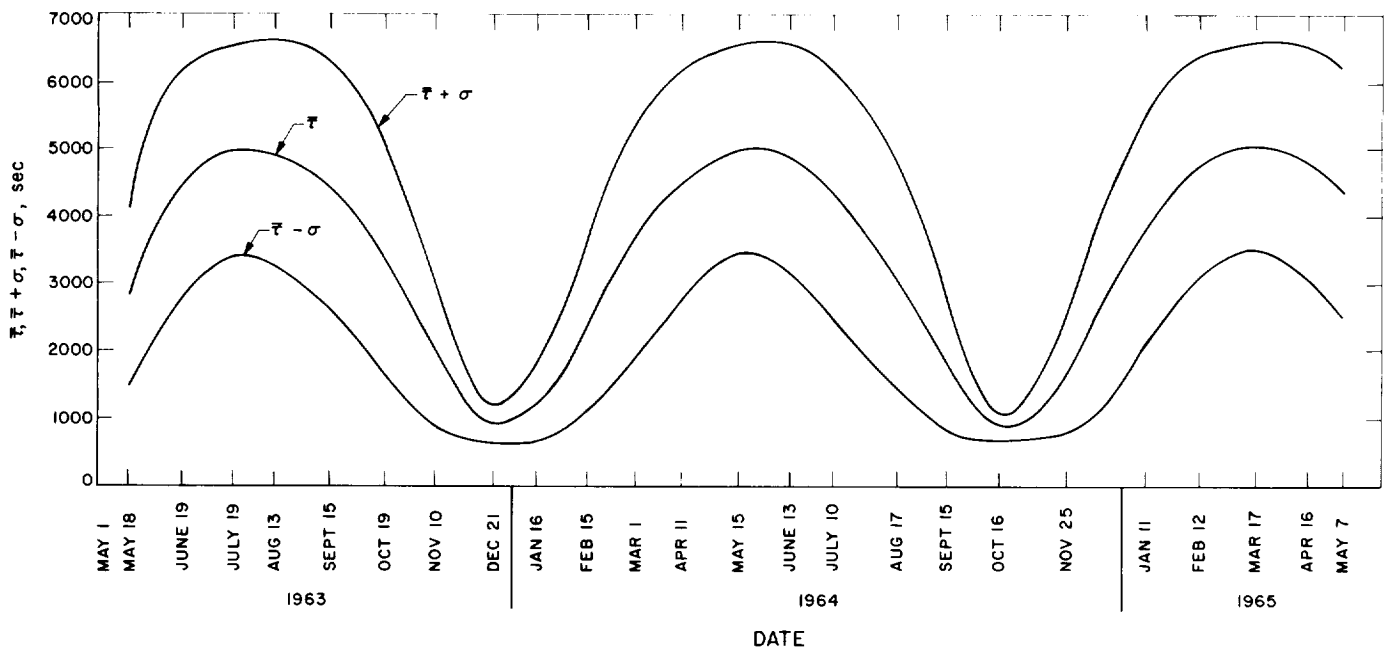


Fig. 11. Average view periods for *Telstar II*

done by Mrs. Susann Chesne of the Systems Analysis Section. The author wishes to acknowledge her significant contribution to this work.

C. Periodic Comet Orbit Determination Capabilities for Spacecraft Intercept Missions from 1970 to 1973

G. E. Pease

1. Comets and Their Orbits

For the period of interest from 1970 to 1973, four short-period comets have been noted by previous studies (Refs.

6, 7, 8) as being worthy of consideration for a spacecraft intercept mission. These objects and their approximate orbits (Refs. 9, 10) are listed in Table 6. The extrapolated orbits, which are presented in the lower half of the table, were obtained by Cowell integration of the starting orbits with the JPL Orbit Determination Program (Ref. 11) for the IBM 7094 computer.

Approximate times of launch, encounter, and flight were derived for minimum-energy Type I spacecraft transfer trajectories in an STL study (Ref. 8). Comet acquisition times given in Table 6 may be uncertain by ± 1 month or more, depending upon the telescope used, the zenith distance of the comet, the phase angle with respect to the Sun, the weather, the seeing conditions, and the phase of the Moon.

Table 6. Selected comets and orbit data

Elements	Comet Giacobini-Zinner	Comet Kopff	Comet Pons-Winnecke	Comet Tuttle-Giacobini-Kresak
Starting orbit, mean 1950 heliocentric ecliptic elements				
Epoch, date	59/10/19	64/05/05	64/03/26	62/04/26
<i>T</i> (UT)	Oct. 26. 9182, 1959	May 16.0900, 1964	March 23.2561, 1964	April 23.8771, 1962
<i>P</i> (yr)	6.42	6.31	6.30	5.48
<i>a</i> (AU)	3.452856	3.415018	3.409810	3.109118
<i>e</i>	0.728934	0.555014	0.639244	0.638959
<i>i</i>	30°9041	4°7075	22°3264	13°7608
Ω	196°0299	120°8694	92°8783	165°5742
<i>w</i>	172°8433	161°9253	172°0173	38°0051
True-of-date extrapolated heliocentric ecliptic elements, epoch of encounter, with proposed spacecraft launch and encounter dates				
<i>T</i> (UT)	Aug. 03.6320, 1972	Oct. 04.6406, 1970	July 19.0443, 1970	May 28.0066, 1973
<i>a</i> (AU)	3.48785	3.455315	3.426395	3.137830
<i>e</i>	0.715209	0.546537	0.635920	0.632887
<i>i</i>	31°7134	4°7223	22°3233	13°5910
Ω	195°4476	120°6655	93°0658	165°4788
<i>w</i>	171°9161	162°7225	172°2439	38°7871
Acquisition date	72/03/06	70/01/04	69/12/15	73/01/06
Magnitude	20.0	20.9	20.4	20.7
Launch date	72/04/01	70/02/03	70/01/30	72/12/10
Encounter	72/08/29	70/09/21	70/07/19	73/03/30
Flight time, days	150	230	170	110

2. Characteristics of Cometary Orbit Determination

Previous comet orbit studies (Refs. 6, 7, 8, 12, 13) have indicated the following problems:

a. Time uncertainties. Perihelion times are very difficult, if not impossible, to accurately predict one revolution in advance using observations from one comet apparition only. This is because the mean daily motion cannot be determined accurately during one apparition by optical observations near perihelion, usually the only part of the orbit at which these faint objects may be observed. Typically, the predicted perihelion times for the next apparitions may be uncertain by several days, or as much as a month. These errors may be reduced substantially by linking observations from as many previous apparitions as possible.

b. Position uncertainties. With no a-priori orbit information from previous comet apparitions, the $1-\sigma$ position uncertainties of the comet may remain many thousands of kilometers, even after 8 months or so of optical tracking (in the form of photographic plates). Thus spacecraft position uncertainties pale into insignificance in comparison.

Because of the above considerations, comet intercept investigators have usually recommended a mission program of using all available observations, obtained during previous apparitions, combined with a continuous schedule of observing and rapidly reducing the photographic plates from acquisition, or as soon as possible before spacecraft launch, to intercept, in an effort to minimize target errors throughout the flight.

In this study, the following statistical information has been obtained for the comets of interest:

c. A-priori information. The magnitude and orientation in space of the comet position and velocity uncertainties at a time near spacecraft encounter have been mapped out from simulated observations at the previous apparitions. This will henceforth be referred to as the a-priori statistical information.

d. Tracking information. The same statistical information has been computed as a function of optical tracking data to intercept. This reveals the state of knowledge of cometary position and velocity uncertainties throughout the flight, and it also indicates the optimum times for spacecraft maneuvers.

3. Limitations of the Analysis

a. A-priori information from more than one previous apparition. In this study, comet orbits were only integrated through one revolution, with the exceptions of Comets Giacobini-Zinner and Tuttle-Giacobini-Kresak. For these two, the orbits were integrated through two revolutions because of the poor Earth-comet-Sun geometry in 1965 for Giacobini-Zinner and in 1967 for Tuttle-Giacobini-Kresak. Consequently, only four observations were obtained at these times for Giacobini-Zinner, and none for Tuttle-Giacobini-Kresak. It is believed that the inclusion of another apparition in the a-priori statistics substantially reduces the derived uncertainties.

b. Correlated observations or systematic errors. Only random errors with a Gaussian distribution are analyzed in this study. In general, observations are separated by many days, which would tend to eliminate correlations depending on time in real observations. In reality, instrumental effects may be expected to be present, both in the telescope and plate-measuring device. For example, great care must be taken to ensure that the center of mass, or nucleus, of the comet is measured rather than the center of light. This means that observations must be made with a telescope of long focal length to ensure the necessary photographic resolution. Systematic errors in position are known to exist in at least two forms: (1) zone errors in right ascension and declination of $\Delta\alpha_s$, $\Delta\alpha_s$, $\Delta\delta_s$, $\Delta\delta_s$ types, and (2) positional errors depending upon apparent brightness of both comet and reference stars used in the plate reductions. Both of the above types of errors are dependent upon the star catalogue used for obtaining reference star positions. They are at a minimum in modern catalogues, such as the Yale Zone or AGK3, but they may be substantial in the *Astrographic Catalogue*, which unfortunately must be used for the faint reference stars usually encountered in this type of work. In such a catalogue, errors from unknown proper motions propagating over a long period of time are perhaps the greatest problem. They have a systematic effect because of the component of galactic motion and because some of the same reference stars may be used for more than one observation.

4. Input Data

Simulated tracking data only has been used in the present analysis. This hour-angle-declination (HaDec) type data is manufactured with a $1-\sigma$ white noise of $0^{\circ}00055$, or approximately 2 arc sec. In all cases, the Goldstone *Pioneer* Station (DSIF 11) has been used as the simulated observatory, while the number and dates of observations used for the a-priori statistics roughly

Table 7. Simulated comet data

Comet	A-priori data, date	Number of a-priori observations	Mission data, date	Number of mission observations	Total number observations
Giacobini-Zinner	59/05/08-60/04/14	37	72/03/06-72/08/21	22	63
	65/09/17-65/09/23	4			
Kopff	63/12/18-65/01/28	30	70/01/04-70/09/07	33	63
Pons-Winnecke	64/02/19-64/09/27	14	69/12/15-70/07/11	27	41
Tuttle-Giacobini-Kresak	62/01/28-62/07/29	14	73/01/06-73/03/25	12	26

simulate those of Elizabeth Roemer (Ref. 14), obtained with the 40-in. reflector at the Flagstaff station of the U.S. Naval Observatory. Dr. Roemer has been nearly the sole observer of these faint periodic comets. Observations have been simulated at the rate of one every 8 days after predicted acquisition in the extrapolated orbits, except for Tuttle-Giacobini-Kresak (one every 7 days, see Table 7). An attempt has been made to use pointing times that are (1) after sunset and before sunrise at Goldstone and (2) such that the comet is above the Goldstone horizon for all observations; 1- σ data weighting has been used throughout. Although refraction has been turned off in the orbit determination program, it nevertheless makes an additional weighting correction depending upon the zenith distance.

In addition to the statistics resulting from the simulated data fitting process, uncertainties in the mass of Jupiter, the astronomical unit, and the station location were considered. The 1- σ uncertainties on these quantities were, respectively, considered to be 0.6×10^{-7} solar masses, 500 km, and 30 meters (in geocentric radius and longitude). Non-gravitational secular accelerations are thought to exist in the case of many comets. Such forces have not been considered in these runs. They are thought to be small, and a test case for comet Giacobini-Zinner for which a large solar pressure force was solved demonstrated that the solution does not corrupt the state vector statistics.

5. Mapping A-Priori Statistics

After simulating the a-priori data from the starting elements listed at the top of Table 6, this data is then used to solve for a new state vector,

$$Q = [x, y, z, \dot{x}, \dot{y}, \dot{z}]$$

the geocentric position and velocity, in equatorial rectangular coordinates, of the comet at some epoch t_0 . The covariance matrix of Q , formed from the weighted least-squares fit and from the covariance matrix of considered

parameters, is then mapped to a future epoch at the next apparition. Since it is unusual to map statistics over such long intervals, it was decided to check the matrix of the state vector partial derivatives for each of the two steps necessary to map statistics for Pons-Winnecke from 1964 to 1969. This was done by perturbing the starting conditions, one at a time, by a small amount (1,000 to 100,000 km and 1 m/sec), mapping from t_0 to a future epoch t , and comparing the resulting $\Delta Q(t)/\Delta Q(t_0)$ with the mapping partials $\partial Q(t)/\partial Q(t_0)$. Typically, the partials maintain linearity to one part in 10^3 at worst and one part in 10^5 at best, and check to the same degree of accuracy, which is sufficient for mapping gross statistics.

6. The Extrapolated Orbit

If one now chooses a new epoch slightly before optical acquisition of the comet during the mission phase of the trajectory, one has merely to again simulate optical angle data from acquisition to shortly before encounter. This data may be fitted with or without the mapped, or a-priori, covariance matrix on the updated state vector. The resulting covariance matrix may then be mapped to encounter, at which time we would like to know the position and velocity errors of the comet. In this study, data at intervals successively differing by approximately 1 month was fitted and mapped to encounter for each of the four objects, with the exception of Tuttle-Giacobini-Kresak, which cannot be acquired until nearly a month after launch, and can only be tracked for about 3 months for a Type I trajectory. By varying the data interval from comet acquisition, it is possible to arrive at a plot of uncertainties in position and velocity, as a function of tracking data (see Figs. 17-24).

7. The Comet-Centered Dispersion Ellipsoid

The comet-centered dispersion ellipsoid of 1- σ position and velocity uncertainties is of statistical interest. The position uncertainty ellipsoid, in particular, may be readily projected into a miss ellipse for any given spacecraft

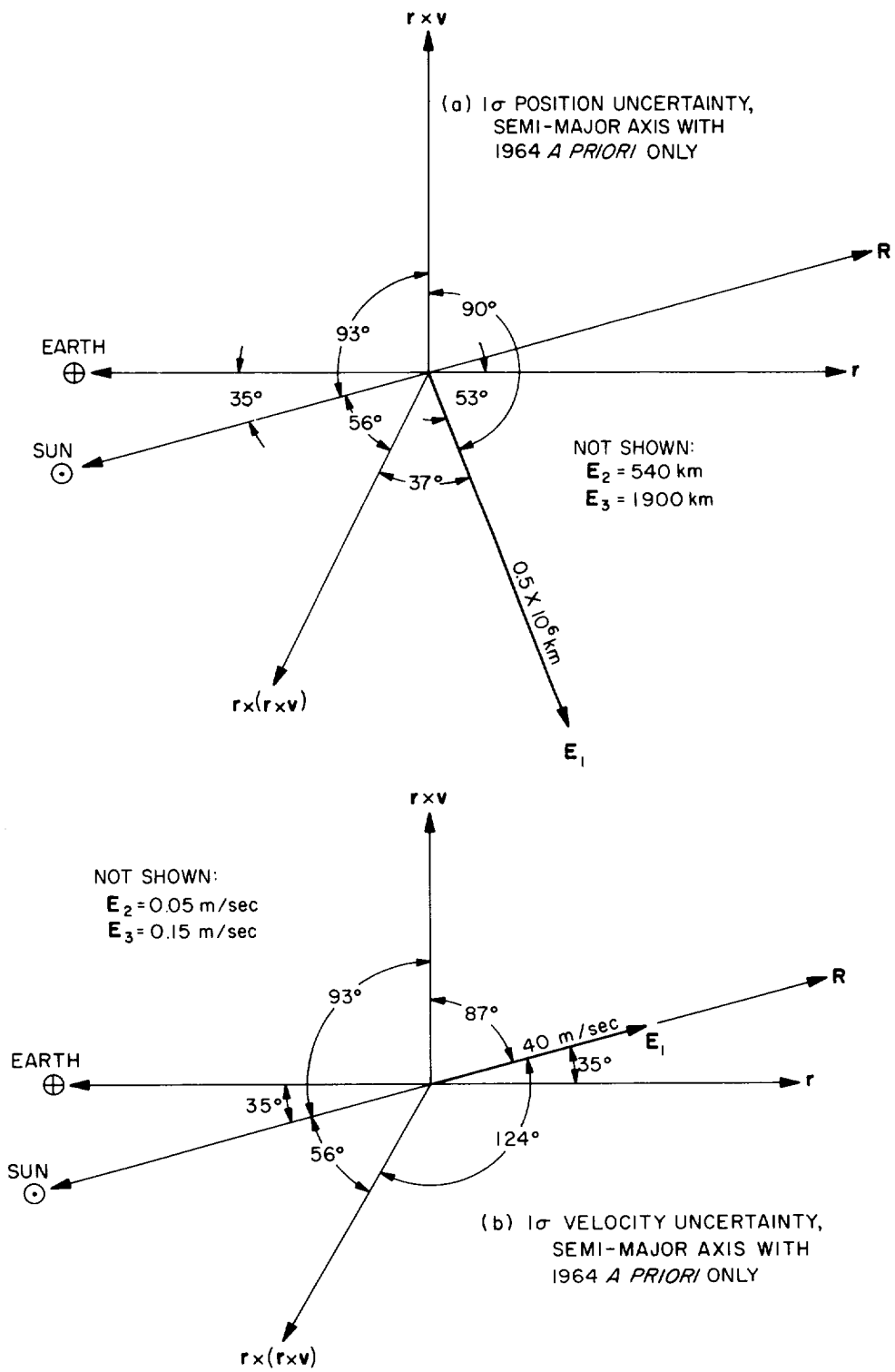


Fig. 12. Comet Kopff dispersion ellipsoid semi-axes mapped to 70/09/21 encounter from 1964

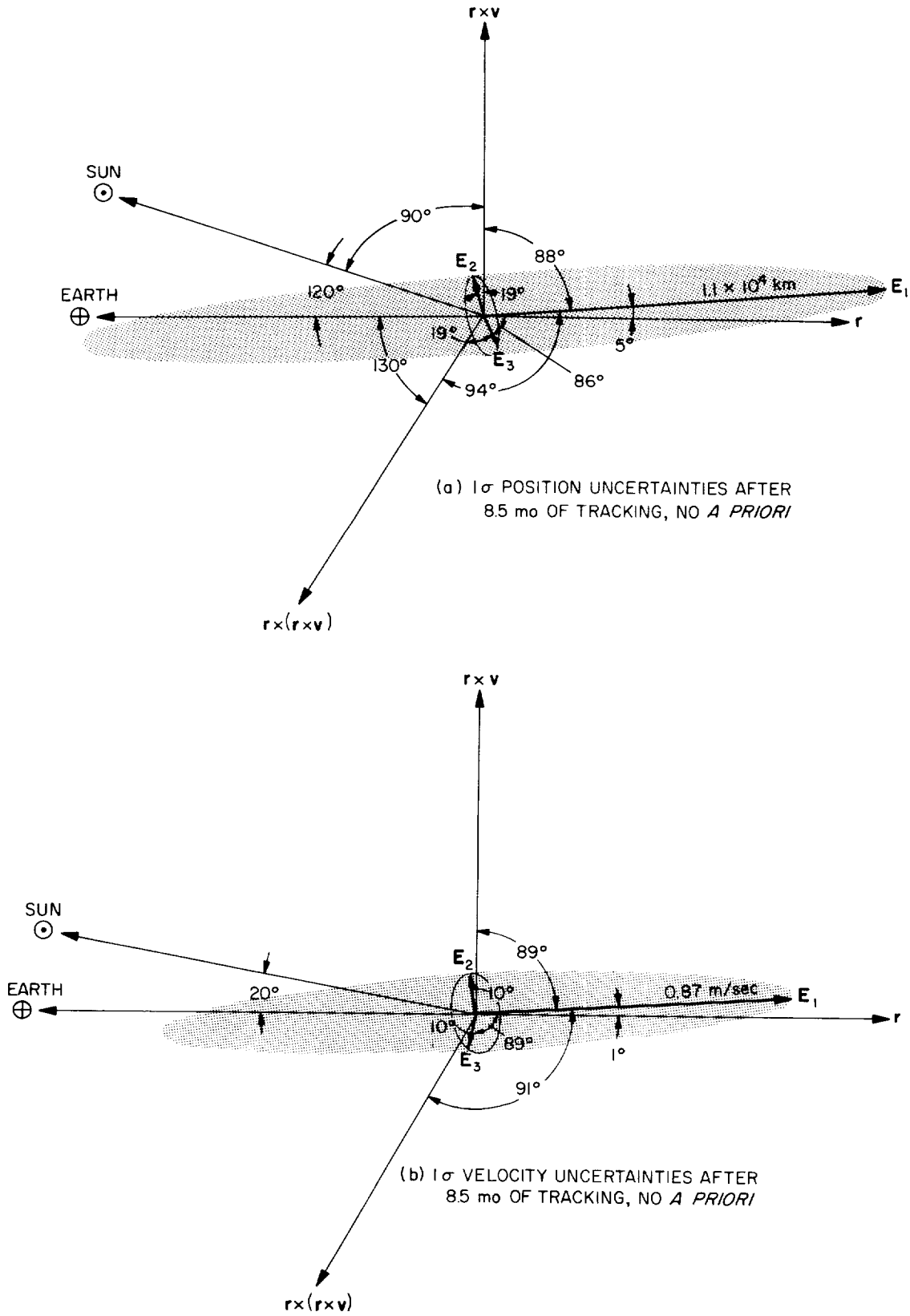


Fig. 13. Comet Kopff dispersion ellipsoid semi-axes at 70/01/01 data-fit epoch

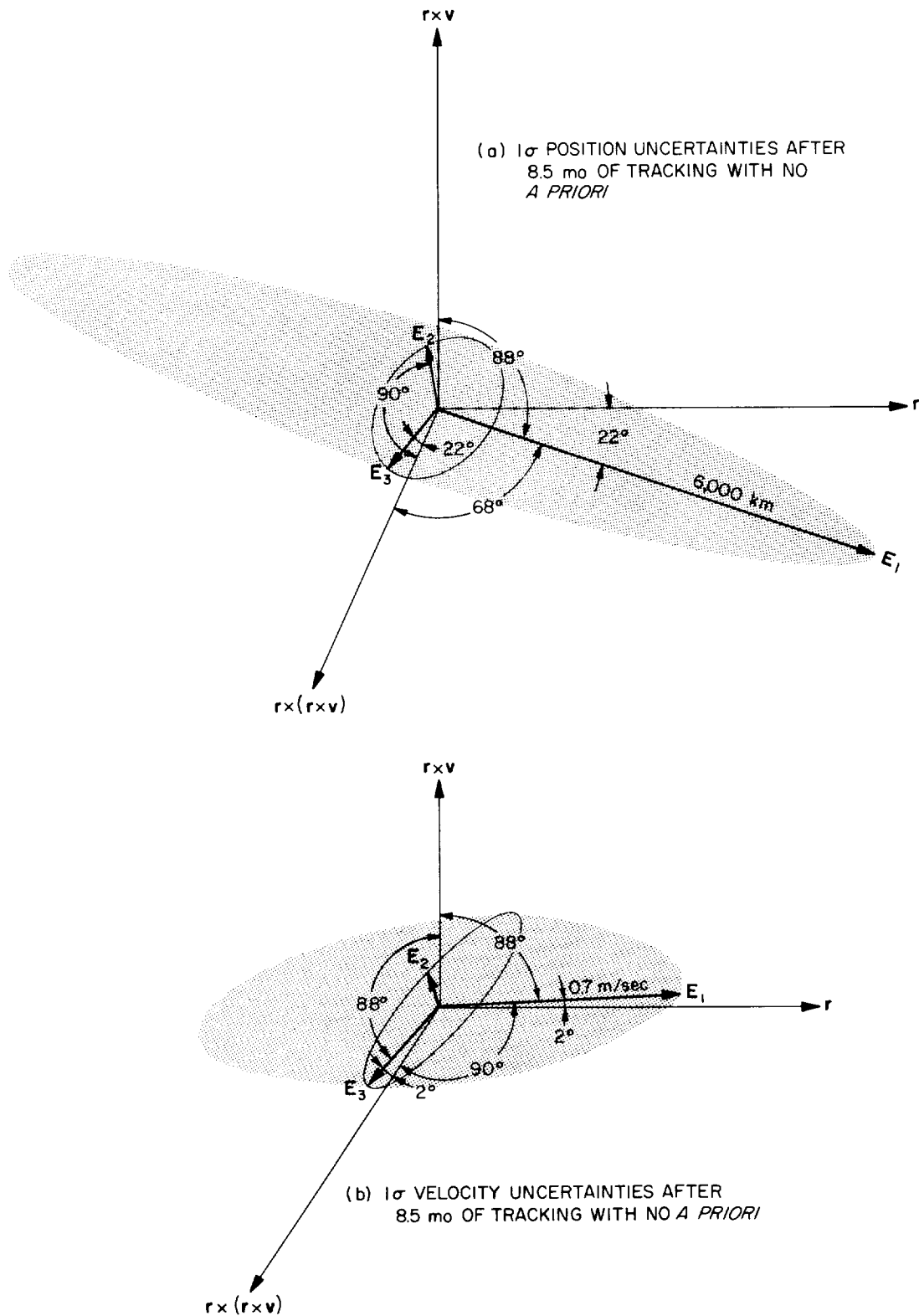


Fig. 14. Comet Kopff dispersion ellipsoid semi-axes mapped to 70/09/21 encounter from 70/01/01

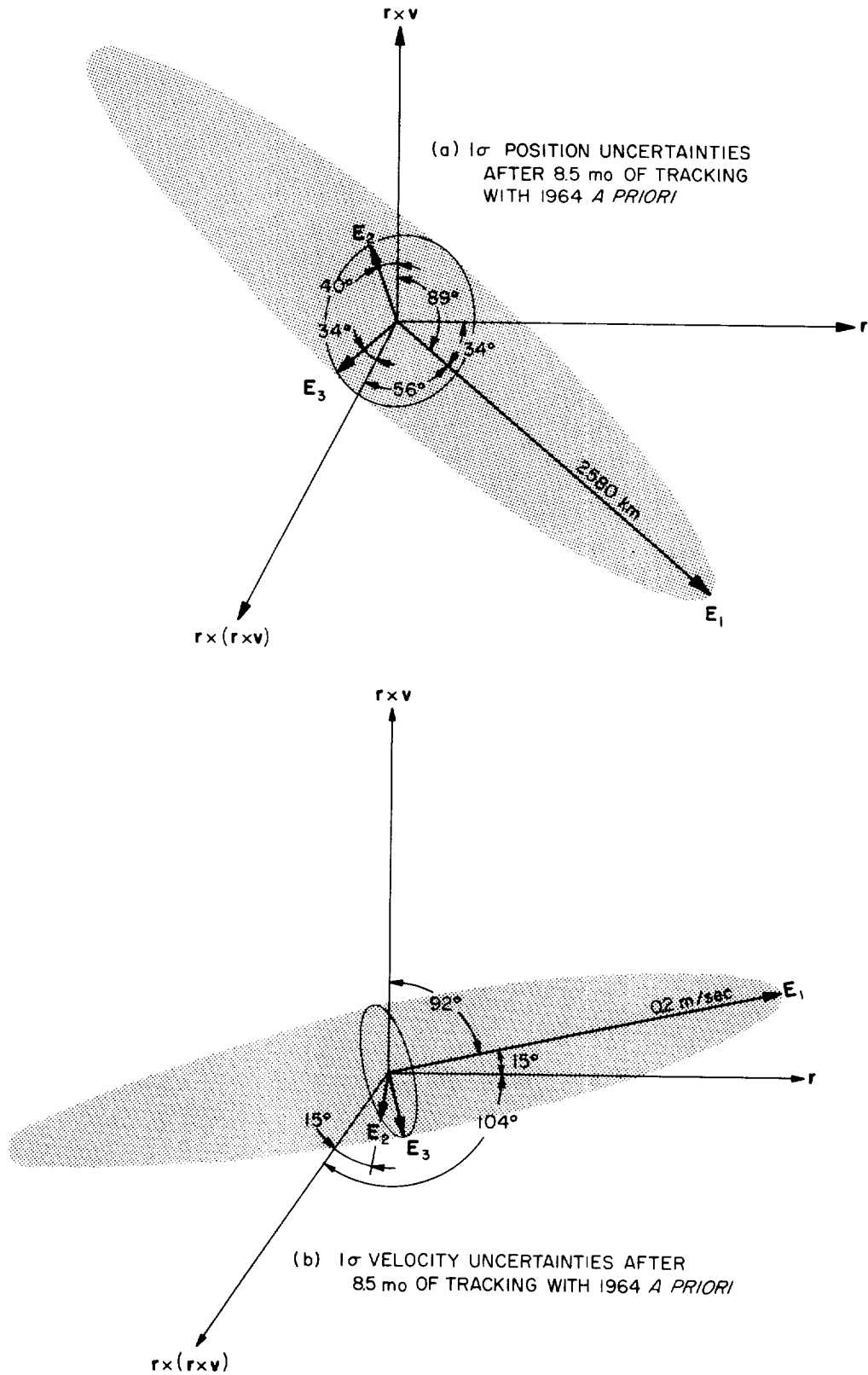


Fig. 15. Comet Kopff dispersion ellipsoid semi-axes mapped to 70/09/21 encounter from 70/01/01 with 1964 a-priori

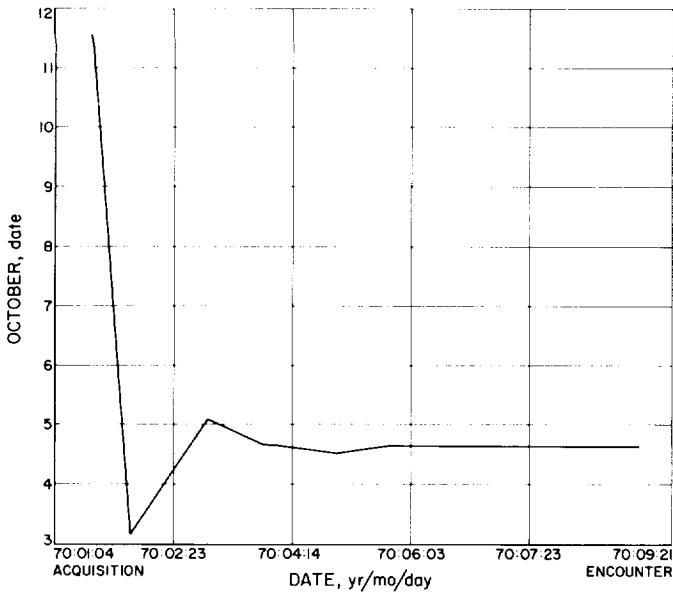


Fig. 16. Comet Kopff predicted perihelion time as a function of optical tracking with no a-priori

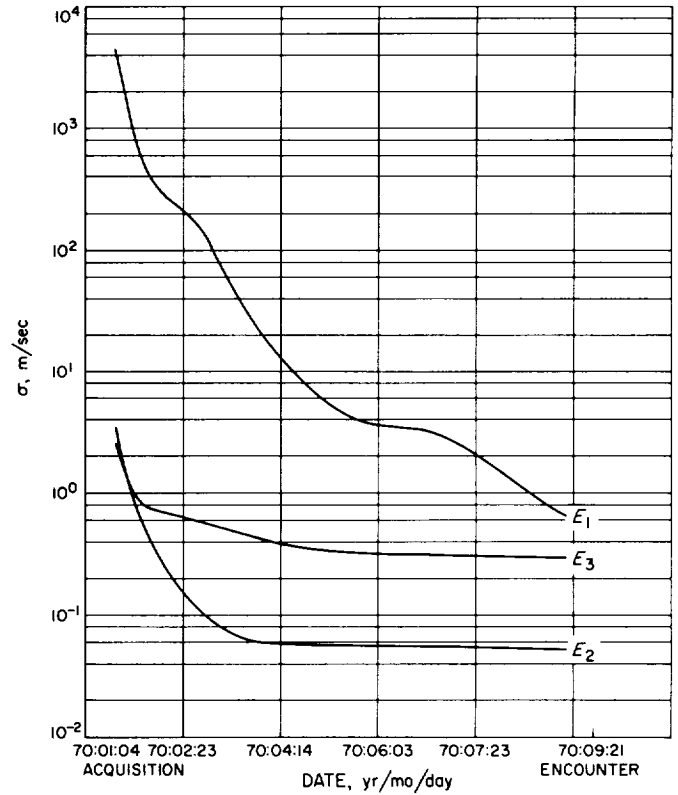


Fig. 18. Comet Kopff 1-sigma velocity dispersion ellipsoid at 70/09/21 encounter, as a function of optical tracking with no a-priori

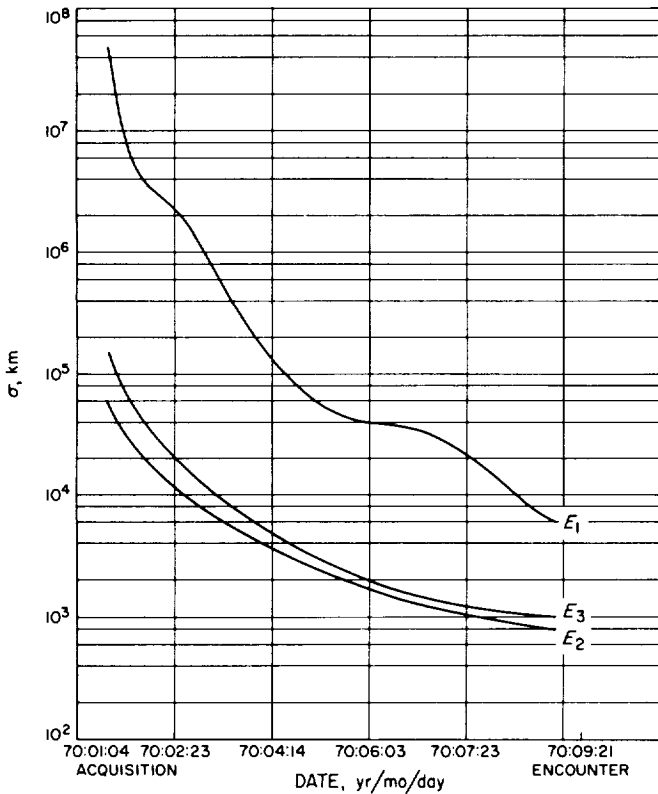


Fig. 17. Comet Kopff 1-sigma position dispersion ellipsoid at 70/09/21 encounter as a function of optical tracking with no a-priori

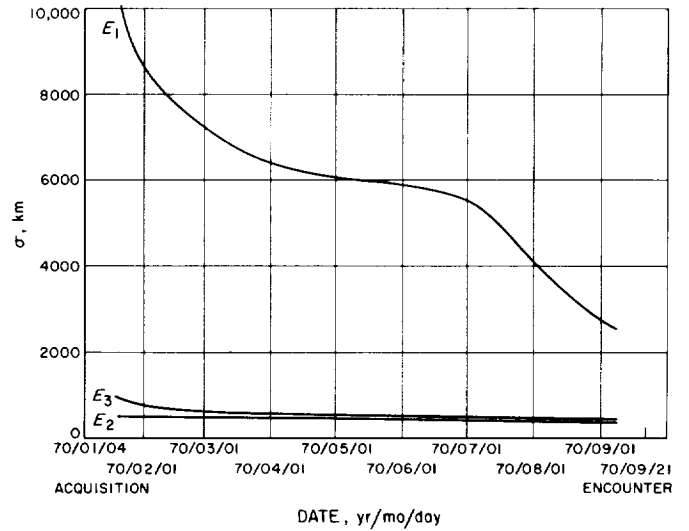


Fig. 19. Comet Kopff 1-sigma position dispersion ellipsoid at 70/09/21 encounter, as a function of optical tracking with 1964 a-priori

trajectory to the comet. To obtain the dispersion ellipsoids at encounter, the eigenvectors of the 3×3 position and velocity covariance matrices have been solved for from the 6×6 covariance matrix at the map-to time (Ref. 12). The square roots of the eigenvalues form the three $1-\sigma$ semi-axes, E_1 , E_2 , and E_3 , of the dispersion ellipsoids, as shown in the polar diagrams (Figs. 12-15) and the tracking plots (Figs. 16-22). The polar diagrams are in the comet-centered \mathbf{r} , $\mathbf{r} \times \mathbf{v}$, $\mathbf{r} \times (\mathbf{r} \times \mathbf{v})$ coordinate system, where \mathbf{r} is the geocentric range vector and \mathbf{v} the geocentric velocity of the comet in inertial space. In these diagrams only the orientations, not the magnitudes, of the various vectors are represented with the exception of those showing all three \mathbf{E} vectors, in which cases *relative* magnitudes of the \mathbf{E} vectors only are indicated. In Fig. 12, the orientation of the heliocentric radius vector has been indicated for comet Kopff at an hypothesized 1970 spacecraft close approach. It is readily apparent that the 1964 tracking errors have mapped into long pencil ellipsoids near 1970 perihelion, with the greatest position uncertainty tangential to the heliocentric orbit and the principal velocity uncertainty radial. These uncertainties correspond to a lack of knowledge of position in orbit or, expressed in terms of classical elements, a large uncertainty in the time of perihelion passage. This is precisely the effect other investigators of comet orbits have noted. Fig. 13 shows the types of errors produced by fitting data for Kopff in 1970 prior to mapping, with no a-priori statistics. The principal position and velocity errors lie along the geocentric range vector, a not very surprising result considering the nature of optical angle measurements, i.e., good determination in a plane perpendicular to the geocentric radius vector, and no direct measurement of range or range

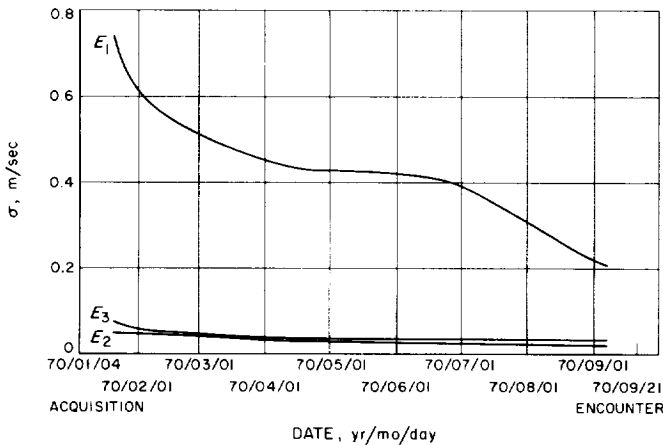


Fig. 20. Comet Kopff $1-\sigma$ velocity dispersion ellipsoid at 70/09/21 encounter, as a function of optical tracking data with 1964 a-priori

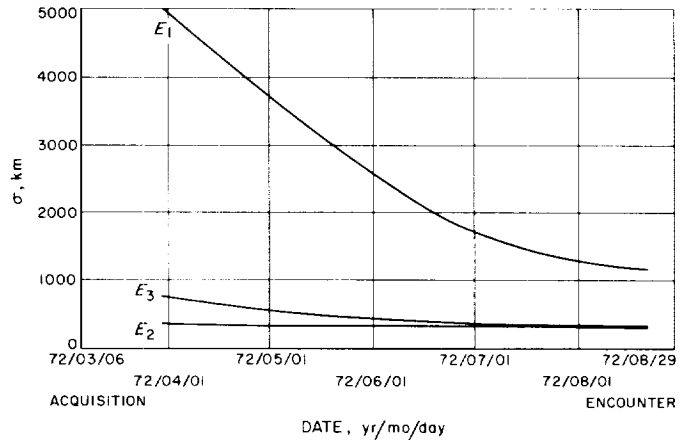


Fig. 21. Comet Giacobini-Zinner $1-\sigma$ position dispersion ellipsoid at 72/08/29 encounter, as a function of optical tracking data with 1959, 1965 a-priori

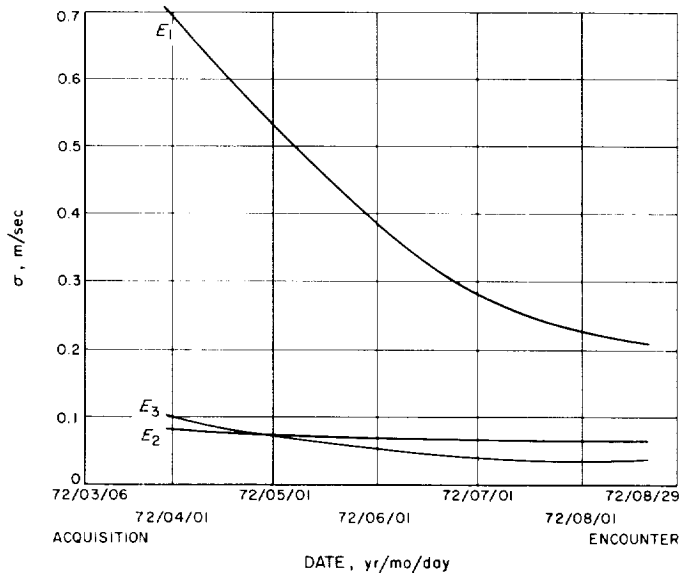


Fig. 22. Comet Giacobini-Zinner $1-\sigma$ velocity dispersion ellipsoid at 72/08/29 encounter, as a function of optical tracking data with 1959, 1965 a-priori

rate. Fig. 14 shows the 1970 tracking statistics mapped to the STL encounter time. Comparison with Figs. 12 and 13 shows that the major axis of the dispersion ellipsoid has twisted towards the orientation of the uncertainties mapped from 1964; i.e., the position in orbit has become less well known as a result of mapping the statistics. A seemingly inconsistent phenomenon has also occurred; namely the position uncertainties are lower after mapping than before. The explanation lies in the fact that the full 6×6 covariance matrix has been mapped, and

the correlations are such that the E_3 velocity uncertainty is the principal one affected by the mapping, increasing by nearly a factor of four. In Fig. 15 is seen the effect of the 1964 a-priori on the 1970 tracking data. The intersection of the ellipsoids of Fig. 14 with the a-priori ellipsoids of Fig. 12 has strikingly improved the 1970 statistics. The effect is even more striking with less tracking data in 1970 (see Fig. 17). Here it may be seen that without a-priori knowledge of the orbit, the $1-\sigma$ E_1 position uncertainty of comet Kopff at 70/02/03 launch mapped out to 70/09/21 encounter is about 5×10^6 km. At 70/09/21, the heliocentric velocity of Kopff is 29 km/sec, or 2.5×10^6 km/day. Thus, with a $1-\sigma$ tangential position error of 5×10^6 km, the predicted perihelion time could easily be 2 days off. The predicted perihelion times produced by fitting various spans of simulated data in 1970 show this effect (see Fig. 16). Looking at Fig. 19, it is seen that the influence of the 1964 a-priori information on E_1 , mapped from 70/02/03 to 70/09/21 is such as to reduce it from over 5×10^6 km down to 8500 km.

Note that the position uncertainties for comet Giacobini-Zinner (Fig. 21) are roughly half those for Kopff (Fig. 19) and Pons-Winnecke (Fig. 23). This seems to be the effect

of linking two previous apparitions for a-priori statistics, thus improving the knowledge of the mean motion. It should be remembered that only four observations were simulated for Giacobini-Zinner in 1965; the principal a-priori tracking uncertainties being mapped out all the way from 1959. One would normally expect to do even better with a more favorable data span at the previous apparition.

8. Conclusions

The principal initial tracking uncertainties for optical angle tracking are in the geocentric range direction, and are of the order of 10,000 km and 1 m/sec with 8.5 months of tracking (see Fig. 13). This result is in agreement with the findings of others (Ref. 14).

As they are mapped out, the principal position uncertainty, E_1 , twists toward a tangential alignment with the heliocentric comet orbit; the principal velocity uncertainty twists toward the Sun-comet axis (Fig. 15). If uncertainties are mapped for a whole comet revolution, the tangential position uncertainty may become many thousands of kilometers (Fig. 12); the corresponding

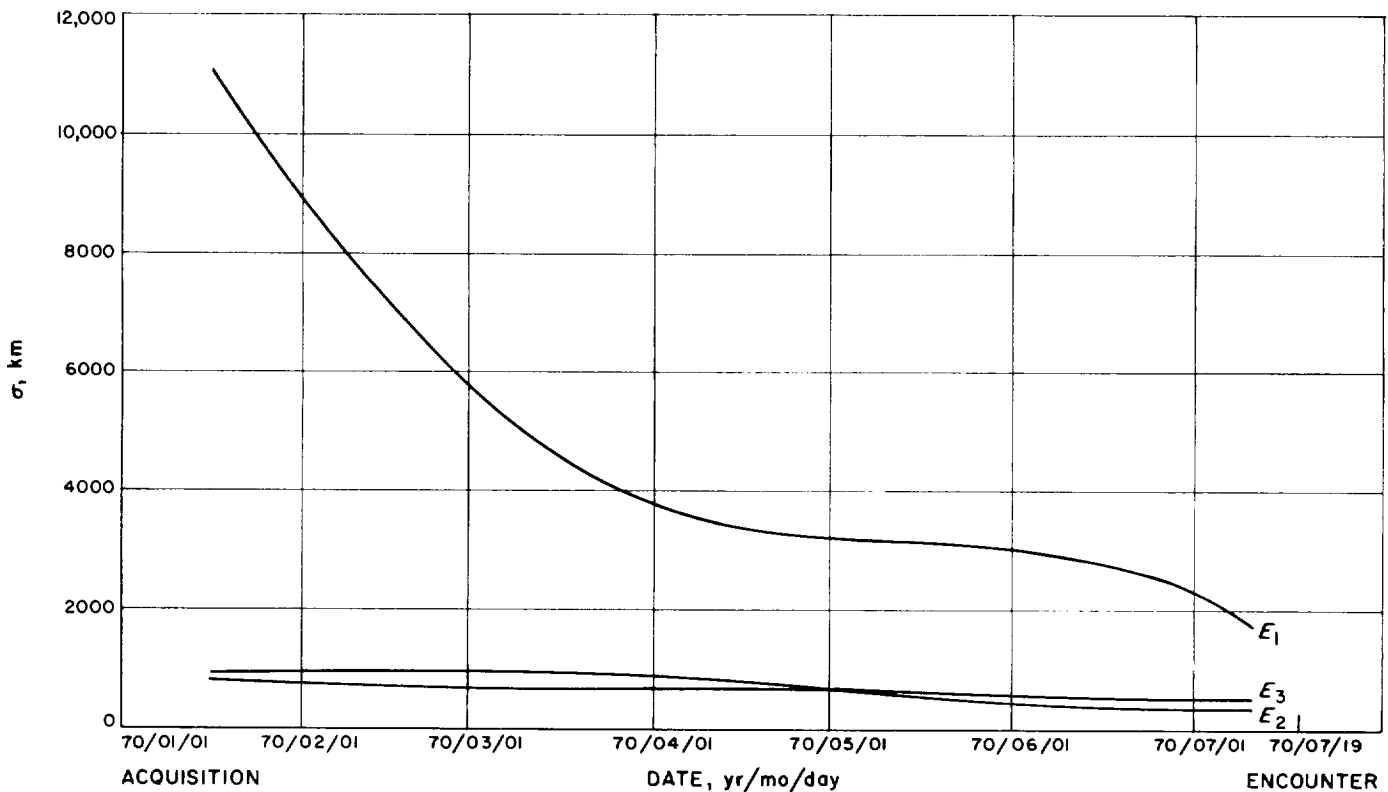


Fig. 23. Comet Pons-Winnecke $1-\sigma$ position dispersion ellipsoid at 70/07/19 encounter, as a function of optical tracking with 1964 a-priori

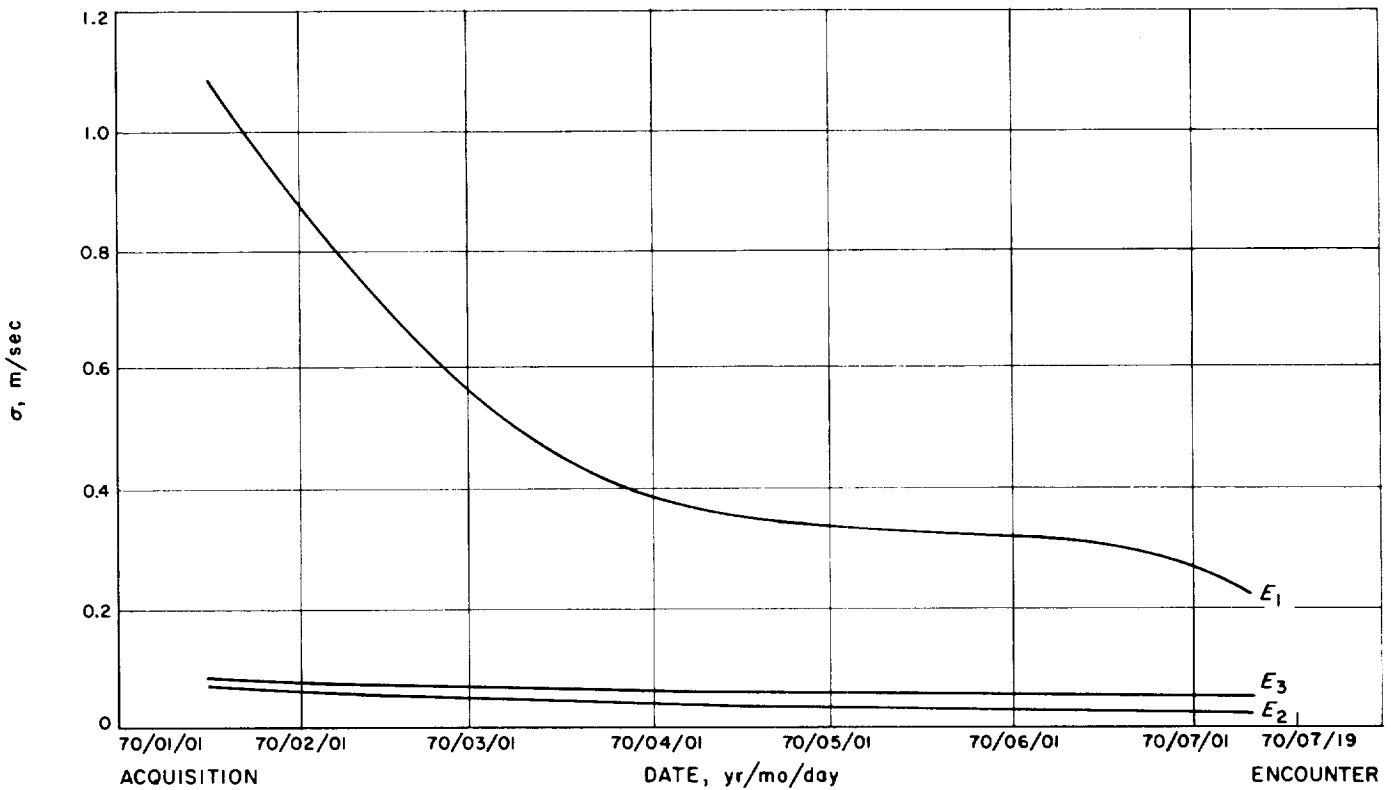


Fig. 24. Comet Pons-Winnecke 1- σ velocity dispersion ellipsoid at 70/07/19 encounter, as a function of optical tracking data with 1964 a-priori

radial velocity uncertainty may be hundreds of meters per second (Fig. 12).

The information obtained by fitting one or more previous apparitions has a dramatic effect in reducing errors when combined with new observations, even though the a-priori information alone leads to tracking errors of millions of kilometers. This is possible because we have the intersection of two pencil ellipsoids, i.e., the a-priori statistics and the statistics from the new observations. The result is that the length of the error ellipsoid from the new observations is greatly reduced. With only three new observations in 16 days of tracking, the uncertainty goes from 5×10^7 km without a-priori information down to 1×10^4 km with a-priori information (Figs. 17, 19). The final uncertainty after 8.5 months of tracking is reduced from 6000 km with no a-priori to 2600 km with a-priori information.

It would appear from the preceding paragraph that final uncertainties can be reduced by at least a factor of 2 over estimates made by other investigators (Ref. 14) who did not include the effect of the a-priori data. From

the results obtained with comet Giacobini-Zinner, one might expect a further improvement by a factor of 2 from fitting data in more than one previous apparition.

9. Recommendations For Comet Intercept Missions

From the orbit determination point of view, comet Tuttle-Giacobini-Kresak may be rejected as a possible target in 1973. The spacecraft would have to be launched days before optical acquisition of the comet, relying on the a-priori comet orbit information alone which, as has been shown, could lead to an error of hundreds of thousands of kilometers in the target position. This would make serious demands upon the spacecraft midcourse correction system. Total amount of time available for optical tracking before encounter is also very short for this object compared with the other three analyzed. The other three comets appear almost uniformly suitable as targets, with a good probability of some tracking before launch. It should be possible, utilizing two spacecraft maneuvers with the last shortly before encounter, to attain final miss accuracies no worse than 1500 km, 1- σ (Fig. 21).

Data from at least two previous apparitions should be carefully fitted before the mission so that the comet may be acquired as rapidly as a-priori knowledge permits and new observations may then be easily fitted with the old ones. After acquisition it is important to be able to reduce the photographic positions within a day or two of the observation in order that the orbit knowledge may be kept current. It will be necessary to carefully examine all observations for systematic errors, and it may be necessary to re-reduce the bulk of the a-priori observations to take out the effects of proper motions in the plate constants. This may be done where field plates containing fundamental stars exist near the epoch of the comet observations.

10. Determination of Cometary Mass by a Close Approach

It is of interest to know whether or not the possibility exists of measuring the mass of the nucleus of a comet by a close spacecraft encounter. It shall be assumed that the object attracts as a point mass. It is desired to know the relation between the cometary mass and the velocity perturbation, \dot{r} (see Fig. 25).

The relative velocity of comet and spacecraft at closest approach is given by

$$V^2 = GM \left(\frac{2}{q} - \frac{1}{a} \right)$$

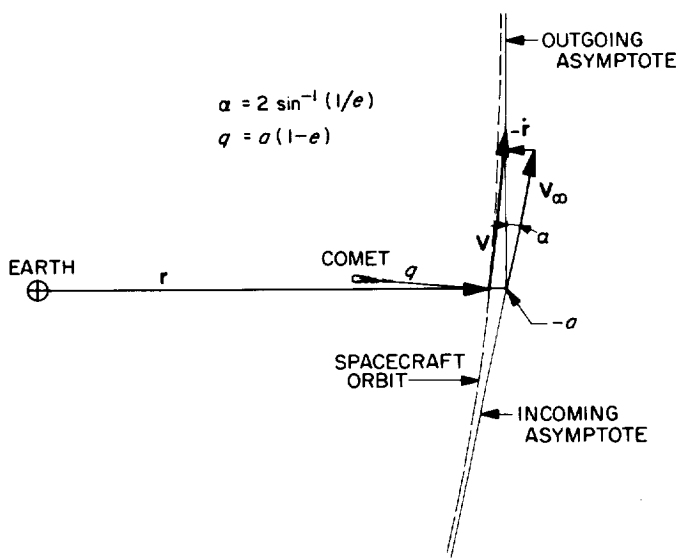


Fig. 25. Spacecraft orbit bending near comet

where

V is the relative velocity at closest approach,

G the gravitational constant,

M the combined mass of comet and spacecraft,

q the distance of closest approach,

$a = q/(1-e)$, where e is the eccentricity of the comet-centered hyperbolic spacecraft orbit (see Fig. 25).

For such an encounter, e is much larger than unity, hence

$$a \approx - \frac{q}{e}$$

$$M \approx \frac{V^2}{G \left(\frac{2-e}{q} \right)} \approx - \frac{qV^2}{Ge}$$

From Fig. 25,

$$\sin \alpha = \sin \left[2 \sin^{-1} \left(\frac{1}{e} \right) \right] = - \frac{\dot{r}}{V_\infty}$$

For very small angles, as in this instance (the angle α is very much exaggerated in Fig. 25),

$$\frac{2}{e} = - \frac{\dot{r}}{V_\infty}$$

$$V \approx V_\infty$$

and

$$M \approx \frac{q\dot{r}V}{2G}$$

Masses of period comet nuclei are estimated to be 10^{17} to 10^{20} grams. Suppose we have for comet Kopff,

$$M = 10^{17} \text{ grams}$$

$$q = 2000 \text{ km}$$

$$V = 10 \text{ km/sec (see Ref. 14, Sect. 4-39).}$$

If the Earth-comet-probe geometry is such as is shown in Fig. 25 then \dot{r} , the total detectable velocity perturbation, will be 6.67×10^{-7} m/sec, or 10^{-5} cps with S-band doppler tracking. This is at least an order of magnitude smaller than the accuracy of any conceivable doppler tracking system in the near future. If the comet mass should be 10^{20} grams, however, only 10^{-2} cps S-band capability is required to detect the velocity perturbation. Of course, the above figures presume that V and q are reasonably well determined. It has been seen that the geocentric velocity of the comet may be determined to a

fraction of a meter per second by optical tracking, and certainly the probe velocity is known at least as well. Thus a 10 km/sec relative velocity would be well measured. However, an onboard ranging system would probably be required to determine q well enough. If photographs of the comet nucleus could be taken against a star background as one of the scientific experiments, it is possible that q could be determined by the parallax shift of the image of the nucleus.

D. Optimum Collocation Method for Two-Point Boundary Value Problems

W. Kizner

As a result of previous work in solving initial value problems of ordinary differential equations (SPS 37-31, Vol. IV, pp. 4-16), and a remark of the referee (Dr. C. W. Clenshaw of the National Physical Laboratory, England) on a version of the SPS article submitted for outside publication, it became evident that the same ideas can be used to obtain an optimum method of collocation for the solution of a certain class of two-point boundary value problems of ordinary differential equations. The class of applicable problems includes those of orbit selection, such as the case where one would like to calculate an orbit going from one planet and passing close to a number of others. In its present form, the method is applicable to second-order ordinary differential equations

$$\ddot{x} = f(x, \dot{x}, t) \tag{1a}$$

with boundary conditions

$$x(t_I) = a, x(t_F) = b \tag{1b}$$

where $x, \dot{x}, f, a,$ and b are vectors of the same dimension, and t_I and t_F are the initial and final times, respectively.

The general idea of solving Eq. (1) by collocation or "selected points" is well known (Ref. 15). The present contribution lies in showing how one can make an optimum a-priori choice of the collocation points so as to keep the error in the positions x as small as possible, and in showing a simplified scheme for calculation of solutions. For the applications that we have in mind, f is a very weak function of the velocities \dot{x} , and we shall not be concerned with the errors in the velocities.

The form of the optimum error curve for solutions of the differential has been discussed previously (SPS 37-31, Vol. IV). Let q_n be any n th degree polynomial approximation for a component of x which satisfies the boundary conditions. For simplicity, assume there is only one component.

Define

$$\bar{E}_n = \inf_{q_n} \|x(t) - q_n(t)\| \tag{2}$$

where $\|f(t)\|$ denotes the uniform norm of a function $f(t)$.

The Theorem 6 of SPS 37-31, Vol. IV, states that

(1) There exists a member of q_n, \bar{q}_n such that

$$E_n = \|x(t) - \bar{q}_n(t)\|$$

(2) For $\bar{q}_n(t)$ to have this property, it is necessary and sufficient that $x(t) - \bar{q}_n(t)$ attain its maximum absolute value M in at least n points of (t_I, t_F) , and that the maxima shall alternate with the minima at these points.

(3) The polynomial $\bar{q}_n(t)$ is unique.

If we assume that the functions to be approximated are very smooth and the optimum error curves $x(t) - q_n(t)$ are accurately represented by a polynomial of one higher degree than we show in SPS 37-31, Vol. IV, that the error curve, defined on the normalized interval $-1 \leq t \leq 1$, is proportional to the "stretched" Chebyshev polynomial $T_{n+1}^{**}(t)$, where

$$T_{n+1}^{**} \left(\frac{\tau}{\cos \frac{\pi}{2} \frac{1}{n+1}} \right) \equiv T_{n+1}(\tau) \quad n \geq 1 \tag{3}$$

We now apply this to equations of the form (1). To satisfy the boundary conditions we assume that the approximation for $x(t), \bar{x}(t)$ is of the form

$$\begin{aligned} \bar{x}(t) = & \frac{x(-1) + x(1)}{2} + \frac{x(1) - x(-1)}{2} t \\ & + (t^2 - 1) \left[\sum_{i=0}^{n-3} a_i T_i(t) \right] \end{aligned} \tag{4}$$

where n is the degree of the ideal error curve, and $T_i(t)$ are the usual Chebyshev polynomials. The advantage of

using Chebyshev polynomials over monomials is that the coefficients a_i tend to zero much faster with increasing i .

It can be shown that a good approximation for the collocation points, or "selected points," for calculating the derivatives is

$$t_i = \frac{n^2}{n^2 - 1} \frac{\cos \frac{\pi}{2n} (1 + 2i)}{\cos \frac{\pi}{2n}} \quad i = 1, 2, \dots, n - 2 \quad (5)$$

The points occur at the roots of the second derivative of $T_n^{**}(t)$.

where $a_e = a_0, a_2, a_4, \dots, a_0 = a_1, a_3, a_5, \dots$ B_e and B_0 can be found by matrix inversion from the equations

$$\begin{aligned} B_e^{-1} a_e &= \ddot{x}_e \\ B_0^{-1} a_0 &= \ddot{x}_0 \end{aligned} \quad (7)$$

where all the elements can be determined.

We exhibit the "selected points," B_e, B_0 for the case n , the degree of the error polynomial, is ten. This makes the number of "selected points" equal eight. We number the "selected point" starting with the largest, and give only the positive ones (since the negative ones are symmetric).

$S \cdot P \cdot =$	(0.91128795	0.72316493	0.46429453	0.15998435)	
$B_e =$	(0.020754808	0.047650719	0.082624655	0.098969817
		0.020509051	0.0097638866	-0.0027881677	-0.027484770
		0.0078745418	-0.011862335	-0.0023046847	0.0062924782
		0.0018336420	-0.0059351906	0.0077704814	-0.0036689327
)				
$B_0 =$	(0.030321658	0.040773513	0.053423000	0.0088233037
		0.013634698	-0.0086812273	-0.0071186684	-0.017764351
		0.0045073875	-0.011655523	0.010048733	-0.0021516732
		0.00078250018	-0.0031917058	0.0065084847	-0.0089184169
)				

More exact values are obtained by a modified Newton-Raphson method.

For linear differential equations, the unknown coefficients a can be obtained by a matrix inversion. For non-linear equations, we use a Picard iteration method. We calculate second derivatives at the "selected points" and then curve fit to obtain a . The resulting polynomial can be evaluated, and new x and \dot{x} can be obtained for use in calculating the next second derivatives.

In curve fitting to find a , we make use of the symmetries of the problem. We transform the array of second derivatives into an "even" and "odd" array \ddot{x}_e, \ddot{x}_o by adding or subtracting the second derivatives at symmetrically spaced collocation points.

Then

$$\begin{aligned} a_e &= B_e \ddot{x}_e \\ a_0 &= B_0 \ddot{x}_0 \end{aligned} \quad (6)$$

Thus one can judge from the size of the elements of B_e and B_0 that the errors in calculating a due to roundoff should be small.

A program has been prepared and checked by calculating known solutions to Eq. (1), and by examining the error curves.

E. Solution of the N-Body Problem with Recurrent Power-Series

R. Broucke

In 1955 to 1957, a few articles were published by Steffensen (Ref. 16), describing the solution of both the restricted and the general three-body problem in terms

of power-series in time. The method proposed by Steffensen is particularly well adapted to modern computing machines. The method is made practical by the introduction of a certain number of auxiliary dependent variables, which transform the system of differential equations of motion into a new system of differential equations where all denominators have been removed, as well as the powers r^3 . Steffensen calls his system of "second degree," because in the final form, only products of two dependent variables appear. This form is particularly well-adapted for the substitution of power series and the identification of equal powers in t . In several of his papers, Steffensen also gave convergence criteria for the series. The application of the series is particularly interesting because the square roots are completely avoided in the computations and the number of divisions is reduced to a minimum. The reason why the method is so well adapted to automatic computers is that the calculation of all the coefficients of the power series is done in a recurrent way; for each order, the coefficients are functions of all the preceding computed coefficients.

In the last two years, this method has been effectively used by several authors, such as Deprit and Fehlbeg (Refs. 17, 18), for the numerical integration of the restricted three-body problem on computers, and it appears that the results are superior both in speed and in precision, to those obtained with most of the classical numerical integration methods.

Table 8. Differential equations for the heliocentric N-planet problem

$$\begin{array}{l}
 i = 1, 2, 3, \dots, N \\
 \left\{ \begin{array}{l} \frac{dx_i}{dt} = u_i \\ \frac{dy_i}{dt} = v_i \\ \frac{dz_i}{dt} = w_i \end{array} \right. \quad \left\{ \begin{array}{l} m_0 = \text{central body (=Sun)} \\ m_i = N \text{ planets} \end{array} \right. \\
 \left. \begin{array}{l} \frac{du_i}{dt} = -(m_0 + m_i) \frac{x_i}{r_i^3} - \sum_{\substack{j=1 \\ j \neq i}}^{j=N} m_j \left(\frac{x_i - x_j}{r_{ij}^3} + \frac{x_j}{r_j^3} \right) \\ \frac{dv_i}{dt} = -(m_0 + m_i) \frac{y_i}{r_i^3} - \sum_{\substack{j=1 \\ j \neq i}}^{j=N} m_j \left(\frac{y_i - y_j}{r_{ij}^3} + \frac{y_j}{r_j^3} \right) \\ \frac{dw_i}{dt} = -(m_0 + m_i) \frac{z_i}{r_i^3} - \sum_{\substack{j=1 \\ j \neq i}}^{j=N} m_j \left(\frac{z_i - z_j}{r_{ij}^3} + \frac{z_j}{r_j^3} \right) \end{array} \right. \quad \left\{ \begin{array}{l} 6N \text{ differential equations} \\ 6N \text{ unknowns} \end{array} \right.
 \end{array}$$

We have adapted the method to the solution of the Equations of Motion of N planets around the Sun, instead of having only a total number of three bodies. The results are reported in Tables 8 to 11. Table 8 gives the explicit form of the equations, which are the starting point for

Table 9. Linearized differential equations for the N-planet problem

$$\left\{ \begin{array}{l} \dot{x}_i = u_i \\ \dot{y}_i = v_i \\ \dot{z}_i = w_i \end{array} \right. \quad \left\{ \begin{array}{l} N(N+7) \text{ differential equations} \\ N(N+7) \text{ unknowns} \end{array} \right.$$

$$\left\{ \begin{array}{l} \dot{u}_i = -(m_0 + m_i)x_i s_i - \sum_{\substack{j=1 \\ j \neq i}}^{j=N} m_j [(x_i - x_j)s_{ij} + x_j s_j] \\ \dot{v}_i = -(m_0 + m_i)y_i s_i - \sum_{\substack{j=1 \\ j \neq i}}^{j=N} m_j [(y_i - y_j)s_{ij} + y_j s_j] \\ \dot{w}_i = -(m_0 + m_i)z_i s_i - \sum_{\substack{j=1 \\ j \neq i}}^{j=N} m_j [(z_i - z_j)s_{ij} + z_j s_j] \end{array} \right.$$

$$\left\{ \begin{array}{l} r_i \dot{r}_i = x_i \dot{x}_i + y_i \dot{y}_i + z_i \dot{z}_i \\ r_{ij} \dot{r}_{ij} = (x_i - x_j)(\dot{x}_i - \dot{x}_j) + (y_i - y_j) \\ \quad \times (\dot{y}_i - \dot{y}_j) + (z_i - z_j)(\dot{z}_i - \dot{z}_j) \end{array} \right.$$

$$\left\{ \begin{array}{l} r_i \dot{s}_i = -3s_i \dot{r}_i \\ r_{ij} \dot{s}_{ij} = -3s_{ij} \dot{r}_{ij} \end{array} \right. \quad \left\{ \begin{array}{l} i = 1, 2, 3, \dots, N \\ j = 1, 2, 3, \dots, N \end{array} \right.$$

Table 10. Power series for the $N(N+7)$ unknowns of the N-planet problem

$$\left\{ \begin{array}{l} x_i = \sum_{u=1}^{\infty} X_{iu} t^{u-1} \\ y_i = \sum_{u=1}^{\infty} Y_{iu} t^{u-1} \\ z_i = \sum_{u=1}^{\infty} Z_{iu} t^{u-1} \\ u_i = \sum_{u=1}^{\infty} U_{iu} t^{u-1} \\ v_i = \sum_{u=1}^{\infty} V_{iu} t^{u-1} \\ w_i = \sum_{u=1}^{\infty} W_{iu} t^{u-1} \end{array} \right. \quad \left\{ \begin{array}{l} r_i = \sum_{u=1}^{\infty} R_{iu} t^{u-1} \\ r_{ij} = \sum_{u=1}^{\infty} R_{ij} t^{u-1} \\ s_i = \sum_{u=1}^{\infty} S_{iu} t^{u-1} \\ s_{ij} = \sum_{u=1}^{\infty} S_{ij} t^{u-1} \end{array} \right. \quad \left\{ \begin{array}{l} i = 1, 2, \dots, N \\ j = 1, 2, \dots, N \end{array} \right.$$

Table 11. Recurrent relations for the coefficients of the $N(N + 7)$ power series

$$\begin{aligned}
 nX_{i(n+1)} &= U_{in} && \text{for } n = 1, 2, 3, \dots, (n_i - 1) \\
 nY_{i(n+1)} &= V_{in} && \text{where } n_i = \text{number of terms in the power series} \\
 nZ_{i(n+1)} &= W_{in} && \text{and for } i, j = 1, 2, \dots, N \\
 \\
 nU_{i(n+1)} &= -(m_0 + m_i) \sum_{\substack{p+q=n+1 \\ p=1, \dots, n}} X_{ip} S_{iq} - \sum_{j=1, \neq i}^N m_j \left\{ \sum_{\substack{p+q=n+1 \\ p=1, \dots, n}} [(X_{ip} - X_{jp}) S_{iq} + X_{jp} S_{iq}] \right\} \\
 nV_{i(n+1)} &= -(m_0 + m_i) \sum_{\substack{p+q=n+1 \\ p=1, \dots, n}} Y_{ip} S_{iq} - \sum_{j=1, \neq i}^N m_j \left\{ \sum_{\substack{p+q=n+1 \\ p=1, \dots, n}} [(Y_{ip} - Y_{jp}) S_{iq} + Y_{jp} S_{iq}] \right\} \\
 nW_{i(n+1)} &= -(m_0 + m_i) \sum_{\substack{p+q=n+1 \\ p=1, \dots, n}} Z_{ip} S_{iq} - \sum_{j=1, \neq i}^N m_j \left\{ \sum_{\substack{p+q=n+1 \\ p=1, \dots, n}} [(Z_{ip} - Z_{jp}) S_{iq} + Z_{jp} S_{iq}] \right\} \\
 \\
 nR_{ij}R_{i(n+1)} &= - \sum_{\substack{p+q=n+1 \\ p=2, \dots, n}} qR_{ip}R_{i(q+1)} + \sum_{\substack{p+q=n+1 \\ p=1, \dots, n}} q [X_{ip}X_{i(q+1)} + Y_{ip}Y_{i(q+1)} + Z_{ip}Z_{i(q+1)}] \\
 nR_{ij}R_{j(n+1)} &= - \sum_{\substack{p+q=n+1 \\ p=2, \dots, n}} qR_{ijp}R_{ij(q+1)} + \sum_{\substack{p+q=n+1 \\ p=1, \dots, n}} q \left\{ \begin{aligned} &(X_{ip} - X_{jp}) [X_{i(q+1)} - X_{j(q+1)}] \\ &+ (Y_{ip} - Y_{jp}) [Y_{i(q+1)} - Y_{j(q+1)}] \\ &+ (Z_{ip} - Z_{jp}) [Z_{i(q+1)} - Z_{j(q+1)}] \end{aligned} \right\} \\
 \\
 nR_{ij}S_{i(n+1)} &= - \sum_{\substack{p+q=n+1 \\ p=2, \dots, n}} qR_{ip}S_{i(q+1)} - 3 \sum_{\substack{p+q=n+1 \\ p=1, \dots, n}} qS_{ip}R_{i(q+1)} \\
 nR_{ij}S_{j(n+1)} &= - \sum_{\substack{p+q=n+1 \\ p=2, \dots, n}} qR_{ijp}S_{ij(q+1)} - 3 \sum_{\substack{p+q=n+1 \\ p=1, \dots, n}} qS_{ijp}R_{ij(q+1)}
 \end{aligned}$$

our derivation of the new equations. The key of the method is in the introduction of N new variables.

$$s_i = r_i^{-3} \tag{1}$$

and $N(N - 1)/2$ new variables

$$s_{ij} = r_{ij}^{-3} . \tag{2}$$

The preceding equations give clearly the relation between the new variables s_i, s_{ij} and the variables $r_{0i}, r_{ij}, (r_{0i} = r_i)$ while r_i and r_{ij} are related to (x_i, y_i, z_i) by

$$r_i^2 = x_i^2 + y_i^2 + z_i^2 \tag{3}$$

$$r_{ij}^2 = (x_i - x_j)^2 + (y_i - y_j)^2 + (z_i - z_j)^2. \tag{4}$$

However, these relations (1) to (4) shall never be used in the computations, except for computing the initial values of these expressions as functions of the initial coordinates.

Instead of directly using these equations, we first differentiate them once, in order to obtain new relations which contain the time derivatives and which are thus to be treated as differential equations. The complete set of new (all first-order) differential equations is given in Table 9. We see that there are $6N$ differential equations

for the coordinates and the velocity components, $2N$ equations for the variables r_i and s_i , and finally $N(N - 1)/2 + N(N - 1)/2 = N(N - 1)$ equations for the variables r_{ij} and s_{ij} . The total number of differential equations, and, of course, the total number of unknowns is thus equal to $N(N + 7)$. For a few possible values of N we have, for instance

N	$N(N + 7)$
2	18
5	60
8	120
10	170

After the differential equations of Table 9 are obtained, we define $N(N + 7)$ Taylor expansions, as shown in Table 10. It can be seen that we have used small letters for the unknowns and capital letters for the coefficients in their Taylor series expansion. It is also seen that we have used a rather unusual convention of starting the zero-degree coefficients of the series with the subscript one; we have taken this convention, having in mind the Fortran-programming of these equations, Fortran not allowing for zero values for subscripts.

The next step in the work is to make the substitution of the series of Table 10 in the differential equations of Table 9. This task is maintained relatively easy because of the simple form of the equations in Table 9, and mainly because no products of more than two variable quantities occur. If all the substitutions are made, and if the coefficients of equal powers of t in both members are set equal, we finally obtain the results collected in Table 11. We see that, if the equations are used in the order where they are given, they are perfectly recurrent; each coefficient depends only on the preceding coefficients. All the zero-order coefficients are given by the initial conditions. The equations of Table 11 form the main part of the computer program for the practical applications.

We have programmed the equations in Double Precision on the IBM-7094 in order to test their practical validity. We have restricted the program to a maximum of 10 bodies revolving around the Sun and a maximum of 25 terms in the power series. A few integrations with different step sizes and different numbers of terms have been performed, and verifications with the known first integrals of the N -body problem give favorable conclusions.

F. On Changes of Independent Variable in Dynamical Systems

R. Broucke

1. Introduction

We observe that in many dynamical problems which arise in celestial mechanics, changes of independent variable are performed. On the other hand we also notice that probably no general theory for performing this operation exists. In conservative systems, general rules have been given, but nonconservative systems are much less studied. We meet changes of independent variable in most publications on the regularization of the three-body problem. We also meet them in the study of Liouville systems and Stackel systems, where the separation of variables plays the important role. All the preceding cases are for conservative systems. In a few books on analytical dynamics we also find the general rules for a change of independent variable in a conservative Lagrangian (Ref. 19). In nonconservative systems (SPS 37-34, Vol. IV, pp. 11-15), we also find changes of independent variables,

for instance in Brown and Shook (Ref. 20), where transformations are made from time to true or eccentric anomaly. We know also another important case in the elliptic restricted three-body problem, with the Nechville transformation (Ref. 21), where a change is made from time to true anomaly. In the treatment of the preceding nonconservative problems, no general rules are used, and the transformations are made in the equations of motion directly.

It is the purpose of this text to show that even for non-conservative systems a general rule can be found for the transformation of the Lagrangian, when a new independent variable is chosen. We do this in the next section. In the two last sections, we apply the theory to the two-body problem and to the elliptic restricted three-body problem.

2. Changes of Independent Variable in a Lagrangian

It is possible to describe in a general way how a change of independent variable affects the Lagrangian and the corresponding equations of motion. In classical dynamics, the Lagrangian is a nonhomogeneous quadratic form in the velocity components dq^i/dt . In order to simplify the writings, we use in this paragraph a few well-known tensor notations, and in particular we take advantage of Einstein's summation convention. The Lagrangian may then be written in the form

$$L\left(q^i, \frac{dq^i}{dt}, t\right) = \frac{1}{2} g_{ij} \frac{dq^i}{dt} \frac{dq^j}{dt} + A_i \frac{dq^i}{dt} + U \quad (1)$$

the g_{ij} , A_i and U being all functions of q^i , t , but not of the velocity components.

We shall now introduce a change of independent variable, from t to s , defined by the differential relation:

$$dt = r(q, s) ds \quad (2)$$

and it is our intention to find what is the new form of the Lagrangian and of the corresponding equations of motion. The original equations of motion are

$$\frac{d}{dt} \left[\frac{\partial L}{\partial (dq^k/dt)} \right] - \frac{\partial L}{\partial q^k} = \frac{d}{dt} \left(g_{kj} \frac{dq^j}{dt} + A_k \right) - \left(\frac{1}{2} \frac{\partial g_{ij}}{\partial q^k} \frac{dq^i}{dt} \frac{dq^j}{dt} + \frac{\partial A_i}{\partial q^k} \frac{dq^i}{dt} + \frac{\partial U}{\partial q^k} \right) = 0 \quad (3)$$

Replacing now in the preceding equations dt by the expression given in Eq. (2) we obtain the new equations

of motion (using from here on a dot to indicate a derivative with respect to s):

$$\frac{d}{ds} \left(g_{kj} \frac{\dot{q}^j}{r} + A_k \right) - \left(\frac{1}{2} \frac{\partial g_{ij}}{\partial q^k} \frac{\dot{q}^i \dot{q}^j}{r} + \frac{\partial A_i}{\partial q^k} \dot{q}^i + r \frac{\partial U}{\partial q^k} \right) = 0 \quad (4)$$

However, we like to write these equations in another form using an expression which is similar to the first expression at the left side of Eq. (3). For this reason we define a new expression L , which is not a Lagrangian, but which we shall call a pseudo-Lagrangian:

$$\bar{L} = r(q^i, s)L(q^i, \dot{q}^i, t) = \frac{1}{2} g_{ij} \frac{\dot{q}^i \dot{q}^j}{r} + A_i \dot{q}^i + rU \quad (5)$$

We have thus replaced in the Lagrangian (1) all the dt 's by rds in order to form s -derivatives instead of t -derivatives, and then we have multiplied it by r . The expression \bar{L} is to be considered as a function of q^i , t and of the s -derivatives \dot{q}^i . Using the partial derivatives of \bar{L} , the equations of motion (4) take the form

$$\frac{d}{ds} \left(\frac{\partial \bar{L}}{\partial \dot{q}^k} \right) - \frac{\partial \bar{L}}{\partial q^k} = W \frac{\partial r}{\partial q^k} \quad (6)$$

where W represents the work function associated with the Lagrangian (1):

$$W = \frac{1}{2} g_{ij} \frac{dq^i}{dt} \frac{dq^j}{dt} - U = \frac{1}{2} g_{ij} \frac{\dot{q}^i \dot{q}^j}{r^2} - U \quad (7)$$

Eq. (6) gives the final form of the equations of motion, using the new independent variable. However, we see that, at the right side, an extra term resembling an external force nonderivable from the pseudo-Lagrangian \bar{L} , has been introduced. We do not have a Lagrangian system generally, after the change of independent variable. However, the simple form of Eq. (6) makes the equations still very attractive for practical derivation of equations of motion. We can see that there are two cases where the Lagrangian form is not lost. First of all, the extra term on the left of Eq. (6) disappears in all cases where r is a function of s only, and not of q^i . This case is met for instance when a transformation is made in the two-body problem from time t to eccentric or true anomaly. Secondly, in conservative systems, where the energy W is constant, the Lagrangian form of the equations of motion can be restored. Define a new Lagrangian (which is not a "pseudo"-Lagrangian here):

$$L^*(q^i, \dot{q}^i, s) = \bar{L} + hr = (L + h)r \quad (8)$$

Then the equations of motion become

$$\frac{d}{ds} \left(\frac{\partial L^*}{\partial \dot{q}^k} \right) - \frac{\partial L^*}{\partial q^k} = 0 \quad (9)$$

and the energy equation may be written in the form

$$\frac{1}{2} g_{ij} \frac{\dot{q}^i \dot{q}^j}{r} - r(U + h) = 0 \quad (10)$$

3. Application to the Three-Dimensional Perturbed Two-Body Problem

The Lagrangian for a perturbed two-body problem is:

$$L = \frac{1}{2} (x_1'^2 + x_2'^2 + x_3'^2) + \frac{M}{r} + U(x_1, x_2, x_3, t) \quad (11)$$

where U is the perturbing function, and where the two first terms are the classical two-body kinetic energy and potential energy terms. The equations of motion derived from the Lagrangian are:

$$x_i'' = -M \frac{x_i}{r^3} - U_i \quad i = 1, 2, 3 \quad (12)$$

We shall indicate a t -derivative by a prime and later on an s -derivative by a dot. To the preceding equations of motion, we associate what we call the two-body or Keplerian energy E (not a constant!):

$$\begin{aligned} E &= \frac{1}{2} (x_1'^2 + x_2'^2 + x_3'^2) - \frac{M}{r} \\ &= E_0 + \int_0^t (x_1' U_1 + x_2' U_2 + x_3' U_3) d\bar{t} \\ &= E_0 + U - \int_0^t \frac{\partial U}{\partial \bar{t}} d\bar{t} \end{aligned} \quad (13)$$

where E_0 is the initial value of the energy E . By differentiating E , we obtain what we shall call the "energy equation"

$$\frac{dE}{dt} = E' = (x_1' U_1 + x_2' U_2 + x_3' U_3) = \frac{dU}{dt} - \frac{\partial U}{\partial t} \quad (14)$$

This equation plays the role of the energy integral in the nonperturbed problem, but here, because of the perturbations, the energy E is variable rather than being a constant of the motion.

Several authors have proposed to change the independent variable in the two-body problem according to the relation

$$dt = rds \quad (15)$$

where s is the new time, replacing t . Let us use the results of the preceding paragraph to transform the Lagrangian: The new pseudo-Lagrangian becomes

$$\bar{L} = rL = \frac{1}{2r} (\dot{x}_1^2 + \dot{x}_2^2 + \dot{x}_3^2) + M + rU \quad (16)$$

while the new equations of motion are

$$\frac{d}{ds} \left(\frac{\partial \bar{L}}{\partial \dot{x}_i} \right) - \left(\frac{\partial \bar{L}}{\partial x_i} \right) = (E - U) \frac{\partial r}{\partial x_i} \quad (17)$$

Developing the partial derivatives, we obtain the final set of differential equations for the two-body problem, having s as independent variable.

$$\begin{aligned} \ddot{x}_i - \frac{\dot{x}_i}{r^2} (x_1 \dot{x}_1 + x_2 \dot{x}_2 + x_3 \dot{x}_3) + M \frac{x_i}{r} &= r^2 U_i \\ \dot{E} &= \dot{x}_1 U_1 + \dot{x}_2 U_2 + \dot{x}_3 U_3 \\ \dot{t} &= r \end{aligned} \quad (18)$$

These equations for the two-body problem have the advantage that when integrated in constant steps Δs , then the pericenter region is traversed with smaller Δt steps, because Δt is proportional to r , according to the last equation. However, these equations may not be called regularized, because the curvature of the trajectory tends to infinity in the pericenter region when the eccentricity tends to 1. This reflects in the equations of motion by the presence of factors such as x_i/r which are undetermined at the singularity and which are a source of numerical difficulties.

However, these difficulties can be avoided if a true regularization is made by a suitable coordinate transformation. As a matter of fact, there exist several coordinate transformations which remove the central collision singularity. We propose here the Levi-Civita variables (or parabolic coordinates). The Levi-Civita variables give only a two-dimensional transformation, but they have been generalized to three dimensions by Stiefel and Kustaanheimo (Ref. 22). We use here this three-dimensional generalization. This is in fact a transformation from the three coordinates (x_1, x_2, x_3) to four new variables u_1, u_2, u_3, u_4 , defined by the relations:

$$\begin{aligned} x_1 &= u_1^2 - u_2^2 - u_3^2 + u_4^2 \\ x_2 &= 2(u_1 u_2 - u_3 u_4) \\ x_3 &= 2(u_1 u_3 + u_2 u_4) \end{aligned} \quad (19)$$

The full description of these new coordinates has been given by Stiefel (Ref. 22).

In order to apply these coordinates to the perturbed two-body problem, we have to make both transformations, for the time t and for the coordinates x_1, x_2, x_3 , in the Lagrangian (Eq. 11), but the order in which we do these two operations is irrelevant. We find the following simple pseudo-Lagrangian:

$$\bar{L} = 2r(\dot{u}_1^2 + \dot{u}_2^2 + \dot{u}_3^2 + \dot{u}_4^2) + M + rU \quad (20)$$

The general equations of motion have a form similar to Eq. (17), and when they are all written out we find:

$$\begin{aligned} \ddot{u}_i + \omega^2 u_i &= \frac{r}{4} U_i \\ \dot{E} &= \dot{u}_1 U_1 + \dot{u}_2 U_2 + \dot{u}_3 U_3 + \dot{u}_4 U_4 \\ \dot{t} &= r \end{aligned} \quad (21)$$

where we have written $2\omega^2 = -E$, and where the U_i are now the partial derivatives of the perturbing function with respect to the regularized variables u_i .

4. Application to the Elliptic Restricted Three-Body Problem

In the preceding paragraph, we have given an application of changes of the independent variable in a nonconservative system, using a function $r(q)$ of the coordinates but not of the new time s . We shall give here another application in a nonconservative system, but where the function $r(s)$ depends only on s , and not on the coordinates: the well-known elliptic restricted three-body problem.

If we refer this problem to an inertial barycentric coordinate system $(\bar{x}, \bar{y}, \bar{z})$, the equations of motion can be derived from the Lagrangian

$$L = \frac{1}{2} (\bar{x}'^2 + \bar{y}'^2 + \bar{z}'^2) + \left(\frac{m_1}{r_1} + \frac{m_2}{r_2} \right) \quad (22)$$

where r_1 and r_2 are two time-dependent functions: the distances from the satellite to both main masses which are supposed to revolve in elliptic orbits around their barycenter. The coordinates of these two masses, at the time $t = 0$ are supposed to be $(m_1 + m_2 = +1)$:

$$\begin{aligned} \bar{x}_1 &= -m_2, & \bar{y}_1 &= 0, & \bar{z}_1 &= 0, \\ \bar{x}_2 &= +m_1, & \bar{y}_2 &= 0, & \bar{z}_2 &= 0. \end{aligned} \quad (23)$$

We shall now refer the problem to a rotating barycentric system, the angular velocity not being constant, but such that the angle v is equal to the true anomaly of the motion of m_1 and m_2 .

The rotation equations are

$$\begin{aligned}\bar{x} &= x \cos v - y \sin v \\ \bar{y} &= x \sin v + y \cos v\end{aligned}\quad (24)$$

In this way, the two masses m_1 , m_2 stay permanently on the moving x -axis at the coordinates

$$\begin{aligned}x_1 &= -m_2 r, & y_1 &= 0, & z_1 &= 0, \\ x_2 &= +m_1 r, & y_2 &= 0, & z_2 &= 0,\end{aligned}\quad (25)$$

where r is the distance between the two bodies m_1 , m_2 on the x -axis. In the (x, y, z) coordinate system, the Lagrangian becomes

$$\begin{aligned}L &= \frac{1}{2}(x'^2 + y'^2 + z'^2) + \frac{1}{2}(x^2 + y^2)v'^2 \\ &+ (xy' - yx')v' + \left(\frac{m_1}{r_1} + \frac{m_2}{r_2}\right)\end{aligned}\quad (26)$$

where v is the true anomaly of the motion of m_1 and m_2 , and where a prime indicates a derivative with respect to t . The distance r being variable, the masses m_1 and m_2 are moving on the x -axis, but with a further coordinate transformation we make the coordinates of m_1 and m_2 constants. We make the coordinate transformation

$$x = r\xi, \quad y = r\eta, \quad z = r\zeta, \quad (27)$$

in order to make the coordinates of m_1 and m_2 constants:

$$\begin{aligned}\xi_1 &= -m_2, & \eta_1 &= 0, & \zeta_1 &= 0, \\ \xi_2 &= +m_1, & \eta_2 &= 0, & \zeta_2 &= 0.\end{aligned}\quad (28)$$

We have now for the distances r_1 , r_2 :

$$\begin{aligned}r_1 &= rs_1, & s_1^2 &= (\xi - \xi_1)^2 + \eta^2 + \zeta^2, \\ r_2 &= rs_2, & s_2^2 &= (\xi - \xi_2)^2 + \eta^2 + \zeta^2.\end{aligned}\quad (29)$$

The Lagrangian of the motion takes the form

$$\begin{aligned}L &= \frac{r^2}{2}(\xi'^2 + \eta'^2 + \zeta'^2) + rr'(\xi\xi' + \eta\eta' + \zeta\zeta') \\ &+ \frac{r'^2}{2}(\xi^2 + \eta^2 + \zeta^2) + \frac{p}{2r^2}(\xi^2 + \eta^2) + (\xi\eta' - \eta\xi')p^{1/2} \\ &+ \frac{1}{r}\left(\frac{m_1}{s_1} + \frac{m_2}{s_2}\right)\end{aligned}\quad (30)$$

where p is the semi-latus rectum for the motion of m_1 and m_2 . This parameter p was introduced in the Lagrangian through the derivative of the true anomaly v :

$$r = \frac{p}{1 + e \cos v}; \quad r^2 \frac{dv}{dt} = p^{3/2}. \quad (31)$$

This last equation suggests that the Lagrangian (30) could be simplified if a change of independent variable is made, using the true anomaly v instead of t as independent variable. This transformation is easy to perform if we use the rules of the preceding Section 2 and the relation (31) between dv and dt . After carrying out the simplifications and dividing the whole Lagrangian by the constant $p^{1/2}$, we obtain

$$L = \frac{1}{2}(\dot{\xi}^2 + \dot{\eta}^2 + \dot{\zeta}^2) + (\dot{\xi}\dot{\eta} - \dot{\eta}\dot{\xi}) + U \quad (32)$$

with

$$U = \frac{1}{2} \frac{r}{p} (\xi^2 + \eta^2 + \zeta^2) - \frac{1}{2} \zeta^2 + \frac{r}{p} \left(\frac{m_1}{s_1} + \frac{m_2}{s_2}\right) \quad (33)$$

The final equations of motion which are in a suitable form for numerical integration are then:

$$\begin{aligned}\ddot{\xi} - 2\dot{\eta} - \frac{r}{p}\xi &= -\frac{r}{p} \left[\frac{m_1(\xi - \xi_1)}{s_1^3} + \frac{m_2(\xi - \xi_2)}{s_2^3} \right] \\ \ddot{\eta} + 2\dot{\xi} - \frac{r}{p}\eta &= -\frac{r}{p} \left(\frac{m_1\eta}{s_1^3} + \frac{m_2\eta}{s_2^3} \right) \\ \ddot{\zeta} + \left(1 - \frac{r}{p}\right)\zeta &= -\frac{r}{p} \left(\frac{m_1\zeta}{s_1^3} + \frac{m_2\zeta}{s_2^3} \right)\end{aligned}\quad (34)$$

It is important to note that we have here a system of differential equations and a Lagrangian, which depends explicitly on the independent variable v , through the factor r/p only. In the circular case this factor becomes equal to unity.

References

1. Sturms, F. M., Jr., and Cutting, E., "Trajectory Analysis of a 1970 Mission to Mercury Via a Close Encounter With Venus," presented at AIAA 2nd Aerospace Sciences Meeting (Paper No. 65-90), New York, N.Y., January 25-27, 1965.
2. Gates, C. R., *A Simplified Model of Midcourse Maneuver Execution Errors*, Technical Report No. 32-504, Jet Propulsion Laboratory, Pasadena, California, October 15, 1963.
3. Kizner, W., *A Method of Describing Miss Distances for Lunar and Interplanetary Trajectories*, External Publication No. 674, Jet Propulsion Laboratory, Pasadena, California, August 1, 1959.
4. Thornton, T. H., "Measuring Flight Time Variations for Lunar and Interplanetary Trajectories," *Research Summary No. 36-13*, pp. 12-15, Jet Propulsion Laboratory, Pasadena, California, March 1, 1962.
5. Elements of *Telstar II* were supplied by the Satellite-Situation Report Section of Goddard Space Flight Center, Greenbelt, Md.
6. *Comet and Close Approach Asteroid Mission Study*, Final Report WDL-TR2366, Vol. 3, Philco Corporation, Palo Alto, California, January 2, 1965.
7. Roberts, D., *A Compendium of Data on Some Periodic Comets*, Report P-9, IIT Research Institute, Chicago, Illinois, July 20, 1964.
8. *Comet Intercept Study*, Final Report NASw-414, 8668-6002-RU-000, Space Technology Laboratories, Inc., Redondo Beach, California, March 28, 1963.
9. Marsden, B. G., "Periodic Comets," *British Astronomical Association Handbook*, p. 57, Burlington House, London, 1963.
10. Porter, J. G., "Reports on the Progress of Astronomy: Comets," *Royal Astronomical Society, Quarterly Journal*, Vol. 2: p. 158, 1961; Vol. 4: p. 310, 1963, Vol. 5: p. 234, 1964.
11. Hudson, R., Nead, M., and Warner, M., *The Orbit Determination Program of the Jet Propulsion Laboratory*, Technical Memorandum 33-168, Jet Propulsion Laboratory, Pasadena, California, March 8, 1964.
12. Roemer, E., *Astronomical Journal*, Vol. 66 (No. 8): pp. 368-371, 1961.
13. Roemer, E., *Comets: Discovery, Orbits, Astrometric Observations*, Reprint 40, U.S. Naval Observatory, Washington, D.C.; reprinted from "The Moon, Meteorites, and Comets," Vol. 4 of *The Solar System*, edited by Middlehurst and Kuiper, University of Chicago Press, Chicago, Illinois, 1963.
14. Roemer, E., *Astronomical Journal*, Vol. 70 (No. 6): pp. 397-400, 1965.
15. Collatz, L., "The Numerical Treatment of Differential Equations," 3rd Ed, p. 181, Springer, 1960.
16. Steffensen, J. F., "On the Problem of Three Bodies in the Plane," *Mat. Fys. Medd. Dan. Vid. Selsk.*, Vol. 31, (No. 3): 1957.

References (Cont'd)

17. Fehlberg, E., *Numerical Integration of Differential Equations by Power Series Expansions, Illustrated by Physical Examples*, TN-D-2356, National Aeronautics and Space Administration, Washington, D.C., October 1964.
18. Deprit, A., and Price, J. F., *The Computation of Characteristic Exponents in the Planar Restricted Problem of Three Bodies*. Boeing Scientific Research Laboratories, Seattle, Washington, 1965.
19. Pars, L. A., *A Treatise on Analytical Dynamics*, John Wiley and Sons, Inc., New York, 1965.
20. Brown, E. W., and Shook, C. A., *Planetary Theory*, Cambridge University Press, Cambridge, 1933.
21. Nechville, V., "Sur une nouvelle forme d'equations differentielles du problème restreint elliptique," *Comptes Rendus*, Vol. 182, pp. 310-311, 1926.
22. Stiefel, E., and Kustaanheimo, P., "Perturbation Theory of Kepler Motion Based on Spinor Regularization," *Journal für reine und angewandte Mathematik*, pp. 204-219, 1964.

II. Deep Space Network System

A. Operational Requirements for a Remote Control Station

W. Wong and K. Heftman

This study on remote control station (RCS) requirements is being carried out by Serendipity Associates, a systems engineering and analysis organization in Chatsworth, California. The study was begun 25 October 1965, and the effort is being conducted according to the plan presented in the contractor report¹.

1. Objectives and Scope

The objectives of this study are twofold: (1) to develop a method which will provide a framework for identifying and evaluating present and potential requirements for the operator in the command/control loop during space flight operations, and (2) to derive a conceptual configuration of equipments and operations which satisfy the operator requirements and which illustrate the application of the study method.

¹Program Plan for a Study to Develop Conceptual Design for Ground Control Station, TR 34-65-23, Contract No. 951313, Serendipity Associates, Chatsworth, California, November 1965.

The control problems of future deep space missions (e.g., *Surveyor*, *Voyager*) are considerably greater than those experienced in previous space flight operations because of: (1) the desire for direct command capability from the Space Flight Operations Facility, (2) the increased quantity of control command, (3) the increased requirement for real time or near-real time control, and (4) the now significant time delay in the control loop.

This study is intended to investigate the implication of these command requirements for SFOF operations, and to arrive at methods and concepts which permit more effective planning and operations to be performed for future missions.

2. Progress

As an initial step in determining control station requirements, candidate missions are being reviewed to define the functional requirements that a generalized spacecraft (object system) would impose on the control station. The object system review partitions the spacecraft system data in a systematic manner to facilitate subsequent identification and analysis of the requirements of the RCS. The space vehicle system is described at increasing levels of

detail by way of block schematic diagrams which represent a configuration of given physical means; i.e., the resources used to accomplish a function or objective.

In the present study, physical means are analyzed to the point necessary to identify the requirements for the supporting system(s). Even when the spacecraft is specified, this method helps to separate the functional demands of the spacecraft on the RCS from those that originate from a particular physical means selection. Just as important, it shows the relative role of commands (from the RCS) in the mission by showing (1) the function they must control and (2) the role of the function in meeting the objective.

Each block schematic diagram has its counterpart in the form of functional flow logic diagrams (FFLD). This functional treatment of the spacecraft system places emphasis on the objectives and the functions necessary for their accomplishment. The function is the process used to reach a specified state.

The representation of the spacecraft in the form of block schematics has been accomplished. Generalization of the spacecraft system in functional terms is currently in progress. A similar process will be followed for the analysis of the RCS requirements during the next report period. The functions required will be developed at successive levels and physical means allocated to them to arrive at the conceptual design configuration.

GUIDANCE AND CONTROL DIVISION

III. Spacecraft Power

A. Thermoelectric Performance Testing

L. Selwitz

Performance testing of thermoelectric modules and generators is being conducted to aid in evaluating the state-of-the-art of thermoelectric power conversion. Tests were initiated with a silicon-germanium (SiGe) thermoelectric module procured from RCA under Contract 951136.

At present, the test facility includes four vacuum test stations, two dual-station monitoring and control centers, and an automatic data readout system which records performance data on an hourly basis. Thermoelectric devices scheduled for testing include a 20-watt high-temperature (1200°C) unit being fabricated by Monsanto Research Corporation under Contract 951426; a 100-watt generator being built by Westinghouse Astronuclear Laboratories under PO CU-388002; and small SNAP-27 type modules currently under negotiation with Minnesota Mining & Manufacturing Company.

The RCA test unit is a water-cooled electrically heated device built around four six-couple silicon-germanium

modules (Fig. 1). The couples are cantilevered, being supported only on the cold side, with the heat transferred by radiation from the electric heater to the face of the hot shoes (Fig. 2).

After 1300 hr of continuous testing, no degradation has been observed in performance. Operating with the hot junction at 900°C and the cold junction at 150°C, the test device is producing 24 watts and 4.2 volts with a matched load. The recorded open-circuit voltage coincides exactly with the calculated value obtained from the Seebeck characteristic curve for doped silicon-germanium thermoelectric material.

The measured internal resistance of the device is approximately 30% above the calculated resistance for the silicon-germanium couples in this generator, indicating the presence of a significant contribution to the electrical resistivity by other components, such as hot and cold shoes, electrical connectors, and expansion compensators. Thus, sizing calculations for silicon-germanium thermoelectric generators must include a secondary resistance factor in order to accurately determine the number of thermoelectric couples and the element geometry necessary to produce a given power output.

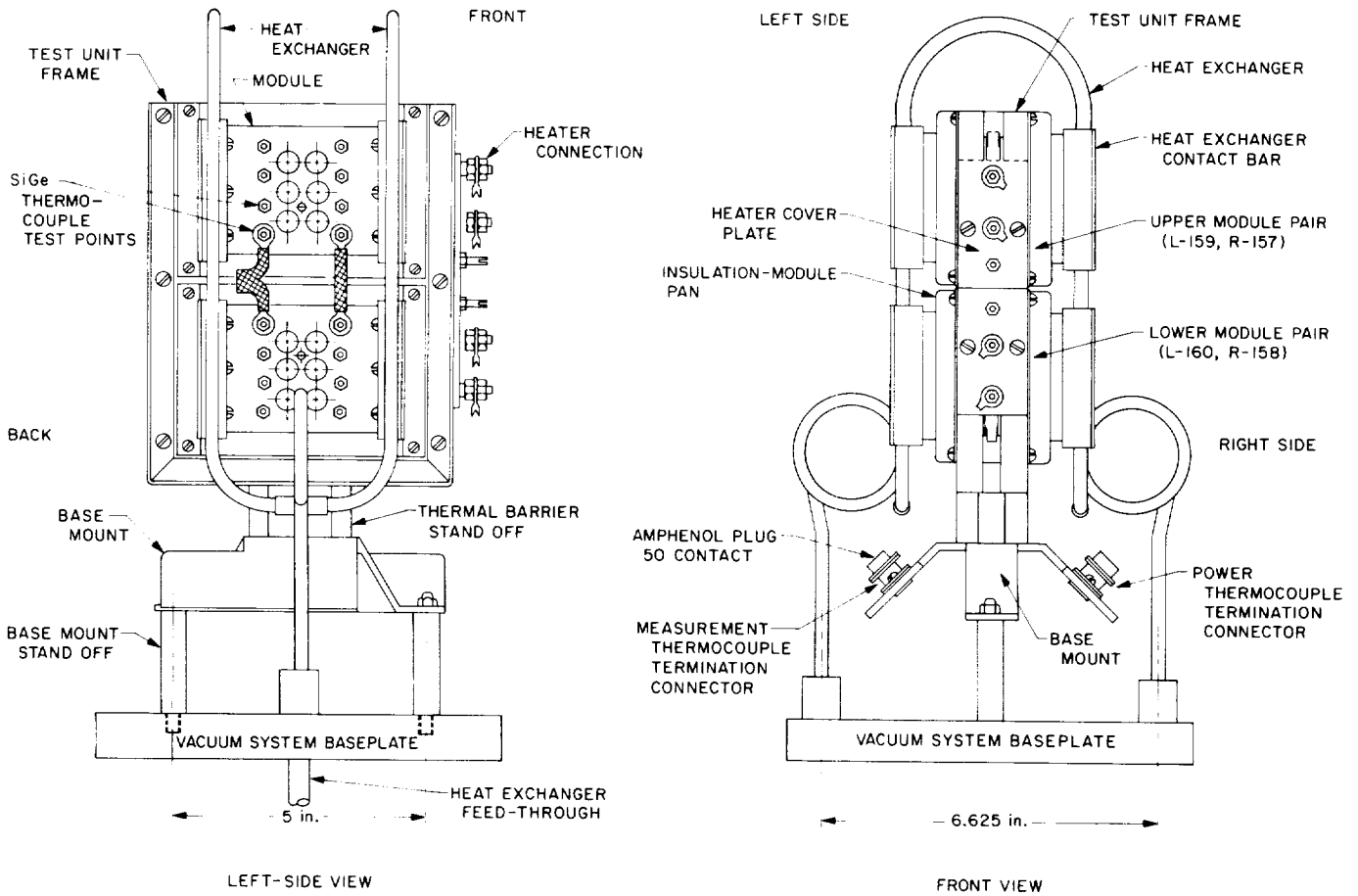


Fig. 1. Thermoelectric module test unit assembly

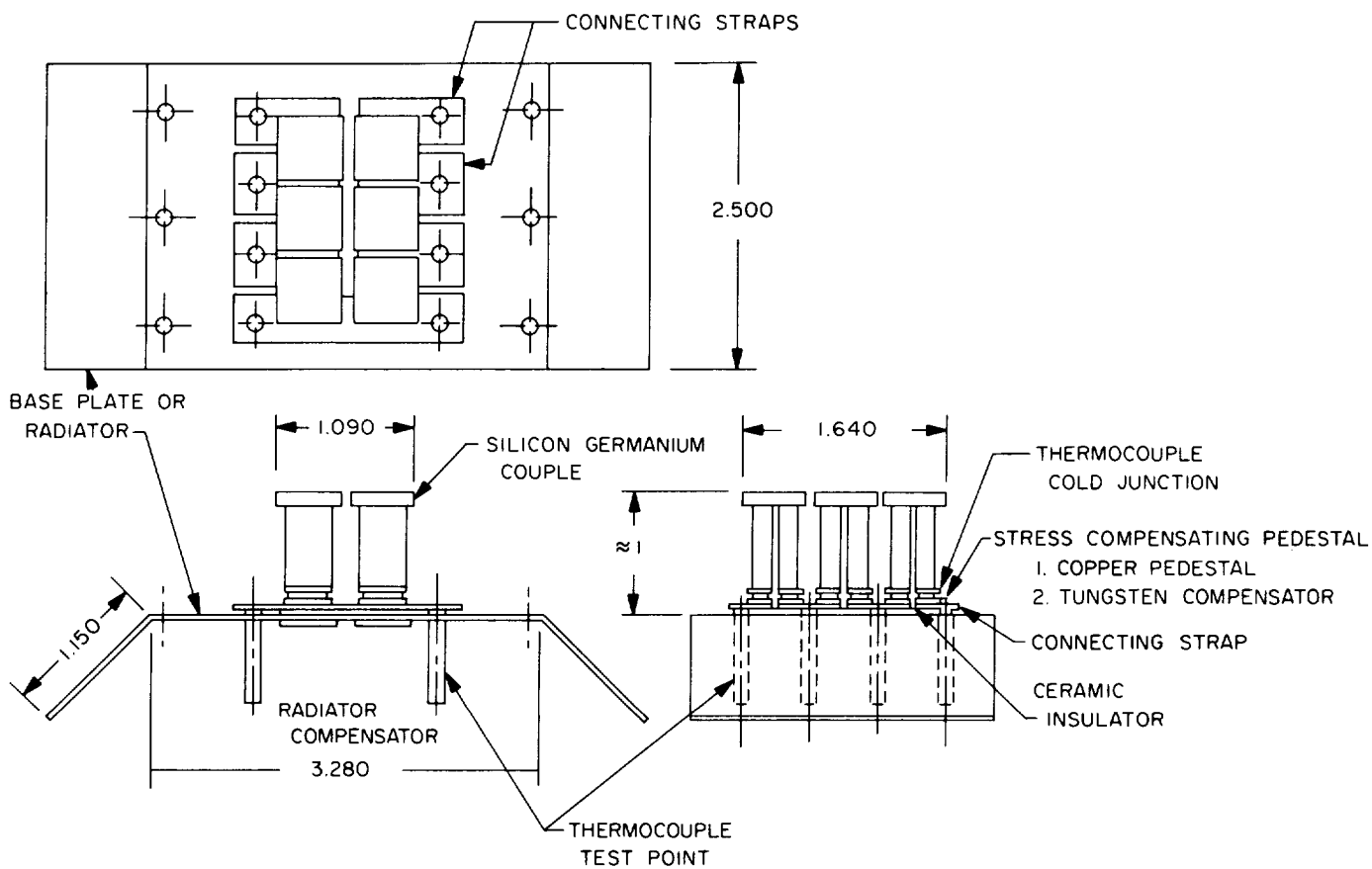


Fig. 2. Modified six-couple thermoelectric power module structure

IV. Spacecraft Control

A. Solid Propellant Electrical Thruster

G. S. Perkins

A contract was established between General Electric/MSD Spacecraft Department and JPL for the study of the application of a solid propellant electrical thruster (SPET) to a JPL space mission. The thruster can be used for spacecraft attitude control actuation. The study is now complete, and a final report was submitted to JPL by GE (Ref. 1).

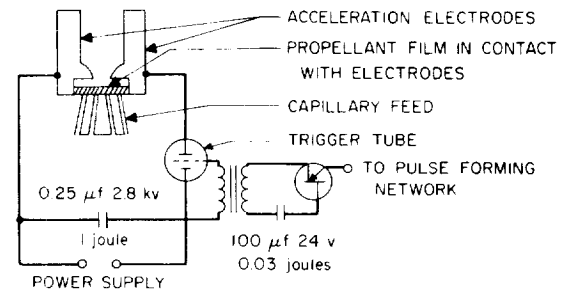
The SPET concept is a simple one. Fuel is retained in capillary fashion and is wick-fed to a trough between two accelerating electrodes. Current, stored in a capacitor, is then discharged through the fuel. The accompanying diagrams (Fig. 1) show two electronic firing configurations.

The points which were to be carefully discussed in the GE report for JPL to make a good objective evaluation of the SPET system are the following: (1) specific impulse, (2) pulse repetition rate capability, (3) impulse per pulse, (4) power profile per pulse, and (5) reliability.

The following is data preliminary to the report: (1) The SPET motor is capable of more than 10^6 pulses without

reduced performance. (2) The impulse per pulse is scalable at the rate of 5×10^{-4} lb-sec/joule. (3) The mass expulsion frontal velocity is 4×10^6 cm/sec; this value is the result of laboratory measurement; it occurs with a specific impulse of 4000 sec, with a power demand of

(a) COLD CATHODE TRIGGER TUBE CIRCUIT



(b) CIRCUIT ELIMINATING TRIGGER TUBE

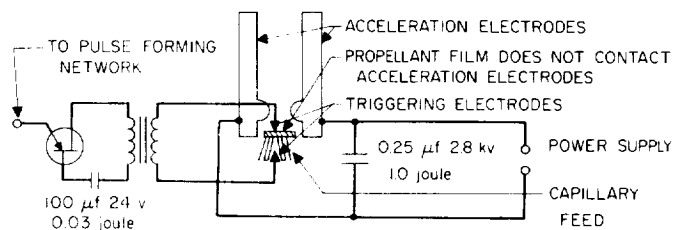


Fig. 1. Electronic configurations for firing SPET motor

1 joule. (4) A spacecraft attitude control system using the SPET will not require a central fuel storage and distribution system; the SPET system is capable of redundancy by having multiple thrusters on the same fuel capillary. (5) The analytical study by GE in determining the optimum fuel produced the following desired characteristics: Low viscosity (liquid), low vapor pressure, wetting characteristics leading to capillary flow, low ionization potential, low residues after discharge, controllable electrical conductivity, low separation on standing, low freezing point, and low handling hazard.

The fuel selected is phosphonitrilic iron chloride. It is a high-temperature synthetic lubricant developed by DuPont Research for high-temperature gyroscope spin bearings. This fluid has the closest conformity to the requirements of any evaluated.

Its bulk vapor pressure at standard temperature is 10^{-5} Torr. The thin-film vapor pressure, which is the way the fuel will be used, is expected to be much less although this has not been measured. The fuel viscosity is 25 centistokes; its specific gravity is 2.0. There is a residue after discharge from this fuel, it appears to be amorphous crystalline iron and phosphorous solids. It is not thought to be a problem, however, because it leaves the motor with a velocity of 4×10^3 cm/sec and does not plume. The contaminant dispersion at a distance of 2 ft is approximately 1-ft diameter and is only visible on the top surface of the vacuum belljar, the direction the motor is test-fired, after many hours of pulsing the motor. This residue is now being analyzed.

There are two electronic firing configurations possible for the SPET motor (Fig. 1). The first, the one in common use, makes use of a cold cathode trigger tube. This firing scheme has two problems: (1) The use of the switching tube adds to the resistance and inductance of the circuit requiring power. (2) The tubes available are not able to handle the large currents and rapid current rise of the SPET; as a consequence their life is shortened; GE has a SPET switching tube currently under development that will tolerate this load demand and will not be subject to breakdown.

The second circuit (Fig. 1) eliminates the trigger tube by applying the same small energy pulse, which previously went to the grid of the switching tube, across two small triggering electrodes in contact with the propellant film. This causes the propellant to vaporize in a small amount which is sufficient to switch the main discharge across the exploding accelerating electrodes. This mode

of firing greatly increases the efficiency of the engine. There is one problem involved with this mode of firing. After about 200,000 pulses, the contaminant residue from the fuel builds up on the primary electrodes causing a general deterioration of motor efficiency. Continued firing leads to motor shorting. This phenomenon does not occur with the trigger tube configuration of firing.

B. Sterilization of Capsule Control Systems

R. J. Mankovitz

1. Introduction

Capsule control system components can be broadly placed into five categories: (1) Actuators, e.g., stepping motors and valves; (2) celestial sensors, e.g., photo-cathode image dissectors; (3) inertial sensors, e.g., gyros and accelerometers; (4) Sun sensors, e.g., photoconductive detectors; (5) control electronics, e.g., servoamplifiers and switching logic. In addition to assessing the effects of sterilization on these five categories, one must also evaluate the compatibility of the system functional test requirements with system sterilization techniques.

The discussion below indicates the problems anticipated in the sterilization of control electronics, and the steps being taken to ensure meeting the time-temperature cycle goal of 145°C for 36 hr in 3 cycles. The problem of system functional compatibility with the sterilization tests has also been investigated.

2. Control System Electronics

An electronic component sterilization test program has been initiated to determine the parts capable of withstanding several 36-hr periods of non-operational storage at 145°C without significant degradation. Preliminary results indicate that a major problem area may be large-value electrolytic capacitors. Presently, solid and foil tantalum units, with ratings up to 47 μ f, 35 v have been tested successfully.

Capacitors used in the attitude control system for timing applications (e.g., the roll search inhibit circuit uses 270- μ f 15-v units), derived rate feedback (540 μ f, 10 v), and gyro loop feedback (four 1020- μ f 20-v units per loop)

require the use of wet-slug and -foil type capacitors. It is believed unlikely that these types will survive; however, no tests have been conducted on these units. Anticipating failure of the units, alternate circuit mechanizations that do not require these units were investigated.

a. Timing circuits. Fig. 2 shows the mechanization for a timing circuit yielding time intervals up to 100 sec using a 2- μ f capacitor. The circuit is basically a digital counter (100) operating from a 1 pps source. The pulse source could be a unijunction oscillator, or it may originate from the CC&S clock. The counting is accomplished by two ($\div 10$) microelectronic counters, serially coupled through a "nand" gate. Any number of counters can be connected serially, with the output of the n th counter yielding a pulse every 10^n seconds. Outputs can be obtained at any count by merely connecting "nand" gates to the proper Z outputs (see table of output states in Fig. 2). To assign a figure of merit to the circuit for its ability to decrease the size of the timing capacitor, it is apparent that the counter decreases the R-C time constant

equivalent, by the number of counter stages (e.g., 100 in this case). The size of each ($\div 10$) counter is the same as a single TO-5 transistor case, and they have a non-operating temperature range to 150°C. It is interesting to note that a single-pulse generator (and hence capacitor) can be used to operate many counter circuits, each controlled by a separate gate. With the pulse generator free-running, the maximum error in the count is 1 sec. Due to the high reliability of silicon semiconductors, the reliability of this type of timing circuit may be considerably greater than the conventional R-C circuit.

b. Derived-rate circuit. Fig. 3 shows the mechanization for a derived rate circuit yielding charge-discharge time constants of about 100 sec. To decrease the capacitance necessary for D/R feedback, an active integrator, using a micro-electronic operational amplifier, is used. Circuit operation is as follows: Assume the switching amplifier (+) output is energized due to a position error signal. A voltage (e_1) appears as an input to the integrator. As the integrator output begins to ramp, the high-gain feedback

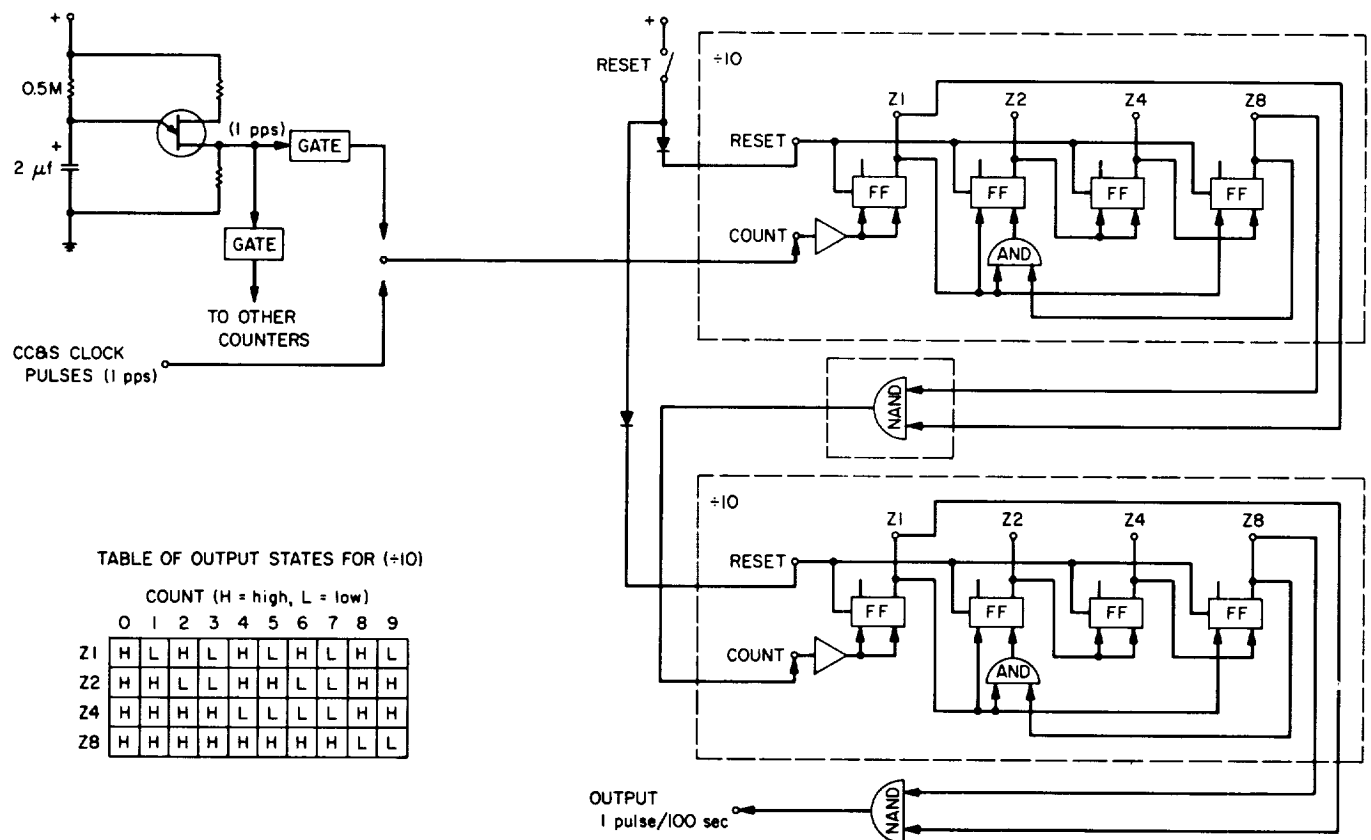


Fig. 2. Timing circuit mechanization

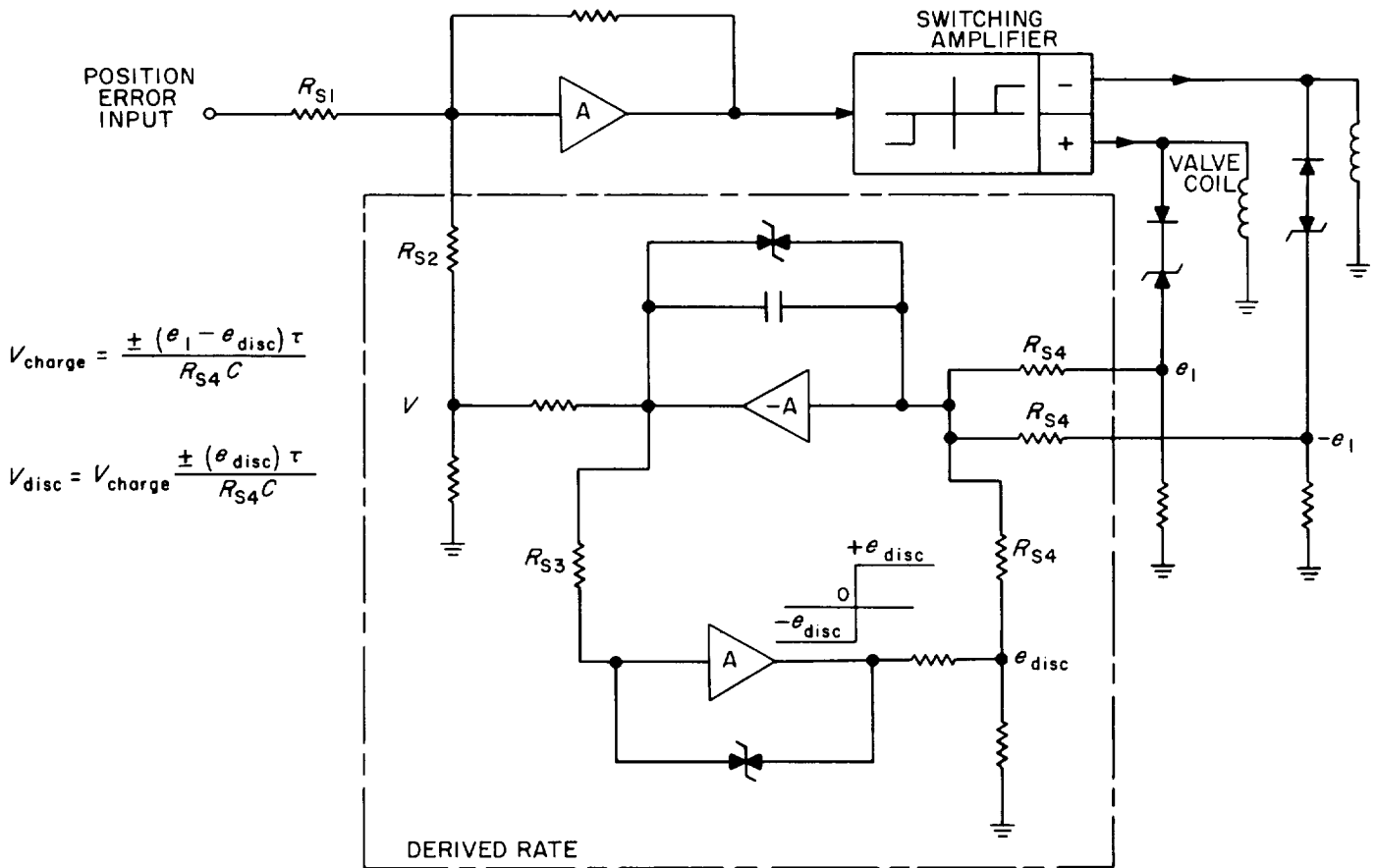


Fig. 3. Derived rate mechanization

amplifier saturates, generating $(-e_{disc})$ as a second integrator input. The voltage (V_{charge}) which is summed with the position error signal, is hence

$$V_{charge} = \left[\frac{-(e_1 - e_{disc}) t}{R_{S4} C} \right] \quad (1)$$

When the switching amplifier goes off, (e_1) is zero and the voltage

$$V_{disc} = \left[V_{charge} \mp \frac{(e_{disc}) t}{R_{S4} C} \right] \quad (2)$$

It appears that the discharge time constant is the determining factor in choosing D/R feedback networks; hence to assign a figure of merit to this circuit, Eq. (2) must be compared with that of an ordinary $R-C$ circuit. For an $R-C$ circuit:

$$V_{disc} = V_{charge} (e^{-t/RC}) \quad (3)$$

expanding $e^{-t/RC}$ for $T < RC$ yields

$$V_{disc} = V_{charge} - \left(\frac{t V_{charge}}{RC} \right) \quad (4)$$

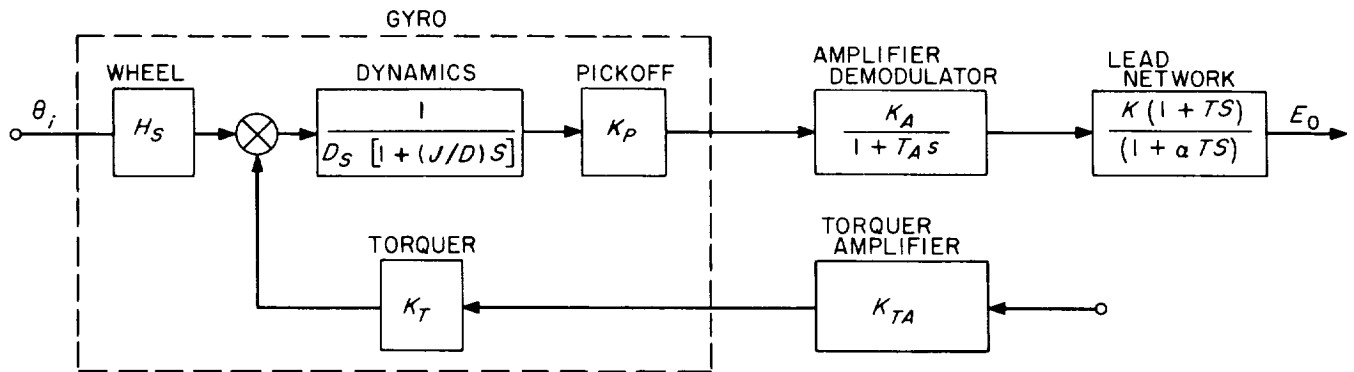
Comparing Eqs. (2) and (4), it is apparent that (V_{charge}/e_{disc}) represents the capacitor reduction factor. If (e_{disc}) is equal to $0.05 V_{charge}$, for example, the D/R capacitor can be reduced by twenty, yielding $27 \mu f$ instead of $540 \mu f$ for the $R-C$ case. Although $27 \mu f$ is not a small value, it does allow the use of non wet-slug type capacitors for this application.

The zener diodes in series with the switching amplifier outputs prevent transistor switch leakage from appearing as an input to the integrator in the "off" condition.

The high-gain feedback loop around the integrator prevents drift (which could be considerable over long time periods) due to noise or offset voltages. The circuit is essentially locked to zero. The small size and high reliability of microelectronic analog circuits makes them ideal for this application. The units have been stored at temperatures to $150^\circ C$.

c. Gyro rate + position circuit. Fig. 4 shows the mechanization for a rate-plus-position gyro circuit which can

(a) POSITION GYRO WITH LEAD NETWORK



(b) LEAD NETWORK

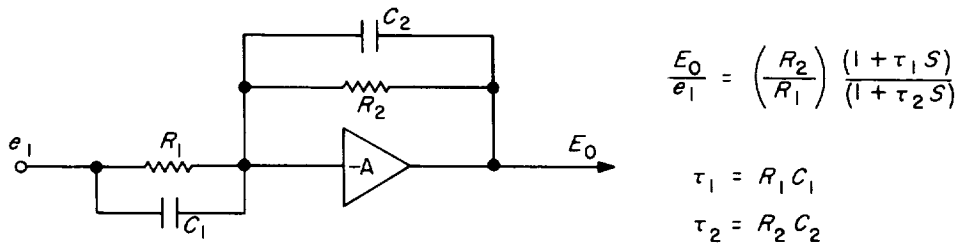


Fig. 4. Gyro rate plus position circuit

be used to eliminate large feedback capacitors. The approach used in the past was that of feeding back a current to the torquer through a series capacitor. This closed-loop system requires large capacitance values (4080 μ f), which, in addition to the sterilization problem, requires large volumes, and degrades the accuracy of the system (due to leakage currents).

The circuit shown in Fig. 4 uses a wide-angle gyro in an open-loop position feedback configuration, with the output passed through a lead-lag network. To assign a figure of merit to this circuit for decreasing the value of capacitance, let us examine a typical active lead-lag network (Fig. 4). Investigation of previous systems indicates that a lead time constant (τ_1) of 10 sec is typical. Assuming (R_1) and (R_2) are 500K resistors, and a lead-lag ratio of 10 is desired, the values for (C_1) and (C_2) are 20 μ f and 2 μ f, respectively. Comparing this with the 4080 μ f for closed-loop systems, it is evident that a reduction factor of 200 is possible with this mechanization. It is planned to breadboard these circuits and subject them to functional and sterilization testing.

3. Overall System Testing

Based on system reliability considerations, a decision can be made for employing subsystem tests only, based on a high confidence level, rather than system-level testing of critical functions after entire system sterilization. If post-sterilization testing is considered, methods for minimizing degradation of sterilization must be considered.

a. Testing: reliability considerations. Assuming each subassembly (e.g., gyro package, optical sensors, electronics, and gas system) has been thoroughly post-sterilization tested at its own level, using both actual and simulated inputs and loads, there still remains one basic flaw in not post-sterilization testing the assembled system. The weak links are the interface connections between the individual subassemblies and between the control system and other systems (e.g., power, CC&S). To preserve overall capsule reliability, verification of the interfacial integrity is imperative. Therefore, the critical functions to be post-sterilization tested are those which maximize the verification of the interfaces. For example, a function which would not be tested is one where the input and

output are monitored in the same subassembly (e.g., apply an input to a switching amplifier and monitor its output). A function, such as generating a signal in a star sensor and monitoring valve current would be a valid post-sterilization test, since it verifies many interface connections.

A separate "test" connector should be provided on the capsule to allow the application of inputs and power, and the monitoring of outputs. Those assemblies which may be damaged if operated (e.g., Canopus sensor) should have the capability of having a signal injected from the "test" connector into the unit, passing through the same interface connections as the actual signal.

As the capsule system is defined in detail, analyses will be conducted to determine the minimum number of post-sterilization tests required to verify all interface connections.

b. Testing: sterilization considerations. To facilitate post-sterilization testing without degrading the sterilization effectiveness, the following test methods are suggested. The capsule will be sterilized in an oven in a bio-clean area. The test equipment will not be sterilized and is located outside of this area. All connections to the capsule are made through hermetically sealed connectors.

The test equipment itself is automated to the point where only a "start button" need be pressed, and the equipment performs all tests sequentially. The results will be permanently recorded on an oscillograph. This method allows the entire test sequence to be performed by a single technician from inside the bio-clean area. The capsule is never exposed to the unsterilized test equipment.

Methods for implementing automated (and possibly remotely programmable) test equipment will be investigated with the aid of industry.

With regard to system sterilization, although the goal is to have all subsystems pass the time-temperature cycle of 145° C for 36 hr in 3 cycles, thus enabling the entire system to undergo this same cycle, it is possible that certain subsystems will not be able to survive this test.

Table 1 is a list of sterilization cycles approved by NASA, any one of which can be used for a single mission. If it is determined that a subsystem cannot survive the high-temperature cycle goal, it would be possible to use any of the other cycles for both the subsystem and overall system tests.

Table 1. Approved sterilization cycles

Temperature, °C	Sterilization time, hr
135	22
130	34
125	53
120	84
115	132
110	210
105	336

It should be noted, however, that while hardware can pass the high-temperature cycle goal, it is not necessarily true that they will survive the lower-temperature longer-time cycles. Since the failure mechanisms of certain components may be more time-dependent than temperature-dependent, all qualified hardware should be subjected to *both* cycle extremes to ensure system success.

C. Horizon Scan Platform System

T. Kerner

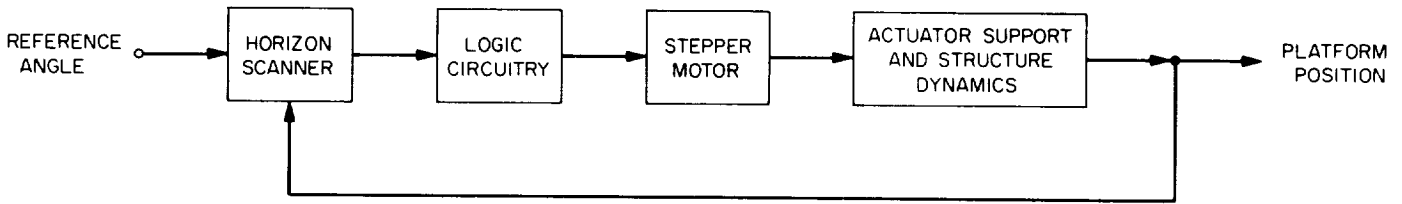
1. Introduction

A summary of the work done on the horizon scan platform system subsequent to the report in *SPS 37-35*, Vol. IV, pp. 33-35 is presented herein. Analog computer runs simulating a stepper motor-driven platform have been made; some of the results are shown here. Work has been done in exploring methods of platform erection. On the premise that the platform system has three degrees of freedom, with tracking being performed about one axis, criteria have been established for the maximum excursions experienced about the tracking axis as a function of the orbit and of the time spent in orbit.

2. Analog Simulations

Fig. 5 shows both the functional and the analytical block diagram of the system that was simulated on the analog computer. In Fig. 5(a), the horizon scanner output is processed by logic circuitry. The presence or absence of an error signal and the polarity thereof is sensed for each scan period. The logic circuitry output is fed into a stepper motor, with the motor being driven one step per

(a) FUNCTIONAL BLOCK DIAGRAM



(b) ANALYTIC BLOCK DIAGRAM

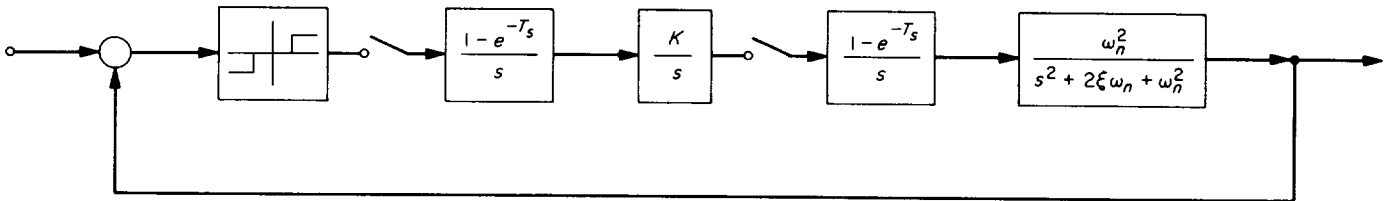


Fig. 5. Logical circuitry for stepper motor-driven platform

scan in a direction dictated by the polarity of the error signal. The stepper motor drives the actuator support and the structure dynamics of the platform. In Fig. 5(b), the horizon scanner is represented as a nonlinear transfer block with a deadband and a saturated amplitude output. This is fed, through a sampler, into a zero-order hold circuit. The stepper motor is represented by an integrator, a sampler, and a zero-order hold. The platform is represented by a second-order system transfer function.

A parametric study of the effects of the structural characteristic variations on the system performance was made. Both the resonant frequency and the damping ratio of the platform were varied. Fig. 6 shows the results of a typical run on the analog computer. Shown is the platform response to an angular planet rate of $0.2^\circ/\text{sec}$. The stepper motor output shaft monitored and recorded in Fig. 6(a) shows the step-like response. Because the tracking rate commanded Fig. 6(b), is one-half of the maximum capability of the system ($0.4^\circ/\text{sec}$), as expected it can be seen that the motor turns over once per every two periods, on the average. The actual platform position is shown in Fig. 6(c). Fig. 6(d) shows that the system operates at an approximate steady-state position error of 0.66 . For this particular run, the platform was considered to have a resonant frequency of 62.8 radians and a damping ratio of $\xi = 0.07$.

Fig. 7 is a phase plane diagram for the same set of parameters. It shows how given a positional offset, the system responds in reaching its steady-state position. The

vertical axis corresponds to the velocity, and the horizontal axis to the position of the platform. The system, as seen in Fig. 7, is stable.

3. Deployment Mode

The relative merits of a three-degree versus a two-degree of freedom platform system was investigated. The three-degree of freedom system would be controlled by the central computer and sequencer (CC&S) in two axes. The CC&S would command the platform to be erected into a plane perpendicular to the plane of the orbit. The sensor would control the remaining axis with the planet local vertical being tracked about it. One advantage of this system over the two-degrees of freedom system lies in the slit-like field of view required for the scanner versus a conical field of view required with the two-degrees of freedom. Another advantage lies in the fact that a three-degrees of freedom system would be mechanized so that the two CC&S controlled axes would be updated infrequently; a failure in any one of these two axes would be tolerable and could be updated by ground command easily. A two-degree of freedom system would require larger excursions around each axis and thus make a failure less tolerable.

Fig. 8(a, b) shows the scan platform deployment sequence. In the stowed position, the platform (*pl*) subsystem reference coordinates, $Roll_{pl}$, Yaw_{pl} , and $Pitch_{pl}$, are lined up with the spacecraft (*sc*) coordinate system, $Roll_{sc}$, Yaw_{sc} , and $Pitch_{sc}$. As shown in Fig. 8(a), the first

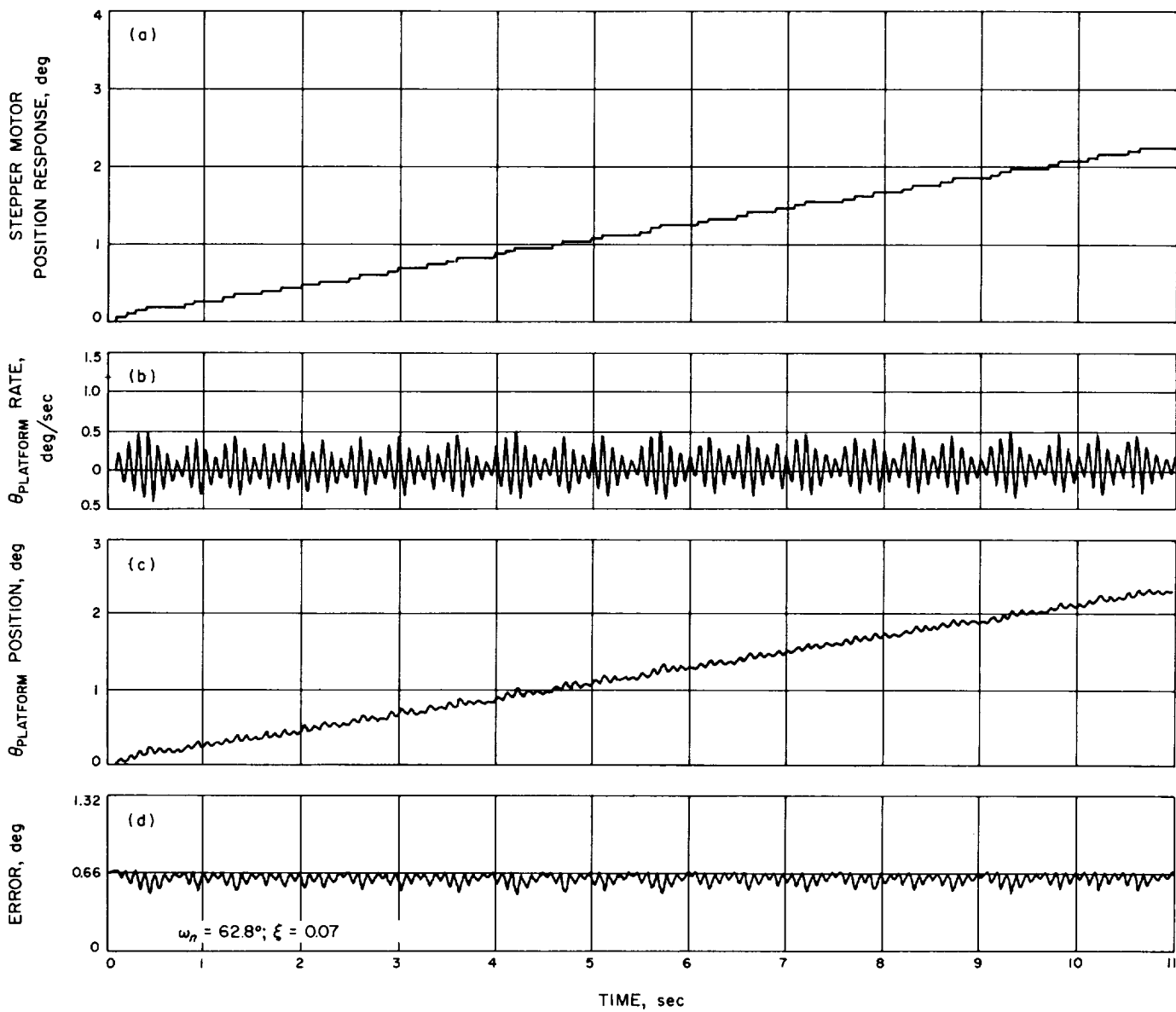


Fig. 6. Effects of variations in structural characteristics on system performance

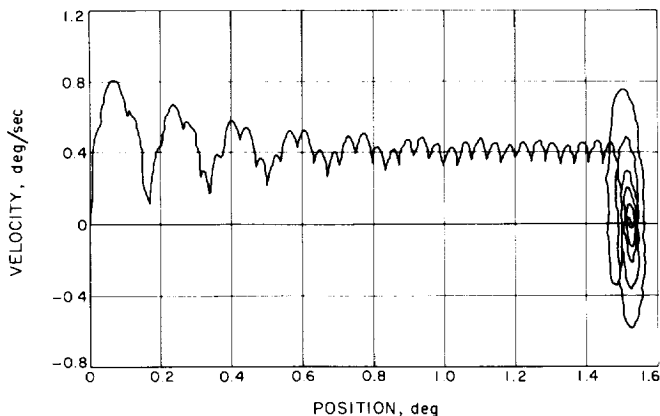


Fig. 7. Scan platform phase plane diagram

step in the deployment sequence is to rotate the scan platform subsystem about the $Pitch_{sc}$ axis by an angle θ such that $Roll_{pl}$ is in the plane of the orbit. Next the subsystem is rotated about the $Roll_{pl}$ axis by an angle ϕ such that Yaw_{pl} is perpendicular to the plane orbit.

Fig. 8(c) shows the platform coordinate orientation with respect to the spacecraft coordinates. The horizon scanner causes the $Pitch_{pl}$ axis to rotate about the Yaw_{pl} axis. The orientation of the $Roll_{pl}$ and Yaw_{pl} axes will be updated by CC&S as needed, depending upon the orbit characteristics.

During an orbital mission, tracking is normally performed as the orbiter moves from the morning terminator to the evening terminator, the scan platform is then reset to a position appropriate to the commencement of scanning on the following day. The following mathematical development results in an expression relating the angles θ and ϕ through which the two CC&S controlled axes are commanded to the angle γ , which is the angle by which the platform has rotated about the Yaw_{pl} axis so as to point at the local vertical located at the terminator.

With reference to Fig. 8(a, b, c), rotation about the $Pitch_{sc}$ axis by an angle θ

$$\begin{vmatrix} Pitch_{sc} \\ Yaw_{sc} \\ Roll_{pl} \end{vmatrix} = \begin{vmatrix} 1 & 0 & 0 \\ 0 & \cos \theta & \sin \theta \\ 0 & -\sin \theta & \cos \theta \end{vmatrix} \begin{vmatrix} Pitch_{sc} \\ Yaw_{sc} \\ Roll_{sc} \end{vmatrix}$$

Rotation about the $Roll_{pl}$ axis by angle ϕ

$$\begin{vmatrix} Pitch_{pl} \\ Yaw_{pl} \\ Roll_{pl} \end{vmatrix} = \begin{vmatrix} \cos \phi & -\sin \phi & 0 \\ \sin \phi & \cos \phi & 0 \\ 0 & 0 & 1 \end{vmatrix} \begin{vmatrix} Pitch_{sc} \\ Yaw_{sc} \\ Roll_{pl} \end{vmatrix}$$

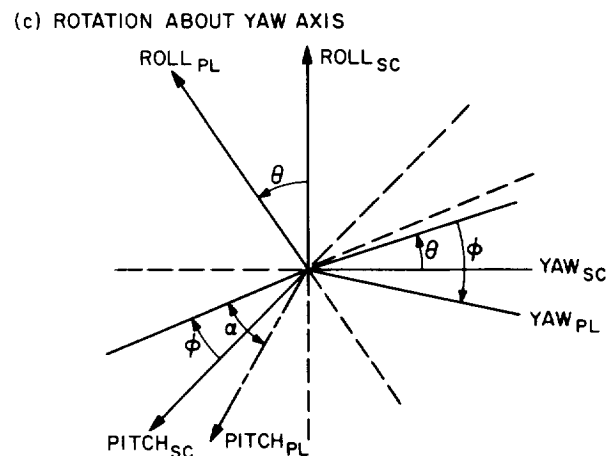
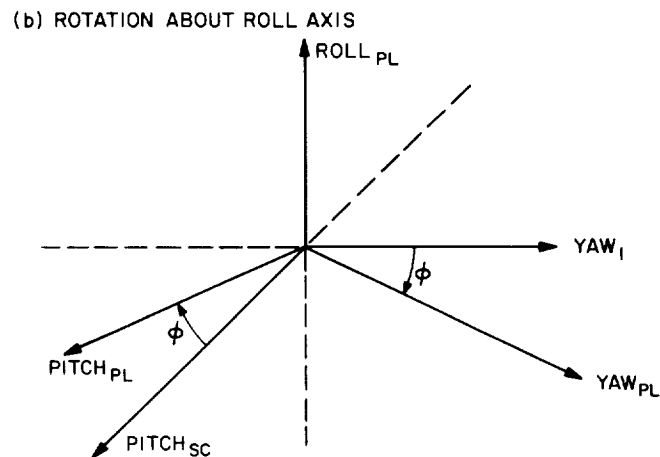
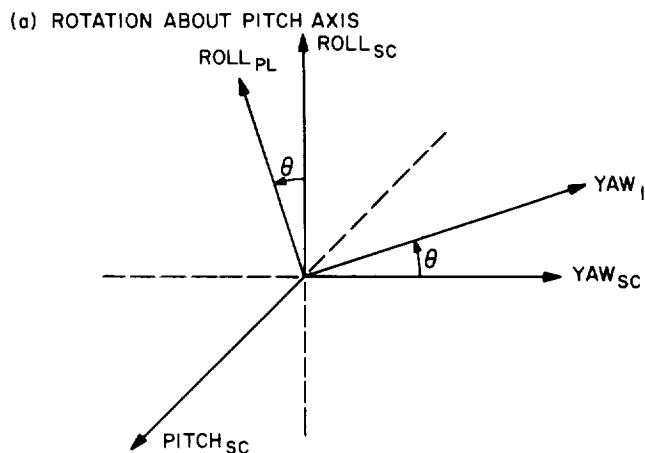


Fig. 8. Scan platform deployment sequence

Tracking in the $Pitch_{pl}$ axis by an angle γ

$$Pitch_{pl, track} = Pitch_{pl} \cos \gamma - Roll_{pl} \sin \gamma$$

When pointing at the terminator $Pitch_{pl, track}$ has no $Roll_{sc}$ component since it is parallel to the $Pitch_{sc} Yaw_{sc}$ plane.

Combining the above matrices

$$\begin{vmatrix} Pitch_{pt} \\ Yaw_{pt} \\ Roll_{pt} \end{vmatrix} = \begin{vmatrix} \cos \phi & -\sin \phi \cos \theta & -\sin \phi \sin \theta \\ \sin \phi & \cos \phi \cos \theta & \cos \phi \sin \theta \\ 0 & -\sin \theta & \cos \theta \end{vmatrix} \begin{vmatrix} Pitch_{sc} \\ Yaw_{sc} \\ Roll_{sc} \end{vmatrix}$$

or

$$Pitch_{pt} = Pitch_{sc} \cos \phi - Yaw_{sc} \sin \phi \cos \theta - Roll_{sc} \sin \phi \sin \theta$$

$$Roll_{pt} = -Yaw_{sc} \sin \theta + Roll_{sc} \cos \theta$$

$$\begin{aligned} Pitch_{pt, track} &= Pitch_{sc} \cos \phi \cos \gamma - Yaw_{sc} \sin \phi \cos \theta \cos \gamma \\ &\quad - Roll_{sc} \sin \phi \sin \theta \cos \gamma + Yaw_{sc} \sin \theta \sin \gamma \\ &\quad - Roll_{sc} \cos \theta \sin \gamma \end{aligned}$$

Since the $Roll_{sc}$ component must be zero when viewing the terminator

$$\sin \phi \sin \theta \cos \gamma = -\cos \theta \sin \gamma$$

or

$$\tan \gamma = -\sin \phi \tan \theta \quad (1)$$

If the angles ϕ and θ are known, the shift in the 180 deg of motion necessary to track from the morning to the evening terminator could be derived from Eq. (1). If mechanical stops were to be used to recycle the platform at the end of each day, Eq. (1) would define the limit on its placement.

D. Antenna Pointing Study

G. Fleischer and J. C. Nicklas

1. Introduction

It is apparent that the use of high-gain directive antennas on the spacecraft is most beneficial in improving telecommunication system performance. However, if the increased gain and accompanying information rate improvement are to be realized, the directivity of the antenna must be controlled accurately, perhaps in the region of 0.5 to 2 deg of pointing error.

Proposals for spacecraft high-gain antenna pointing systems have generally begun by considering a one- or two-degree of freedom, servoactuated antenna whose

position is controlled by a preselected program generated by the on-board computer. This choice stems from the standpoints of proven feasibility, simplicity, relatively small design effort, and past experience. However, the ultimate accuracy offered by programmed pointing is open to question. Further, the problems of calibrating and compensating such an open-loop system for static and thermal structural errors have not been resolved. In the event that some auxiliary system such as an RF or optical Earth link is used as a fine-pointing method, what are the results in terms of system reliability, weight, power requirements, and flexibility?

2. Study Objectives

The objectives of this study are to examine the programmed pointing system in detail, to determine its ultimate accuracy as a function of system complexity, and to further determine accuracy versus complexity for the programmed system in combination with a closed-loop optical or RF system.

As a result, a mathematical model should be developed which is capable of (1) incorporating all pointing system and spacecraft component contributions to pointing error, (2) accepting as inputs the selected trajectories, i.e., Earth cone and clock angle tables, and (3) providing as an output a measure of total system pointing error. The error may be viewed as a time function or simply in terms of the maximum to be expected for the system and trajectory chosen.

Evaluation of the corresponding complexity of a particular pointing system mechanization may be a significant

problem. A method of weighing the several contributing factors appears to be a reasonable procedure for obtaining quantitative information. Complexity factors include system weight, calibration and checkout requirements, relative reliability, and power requirements.

The relative merits of the various systems with regard to ground control capabilities, adaptability to nonstandard trajectories, and sensitivity to reference body geometries will be closely examined. Trajectory selections will be made from Mars '71 or '73 and Jupiter '74 or '75 opportunities in the form of Earth cone-clock angle tables.

3. Study Outline

A tentative outline for pointing system investigations is listed in Table 2. Currently, work is progressing on an examination of the one-degree of freedom positioning

Table 2. Antenna pointing study

<ol style="list-style-type: none"> 1. Programmed pointing <ol style="list-style-type: none"> a. Selected trajectories, Earth cone-clock profiles b. One-degree of freedom antenna positioning <ol style="list-style-type: none"> (1) Optimum hinge-axis location (2) Pointing errors due to discrete hinge angle rotations c. Two-degree of freedom antenna positioning <ol style="list-style-type: none"> (1) Gimballed axes (2) Hinge angle with roll angle degree-of-freedom d. Central computer mechanization complexities <ol style="list-style-type: none"> (1) Timer-oriented computer (2) Memory-oriented computer (3) Ground command capabilities 2. Effects of attitude control errors <ol style="list-style-type: none"> a. Pitch, yaw, and roll deadband error contributions b. Sensor and amplifier null offset errors c. Stored program pointing with attitude sensor error signal corrections <ol style="list-style-type: none"> (1) Mechanizations (2) Error improvement versus added complexity 3. Antenna servo errors <ol style="list-style-type: none"> a. Servo tracking and deadband errors b. Gear train errors c. Mounting errors 4. Spacecraft and antenna structural misalignments <ol style="list-style-type: none"> a. Static errors b. Thermally generated errors 5. Programmed coarse pointing with RF fine pointing 6. Programmed coarse pointing with optical fine pointing 7. Summary of pointing error versus complexity for several pointing systems

system. This being the most simple of the antenna directing systems, the question of what its ultimate capabilities are should be answered. More specifically, what does the single-degree of freedom system cost in terms of pointing accuracy in exchange for its simplicity? Assuming a structurally and mechanically perfect pointing device and a perfectly attitude-controlled spacecraft, the only pointing errors would be due to the geometry involved and the discrete nature of the pointing program. The geometry of the situation is depicted in Fig. 9.

The right-handed cartesian coordinate system, $L-M-N$ is used as the set of reference axes. This is the familiar spacecraft-centered cone-clock coordinate system, where ON is the Sun line and the $L-N$ plane contains the probe-Canopus pointing vector, C . Since the craft is perfectly aligned in attitude, its $X-Y-Z$ system coincides with $L-M-N$. Also shown is the probe-Earth pointing vector e .

Of concern then is the location of the axis about which the antenna has its degree of rotational freedom, i.e., the hinge axis, as well as the angle ψ , between the antenna feed vector, f , and the hinge axis. That combination of hinge axis location and ψ value which results in an optimum fit of feed-axis location to the Earth vector track is desired.

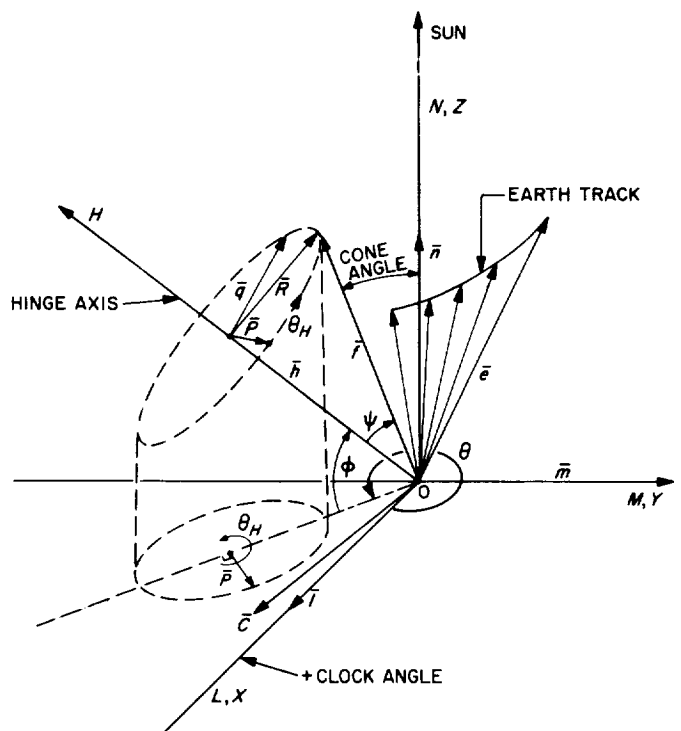


Fig. 9. Antenna pointing geometry

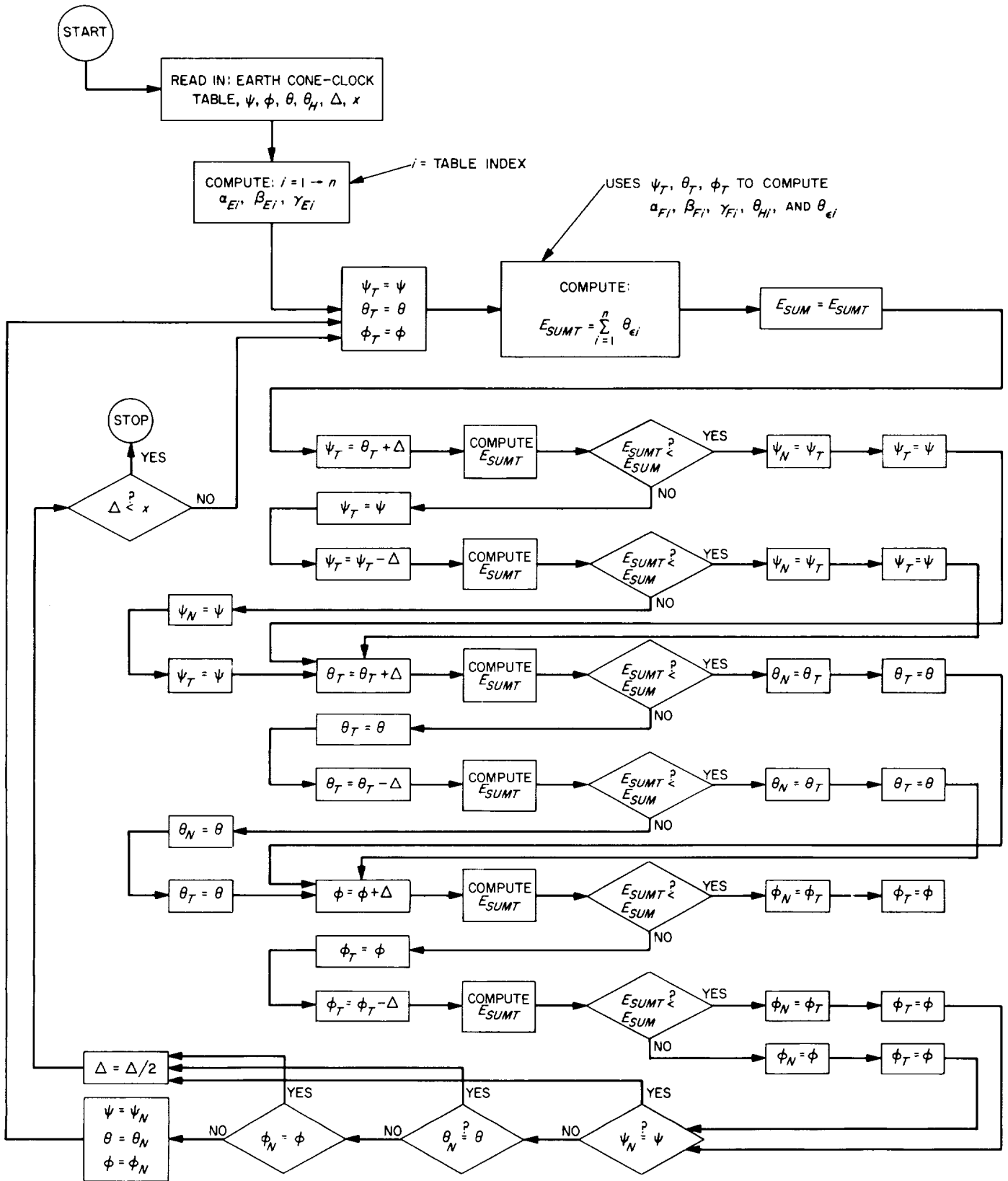


Fig. 10. Computer program optimization routine

The components of the unit feed vector, \mathbf{f} , may be developed as follows:

$$\begin{aligned} \mathbf{h} &= \text{unit vector along hinge axis} \\ \mathbf{h} &= \cos \phi \cos \theta \mathbf{l} + \cos \phi \sin \theta \mathbf{m} + \sin \phi \mathbf{n} \\ \mathbf{f} &= \cos \psi \mathbf{h} + \mathbf{R} \\ \mathbf{R} &= \sin \psi \cos \theta_H \mathbf{p} + \sin \psi \sin \theta_H \mathbf{q} \end{aligned}$$

where:

$\theta_H =$ hinge angle

$$\begin{aligned} \mathbf{p} &= \frac{\mathbf{n} \times \mathbf{h}}{|\mathbf{n} \times \mathbf{h}|} = -\sin \theta \mathbf{l} + \cos \theta \mathbf{m} \\ \mathbf{q} &= \frac{\mathbf{h} \times \mathbf{P}}{|\mathbf{h} \times \mathbf{P}|} = -\cos \theta \sin \phi \mathbf{l} - \sin \theta \sin \phi \mathbf{m} + \cos \phi \mathbf{n} \\ \therefore \mathbf{f} &= (\cos \theta \cos \psi \cos \phi - \sin \theta \sin \psi \cos \theta_H \\ &\quad - \cos \theta \sin \psi \sin \phi \sin \theta_H) \mathbf{l} \\ &\quad + (\sin \theta \cos \psi \cos \phi + \cos \theta \sin \psi \cos \theta_H \\ &\quad - \sin \theta \sin \psi \sin \phi \sin \theta_H) \mathbf{m} \\ &\quad + (\cos \psi \sin \phi + \sin \psi \cos \phi \sin \theta_H) \mathbf{n} \\ &= \alpha_F \mathbf{l} + \beta_F \mathbf{m} + \gamma_F \mathbf{n} \\ \mathbf{e} &= \alpha_E \mathbf{l} + \beta_E \mathbf{m} + \gamma_E \mathbf{n} \end{aligned}$$

In terms of cone and clock angles:

$$\begin{aligned} \theta_{CLF} &= \tan^{-1} \beta_F / \alpha_F = \text{feed vector clock angle} \\ \theta_{COF} &= \cos^{-1} \gamma_F = \text{feed vector cone angle} \end{aligned}$$

The pointing error angle, θ_ϵ , may be described by:

$$|\mathbf{f} \times \mathbf{e}| = \sin \theta_\epsilon, \text{ where } \mathbf{e} = \text{unit Earth vector}$$

and,
$$\theta_\epsilon \cong [(\beta_F \gamma_E - \gamma_F \beta_E)^2 + (\gamma_F \alpha_E - \alpha_F \gamma_E)^2 + (\alpha_F \beta_E - \beta_F \alpha_E)^2]^{1/2},$$

for small θ_ϵ .

A computer program is being developed using the above relations and a table of Earth cone-clock angles to determine the values of θ , ϕ , and ψ which minimize the sum of θ_ϵ 's computed at each tabulated point on the Earth track. The optimization routine flow diagram is shown in Fig. 10.

The result of these computations for a particular trajectory will be a function $\theta_H(t)$ which provides a minimum pointing error at each point in time along the trajectory. The maximum θ_ϵ which results will be a measure of the cost of using the simple single-degree of freedom system.

4. Future Work

Following the described determination of the intrinsic cost of a single-degree of freedom system, a study of the digital approximations used to actuate the antenna servo, i.e., the stored pointing program, will be made. Of interest are the best accuracies obtainable from these approximations beginning with low-order steps and line segments to higher-order polynomials. This will be done for both one- and two-degrees of freedom. The extent of complexity that each of these programmed approximations imposes on the spacecraft central computer can then be closely determined.

E. Attitude Control of a Spin-Stabilized Spacecraft

B. M. Dobrotin and J. C. Nicklas

This report presents the results of a design study of a spin stabilized spacecraft. Previous articles (SPS 37-34, Vol. IV; SPS 37-35, Vol. IV) have presented some background material for spin-stabilized spacecraft. This article attempts to utilize this material in a systems study of the spin concept to achieve a practical example. In addition several areas for future study are indicated.

The example selected consists of a 600-day Jupiter flyby mission. Attitude control requirements are to maintain the spin axis coincident with the Sun line. The midcourse correction maneuver is to be a Sun line maneuver in either a negative (towards the Sun) or positive (away from the Sun) direction. Thus, the body dynamics must be constrained to keep the pointing errors to a minimum during the entire flight while the active attitude control system must acquire the Sun and update the Sun-roll axis look angle. Table 3 presents the assumed spacecraft parameters.

Table 3. Spacecraft configuration

Weight	500 lb
Roll inertia	100 slug-ft ²
Pitch inertia	yaw inertia = 52.6 slug-ft ²
Midcourse correction acceleration	3.2 ft/sec ²
Midcourse motor misalignment lever arm	1 ft

The first consideration is the selection of a design spin rate. While a large spin rate minimizes the pointing errors, the lower spin rate will minimize the attitude control system requirements. Since the autopilot portion of the attitude control system is to be completely passive, it seems likely that this phase of the flight should determine the spin requirements. The autopilot is defined as the mechanism for controlling the heading of the ΔV vector introduced during the midcourse maneuver. The equation for the midcourse heading error, α , is derived in Ref. 2 and is:

$$\alpha(\tau) = \frac{1}{\tau} \left(\frac{\xi}{\omega_R} - \frac{N}{\lambda \omega_R} \right) (e^{i\omega_R \tau} - 1) + \frac{1}{\tau} \left(\frac{N}{\lambda(1+\lambda)^2 \omega_R^2} - \frac{\theta_0}{(\lambda+1)\omega_R} \right) (e^{i\omega_R(1+\lambda)\tau} - 1) + \frac{iN}{(1+\lambda)\omega_R^2} \quad (1)$$

where:

$N = \frac{Fl\xi}{I}$ = normalized torque generated by the thrust misalignment

F = motor thrust, lb

ξ = angular misalignment, rad

l = lever arm through which misalignment acts, ft

τ = burning time, sec

$\lambda = \frac{\Delta I_R}{I} - 1$

ω_R = spin rate, rad/sec

I_R = roll moment of inertia

$I = I_{pitch} = I_{yaw}$ = cross-axis moment of inertia

$i = \sqrt{-1}$

This equation was derived under the following assumptions. First, the motor thrust is a constant. Second, there is no component of the misalignment which produces a torque about the roll axis. This assumption is required to maintain a constant spin rate. Third, α and θ_0 , the initial cone angle, remain small.

Eq. (1) is bounded by two limits: $\tau = 0$ and $\tau = \infty$. As $\tau \rightarrow 0$, $\alpha \rightarrow \xi$ as would be expected for an impulse. As

$$\tau \rightarrow \infty, \alpha \rightarrow \frac{Fl\xi}{I \lambda \omega_R^2}$$

which is constant in both direction and magnitude. In addition to these two limits, Eq. (1) may be maximized to produce some upper bound on the heading error for other cases. The value of Eq. (1) reaches a maximum when the exponential terms on the right-hand side are purely real and negative. Eq. (1) then reduces to

$$\alpha_{max}(\tau) = \frac{\xi}{\omega_R} \left\{ \frac{2}{\tau} \left[1 - \frac{Fl}{I} \left(\frac{(1+\lambda)^2 - \omega_R \tau}{\lambda \omega_R^2 (1+\lambda)^2} \right) \right] + i \frac{Fl}{I \lambda \omega_R} \right\} \quad (2)$$

where it is assumed that $\theta_0 = 0$. This is based on the assumption that a nutation damper will have removed any coning angle. However, a nutation damper will not remove any residual pointing error due to the dead zone of the attitude control system. This initial bias must be added to the pointing error introduced by the midcourse maneuver itself. A plot of equation (2) for various spin rates is shown in Fig. 11. As the limit of α is ξ as $\tau \rightarrow 0$, it is seen that Eq. (2) becomes invalid as an approximation to Eq. (1) when $t \rightarrow 0$. In an attempt to provide some estimate of the pointing error for small burn times, the case of the non-spinning spacecraft is shown in Fig. 11 for $\tau < 1$ sec; $\alpha(\tau)$ for $\omega_R = 0$ is:

$$\alpha(\tau) = \tan^{-1} \frac{V_x}{V_z} \approx \frac{V_x}{V_z} = \frac{\int \sin K\tau^2 d\tau - \xi \int \cos K\tau^2 d\tau}{\int \cos K\tau^2 d\tau + \xi \int \sin K\tau^2 d\tau}$$

when

$$K = \frac{Fl\xi}{2I}$$

On the basis of the information presented in Fig. 11 and an upper limit on the pointing error of 3 deg, a spin

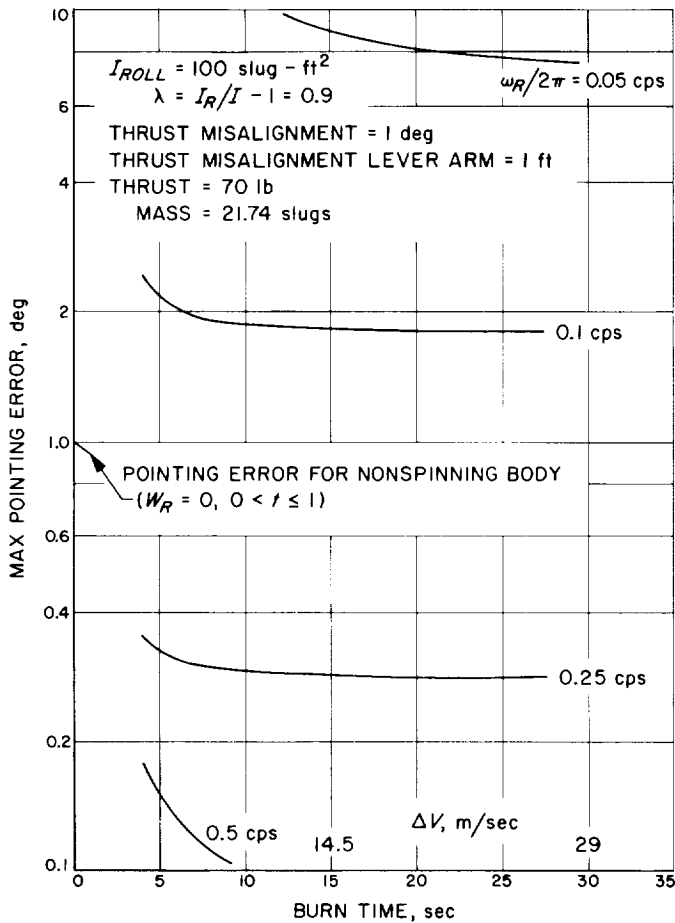


Fig. 11. Maximum pointing error versus burn time

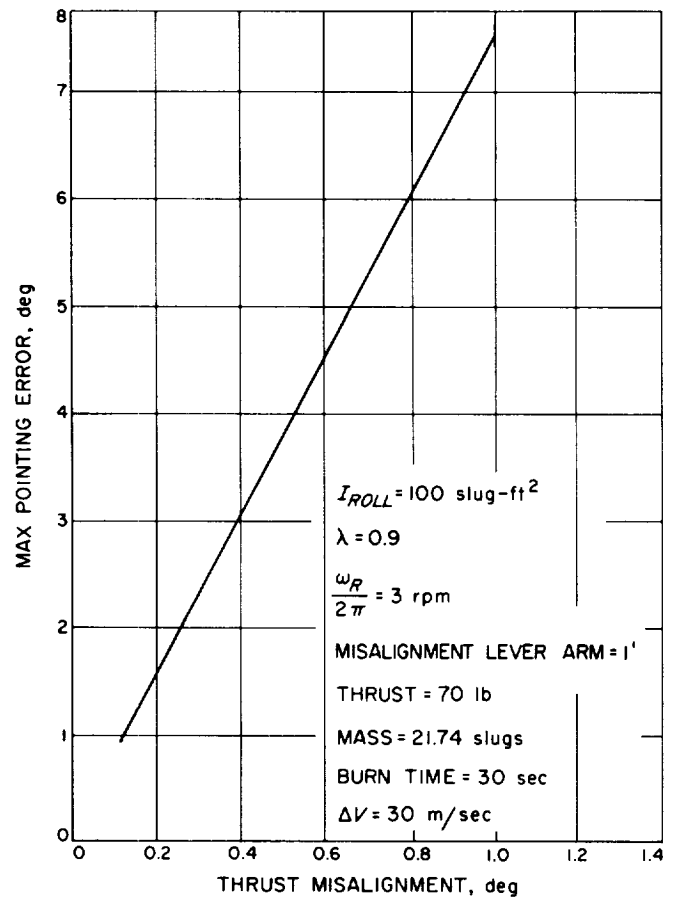


Fig. 12. Maximum pointing error versus thrust misalignment

rate of 0.1 cps or 6 rpm was selected. This assumes 2 deg generated by motor misalignment and 1 deg for residual pointing error prior to motor burn. In the event that the motor can be aligned to greater accuracy than assumed in Fig. 11, Fig. 12 shows the reduction in pointing error with reduction in misalignment (for large τ). At this time it is important to mention that λ must be > 0 for all portions of the flight.

If the spacecraft is suitable for thrusting (e.g., booms retracted) only in a configuration such that $\lambda < 0$, instability will result.

Once an estimate of the spin rate is obtained, the active attitude control system may be designed. The proposed mechanization is shown in Fig. 13. This figure shows a two-jet system as outlined in Ref. 3.

A two jet system is required for two reasons. First, two completely redundant half systems are required for re-

liability. Each half-system must contain enough gas to complete the mission. Secondly, a two-jet system may be arranged on the spacecraft so as to minimize the generated cone angle. Fig. 14 shows the generated cone angle as a function of λ . It may be seen that the cone angle is minimized when $\lambda = 0.5$ if a single jet system is used. The same minimization is achieved with a two-jet system if the two control jet pairs (and the controlling Sun sensors) are arranged as shown in Fig. 13. In the event of failure of one jet-sensor pair, the remaining jet-sensor will operate satisfactorily as a single-jet system. However, there will be an attendant increase in the maximum cone angle, depending on the inertia ratio of the spacecraft. For the configuration under consideration (with a $\lambda = 0.9$) the cone angle will increase by a factor of 3.

The analysis presented in SPS 37-35, Vol. IV, indicated that the system described in Ref. 3 will be unstable. Therefore, a hysteresis band has been added to the dead-zone. Thus, the pointing error will oscillate between the

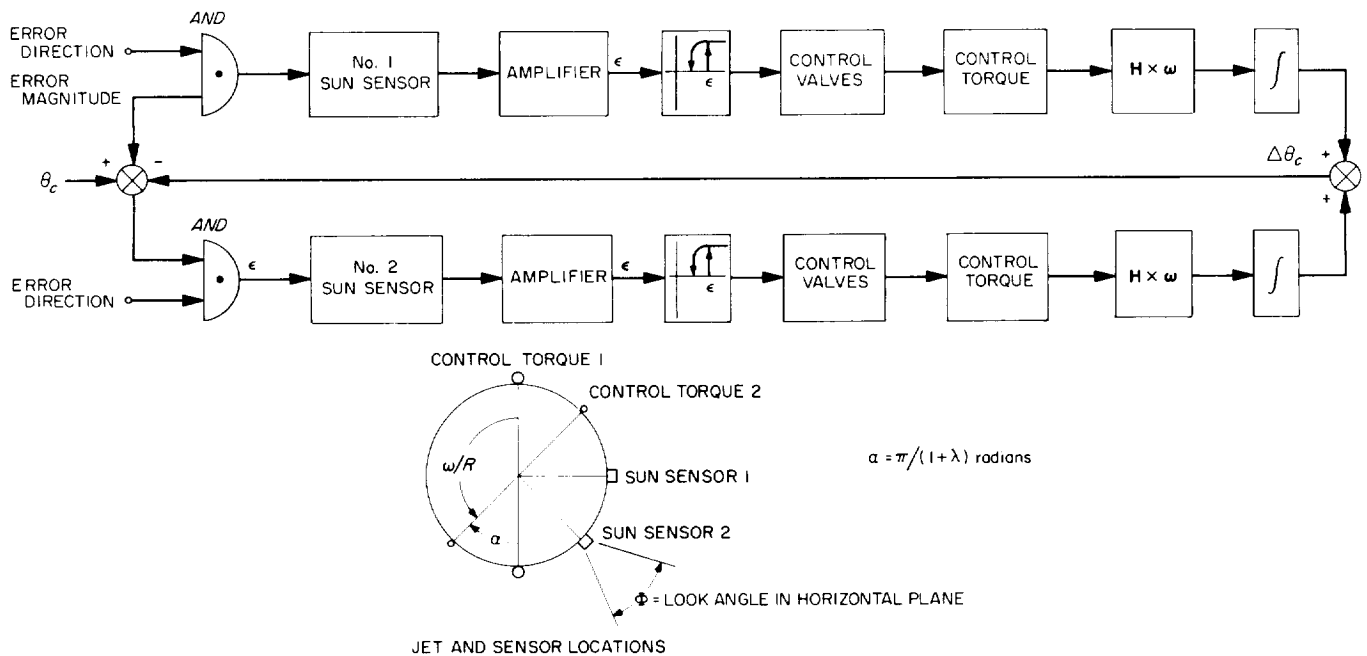


Fig. 13. Mechanization of attitude control for spin-stabilized spacecraft

deadband and the sum of the deadband and the hysteresis band. The oscillations will be caused by external (e.g., solar, meteor) torques and the relative motion of the Sun and spacecraft.

For a control system with a maximum pointing error of 1.5 deg, a spin rate of 0.1 cps (6 rpm) and $I_R = 100$ slug-ft², a jet thrust level may be selected as follows: From Fig. 15, a thrust level of 0.02 lbf per jet pair (0.01 lbf/valve) produces a maximum cone angle of 0.1 deg. For the event of one valve failing open and producing a constant body-fixed torque, a cone angle of ~0.35 deg will allow the spacecraft to point between 0.5 deg and 1.5 deg while the two-jet system is operative. In the event that one valve sticks open, the spacecraft will cone within the hysteresis zone until the gas in the failed half-system is expended.

Sizing the gas supply is independent of the thrust level and deadzone. The gas requirements are given by:

$$W_p = \text{lb propellant} = \frac{I_R W_R \theta}{I_{sp} l} \left(\frac{\phi/2}{\sin \phi/2} \right)$$

where

I_{sp} = specific impulse of propellant used

l = lever arm of control jet

θ = total angle of precession

ϕ = angle of rotation during which torque is applied (torquing angle)

Propellant weight is shown in Fig. 16 for various total precession angles. System weight versus precession angle is given by:

$$W_s = 2 [(W_p + W_L)(1 + 1.6) + 5]$$

where W_p is obtained from Fig. 16, and W_L is the gas leakage requirement:

$$\begin{aligned} W_L &= 3 \text{ cc/hr/valve} \times 4 \text{ valves} \times 600\text{-day/mission} \\ &= 0.44 \text{ lb.} \end{aligned}$$

Fig. 17 shows system weight as a function of total precessional angle. For the hot-gas system, system weight is:

$$W_s = 2 (1.26 W_p + 5)$$

Both system weights include enough propellant to allow either half-system to complete the mission.

Fig. 18 gives the average precession rate for various thrust levels. At the selected design point, worst-case capture (108 deg) would take 5 hr. Many problem areas

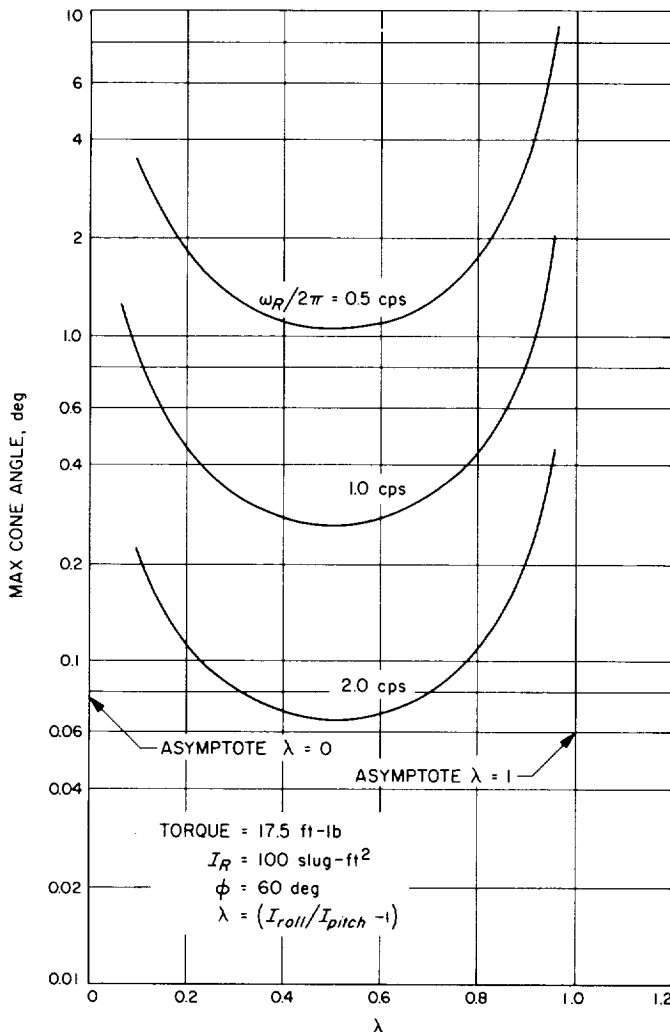


Fig. 14. Maximum cone angle versus inertia ratio for single-jet system

remain in predicting the performance of a spinning spacecraft. In the area of autopilot pointing error, a detailed study of anticipated configurations should be made. Previous discussion has merely provided upper bounds for the error, which, for the low spin rate selected, may be quite high. A six-degree of freedom computer program should be utilized.

However, of even more importance is the interaction of the control elements as a whole. There has been tacit assumption of the presence of a passive nutation damper, but no analysis has been made (in this study) of the properties of such a device. Additionally, the performance of the control system has been based on the validity of Euler's moment equations assuming that the only torques present are the desired control torques. This is certainly valid for high spin rates (> 1 cps) and large

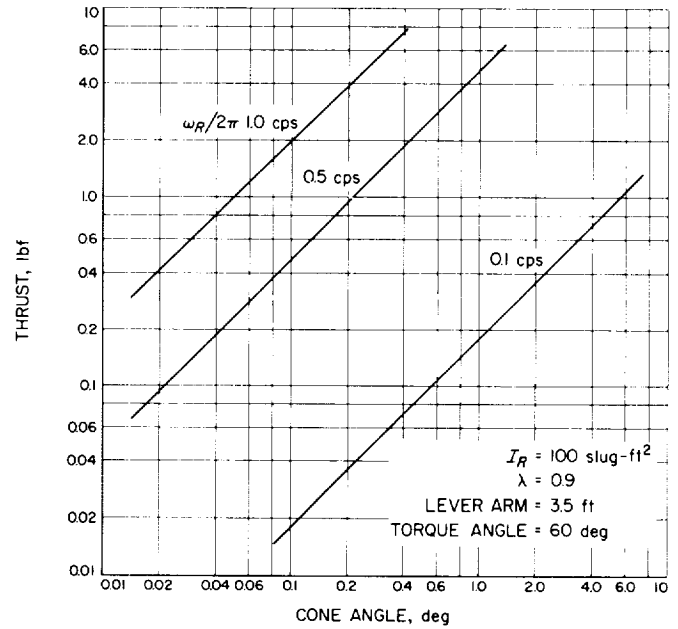


Fig. 15. Precessional cone angle versus thrust level for two-jet system

control torques (> 1 ft-lb), but for the present configuration this is not necessarily true. In the first place, the spacecraft is not a rigid body, as Euler's equations demand. Secondly, it may be that the nutation damper torques will interact with the low control torques required (~ 0.07 ft-lb). Third, the operation of the control system in the failed mode (i.e., one valve stuck open) with additional control moments being applied must be closely studied. In essence, it appears that several sections of the control problem have been presented. If further development of the spin-stabilized concept is desired, the interaction of the various bits and pieces must be defined.

One last question is, "How is the spacecraft spun up?" Since the spacecraft is to be spinning for the entire duration of the flight, the spinup must be done at the earliest possible moment; at, or immediately after, separation from the booster. Thus, it seems logical to leave the spinup function to the booster where it may be simply mechanized. Spinup on the booster would have the additional advantages of minimizing tipoff errors. As in past launches, a mechanization may consist of a spin table driven by the residual pressurization gasses from one of the booster propellant tanks. If data from future space flights indicate that windage in space is a problem, the spacecraft would have to carry a small spin-speed control system.

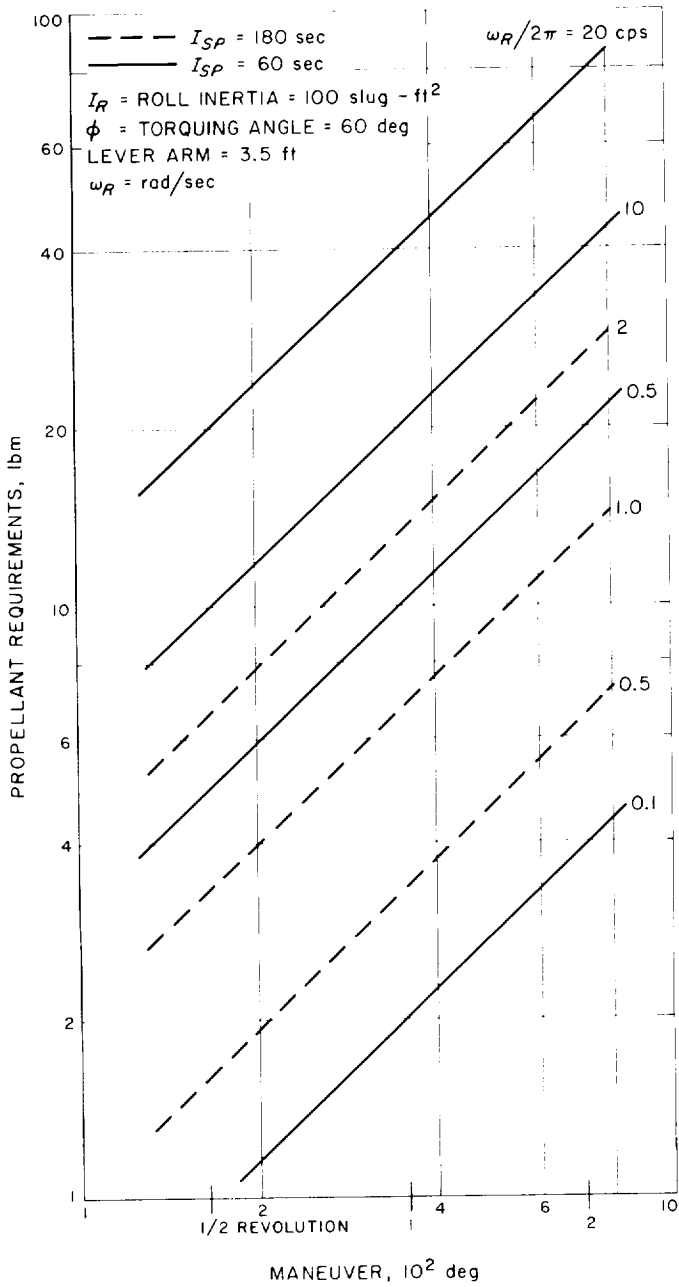


Fig. 16. Propellant requirements for precessional control system

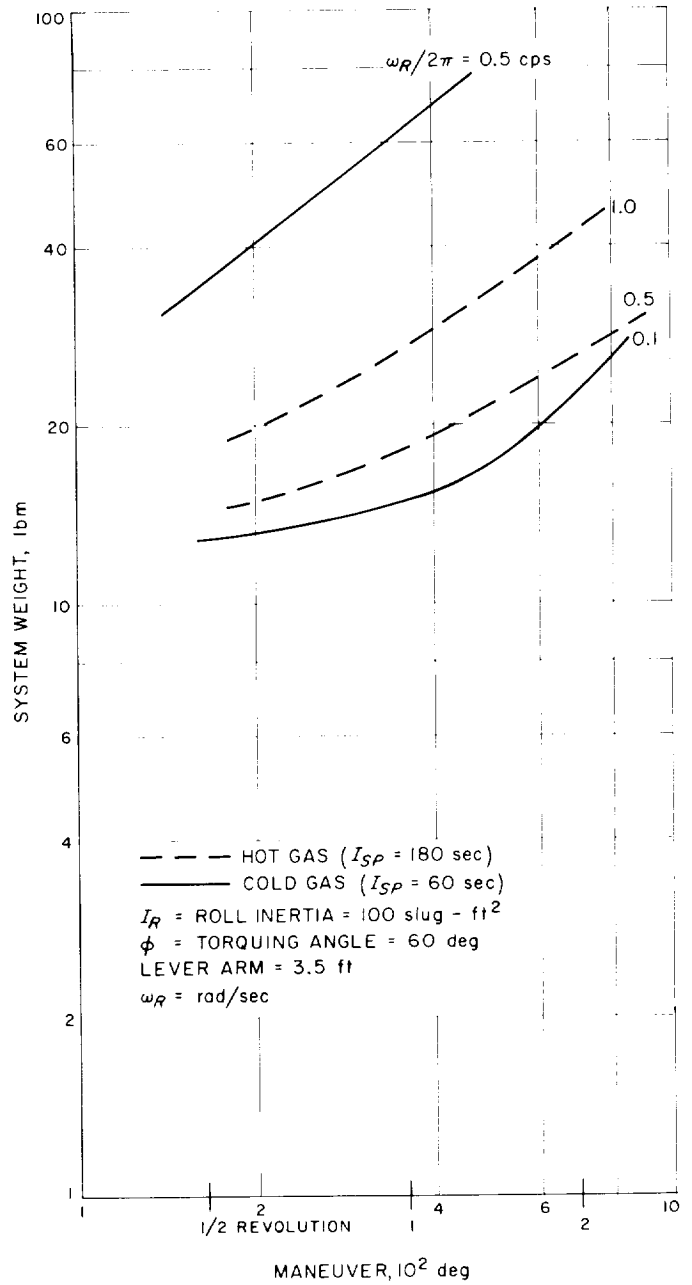


Fig. 17. System weight for precessional control system

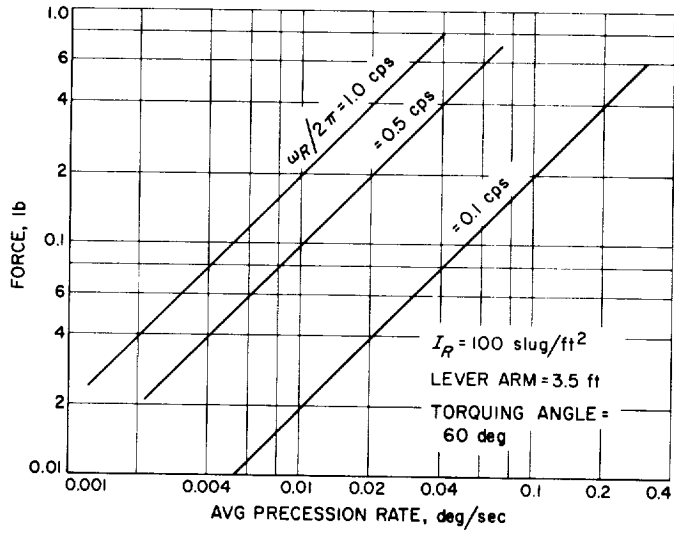


Fig. 18. Average precessional rate versus thrust level

References

1. *Feasibility Study, Solid Propellant Electrical Thruster in the Detonation Mode*, Contract 951102, General Electric Company, Missiles and Space Division, Spacecraft Department, Philadelphia, Pennsylvania, March 1966.
2. Armstrong, R. S., *Errors Associated With Spinning-up and Thrusting Symmetric Rigid Bodies*, Technical Report 32-644, Jet Propulsion Laboratory, Pasadena, February 15, 1965.
3. Windecknecht, T. G., *A Simple System for Sun Orientation of a Spinning Satellite*, ARS Paper G1-204-1898, June 1961.

V. Guidance and Control Research

A. Titanium Oxide Thin Films

J. Maserjian

The investigation of the electrical properties of titanium-oxide thin films has continued during recent months. The experimental procedure and some of the initial measurements were described previously (*SPS 37-31*, Vol. IV, p. 98). As discussed in that report, one objective of this investigation is to develop a physical model which provides a consistent interpretation of the observed properties. From this, one can hope to find better ways of exploiting thin films for device applications as well as recognize certain physical limitations on existing thin-film devices.

The approach has been to treat the limiting case where extremely high densities of impurities exist in the oxide film. Since the films have been shown to be amorphous (*SPS 37-31*, Vol. IV), impurities are introduced by the various structural defects present. Also, because of the relative ease with which titanium oxide is reduced, one can expect excess concentrations of oxygen vacancies to

occur with the evaporation method used. These vacancies act like donor impurities and make the oxide a heavily doped *n*-type semiconductor. It was previously stated that the thin aluminum-titanium oxide-aluminum sandwich type samples studied give very stable electrical characteristics in contrast to large creep effects observed with other methods tried (*SPS 37-31*, Vol. IV). This is attributed in part to a near-saturation effect of the impurities, so that large applied or built-in fields have little effect on redistributing impurities within the film. Also, the aluminum films in contact with the titanium-oxide films are more stable as compared with certain other materials such as gold.

Measurements of the electrical conductance through the oxide films as a function of voltage and temperature (see *SPS 37-31*, Vol. IV, for typical curves) cannot be explained by the familiar theories. Since the films considered exceed 100 Å in thickness, the calculated conductance would be much too small if explained on the basis of the usual theory of quantum-mechanical tunneling between electrodes. Also, the marked temperature dependence at low voltages is inconsistent with a "pure"

tunneling mechanism and yet is too small to be consistent with a purely thermionic process. The latter requires in this case an activation energy of the order of only 0.1 eV, and if a purely thermionic process were involved, excessively high conductance would result. A process intermediate between these extremes is clearly required. This arises naturally if, as already postulated, extremely large impurity concentrations are assumed to be present in the oxide. The effect of these impurities results in space-charge layers in the oxide, one adjacent to each contact which determines the effective energy barrier at the contact. One can show this from Poisson's equation which in one dimension can be written

$$\frac{1}{q} \frac{d^2U}{dx^2} = \frac{4\pi}{\kappa} \rho, \tag{1}$$

where U is the electron potential, ρ , the space-charge density, and κ , the dielectric constant of the oxide. The simplest case assumes ρ to be constant, equal to qN , where N is the density of positively ionized impurities. This is a valid assumption if the oxygen vacancies are the dominant impurity and are uniformly distributed through the oxide. It is known that these impurities are easily ionized, that is, they possess a small ionization energy (≈ 0.01 eV). Since the energy gap of the oxide is large (3 eV), one may neglect the effect of intrinsic ionization. In the case being considered for large values of N , charge neutrality can only be satisfied when the electron potential U is approximately zero. That is, the density of electrons available to neutralize the donors falls off as $\exp(-U/kT)$ for $U \gtrsim kT$, with ρ becoming very nearly equal to qN .

Eq. (1) may then be readily integrated subject to the boundary conditions imposed at the contacts, i.e., $U(x=0) = \phi$, the metal-to-oxide work function. For sufficiently thick films, the solution becomes

$$U(x) = \phi(1 - x/s)^2 \tag{2}$$

where

$$s^2 = \frac{\kappa\phi}{2\pi q^2 N}$$

Eq. (2) describes the shape of the potential barrier created by the impurity space-charge as measured from each contact when the above assumptions are valid. Barriers of this kind have already been extensively treated in the literature for cases involving more moderate concentrations of donors where a pure thermionic process results (Schottky emission).

The electron current that crosses a barrier can be written:

$$J = \frac{A}{kT} \int_{-\infty}^{\infty} P(E) \ln \left[\frac{1 + e^{-E/kT}}{1 + e^{-(E-V)/kT}} \right] dE \tag{3}$$

where $A = 120T^2$ amp/cm² is Richardson's coefficient, and $P(E)$ is the transmission probability of the barrier at energy E . The quantity A/kT times the log term in the integrand represents the difference in the flux of electrons along the x -direction in the range E to $E + dE$ incident from opposite sides of the barrier.

The transmission probability can be written to a good approximation by

$$P(E) = \frac{1}{1 + e^{\theta(E)}} \tag{4}$$

where

$$\theta(E) = \alpha \int_{x_1}^{x_2} (U - E)^{1/2} dx,$$

x_1, x_2 are given by the roots of $U(x) - E = 0$, and α is a constant $= (8m^*)^{1/2}/\hbar$.

Eq. (4) can be solved exactly for the potential barrier given by Eq. (2). The effect of image forces on U may be included as a correction. The nature of the assumed barrier is to make $P(E)$ increase rapidly with increasing E . Offsetting this is the Boltzmann probability which appears out of the log term in Eq. (3) for $E/kT > 1$, and which decreases exponentially with energy. The effect of an intermediate type process is clearly indicated. Eq. (3) can then be solved by the saddle-point approximation, that is, by integrating about the energy in which the integrand is a maximum. The final result which must take into account both barriers is greatly simplified in the limit of zero field. The dependence obtained for the zero field conductance is given by

$$G = G_0 \frac{[(\phi/kT_0) \tanh(T_0/T)]^{1/2}}{\cosh(T_0/T)} e^{-(\phi/kT_0) \tanh(T_0/T)}$$

where $G_0 = 5.0 \times 10^6 T_0$ mhos/cm², and the parameter T_0 has been defined by $kT_0 = \phi^{1/2}/2as$.

A fit of this theory to experimental results obtained from a typical sample is shown in Fig. 1, where the values for ϕ and T_0 have been chosen to give the best fit between experiment and theory.

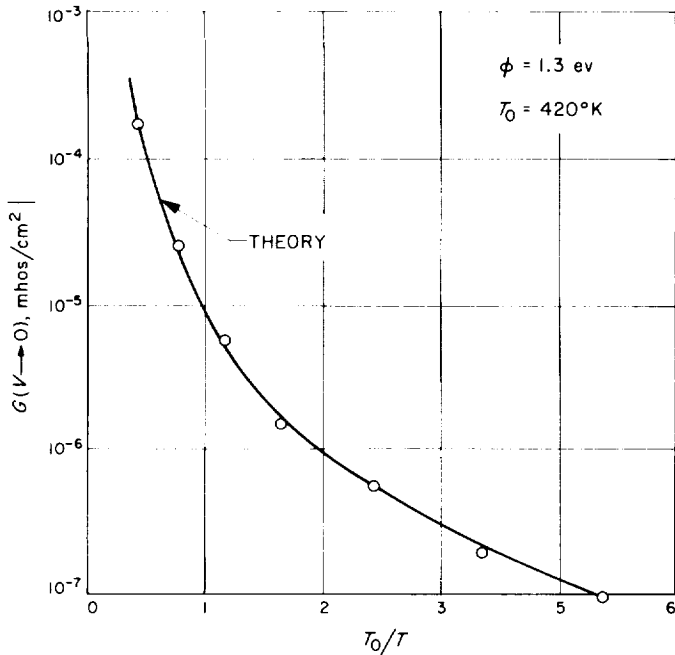


Fig. 1. Zero field conductance per unit area versus reciprocal absolute temperature, normalized

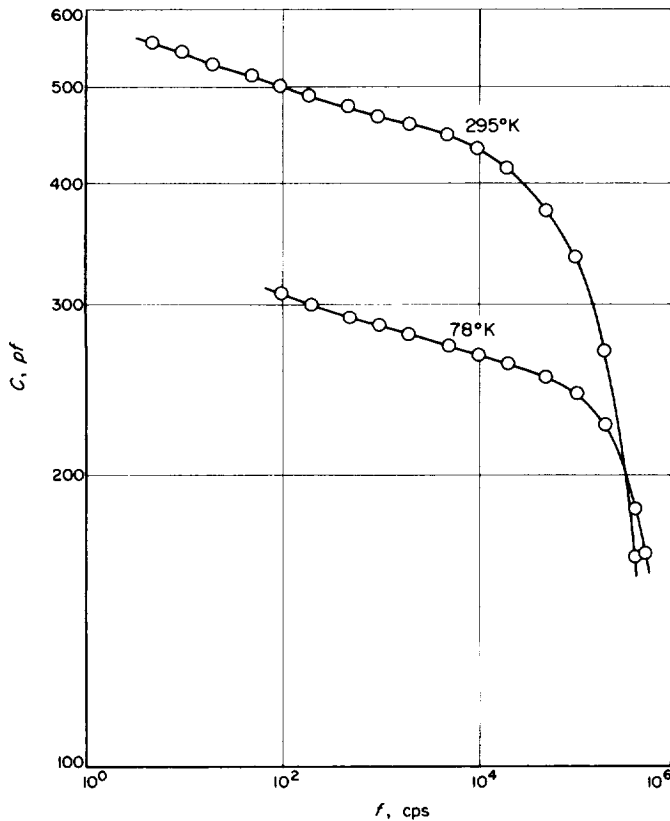


Fig. 2. Capacitance versus frequency at room temperature and liquid nitrogen temperature

The barrier height has been independently determined from photo-response measurements taken from a similar sample which gave 1.24 eV, in good agreement with the value of 1.30 eV used in the theoretical fit. The characteristic temperature T_0 of 420°K may be compared with capacitance measurements as discussed below and is also found to be consistent. The over-all agreement with the zero-field-conductance data is considered good, considering the simplifying assumptions used. At finite fields, the problem is considerably more complicated and will not be discussed in this report.

Measurements of the capacitance and conductance of the same sample as a function of frequency at two temperatures are plotted in Figs. 2 and 3, respectively. The large temperature dependence of the capacitance is particularly interesting because it cannot be explained on the basis of any well-known theory. For example, the effect of change of dielectric constant with temperature is much too small to account for the observed result. On

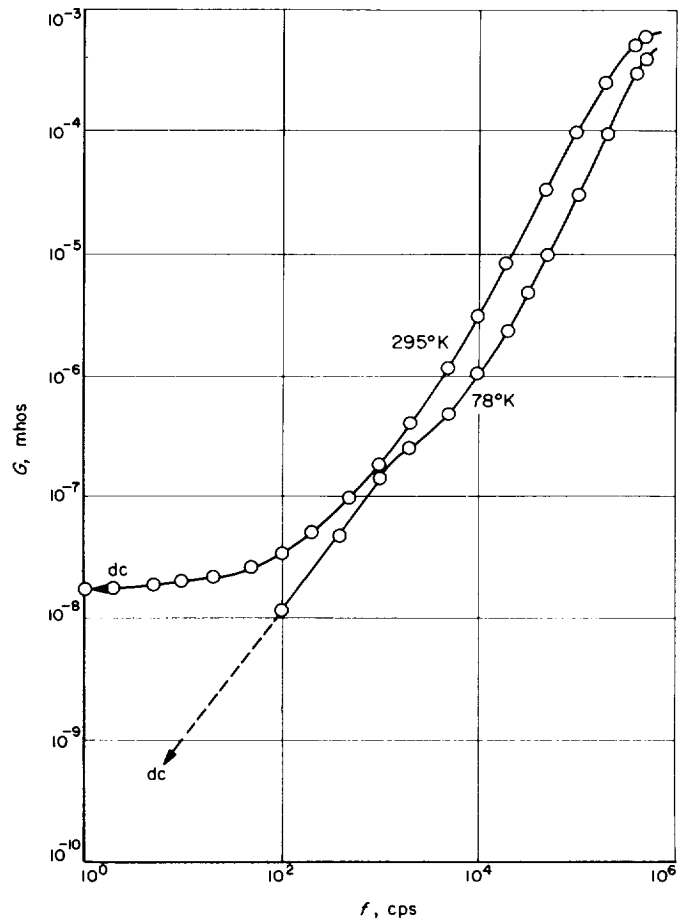
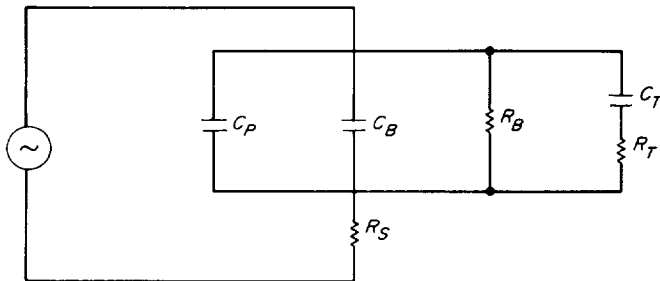


Fig. 3. Conductance versus frequency at room temperature and liquid nitrogen temperature

the basis of the theory discussed above, one obtains an effective barrier thickness corresponding to the saddle-point energy used in evaluating Eq. (3). The barrier capacitance which results predicts a temperature dependence requiring approximately the same value of T_0 used above when proper correction is made for the effect of the parallel-plate capacitance C_p , estimated at 70 pf (Fig. 4).

The dependence of capacitance and conductance on frequency can be explained if one includes the effect on the space-charge capacitance of electron trapping in impurity states. The theory of such a mechanism was introduced by A. Rose (Ref. 1), and has been considered further by others (Refs. 2, 3). This should be appropriate here since we are dealing with extremely high concentrations of impurities. The effect of trapping increases the capacitance at low frequencies where the occupancy of traps can follow the field oscillations. This may be conveniently represented in the equivalent circuit of Fig. 4 by a capacitance C_T and resistor R_T (see Ref. 3).

The cutoff in the curve of capacitance versus frequency arises from the series resistance introduced by the electrode films ($\approx 1 \text{ K}\Omega$). The important features of the dependence of both the conductance and the capacitance on frequency can be satisfactorily interpreted in terms of the equivalent circuit shown.



- C_B = TOTAL BARRIER CAPACITANCE
- C_T = EFFECTIVE CAPACITANCE OF DISTRIBUTED TRAPS
- C_p = PLATE CAPACITANCE
- R_B = TOTAL BARRIER RESISTANCE
- R_T = EFFECTIVE RESISTANCE OF DISTRIBUTED TRAPS
- R_S = SERIES RESISTANCE OF METAL FILM LEADS

Fig. 4. Equivalent circuit of sample; C_B is total barrier capacitance, C_T , effective capacitance of distributed traps, C_p , plate capacitance, R_B is total barrier resistance, R_T , effective resistance of distributed traps, R_S , series resistance of metal film leads

B. Pure Space-Charge-Limited Electron Current in Silicon

M-A. Nicolet¹ and S. Denda

1. Introduction

The idea that space-charge-limited current (sclc) can flow through a solid much as it does through vacuum can be traced to early workers (Ref. 4) and is stated explicitly and analytically in Mott and Gurney's book of 1940 (Ref. 5). But it is only in recent years that the subject has attracted wider attention, motivated at least in part by the promises which the phenomenon has been claimed to hold in device applications. The general picture which has emerged as a result of these recent efforts is that, as a rule, unipolar sclc is dominated by the presence of charge carrier traps. The physical nature and identity of most of these traps is unknown, but an obvious guess is to link them with imperfections in the solid. As a result, pure (that is, trap-free) sclc has not been observed often. To find a solid in which pure sclc can flow, emphasis should therefore be laid on extreme perfection. This immediately suggests germanium and silicon because these are the elements available in single-crystal form of the highest perfection achieved to date.

Dacey (Ref. 6) and Shumka (Ref. 7) have studied sclc of holes in germanium. Dacey's results indicate that the simple theory of Mott and Gurney has to be modified to take into account the field-dependence of tepid charge carriers. Dacey developed an improved theory assuming that the charge carrier mobility varies with the electric field as $E^{1/2}$. The verification of this theory was later provided by Shumka, whose work is the first detailed experimental analysis of pure sclc in a solid. But it is known that at high field strengths the drift velocity of charge carriers in germanium saturates (hot charge carriers). One should therefore expect that in extending Shumka's observation to still higher current densities, drift velocity saturation should appear if breakdown effects can be avoided.

Sclc in silicon has not been studied extensively. Gregory and Jordan (Ref. 8) have recently investigated the flow of sclc of holes at 4.2°K. Trapping was found to dominate at these low temperatures, but there is evidence that this may not be the case at 300°K (Ref. 9). Because of the lesser attention that silicon has received, it has been

¹At the California Institute of Technology, performing work supported by the Jet Propulsion Laboratory.

selected as the host lattice for the experiments described below, using electrons as charge carriers. Silicon also has smaller ionization rates than germanium for both electrons and holes (Ref. 10). This moves the limit of avalanche breakdown to higher voltages and eases the access to the range of drift velocity saturation.

2. Experimental Procedure

The preparation of devices adapted to the present purpose has been discussed in a previous report (SPS 37-33, Vol. IV, p. 57-65). Electrical measurements are performed by applying a sawtooth voltage of variable amplitude, duration and repetition rate across the device at ambient temperatures between 78°K and room temperature. The ramp was normally 20 μs long, a duration

found experimentally to be short enough to eliminate any observable heating of the sample and long enough to avoid transient phenomena in sample and circuit. The voltage across the sample and the current flowing through it are displayed on the x and y axis of an oscilloscope and recorded photographically or visually point by point.

3. Experimental Results and Evaluation

Fig. 5 shows a family of V-I characteristics obtained at room temperature on samples of 300 Ωcm base material and various base widths. The characteristics of the same samples at liquid nitrogen temperature are given in Fig. 6. The V-I plane of these plots is subdivided into three distinct fields of operating points by the boundary lines 1,1' to 4,4'. These boundaries have been obtained

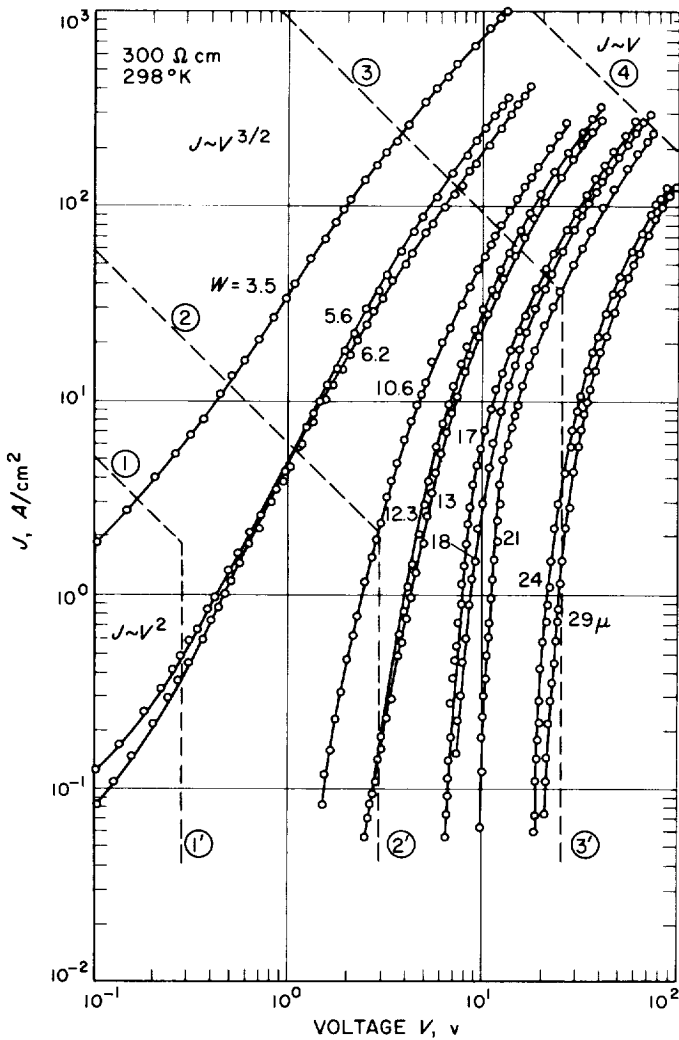


Fig. 5. V-I characteristics at room temperature of n⁺πn⁺ structures with 300 Ωcm base material

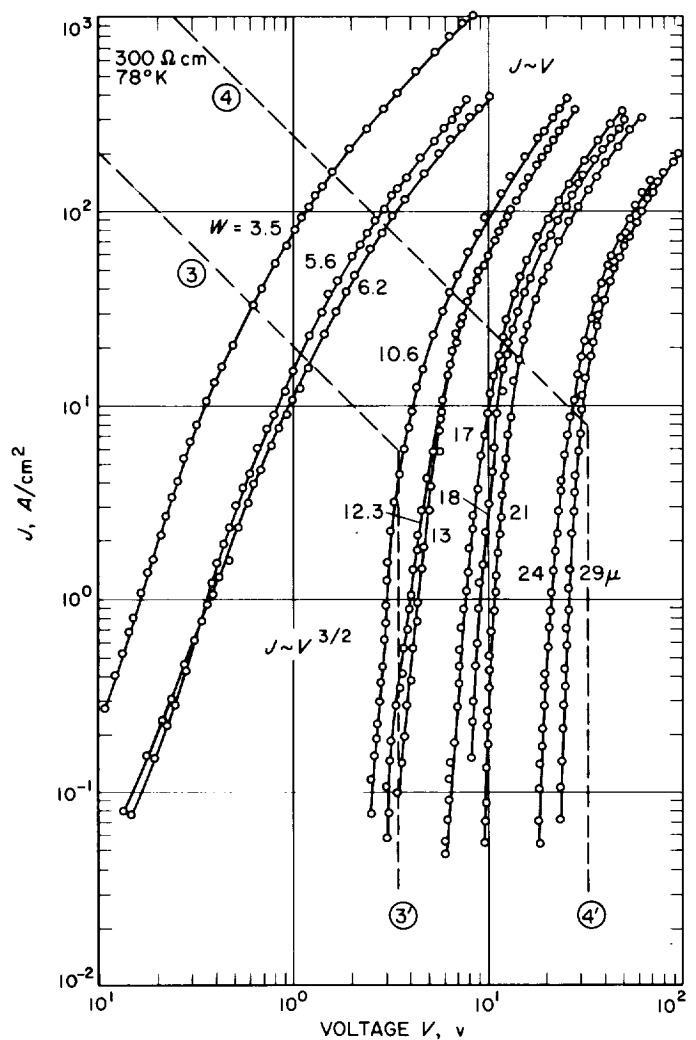


Fig. 6. V-I characteristic at 78°K of the n⁺πn⁺ structures of Fig. 5

from order-of-magnitude considerations, using all available information on the field dependence of the drift velocity of electrons in silicon (Refs. 11, 12). For operating points in the field delineated by the boundaries 1,1' and $V = 0, J = 0$, the electrons are essentially in thermal equilibrium with the lattice and the characteristics should follow a square law as predicted by Mott and Gurney (Ref. 5). In the field limited by the boundaries 2,2' and 3,3' the drift velocity of electrons is no longer proportional to the electric field strength, but increases less rapidly (tepid electrons). If one assumes, as Dacey, that the carrier mobility varies as $E^{-1/2}$, then a $V^{3/2}$ power law should result. The drift velocity has reached saturation at operating points lying beyond the boundary 4,4'' (hot electrons). The current density should now be proportional to V .

This discussion neglects the limitations imposed on the V - I characteristic by the existence of a punch-through voltage V_{pt} at which the current rapidly decreases to low values. The effect is caused by residual doping in the base material. It has been incorporated into the simple model of Mott and Gurney by Shockley and Prim (Ref. 13), and has been treated for tepid charge carriers by Dacey himself (Ref. 6). In Sect. 4, the corresponding analysis for hot charge carriers will be outlined. Fig. 7 gives the results obtained in the three cases. Voltages are normalized with respect to

$$V_{pt} = qNW^2/2\epsilon\epsilon_0,$$

the punch-through voltage as obtained from the simple full depletion approximation of a reverse-biased junction (q = electronic charge, N = concentration of residual doping ions in the base, W = base width, $\epsilon\epsilon_0$ = dielectric constant). Currents are normalized with respect to that particular pure sclc density J_{pt} that would flow in each particular case if the applied voltage were equal to V_{pt} and if the base were free of doping ions, e.g.,

$$J_{pt} = \begin{cases} (9/8)\epsilon\epsilon_0\mu_0 V_{pt}^2/W^3 & \text{for thermal charge carriers} \\ (2/3)(5/3)^{3/2}\epsilon\epsilon_0\mu_0 E_c^{1/2} V_{pt}^{3/2}/W^{5/2} & \text{for tepid charge carriers} \\ 2\epsilon\epsilon_0 v_s V_{pt}/W^2 = v_s qN & \text{for hot charge carriers} \end{cases}$$

where μ_0 is the low field mobility of the charge carriers, E_c the critical electric field, and v_s the drift velocity of saturation. The asymptotes for $V_{pt} \ll V$ are those predicted for pure sclc flow of thermal (Mott and Gurney), tepid (Dacey) and hot charge carriers.

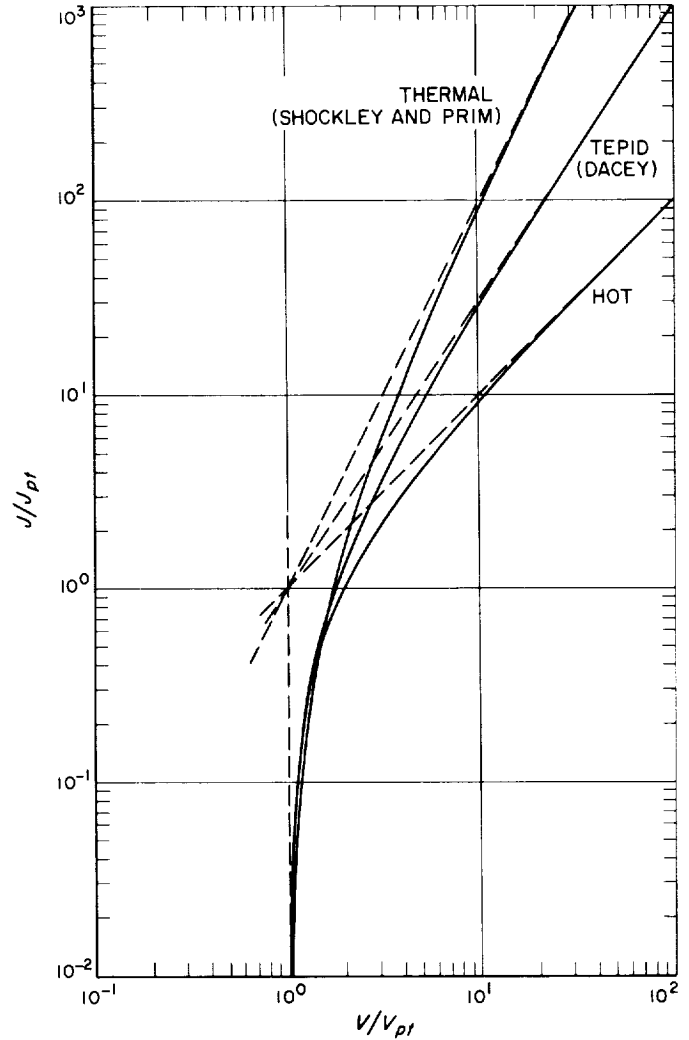


Fig. 7. Theoretical V - I characteristics of pure sclc, including punch-through effect, derived under the assumption of thermal, tepid and hot charge carriers

Fig. 8 shows two experimental curves of Figs. 5 and 6 represented in superposition with the proper theoretical curves of Fig. 7. The fit is excellent and indicates that the models used are adequate to reproduce the main features of the dc characteristics of the device. Specifically, it is

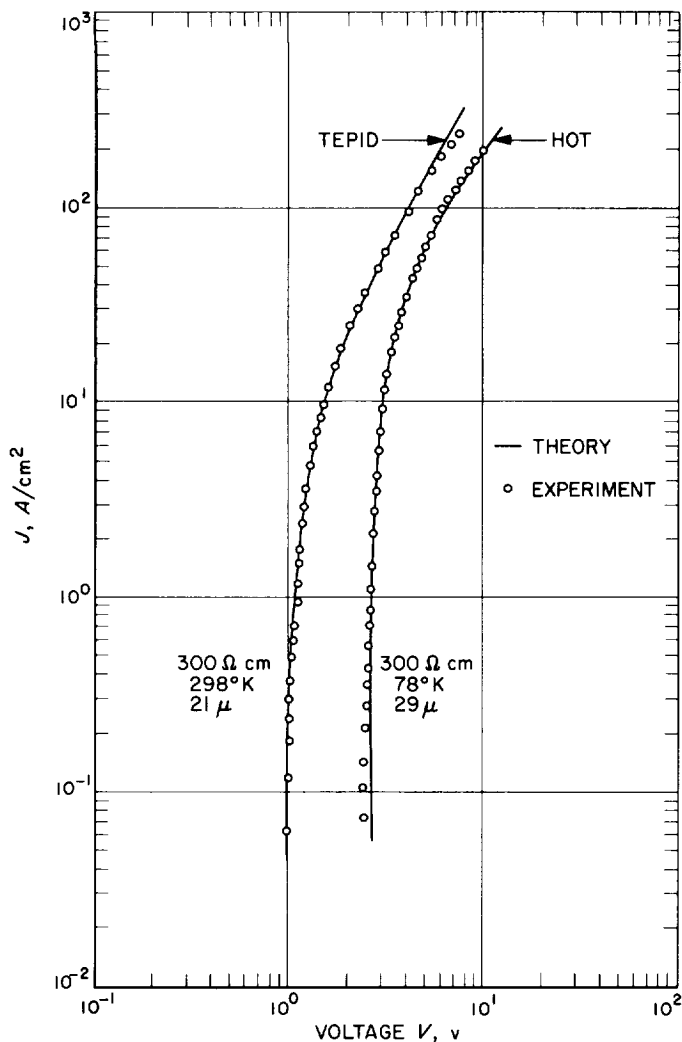


Fig. 8. Comparison of experimental results obtained on 300 Ωcm samples of 21 and 29 μ base width at room temperature and at liquid nitrogen temperature with the theoretical curves of Fig. 7 for sclc of tepid and hot charge carriers, respectively

concluded that current flow is purely space-charge-limited and that at 78°K, and to some extent even at room temperature, the current at the highest operating points is carried by hot electrons in a state of complete velocity saturation. However, the theoretical curves of Fig. 7 are inadequate to explain the V-I characteristics of the thinner samples in Figs. 5 and 6. The discrepancy is believed to be due to the finite extent of the Debye length which can not be neglected at small base widths. This range of operation awaits clarification.

A numerical analysis yields $1.0 \cdot 10^7$ cm/s $\pm 10\%$ for the saturation velocity of electrons in silicon at 78°K.

The temperature dependence of the current at fixed bias voltages in the sclc range of the V-I characteristics is in general agreement with the variation of the low field mobility.

4. Analysis of Sclc

The equations governing the flow of sclc in a planar structure with a uniform concentration N of residual doping ions are

$$j = \rho v \tag{1}$$

$$\epsilon \epsilon_0 \frac{dE}{dx} = \rho + qN \tag{2}$$

where E is the electric field, and the equations are written for positive mobile charge carriers and doping ions. The charge carrier velocity depends upon the electric field strength according to

$$v = \mu_0 E \quad \text{for thermal charge carriers} \tag{3a}$$

$$v = \mu_0 (E_t E)^{1/2} \quad \text{for tepid charge carriers} \tag{3b}$$

$$v = v_s \quad \text{for hot charge carriers.} \tag{3c}$$

Three cases can thus be distinguished (Fig. 7).

a. Punch-through and thermal charge carriers. The solution has been given first by Shockley and Prim (Ref. 13) and is of the parametric form

$$a^2 = \frac{9}{16} \bar{J} + \bar{V}$$

$$a - \frac{9}{32} \bar{J} \log \left(1 + \frac{32a}{9\bar{J}} \right) = 1 \tag{4}$$

b. Punch-through and tepid charge carriers. The solution has been given by Dacey (Ref. 6) and is of the parametric form

$$\bar{V} = \frac{3e^{2u} - 16e^{u/2} + 36e^u - 48e^{u/2} + 6u + 25}{3(e^u - 4e^{u/2} + u + 3)^2}$$

$$\bar{J} = 1.98 (e^u - 4e^{u/2} + u + 3)^{-1/2} \tag{5}$$

c. Punch-through and hot charge carriers. Substituting Eq. (3c) into Eq. (1) and eliminating ρ from Eq. (2) by Eq. (1) yields a simple linear differential equation. After two-fold integration with the boundary condition $E(0) = 0$ and normalization, one obtains

$$\bar{J} = \bar{V} - 1 \tag{6}$$

In Eqs. (4-6), current and voltage are normalized to J_{μ} and V_{μ} , as explained in the text. The three results of Eqs. (4-6) are plotted in Fig. 7.

C. Variable-Frequency NMR Spectrometer for the 20- to 200-Mc Range

D. I. Tchernev, H. G. Vorkink, and J. E. Guisinger

1. Introduction, *D. I. Tchernev*

In order to study the magnetic interaction between γ iron oxide particles by means of the nuclear magnetic resonance (NMR) of Fe^{57} , it was necessary to design and construct a spectrometer for the 20- to 200-Mc frequency range. Since this spectrometer is a generally useful laboratory instrument for various applications, this article has been prepared to describe its features, while its specific application to the study of the interaction between magnetic iron oxide particles dispersed in a nonmagnetic binder will be the subject of a later article.

The magnetic-resonance phenomenon has attracted considerable interest in recent years and has been shown to be extremely useful as a research tool in many fields of science and engineering. It is based on the fact that any particle possessing a magnetic moment and an angular momentum, when in the presence of an external magnetic field, will precess about the direction of this field with a Larmor Precession Frequency $\Omega_L = \gamma H$, where H is the external field and γ is the ratio of magnetic moment to angular momentum (erroneously called gyro-magnetic ratio). The most common particles exhibiting such a resonance are the electron (Electron Paramagnetic Resonance — EPR), and the nuclei of most elements with odd mass number (Nuclear Magnetic Resonance — NMR); however, the phenomenon is not restricted to atomic particles only. As a matter of fact, large samples of ferro-, ferri-, and antiferromagnetic materials exhibit the same effect when the magnetization of such samples is in the presence of an applied magnetic field. In general we can say that magnetic resonance is the natural resonance of any system possessing magnetic moment and angular momentum. In nature, however, there are always losses associated with systems in motion and, therefore, the resonance phenomena can be observed experimentally only when the system is driven

with an external electromagnetic field. If the frequency of the driving field is equal to, or in the neighborhood of, the natural resonance frequency of the driven system, there will be a large energy transfer from the driving field to the resonating system, which can be easily detected. On the other hand, a magnetic moment precessing at a given frequency induces a voltage in a properly oriented coil and this voltage is a maximum at resonance, since at this frequency the precession amplitude is a maximum. This method (called Nuclear Induction when used in NMR experiments) is used in the equipment described here.

The driving electromagnetic field in most NMR equipment is produced by a driving coil, while the voltage at resonance is induced in a pickup coil. Since the driving field is many orders of magnitude larger than the field produced by the precessing magnetic moment, the voltage induced in the pickup coil by the driving field will wipe out any useful signal unless some measures are taken to prevent this. This is done by physically decoupling the drive and pickup coils by orienting them perpendicular to each other. In this case, if the driving frequency is varied over a range of frequencies, the pickup coil will send a signal only when there is a resonance excited in the system under study. An instrument built in this way, which can determine the frequency of nuclear magnetic resonance, is called an "NMR spectrometer." The main parts of the spectrometer are a variable frequency oscillator and amplifier for driving the system at resonance, and a very high-gain superheterodyne receiver for detecting the low-level signal from the pickup coil.

The spectrometer described in this article is unique for its variable frequency, extremely high gain, and possibility of use at cryogenic temperatures. Since Fe^{57} has a natural abundance of 2.245% (the more common Fe^{56} isotope has zero nuclear magnetic moment), it was necessary to detect extremely weak signals and therefore it was required that the spectrometer have a total gain of over 140 db (10^7 times). This, in combination with the requirement of variable frequency over a wide range, made the choice of a superheterodyne system a natural one. After this choice was made, it was necessary to use the "nuclear induction" crossed-coil method, instead of the more common "marginal oscillator" method where the large change of transfer of energy is detected at resonance.

Since the induced nuclear signal is about 10^{-6} times smaller than the driving signal, the accuracy of adjustment of the axes of the two coils must be better than

15 arc sec. This puts severe requirements on the mechanical stability and accuracy of adjustment of the cross-coil system. This, in combination with the requirement for use at cryogenic temperatures, made it necessary to search for a new material which was nonconducting, had low thermal conductivity, and good mechanical properties. It was required that the material withstand thermal shock from room temperature to 77°K and below. These were the constraints under which the system was designed and which forced the selection of the specific way in which the spectrometer was constructed.

2. System Description, *D. I. Tchernev*

In order to simplify and speed up the construction of the spectrometer, an attempt was made to use commercially available components and systems whenever possible. The complete block diagram of the spectrometer is shown in Fig. 9. The master drive oscillator covers the frequency range from 10 to 200 Mc, and can be frequency-modulated with a maximum modulation deviation of 100 Kc. For the regular search for the resonance, a Marconi Instruments, Ltd., FM signal generator Model TF 1066 B/6 is used as the master drive oscillator while the accurate measurement of the resonance frequency to 1 part in 10^6 requires the use of a Rohde & Schwarz frequency synthesizer as the master drive oscillator.

The output of the master drive oscillator is amplified through two wide-band distributed amplifiers; the first is a voltage amplifier with 20 dB gain, while the second one is a 1.5 watt power amplifier, driving the two drive coils. Since the impedance of these coils varies with frequency, and the NMR experiment requires a constant driving magnetic field, the current through the drive coils is monitored by a Tektronix current transformer (CT-2) and kept constant through a feedback loop. A second current transformer (CT-1) is used to produce a reference voltage for the frequency-lock loop. The master drive oscillator can be swept by the use of a constant-speed mechanical drive. The sweep speed can be varied continuously from a few Kc/sec to about 2 Mc/sec.

A second oscillator, covering the 20- to 210-Mc range, is slaved to the master oscillator so that it always is at a 10.7-Mc higher frequency than the master oscillator. For this purpose, a Kay Electric Company Model 990A Utilator was modified as described in detail in Part 4. The output of the slave oscillator is fed through an isolation amplifier to a diode mixer, where the frequencies of the master and slave oscillators are mixed together and the difference-frequency of 10.7 Mc is obtained. This is further amplified through a tuned amplifier and a 10.7-Mc

frequency discriminator. The output of this discriminator is a DC signal with a polarity and amplitude depending on the deviation of the difference-signal from 10.7 Mc.

In order to make the output of the discriminator amplitude-independent, the gain of the tuned 10.7-Mc amplifier is controlled through a feedback loop and its output maintained at 1 volt.

The error signal from the frequency discriminator is split in two parts. One part is amplified through a Kin-Tel DC amplifier and used to electrically control the frequency of the slave oscillator with a time constant of 0.1 sec. The range of this control depends on the actual frequency of the slave oscillator and is, in general, of the order of 5 Mc.

The second error signal is amplified through another Kin-Tel DC amplifier and used to drive a servomotor, mechanically coupled to the tuning shaft of the slave oscillator. In this manner the electrical tuning provides fine and fast correction of the slave oscillator's frequency while the mechanical tuning permits coverage of the whole frequency-band of interest. Once the two oscillators are locked 10.7 Mc apart, they remain locked within a 500-cycle accuracy while their nominal frequency varies over a factor of 10. This system has proved to be extremely efficient and reliable.

The pickup part of the spectrometer is mounted in a separate rack from the drive part in order to reduce coupling between the two parts, and to eliminate possible oscillations at the extremely high gain of 10^6 times. Because of the variable-frequency nature of the spectrometer, it is difficult to construct tuned amplifiers with variable frequency and have them remain tuned while the driving frequency is swept. For this reason the voltage induced at resonance in the pickup coil is heterodyned to 10.7 Mc in a low-level balanced mixer located at the coil. The signal from the slave oscillator is fed to the balanced mixer through an isolation amplifier, and the resulting difference-frequency of 10.7 Mc is amplified in a 36-dB tuned and balanced preamplifier located at the top of the coil assembly. The output of this preamplifier is then fed to the pickup rack and to the main tuned amplifier. The gain of this amplifier can be controlled manually from 0 to 90 dB.

The induced NMR signal, which so far has been amplified more than 10^6 times, is now delivered to a phase-sensitive detector, where the phase reference is taken from the output of the locking loop and delayed through

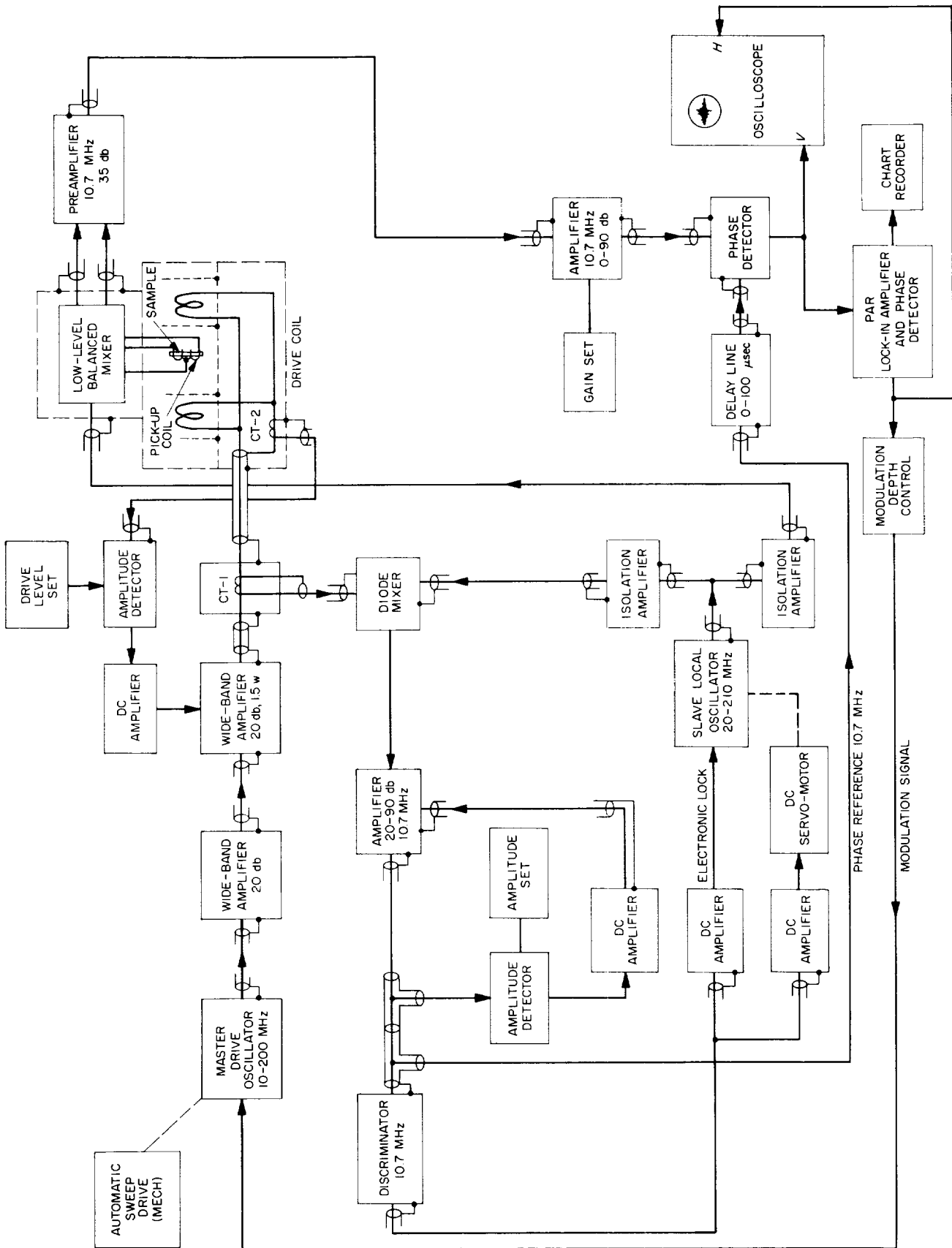


Fig. 9. Block diagram of variable-frequency NMR spectrometer

a variable 0- to 100- μ sec delay line. By varying the time delay of the reference signal, and consequently its phase, one can select to display either the dispersion or the absorption mode of the nuclear magnetic resonance. The output of the phase-sensitive detector is displayed on an oscilloscope, where the horizontal deflection is controlled by the signal used for FM modulation of the master drive oscillator. If the FM modulation depth is larger than the width of the resonance, one can observe the absorption or dispersion line directly on the screen of the scope.

Alternatively, one can feed the output of the phase-sensitive detector to a Princeton Applied Research lock-in amplifier and phase-sensitive detector (Model JB-5), and for a small FM modulation depth of less than the line-width, one can obtain a signal proportional to the derivative of the absorption or dispersion line. This signal then is recorded on a strip-chart recorder.

The lock-in amplifier produces an additional improvement of signal-to-noise ratio of over 100 times (40 dB), and can detect signals well below the noise level of the tuned amplifiers. The built-in audio oscillator in this amplifier is also used to frequency-modulate the master drive oscillator.

A view of the complete spectrometer is shown in Fig. 10. The complete system has a detection capability better than 100 nanovolts without the lock-in amplifier at room temperature. Further improvements can be made

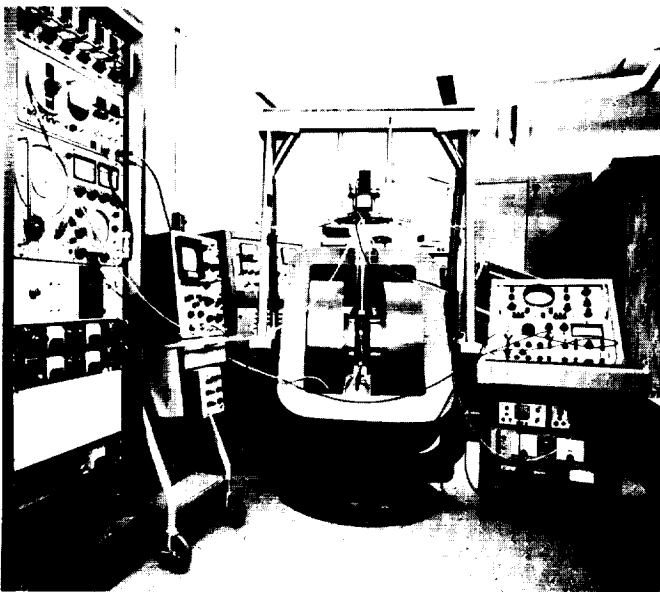


Fig. 10. Overall view of complete NMR spectrometer

by reducing the bandwidth of the tuned 10.7-Mc amplifiers. For this purpose, a set of quartz-crystal filters with a matched discriminator was obtained, which enables the reduction of the bandwidth from 1 Mc to 10 Kc. However, it was not necessary to use them for the present experimental setup.

More detailed discussion of the low-level balanced mixer will be given in Part 4.

3. Design of the Coil Assembly, H. G. Vorkink

The mechanical limitations imposed on the coil assembly were rather severe. The mutual orientation between the axes of the drive and pickup coils had to be maintained with an accuracy of 15 arc sec over a wide temperature range. The assembly was also required to withstand thermal shock from room temperature to 4.2 K. For this reason, it was necessary to find a material with low dielectric losses, high resistivity, low coefficient of thermal expansion, dimensional stability, resistance to thermal shock, and which could be easily machined. After exhaustive tests of many materials, the choice was a polycarbonate manufactured by G.E. under the trade name "Lexan." This material was used almost exclusively for the coil assembly, with the exception of metallic shields whenever necessary.

It was decided to keep the pickup coil with the sample stationary and to adjust the driving coil pair around two mutually perpendicular rotational axes. Considering that mechanical stability was of utmost importance, it was chosen to use flexure pivots on all moving parts, rather than regular pivots or bearings, thus eliminating any backlash or take-up. An assembly drawing of the coil system is shown in Fig. 11. The driving coil pair, of the Helmholtz type, is wound around a cylinder, which is fixed to a tuning plate. This plate is milled out in such a way that applying pressure to the two tuning points causes angular deflection about the flexure pivots. The angular motion is thus transferred into linear motion. Two Lexan rods are connected to the tuning points of the plate and surrounded by Lexan tubing of the proper dimension. In this way, the linear translation of the rods with respect to the tubing is used to adjust the position of the drive coils.

The entire coil assembly extends down for 22 in. in a cryogenic dewar. On the upper end, the Lexan rods and tubing end at a 0.5-in. brass plate, where a lever system transfers the linear motion to two Sherr-Tumico direct-reading micrometers with a resolution of 0.0001 in., as

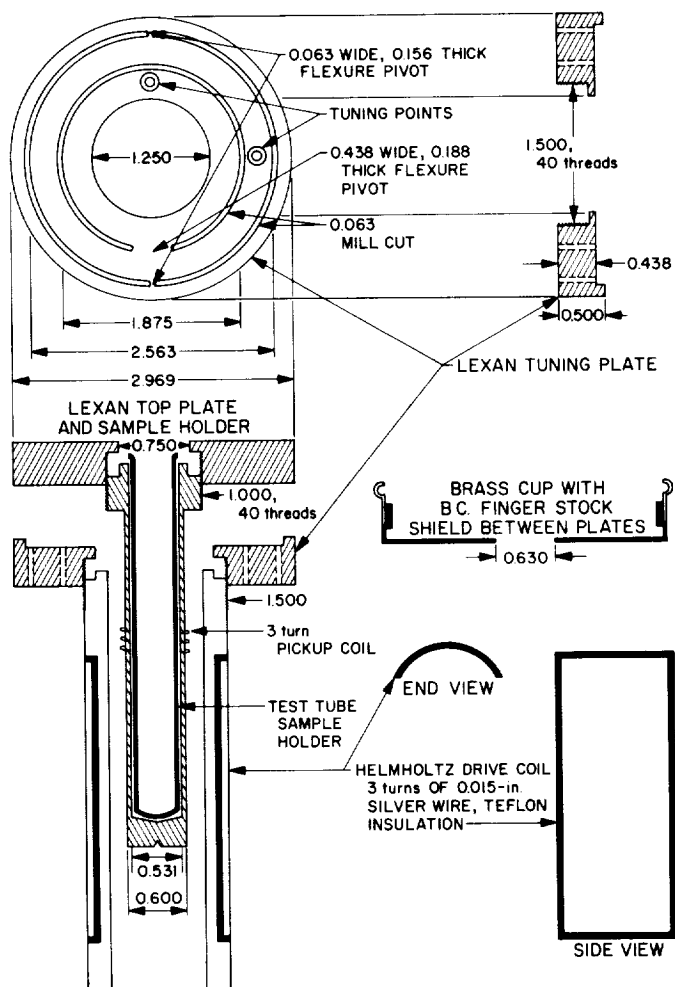


Fig. 11. Coil assembly for NMR spectrometer

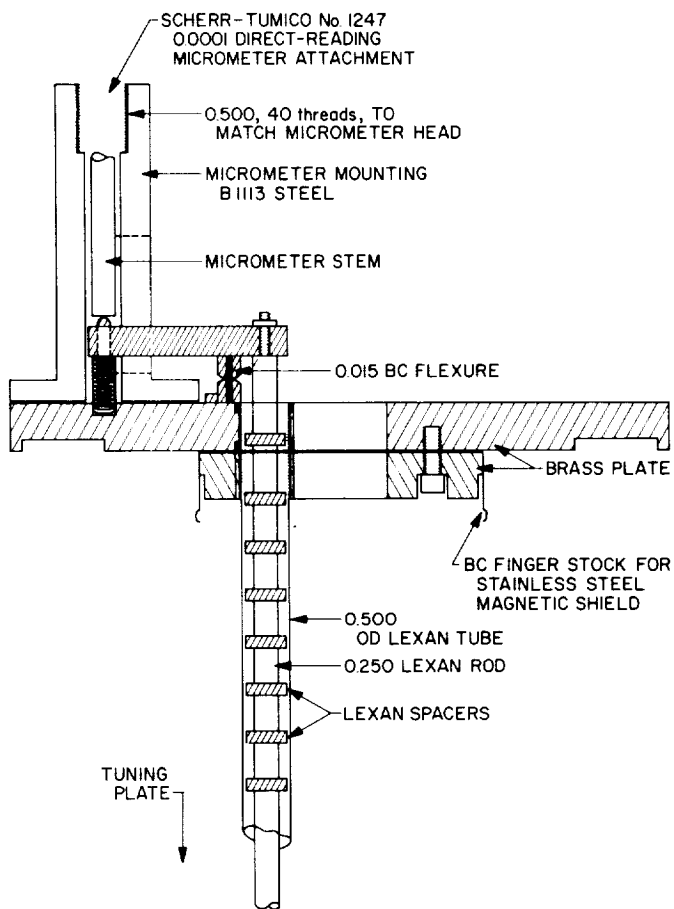


Fig. 12. Upper plate and lever system for NMR spectrometer

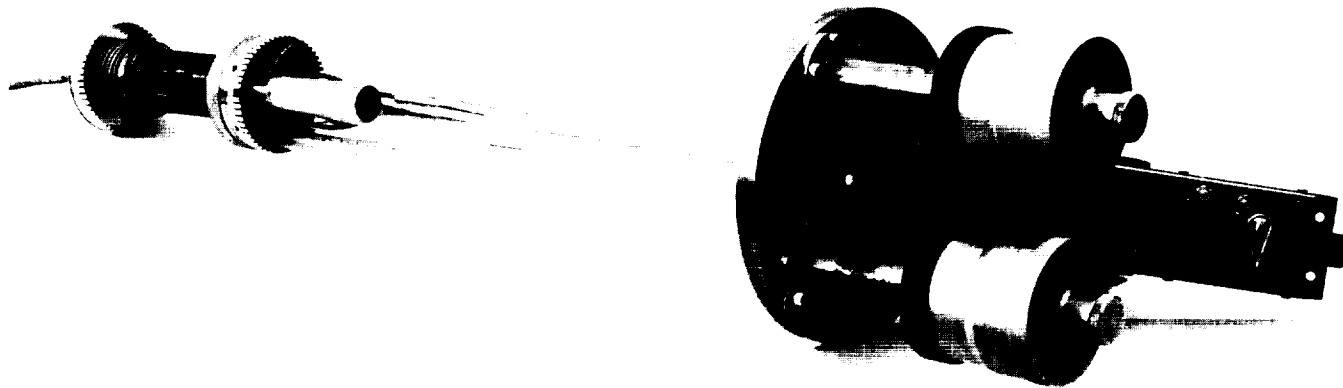


Fig. 13. Views of complete coil assembly with preamplifier

shown in Fig. 12. The entire coil assembly is surrounded by a 3-in. OD, 16-mil wall, nonmagnetic stainless-steel (No. 304) tube for shielding purposes. For the same reason, there is a brass cup shield between the tuning plate and the pickup plate in the coil assembly.

In Fig. 13 we show a picture of the total assembly. The 10.7-Mc preamplifier, which is also mounted on the top brass plate in order to reduce the length of the lead wires and the noise pickup, is visible next to the two micrometers.

4. Electronic Circuits, J. E. Guisinger

a. Modification of the slave oscillator. For the purpose of electronic tuning and frequency lock, a Kay Electric

Company Utilator Model 990A was modified. The tuned circuit was changed from the grids to the plates of the push-pull oscillator (tubes 5719), as shown in Fig. 14. In addition, two capacitive diodes (type MM 1861, by Motorola) were added across the tuned circuit of the oscillator, where they are automatically back-biased by the tube-plate voltage at 24 volts. The error DC signal from the lock-in loop was then applied between the centerpoint of the diodes and ground, thus changing the negative bias and, consequently, varying their capacity.

Two cathode-followers were added to the oscillator (tube 6021), thus separating the two outputs for the locking loop and the balanced mixer. In order to control the amplitude of the output voltage, the cathode followers were supplied with plate voltage from the automatic gain

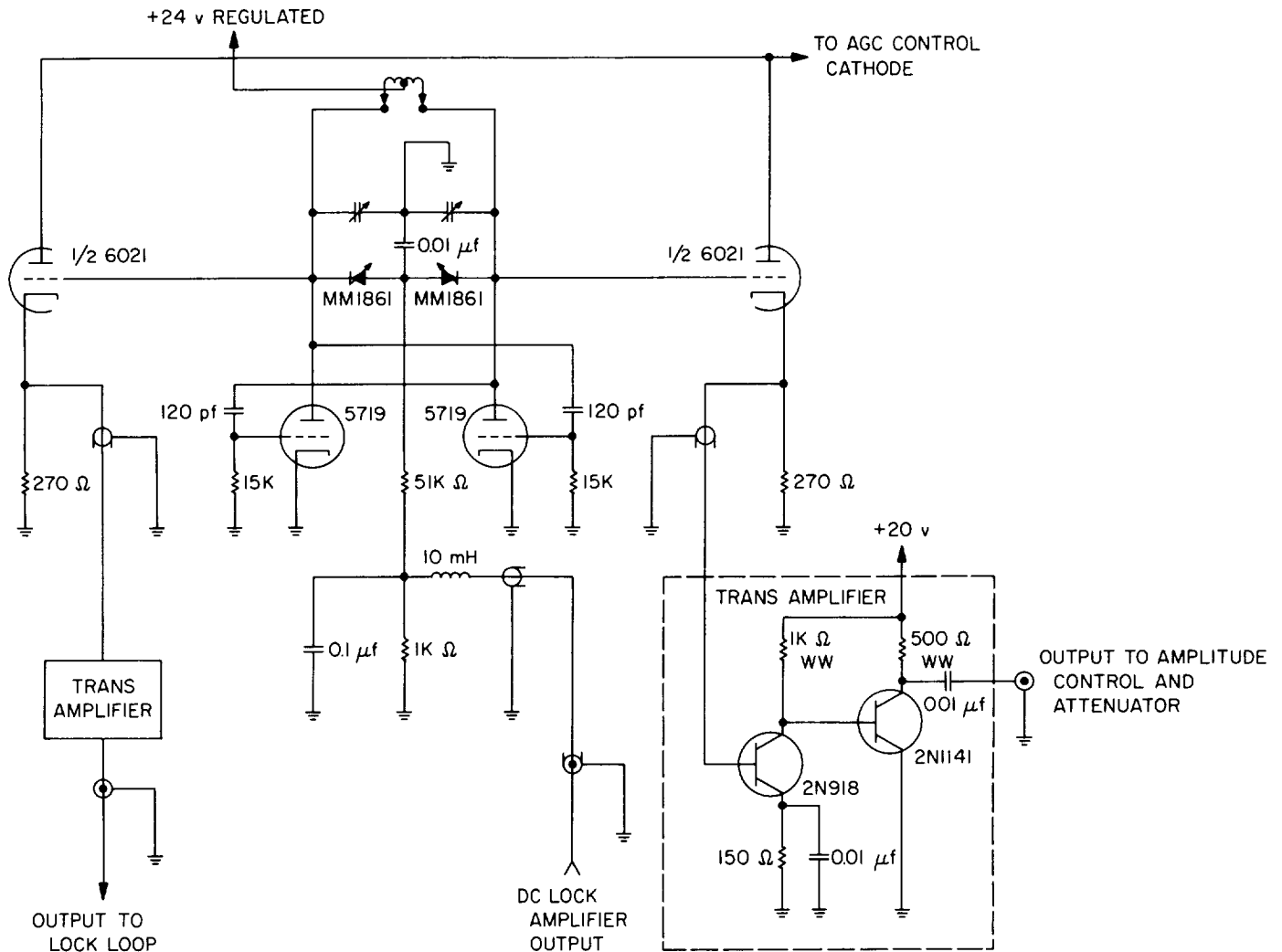


Fig. 14. Modification of slave oscillator for electric tuning

control (AGC) loop in existence in the Utilator. Two double-stage wide-band transistor amplifiers were added to increase the output to about 1 volt in the range from 20 to 210 Mc. This output can then be reduced by using the built-in attenuator of 56-dB total attenuation.

The time constant of the DC error signal was set to 0.1 sec in order to prevent oscillations in the frequency lock loop while still permitting quick tuning to the necessary frequency during operation.

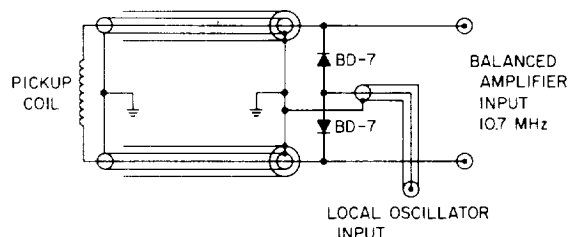
b. Low-level balanced mixer. Heterodyning of signals of about 100 nanovolts is difficult, because the local oscillator signal is 10^7 times larger, and any small variation in amplitude will be amplified and detected as noise or signal fluctuation. Furthermore, hum and other types of amplitude modulation of the local oscillator will also be present in the difference-frequency, and will totally mask the small signal. Therefore it is imperative to use a balanced mixer, where such variations and modulations are cancelled while the incoming signal is doubled. Three possible schemes are shown in Fig. 15, and all were tried for our purpose.

In Fig. 15(a), the balanced mixer uses two backward diodes (a type of tunnel diode, type BD-7, by G.E.), which are especially suited for low-level signals, since the break point is at zero volts and no bias is required. The noise level is low, and operation at cryogenic temperatures is possible because the diode characteristic is due to tunneling. The main disadvantage of the circuit is the fact that the pickup coil cannot be tuned to resonance with any useful Q factor. The backward diodes have too large resistance to be in series with the tuned circuit, and not high enough to be in parallel. Since tuning of the pickup coil increases the signal by a factor of 50, this scheme was abandoned.

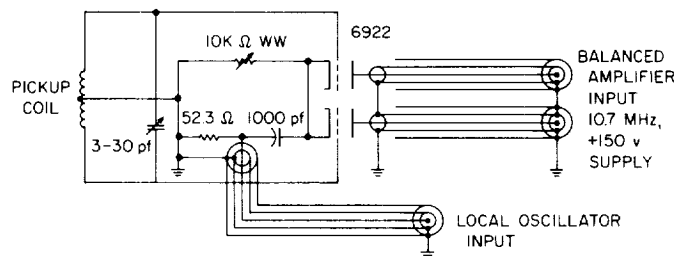
Fig. 15(b) shows a balanced mixer using the type 6922 tube (a low-noise high-frequency double triode). In this case, the mixer has a net conversion gain of about 10, instead of a conversion loss, as in the case of diodes, and high Q of the tuned pickup coil. The main disadvantage is that the mixer has to be physically located next to the coil and this prevents the system from operating at cryogenic temperature, or at least makes such operation difficult.

The third circuit that was tried is shown in Fig. 15(c). In this case, the tube is replaced by two MOS field-effect transistors. Since the gate resistance of the FET is very high, the pickup coil can be tuned satisfactorily and the system can operate at moderately low temperatures.

(a) BALANCED MIXER USING BACKWARD DIODES



(b) BALANCED MIXER USING TWIN TRIODE



(c) BALANCED MIXER USING MOS FIELD-EFFECT TRANSISTORS

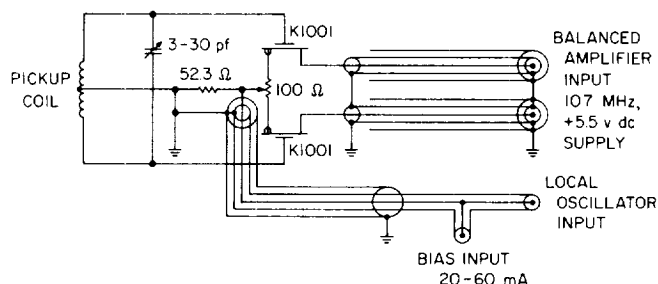


Fig. 15. Low-level balanced mixer circuits

The main difficulty, however, is the higher noise level and the lower transconductance of the FET in comparison with the tube triode and, consequently, the lower signal-to-noise ratio of the mixer. The final choice between the last two circuits will be made on the basis of the system's use at cryogenic temperatures.

5. Conclusions, D. I. Tchernev

It has been shown that it is possible to build a variable-frequency NMR spectrometer of extremely high gain, capable of operation at cryogenic temperatures. The complete system was tested at frequencies up to 55 Mc using the proton resonance of heavily doped water in an externally applied magnetic field, and the performance was found to be according to specifications. The signal-to-noise ratio obtained in this test was better than 40 dB without the use of the lock-in amplifier, and signals lower than 100 nanovolts were detected without any difficulties. The self-resonance of the pickup coil with three turns of

silver wire is at 140 Mc, which limits the upper frequency of the system. However, using a single-turn pickup coil will permit operation above this limit with perhaps

slightly lower sensitivity. The possibility of using the pickup coil above its natural resonance will also be investigated.

References

1. Rose, A., *Physical Review*, 97: 1538, 1955.
2. Lampert, M., *Physical Review*, 103: 1648, 1956.
3. Muller, R. S., "Physics of Semiconductors," *Proceedings of the 7th International Conference, Paris*, p. 631, Academic Press, 1964.
4. Wright, G. T., "Space-Charge-Limited Solid-State Devices," *Proceedings of IEEE*, 51: 1642-1652, 1963.
5. Mott, N. F., and Gurney, R. W., *Electronic Processes in Ionic Crystals*, 2nd Ed, p. 172, Oxford University Press, Oxford, England, 1957.
6. Dacey, G. C., "Space-Charge-Limited Hole Current in Germanium," *Physical Review*, 90: 759-764, 1953.
7. Shumka, A., and Nicolet, M-A., "Space-Charge-Limited Current in Germanium," *Proceedings of the 7th Int. Conference on the Physics of Semiconductors*, p. 621, Dunod, Paris, Academic Press, 1964.
8. Gregory, B. L., and Jordan, A. G., "Experimental Investigations of Single Injection in Compensated Silicon at Low Temperatures," *Physical Review*, 134: A1378-1386, 1964.
9. Gregory, B. L., and Jordan, A. G., "Single-Carrier Injection in Silicon at 76° and 300°K," *Journal of Applied Physics*, 35: 3046-3047, 1964.
10. Moll, J. L., *Physics of Semiconductors*, p. 222, McGraw Hill, New York, N.Y., 1964.
11. Ryder, E. J., "Mobility of Holes and Electrons in High Electric Fields," *Physical Review*, 90: 766-769, 1953.
12. Prior, A. C., "The Field-Dependence of Carrier Mobility in Silicon and Germanium," *Journal of Physics and Chemistry of Solids*, 12: 175-180, 1959.
13. Shockley, W., and Prim, R. C., "Space-Charge-Limited Emission in Semiconductors," *Physical Review*, 90: 753-759, 1953.

VI. Flight Computers and Sequencers

A. The Diagnosable Arithmetic Processor

A. Avizienis

1. System Design of the Diagnosable Arithmetic Processor

The preceding studies of arithmetic with coded binary operands (Refs. 1, 2) were motivated by the objective to design a spacecraft guidance computer which stores, transmits, and processes binary numbers exclusively in a coded form. Given a fast and relatively inexpensive checking algorithm, all binary numbers which are being moved between the functional subsystems (arithmetic processors, memories, input-output buffers, sequence generators) of a computer can be checked to generate real-time diagnostic information concerning the sources of the numerical data. This diagnostic information is then available to initiate immediate replacement, repair, or reorganization actions in the computing system in the case of a detected fault.

The favorable properties of product codes with the check factor 2^a-1 led to the selection of the code with the check factor $a = 15$ for the use in the experimental model of the JPL Self-Testing-And-Repairing (JPL-STAR) spacecraft guidance computer, which is intended to serve as a potential prototype for guidance computers in very long exploratory missions (from one to several years). One of the initial steps in the development of the JPL-STAR computer system was the design of a diagnosable arithmetic processor which receives product-coded operands and performs all algorithms with product-coded forms.

The operand precision of 28 bits was selected for the expected guidance problems, and the check factor $a = 15$ was chosen in order to provide complete detection of single determinate faults when binary numbers are transmitted and added in four-bit bytes. Total length of coded numbers (15X) is then 32 bits. It is to be noted that the choice of $a = 15$ provides complete detection of single determinate faults for binary coded numbers up to 56 bits in length. The JPL-STAR computer is a replacement

system, and information is transmitted between its sub-systems in four-bit bytes in order to reduce the size of the replacement switches.

The block diagram of the arithmetical processor for the JPL-STAR computer is shown in Fig. 1. The processor accepts six operation codes: "Clear Add," "Add," "Subtract," "Multiply," "Divide," and "No Operation." The operation codes are protected by a two-out-of-four encoding for fault detection. After completing an algorithm, the processor issues an "end of algorithm" control signal, which serves as a request for new work. The request is satisfied by delivering a one-byte operation code, followed by an 8 bytes long operand on the four data input (DI) lines. An exception is the "No Operation" code, which

causes the processor to ignore the input operand, and to issue the work request again after one idle internal cycle. The internal cycle, which is the main time unit of the processor, consists of 10 byte-times. The byte-time is determined by the clock frequency of the computer, and it consists of two phases.

Results of arithmetic algorithms are delivered on the four data output lines (DO). Partial results (partial sums, products, remainders) may be up to 10 bytes long, and the last byte is accompanied by a "perform check" signal on a control line. The final results (sum, difference, product, quotient) are always 8 bytes long and also have the "perform check" signal along with the eighth byte. They are followed by one non-numerical *code byte*, which

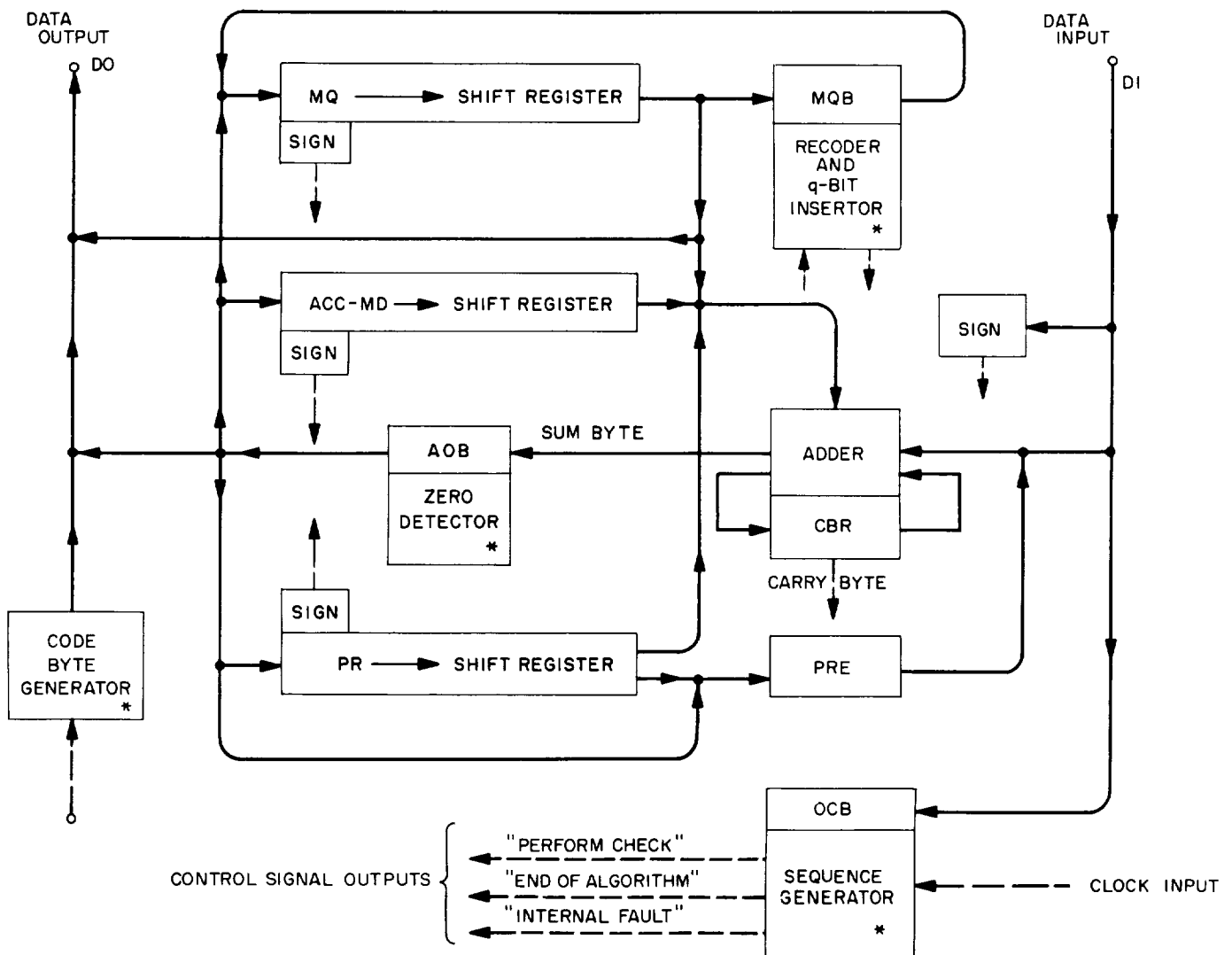


Fig. 1. Diagnosable arithmetic processor block diagram

conveys additional information on the result using a two-out-of-four code. There are three *singularity codes*: "sum overflow," "quotient overflow" and "zero divisor," and three *good result codes*: "positive," "zero," and "negative." The latter three are obviously redundant and serve as useful checks and as branching information for "jump" class instructions. The work request is issued on a control line during the last byte-time of the output cycle. All partial and final results are sent to the *checker*, which is a four-bit adder and accumulator. The adder performs the modulo 15 summation (with an end-around carry) of the incoming bytes of the results. Upon receipt of the "perform check" signal, the four-bit accumulator is inspected for the "all ones" check result. Any other check result indicates that the result was not a properly product-coded binary number, and a fault warning is issued to the central control of the system.

Internally, the processor contains three eight-byte double-ranked registers (see Fig. 1): the "Accumulator/Multiplicand/Divisor" (ACC-MD) register, the "Product-Remainder" (PR) register and the "Multiplier-Quotient" (MQ) register. There also are four one-byte registers: "Adder Output Buffer" (AOB), "Multiplier-Quotient Buffer" (MQB), "PR Extension" (PRE) and the "Operation Code Buffer" (OCB), and several one-bit storage elements for recording signs and similar information.

The *adder* is an eight-bit parallel adder which generates a *sum-byte* SB and a *carry-byte* CB. The carry byte CB is stored in an internal four-bit double-ranked Carry Byte Register (CBR). The eight-bit adder is needed because the ACC-MD input to the adder supplies the multiples ± 1 , ± 2 , ± 4 and ± 8 of ACC-MD contents as operands for multiplication and division. Fig. 1 also demonstrates the interconnections of the registers.

It is to be noted that all movement of numerical information takes place *four bits at once*, or in the so-called series-parallel mode. At no point do the bits of one byte pass through the same logic element; consequently, a fault will not damage more than one bit in the byte, and the same bit position will be subject to damage in a sequence of bytes passing through the point of fault. All solid lines in Fig. 1 designate four parallel data lines; the dashed lines are control signal lines. Asterisks designate parts of the control.

2. Algorithms of the Diagnosable Arithmetic Processor

The product-coded binary operands consist of 32 bits. The "one's complement" notation is used to represent

negative numbers, and the binary point is assumed to be at the left end of the encoded 32-bit number, giving the range $-1/2 < z < 1/2$ for any coded operand z , and the range $-1/30 < x < 1/30$ for the uncoded operands x . This range was most convenient for the experimental model; other ranges can be readily employed by moving the binary point and appropriately adjusting the algorithms. It is to be noted that the range $-1 < x < 1$ is not available for uncoded operands in this case, since moving the binary point will scale the range of x by 2^j , and the jump in range around one will be from $16/30$ to $32/30$. The location of the binary point must be in reference to the coded numbers in order to obtain simple sign detection and overflow detection algorithms. Zero is represented by a string of 32 ones; the all-zero number is not a properly coded number and is not permitted as an input.

The *Clear Add* or *CAD* algorithm needs one cycle for its execution. It replaces the contents of the ACC-MD by the input operand, which is added to zero and then stored in the ACC-MD. At the same time this sum is also returned on the output lines to the checker.

The *ADD* and *Subtract* or *SUB* algorithms add the input operand or its digitwise complement, respectively, to the operand in the ACC-MD, store the sum in the ACC-MD, and also feed it to the checker. Additions which do not generate an end-around carry (e.a.c.) are completed in one cycle. If an e.a.c. is detected, the carry byte is sent to the checker, a check performed on this incomplete result, and a second cycle (always final) is employed to add the e.a.c. to the contents of ACC-MD. In case of overflow the "additive overflow" singularity code follows the result on the output lines.

The *Multiply* or *MUL* algorithm requires that the $15X$ should be already in the ACC-MD register; it is placed there by a *CAD* command, or is left there by the preceding operation. One cycle is employed to load the multiplier $15Y$ into the MQ register and to derive sign information for the product. The multiplier is then sensed one byte at a time; consequently, there are eight iterative steps, each one consisting of from one to three cycles. The multiplier byte is recoded into a form possessing not more than two non-zero (± 1) bits, and appropriate multiples (± 1 , ± 2 , ± 4 , ± 8) of the multiplicand are added to the partial product in *PR*. Every partial result (nine bytes, plus the end-around carry byte) is also delivered to the checker for diagnosis of the addition. None, one, or two cycles may be required. Each step is concluded with a contraction-and-shift cycle for the nine-byte partial result P^* of preceding additions. This cycle rounds the partial

result P^* to a nine-byte result P (which is a multiple of 16) by subtracting a constant $15N_i$ to get:

$$P = P^* - 15N_i = 15(16T), \text{ since } P^* = 15(16T + N_i)$$

Simultaneously, P is shifted one byte right (divided by 16) and the value of N_i ($0 \leq N_i \leq 15$) is stored in one byte of MQ, which has delivered a multiplier byte for decoding and thus can accommodate the correction byte N_i . After the end of the eighth step, the PR contains the result

$$P^{(8)} = (15X)(15Y) - 15N = 15(15XY - N)$$

The terminal step now is performed to get an eight-byte rounded product P as a result. One cycle is used to divide $P^{(8)}$ by 15, and the eight-byte result

$$P^{(8)}/15 = 15XY - N$$

(which is usually not a multiple of 15) is returned to PR and the checker. However, the value of N has been stored in the MQ and is now available to form the 16 byte result by attaching MQ at the right end of PR

$$P_{\text{term}} = (15XY - N) + N \text{ (16 bytes long)}$$

During the next cycle, N is sent to the checker and added to the check sum of $15XY - N$, which was not tested. Internally, the roundoff constant G is computed during this cycle from the bytes of N . The algorithm is concluded by adding the coded roundoff constant $15G$ to get the final eight-byte rounded result:

$$P_{\text{out}} = (15XY - N) + N \pm 15G = 15(XY \pm G)$$

where G is the up- or down-rounding constant which would have been used for an uncoded product XY . Although "one's complement" is being used for subtractions, only nine bytes of the partial products were needed for the steps of the algorithm. The contract-and-shift cycle permits this time-saving variation of "one's complement" multiplication. The multiplication time for non-zero operands is

$$t_m = 1 + 8(k_i + 1) \pm 3 \text{ cycles,}$$

where k_i is the count of non-zero digits in the i th multiplier byte. Since a multiplier can have as many as 16 and as few as two non-zero digits (one ± 1 and one ∓ 1) in its recoded form, the variation of t_m is

$$14 \leq t_m \leq 28 \text{ cycles.}$$

Zero operands are detected upon receipt, and a zero result is delivered immediately, taking only two cycles.

The *Divide* or *DIV* algorithm requires that the divisor $15Y$ should be already in the ACC-MD register. One

cycle is used to load the single-length (eight-byte) dividend $15X$ into the PR register and to record the signs. Tests for zero dividend (giving an immediate zero result) and zero divisor (a singularity) are performed during this cycle; in either case only one additional cycle is needed to complete the algorithm. The divisor is returned to the checker in case of a "zero divisor" singularity. In the non-zero cases the next cycle is used to form $15(15X)$, that is, to multiply the dividend by 15 in order to get a properly coded quotient $15Q$, such that

$$15^2 X = (15Y)(15Q) \pm 15^2 R$$

is satisfied, where R is the remainder in uncoded division. The quotient $15Q$ is then generated in eight steps; one byte of the quotient per step. Restoring division is employed, generating one bit of the quotient at a time. The first cycle of each step is employed to finish restoring the remainder (if required by the preceding step) and to shift the remainder one byte left (multiplying by 16). Four cycles of quotient generation follow. First, the magnitude of the remainder is diminished by eight times the divisor. The sign of this result selects the leftmost bit of the new quotient byte and decides whether ± 4 (restoration) or ∓ 4 (further decrease) will be the next multiple of the divisor; the next two cycles use ± 2 and ± 1 as trial multiples of the divisor. If restoration is called for in the last cycle, it will be performed during the shift cycle of the next step. All partial results are returned to the PR register and also are sent to the checker. Two cycles are needed for the terminal step: one completes the storage of the quotient into MQ, the other is used to move the quotient into ACC-MD and to deliver it to the checker. The total time for division is:

$$t_d = 2 + 5 \times 8 + 2 = 44 \text{ cycles}$$

The "quotient overflow" singularity occurs whenever the allowed operand range $-1/30 < Q < 1/30$ is exceeded. This implies $|15Q| < 1/2$ as a requirement, and the test is an attempt (during the first step, second cycle) to generate a bit of value 1 for the leftmost position of the coded quotient magnitude; if it succeeds, the quotient will overflow. This condition leads to an immediate termination of the algorithm (in one cycle), and an output of a zero operand and an appropriate singularity code. The remainder of any division is not made accessible in this experimental model of the processor, although it can be obtained from the contents of PR.

No Operation or *NOP* algorithm retains the ACC-MD unchanged and ignores any possible external input for one cycle, issuing an "end of algorithm" work request at its end. It is noted that a "Store Accumulator" operation

code is not provided for the arithmetic processor. The result of an algorithm is always placed into the ACC-MD and also sent to the checker. In this model of the JPL-STAR computer system a duplicate accumulator (DAC) is maintained in the memory module. The DAC receives the result from the checker and always holds a copy of the contents of the ACC-MD, therefore "Store Accumulator" is a command to the memory module. A more elaborate set of arithmetic processor commands was considered to be unnecessary for the experimental model.

3. Control of the Diagnosable Processor

A two-phase 1-Mc clock is employed to provide the basic frequency of the processor (one byte-time), with higher frequencies being quite feasible. The clock may be either internal or external with respect to the processor; an external clock provides an opportunity for independent monitoring and replacement. In the sequence generator, one "two-out-of-five" coded ten-step counter generates timing for the basic cycle, and another similar counter generates the timing for multiplication and division (one preliminary, eight iterative, and one terminal step). Five individual storage elements serve for conditional and intra-step sequencing, and the current operation code is stored in the four-bit buffer OCB. All control sequencing is performed in the processor after receipt of the operation code. Control functioning is monitored by the protective encoding of counters and by

duplication of a few critical functions; any discrepancy is indicated on a special "internal fault" output line. Furthermore, it is very likely that a control fault will generate an unacceptable (not properly coded) result, which will be detected by the checker. Further analysis of this property may permit a reduction in the redundancy of arithmetic control.

Three control lines are needed to supply control information to the outside: the "perform check" signal, the "end of algorithm" signal, which serves as the request for work, and the "internal fault" signal obtained from internal monitor circuits. Besides these lines, the clock input, four data input lines, and four data output lines are needed for connections of the arithmetic processor to the remaining part of the JPL-STAR computer system. The self-contained control facilitates the replacement of the processor as a single unit with relatively few input-output lines.

The logic design of the "hard core" central control and of other functional replaceable units is presently under way and will be reported in future *Summaries*. A complete and detailed description of this Diagnosable Arithmetic Processor for the JPL-STAR system is being prepared for publication as a JPL Technical Report. The construction of the breadboard model is about 80% complete, and checkout procedures are presently being devised for the breadboard.

References

1. Avizienis, A., *A Set of Algorithms for a Diagnostic Arithmetic Unit*, Technical Report No. 32-546, Jet Propulsion Laboratory, Pasadena, California, March 1, 1964.
2. Avizienis, A., *A Study of the Effectiveness of Fault-Detecting Codes for Binary Arithmetic*, Technical Report No. 32-711, Jet Propulsion Laboratory, Pasadena, California, September 1, 1965.

ENGINEERING MECHANICS DIVISION

VII. Materials

A. Carbon and Graphite Research

D. B. Fischbach and W. V. Kotlensky

1. Shear Deformation of Pyrolytic Carbons Parallel to the Substrate

The study of high-temperature shear deformation of pyrolytic carbons parallel to the substrate (SPS 37-35, Vol. IV), formerly called basal shear deformation, has continued with an investigation of the effect of strain rate $\dot{\epsilon}$ and temperature on the shear flow stress σ_f . The double-shear technique (SPS 37-31, Vol. IV) was used and all specimens had been preannealed at 3000°C with the exception of one which had been compression-annealed at 2900°C. Tests were run with monotonically increasing strain rates at temperatures of 2500–2900°C. The results, shown in Fig. 1, can be fitted approximately by

$$\dot{\epsilon} = S \exp(-\Delta H/RT) \sigma_f^n \quad (1)$$

where S is a constant depending on the microstructure (especially the degree of preferred orientation) of the sample, ΔH is the effective activation energy, R is the gas constant, and T is the absolute temperature. A ΔH value of approximately 270 kcal/mole was obtained from these data. The positive deviations of the data points from a σ_f^n

relationship at 2700–2900°C are attributed to an approximation made in calculating σ_f . Shear on a single plane was assumed, but the actual situation is intermediate

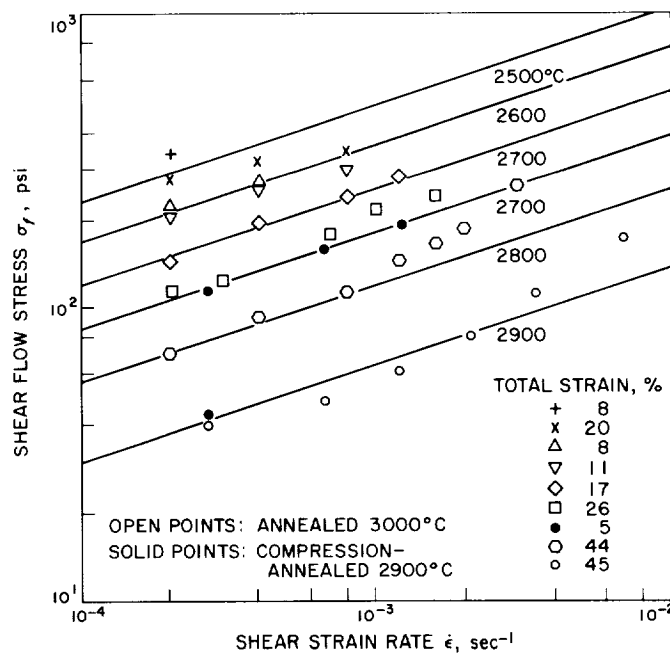


Fig. 1. Dependence of shear flow stress of pyrolytic carbon parallel to the substrate on strain rate at several temperatures

between this case and that of uniform shear. The resultant error increases with shear strain and becomes significant above approximately 20% strain (the total strain is shown in parentheses by the curves in Fig. 1). The negative deviations at 2500–2600°C appear to result from partial failure of the specimen at the higher strain rates in this temperature range.

Eq. (1) is of the same form as that found by Dorn (Ref. 1) for the creep of metals at low stresses, and had been successfully applied earlier (Ref. 2 and SPS 37-30, Vol. IV) to the tensile creep of pyrolytic carbons parallel to the substrate. The application of creep formalism to shear flow stress studies is justified by the equivalence of a constant flow stress value at constant strain rate and a steady-state (constant) creep strain rate under constant stress. Eq. (1) may also be applied to data obtained earlier (SPS 37-35, Vol. IV) on the dependence of shear flow stress on temperature at constant strain rate. The effective activation energy is again found to be near 270 kcal/mole. Approximately this value of activation energy has also been observed for tensile creep of pyrolytic carbons and for graphitization of both coke-pitch and pyrolytic carbons (Ref. 3). It therefore appears to correspond to a definite, fundamental diffusion or mass transport mechanism in carbons and graphite. A detailed identification of this mechanism has not yet been achieved, but present evidence suggests that it is associated with crystallite boundary processes.

B. Directional Solar Absorptance of Temperature-Control Surface Finishes

W. M. Hall

A series of measurements of spectral reflectance was made on a number of spacecraft finishes to determine the effect of variation of the angle of incidence. Solar absorptances were then calculated from the reflectance values.

These measurements were performed by directing a collimated beam of monochromatic light upon a flat specimen, at the desired angle of incidence, and collecting the reflected radiation within an integrating sphere, as shown in Fig. 2. In the figure, light from a monochromator enters the sphere through a small aperture and is reflected

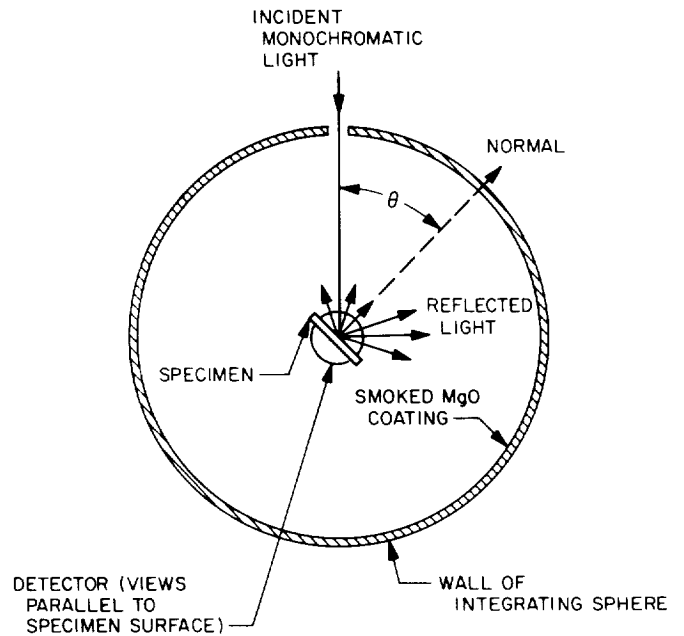


Fig. 2. Integrating sphere

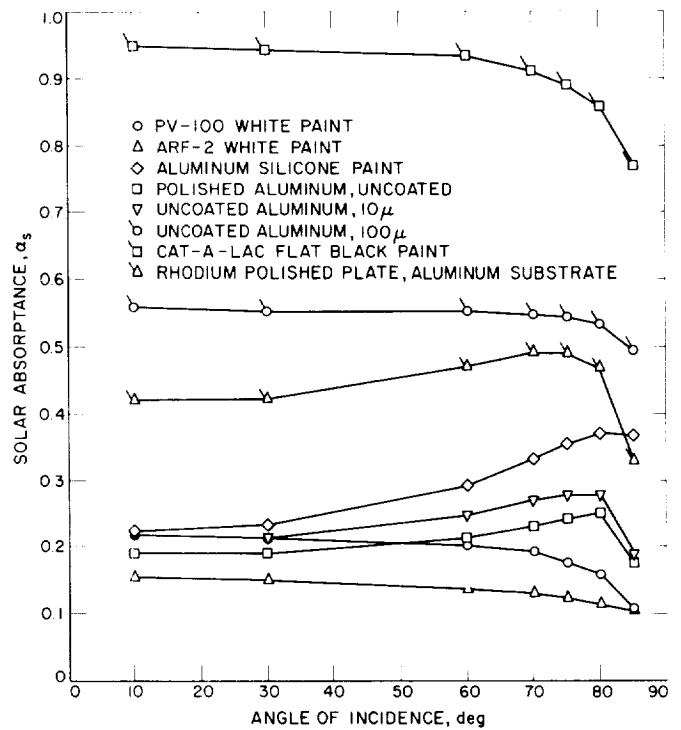


Fig. 3. Calculated solar absorptance for eight spacecraft finishes at various angles of incident light

by the specimen with a certain amount of scattering. The incidence angle θ is varied by rotating the specimen. The reflected light illuminates the sphere walls, which are covered with a diffusely reflective coating of magnesium oxide smoke. A photo-detector located at an aperture in the sphere wall, as shown in Fig. 2, is illuminated uniformly by the light reflected from the wall. The relative position of the specimen and the aperture prevents direct reflection from the specimen surface to the detector.

The calculated solar absorptance as a function of incidence angle is shown in Fig. 3. It will be noted in the figure that the metallic finishes tend to increase in solar absorptance with increasing angle of incidence, measured from the normal. An exception is the aluminum of 100 μ n.-surface roughness. As an angle of incidence approaches grazing (90 deg), the absorptance of all the finishes decreases.

Near-normal values of α_s , which are the values usually reported in optical properties tabulations, appear from the curves to show insignificant change until the angle of incidence exceeds approximately 30 deg.

The effect of the variation of α_s with angle of incidence on the effective α_s/ϵ_h ratio is shown in the following examples:

	ϵ_h	α_s/ϵ_h , 10 deg	α_s/ϵ_h , 60 deg	Change of ratio, %
ARF-2 white paint	0.9	0.176	0.151	-16.6
Polished aluminum	0.05	3.86	4.26	+10.4

One application of these measured variations of solar absorptance is to the calculation of the effective solar absorptance of a curved surface. A particularly simple example is the calculation of the effective absorptance of a hemisphere which is irradiated from a direction parallel to its symmetry axis. For purposes of analysis, the hemispherical surface is divided into area sectors located by a polar angle corresponding to each incidence angle for which the solar absorptance curve shows a data point. If θ_M is the polar angle, then θ_{1M} and θ_{2M} are designated as the angles defining the boundaries of the hemispherical area sectors.

The area elements ΔA_M required for the absorptance calculation are the projections of each hemispherical area

sector onto a plane perpendicular to the direction of irradiation. These plane area elements are circular annuli of area $\Delta A_M = \pi(\sin^2 \theta_{2M} - \sin^2 \theta_{1M})$.

A rough numerical integration yields as the absorption of a hemisphere of unit radius:

$$\pi \sum_M \alpha_M (\sin^2 \theta_{2M} - \sin^2 \theta_{1M}),$$

where α_M is the solar absorptance at incidence angle, θ_M .

Substituting numerical values for ARF-2 paint indicates an effective solar absorptance, α_s (effective) = 0.139. This amounts to a decrease of 12% from a plane surface coated with ARF-2 paint.

For a polished aluminum hemisphere α_s (effective) = 0.209, an increase of 8.3% from a plane polished aluminum surface.

The angular reflectance data for polished metals can be used to calculate their optical constants. Comprehensive tables of the directional reflectance as a function of angle of incidence and of the optical constants n and k (where n = index of refraction and k = absorption constant) have been published for this purpose by Vasicek, Ref. 4.

A simple analytical procedure is required in order to use the tables to establish the unique set of optical constants. Using this method, with directional reflectance data from polished aluminum, the following values were established: n = 1.48, k = 4.44.

Data for the foregoing calculations have been taken from the final report by TRW, Inc., "Directional Reflectance Measurements of Spacecraft Temperature Control Surfaces," under JPL Contract CN5-356146.

C. Pure Oxide Ceramic Research

M. H. Leipold and T. H. Nielsen

Fabrication of MgO specimen blanks for mechanical properties evaluation is continuing. There are still difficulties with the procedure, and attempts are being made to eliminate them; however, a stockpile of specimens suitable for testing is developing.

Much of the recent effort in the program has been directed toward the determination of impurities and their distribution in the MgO. Work similar to that reported in SPS 37-34, Vol. IV, has continued. Several conclusions may now be drawn from results obtained in the studies. These are: (1) impurities in MgO are segregated to the grain boundaries when the total quantity of impurity present is far below the equilibrium solubility limit; for example, calcium oxide present at approximately 50 ppm atomic is segregated to the grain boundary at temperatures where the equilibrium solubility is approximately 5 wt %; (2) impurities many form multiple phases at the grain boundaries; for example, calcium oxide and silicon oxide form one discrete impurity phase at the grain boundary in MgO, while aluminum oxide is located in an entirely separate impurity phase; (3) the lack of visible second phase at a grain boundary is not sufficient evidence to neglect impurity segregation; (4) anion impurities are significant in MgO, although present distribution studies are not sufficiently sensitive to confirm or exclude grain boundary segregation; (5) many impurities in MgO are introduced in the form of agglomerates, but the presence of such agglomerates is not related to the ultimate existence of segregated impurities. These studies, employing the electron beam microprobe, have become limited by the sensitivity of the technique and further efforts must await improved techniques for analysis of distribution. Such development is being undertaken as part of a chemical analysis contract with Sperry Rand Research Center, Sudbury, Massachusetts.

Many of the findings of this research have been contingent upon the existence of satisfactory analytical techniques for impurities in MgO. Since previous experience indicated that even bulk analyses showed considerable disagreement among analysts and techniques, a program to develop dependable analytical procedures was initiated approximately 1 yr ago by a contractual arrangement with Sperry Rand. A detailed literature survey of the analytical methods was made, and solid source mass spectroscopy was selected for confirmation and development. After considerable refinement of procedures, results comparable to those in Table 1 were obtained. It should be pointed out that early results were not nearly so satisfactory; for example, routine silicon analyses by emission spec were found to be low by more than two orders of magnitude. In general, mass spectroscopy has proved to be entirely satisfactory for analysis of all metallic impurities in MgO. Further confirmation of results is under way with respect to silicon and various anions such as sulphur and chlorine and hydroxyl. Finally, the problem of application of mass spectroscopy techniques to distribution analysis is being

Table 1. Analysis of JPL high purity MgO

Specie	Powder		Hot-pressed compact
	Mass spec, ppm atomic	Emission spec, ppm atomic	Mass spec, ppm atomic
B	2	<10	3
N	50	N.D. ^b	100
F	40	N.D.	2
Na	<1	<30	<1
Al	35	50	10
Si	75	65	25
P	<1	N.D.	7
S	115	N.D.	5
Cl	75	N.D.	50
K	<1	N.D.	4
Ca	30	20	25
Ti	<1	<10	<1
Cr	3	<5	<1
Mn	<1	<5	<1
Fe	15	15	4
Co	<1	<8	<1
Ni	<1	<5	<1
Cu	10	10	<1
Zn ^a	2	<5	<1
OH ^a	5000	—	500

^aValues are very tentative.
^bN.D.: not determined.

investigated. Considerable detail of results and procedures developed in this analytical program is available in monthly letter reports and quarterly summary reports from Sperry Rand Research Center.

One of the impurities whose presence has appeared in this analytical program and whose distribution is almost completely unknown is the hydroxyl ion. Evidence exists in the literature for its presence as a vacancy former (Ref. 5), and studies of hydroxyl on the surface of MgO grains (Refs. 6 and 7) make extrapolation of its existence to the grain boundaries very high. Since a very likely source for hydroxyl contamination in MgO would be the presence of a surface layer adsorbed from the atmosphere, a literature and theoretical study of this behavior was made to ascertain whether hydroxyl or other contaminants might appear from such a source. The approach consisted of a literature search and detailed application of the findings to the MgO being used at this laboratory. A thermodynamic study was also conducted on the decomposition reaction occurring in the preparation of MgO. Detailed findings of this investigation are being prepared as a JPL Technical Report. Briefly summarized the conclusions are:

- (1) Hydroxyl ions are the most likely contaminants to be adsorbed on the surface of MgO.

- (2) Hydroxyl ions held in active sites (corners, edges, steps) are below present limits of detection by infrared spectroscopy or by gravimetric studies. They can, however, be detected by mass spectrographic analysis.
- (3) Hydroxyl ions in some of the most active sites may be capable of existing at these sites to temperatures of the order of 2200°C.
- (4) Hydroxyl impurity atoms in MgO are associated with vacancies and since the vacancy concentration is higher at the grain boundaries, the hydroxyl impurity atoms are likely to be located there.
- (5) The likelihood of reducing hydroxyl contamination, either from the surface or from the interior of the material by subsequent treatment, is small. A more satisfactory approach involves shielding active surface sites, using larger adsorbed molecules such as $\text{CH}_3\text{CH}_2\text{OH}$, or preferentially occupying the sites by more easily removed species such as helium.
- Thermodynamic studies of the decomposition reaction used in the production of MgO at JPL suggest that if the hydroxyl contamination can be maintained at a satisfactorily low level, superior pressure sintering should occur with the use of material calcined at the lowest possible temperature. This improvement would be the result of greater surface area and higher reactivity.

References

1. Dorn, J. E., "Some Fundamental Experiments on High Temperature Creep," *Journal of the Mechanics and Physics of Solids*, Vol. 3, pp. 85-116, 1954; "The Spectrum of Activation Energies for Creep," *Creep and Recovery*, American Society for Metals, pp. 255-283, Cleveland, Ohio, 1957.
2. Kotlensky, W. V., "Analysis of High Temperature Creep in Pyrolytic Carbon," TR No. 32-889, Jet Propulsion Laboratory, Pasadena, California (to be published).
3. Fischbach, D. B., "Kinetics of Graphitization. I. The High Temperature Structural Transformation in Pyrolytic Carbons," TR No. 32-532, Jet Propulsion Laboratory, Pasadena, California, February 1, 1966; "Kinetics of High Temperature Structural Transformation in Pyrolytic Carbons," *Applied Physics Letters*, Vol. 3, pp. 168-170, 1963; "Kinetics of Graphitization of a Petroleum Coke," *Nature*, Vol. 200, pp. 1281-1283, 1963.
4. Vasicek, A., "Tables of Determination of Optical Constants From The Intensities of Reflected Light," *Nakladatelství Československé Akademie Věd*, Prague, Czechoslovakia, 1964.
5. Konklin, P. W., Auzins, P., and Wertz, J. E., "A Hydrogen-containing Trapped Hole Center in Magnesium Oxide," *Journal of the Physics and Chemistry of Solids*, Vol. 26, pp. 1067-1074, 1965.
6. Anderson, P. J., Horlock, R. F., and Oliver, J. F., "Interaction of Water with Magnesium Oxide Surface," AERE R4958 Metallurgy Division UKAEA Research Group, Atomic Energy Research Establishment, Harwell, England.
7. Webster, R. K., Jones, T. L., and Anderson, P. J., "Proton Magnetic Resonance Studies of Adsorbed Water on Magnesium Oxide," AERE Report R4959, Atomic Energy Research Establishment, Harwell, England.

VIII. Lunar Spacecraft Development

A. High Impact Technology

J. L. Adams

This report summarizes accomplishments of the JPL high impact program during the reporting period.

1. Ruggedized Gas Chromatograph

The prototype instrument is shown in Fig. 1, which is an over-all view of the electrometer circuitry before coating, and in Fig. 2, which is an interior view of the instrument showing the pressure regulator, sample loop, sample valve, delay line, columns and detectors, and jet

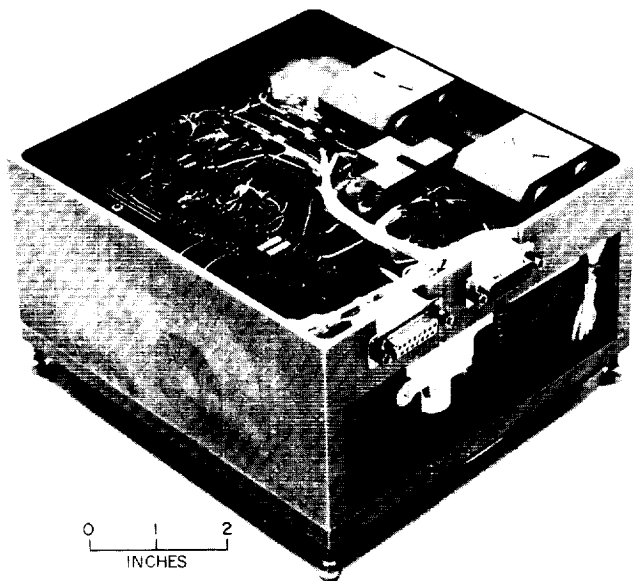


Fig. 1. Prototype gas chromatograph

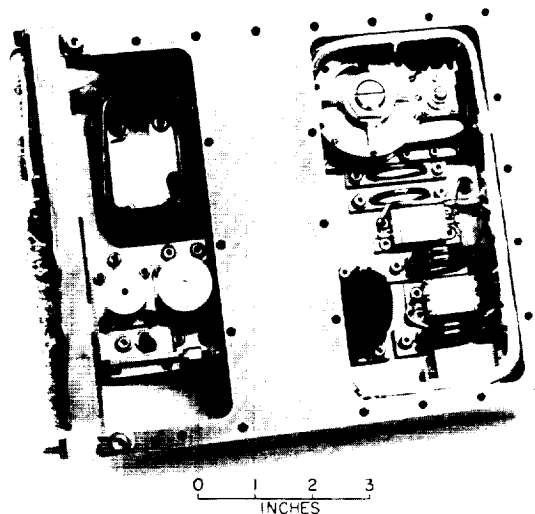


Fig. 2. Interior of ruggedized gas chromatograph

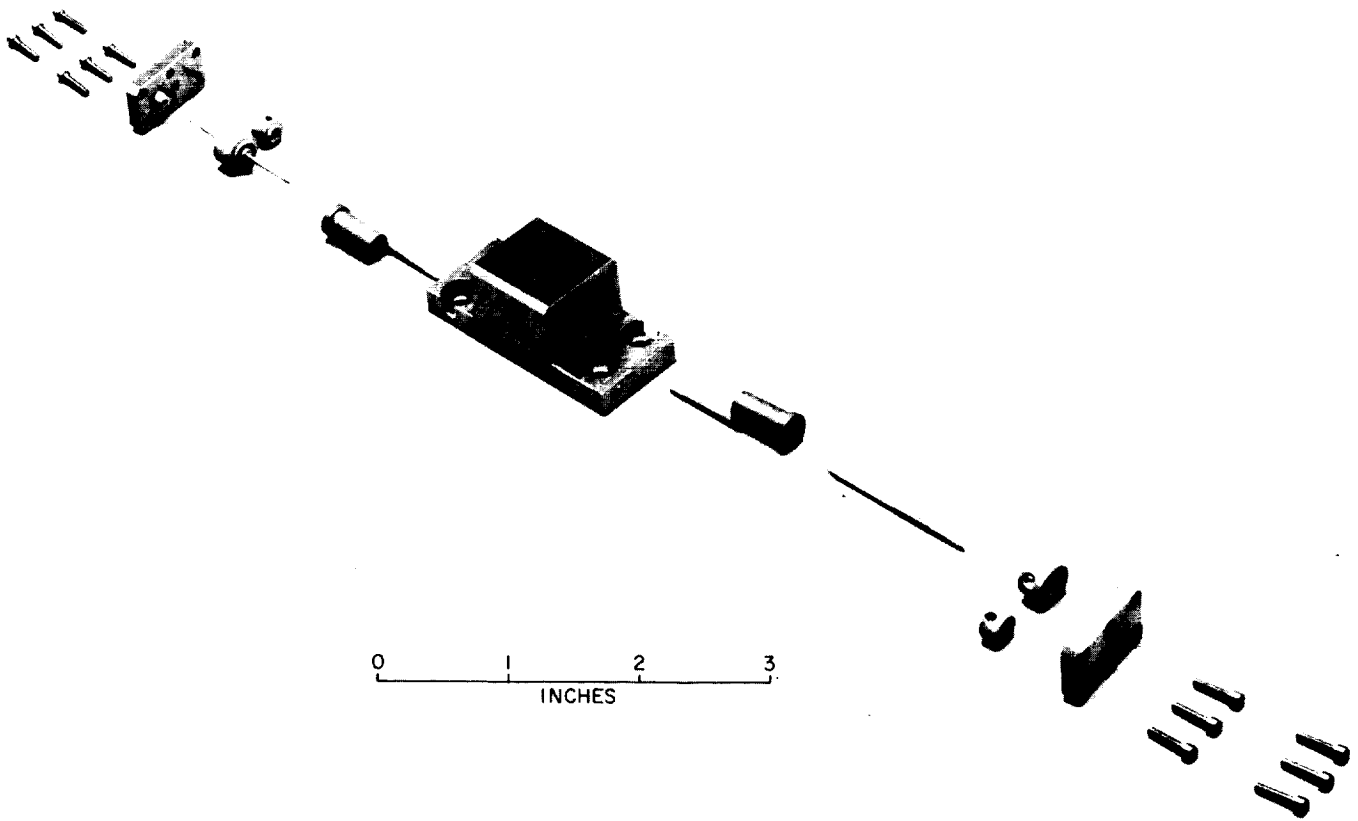


Fig. 3. Ionization detector

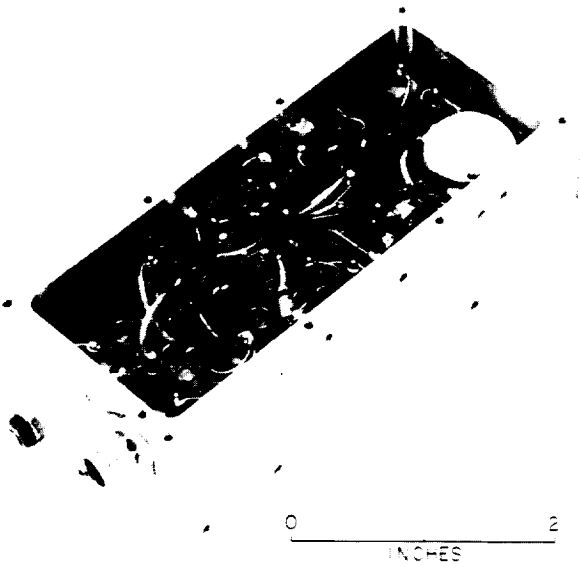


Fig. 4. Module, DC side

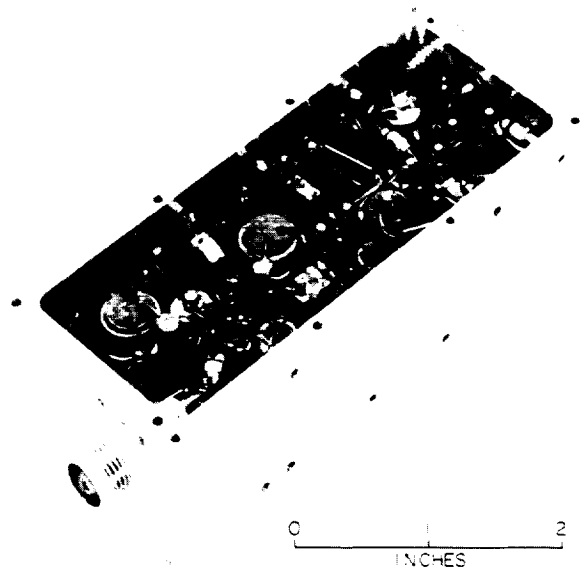


Fig. 5. Module, RF side

pump. Fig. 3 is an exploded view of the ionization detector developed for this instrument. Like all components developed for the gas chromatograph, this detector is sufficiently rugged to survive impacts of several thousand g in all principal directions from impact velocities of several hundred ft/sec.

2. Ruggedized S-Band Transmitter

The first module of the three-module, 3-w, S-band, solid-state, high-impact resistant transmitter being developed by the JPL Telecommunications Division successfully survived impacts of 10,000 g from 200 ft/sec in all principal directions. This module contains the oscillator, two stages of amplification, a doubler, and a tripler.

Figs. 4 and 5 show the two sides of the module. The second module (amplifier) had previously survived 10,000 g impacts in all directions.

3. Mechanisms

Fig. 6 is an exploded and an assembled view of an impact-resistant pressure regulator. This device utilizes diaphragms both for pressure sensing and spring force. It is a two-stage device capable of regulating a supply at several thousand psi to outputs on the order of 60 psi at low flow rates (50 ml/min). Regulation is within 0.5 psi at the output over an input range of 200-1500 psi. The regulator has been impact-tested at 10,000 g from 200 ft, sec, axially and radially. Regulation has remained within 1 psi over the 200-1500 psi input range.

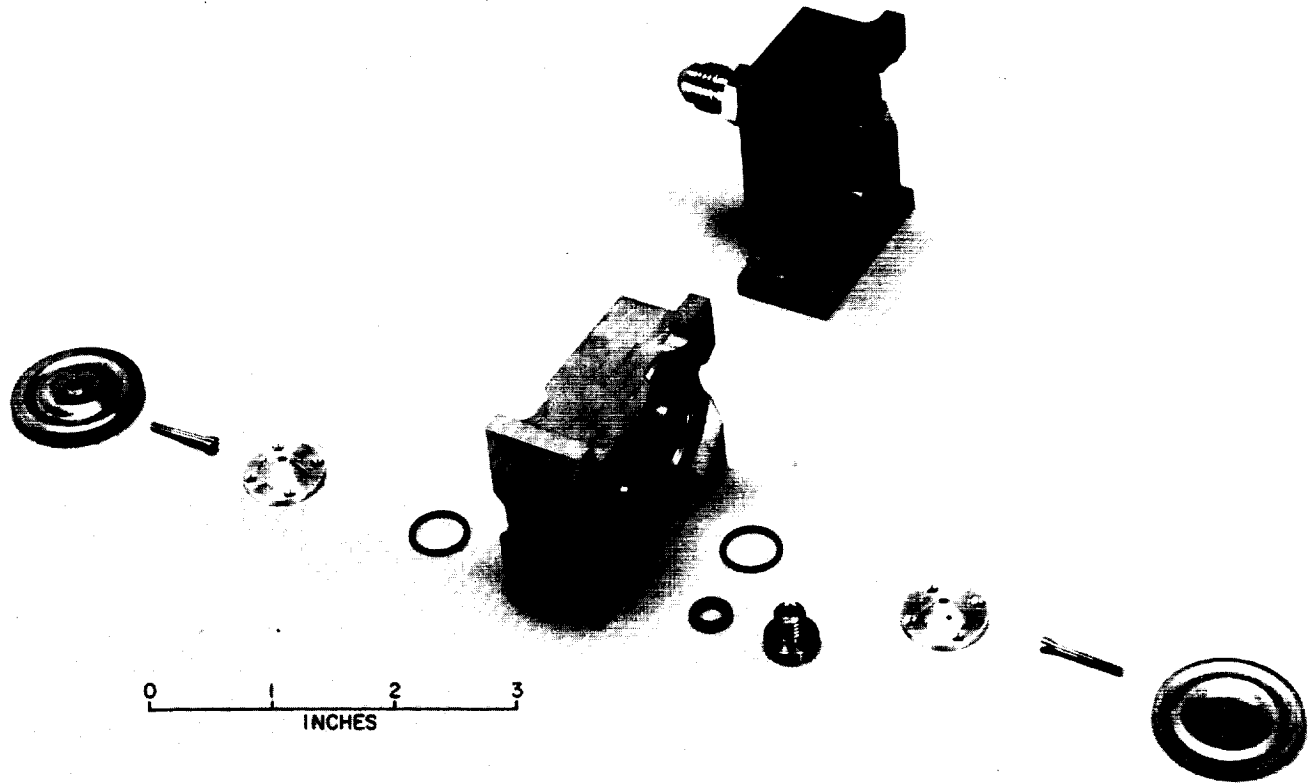


Fig. 6. Impact-resistant pressure regulator

IX. Electro-Mechanical Engineering

A. High Voltage Insulation Using Foams in Vacuum

E. R. Bunker, Jr.

The advisability of using foam-encapsulating resins for insulation of voltages greater than 270 v, when such foams will be exposed to hard vacuum, is still open to controversy. It appears to some that the gradual diffusion of the blowing gas out of the individual cells will, in time, cause the region between the high voltage conductors to pass through the critical air pressure region where, with no insulation, voltages greater than 270 v will arc over. With foam interdicting the path, an arc will not form, but it seems reasonable that with sufficient conductor separation, a partial breakdown or corona could occur in some of the individual foam cells. As was verified in a previous voltage breakdown test of a polyurethane foam, the effect of such corona is to break down the cell walls gradually until a complete conductive path between the electrodes is developed, whereupon arcing occurs.

To date, attempts to measure the decay of pressure in the foam cells by means of pressure transducers have not been too successful, because the volume of gas in the individual foam cells was extremely small compared to the volume required to actuate even the smallest pressure transducer. To overcome this difficulty, an approach was proposed which would use the pressure-calibrated corona onset voltage level between fixed conductors as

a measure of the average gas pressure existing in the foam between the electrodes.

As shown in Fig. 1, four samples of CPR 23-8 foam, 8 lb/ft³ density, were prepared. Sample 1 consisted of a 4- × 4- × 2-in. block in which holes were carefully

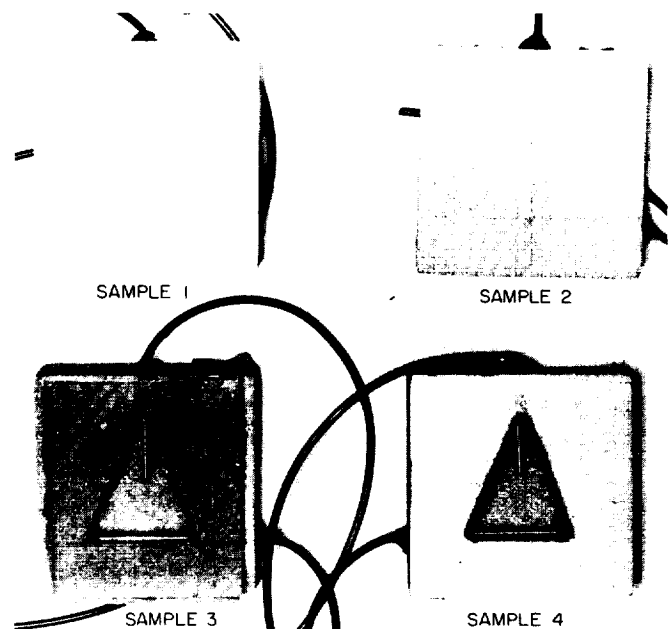


Fig. 1. Polyurethane foam samples for determining rate of gas diffusion in vacuum by corona onset voltage measurements

drilled and $\frac{3}{32}$ -in. diameter stainless steel electrodes were inserted in a planar "T" configuration, identical to the geometry visible in Samples 3 and 4. The stainless steel electrodes were spaced 1 in. apart at the closest points. The electrode ends were rounded and high voltage insulated wire was silver-soldered to the opposite ends of the electrodes. An ultrasonic cleaner was used to carefully clean the electrodes in order to eliminate any possible surface contamination which would affect the corona onset voltage. The conductor-foam interfaces were sealed with adhesive to achieve adequate insulation so that the voltage could be applied continuously to the electrodes during passage through the critical pressure region. This procedure would detect possible transient effects of cell rupture or surface anomalies due to a rapid decrease in pressure.

Test Sample 2 was split in half through the 4-in. sides, with a triangular cavity hollowed out and electrodes positioned similar to Samples 3 and 4. The two halves were then bonded together to make an air-tight seal. Sample 3 was constructed in a similar manner, except that a plexiglas window was bonded to the foam to enable visual observation of the electrical breakdown inside. Construction of Sample 4 was similar to the others, except that the cavity was exposed to the ambient pressure.

Using Sample 4 only, a curve of corona onset voltage versus pressure was taken through the critical region to serve as a calibration reference. All samples were then

installed in the vacuum chamber with a test setup capable of applying the high voltage to the vertical electrode of each sample individually. The corona detection network measures the corona current collected by the lower electrode which is returned to ground through the corona detection network.

During the first test, voltage was applied continuously to Samples 1, 2, and 3 while passing through the critical region. Breakdown of the wire and sealing adhesive of Sample 3 required that the test be terminated, and the sample repaired. During a second run, the pressure was reduced as quickly as possible to below the critical region and the high voltage was then applied.

During the test currently in progress, approximately once a day, while the samples are exposed to a continuous vacuum of 10^{-5} mm Hg, voltages are applied to each sample in turn. The voltage applied is 11.8 kv or the corona onset voltage, whichever is lower. The corona detection network employed indicates currents of fractions of a microampere. In addition to reducing the corona onset voltage where continuous corona occurs, the voltage is reduced slowly until complete corona extinction takes place, and this value is recorded.

After a month of tests, the results are still inconclusive; however, Samples 2 and 3 are showing a decreasing corona onset voltage from the value originally measured at room pressure. The work is continuing and complete results will be summarized in a future report.

ENVIRONMENTAL SIMULATION DIVISION

X. Aerodynamic Facilities

A. Wind Tunnels

*E. Laumann, G. Herrera, H. Holway, H. Enmark, D. Lund,
and R. Prislin*

1. Wakes of Wire-Supported Models, E. Laumann

The characteristics of supersonic and hypersonic wakes continue to intrigue the fluid physicist and aerodynamicist. The facilities are often asked to produce experimental three-dimensional wake characteristic data that are free of any support-interference effects. Whereas it is preferred to make these measurements using free-flight techniques, the lack of position and attitude control and the increased complexity of the technique tend to cause investigators to prefer more conventional techniques.

Recently the facilities were asked to make some pitot and static pressure wake surveys behind sharp and blunted cones on which the boundary layers were tripped. We suggested that the experiments be conducted using the free-drop technique, wherein a very heavy model is allowed to fall ahead of a fixed probe. However, the experimenter felt that because the boundary layer would

be turbulent, wire-support interference effects would be minimal and therefore, by supporting the model on a thin wire, more definitive data could be obtained. Having no data on which to base opposition to this opinion, we agreed to conduct his experiment.

The models consisted of 10-deg half-angle cones with bluntness ratios ranging from 0 to 0.4 and a common base diameter of 1.5 in. They were constructed with solid aluminum noses and hollow plastic afterbodies. Trip rings made from 0.020-in. D wire were mounted approximately $\frac{1}{4}$ in. aft of the model nose. All tests were run in the 20-in. Supersonic Wind Tunnel at $M = 4$ and a unit Reynolds number of 0.34×10^6 in.

A brief investigation of support configurations was performed. An attempt to support the models on shim-stock ribbons failed because of ribbon flutter. The wakes of models supported on vertical wires 0.007, 0.010, and 0.015 in. in diameter were recorded on schlieren photographs and compared with the wakes of identical free-flight models. The neck of the wake of each wire-supported model appeared to be 0.15-in. D closer to the

base than the neck of the free-flight wake. There was no significant difference between the wire-supported wakes. Because the 0.007-in. wire tended to break under air load, the 0.010-in. wire was used throughout the experiment.

All data were obtained using probes mounted on an X-Y-Z traversing mechanism. A round cross section pitot probe of 0.032 in. OD, or a static pressure probe duplicating the design described in Ref. 1, could be used to make pressure measurements. A pressure transducer was close-coupled to the pressure probes. The repeatability of the pressure data appears to be $\pm 2\%$.

The characteristics of the flow field are shown in Fig. 1. Figs. 2-5 show some typical pressure surveys taken normal to the free-stream direction where X/D is the distance from the model base normalized by the base diameter, and Y is the distance from the axis of symmetry, in inches. All data indicated by circle symbols were measured in a plane normal to the wire and passing through the wake centerline. Triangle and plus symbol data were measured in a plane parallel to the wire and passing through the wake centerline. A viscous effect

correction and a constant zero shift correction have not been applied to the static pressure data; however, for comparative purposes these effects cancel. Arrows on the figures indicate the apparent position of shock waves and the forward position of expansion fans as indicated by the schlieren photographs. *RS* is recompression shock; *LE*, lip expansion; and *BS*, bow shock.

A limited flow symmetry comparison is shown in Table 1. The numbers in the table represent the ratio of pressures measured in a vertical plane to those measured in a horizontal plane at the noted locations in the wake flow field. Some data are questionable and the results are far from complete. Nevertheless, trends are definitely apparent. The model wake core appears to be very symmetrical. In the outer wake regions, however, pitot pressures measured in the wire-support wake show a reduction of as much as 50% and static pressures are reduced as much as 40%. This is interesting when it is realized that the measuring stations represent X/D_{wire} values of 200, 400, 600, and 1200. The wire wake effects do not diminish rapidly as would those of a wire supporting no model. Asymmetries are somewhat less pronounced for the blunt cone.

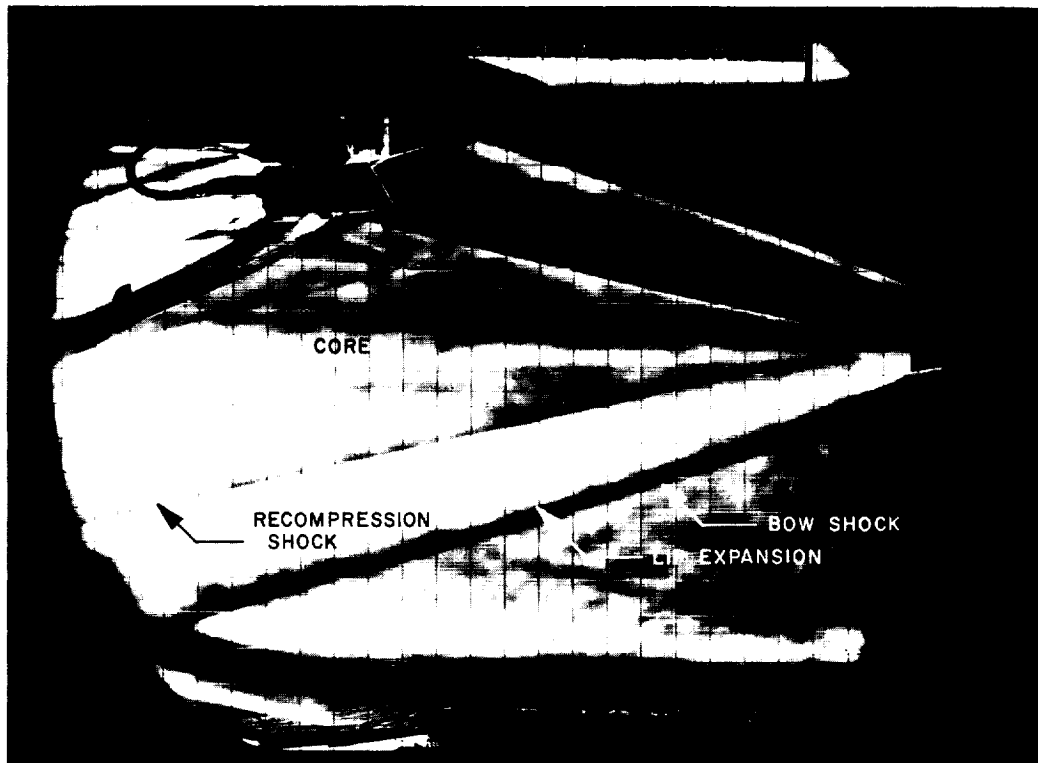


Fig. 1. Characteristics of flow field

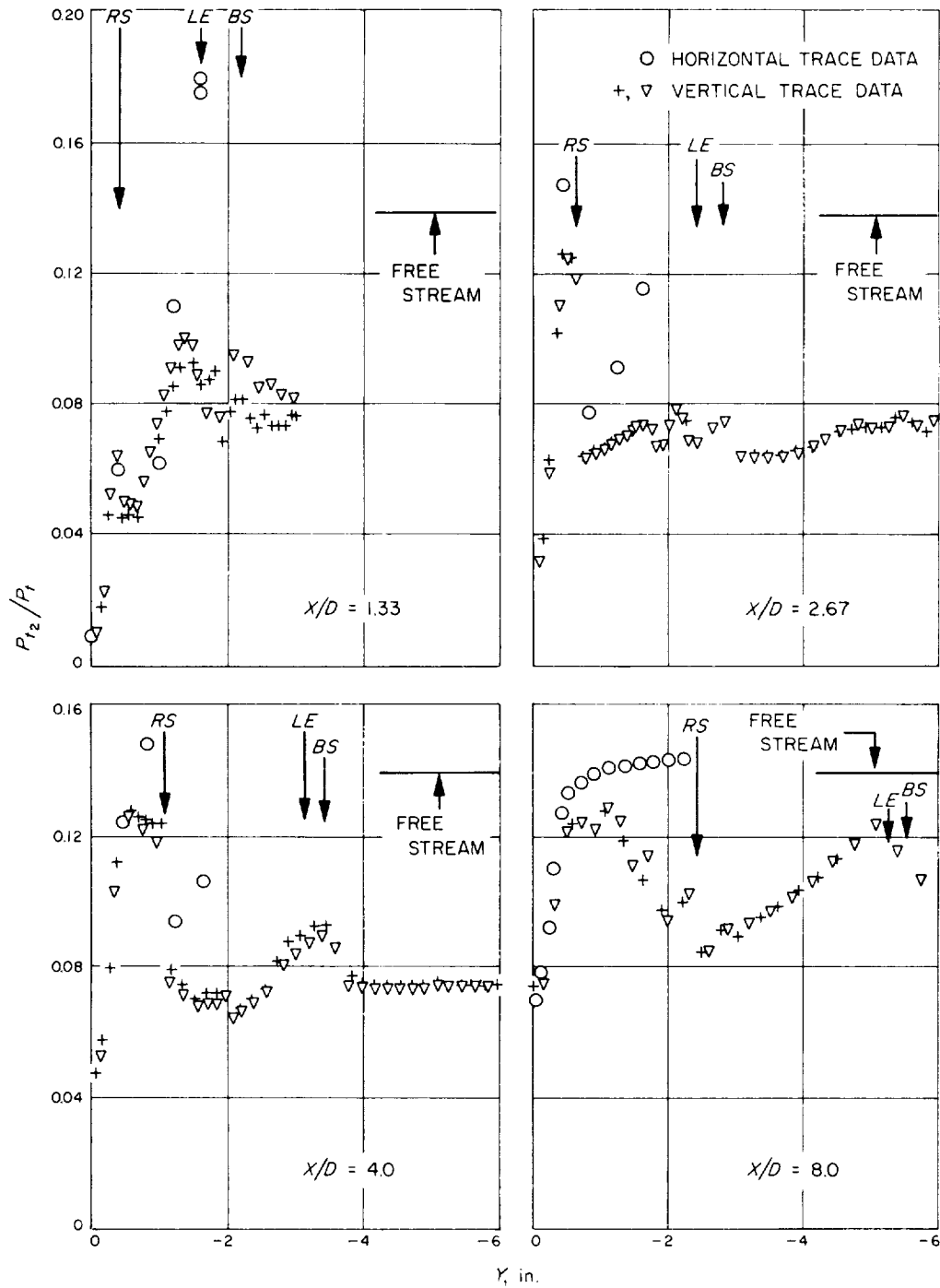


Fig. 2. Pitot pressure profiles for sharp cone

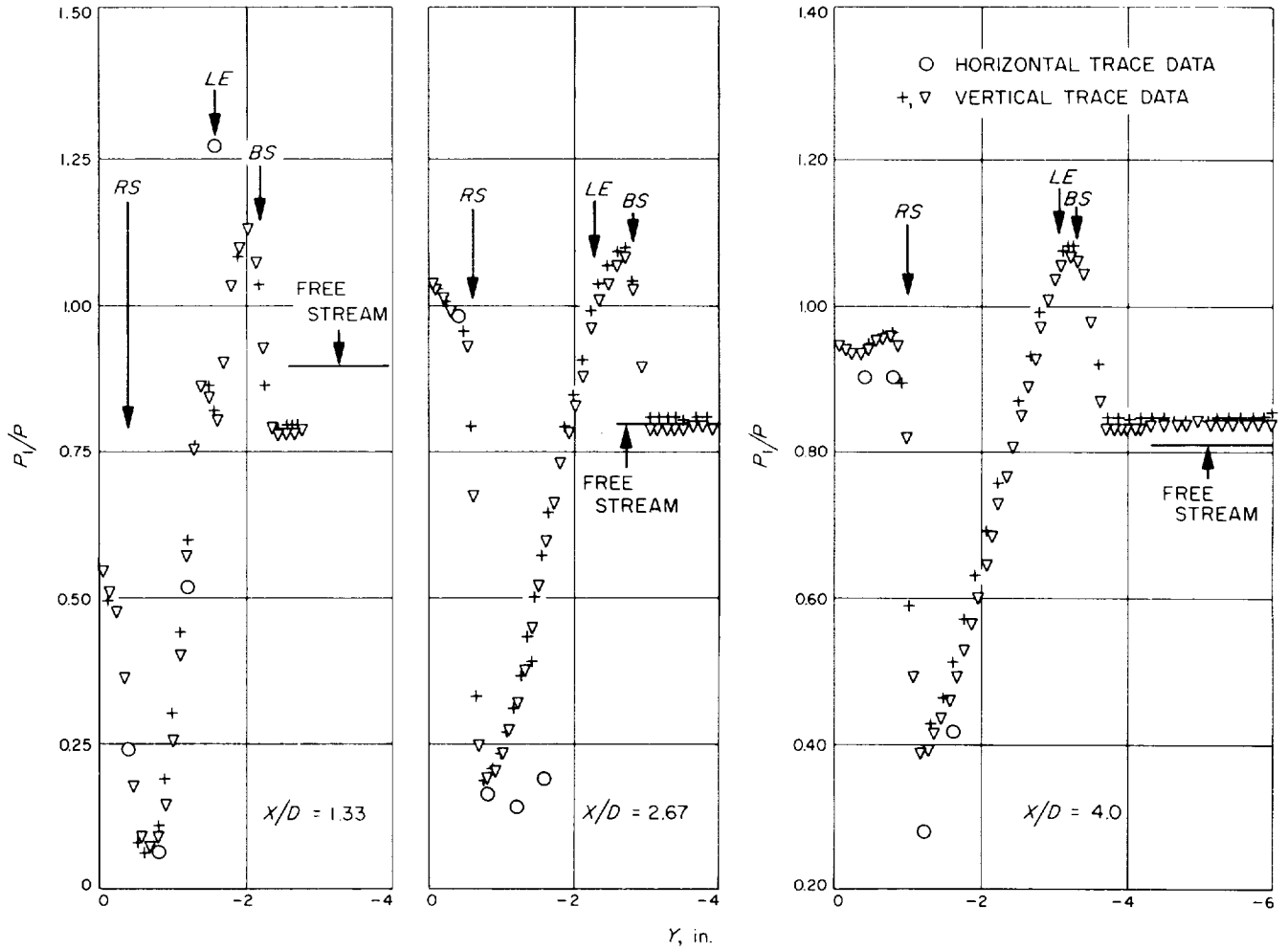


Fig. 3. Static pressure profiles for sharp cone

Table 1. Ratios of pressures in vertical planes to pressures in horizontal planes

Sharp cone ($r_s/r_b = 0$)								
Location	X/D							
	1.33		2.67		4		8	
	Pitot	Static	Pitot	Static	Pitot	Static	Pitot	Static
Core	1.0	1.0	^a	1.0	1.0	1.1 ^b	1.0	^a
RS	1.0	1.0	0.8	1.0	0.8	1.1 ^b	0.7	^a
LE	0.5	0.6	^a	^a	^a	^a	^a	^a
Outside BS	0.6 ^b	0.6	0.5	1.0	0.5	1.0	0.8	^a

Blunt cone ($r_s/r_b = 0.4$)								
Location	X/D							
	1.33		2.67		4			
	Pitot	Static	Pitot	Static	Pitot	Static		
Core	1.0	^a	1.0	1.0	1.0	1.0		
RS	1.0	^a	1.0	1.0	1.0	1.0		
LE	0.9	^a	^a	^a	^a	^a		
Outside BS	^a	^a	0.5	1.0	0.7	1.0		

^aNot measured
^bData questionable

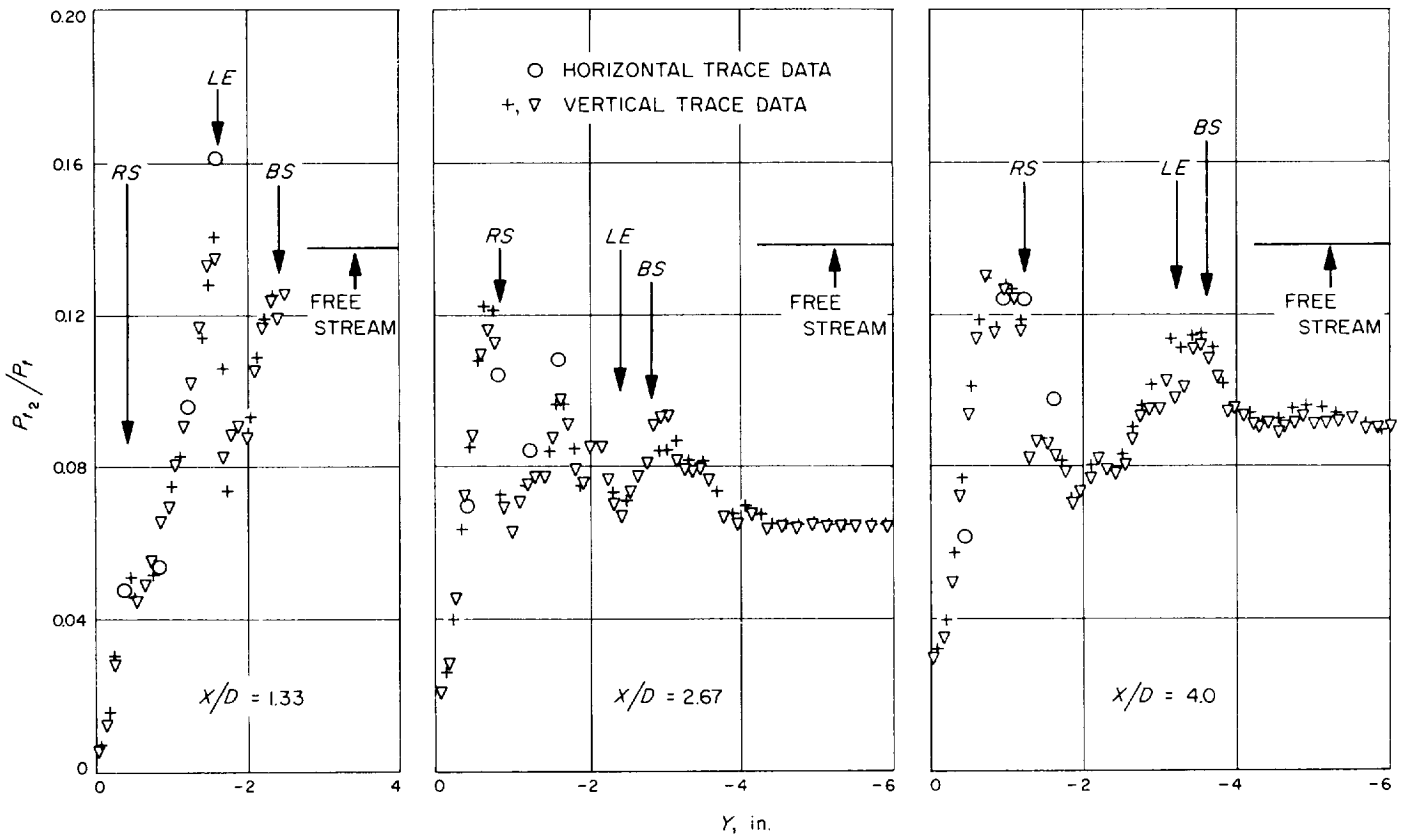


Fig. 4. Pitot pressure profiles for blunt cone

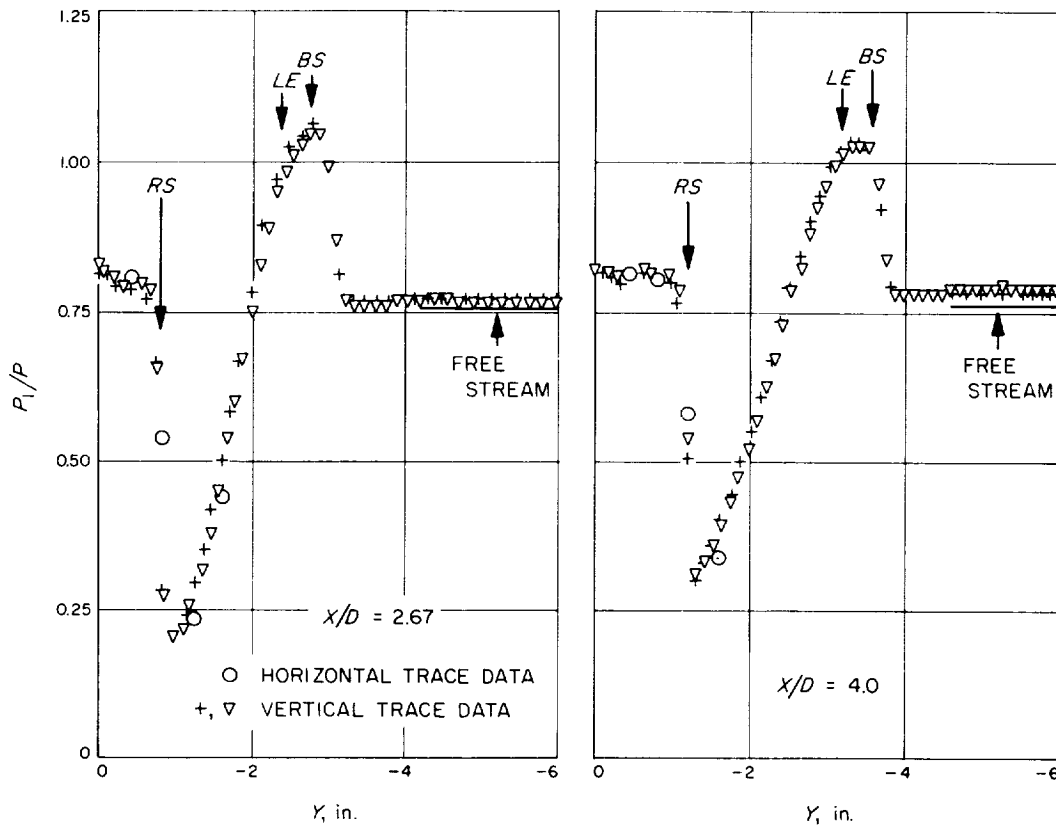


Fig. 5. Static pressure profiles for blunt cone

A region for unsteady pitot pressure, observed in the vertical trace data, extended from approximately 1.5 to 3.0 in. from the core centerline and parallel to the free stream from 2 to beyond 12 in. aft of the model. The interpretation of this observation is not clear at the present time.

Based upon these observations, it is suggested that the wake profiles measured were not entirely free of support interference. The level of error is unknown but future free-drop investigations may be informative.

2. 20-in. Supersonic Wind Tunnel Nozzle Flow Calibration, J. G. Herrera

A calibration of the nozzle flow was conducted to determine the pitot pressure and Mach number distribution in the test rhombus (Test 20-618). The 19 calibrated Mach numbers, ranging from 1.33 to 5.01, were checked at their maximum supply pressures. For some Mach numbers, adjustments were applied to the contour in order to establish a Mach number variation less than ± 0.01 on the tunnel centerline (in the test region). The majority of contours compared favorably with results

of the last flow calibration made approximately 3 yr ago. Before the current calibration, the nozzle was realigned with the aid of a template.

3. Tandem-Model Release for Free-Flight Testing, H. Holway

Since inception of the wire-released free-flight technique in 1962 (SPS 37-16, Vol. IV, p. 128), many valuable tests have been conducted for the purpose of measuring total drag, wakes, and dynamic stability. Test 20-620 recently evaluated the development of a small mechanism embedded in the base of the upstream model which, when assembled, secures the aft shape in tandem, and releases it simultaneously along with the forebody.

The cone-cone configuration, Fig. 6, with the various parts of the mechanism, is shown unassembled, and assembled in the tandem position. Three other shape combinations (Fig. 7) were tested to more fully document the capabilities of this technique.

To record the separation and flight path of the models, the conventional free-flight method of using a 35mm

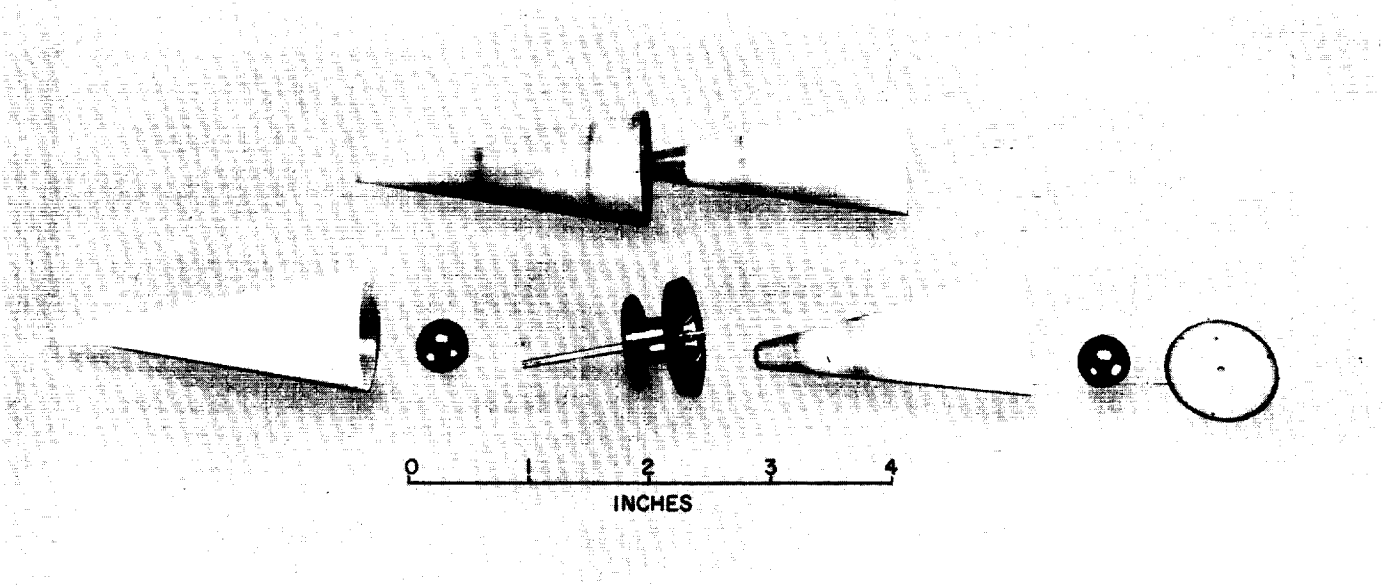


Fig. 6. Tandem release model

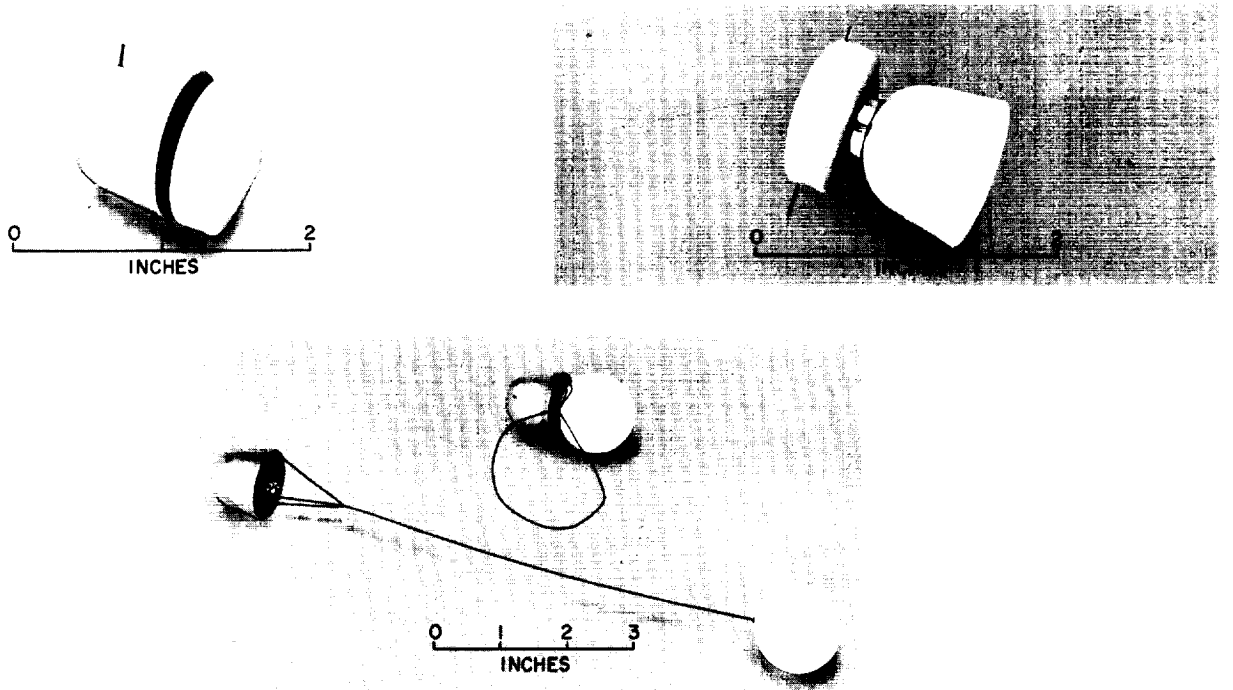


Fig. 7. Other shape combinations tested

high-speed camera timed by the wire-release was employed. A composite of the flight path of the cone-cone configuration is shown in Fig. 8, in which separation occurs 0.0017 sec after the initial breaking of the main

supporting wire. Not all configurations tested were as successful as the cone-cone, primarily because of inadequate ballistic parameter relationships between the models. More suitable mass ratio configurations are

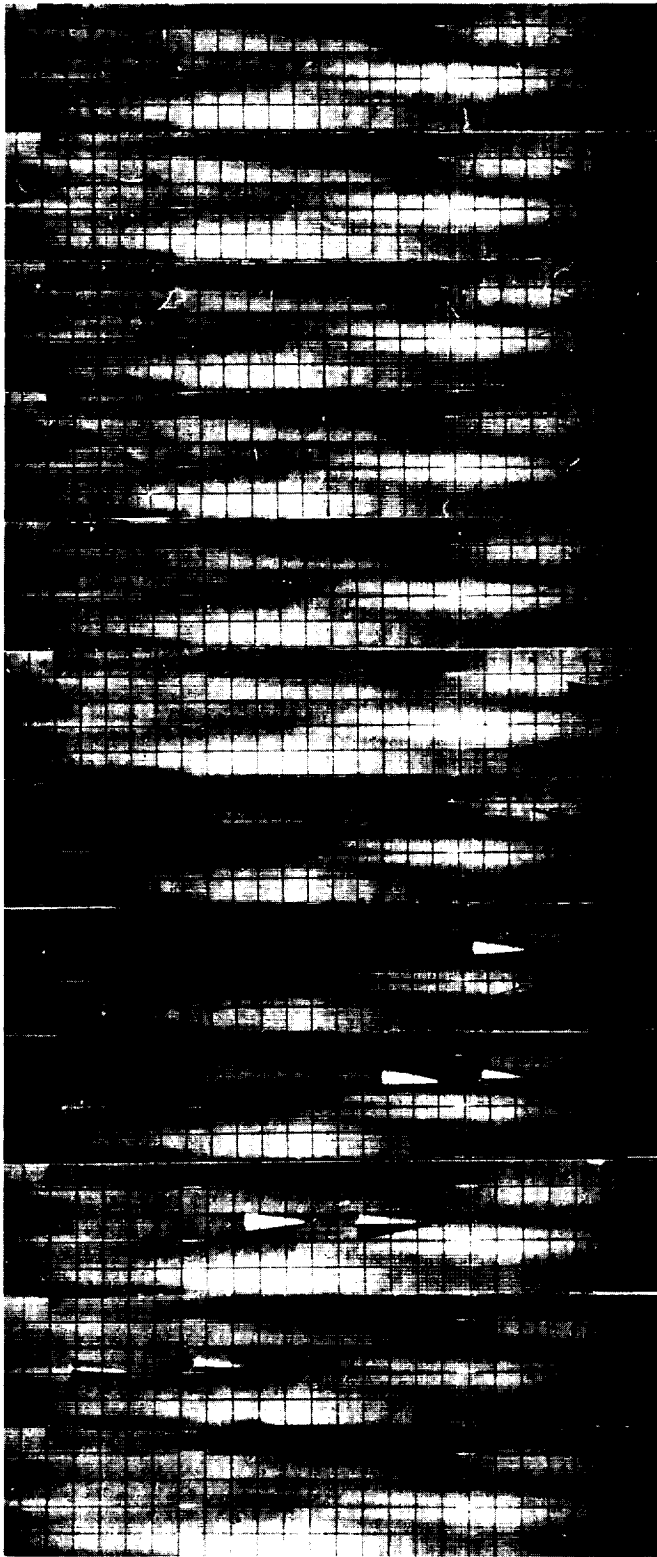


Fig. 8. Composite of 35mm high-speed photographs showing free flight of tandem model

planned for another test which will be conducted soon. Several additional combinations will be attempted, such as aft cover ejection, and perhaps parachute deployment.

4. JPL Tunnel Development: Sector Mock-Up Performance Check, H. T. Enmark

Test 20-617 was run to determine the effect of a new sector design on the performance of the 20-in. Supersonic Wind Tunnel. A mock-up of the sector was tested at two pitch angles, -10 and $+30$ deg, representing the two extremes possible with the new design. These two configurations were tested at four Mach numbers: 1.33, 2.61, 4.54, and 5.01.

Maximum and minimum tunnel running conditions were determined for each sector mock-up configuration at each of the four Mach numbers. Also, each sector configuration was run with and without a sting and model.



Fig. 9. Sector configuration (-10 deg)

The -10 -deg sector configuration (Fig. 9) had no adverse effect on tunnel performance. The maximum and minimum running conditions were limited by compressor plant capability only, and the tunnel started easily.

The $+30$ -deg sector configuration (Fig. 10), however, caused the flow to be severely separated at the floor of the tunnel and caused difficult tunnel starting at the two highest Mach numbers.



Fig. 10. Sector configuration (+ 30 deg)



Fig. 11. Fairing between apex of sector and floor

To improve tunnel performance, two changes in the configuration were tried. A fairing between the apex of the sector and the floor (Fig. 11) had little or no effect on the separated flow conditions. However, removal of floor plates around the base of the sector (Fig. 12) improved flow considerably. The separation point moved downstream and tunnel compression ratio was increased.

Although the +30-deg sector configuration produced tunnel operation limitations, the flow conditions in the test section are not affected. The limitations are no worse than those historically produced by similar configurations protruding from the floor or ceiling through the flow boundary layer.



Fig. 12. Base of sector with floor plates removed

5. Saturn Cold Wall Studies, D. Lund

Test 21-174D provided additional *Saturn IB/V* force and stability data which supplemented that obtained from Test 21-174A.

The approximate aerodynamic parameter ranges of the test were: Mach numbers from 4.0 to 8.0, and Reynolds numbers/in. from 0.033 to 0.313×10^6 . The test variables and ranges were: angle of attack from -5 to 15 deg, and wall temperature to stagnation temperature ratios from 0.10 to 0.92.

Model configurations tested were the same as those in Test 21-174A. Along with some typical Reynolds number and wall temperature effects, these configurations were shown in *SPS 37-34*, Vol. IV, pp. 106-107.

Some of the test techniques were:

- (1) An external heat shield was used to cool the model with LN_2 while the tunnel was running. When the model was sufficiently cool, the heat shield was quickly retracted and data taken.
- (2) The control of model wall temperatures from adiabatic recovery to -320°F was demonstrated and can be improved upon with additional wind tunnel LN_2 valving.

- (3) The internal force strain gage balance was maintained at a temperature of approximately 100°F, while the model wall temperatures were approximately -300°F.
- (4) Model force data and model wall temperature data were taken simultaneously.
- (5) Data could be taken while angle of attack was changing. The rate of pitch was as high as 4.2 deg/sec and averaged 3.5 deg/sec. Data were acquired at 0.2-sec intervals.

Test 21-174D was completed January 4, 1966; data reduction is in process.

6. Nonplanar Free-Flight Testing in a Conventional Wind Tunnel, *R. H. Prislun and H. P. Holway*

Considerable wind tunnel static and dynamic stability testing has been performed at JPL using the planar free-flight technique (Ref. 2). However, as shown by Murphy (Ref. 3), planar damping characteristics are not always applicable to the prediction of general free-flight motion. In addition, other coefficients such as Magnus coefficients cannot be determined from a planar motion analysis.

Thus, in some instances an experimenter may require a more exact simulation of the actual free-flight motion of a vehicle than that provided by planar testing. Described here is a nonplanar motion free-flight testing capability which will supplement the planar technique. The description is referenced to the JPL 20-in. Supersonic Wind Tunnel; however, the technique could easily be instrumented in most conventional wind tunnels.

The major criteria which shaped the system design were:

- (1) The model trajectory must be viewed in two planes simultaneously to determine nonplanar free-flight angular histories from motion picture data. Obtaining these two views without a major modification to the tunnel was the primary limitation considered in the development of this system.
- (2) Parallax distortions are prevented and flow visualizations are obtained if a schlieren system can be used for both views of the model motion.
- (3) It is simpler and cheaper to record both views simultaneously on each frame of data with a single camera.

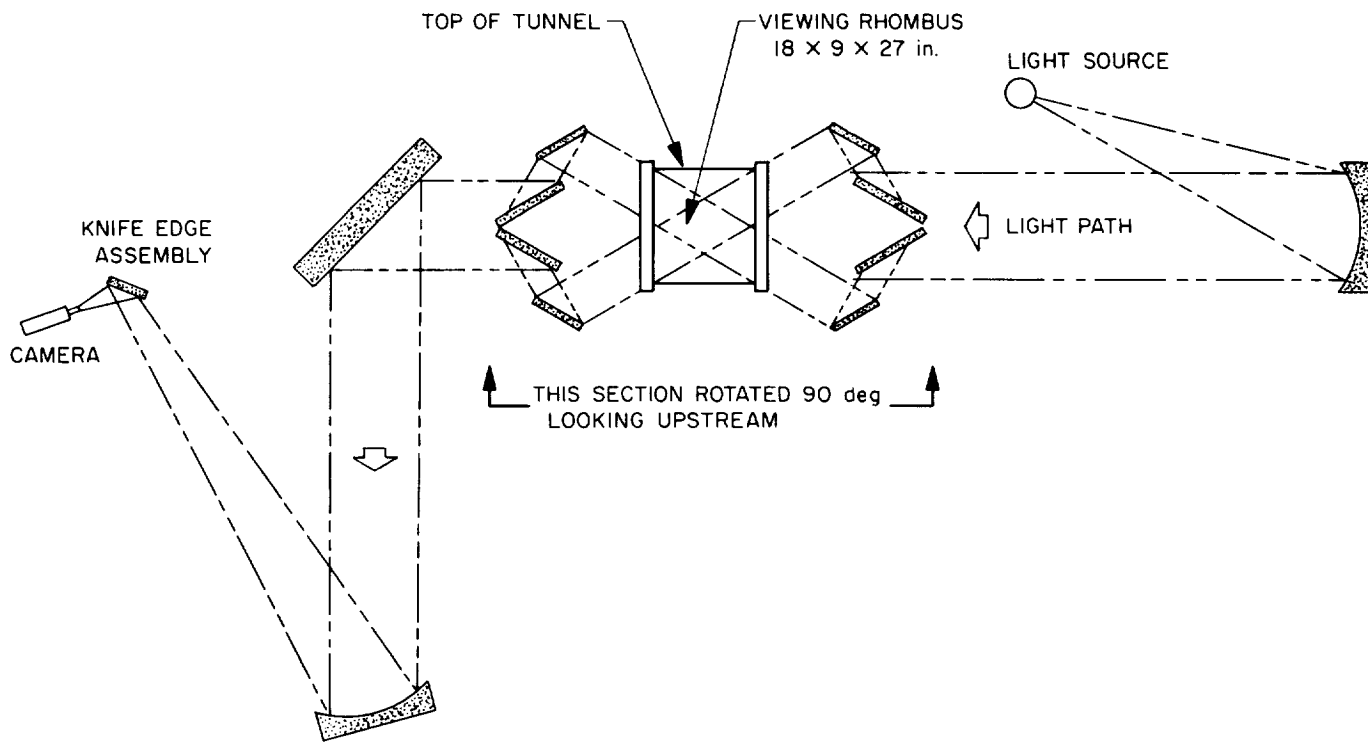


Fig. 13. Schlieren system nonplanar free flight

By revising the schlieren optical system, these criteria were satisfied without modification to the tunnel. A set of front surface mirrors is positioned to split the schlieren beam and redirect it through the test section viewing windows at angles of 30 deg above and below the original horizontal light path. Thus, the angle between the intersecting beams is 60 deg. A second set of mirrors realigns the light beams onto the original schlieren path. Consequently, one camera placed at the focal point of the schlieren system records both views simultaneously. Fig. 13 is a schematic representation of the light path.

A full-frame Fastax camera operating at approximately 2000 frames/sec has been used to record both views of the model motion. The individual size of each image is equivalent to that which would be obtained by using a 35-mm half-frame camera for one view only. Since parallel light is used for both views, a single reference grid may be placed in the light path either before or after both sets of front surface mirrors. To eliminate picture smearing during exposure (at 2000 frames/sec, a model could move as much as 0.2 in. during normal exposure), a multiframe strobe light source was used. Flash durations are 1–2 μ sec, reducing the model motion during exposure to well below film reading accuracies. The flight trajectory must be controlled so that the model stays in the illuminated volume, the cross section of which is a rhombus (Fig. 13).

The data reduction process transforms the model angular orientation into two orthogonal views. The transformation equations converting the observed angles to the orthogonal angles are linear in the tangents of these angles. This transformation permits the use of standard ballistic range data reduction procedures to obtain aerodynamic coefficients.

B. Hypervelocity Laboratory

*F. Livingston, G. Stickford, T. Babineaux, W. Menard,
G. Thomas, B. Riale, and T. Horton*

1. 43-in. Diameter Shock Tunnel,

F. R. Livingston and G. Stickford

The 43-in. diameter shock tunnel was designed for operation from the reflected region of a 6760 ft/sec incident shock propagated into 12.5 cm Hg of air in the 3-in.

diameter shock tube. Unheated hydrogen is used as the driver gas in the shock tube.

Tests during the last half of 1965 were concerned with: (1) determining the shock tube tailored conditions with hydrogen-driving nitrogen test gas and, (2) shakedown of the tunnel and pitot pressure rake system. Using theoretical real gas values for all quantities and assuming a diaphragm pressure ratio based upon steady flow through the diaphragm section, a value of the tailoring Mach number of 5.90 was computed for nitrogen. In two separate series of tests of nine and seven runs each, two different values of tailoring Mach number were obtained:

Runs 55–63, $M = 5.78$

Runs 64–70, $M = 5.54$

Other sources predict a tailored Mach number in the vicinity of 6.0, e.g., later data with the system operating in the shock tunnel mode.

Data obtained in 30 shock tunnel runs indicate a test time of approximately 1 msec. Test time computed on the basis of turbulent wall boundary layer theory is about 3 msec. The discrepancy is thought to be due to contact surface acceleration or mixing during the reflected shock cycle. The test time was increased to 1.5 msec by adding a 5-ft section onto the existing 17-ft driven tube. Now, sufficient steady-state time exists to make pressure and heat transfer measurements.

Using the Kistler Model 701A quartz pressure transducers in pitot heads has proved to be of marginal value due to a flow-excited vibration mode of 8000 cps in the flat plate strut spanning the test section. Vibration isolation devices and electronic low-pass filters have helped, but not eliminated, the problem. A windshield will be installed to isolate the strut from the gas flow.

Considerable effort has gone into completing the vacuum, venting, and remote firing systems during this period. A hydrogen bottle bank has been designed and is to be constructed in January and February, 1966.

2. Electric Arc-Driven Shock Tube, *T. L. Babineaux*

The JPL 6-in. diameter electric arc-driven shock tube has been in operation for almost 4 yr and has produced valuable data in the study of convective and radiative heat transfer. A total of 120 runs was obtained in this facility in the last 6 mo and major development programs were initiated and completed to extend its performance capabilities.

A new test section was installed and provides 18 additional instrument ports to increase data-gathering capabilities and to provide more accurate shock-speed measurements. To extend the shock-speed and test-time capabilities of the facility, a new driver was designed and more capacitors were purchased. The new driver, being fabricated under contract with Inca Engineering Corp., will improve performance in two ways: (1) the driver diameter (6 in.) will give a one-to-one area ratio between driver and driven tube, thus increasing shock speed and test time; (2) a new liner design, fused quartz shrink-fitted into the driver, replacing the present teflon liner, will reduce contaminant levels in the driver which will increase the shock speed and decrease the effect of contaminant radiation on shock-tube data. Since the overall volume of the driver will be increased with this new driver, the additional capacitors will raise the available energy to 300,000 j so that the energy per unit volume will be sufficient to produce shock speeds to 40,000 ft/sec. The capacitors and driver are to be installed in the next 3 mo.

A new data-gathering system for the 6-in. shock tube, which will handle all facilities in the Hypervelocity Laboratory, has been designed and some subsystems have been purchased. Bids have been received for the remaining subsystems and final design criteria are being established. The initial function of this system will be to record and transmit (for reduction) to an available computer, shock-speed data for all the facilities. Later, this function will be expanded to record and transmit all data being taken from shock tube equipment. The purpose of this system is to reduce costs in data recording and reduction and to increase the accuracy of final data.

A major modification to this facility was its conversion to a cold-driven shock tube for a limited time. This was accomplished by replacing the electric driver with a 6-in. driver and by using hydrogen at pressures up to 1400 psia to drive a shock into argon at 13,000 ft/sec. The facility was reconverted to electrical drive but the capability to convert to cold-driven operation has been established and all necessary hardware and instrumentation are available.

3. Ultraviolet Radiation Measurement Capability,

W. A. Menard and G. M. Thomas

In SPS 37-32, Vol. IV, p. 104, the problems involved with making ultraviolet radiation measurements in a shock tube were discussed. These problems have been solved and successful side wall measurements in the 2000-

3000-Å region were obtained with the Jarrell-Ash $f/6.3$ spectrometer. To eliminate unwanted visible stray light from the measurements, a grating blazed for 3000 Å and a solar blind detector were used. The grating was supplied by the Jarrell-Ash Co. It has 1180 grooves/mm and disperses the spectrum approximately 10 Å/mm at the focal plane. The detector is a Model 541F-05M-14 multiplier phototube made by Electro-Mechanical Research, Inc. It has a sapphire window and uses a semitransparent cesium telluride coating as the photocathode. As Fig. 14 shows, the photocathode has a high quantum yield in the ultraviolet but drops off rapidly toward the visible.

Preliminary data (Fig. 15) show that the signal-to-noise ratio is excellent. In Fig. 16, measurements of the ultraviolet spectrum of high temperature ($T_2 = 7000^\circ\text{K}$) air are given. A plot of relative, instead of absolute, intensity is presented because these preliminary data were not

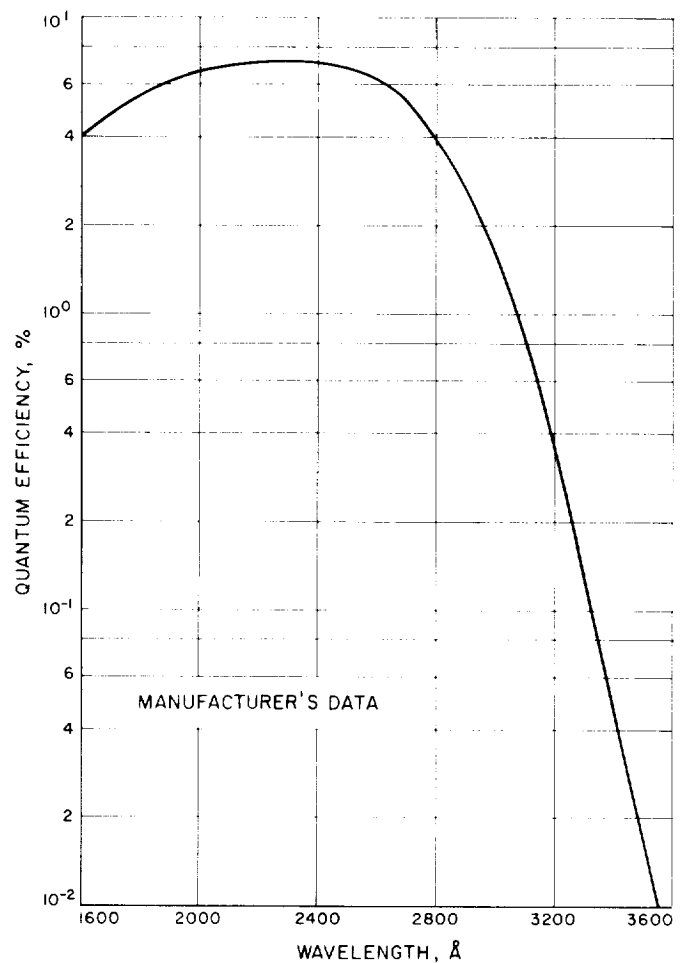
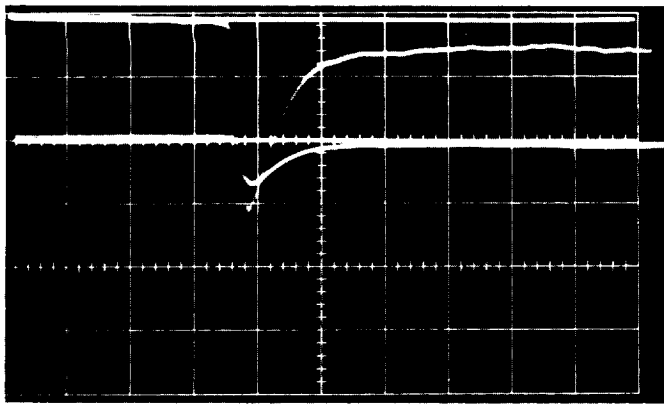


Fig. 14. Spectral response of solar blind multiplier phototube



SWEEP: 1 μ sec/cm
 TEST CONDITIONS: GAS= AIR; $\lambda = 2280 \text{ \AA}$
 $U_s = 29,000 \text{ ft/sec}$; $P_1 = 0.25 \text{ mm Hg}$

Fig. 15. Typical oscillogram of ultraviolet radiation (same data recorded at different gains)

completely calibrated. A formal experimental investigation of this spectral region is planned.

4. Performance Evaluation of a 12-in. Diameter Free-Piston Shock-Tube Driver, B. R. Riale

Much progress has been made in the free-piston shock-tube driver investigation.¹ Approximately 6000 lb additional weight was added to the driver early in November 1965, in an attempt to control vibration of the driver during operation. The added weight has kept vibrations at a

¹SPS, Vol. IV of the following: 37-32, p. 101; 37-34, p. 111; 37-35, p. 89.

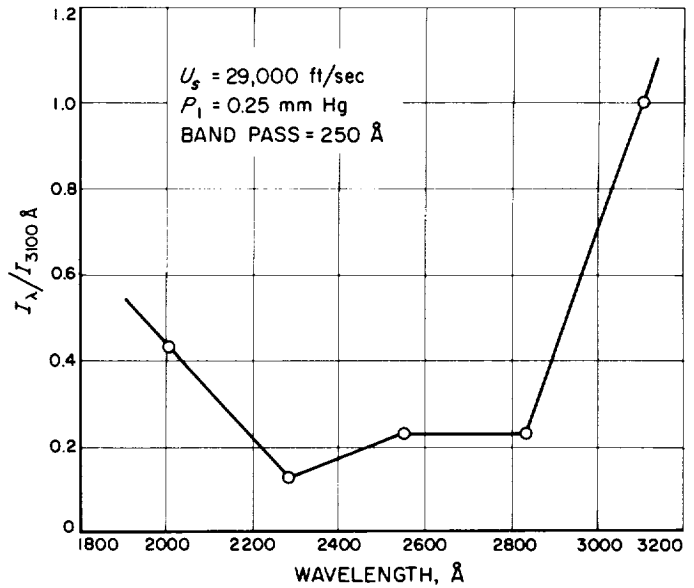


Fig. 16. Ultraviolet air radiation

level low enough so that the present slip joint may be used with all driver conditions given in Table 2. More data on the magnitude of the vibrations will be taken as other driver conditions are investigated.

All driver investigation runs made in November and December 1965, are plotted in Fig. 17. The abscissa is the measured value of the initial driver volume before the piston is released, divided by the measured value of the final driver volume. The ordinate is a calculated value obtained by measuring the initial and final pressures in

Table 2. Shock speed prediction in free-piston shock tube

P_{a0}/P_{b0} , psi	P_{bf} , psi	T_{bf}/T_{b0}	Insert diameter, in.	U_s , ft/sec		
				$P_1 = 0.25 \text{ mm Hg}$	$P_1 = 0.10 \text{ mm Hg}$	$P_1 = 0.05 \text{ mm Hg}$
$\frac{265 \text{ He}}{2 \text{ He}}$	1309	9.95	6	19,000	20,200	21,000
$\frac{690 \text{ He}}{5 \text{ He}}$	3538	10.85	6	21,000	22,000	22,800
$\frac{1450 \text{ He}}{10 \text{ He}}$	7055	11.70	6	22,400	23,300	24,100
$\frac{360 \text{ He}}{2 \text{ He}}$	2699	13.6	4.5	21,000	22,300	23,200
$\frac{980 \text{ He}}{5 \text{ He}}$	8150	14.7	4.5	23,200	24,200	25,000
$\frac{590 \text{ N}_2}{2 \text{ He}}$	9110	19.25	3	23,800	24,000	26,000

(Considering real gas effects, driven gas is air)

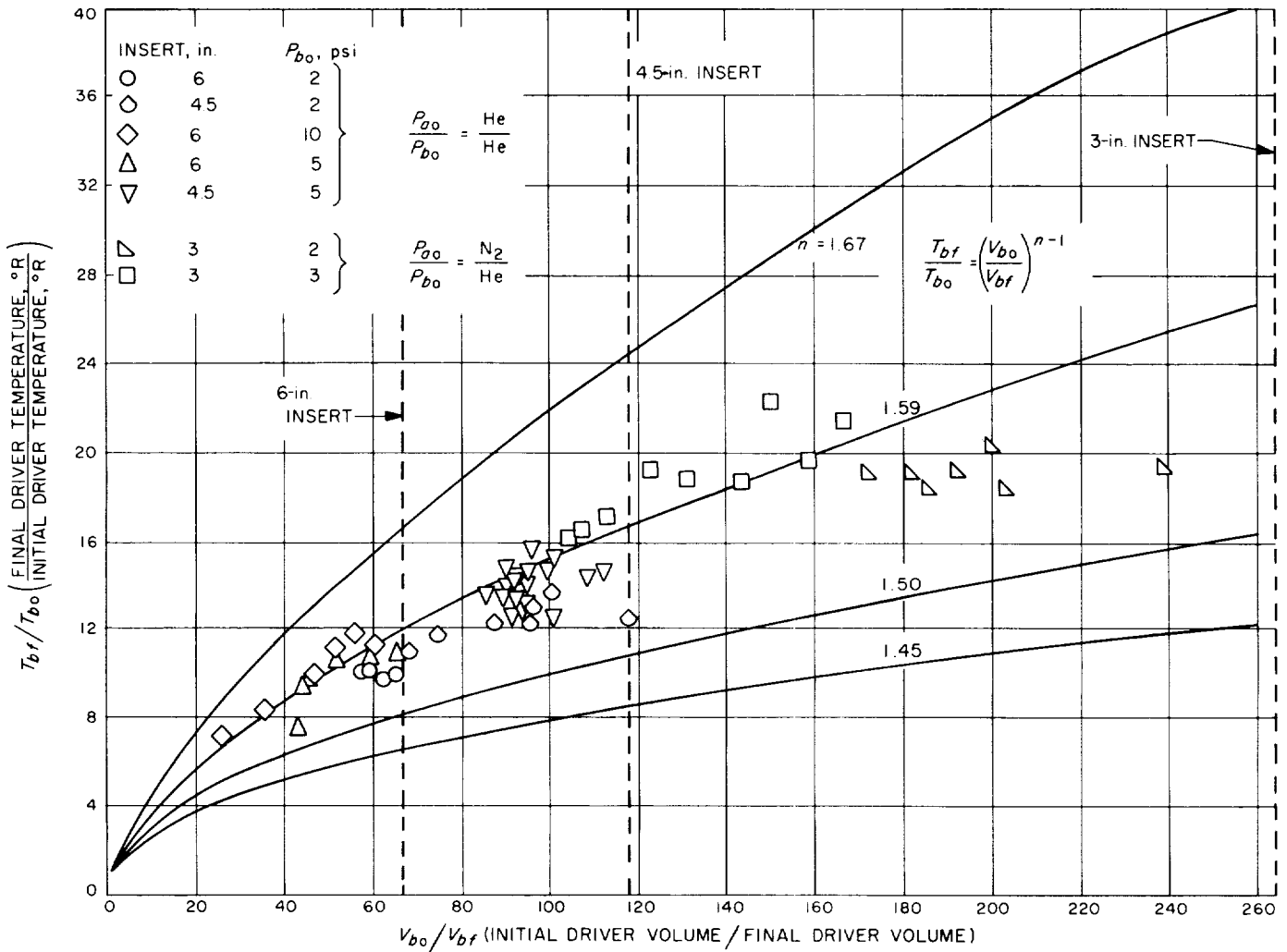


Fig. 17. Driver temperature ratio as a function of driver volume ratio

the driver chamber and calculating the polytropic exponent n for the compression by the equation

$$\left(\frac{V_{bo}}{V_{bf}}\right)^n = \frac{P_{bf}}{P_{bo}}$$

Knowing n , the ratio of final-to-initial absolute temperatures in the driver can be calculated from the expression:

$$\frac{T_{bf}}{T_{bo}} = \left(\frac{V_{bo}}{V_{bf}}\right)^{n-1}$$

The vertical lines in Fig. 17 represent the limits in driver volume ratio using the three different diameter driver inserts. To date, six different driver conditions have been reached and are given in Table 2 with their respective predicted shock speeds in air.

Recently, the piston driving gas was changed from bottled helium to nitrogen because the nitrogen was more readily available in larger quantities.

The problem of black ablation deposits in the driver has been solved by removing a molded teflon ring from the front of the piston and replacing it with an aluminum ring. Also, a silicone rubber bumper was removed from the driver after semiquantitative spectrographic analysis of the ablation deposits showed that the silicone rubber was a contributor to the ablation.

Since many problems and much down-time have resulted from wear on the thin spray coating of teflon which covers the aluminum piston, a new piston has been designed. A 0.375-in. molded teflon sheath replaces the spray coating.

Definition of symbols

- V volume
- P absolute pressure
- T absolute temperature
- n polytropic exponent

Subscripts

- a0 conditions behind piston before it is released
- af conditions behind piston after it is released
- b0 conditions ahead of piston before it is released
- bf conditions ahead of piston after it is released

5. An Experimental Assessment of the Effect of Large Amounts of Argon on Stagnation Point Convection Heating in a Planetary Atmosphere,² T. E. Horton and T. L. Babineaux

This experimental investigation assessed the effect of significant amounts of argon on stagnation point convective heating. The primary gas mixtures investigated consisted of 65% CO₂-35% A and 30% CO₂-40% N₂-30% A. Also, tests were conducted in air and a mixture of 9% CO₂-90% N₂-1%A. The intent of the tests in the latter two mixtures was to establish a base to which the heating rates in the argon concentrated mixtures could be compared.

The data were obtained utilizing an arc-heated shock tube with a 6-in. diameter driven section to simulate flight velocities in the range of 18,000 to 34,000 ft/sec. Hemisphere models of 1 in. diameter were used with 0.001-in. thick platinum calorimeter gages mounted at the stagnation point. The particular care placed on the design of the models, the measurement of the calorimeter-gage

²Horton, T. E., and Babineaux, T. L., "An Experimental Assessment of the Effect of Large Amounts of Argon in a Planetary Atmosphere on Stagnation Point Convective Heating," AIAA Paper No. 66-29, AIAA 3rd Aerospace Sciences Meeting, New York, New York, January 24-26, 1966.

properties, and calibration of the instrumentation contributed to the high degree of repeatability of the data. The quality of the data was such that smooth curves could be fitted to it with an average deviation of less than ±10%.

The thermodynamic properties behind the incident and model bow shocks were calculated for the various mixtures. Chemical compositions were used to evaluate the radiative intensity of the gases behind the bow and incident shocks. Using these data, the convective heating results were corrected for the estimated radiative contribution to the data. By comparing data taken with 1- and 2-in. models in the 65% CO₂-35% A mixture, an excellent confirmation of the theoretical radiation correction was obtained.

The results of the investigation indicate that the effect of argon in an atmosphere is to slightly increase the heat transfer in the flight range where ionization is important (Fig. 18). For the mixtures investigated, this increase above the values obtained in air was less than 30%. For Martian entry, (H_s - H_w) below 12,000 Btu/lb, the ionization is not significant and heat transfer rates are similar to these in the nonargon atmospheres.

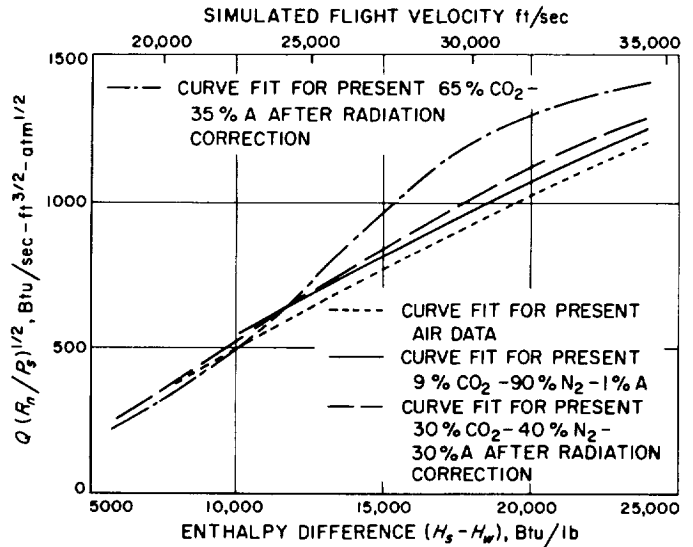


Fig. 18. Comparison of curves of stagnation point heat transfer data for various atmospheres

References

1. Behrens, W., "Viscous Interaction Effects on a Static Pressure Probe at $M = 6$," *AIAA Journal*, Vol. 1, No. 12, p. 2864, December, 1963.
2. Prislin, R. H., "The Free-Flight and Free-Oscillation Techniques for Wind Tunnel Dynamic Stability Testing," Technical Report No. 32-878, Jet Propulsion Laboratory, Pasadena, California, February 1966.
3. Murphy, C. H., "An Erroneous Concept Concerning Nonlinear Aerodynamic Damping," *AIAA Journal*, Vol. 1, No. 6, June 1963.

XI. Space Simulators and Facility Engineering

A. Advanced Solar Simulation Development

C. L. Youngberg

To improve the performance of solar simulation systems, especially those at JPL, is the object of this program. That portion of the current effort covered by this report involves development of an advanced light source module consisting of an appropriate concave reflector enclosing a high output source, as depicted in Fig. 1.

The reflector geometry consists of a 27-in. diameter prolate ellipsoid with foci at 4 and 544 in. from the vertex. The reflector is fabricated of 0.5-in. 6061 aluminum with appropriately thicker support areas, is coated with electroless nickel as the optically polished substrate, and coated with vacuum-deposited aluminum for maximum specular reflectivity. The polished surface contour departs from a true ellipse by less than 2 min of arc. Temperature control is accomplished by water circulation through 50 ft of 3/8-in. copper tubing attached to the rear surface of the reflector with aluminum-filled epoxy. Operation with a 20-kw arc at the first focus produced an equilibrium cooling water ΔT of 16°F at a flow rate of 0.25 g/min. Thermocouples located on the rear of the reflector registered maximum temperatures of 100°F at the

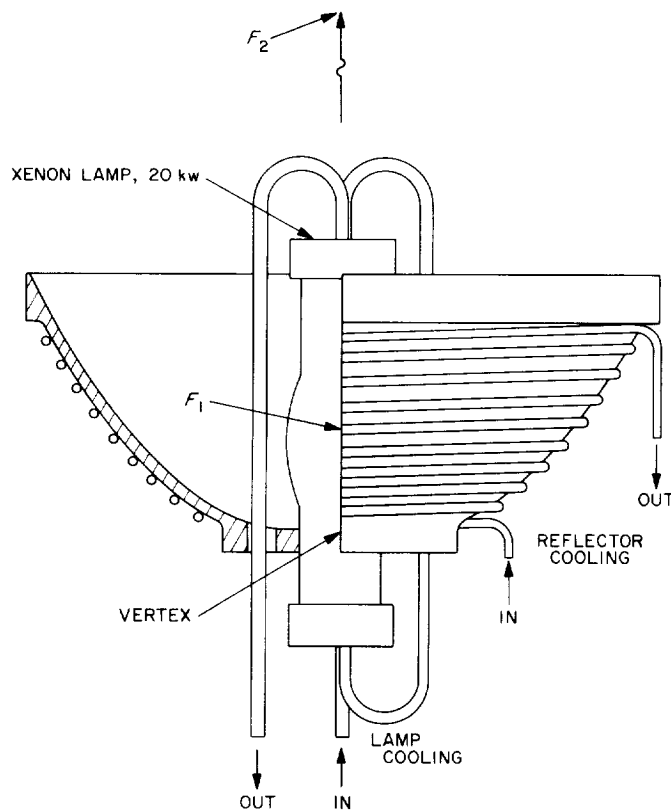


Fig. 1. Light source module

edge and 115°F at the center. After more than 275 hr of operation and several cleanings, the reflective surface showed no visual degradation.

The requirements of the 25-ft Space Simulator modification dictated a need for a 20-kw compact arc lamp capable of reliable operation for several hundred hours. Emphasis was placed on the commercially available xenon lamp shown in Fig. 2. It has water-cooled electrodes and a clear fused silica envelope. A number of these lamps has been procured and operated in an environment similar to that of their intended use. A problem concerning overheating of the brass clamp blocks at each end of the lamp was overcome by polishing and chrome plating the blocks, thus reflecting incident radiation previously absorbed. A more severe problem is failure of the copper anode by perforation during

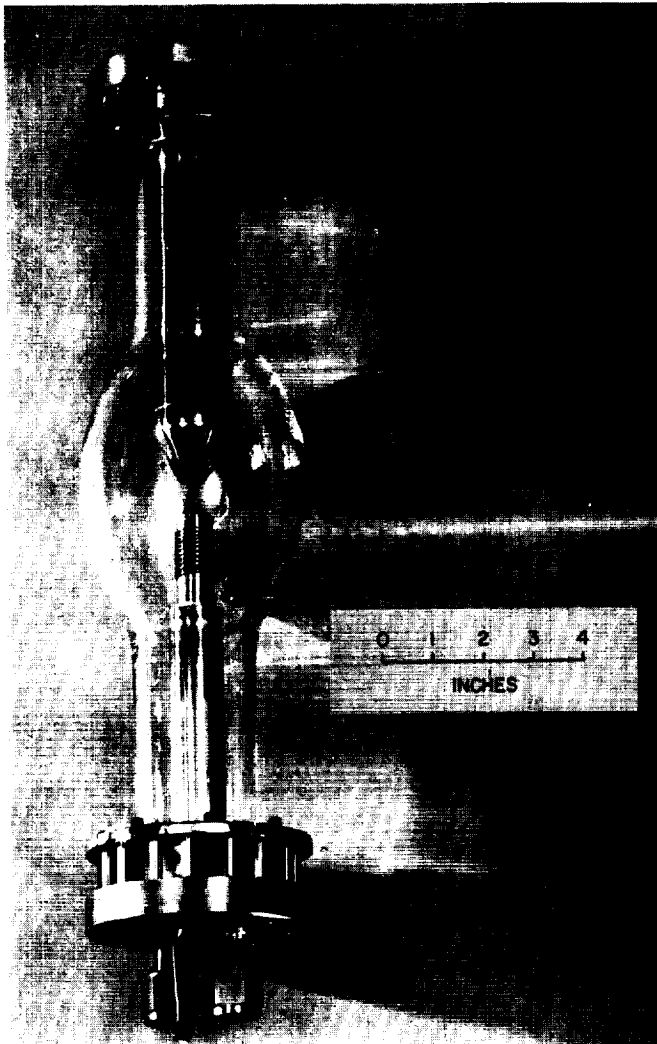


Fig. 2. 20-kw xenon lamp

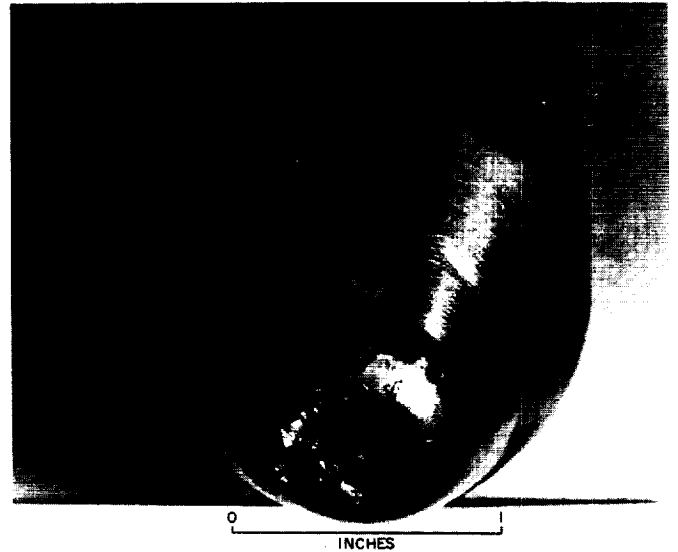


Fig. 3. Perforated anode

operation. This generally causes fracture of the silica envelope. A typical failed anode is shown in Fig. 3. This mode of failure appears to have several defined steps that happen in rapid succession:

- (1) Inadequate internal cooling, possibly by formation of a coolant stagnation area, allows local overheating of the spherical anode tip.
- (2) The copper softens and is deformed inward toward the coolant nozzle by the high-pressure xenon gas.
- (3) The deformation further restricts the water flow, causing the tip temperature to continue its rise.
- (4) The temperature reaches the melting point, the perforation forms.
- (5) Xenon gas vents through the hole into the cooling system until pressure equalization occurs and the water, at 180 psig, can flow out of the hole, impinge on the envelope and shatter it.

One lamp failed in this manner after 403 hr of operation. Most other failures have occurred at less than 50 hr. Parallel programs are being pursued by JPL and the vendor to solve this problem. Improved coolant passage contours, pressurized coolant systems, and higher melting point anode tips are being explored in these programs.

One lamp was checked for degradation during the latter 278 hr of a 403-hr life. Output degraded less than 10% and the envelope remained visually clear where a nonwater-cooled lamp would have displayed tungsten

deposit on the inside of the envelope. This lamp has a tungsten cathode which is also water cooled; thus, it may produce less spectral change during its useful life than nonwater-cooled lamps.

Total energy measurements were made with an appropriate 19.5-in. aperture in front of a 24-in. copper spiral calorimeter placed at the second focus of the reflector with the lamp at the first focus, as shown in Fig. 4. The flat black calorimeter surface absorbs about 96% of the total energy delivered through the aperture which is identical in size and shape to the outline of a JPL solar simulator lens systems. Thus the energy measurements are directly applicable to a specific JPL-type system. With data normalized to 20-kw input, 10 total-energy measurements made near the end of the 403-hr life mentioned above show an average capture of 2849 w, an average efficiency of 14.2%.

A profile of the energy distribution across the beam in the plane of the second focus was necessary for lens system design and uniformity predictions. The energy was

attenuated without spectral shift by using a black screen to allow use of a high intensity thermopile as a survey sensor. This distribution is presented in Fig. 5 and demonstrates a symmetry made possible by the accuracy of the ellipsoidal reflector.

Concurrent with lamp energy and life tests, several other lamp operation parameters were investigated and defined. These included the 50-kv pulse starting of the lamp, lamp cooling by heat exchanger, reflector cooling, high amperage switch operation, starter bypassing, and remote control of the rectifiers for lamp power.

Total energy and survey measurements have demonstrated that this light source module will satisfy its intended objectives. The most important remaining step is solution of lamp design problems to raise the expected lamp life to 400 hr or more.

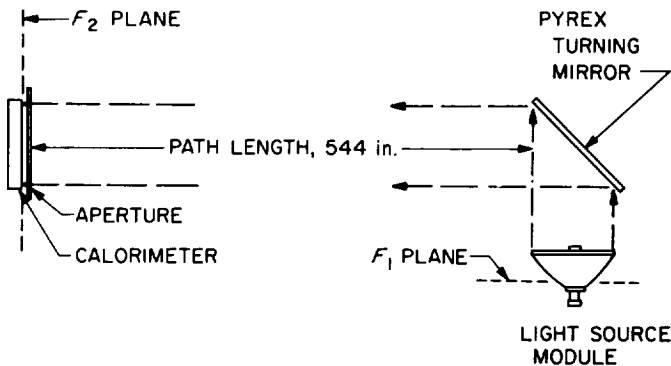


Fig. 4. Total energy test

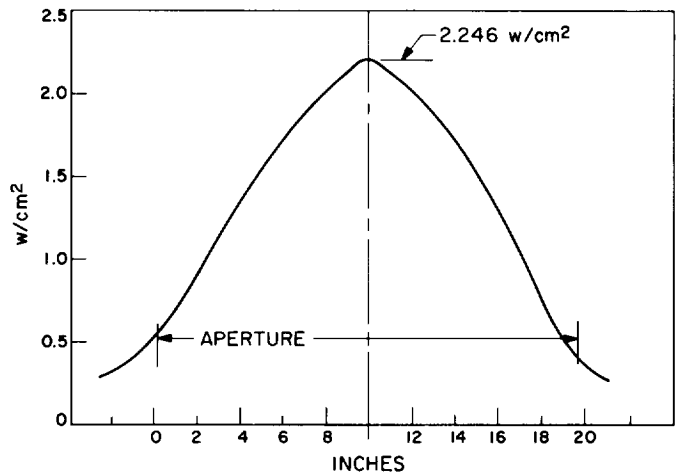


Fig. 5. Energy profile

PROPULSION DIVISION

XII. Research and Advanced Concepts

A. Thermal Radiation From Ionized Argon As Determined by Application of Near-Black Cavities: Effect of Quartz Window Between Gas and Cavity*E. J. Roschke***1. Introduction**

The description and use of a hohlraum, designed for measuring total radiation from an ionized gas flowing in a circular duct, was presented in *SPS 37-36*, Vol. IV, pp. 87-92. This hohlraum had an annular opening and window which formed a portion of the wall of the circular duct. Preliminary experimental data were presented and analyzed for the simplest case of neglecting the presence of the quartz window; those results indicated that approximately 2% of the total heat transfer to the duct wall was in the form of thermal radiation. The purpose of this paper is to extend the thermal analysis, reported in *SPS 37-36*, by taking into account the presence of the quartz window, and to apply the analysis to the experimental data of one

of the tests. The results indicate that the quartz window, particularly its temperature, is an important consideration but that by neglecting its presence, one is likely to determine an upper bound on the magnitude of the thermal radiation. A further purpose for the present work is to assess the feasibility of making total radiation measurements by means of the hohlraum technique.

2. Thermal Analysis, Including Effect of Window

The following analysis is a further step toward understanding the functional operation of the hohlraum as a total radiation measurement device. Unfortunately, some type of transmitting window appears necessary to isolate the cavity from direct or indirect gas convection effects especially when, as in the present experiments, run time is of the order of 30 min per test. The effect of the quartz window on the performance of the hohlraum appeared superficially as a possible source of considerable error. The following very approximate analysis confirms that thought.

Thermal radiation incident on the quartz window (Fig. 1) is not due entirely to gas radiation if the gas is

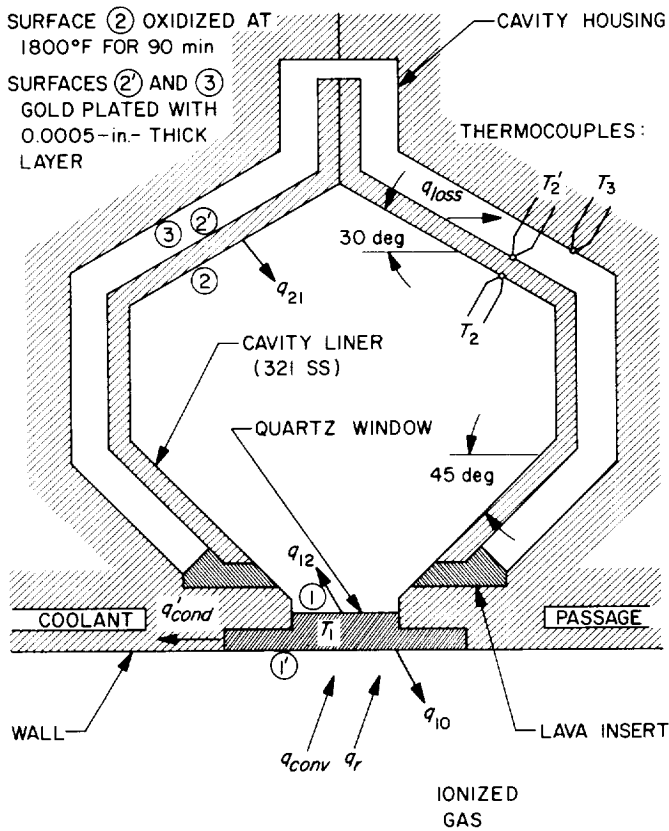


Fig. 1. Details of uncooled hohlraum and terminology for thermal analysis

optically thin which, in the present case, it probably is, since the pressure is not high and the path length is relatively small. The quartz window also receives radiation from itself and from the duct walls, both directly and by reflection. The gas shall be constructed as a fictitious surface area and all former effects may be lumped in a configuration factor F_{10} from window to gas. It is anticipated that F_{10} approaches unity in the present apparatus; however the thermal analysis, on a comparative basis, does not depend on F_{10} .

The problem is summarized in Table 1 (a description of terms may be found in Fig. 1 and the definition of symbols). Since the window temperature T_1 has not yet been measured experimentally, it is treated as a parameter in the analysis. Thus, the problem is reduced to five equations in five unknowns; the desired quantity is q_r , the rest are incidental to the solution. The leaving radiant flux from any surface includes emission, reflection of radiation received from other surfaces including itself and, in the case of the window, transmission. Note that $A_1 \neq A_1'$ and $A_2 \neq A_2'$. Convective heat transfer to the

Table 1. Thermal analysis of uncooled hohlraum

Assumptions	
<ol style="list-style-type: none"> 1. Radiation from ionized argon is diffuse and uniformly distributed. 2. Presence of hohlraum does not alter q_r significantly. 3. Hohlraum is in thermal equilibrium with surroundings. 4. Hohlraum cavity is isothermal (T_2 is uniform). 5. Quartz window is at uniform temperature T_1. 6. Window and cavity liner reflect and emit diffusely. 7. Cavity is filled with nonabsorbent medium. 8. There is no heat transfer by conduction between window and cavity liner. 9. Multiple reflections internal to cavity are not considered. 10. All optical properties, configuration factors, and surface areas are known or can be determined. 	
Known (Measured or assumed)	Unknown (Calculated)
<ol style="list-style-type: none"> 1. q_{in} 2. q_{loss} 3. T_1 4. T_2 5. All optical properties 	<ol style="list-style-type: none"> 1. q_{in} 2. q_{12} 3. q_{21} 4. q'_{cond} 5. q_r
Equations for determining q_r ($T_1 \neq T_2$)	
<ol style="list-style-type: none"> 1. Thermal balance on hohlraum cavity. 2. Thermal balance on window. 3. Leaving radiant flux^a expression for q_{10}. 4. Leaving radiant flux^a expression for q_{12}. 5. Leaving radiant flux^a expression for q_{21}. 	
^a Also known as radiosity.	

quartz window occurs over area A_1' . In this analysis all radiant heat flux terms referred to the window are assumed to occur over surface A_1 only, hence, emission from the window to the gas will be too small. The effect of this assumption is discussed later. The following relations between configuration factors have been utilized:

$$A_0 F_{01} = A_1 F_{10}, F_{10} \sim 1$$

$$A_1 F_{12} = A_2 F_{21}, F_{12} = 1$$

$$F_{21} + F_{22} = 1$$

From these relations it is determined that $F_{21} = A_1/A_2$ and $F_{22} = 1 - A_1/A_2$. F_{12} is unity because the quartz window is completely enclosed by the cavity and, on the cavity side, cannot view itself.

The equations listed 1 to 5 in Table 1 are reduced to final form below in Eqs. (1) to (5), respectively. Note that the total heat flux incident on the cavity q_{tot} has been resolved into the radiative component q_r acting on area A_1 and the convective component (gas conduction and convection) q_{conv} acting on area A'_1 .

$$(q_{12} - q_{21}) = (A'_2/A_1) q_{loss} \quad (1)$$

$$F_{10} q_r = \left(q_{10} + \frac{A'_2}{A_1} q_{loss} \right) + \left(q'_{cond} - \frac{A'_1}{A_1} q_{conv} \right) \quad (2)$$

$$q_{12} = e_{12} + t_{12} + (1 - \alpha_1 - \tau_1) q_{21} \quad (3)$$

$$q_{10} = e_{10} + t_{10} + (1 - \alpha_1 - \tau_1) F_{10} q_r \quad (4)$$

$$q_{21} = \left[e_{21} + (1 - \alpha_2) \frac{A_1}{A_2} q_{12} \right] / C_1 \quad (5)$$

where

$$\left. \begin{aligned} e_{10} &= e_{12} = \epsilon_1 \sigma T_1^4, & e_{21} &= \epsilon_2 \sigma T_2^4 \\ t_{12} &= \tau_1 F_{10} q_r, & t_{10} &= \tau_1 q_{21} \\ C_1 &= 1 - (1 - \alpha_2) (1 - A_1/A_2) = \alpha_2 + (1 - \alpha_2) A_1/A_2 \end{aligned} \right\} \quad (6)$$

Eqs. (1)-(5) may be solved simultaneously for each of the five unknowns in terms of the knowns. Note that solution of the quantity q_r , which is of chief interest, does not depend on q'_{cond} or q_{conv} if T_1 is known or specified. From experiment, only q_{tot} is known but for practical purposes in the present case $q_{tot} \sim q_{conv}$. The solutions for q_{10} , q_{12} , q_{21} , q'_{cond} and q_r are given in Eqs. (7)-(11) in the order of their solution:

$$q_{12} = (1/\alpha_2) [e_{21} + (A'_2/A_1) C_1 q_{loss}] \quad (7)$$

$$q_{21} = (1/\alpha_2) [e_{21} + (1 - \alpha_2) (A'_2/A_1) q_{loss}] \quad (8)$$

$$\tau_1 F_{10} q_r = (\alpha_1 + \tau_1) e_{21}/\alpha_2 - e_{12} + (A'_2/A_1) C_2 q_{loss} \quad (9)$$

$$q_{10} = C_3 e_{10} + \frac{C_4 e_{21}}{\alpha_2} + \frac{A'_2}{A_1} q_{loss} \times \left\{ (1 - C_3) + \frac{(1 - \alpha_2) A_1}{\alpha_2} C_1 \right\} \quad (10)$$

$$q'_{cond} = \frac{A'_2}{A_1} \frac{\alpha_1}{\tau_1} C_5 q_{loss} + \frac{A'_1}{A_1} q_{conv} - \frac{(\alpha_1 + 2\tau_1)}{\tau_1} \left(e_{10} - \frac{\alpha_1}{\alpha_2} e_{21} \right) \quad (11)$$

where the coefficient C_1 has been given in Eqs. (6), and

$$\left. \begin{aligned} C_2 &= 1 + \frac{(\alpha_1 + \tau_1)(1 - \alpha_2)}{\alpha_2} (A_1/A_2) \\ C_3 &= 1 - \frac{(1 - \alpha_1 - \tau_1)}{\tau_1} \\ C_4 &= \tau_1 + \frac{(1 - \alpha_1 - \tau_1)(\alpha_1 + \tau_1)}{\tau_1} \\ C_5 &= 1 + \frac{(\alpha_1 + 2\tau_1)(1 - \alpha_2)}{\alpha_2} (A_1/A_2) \end{aligned} \right\} \quad (12)$$

Eq. (9) has two limiting cases: (a) $e_{12} \rightarrow 0$, and (b) $q_r \rightarrow 0$. Case (a) represents the situation when the effect of the window (i.e., the participation of the window in the thermal balance) becomes negligible. For this case, $\alpha_1 = \epsilon_1 \rightarrow 0$, $\tau_1 \rightarrow 1$, $C_2 \rightarrow C_1/\alpha_2$ or $T_1 \rightarrow 0$; if, in addition, $F_{10} = 1$, Eq. (9) reduces to:

$$q_r = \frac{e_{21}}{\alpha_2} + \frac{A'_2}{A_1} C_2 q_{loss} \quad \text{or} \quad q_r = \frac{\epsilon_2}{\alpha_2} \sigma T_2^4 + \frac{C_1 A'_2}{\alpha_2 A_1} q_{loss} \quad (13)$$

Eq. (13) is identical with Eq. (1) in SPS 37-36 except for a minor difference in the apparent absorptivity of the cavity. In Eq. (13) $\alpha_e = \alpha_2/C_1$ where the flatness factor $f = A_1/A_2$, whereas $f = A_1/S = A_1/(A_1 + A_2)$ in Eq. (1) of SPS 37-36. The difference, which has negligible effect on α_e in this case, arises because of the configuration factor between window and cavity surfaces. In the case of a hollow sphere, the flatness factor f merely represents the configuration factor between a spherical cap (of finite or infinitesimal area) and the remaining inside surface area of the sphere (see Section 3: Emission Characteristics of Cavities).

Case (b) represents the condition in which emission from the window accounts for all thermal energy entering the cavity and hence $q_r = 0$. This condition occurs when

$$e_{12} = (\alpha_1 + \tau_1) e_{21}/\alpha_2 + \frac{A'_2}{A_1} C_2 q_{loss} \quad (14)$$

$$\text{or} \quad T_1 = \left[\frac{(\alpha_1 + \tau_1) \epsilon_2}{\alpha_2 \epsilon_1} T_2^4 + \frac{A'_2 C_2}{A_1 \sigma \epsilon_1} q_{loss} \right]^{1/4} \quad (15)$$

The effect of the window on the determination of q_r from typical experimental data is shown in Fig. 2, based

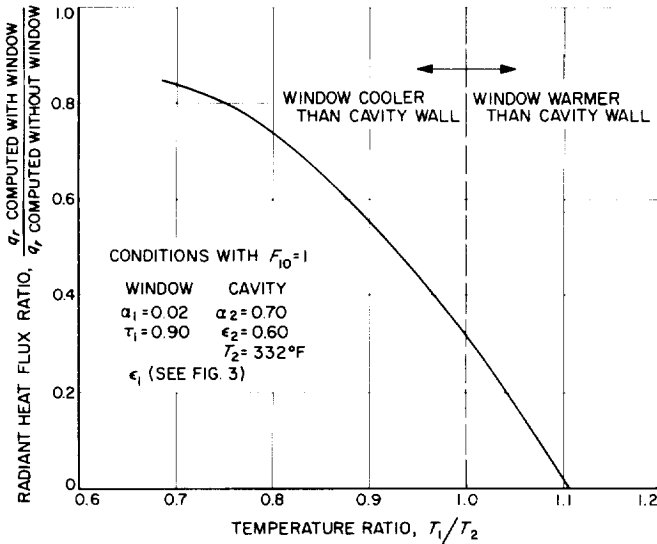


Fig. 2. Effect of window on radiant heat flux incident on hohlraum cavity for various assumed values of window temperature as applied to Test 112-5H

on observations from Test 112-5H. The ordinate represents a ratio of q_r values obtained from Eq. (9) (numerator) and Eq. (13) (denominator) for various assumed values of T_1 plotted on the abscissa as the ratio T_1/T_2 . Values for the emissivity of quartz have been taken from the faired curve in Fig. 3. Other required values of the optical properties are listed as conditions in Fig. 2 (see Section 4: Optical Properties of Hohlraum Materials). For the conditions assumed, it is seen that the "true" value of q_r is markedly affected by the window; at $T_1 = T_2$ the true value of q_r is approximately 30% of the value obtained when disregarding the window. The exact shape and level of the curve in Fig. 2 of course depends on the values assumed for the optical properties involved;

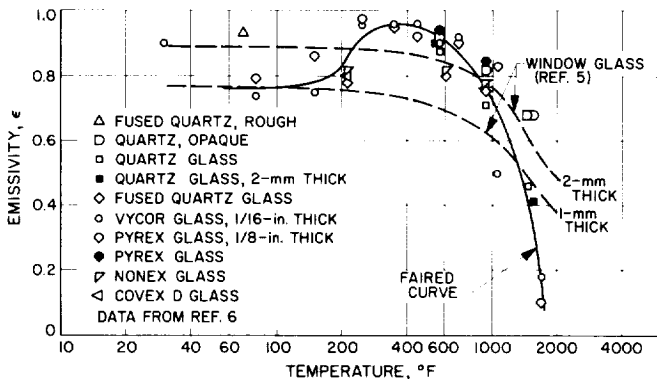


Fig. 3. Total emissivity of various quartz and high-silica glass samples

however, the trend is significant. Since T_1 has not yet been measured, the window effect is not precisely known. It is expected that $T_1 > T_2$ in the present experiments since the quartz was not directly cooled.

This analysis predicts an upper limit on T_1 corresponding to $q_r = 0$, i.e., intersection of the curve with the abscissa in Fig. 2. For this case a maximum value of T_1/T_2 is evident. If an actual measurement indicated that T_1 was significantly higher than this theoretical limit, it could be assumed that the assumptions of the analysis are too restrictive. Large deviations from the theory could not be accounted for solely by incorrect values of the optical properties. The walls of the duct containing the flow of ionized argon were highly cooled in this apparatus (SPS 37-36). For comparison purposes, the approximate gas-side wall temperature adjacent to the quartz window was approximately 105 F in Test 112-5H.

Obviously, uncertainty in the effect of the window on calculating q_r can be greatly reduced by highly cooling the quartz window. For example, $T_1/T_2 = 0.7$ corresponds to $T_1 = 95^\circ\text{F}$ in Fig. 2 (approximately room temperature). It is doubtful that even direct water cooling at the edges of the window could produce this much cooling.

If T_1 is known, q'_{cont} can be calculated directly from Eq. (11). The value of T_1 necessary to produce a direct cancellation of q_{cont} is found from Eq. (11) by setting $q'_{cont} - (A'_1/A_1) q_{cont} = 0$. Thus,

$$T_1 = (\alpha_1 + \epsilon_1 \sigma)^{-1} [C_2 (A'_2/A_1) q_{loss} (\alpha_1 + 2\tau_1) + (\epsilon_2 + \alpha_2) \sigma T_2^4]^{1/4} \quad (16)$$

For the conditions of Test 112-5H and values listed in Fig. 2, this would correspond approximately to $T_1 \sim 150$ F. At this temperature, the window could be disregarded with small error.

3. Emission Characteristics of Cavities

In the present application of the hohlraum, information concerning both the emission and absorption characteristics of the cavity are required. Cavity emission depends on the shape and optical characteristics of the cavity walls; cavity absorption, in addition to these factors, depends on the character of the incoming radiation. Certain conditions (Ref. 1) permit derivation of one from the other. In order for $\alpha_w = \epsilon_w$, the cavity must be gray and, with the exception of the spherical cavity, the incident radiation must be diffuse. In the present case

it is felt that the assumptions of nongray cavity walls with diffuse incident radiation are sufficiently accurate to use parallel expressions for α_n and ϵ_n despite the complexity of the cavity shape. Whatever error is incurred, it is probably no worse than some of the other uncertainties involved. The nature of the derivation used in determining window effect amounts to the use of parallel expressions for α_n and ϵ_n such that $\alpha_n/\epsilon_n = \alpha_2/\epsilon_2$. There is no assurance that this is true in the present case.

The following expression for the apparent absorptivity of a spherical cavity was applied to the hohlraum in SPS 37-36:

$$\alpha_n = \alpha_2 / [\alpha_2 + (A_1/S)(1 - \alpha_2)] \tag{17}$$

More complicated expressions than this arise when nonspherical cavities are treated. Some of these are generally applied to cavities of any shape. Ref. 2 contains a discussion of several expressions for ϵ_n available for cylindrical cavities; in addition, these were compared with experimental data. Ref. 3 contains analytical expressions for a variety of cavity shapes and is especially convenient because, to a first approximation, a single expression containing flatness factor f is used for all cavity shapes and f -curves are given for several shapes. The expression for ϵ_n given in Ref. 3 is parallel to Eq. (17) used here, i.e.,

$$\epsilon_n = \epsilon / [\epsilon + f(1 - \epsilon)] \tag{18}$$

where ϵ is the emissivity of the cavity walls.

4. Optical Properties of Hohlraum Materials

The required optical properties are: emissivity and absorptivity of the quartz window, oxidized cavity liner, and gold plated rear surfaces (Fig. 1). Transmissivity of the quartz window to ionized argon radiation is also required; τ_1 was taken as 0.9 for illustrative purposes, for lack of a better value.

The absorption characteristics of the quartz window—at least for clean, uncontaminated quartz—are thought to be of small importance. However, the emission characteristics are of great influence. The radiative characteristics of transparent materials are very complex since they depend on bulk or volume phenomena (Ref. 4). Emissivity measurements on quartz are not readily available. Data from a compilation presented in Ref. 5 is plotted in Fig. 3 and should be considered as merely typical. Also included in Fig. 3, for comparison, are two

curves for window glass as taken from Ref. 4. It is apparent that the total emissivity of quartz is rather high from room temperature to 1000°F.

The emissivity of oxidized stainless steel has been measured by various investigators with varied results (Refs. 5–8). Precise physical conditions of the surface are apparently of great importance. Absorptivity of the oxidized 321 stainless steel to thermal radiation from ionized argon, which in the present case probably does not approximate even a gray body, is unknown. Solar absorptivity values, though available, are of questionable use. Values of α_2 and ϵ_2 listed in Table 2 are judicious guesses for the most part.

Table 2. Nominal and error values assumed for error analysis of radiant heat flux q_r as applied to Test 112-5H

Quantity	Nominal value	Absolute error	Relative error, %
F_{10}	0.90	± 0.10	+ 11.1
τ_1	0.90	± 0.06	+ 6.7
α_1	0.02	± 0.02	± 100.0
ϵ_1	Variable	± 0.10	—
α_2	0.70	± 0.10	+ 14.3
ϵ_2	0.60	± 0.10	+ 16.7
A_2'/A_1	18.48	+ 0.92	+ 5.0
A_1/A_2	0.0508	± 0.0025	+ 5.0
$q_{r, \dots}$ (Btu/ft ² hr)	20	± 8	+ 40.0
T_2 (°R)	768	± 24	+ 3.1
T_1 (°R)	Variable	- 0.05 T_1	+ 5.0

Surfaces 2' and 3, indicated as gold plated in Fig. 1, can probably be considered gray surfaces for practical purposes since they are not subject to external radiation and do not differ appreciably in temperature. Again, data from Refs. 5 and 7 have been utilized to arrive at a reasonable value of $\epsilon = \epsilon'_2 = \epsilon_3 = 0.09$ as used here.

5. Error Analysis

Ref. 9 points out some of the many errors associated with the practical use of hohlraums; however, those results pertain to the use of hohlraums in measuring optical properties of physical specimens. In the present work an error analysis is essential to assess the feasibility of the hohlraum in absolute measurement of total radiation. This has been done by methods outlined below.

Given an analytical expression for a physical quantity, in terms of several physical quantities which are determined experimentally with varying degrees of absolute

error, the most probable error in the desired physical quantity is calculated as indicated.

If a physical quantity M is given in terms of i , other quantities

$$M = f(x_i)$$

and each of the x_i has absolute uncertainty δ_{x_i} , then the most probable error in M associated with these uncertainties is

$$\Delta_M = (\Delta_{x_1}^2 + \Delta_{x_2}^2 + \dots + \Delta_{x_i}^2)^{1/2}$$

or
$$\Delta_M = (\sum \Delta_{x_i}^2)^{1/2} \tag{19}$$

where the error in M due to uncertainty δ_{x_i} in x_i is calculated from

$$\Delta_{x_i} = \frac{\partial M}{\partial x_i} \delta_{x_i} \tag{20}$$

Application to Eq. (9) results in eleven values of Δ_r calculated according to Eq. (20) with nominal x and absolute δ_x given by Table 2. An error analysis for q_{loss} , as determined from Eq. (4) of SPS 37-36, indicated an error in q_{loss} of approximately $\pm 40\%$ for Test 112-5H (Table 2).

Most probable error in radiant heat flux (relative to the total heat flux) has been plotted in Fig. 4. This result is to be compared to the nominal value of q_r/q_{tot} . The curves shown in Fig. 4 are to be construed as typical results which could occur when experimental uncertainties and uncertainties in optical properties are as indicated. It is apparent that heat transfer data of acceptable engineering accuracy can be obtained only if (1) the window temperature is maintained at, or less than, approximately room temperature, or (2) the requisite optical properties are known to much higher precision than indicated in Table 2. For the case considered, the most probable error in q_r is approximately $\pm 80\%$ when $T_1/T_2 = 1$; for this condition the largest contributions to the total error were those due to q_{loss} , t_1 , ϵ_2 , α_2 , ϵ_1 , and T_2 , in that order. Although the relative error in q_r approaches infinity as T_1/T_2 approaches its limiting value (because q_r approaches zero), the absolute error in q_r remains finite. In fact, the absolute error never

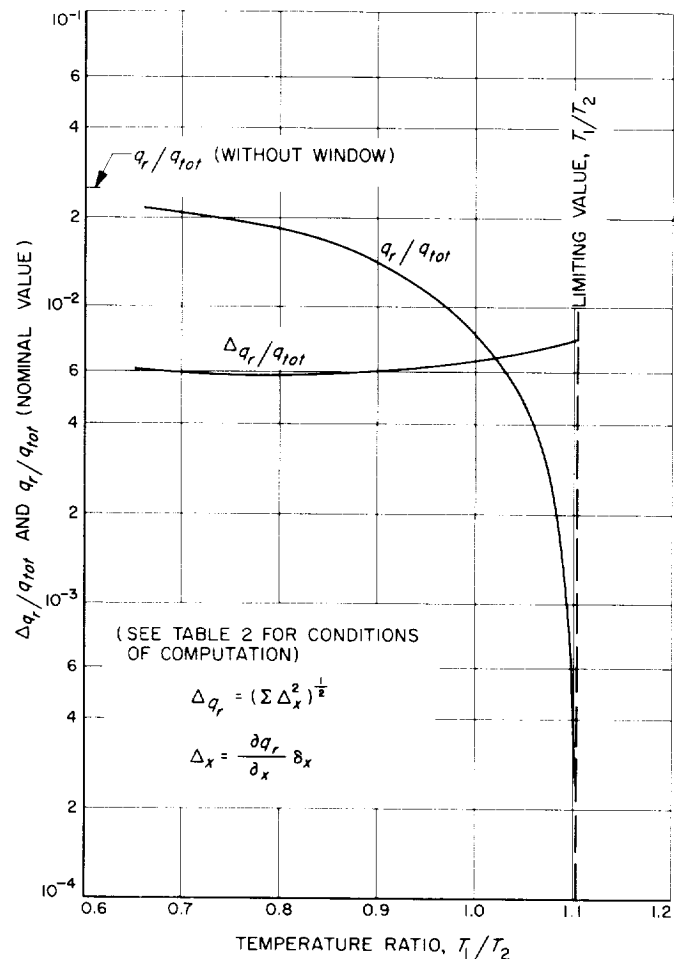


Fig. 4. Results of error analysis for determining radiant heat flux, including effect of window. Comparison of nominal value of q_r and its absolute error for Test 112-5H

approaches or exceeds q_r as determined, neglecting the presence of the window. This is an important distinction.

6. Discussion

In the approximate analysis, thermal radiant exchange between the gas and the quartz window was based on area A_1 ; i.e., only a portion A_1 of the gas-side area A'_1 participated in the exchange (Fig. 1). If the window temperature T_1 is known, q_r may be computed from the relations given since the component q_{10} is not involved. Thus, Eqs. (1), (3), and (5) remain unaffected by this assumption, which greatly simplifies the problem. However, Eqs. (2) and (4) are affected to an extent which is difficult to discuss with rigor. A simplified approach, taken by merely assigning new areas to the terms given in Eq. (4), indicates that q_{10} would actually decrease,

although the total heat transfer from surface A_1' would increase. The total effect would probably result in a small reduction of T_1 .

SPS 37-36 presents some brief remarks concerning the effects of nonisothermal conditions in the hohlraum. The effects of nonisothermal conditions of the quartz are likely to be equally serious. If the quartz temperature T_1 was relatively high compared to the hohlraum temperature, and also highly nonuniform, the quartz emission would be anisotropic and extremely complex. This effect could conceivably overshadow the emission and absorption characteristics of the cavity itself.

Application of the present analysis does not precisely define the window effect because the cavity temperature T_2 has been held constant as the window temperature T_1 was allowed to assume different values. This would not actually occur. In fact, T_2 is likely to increase as T_1 increases. A more precise treatment will have to await experimentally determined values of both T_1 and T_2 ; however, the equations given here may still be applied.

7. Summary and Conclusions

It has been demonstrated that the analysis of thermal radiation data, obtained by means of a hohlraum of the type described here, cannot be accurately carried out without consideration of the effects of the window. The window cannot be considered thermally passive unless it has a temperature considerably lower than that of the cavity. If the window has a high equilibrium temperature, its thermal emission may mask thermal radiation from the gas. Disregard of the window effect therefore leads to a higher computed value of radiation emitted from the gas than actually occurs. Approximately 2% of the heat transfer to the duct walls was in the form of thermal radiation, as predicted by the simple analysis disregarding the window (SPS 37-36).

By means of the hohlraum, it is possible to determine an approximate upper bound on radiation from the gas. Detailed and accurate studies of the gas radiation are not judged possible unless the hohlraum is calibrated against a known radiation standard, or all requisite optical properties are known accurately over the range of the experimental conditions.

Definition of symbols

A	surface area	τ	transmissivity
C_1, C_2, C_3, C_4, C_5	coefficients defined in text	<i>Subscripts and superscripts</i>	
e	heat flux, transfer by radiant emission	a	apparent
f	flatness factor of cavity	<i>cond</i>	conduction component
F	configuration or view factor between surfaces	<i>conv</i>	convection component
q	heat flux, transfer of thermal energy per unit time per unit area	<i>loss</i>	loss term
S	sum of areas A_1 and A_2	<i>tot</i>	total
t	heat flux, transfer by transmission	r	radiative component
T	temperature, absolute unless otherwise specified	0	fictitious surface (gas)
x	denotes general variable	1	window surface
α	absorptivity	2	cavity surface of hohlraum (liner)
δ	absolute error in variable x	3	surface of cavity housing
Δ_r	error in primary quantity due to error in x	12	denotes process originating at Surface 1 toward Surface 2 (typical)
Δ_{q_r}	absolute error in q_r	' (prime)	denotes gas-side of window when used with 1
ϵ	emissivity		denotes outside surface of cavity liner when used with 2
σ	Stefan-Boltzmann constant		denotes flux per unit area of Surface 1 when used with subscript <i>cond</i>

B. Liquid MHD Power Conversion

D. Elliott, D. Cerini, L. Hays, and E. Weinberg

The long lifetimes required of electric-propulsion powerplants make cycles without rotating components desirable. Such a cycle under investigation at JPL is the liquid metal magnetohydrodynamic (MHD) system shown schematically in Fig. 5. In this cycle a fluid, such as cesium, circulates in the vapor loop and causes a liquid metal, such as lithium, to circulate through an MHD generator in the liquid loop. The cesium leaves the radiator (or radiator-loop condenser) as condensate, flows through an electromagnetic pump and regenerative heat exchanger to the nozzle, vaporizes on contact with the lithium, atomizes and accelerates the lithium in the nozzle, separates from the lithium in the separator, and returns to the radiator through the regenerative heat exchanger. The lithium leaves the separator at high velocity (typically 500 ft/sec), decelerates through the production of electric power on the MHD generator, and leaves the generator with sufficient velocity (typically 300 ft/sec) to return through a diffuser to the reactor (or reactor-loop heat exchanger) where the lithium is reheated.

Experiments are beginning on ac power generation. A 70°F NaK-nitrogen conversion system is under construction for system evaluation. High-temperature loops are in preparation for evaluating materials and components for 2000°F operation. Cycle analysis for selecting 2000°F cycle arrangements and working fluids is nearly complete, and analysis of a 300-kw 2000°F conversion system is beginning.

1. AC Generator

Empty-channel ac tests of the 5-kw ac generator were conducted, employing three aircraft alternators mounted on a common shaft as the 3-phase excitation source. The excitation frequency was varied from 900 to 1200 cps. Capacitors were connected across each phase to supply the reactive power. (During tests with NaK the alternators will be disconnected when the generator power is sufficient to supply the core losses, leaving only capacitor excitation.)

The empty-channel tests were conducted at 25 amp phase, instead of the 100 amp required for 5-kw output power, to minimize voltage stress and heating. During the tests the field amplitude was checked, the required capacitance was found, the proper synchronization of the compensating poles through transformer coupling to

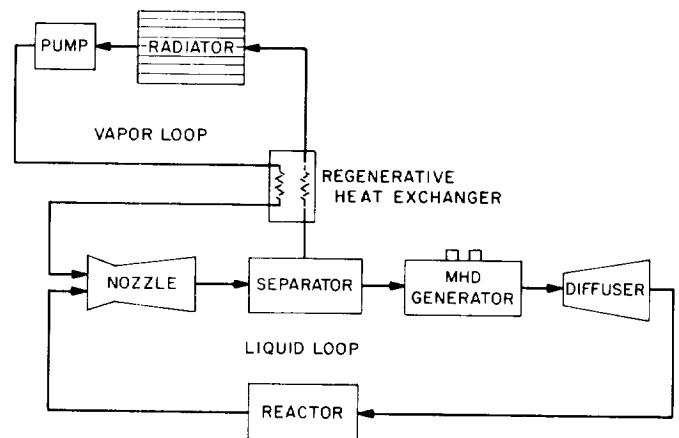


Fig. 5. Liquid MHD power conversion system

the main phases was verified, and the instrumentation was checked out. It was not possible, however, to proceed to the NaK tests because of damage to the flow channel. Heating and excessive clamping forces had loosened the slot plugs and deformed the copper side strips and nylon blocks. The stator blocks are being repaired for tests in February, and a second assembly is in fabrication for later testing.

The empty-channel tests revealed that the core loss at 25 amp was 400 w, three times the predicted value. A check of the calculations showed that the ac/dc resistance ratio of the 0.68- \times -0.128-in. windings at 1200 cps had been incorrectly computed and that the ac/dc ratio of this size wire accounts for most of the observed loss. The second stator assembly is being wound with 0.068-in. diameter wire to reduce the core loss.

2. NaK-Nitrogen Conversion System

Fabrication has begun on the separator and generator housing, and the diffuser drawings have been completed. Estimates of the compensating pole losses indicate that minimum loss would occur with approximately 30 vanes of 0.2-in. spacing and 2-in. length under the compensating poles. Test channels with various vane shapes and boundary gas injection methods are being designed for comparative friction tests with nitrogen and water.

Analysis of the 50-kw generator for the NaK-nitrogen system is continuing. An improved design procedure for the slots was derived from the tapered-slot analysis in SPS 37-36, Vol. IV, p. 102. It was noted that for a given slot depth d and saturation flux density B_{sat} , the slot current I that saturates the iron within the slot width w_1 (Fig. 6) is related to the current density i by a single

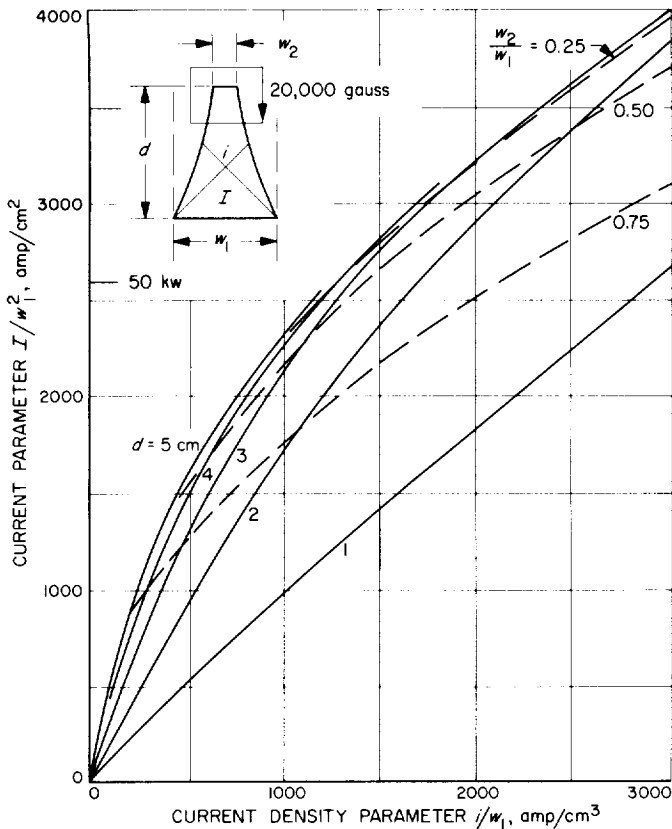


Fig. 6. Universal tapered-slot performance curves

curve of I/w_1^2 versus i/w_1 . Fig. 6 presents such curves for $B_{sat} = 20,000$ gauss and $d = 1, 2, 3, 4,$ and 5 cm. Curves of constant width ratio w_2/w_1 are superimposed. For the 50-kw generator, the peak tooth flux occurs when the adjacent slot currents are 2600 amp, and it is seen that little is gained with a slot depth greater than 3 cm or a width ratio less than 0.5.

3. High-Temperature Tests

The 2000°F lithium loop is being installed and instrumented for tests early in 1966. Construction of the 2000°F cesium-lithium loop will resume upon completion of the lithium loop.

A small Haynes-25 loop is being designed for circulating lithium at temperatures up to 1800°F at velocities up to 200 ft/sec to determine if the 300-kw system could be constructed of that alloy, with attendant reduction in cost and complexity of the test facility.

4. Cycle Analysis

The cycle calculations presented in SPS 37-34 and 37-36, Vol. IV, compared condenser systems with separa-

tor systems under the assumption that the condenser is frictionless. For the usual nozzle shape this is an unrealistic assumption, as illustrated in Fig. 7. The high-velocity two-phase mixture leaves the nozzle along an axial or slightly diverging path. The subcooled liquid

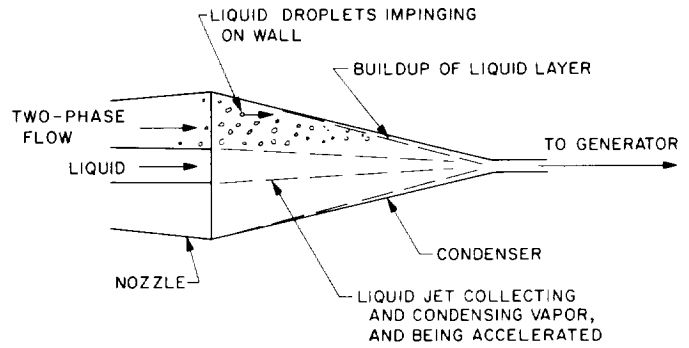


Fig. 7. Liquid impingement in a jet condenser

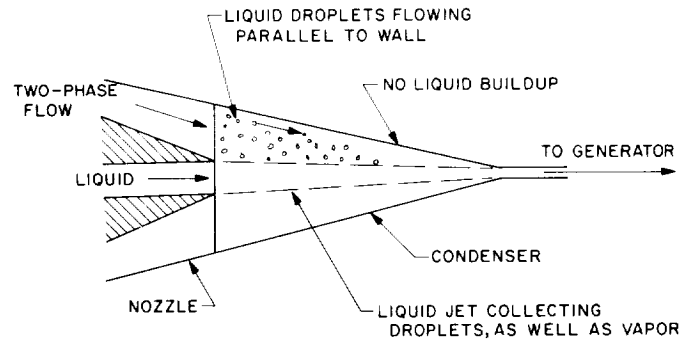


Fig. 8. Elimination of condenser friction through converging nozzle flow

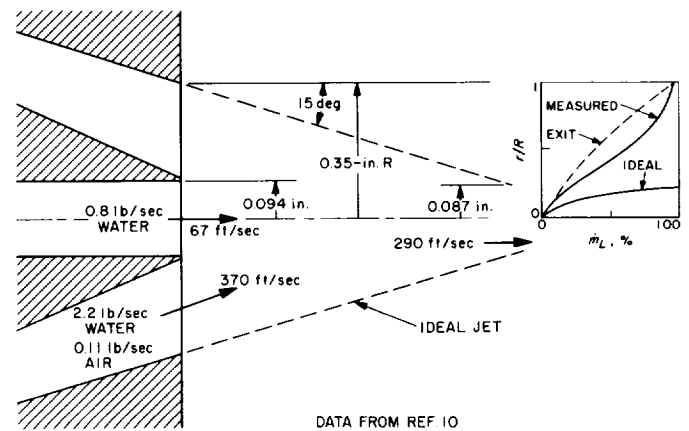


Fig. 9. Comparison of measured and ideal liquid flow distribution downstream of a converging-path nozzle

enters axially and condenses the vapor phase. In the conventional jet condenser, where the nozzle flow is largely vapor, the resulting liquid jet proceeds to the exit tube with little friction because only vapor contacts the wall. In the condensers required for MHD power conversion, however, the nozzle flow is about 75% liquid, by mass, and at the droplet sizes produced by two-phase nozzles most of this liquid will impinge on the wall, giving the same friction loss as with a separator.

If the nozzle geometry is changed so that the flow leaves along a converging path, as illustrated in Fig. 8, then it is conceivable that the impingement friction could be eliminated. An experiment to investigate this possibility was reported in Ref. 10, and the result is shown in Fig. 9. An air-water mixture left a 0.7-in. diameter nozzle at 370 ft/sec and 15-deg inward convergence angle and impinged on a 0.188-in. diameter, 67-ft/sec jet of water. If the ideal process of Fig. 8 had occurred, the jets would

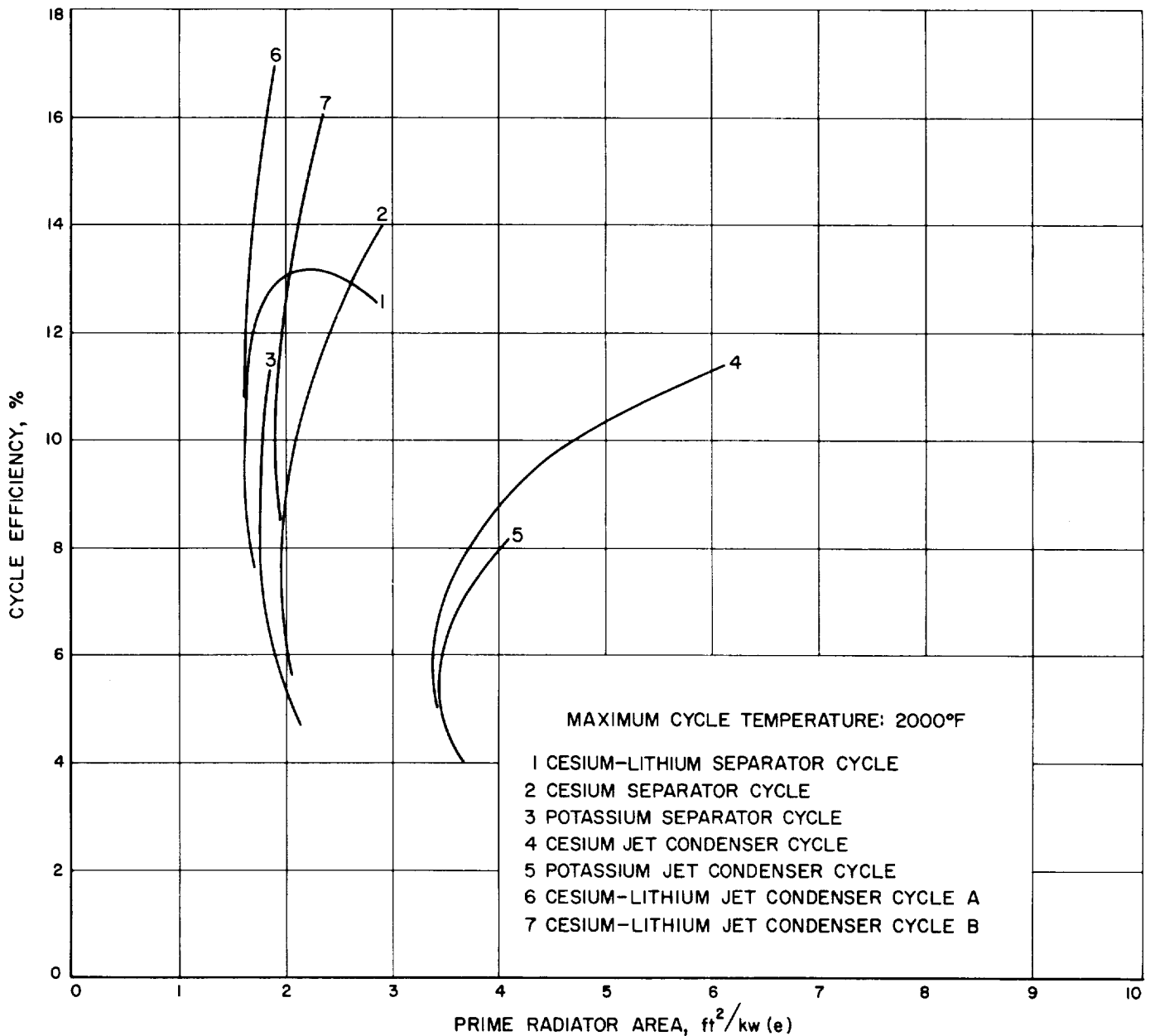


Fig. 10. Performance of liquid MHD cycles with no friction between nozzle exit and generator inlet

have merged into a 0.174-in. diameter, 290-ft/sec water jet having the variation of liquid flow rate with radius shown by the lower curve in Fig. 9. Instead, the water was distributed over the full nozzle diameter with the profile shown by the middle curve. Some increase in concentration relative to the exit distribution was observed, however, encouraging further investigation of this technique.

Reduction of friction through this and any other method should be as possible for separator systems as for condenser systems, and the cycle calculations have been extended accordingly to include condenser cycles with friction and separator cycles without friction. The efficiencies of liquid MHD cycles *without friction* are presented in Fig. 10, with other assumptions remaining as in SPS 37-34. The efficiency of each cycle increases with decreasing radiator temperature while, at the same time, the radiator area decreases until the radiator temperature is approximately 75% of the maximum cycle temperature (2460°R) below which the area again increases.

The cycle with the best performance in the absence of friction is the cesium-lithium condenser cycle wherein two-phase cesium is used in the nozzle, lithium is used as the coolant, and the lithium is separated from the condensed cesium at the exit of the condenser (Cycle 6). Slightly lower performance is obtained if the lithium and cesium are separated after leaving the generator (Cycle 7), since this provides lower lithium injection velocity into the condenser. This use of lithium coolant was suggested by L. Prem, Atomics International.

Performance equal to Cycle 6 in the region of minimum radiator area is provided by the cesium-lithium separator cycle (Cycle 1) which is being investigated at JPL. Increasing lithium vapor flow to the radiator at low nozzle exit pressures limits the frictionless efficiency of this cycle to 13%.

Good performance is also shown by the potassium separator cycle (Ref. 11) and the cesium separator cycle. The potassium and the cesium condenser cycles, wherein the coolant is the same metal as the vapor (Refs. 12 and 13), have the lowest performance in this comparison because of the energy loss of mixing the nozzle exhaust with a relatively large quantity of low-velocity coolant.

Performance values for the separator cycles with friction were presented in SPS 37-34 and 37-36. Condenser system performance with friction is being computed.

5. Cesium-Lithium Conversion System

A 300-kw ac generator for a 2000°F cesium-lithium conversion system would have a lithium flow channel of approximately 9-in. width, 0.25-in. gap, and 7-in. length. The magnetic field required would be 12,000 gauss peak and the frequency for a one-wavelength generator would be approximately 700 cps. A key factor limiting the efficiency is the thickness of thermal insulation required between the 2000°F lithium stream and the stators which are limited to about 1000°F by magnetic material limitations and to perhaps only 500–700°F by winding insulation limitations.

The effects of channel insulation thickness and winding temperature on winding loss were calculated, and the results are shown in Fig. 11. The winding loss (assuming tapered slots, 80% copper fill, 1.5 ac/dc resistance ratio, an end-turn length equal to slot length) is plotted as a function of channel insulation thickness for various winding temperatures. The winding loss increases with insulator thickness because of the increasing slot current required to maintain the same field with a wider gap, and increases with temperature because of the increasing copper resistivity. The significant result is that an acceptable winding loss such as 20 kw (7% of output power) is

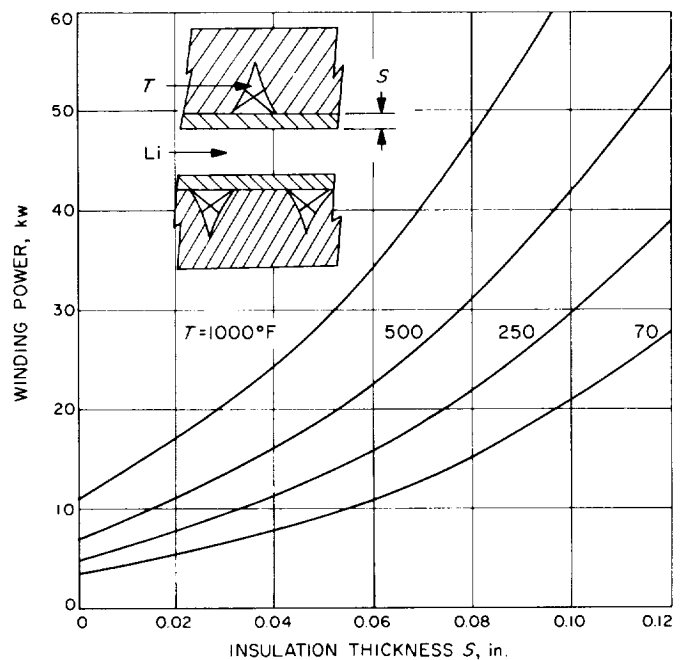


Fig. 11. Effect of channel insulation thickness and winding temperature on winding loss in a 300-kw generator

attainable with practical insulation thicknesses of 0.04–0.08 in. at sufficiently high temperatures for reasonable coolant radiator areas.

If ceramic compatibility with lithium is verified in loop tests, the insulation can be a ceramic sheet. If compatibility is insufficient, the ceramic could be shielded with metal foil divided into strips for low eddy-current loss. A

continuous metal sheet, even 0.001-in. thick, would have unacceptable eddy-current losses.

Analysis of the cesium-lithium design is proceeding toward a reference design in which key problems, such as the generator channel insulation, can be identified for early investigation in the NaK-nitrogen system and the high-temperature loops.

References

1. Sparrow, E. M., "Radiant Emission Absorption and Transmission Characteristics of Cavities and Passages," Symposium on Thermal Radiation of Solids, San Francisco, California, March 1964. Published as NASA SP-55, edited by S. Katzoff, pp. 103–115, 1965.
2. Kelly, F. J., and Moore, D. G., "A Test of Analytical Expressions for the Thermal Emittance of Shallow Cylindrical Cavities," Symposium on Thermal Radiation of Solids, San Francisco, California, March 1964. Published as NASA SP-55, edited by S. Katzoff, pp. 117–131, 1965.
3. Treuenfels, E. W., "Emissivity of Isothermal Cavities," *Journal of the Optical Society of America*, Vol. 53, No. 10, pp. 1162–1171, October 1963.
4. Gardon, R., "Emissivity of Transparent Materials," *Journal of the American Ceramic Society*, Vol. 39, No. 8, pp. 278–287, August 1956.
5. Gubareff, G. G., Janssen, J. E., and Torborg, R. H., "Thermal Radiation Properties Survey," 2nd Edition, Honeywell Publication, Honeywell Research Center, Minneapolis, Minnesota, 1960.
6. Bevans, J. T., Gier, J. T., and Dunkle, R. V., "Comparison of Total Emittances with Values Computed from Spectral Measurements," *Transactions of the ASME*, Vol. 80, No. 11, pp. 1405–1414 (see also Discussion, pp. 1415–1516), October 1958.
7. Ohlsen, P. E., and Etemad, G. A., "Spectral and Total Radiation Data of Various Aircraft Materials," North American Aviation Report No. NA57-330, Engineering Department, Los Angeles, California, July 1957.
8. Herczeg, L. S., "Determination of Emittance and Absorptance Characteristics of Missile Structural Materials," WADC Technical Report 58-506, Franklin Institute of Boston, Massachusetts.
9. Streed, E. R., McKellar, L. A., Rolling, R. Jr., and Smith, C. A., "Errors Associated with Hohlraum Radiation Characteristics Determinations," Symposium on Measurement of Thermal Radiation Properties of Solids, Dayton, Ohio, September 1962. Published as NASA SP-31, edited by J. C. Richmond, pp. 237–252, 1963.
10. Elliott, D. G., "Theoretical and Experimental Investigation of a Gas-Driven Jet Pump for Rocket Engines," Report No. I-58-3 (AD No. 305, 997), p. 109, Purdue University, Jet Propulsion Center, Lafayette, Indiana, December 1958.

References (Cont'd)

11. Petrick, M., and Lee, K. Y., "Performance Characteristics of a Liquid Metal MHD Generator," International Symposium on Magnetohydrodynamic Electrical Power Generation, Vol. 2, pp. 953-969, Paris, France, July 1964.
12. Brown, G. A., and Lee, K. S., "A Liquid Metal MHD Power Generator Cycle Using a Condensing Ejector," International Symposium on Magnetohydrodynamic Electrical Power Generation, Vol. 2, pp. 929-938, Paris, France, July 1964.
13. Prem, L. L., and Parkins, W. E., "A New Method of MHD Power Conversion Employing a Fluid Metal," International Symposium on Magnetohydrodynamic Electrical Power Generation, Vol. 2, pp. 971-984, Paris, France, July 1964.

XIII. Solid Propellant Engineering

A. Nozzle Thrust Misalignment

L. Strand

A research program was formulated to investigate two areas of rocket nozzle aerodynamics that up till now, it is believed, have been relatively neglected: (1) the effects, if any, of nozzle surface irregularities, and (2) throat asymmetry on the position of the nozzle thrust vector. Such irregularities can result from the delamination and/or erosion of nozzle ablative materials during rocket firing.

The initial test program was conducted on the three-dimensional gas-flow test facility, designated the "auxiliary flow channel." Two conical nozzles were used for these tests. One nozzle is axisymmetric (Fig. 1) and was tested both with and without a 0.125-in. square flow protrusion extending 0.150-in. above the surface of the nozzle. The second test nozzle was fabricated with a

known throat asymmetry (Fig. 2). One 180-deg section of the asymmetric throat region is circular, while the opposite 180-deg section is elliptical. Both nozzles are instrumented with over 80 static pressure taps mounted in the walls of both the nozzle throat sections and expansion cones. By numerically integrating the pressure distribution over the nozzle wall, an analytical approximation of the force unbalance normal to the nozzle axis was obtained.

A complete description of the test facility and the test program and results has been published in *SPS 37-35*, Vol. IV. The following are the results of the data analyses that have been pursued to date.

The maximum side force for each of the two nozzles was determined by summing the side force normal to the nozzle axis along the cross sections shown in Figs. 1 and 2. Figs. 3 and 4 show the net side force, summed over

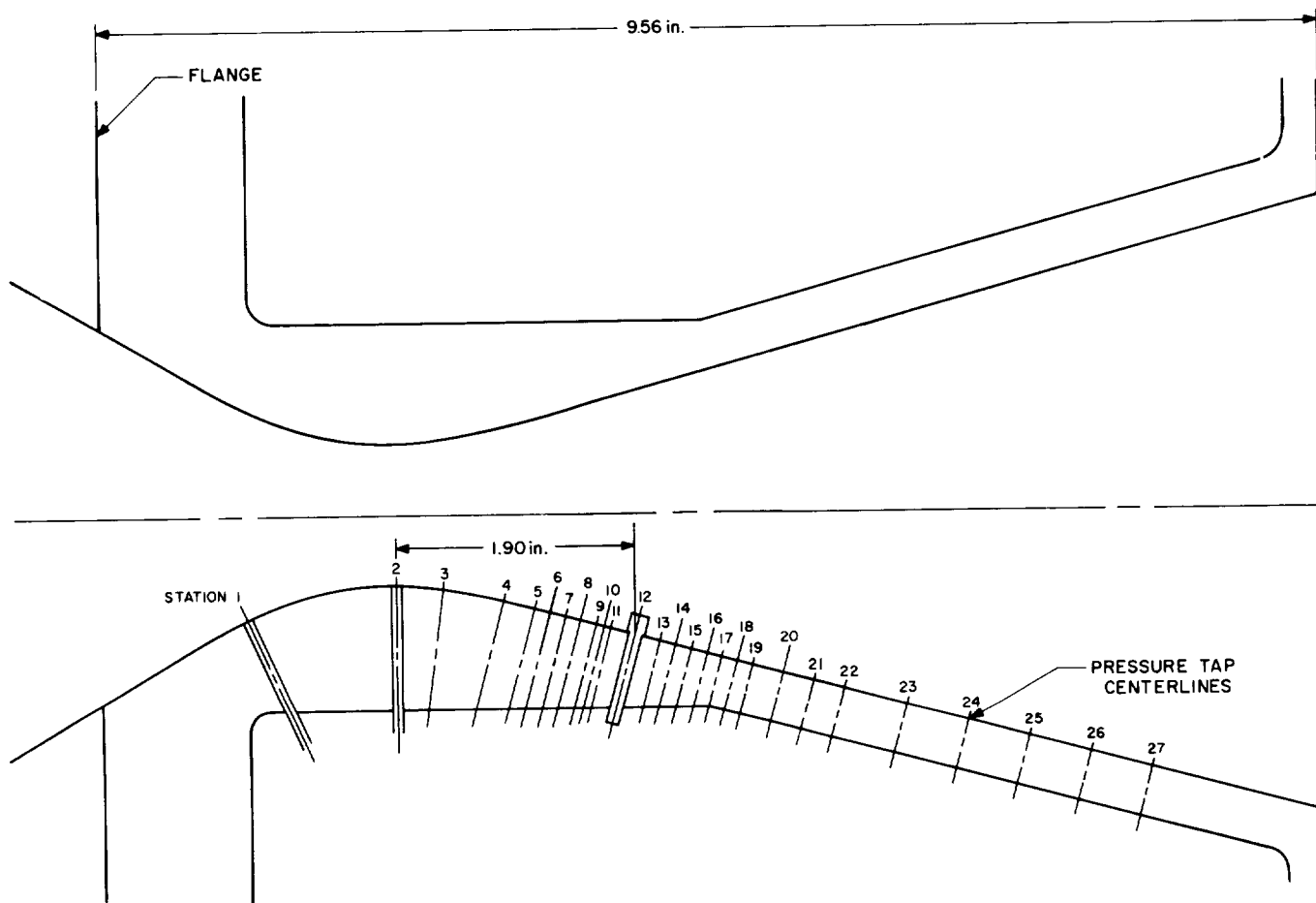


Fig. 1. Symmetric nozzle cross section

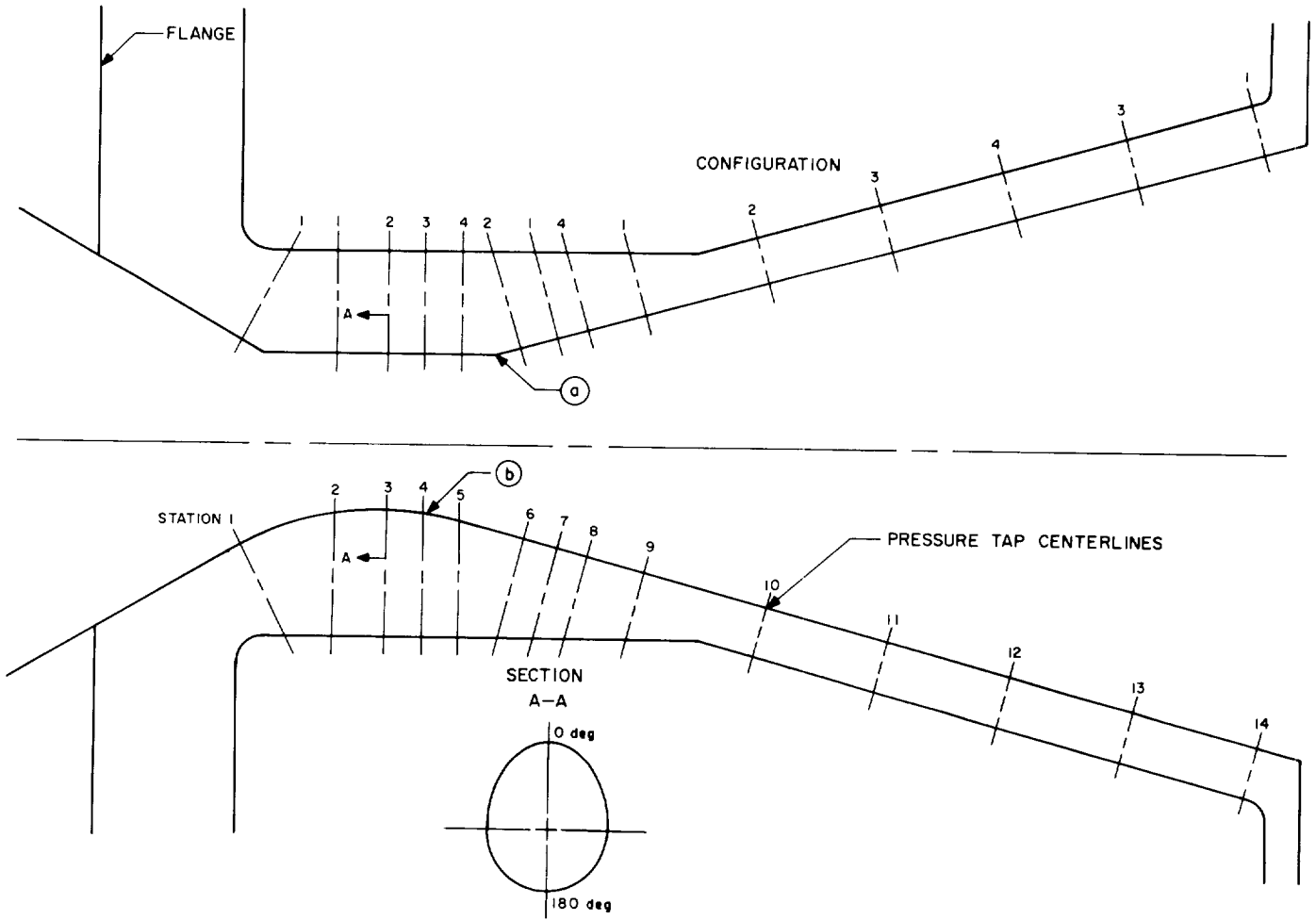


Fig. 2. Asymmetric nozzle cross section

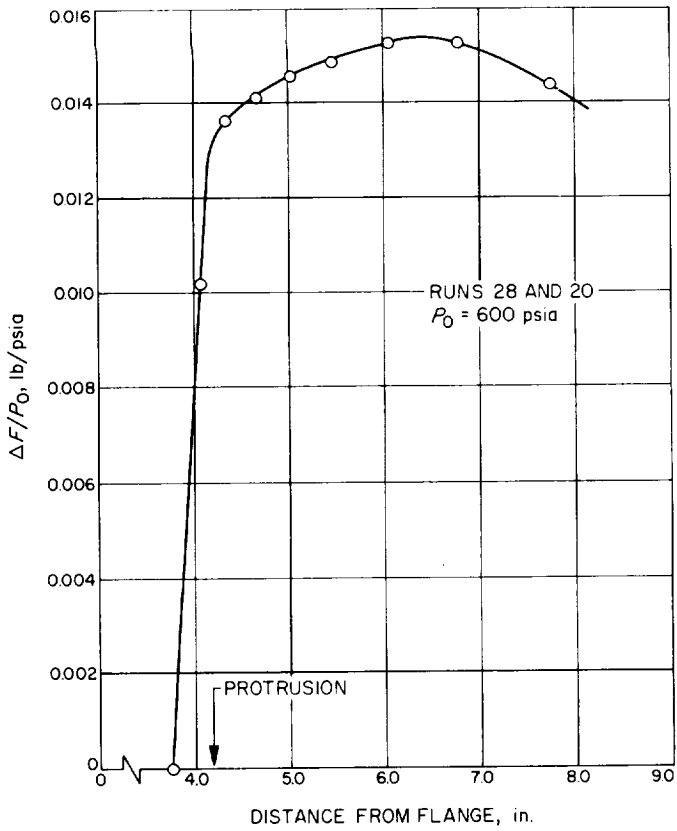


Fig. 3. Summed net side force/supply pressure ratio versus nozzle axial distance, symmetric nozzle

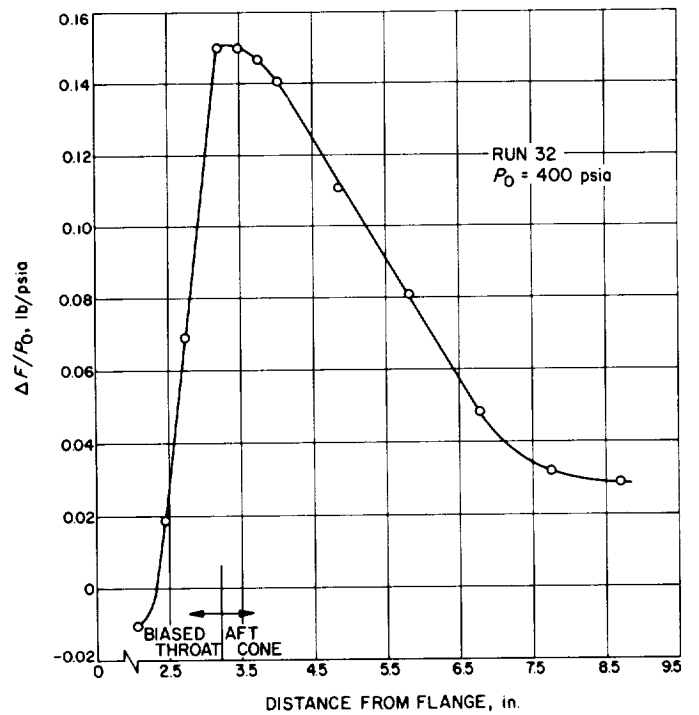


Fig. 4. Summed net side force/supply pressure ratio versus nozzle axial distance, asymmetric nozzle

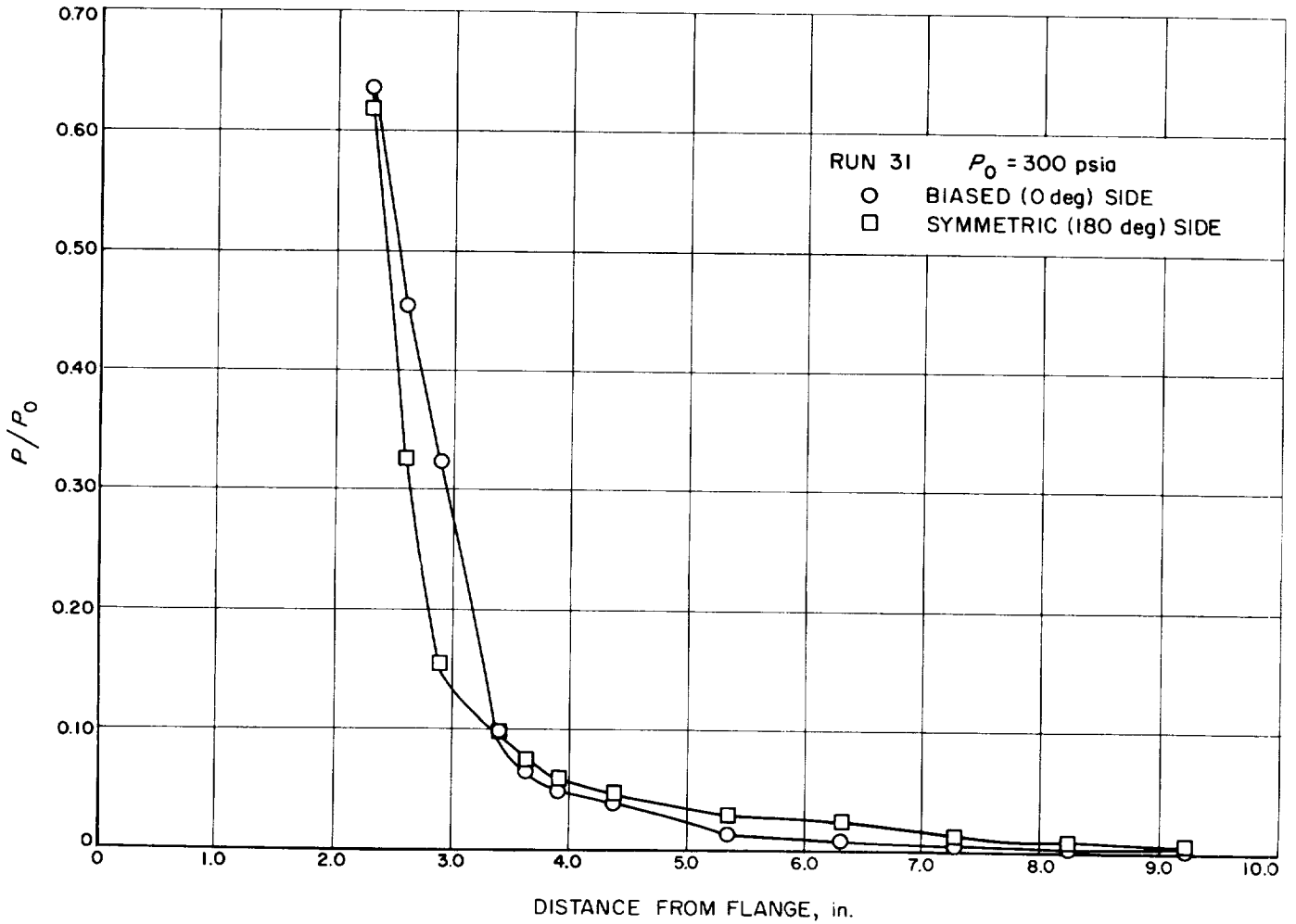


Fig. 5. Measured wall static pressure ratio versus nozzle axial distance, asymmetric nozzle

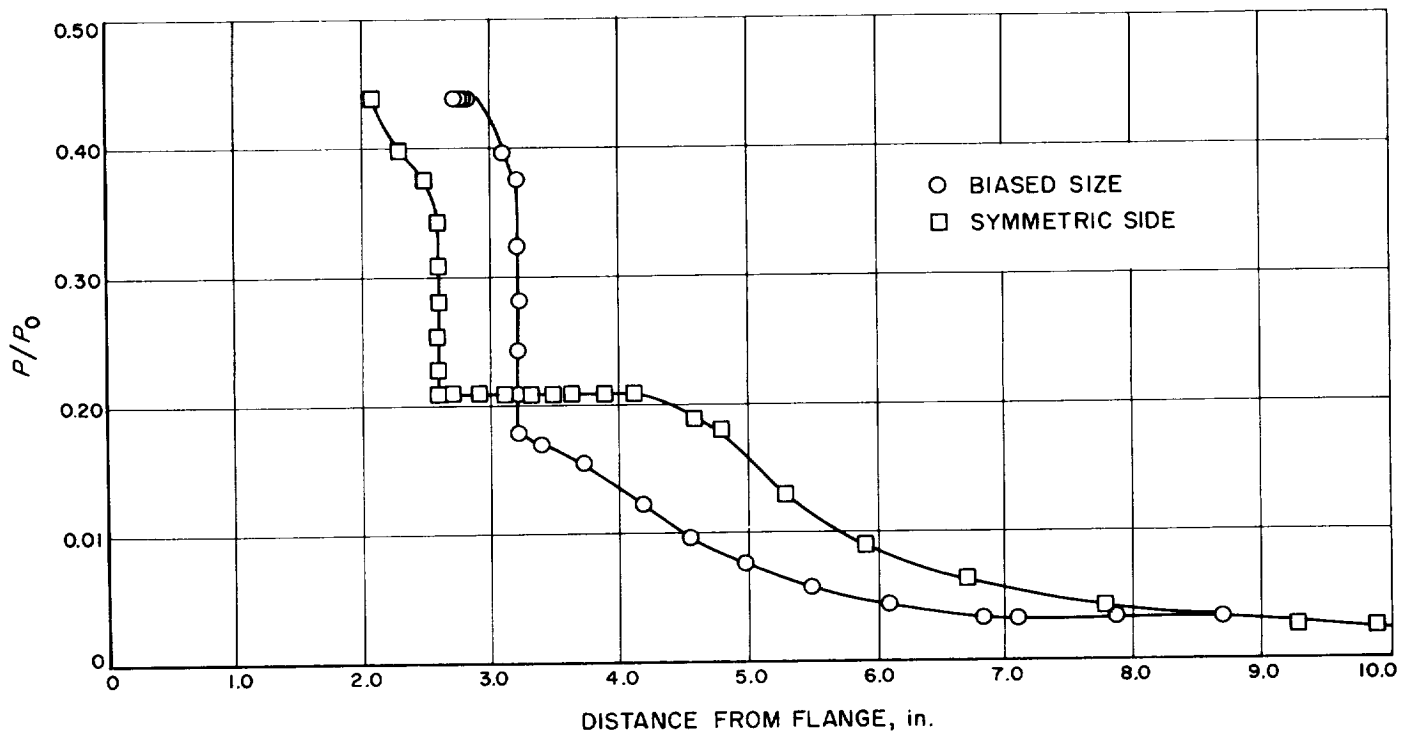


Fig. 6. Calculated wall static pressure ratio versus nozzle axial distance, 2-dimensional biased nozzle

the nozzle axial distance, for the symmetric and asymmetric nozzles, respectively. All test pressure data ratioed by the plenum supply pressure (P_0) was found to be essentially independent of test supply pressure, as previously reported. The summed net side forces were also calculated as ratios of the supply pressures, the two curves thereby describing all test results for each nozzle. For both nozzles the force profile reaches a maximum and then continues to decrease as the nozzle is traversed along its axis. The force profile maxima are due to changing pressure profiles along the nozzle axes for perturbed and asymmetric nozzles and have been analytically shown to not be solely attributable to the particular geometries of the test nozzles.

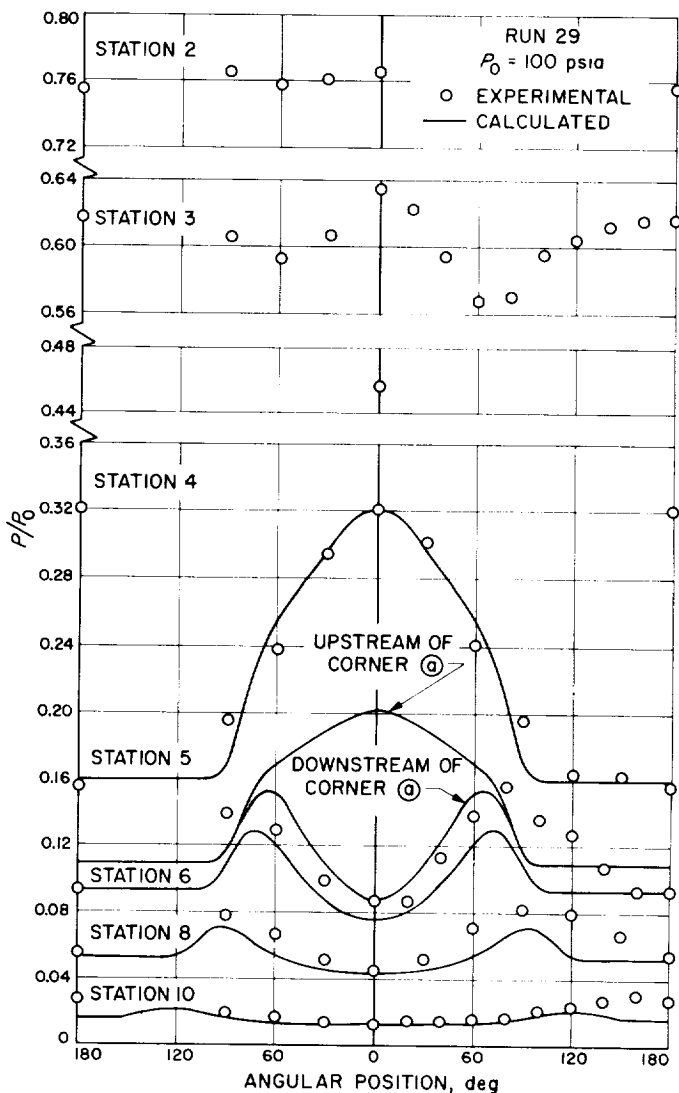


Fig. 7. Wall static pressure ratio versus nozzle angular position, asymmetric nozzle

In addition to the net side force calculations asymmetric nozzle pressure data have been compared with a method of characteristics flow-field solution for a two-dimensional nozzle having the same cross-sectional wall profile as that of the asymmetric nozzle (Fig. 2). Figs. 5 and 6 show the experimental and calculated results respectively. As expected, agreement is only qualitative. The transition corners (a) and (b) in Fig. 2, from the throat region to the aft expansion cone, were assumed sharp for the two-dimensional nozzle, necessitating the use of Prandtl-Meyer corner-flow expansions in the calculated pressure ratio profiles. In the actual nozzle these transition regions were slightly rounded.

A combined one-dimensional isentropic, three-dimensional method of characteristics flow-analysis method was used to obtain a qualitative picture of the flow through the asymmetric nozzle. The calculated axial station circumferential pressure ratio profiles are compared with experimental data in Fig. 7, the angular position and axial station designation shown in Fig. 2 being used. The flow structure within the nozzle is felt to be understood to a fairly high degree of confidence.

B. Applications Technology Satellite (ATS) Motor Development

R. G. Anderson and D. R. Frank

1. Introduction

In January 1963 the Jet Propulsion Laboratory initiated a development program to provide a solid propellant apogee rocket motor for a second-generation *Syncom* satellite. This program, under the management of the Goddard Space Flight Center, was designated *Advanced Syncom*. It was to result in a spin-stabilized, active repeater communications satellite weighing about 750 lb, operating at synchronous altitude (22,300 miles) which would handle voice communications, teletype, and monochrome and color television signals.

In January 1964 the *Advanced Syncom* communication program was redirected to include a number of experimental instruments in addition to the original communication instruments. This expanded program is the

Dev. Code No.	Test conditions					Physical hardware				
	Type of test	Test location	Test date	Run No.	Grain condition temperature, °F	Propellant weight, lbm	Chamber S/N	Nozzle S/N	Igniter S/N	
C-1	Atmospheric	ETS E60	2-26-64	E-127	60	760.8	P-2	F-13	ε=8.5	SYC-231
C-2	Atmospheric		3- 5-64	E-129		761.3	P-7	F-7		SYC-233
C-3	Diffuser		6- 4-64	E-174		762.2	P-7F	F-6		SYC-234
C-3A	Diffuser		6-12-64	E-175		765.8	P-2F	F-5		SYC-235
C-6	Atmospheric		7- 9-65	E-416		765.7	P-24	F-30		SYC-255
G-5	Spin		11-24-64	E-326		768.7	P-16	F-14		SYC-245
C-4	Atmospheric	ETS E60	7-15-64	E-218	10	764.8	P-13	F-11	ε=8.5	SYC-241
H-1	Atmospheric		11- 4-64	E-314		640.4	P-5	F-10	ε=8.5	SYC-244
G-2	Atmospheric		12-16-64	E-343		766.1	P-10	F-17	ε=35	SYC-252
G-7	Spin		8- 6-65	E-434		769.6	P-20	F-19	ε=35	SYC-263
G-9T	Spin		1- 4-66	E-515		759.6	T-6	F-23	ε=35	SYC-256
C-5	Atmospheric	ETS E60	7-23-64	E-237	110	769.3	P-12	F-12	ε=8.5	SYC-243
C-7	Atmospheric		8-10-65	E-435		767.0	P-22	F-29	ε=8.5	SYC-265
G-1	Atmospheric		12-16-64	E-342		766.8	P-11	F-16	ε=35	SYC-253
G-6	Spin		7-16-65	E-431		767.2	P-19	F-21	ε=35	SYC-262
G--BT	Atmospheric		11- 9-65	E-485		759.8	T-4	F-36	ε=35	SYC-264
E-1	Diffuser	AEDC	7-16-64	1426-01	60	765.6	P-9	F-9	ε=35	SYC-240
E-2	Diffuser		10-13-64	1511-01	60	764.4	P-18	F-15	ε=35	SYC-242
G-3	Diffuser and spin		5-28-65	1540-02	75	765.3	P-14	F-24	ε=35	SYC-260
G-4	Diffuser and spin		5-26-65	1540-01	75	768.6	P-15	F-20	ε=35	SYC-261

^a Nozzle expelled approx. 17 sec following motor ignition, voiding all performance data.

^b Data unavailable because of electrical noise during ignition phase of motor.

^c Thrust measurement was not made during spin tests.

^d Vacuum correction does not apply because of incomplete expansion of exhaust gases.

^e Data unavailable due to malfunction of oscillograph recorder.

^f For definitions of motor ballistic parameters, see Table 4.

^g SDI P/N 101120 (all others are SDI P/N 100728).

Table 1. Applications Technol

Squib S/N	Pressure						Time		
	Characteristic velocity \bar{W}_c , ft/sec	Chamber pressure integral, psia-sec	Igniter basket peak pressure, psia (msec)	Chamber ignition peak pressure, psia (msec)	Chamber starting pressure, psia (sec)	Chamber run peak pressure, psia (sec)	Ignition delay t_{DM} , msec	Action time t_A , sec	Run time t_R , sec
9	4981.3	8918.0	1997 (52)	255 (63)	103.9 (0.23)	265.2 (32.1)	34	42.31	42.42
10	4982.0	8921.1	1620 (50)	173 (60)	98.6 (0.27)	260.6 (33.0)	29	42.96	43.04
11	"	"	1828 (59)	249 (71)	115.2 (0.22)	"	40	"	"
12	4972.6	8952.2	2289 (48)	270 (63)	99.6 (0.21)	264.4 (34.1)	35	42.76	42.89
30	4957.8	8951.2	1950 (22)	269 (29)	96.1 (0.25)	254.8 (33.7)	11	44.08	44.18
28	4964.6	9002.8	1930 (33)	225 (42)	98.6 (0.25)	258.9 (33.0)	b	b	c
18	4960.3	8944.5	1853 (34)	228 (45)	98.0 (0.25)	252.3 (34.6)	17	44.45	44.52
27	4965.6	7514.3	2005 (20)	224 (40)	191.1 (0.36)	264.2 (20.3)	12	31.74	31.81
58 ^e	4951.2	8945.5	1527 (22)	212 (32)	92.4 (0.25)	242.7 (36.0)	2	45.48	45.74
60 ^e	4958.6	9019.7	1650 (14)	217 (23)	99.3 (0.27)	245.7 (33.9)	b	b	45.09
40 ^e	4959.2	8901.4	1592 (17)	234 (30)	100.4 (0.34)	243.8 (33.3)	b	b	44.91
20	4972.3	9012.2	3292 (21)	273 (29)	98.8 (0.21)	274.6 (32.8)	9	41.68	41.76
9 ^e	4982.4	8999.2	3000 (12)	320 (16)	96.2 (0.20)	272.3 (33.4)	3	42.35	42.57
38 ^e	4975.3	8997.2	"	"	99.4 (0.21)	277.4 (33.0)	c	"	"
59 ^e	4978.5	9021.9	3485 (16)	276 (23)	100.4 (0.23)	268.5 (30.3)	b	b	41.74
61 ^e	4967.2	8898.8	2863 (12)	296 (22)	99.3 (0.25)	262.7 (30.8)	3	41.76	41.92
6	4982.9	8960.4	1524 (59)	239 (69)	98.1 (0.24)	263.4 (34.0)	26	42.93	43.42
26	4984.4	8937.8	1832 (38)	233 (49)	89.9 (0.20)	261.5 (34.6)	27	43.32	43.59
36	4965.2	8970.1	1626 (33)	241 (44)	99.5 (0.25)	261.7 (32.3)	16	42.52	43.09
31	4985.1	9042.7	1826 (32)	233 (45)	96.6 (0.25)	261.0 (33.1)	22	42.99	43.56

2

og Satellite program apogee motor static test data summary, development phase

Peak vacuum thrust, lbf-sec	Thrust				Nozzle				
	Total measured impulse, lbf-sec	Vacuum total impulse, lbf-sec	Measured specific impulse, lbf-sec/lbm	Vacuum specific impulse, lbf-sec/lbm	Nozzle throat diameter, in.			Nozzle exit initial diameter, in.	Nozzle throat erosion, %
					Initial	Final	Average		
5888 (32.9)	138,450	197,640	182.0	259.8	4.083	4.123	4.103	11.907	1.97
5746 (33.0)	137,560	196,580	180.7	258.2	4.083	4.125	4.104	11.907	2.07
"	"	"	"	"	4.083	"	"	11.906	"
5766 (34.2)	181,110	193,320	236.5	252.4	4.083	4.127	4.105	11.906	2.17
5686 (33.8)	138,710	199,620	181.1	260.7	4.084	4.114	4.099	11.907	1.47
"	"	"	"	"	4.083	4.113	4.098	11.904	1.48
5563 (33.3)	137,560	197,510	179.9	258.2	4.084	4.114	4.099	11.905	1.47
5774 (21.3)	117,080	163,930	182.8	256.0	4.084	4.105	4.094	11.904	1.03
"	127,400	"	166.3	"	4.083	4.115	4.099	24.135	1.57
"	"	"	"	"	4.082	4.105	4.094	24.126	1.13
"	"	"	"	"	4.083	4.106	4.094	24.136	1.13
6034 (32.8)	140,850	198,100	183.1	257.5	4.083	4.118	4.100	11.907	1.72
6018 (33.4)	140,690	200,080	183.4	260.9	4.083	4.120	4.101	11.908	1.82
"	131,360	"	171.3	"	4.083	4.114	4.098	24.137	1.52
"	"	"	"	"	4.082	4.108	4.095	24.127	1.28
"	129,498	"	170.3	"	4.084	4.114	4.099	24.138	1.47
6338 (34.2)	205,060	214,740	267.9	280.2	4.085	4.124	4.105	24.134	1.92
6319 (34.0)	210,730	214,360	275.7	280.2	4.090	4.124	4.107	24.135	1.67
6233 (33.0)	212,190	214,760	277.3	280.6	4.083	4.110	4.096	24.135	1.33
6226 (33.2)	213,240	215,740	277.4	280.7	4.082	4.112	4.097	24.106	1.48



Vertical line on the left side of the page.

Applications Technology Satellite (ATS) program and will result in a general-purpose satellite capable of operation at synchronous altitude with experimental instruments in the areas of meteorology, communications, radiation, navigation, gravity gradient stabilization and various engineering experiments. For those satellites to be placed in synchronous orbit JPL will provide a solid propellant rocket motor to provide the final required velocity increment at the apogee of the elliptical transfer orbit. This rocket motor is designated the JPL SR-28-1 (steel chamber) or JPL SR-28-3 (titanium chamber) rocket motor. It is presently intended that only the JPL SR-28-3 unit will be delivered for flight use.

Previous reports of progress on the development of this motor have been published in SPS 37-20 to 37-33, Vol. V and SPS 37-34 to 37-36, Vol. IV.

2. Program Status Summary

The motor development program calls for static firing of 4 heavywall motors and 25 lightweight motors, including 2 with flight-design titanium chambers, prior to conducting a 9-motor qualification program. To date, the 4 heavywall motors plus 20 lightweight motors have been static-fired, 4 of which were under simulated high-altitude conditions at Arnold Engineering Development Center (AEDC), Tullahoma, Tennessee. All of the lightweight motors tested to date have been with Type 410 chromium steel chambers, with the exception of Dev. G-8T and G-9T, which used titanium chambers.

During the period December to January 1966, one apogee motor (G-9T) was static-tested at ETS. Thermal model D-8TF was delivered to Hughes Aircraft Company. With the delivery of D-8TF, this completes JPL's ATS hardware delivery commitment to Hughes Aircraft Co. (HAC). A total of 6 ATS apogee motors have been sent to HAC. These include 3 thermal models (2 steel chambers, 1 titanium) and 3 apogee units loaded with inert propellant (2 steel chambers, 1 titanium).

A second titanium chamber (B-5T, S/N T-5) was instrumented and hydrostatically burst during this report period. The three storage rounds, cast during September 1965, are presently in storage. These units will be removed after six months of storage (March 1966), and at that time they will receive critical visual and physical inspections. The first of nine qualification units (Q-1T through Q-9T) was cast on schedule. These units will be cast over a 9-wk period, the first unit having been cast during the week of January 2, 1966.

3. Thermal Model

Thermal model D-8TF was delivered to HAC on December 29, 1965. This titanium unit (G-8T) had been previously static-tested on November 9, 1965. No attempt to clean this hardware before delivery was made. The thermal unit consisted of Titanium Chamber T-4 and Nozzle F-36.

4. Static Test of ATS Development G-9T

Development Round G-9T, the last environmental development test for the ATS apogee motor development program, was temperature conditioned at 10°F and statically tested on the spin stand at JPL's Edwards Test Station. This test was completed on January 4, 1966.

The purpose of the test was to evaluate the motor's performance following a prescribed set of environmental tests which included acceleration, vibration, and temperature cycling. A visual inspection of the motor hardware following the test and the results of the data analysis confirmed that the motor operated normally. Presented in Table 1 are the test conditions and important data results of G-9T and all of the apogee motor static tests to this date.

5. Nozzle Alignment Summary

Thirty-six flight design nozzles with a 35:1 area expansion ratio have been accepted by JPL. Each unit undergoes a 100% dimensional in-process inspection, in addition to a precision alignment inspection, prior to acceptance of the unit by JPL. The alignment inspection and total weight are normally the primary criteria used in determining the final use or assignment for the nozzle.

Table 2 lists the assignments, total weight, and critical alignment surface dimensions. Since the A-5 nozzle attachment ring surface is used to center the nozzle during motor assembly, this surface is used as a basic or reference position. The offset and out-of-roundness of the A-7 surface or nozzle exit cone and A-9 surface or nozzle throat are subsequently determined; also the offset with respect to the geometric center of the A-5 surface. The flatness of the B-3 surface is used to evaluate possible nozzle misalignment, prior to assigning the unit to a chamber. The B-4 surface is used as reference to verify that the nozzle has been assembled to the chamber with a minimum misalignment. Fig. 8 shows the location of the alignment surfaces.

Table 2. Applications Technology Satellite apogee motor nozzle alignment summary

Nozzle S/N	Code No.	Nozzle weight, lb	Surface inspection description						
			A-5 out of round, in.	A-7 out of round, in.	A-7 offset from A-5, in.	A-9 out of round, in.	A-9 offset from A-5, in.	B-3 Flatness, in.	B-4 Flatness, in.
F-8	D-1	52.28	0.0005	0.0050	0.0020	0.0007	0.0002	0.0017	0.0020
F-9	E-1	48.50	0.0004	0.0025	0.0008	0.0004	0.0005	0.0018	0.0017
F-15	E-2	37.12	0.0006	0.0060	0.0040	0.0006	0.0005	0.0018	0.0023
F-16	G-1	37.23	0.0006	0.0040	0.0020	0.0004	0.0004	0.0009	0.0018
F-17	G-2	37.61	0.0005	0.0070	0.0020	0.0003	0.0004	0.0011	0.0007
F-18	D-3	37.03	0.0021	0.0040	0.0050	0.0005	0.0002	0.0013	0.0018
F-19	G-7	37.94	0.0006	0.0035	0.0006	0.0003	0.0001	0.0010	0.0008
F-20	G-4	38.00	0.0012	0.0060	0.0007	0.0004	0.0007	0.0019	0.0026
F-21	G-6	38.22	0.0004	0.0030	0.0005	0.0004	0.0004	0.0006	0.0007
F-22	D-5T	39.55	0.0007	0.0020	0.0008	0.0001	0.0003	0.0008	0.0008
F-23	D-6-9T	39.44	0.0018	0.0040	0.0003	0.0003	0.0003	0.0010	0.0015
F-24	G-3	39.72	0.0004	0.0025	0.0013	0.0002	0.0003	0.0010	0.0015
F-25	D-4	39.36	0.0005	0.0025	0.0013	0.0002	0.0001	0.0008	0.0011
F-26	F-1	38.83	0.0018	0.0030	0.0018	0.0003	0.0002	0.0010	0.0017
F-27	F-2	39.15	0.0004	0.0055	0.0018	0.0004	0.0003	0.0019	0.0015
F-28	F-3	38.94	0.0007	0.0025	0.0070	0.0003	0.0003	0.0011	0.0008
F-31	Q-1T	38.27	0.0006	0.0035	0.0008	0.0003	0.0005	0.0015	0.0021
F-32	Q-5T	38.95	0.0005	0.0045	0.0013	0.0003	0.0003	0.0009	0.0013
F-33		37.95	0.0005	0.0045	0.0018	0.0005	0.0003	0.0006	0.0010
F-34	Q-2T	38.23	0.0005	0.0060	0.0020	0.0002	0.0004	0.0012	0.0026
F-35	D-2T	39.25	0.0004	0.0060	0.0020	0.0002	0.0005	0.0020	0.0030
F-36	G-8T	37.88	0.0005	0.0038	0.0020	0.0002	0.0006	0.0013	0.0020
F-37	Q-9T	38.07	0.0007	0.0030	0.0015	0.0002	0.0005	0.0007	0.0022
F-38	Q-3T	38.57	0.0005	0.0065	0.0020	0.0004	0.0010	0.0015	0.0020
F-39	Q-8T	38.31	0.0002	0.0015	0.0010	0.0004	0.0004	0.0013	0.0012
F-40		37.77	0.0004	0.0035	0.0020	0.0004	0.0007	0.0013	0.0017
F-41	Q-6T	37.13	0.0004	0.0045	0.0015	0.0006	0.0006	0.0017	0.0028
F-42	E-3T	38.29	0.0007	0.0060	0.0010	0.0003	0.0003	0.0016	0.0025
F-43	Q-7T	38.33	0.0006	0.0050	0.0025	0.0003	0.0006	0.0023	0.0025
F-44	Q-4T	38.13	0.0008	0.0090	0.0030	0.0003	0.0005	0.0036	0.0053
F-45		37.86	0.0008	0.0090	0.0027	0.0003	0.0010	0.0035	0.0045
F-46		37.94	0.0008	0.0030	0.0015	0.0002	0.0005	0.0016	0.0023
F-47		37.50	0.0010	0.0065	0.0015	0.0004	0.0006	0.0023	0.0033
F-48		37.24	0.0012	0.0055	0.0015	0.0003	0.0004	0.0021	0.0034
F-49		37.70	0.0010	0.0120	0.0030	0.0006	0.0008	0.0033	0.0050
F-50		37.89	0.0006	0.0040	0.0025	0.0009	0.0008	0.0024	0.0033

Nozzles F-22 through F-50 are flight design.

Nozzles without code numbers are unassigned and will be used for flight assignments and spares.

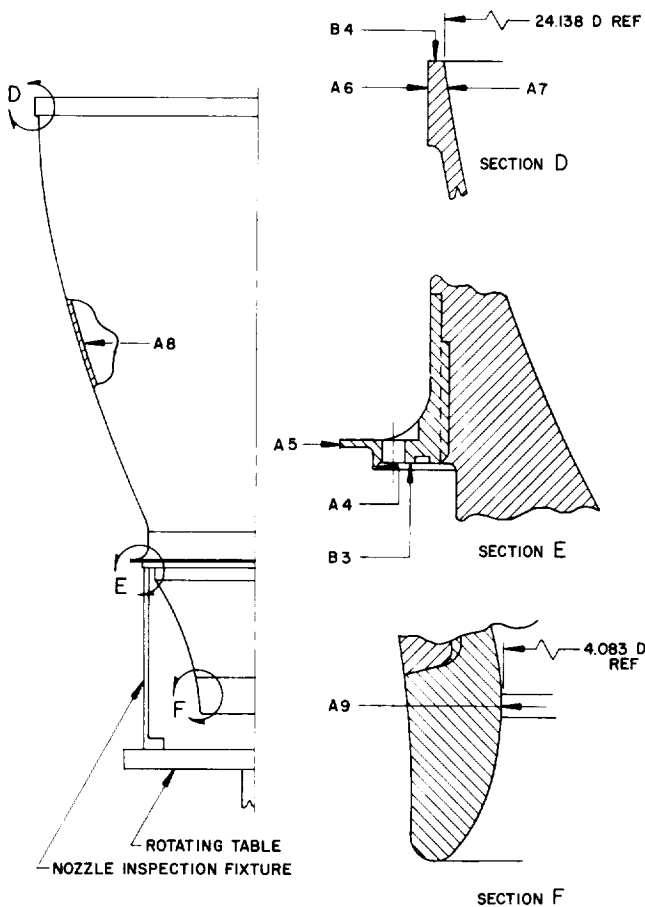


Fig. 8. ATS apogee motor nozzle alignment inspection positions

6. Titanium Chamber Inspection

After fabrication, each of the titanium chambers of the ATS apogee motor undergoes a precision inspection at the manufacturing vendor's plant by JPL inspection personnel. This inspection is performed to provide both determination of drawing conformity and comparison data among chambers. The dimensional data then become a factor in determining the assignment of each chamber, i.e., development test, qualification test, flight or flight backup.

Referring to Table 3, chamber alignment summary, each of the serialized chambers is listed together with its assignment and inspection results. The weight, being an important assignment factor, is also included. The out-of-round inspection is defined as the difference between maximum and minimum radii about a mean center of area of the profile. The offset inspection is the horizontal deviation of the mean center of area of the profile in question from a vertical line originating from the mean

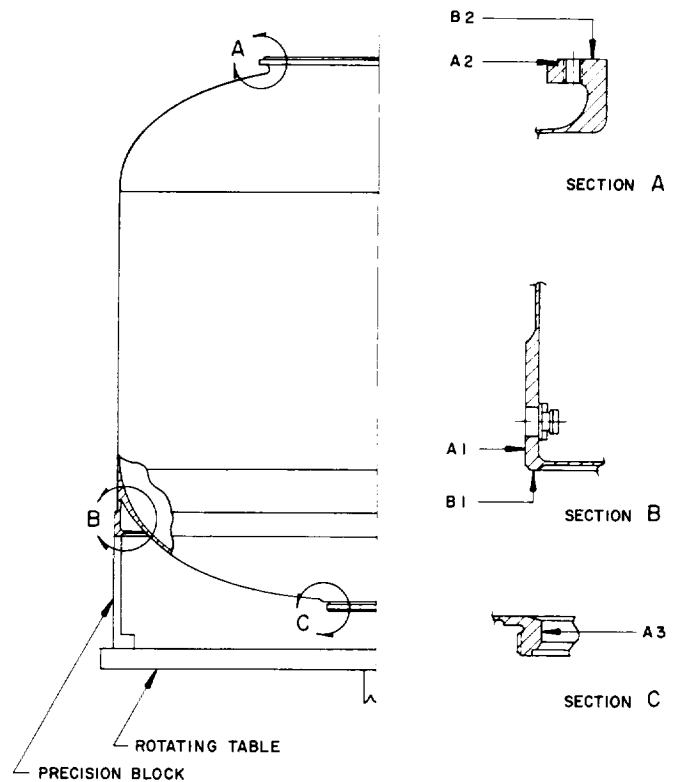


Fig. 9. ATS apogee motor chamber alignment inspection positions

center of the reference diameter A-1. Flatness of surfaces B-1 and B-2 is the vertical distance between the maximum peak and minimum valley of the profile. The above inspection surfaces are defined and located in Fig. 9.

7. Hydroburst Test of Dev. B-5T

The ATS Development Motor B-5T (T-5) was hydroburst on January 4, 1966. Eighteen strain gauge and pressure-volume data were recorded at approximately every 20 psig increment. The post-test results of the hydrotest are shown in Fig. 10. No evidence of buckling was observed.

The test results were as follows:

<i>Data</i>	<i>Proportional limit, psig</i>	<i>Burst pressure, psig</i>
Not normalized	375	440
Normalized ^a	311	363

^aNormalized with respect to wall thickness and material properties.

Table 3. Applications Technology Satellite apogee motor chamber alignment summary

Chamber S/N	ATS code designation	Chamber weight, lb	Surface and inspection description ^a						
			A-1 Out of round, in.	A-2 Out of round, in.	A-2 Offset from A-1, in.	A-3 Out of round, in.	A-3 Offset from A-1, in.	B-1 Flatness, in.	B-2 Flatness, in.
T-1	B-4T	25.23	0.0004	0.0020	0.0017	0.0010	0.0015	0.0007	0.0060
T-2	D-5T	25.00	0.0002	0.0011	0.0018	0.0015	0.0020	no data	0.0035
T-3	D-2T	25.34	0.0005	0.0007	0.0005	0.0012	0.0009	0.0006	0.0016
T-4	G-8T	24.70	0.0008	0.0012	0.0003	0.0005	0.0008	0.0005	0.0010
T-5	B-5T	24.55	0.0003	0.0014	0.0002	0.0032	0.0008	0.0004	0.0016
T-6	G-9T	24.35	0.0003	0.0020	0.0005	0.0003	0.0013	0.0004	0.0020
T-7	Q-1T	23.84	0.0004	0.0012	0.0004	0.0022	0.0010	0.0005	0.0022
T-8	Q-2T	24.40	0.0003	0.0018	0.0002	0.0015	0.0025	0.0004	0.0016
T-9	Q-3T	24.13	0.0004	0.0015	0.0004	0.0020	0.0028	0.0004	0.0025
T-10	Q-4T	24.40	0.0004	0.0018	0.0002	0.0010	0.0015	0.0004	0.0026
T-11	Q-5T	24.74	0.0002	0.0002	0.0008	0.0015	0.0005	0.0006	0.0015
T-12	Q-6T	24.56	0.0004	0.0007	0.0005	0.0010	0.0012	0.0007	0.0013
T-13	Q-7T	24.47	0.0003	0.0010	0.0008	0.0005	0.0020	0.0007	0.0021
T-14	Q-8T	24.13	0.0004	0.0008	0.0010	0.0018	0.0018	0.0008	0.0028
T-15	Unassigned	23.92	0.0005	0.0010	0.0004	0.0016	0.0012	0.0008	0.0018
T-16	Unassigned	23.71	0.0006	0.0012	0.0011	0.0010	0.0016	0.0008	0.0024
T-17	Unassigned	23.83	0.0007	0.0006	0.0007	0.0014	0.0010	0.0005	0.0024
T-18	Q-9T	24.09	0.0006	0.0013	0.0007	0.0012	0.0018	0.0006	0.0020
T-19	Unassigned	23.74	0.0005	0.0018	0.0006	0.0025	0.0020	0.0005	0.0016
T-20	E-3T	24.10	0.0005	0.0015	0.0011	0.0022	0.0011	0.0007	0.0023
T-21	Unassigned	24.63	0.0003	0.0020	0.0007	0.0007	0.0014	0.0008	0.0022
T-22	Unassigned	24.34	0.0002	0.0010	0.0015	0.0007	0.0019	0.0005	0.0029
T-23	Unassigned	24.20	0.0004	0.0008	0.0010	0.0014	0.0007	0.0005	0.0029

^a For definition of inspection surfaces, see Fig. 9.

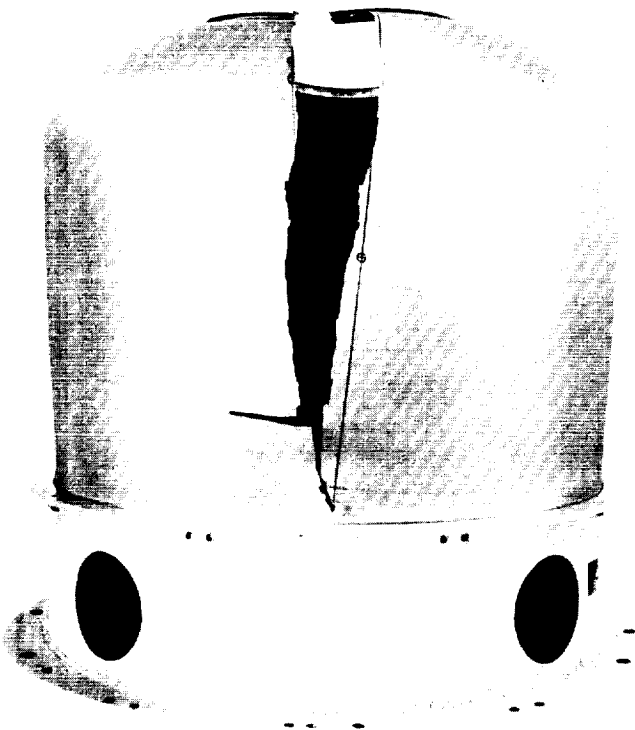


Fig. 10. ATS titanium chamber (T-5) post-test condition

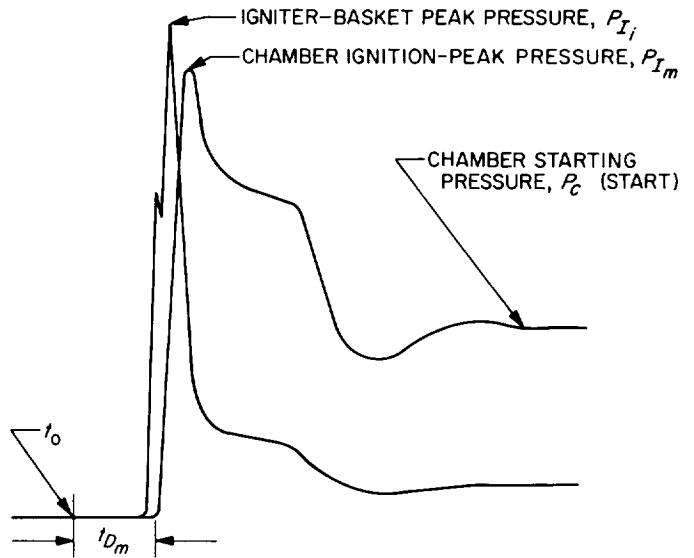


Fig. 11. Measurements made during ignition phase of motor operation

Table 4. (Cont'd)

Table 4. Parameter definitions used in ATS static test data summary

(1) \bar{W}^* , ft/sec, $\frac{g_0 A_t \int_{t_0}^{t_r} P_c dt}{W_p}$

where

g_0 = gravitational constant
(32.14 lbf-ft/lbf-sec²)

A_t = average nozzle-throat area (based on the average of the prefire and postfire measurements)

W_p = loaded propellant weight

t_r = run time (Item 10)

t_0 = zero time (Item 7)

(2) Chamber-pressure integral, psia-sec, $\int_{t_0}^{t_r} P_c dt$

(3) Igniter-basket peak pressure, psia, P_{I_i} (Fig. 11)

(4) Chamber ignition-peak pressure, psia, P_{I_m} (Fig. 11)

(5) Chamber-starting pressure, psia, P_c (start) (Fig. 11)

- (6) Chamber peak pressure, psia, P_c (peak) (Fig. 12)
- (7) Zero time, sec, t_0 , t_0 is the instant electrical current is supplied to the squib (Fig. 11)
- (8) Ignition delay, msec, t_{D_m} , t_{D_m} is the time period between the application of electrical current to the squib until the first indication of motor-chamber pressure (Fig. 11)
- (9) Action time, sec, t_a , t_a is the time period between the time the motor-chamber pressure has reached 10% of its run peak value at ignition until it has decreased to 10% of the run peak value during motor tailoff (Fig. 12)

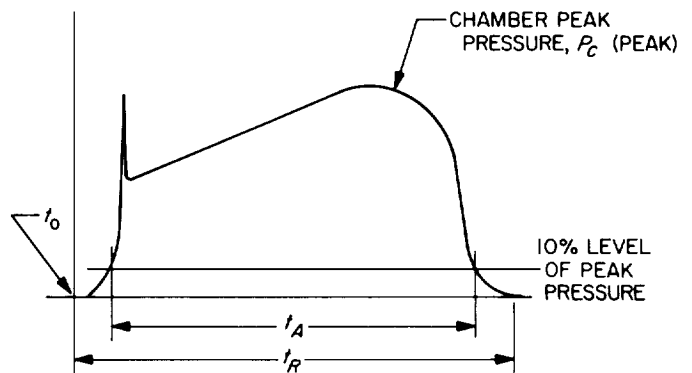


Fig. 12. Measurements made over the entire motor test

Table 4. (Cont'd)

<p>(10) Run time, sec, t_r, t_r is the time period between the application of electrical current to the squib until the motor chamber pressure has returned to ambient conditions following motor tailoff (Fig. 12)</p>	<p>(14) Measured specific impulse, lbf-sec/lbm,</p> $I_{s, mea} = \frac{\int_{t_0}^{t_r} F_{mea} dt}{W_p}$
<p>(11) Peak vacuum thrust, lbf, F_{vac} (peak), measured at the same time as the chamber peak pressure value (Fig. 12)</p>	<p>(15) Vacuum specific impulse, lbf-sec/lbm,</p> $I_{s, vac} = \frac{\int_{t_0}^{t_r} F_{vac} dt}{W_p}$
<p>(12) Total measured impulse, lbf-sec, $I_{mea} = \int_{t_0}^{t_r} F_{mea} dt$</p>	<p>(16) Nozzle throat erosion, %, $\frac{D^2(\text{final}) - D^2(\text{initial})}{D^2(\text{initial})} \times 100$ where D = the nozzle throat diameter</p>
<p>(13) Vacuum total impulse, lbf-sec, $I_{vac} = \int_{t_0}^{t_r} F_{vac} dt$</p>	

Erratum

In SPS 37-36, Vol. IV, Fig. 4 on p. 191 should be replaced by Fig. 4 on p. 198.

XIV. Polymer Research

A. Relationship Between Maximum Extensibility of Networks and the Degree of Crosslinking and Primary Molecular Weight

R. F. Fedors and R. F. Landel

1. Introduction

Based on simple theory (Ref. 1), it has been predicted that $(\lambda_b)_{max} = n^\beta$. Here $(\lambda_b)_{max}$ is the maximum value of the extension ratio at break, as determined by the value of λ_b at which the failure envelope has infinite slope; n is the number of statistical units per network chain; and $\beta = 1/2$. In order to test this relationship, n must first be expressed in terms of parameters which can be experimentally evaluated. The purpose here is to show how this can be accomplished and, furthermore, to subject the derived theoretical equations to an experimental test, using the data of Smith on values of $(\lambda_b)_{max}$ as a function of degree of crosslinking for a Viton elastomer (Ref. 2).

The quantity N_0 is defined as the concentration of statistical units per unit volume of effective network chain

$$N_0 \equiv \frac{nv'_c}{f} \quad (1)$$

where v'_c is the concentration of effective network chains in the gel and f is the fraction of network chains which are terminated at both ends by crosslinked units. This definition of N_0 ensures its independence of both the degree of crosslinking and the primary molecular weight. In Eq. (1), and hereafter, the primed quantities refer to the gel fraction. In terms of N_0 , Eq. (1) becomes

$$(\lambda_b)_{max} = n^\beta = \left(\frac{N_0 f'}{v'_c} \right)^\beta \quad (2)$$

Eq. (2) predicts $(\lambda_b)_{max}$ to vary as $(v'_c)^{-\beta}$ when f' is held fixed. In general, however, f' will vary with both the degree of crosslinking and the primary molecular weight; thus in order to use Eq. (2) directly, it is necessary to estimate f' . This can easily be accomplished if the relationship between the active and inactive portions of the gel, i.e., the free chain end fraction, is known.

Based on differing assumptions and approximations, free chain end corrections have been derived by Flory (Ref. 3), by Berry (Ref. 4), by Scanlan (Ref. 5), by Tobolsky (Ref. 6) and by Mullins (Ref. 7). The relative merits of these different proposals have been discussed by Scanlan (Ref. 5). In Fig. 1, plots of f' as a function of the sol fraction s , are shown for each relationship except for that of Mullins, since this latter correction closely follows the Tobolsky equations (Ref. 7). For the present purposes, it is sufficient to note that at a given value of s , the Berry expression provides a maximum estimate and the Flory expression a minimum estimate of f' . The Flory expression for f' is given by

$$f' = \frac{1}{\left(1 + \frac{2\rho}{v_c' M'}\right)} \quad (3)$$

and the Berry estimate for f' is given by

$$f' = \frac{1}{\left(1 + \frac{\rho}{v_c' M'}\right)} \quad (4)$$

where ρ is the polymer density, v_c' is the concentration of network chains which are terminated at both ends by cross-linked units, and M' is the number-average molecular weight of the primary molecules.

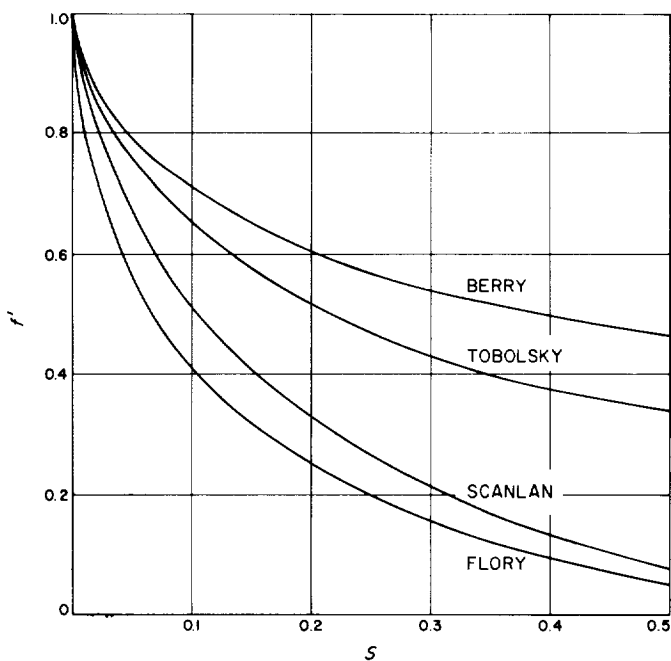


Fig. 1. Variation of the fraction of active gel network as a function of the sol fraction according to the treatments of several theories (Refs. 3-6)

In order to employ Eqs. (3) or (4) directly, values of v_c' and M' must be available. Ordinarily, v_c' , the concentration of elastically effective chains (which can include a significant contribution from chain entanglements), is experimentally obtained rather than the required v_c' . However, both Mullins (Ref. 8) and Kraus (Ref. 9) have shown by means of calibration experiments that v_c' and v_c' can be related by an equation of the form

$$v_c' = (v_c' + a) \left(1 - \frac{b}{v_c' M'}\right) \quad (5)$$

where a is the concentration of network chains contributed by entanglements alone at infinite primary molecular weight, and b is a constant (generally ~ 2 to 3). If a and b are known for a particular system, then v_c' values can be calculated directly. However, the values of a and b are available for only a few systems. Nevertheless, even in the absence of specific knowledge of a and b , it is of significance to note that Eq. (5) requires $v_c' > v_c'$ everywhere, and thus v_c' values can be used as maximum estimates for v_c' .

It is now necessary to estimate M' . In general, compounding (mixing) and vulcanization of an elastomer might be expected to result in both chain scission and crosslinking occurring simultaneously. The relative extents of these two competing processes will depend on the chemical nature of the elastomer, the nature of the vulcanizing system and the conditions, e.g., temperature, used to bring about vulcanization. When both scission and crosslinking occur, M' will vary with the degree of crosslinking, since each scission increases the number of primary molecules by one. Thus, in order to evaluate M' , it is necessary first to determine if scission has occurred, and if so, to what extent.

A method of estimating the extents of chain scission is based on sol-gel relationships. Charlesby (Ref. 10) has derived equations which relate the sol fraction to both the degree of crosslinking and the size and distribution of the primary molecules. In particular, for random chain scission and simultaneous crosslinking of a polymer having a most probable or random molecular weight distribution, Charlesby derived the following equation:

$$s^{1/2}(1 + s^{1/2}) = \frac{p}{v_c'} + \frac{\rho}{v_c' M(0)} \quad (6)$$

where p is the concentration of cuts and $M(0)$ is the number-average molecular weight for the whole polymer

(sol and gel) before crosslinking. For a random molecular weight distribution, M is related to M' by (Ref. 11)

$$M' = (1 + s^{1/2})M \quad (7)$$

Charlesby has shown that almost any initial distribution will closely approach the most probable after about 1 to 3 random cuts per weight average chain have occurred. Data points representing specimens at small extents of scission and crosslinking will be expected to diverge from the predicted behavior if the initial distribution is not random. If no scission occurs, then Eq. (6) predicts that a plot of $s^{1/2}(1 + s^{1/2})$ versus ν_c^{-1} will be linear with zero intercept and slope equal to $\rho/M(0)$. On the other hand, if scission occurs, then the plot will, in general, yield a curve whose slope at any given value of ν_c^{-1} is $[p + \rho/M(0)]$. In this case, if $M(0)$ is known from an independent measurement, p can be evaluated at each value of ν_c^{-1} . A particularly simple relationship prevails if p is directly proportional to ν_c , i.e., if $p = K\nu_c$, then the plot of $s^{1/2}(1 + s^{1/2})$ versus ν_c^{-1} will be linear with intercept equal to K and slope equal to $\rho/M(0)$.

In principle, it is thus possible to determine the values of the necessary parameters required in Eq. (2). Using the Flory chain end correction, Eq. (2) becomes

$$\log (\lambda_b)_{max} = \beta \log \frac{N_0 f'}{\nu'_e} = \beta \log \left[\frac{\nu'_c M'}{\nu'_e (\nu'_c M' + 2\rho)} \right] + \beta \log N_0 \quad (8)$$

and using the Berry estimate for f' ,

$$\log (\lambda_b)_{max} = \beta \log \frac{N_0 f'}{\nu'_e} = \beta \log \left[\frac{\nu'_c M'}{\nu'_e (\nu'_c M' + \rho)} \right] + \beta \log N_0 \quad (9)$$

It is interesting to observe that if $\log (\lambda_b)_{max}$ versus $\log f'/(\nu'_e)$ is linear, or approximately so, for both Eqs. (8) and (9), then the estimate of β from Eq. (8) using the Flory chain end correction will be greater than the estimate of β obtained from Eq. (9) using the Berry estimate for the free chain end fraction. Furthermore, if in addition, the approximation is made that $\nu'_e = \nu'_c$, as is usually the case in practice, then these estimates for β are the maximum estimates.

2. Experimental Test

In order to subject Eqs. (8) and (9) to experimental test, it is necessary to obtain data on the dependence of $(\lambda_b)_{max}$ on the degree of crosslinking. To ensure that N_0 doesn't vary, it is necessary to obtain the data on a single

elastomer since, presumably, N_0 will be a function of the molecular structure of the polymer chain. Fortunately, such data are available in a recent publication by Smith (Ref. 2) who reported $(\lambda_b)_{max}$, ν'_e and s values for a gum Viton elastomer. These data are shown in Table 1.

Table 1. Selected properties of Viton elastomers

Sample	Sol, s	$\nu_e \times 10^5$ moles/cm ³	$c \times 10^5$ moles/g ^a	$(\lambda_b)_{max}$	$M \times 10^{-5}$ g/mole	$M' \times 10^{-5}$ g/mole
Original	—	—	0	—	1.54	—
1	0.49	4.6	6.02	19.1	1.49	2.53
2	0.30	16.7	12.0	15.5	1.27	1.97
3	0.18	28.7	18.1	12.6	1.12	1.60
4	0.10	48.6	24.1	8.9	0.94	1.24
5	0.075	61.4	30.1	7.9	0.86	1.10
6	0.036	118	60.2	5.7	0.61	0.72

^a Concentration of curing agent N,N'-dicinnamylidene-1, 6-hexanediamine in moles/g of elastomer; ρ for Viton taken as 1.84 g/cm³.

In order to estimate the extent of chain scission which has occurred, the plot suggested by Eq. (6) is used with the approximation that $\nu_e = \nu_c$ and these data are shown in Fig. 2 as the unfilled points. Except for the data point representing the lowest degree of crosslinking, the data can be reasonably represented by a linear relationship. The line shown has been fitted by the least squares technique and the slope and intercept are 1.20×10^{-5} moles/cm², and 0.154, respectively. According to Eq. (6), linearity implies that the number of cuts p is directly proportional to ν_e , i.e., $p = 0.154 \nu_e$. Since $p = N_i - N(0)$ where N_i is the concentration of primary molecules present in the i th sample after crosslinking and scission have occurred and $N(0)$ is the initial concentration, it is now possible to estimate M for each sample, and these values are listed in Table 1. It is of interest to note that, provided the $s^{1/2}(1 + s^{1/2})$ versus ν_c^{-1} relation is linear also, these values of M are maximum estimates since $\nu_e > \nu_c$ always, and ν_e was used to estimate ν_c .

In this regard, it is of interest to apply Eq. (6), using the concentration of amine curing agent as an estimate of ν_e . If the plausible assumption is made that the concentration of amine, c , is proportional to the number of crosslinks generated, i.e., $c = k\nu_e$, then a plot of $s^{1/2}(1 + s^{1/2})$ versus c^{-1} should be linear also with slope $\rho k/M(0)$ and intercept ρk . These data are the filled points in Fig. 2, the line shown was fitted by the least

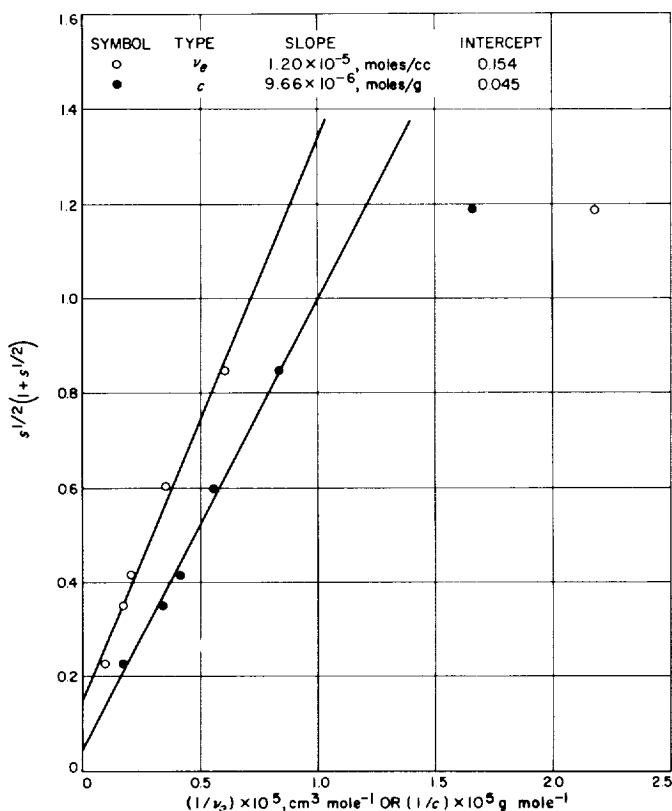


Fig. 2. Variation of the sol fraction, $s^{1/2}(1 + s^{1/2})$ as a function of v_e^{-1} , \bullet , and as a function of c^{-1} , \circ , for a series of Viton elastomers

square technique, which provided a value of the slope and intercept of 9.66×10^{-6} moles/g and 0.045, respectively. The significant point here is that this plot, like that using v_e , is linear also. A linear relationship between v_e and c was obtained by Novikov from studies of Viton elastomers vulcanized by hexamethylene diamine (Ref. 12).

It is also of interest to obtain estimates of k . A maximum estimate can be obtained by assuming that no chain scission occurs during compounding; under this condition, $M(0) = 2.4 \times 10^5$ g/mole which leads to $k = 1.25$. On the other hand, two estimates of the minimum value of k can be obtained; in one, setting $v_e = v_c$ leads to a minimum estimate for $M(0)$ which provides a minimum estimate for $k = 0.86$; in another, the intercept values from Fig. 2 provide $k = 0.54$ in good agreement with the value obtained from the slope. Hence, $0.54 \leq k \leq 1.25$. For a quantitative crosslinker $k = 2$. For Viton vulcanized with hexamethylenediamine, Novikov's data lead to a maximum estimate of $k = 1.23$.

Having evaluated the various intermediate quantities required, it is now possible to subject the theoretical

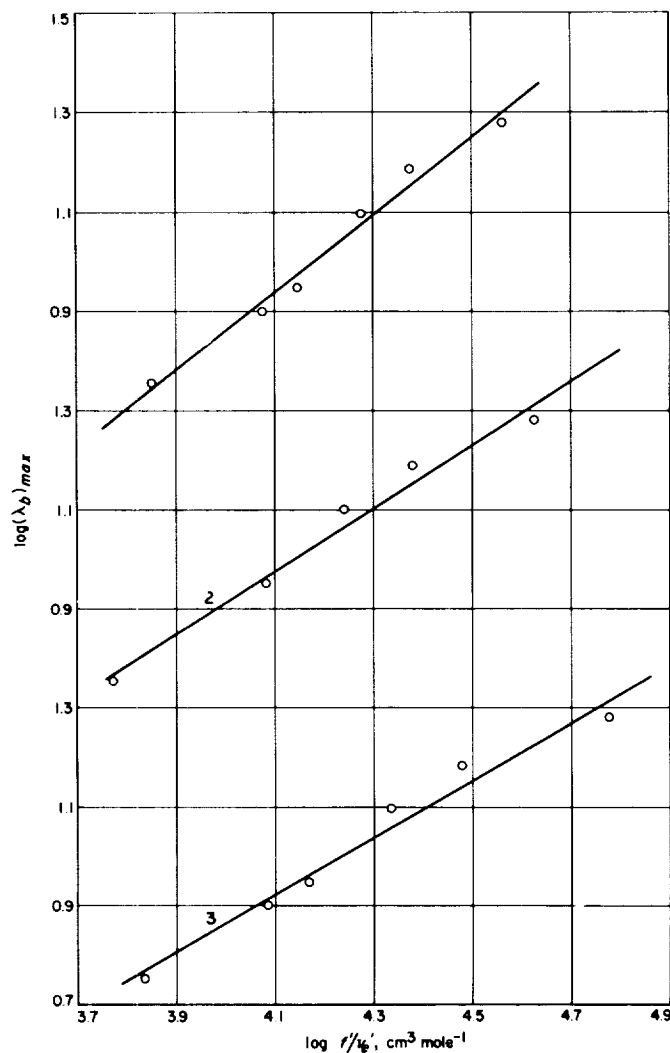


Fig. 3. Dependence of $\log(\lambda_b)_{max}$ on $\log f'/v'_e$ for Viton data of Smith

Eqs. (8) and (9) to an experimental check. Fig. 3 shows $\log(\lambda_b)_{max}$ versus $\log f'/v'_e$. In Curve 1, the data are plotted according to Eq. (8), assuming that $v'_e = v'_c$ and $M' = M = 2 \times 10^5$ g/mole. The line was fitted by the least square technique which provides $\beta = 0.784$. Since $v'_e > v'_c$ and $M' > M$, this value of β is the largest estimate. Curve 2 is a plot of Eq. (8), assuming also only $v'_e = v'_c$; the least square estimate of $\beta = 0.64$. Curve 3 is a plot according to Eq. (9) assuming that $v'_e = v'_c$; the least square estimate of $\beta = 0.58$. Since $v'_e > v'_c$ always, these estimates of β are the *maximum* estimates, and the use of v'_e itself rather than v'_c would yield smaller values of β closer to the theoretical one of $1/2$. In the absence of further data, these Viton results may therefore be taken as a verification of the relationship given by Eq. (2).

B. The Effect of Surface Modifications on the Burning Rate of a Composite Solid Propellant, II

B. G. Moser and R. F. Landel

1. Introduction

In SPS 37-35, Vol. IV and elsewhere (Ref. 13), it was shown that the degree of dispersion or the surface energy of the dispersed oxidizer particles in a composite solid propellant could profoundly affect the burning rate. For example, it was shown that when a surfactant is added to a slurry of oxidizer and binder, a rather large change in burning rate may occur. In a slurry containing 20% by weight of mineral oil and 80% of ammonium perchlorate (AP), the burning rate at 1000 psi is decreased by several hundred percent by the addition of only 0.1 of an effective surfactant, but in a similar slurry in which the liquid phase is poly(propylene oxide) (PPO), the use of a surfactant has a very much smaller effect. It was pointed out that these changes in burning rate could originate either from effects on the decomposition of the AP or from changes in the degree of dispersion. Work has continued on this problem, and additional data have supplied a more definitive answer.

2. Experimental

When common burning rate modifiers, especially accelerators, are used in a composite solid propellant, it is known that there is a shift in the temperature at which decomposition of the oxidizer (ammonium perchlorate) takes place. The question that was not really satisfactorily answered in the last report was whether the change in burning rate as a function of the surface energy of the oxidizer was due to changed decomposition characteristics or truly due to dispersion.

The degree of dispersion of a slurry system can be assessed by measuring the radius of a given volume of slurry after the latter has been freely compressed between parallel glass plates under a constant load for a given length of time. The effectiveness of a surfactant can then be gauged by plotting the radius versus the surfactant concentration. We call such plots effectiveness curves (Ref. 13).

If the degree of dispersion is contributing to the burning rate, then a plot of burning rate versus surfactant

concentration should resemble an effectiveness curve. As was pointed out in SPS 37-35, Vol. IV, this is indeed shown to be the case (Fig. 4). Fig. 5 depicts burning rate versus surfactant concentration for 82 wt% AP in a U.S.P. mineral oil. The startling difference is not too surprising when it is considered that PPO is an effective surfactant, and the oxidizer particles are fairly well dispersed even before the addition of the surfactant. This is discussed in much greater detail in SPS 37-35, Vol. IV and in Ref. 13.

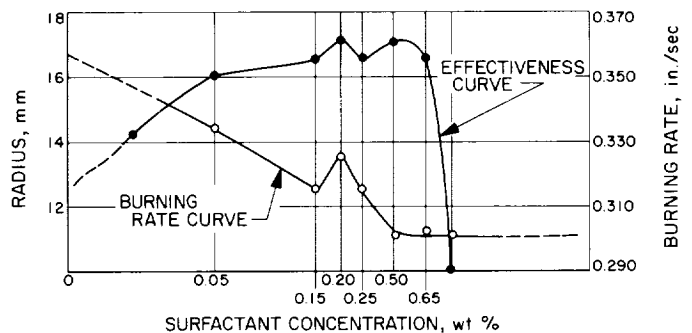


Fig. 4. Effectiveness curve of 75 wt% AP (0/100) and burning rate of 80 wt% AP (30/70) at 1000 psi

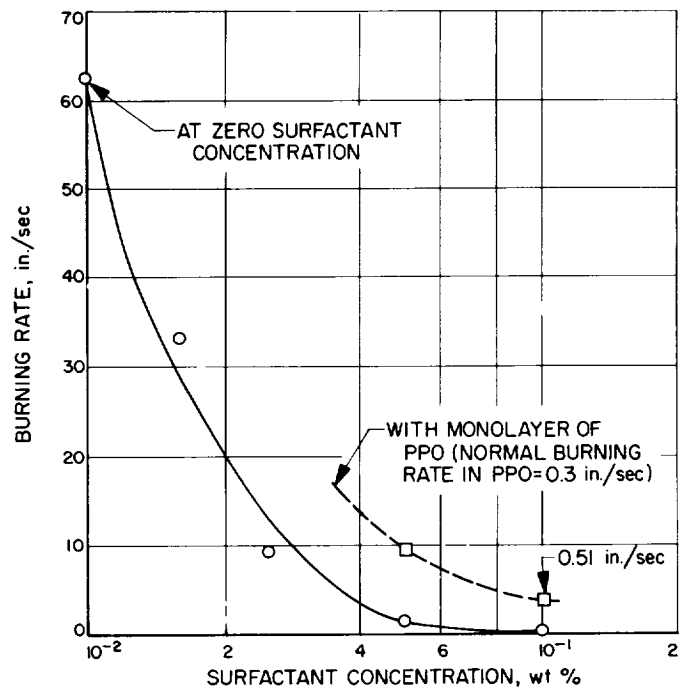


Fig. 5. Burning rate versus surfactant concentration for bimodal AP in USP mineral oil (82 wt% solids)

If one could show that the addition of trace amounts of PPO to an AP mineral oil system resulted in a vastly reduced burning rate, and if one could also show that the decomposition characteristics of such a slurry remained unchanged, then one has a very strong argument for dispersion effects on the burning rate. This has been done in Figs. 5 and 6. Plotted on Fig. 5 is the lower end of the same AP-mineral oil slurry that has had PPO added as a surfactant (dashed line). Note that the burning rate has been drastically reduced. Furthermore, it can be seen in comparison of (a) and (b) of Fig. 6 that there has been no significant change in the decomposition characteristics of a slurry. A differential thermal analysis of a 78% ammonium perchlorate, 2% aluminum, 20% mineral oil slurry is shown in Fig. 6(a). The same slurry with 0.3% of PPO added as a coating on the oxidizer surface is shown in Fig. 6(b).

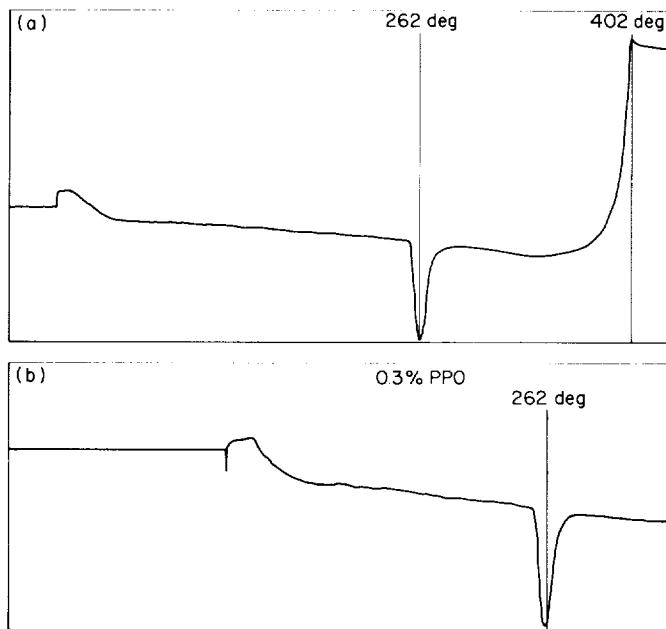


Fig. 6. Differential thermal analysis of (a) ammonium perchlorate in mineral oil (b) ammonium perchlorate in PPO

3. Conclusion

The effects of surface modification on propellant oxidizer is twofold. First, there is a change in the rheological properties, i.e., increased dispersion with attendant decreased mix viscosity, and secondly, there is a change in the burning rate due exclusively to dispersion.

C. Polymer Degradation Mechanisms: C¹⁴-Labeled Adducts of Poly(Propylene Oxide)

J. D. Ingham, E. F. Kopka and G. K. Ostrum

1. Introduction

For studies of polymer degradation, very sensitive means of observing chemical reactions that result in bond scission are required. One method is to monitor formation of a C¹⁴-labeled product involved in the degradation reaction (SPS 37-35, 37-25, and 37-23, Vol. IV). As a means of isolating reactions at the 2- and 4-positions of toluene diisocyanate (TDI) -urethanes and to correlate small extents of bond scission with C¹⁴O₂ evolution, studies of the thermal degradation at moderate temperatures (up to 150°C) of poly(propylene oxide) (PPO) reacted with C¹⁴-labeled *p*-tolyl isocyanate (PTI), *o*-tolyl isocyanate (OTI) and TDI have been carried out.

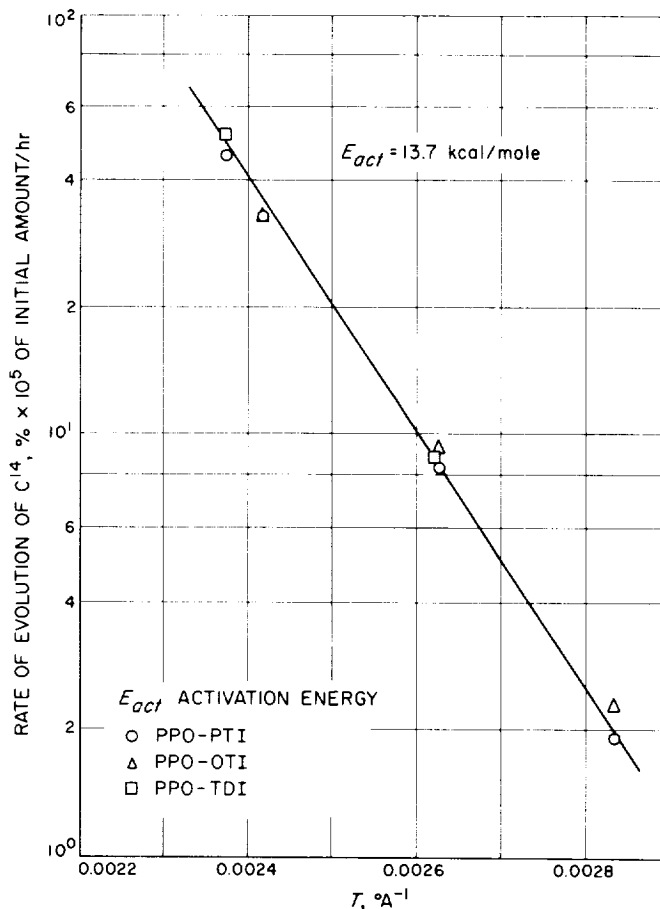


Fig. 7. Rate of evolution of C¹⁴, % × 10⁵ of initial amount per hour

2. Discussion of Results

Previously, the measured rates at 128 and 150°C for PPO-PTI were found to be nearly the same, with a substantially lower rate at 109°C (SPS 37-35). More recent measurements substantiate the observed rate at 150°C and very strongly indicate that the measurement at 128°C was incorrect. The results obtained are summarized in Table 2, and an Arrhenius plot of the rate data is shown in Fig. 7.

Table 2. Rates of $C^{14}O_2$ evolution on heating diisocyanate adducts of poly(propylene oxide)

Product	Temperature, °C	Rate of C^{14} evolution, %/hr $\times 10^5$
PPO-PTI	80	1.92
	109	8.4
	128	44.5 ^a
	141	33.0
	150	46.0
PPO-OTI	80	2.29
	109	9.4
	141	33.0
PPO-TDI	110	8.8
	150	51.6

^a This value is apparently incorrect; it should be $\sim 20 \times 10^{-5}$ %/hr

The two main conclusions from this work are: (1) There is no difference in the rates of $C^{14}O_2$ evolution for urethanes prepared from PPO and either PTI, OTI or TDI. Therefore, the interpretation of degradative studies of TDI polyurethanes is greatly simplified. (2) A linear plot giving an activation energy of ~ 13.7 kcal/mole is obtained between 80 and 150°C. Thus, if it is known that this process is predominant, it is reasonably safe to extrapolate to lower temperatures from data obtained from accelerated tests at $\sim 150^\circ\text{C}$.

This work will be extended to attempt to correlate $C^{14}O_2$ evolution with changes in molecular weight of polyurethanes.

D. Polymer Nuclear Magnetic Resonance Spectroscopy Studies

D. D. Lawson and J. D. Ingham

1. Introduction

In our previous NMR studies we have found that the F^{19} signals from the trifluoroacetate esters of the secondary hydroxyls of poly(propylene oxide) were doublets resulting from differences in the stereoconfiguration of the adjacent end units. The detection of such subtle structural features is fundamentally significant, since they influence the reactivity of the terminal groups and, consequently, may critically affect polymer degradative processes, synthesis, and processing.

2. Poly (Alkylene Oxide) Polymers

The ditrifluoroacetates of poly(epichlorohydrin) and poly(1,3-butylene oxide) were prepared. The ester of the poly(epichlorohydrin) shows (Fig. 8) the F^{19} signal as a doublet, which indicates that two different types of secondary hydroxyl groups are present in the diol. The differences in hydroxyl groups is caused by asymmetric

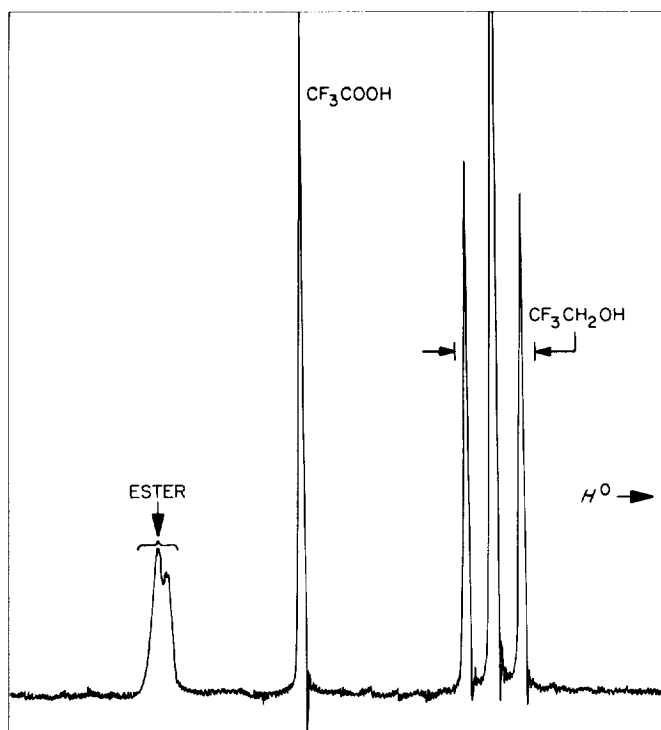


Fig. 8. The F^{19} spectrum of the ditrifluoroacetate ester of poly (epichlorohydrin) in benzene solution

carbons in each monomeric unit with two different diad forms being present at the ends of the polymer chains. In the poly(1,3-butylene oxide) polymer no asymmetric carbons are present, and only primary hydroxyl groups would be expected to be present in the diol. Fig. 9 shows clearly only a single sharp line for the trifluoroacetate ester.

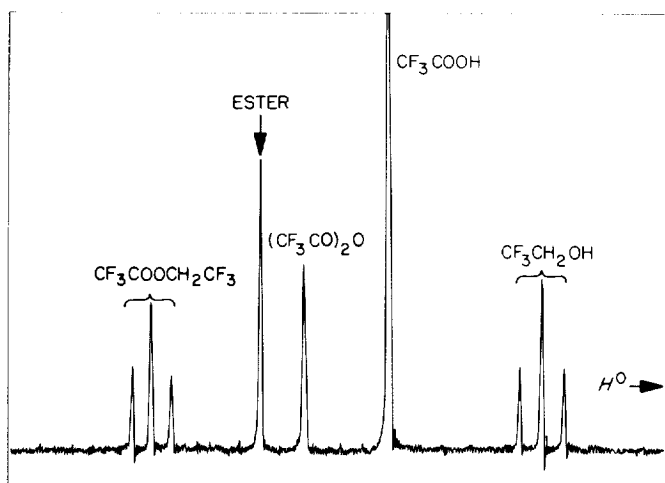


Fig. 9. The F^{19} spectrum of the ditrifluoroacetate ester of poly (1, 3-butylene oxide) in benzene solution

3. Hydroxy-Terminated Butadiene Polymers

Two butadiene polymers were prepared by a living polymer synthesis. The termination of the living polymer systems was obtained with propylene oxide to give a secondary hydroxyl or with ethylene oxide to give a primary hydroxyl as the terminal group. The trifluoroacetate ester of the secondary hydroxyl polymer (Fig. 10) shows a doublet which would indicate that more than one propylene oxide unit reacted to reflect differences in stereoconfiguration of the terminal and next adjacent ether units, or that only one propylene oxide reacted per chain end and a structural variation in the poly(butadiene) is being observed. In the case of the primary hydroxyl terminated polymer (Fig. 11) there appears a slight splitting on the shoulder of the peak, which indicates that a difference in the butadiene structure through the capping ethylene oxide unit is being observed. Although here, again, the splitting may have resulted from two types of primary hydroxyl: one having only one terminal ethylene oxide unit and the other more than one. Work is in progress to clarify these observations unequivocally.

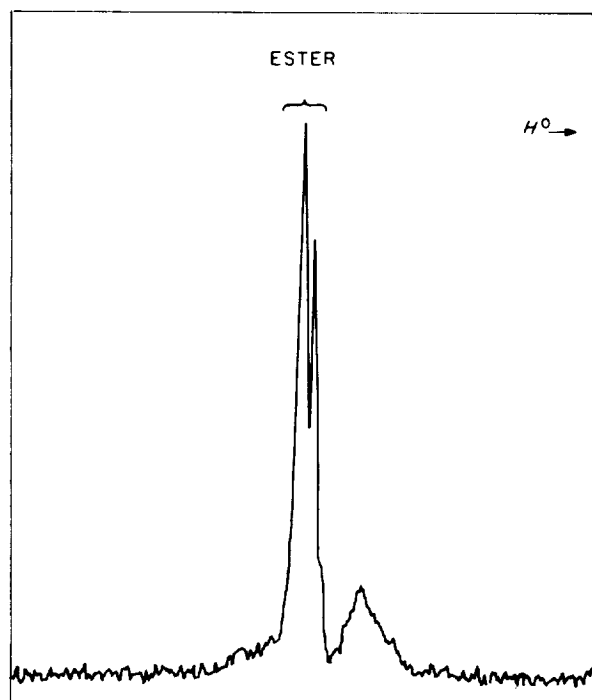


Fig. 10. The F^{19} spectrum of secondary hydroxyl-terminated butadiene polymer in benzene solution

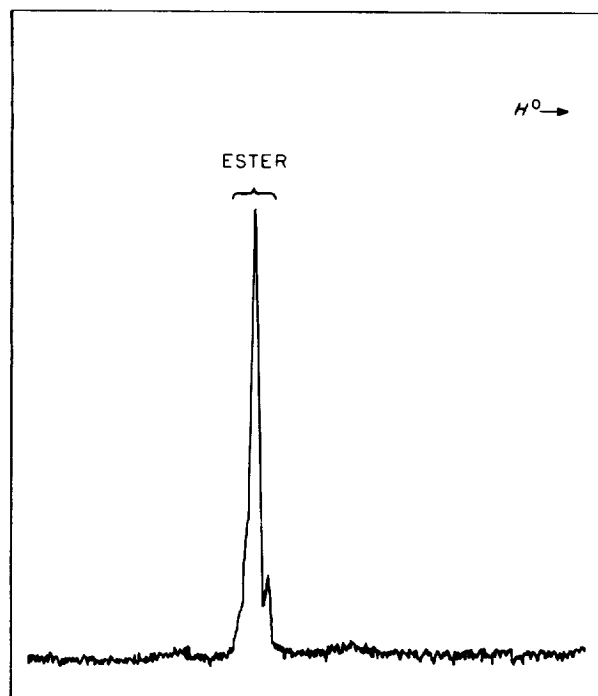


Fig. 11. The F^{19} spectrum of primary hydroxyl-terminated butadiene polymer in benzene solution

E. Acenaphthene Radical Ion

A. Rembaum and A. M. Hermann

1. Introduction

In order to substantiate our proposed degradation mechanism in connection with the study of electron transfer to polyacenaphthylene (Ref. 14), it was found necessary to establish the formation of acenaphthene

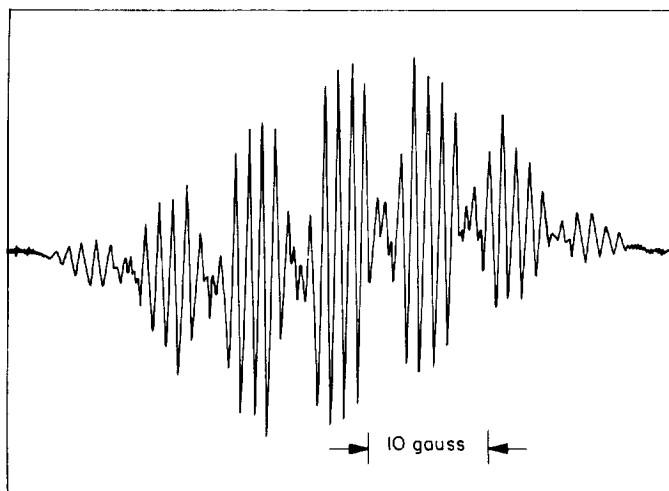


Fig. 12. ESR spectrum of acenaphthene radical ion at 25°C (in THF)

radical ion during the reaction of acenaphthene with sodium. A previous attempt to produce this radical ion in liquid ammonia was not successful (Ref. 15); deBoer and Weissman (Ref. 16) obtained its ESR spectrum using potassium as a reducing agent. However, poor resolution was reported; the hyperfine structure was not published; and the temperature effect was not studied.

As a result of the present investigation we were able to: record a reasonably well-resolved spectrum, show the considerable influence of temperature on the hyperfine structure, confirm the previously proposed equilibrium for other aromatic hydrocarbons (Ref. 17), obtain information on the recently observed counter ion interchange in pyracene (Ref. 18), and reconstruct the theoretical spectrum from the experimentally determined splitting constants.

2. Experimental

All spectra were determined by means of a 4500 Varian spectrometer, using 100-kc modulation and a quartz flat cell. Zone refined acenaphthene dissolved in tetrahydrofuran (THF) or dimethoxyethane was reacted with a freshly prepared sodium film under high vacuum according to well established techniques. The solvents were stirred with finely divided sodium potassium alloy and first distilled into a bulb containing pure sodium and

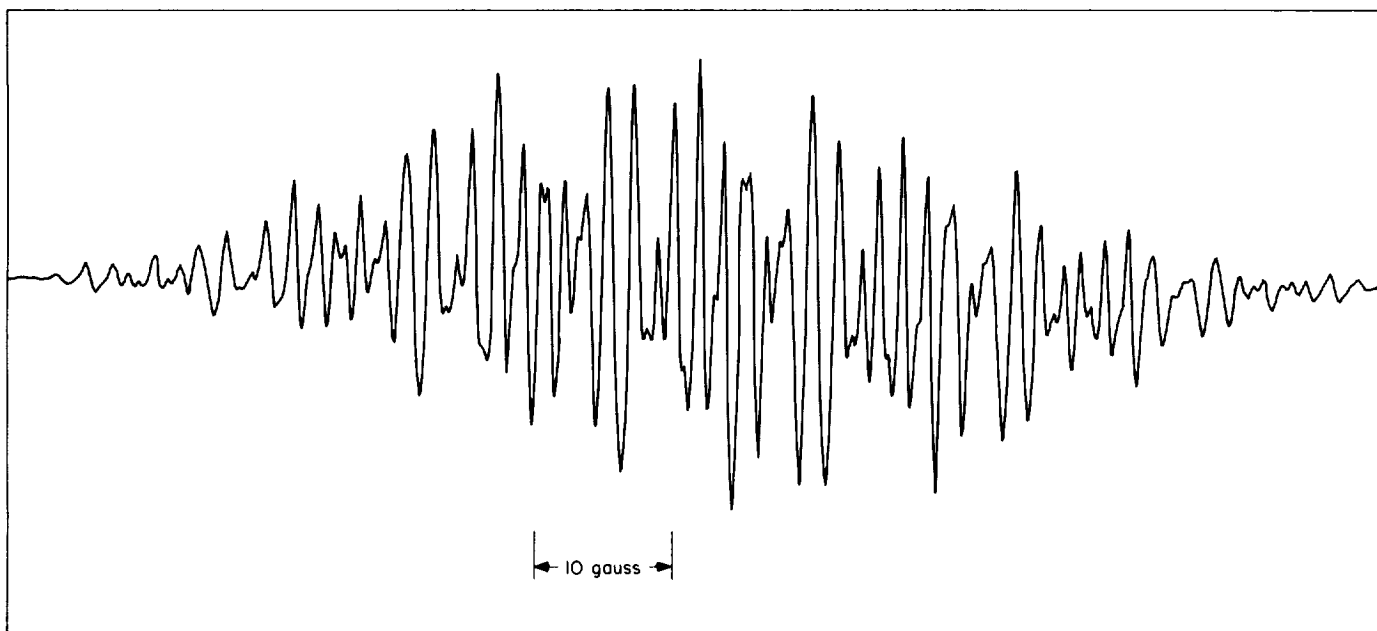


Fig. 13. ESR spectrum of acenaphthene radical ion at -38°C (in THF)

pyrene and then into the ESR cell containing acenaphthene and a film of sodium in a side arm. The radical ion was formed at about -60°C , and its concentration was adjusted according to experimental requirements.

3. Results

The ESR spectrum of acenaphthene radical ion in THF at room temperature is shown in Fig. 12. The change in the appearance of the spectrum on lowering the temperature is shown in Fig. 13. Solutions used to obtain Figs. 12 and 13 contained approximately 10^{-4} moles/liter of radical ions. On increasing the concentration to 10^{-2} mole/liter, and in presence of excess sodium, a single line was obtained, the amplitude of which in-

creased about twelvefold as the temperature was lowered from 25 to -60°C . The optical density at the wavelength of $385\text{ m}\mu$ of a solution of acenaphthene radical ion in presence of excess sodium examined separately by means of a Cary Model 14 spectrophotometer was also found to vary with temperature. A comparison of the changes of the normalized optical density with the normalized free spin concentration as a function of temperature is shown in Fig. 14.

The ESR spectra of acenaphthene radical ion in dimethoxyethane were found to be significantly different. It was not possible to obtain good resolution at 25°C ; however, on lowering the temperature the spectra shown in Figs. 15 and 16 were recorded.

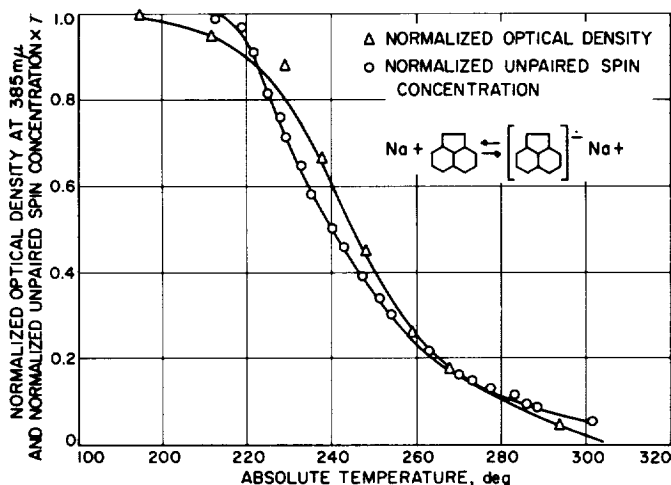


Fig. 14. Extinction coefficient and unpaired spin concentration of acenaphthene radical ion versus absolute temperature

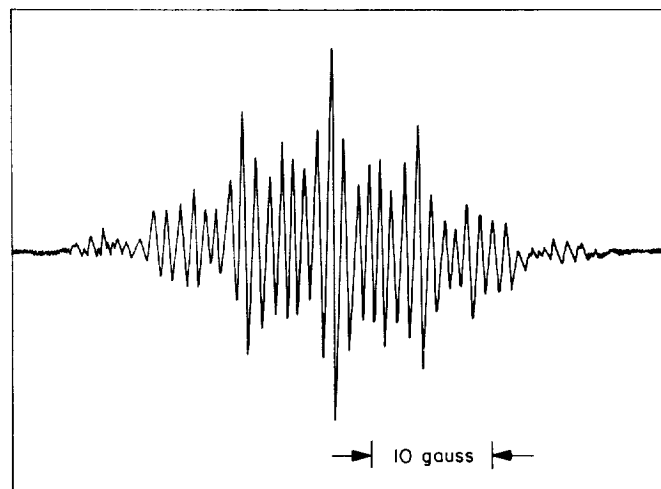


Fig. 15. ESR spectrum of acenaphthene radical ion at -40°C in dimethoxyethane (approx. 10^{-4} M)

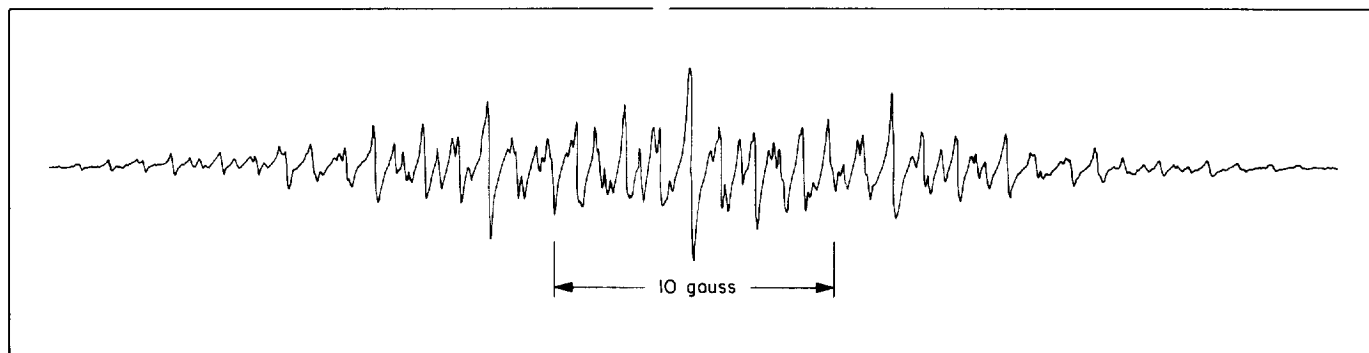


Fig. 16. ESR spectrum of acenaphthene radical ion at -40°C in dimethoxyethane (approx. 10^{-5} M)

The spectrum of Fig. 12 was reconstructed using the following splitting constants:

Aliphatic protons	7.45 gauss
Para protons	4.12 gauss
Ortho protons	0.98 gauss
Meta protons	1.18 gauss
Sodium splitting	0.85 gauss

4. Conclusions

- (1) In Fig. 12, the five lines which are split into quartets originate from the electron interaction with four equivalent protons (Ref. 16), the splitting into quartets being due to the interaction with the sodium nucleus of spin 3/2. On cooling a THF solution of acenaphthene radical ion the sodium interaction is reduced and in dimethoxyethane (Fig. 15) it is diminished to the extent that the quintet, due to the 4 aliphatic protons, may be clearly distinguished. In contrast to the spectrum in THF (Fig. 12) where the intensities are obscured because of sodium interaction, in dimethoxyethane the quintet (Fig. 15) has the theoretical intensities of 1:4:6:4:1.
- (2) The total number of lines expected on the basis of one group of four equivalent protons and three groups of equivalent pairs of protons is 5×3^3 , or 135, but due to the similar values of the splitting constants of *ortho* and *meta* protons a complete resolution could not be achieved. In the best case (Fig. 15) approximately a hundred lines can be distinguished.
- (3) deBoer (Ref. 18) postulated time-dependent modulations in the isotropic coupling constants of pyracene on the basis of an experimental alternating effect in the hyperfine structure. The fact that no alternating effect was observed in any of the acenaphthene ESR signals may be considered as a confirmation of deBoer's results, since in our case the counterion cannot be interchanged between two symmetrical positions. Similarly, the elimination of sodium splittings in dimethoxyethane confirms the previous observations of the effect of solvents (Ref. 19), and indicates greater solvation of the counterion by dimethoxyethane than by tetrahydrofuran.
- (4) The sharp increase of the ESR signal with decrease of temperature (Fig. 13) is in excellent agreement with spectrophotometric results and confirms the equilibrium previously postulated for substituted biphenyls and substituted carbazoles (Ref. 17).

F. Method for Calculating Outgassing Rates of Rigid Closed-Cell Foams

E. F. Cuddihy and J. Moacanin

Previously, results of both theoretical and experimental studies on the outgassing rates of gases in vacuum from rigid closed-cell foams have been reported (SPS 37-34, 37-35, and 37-36, Vol. IV). The purpose of this report is to show how the outgassing rate for a given foam can be calculated from the foam density and the polymer-gas permeation constant, P_c . Values for the latter are available in the literature for a variety of systems. These studies are being carried out in support of our effort to assess the possibility of using cellular plastic materials as encapsulants for spacecraft electronic components.

The following equation describes the pressure profile of the blowing gas within the foam with one specimen surface exposed to vacuum:

$$\frac{P}{P_0} = \frac{4}{\pi} \sum_{k=1}^{\infty} \frac{1}{(2k-1)} \left\{ \sin \frac{(2k-1)\pi x}{2a} \right\} \exp - \left\{ \left[\frac{(2k-1)\pi}{2a} \right]^2 Dt \right\} \quad (1)$$

where

P = pressure of blowing gas

P_0 = initial pressure

a = thickness of foam

t = time

D = diffusion coefficient

x = distance in foam from exposed surface

This equation is the classical one-dimensional solution of Fick's law and describes the pressure as a function of

time at any distance x below the exposed surface. Equivalent equations can also be developed for any other foam geometries and for one-, two-, or three-dimensional diffusion flow (Refs. 20 and 21). From these equations, it will be possible to estimate times at various locations within the foam when the internal gas pressure will be in the ionization region.

It is apparent from the above equation that to characterize a given foam it is necessary to secure the value of D . Values of D for foams are not yet available from the literature. Experimentally, D can be obtained from weight-loss measurements (SPS 37-34, 37-35, and 37-36, Vol. IV), but the technique is time-consuming and requires specialized equipment.

To allow the design engineer to estimate D , an equation was developed which relates D to the density of the foam and the permeation constant P_e of the gas-polymer system

$$D = P_e \left(\frac{3RT}{M} \right) \left(\frac{\rho_0}{\rho} \right) \quad (2)$$

where

ρ_0 = density of the polymer

ρ = density of foam

M = molecular weight of the blowing gas

R = gas constant

P_e = permeation constant of gas-polymer combination

D = diffusion constant

T = absolute temperature, to be equal to the temperatures at which the permeation constant was determined.

Values of P_e have been determined for a variety of materials and recently a table has been published (Table 3), which allows one to estimate P_e values for a wide combination of polymers and gases. Thus D can be calculated from data available in the literature. Using the appropriate diffusion equation one can then predict pressure profiles within a foam-encapsulated component as a function of exposure to vacuum.

Table 3.^a F and G Values^b for permeation at 30°C

Film	F Value
Saran	0.0094
Mylar	0.050
Pliofilm NO	0.080
Nylon 6	0.10
Kel-F	1.3
Pliofilm FM	1.4
Hycar OR 15	2.35
Polyvinyl butyral	2.5
Cellulose acetate P-912	2.8
Butyl rubber	3.12
Methyl rubber	4.8
Yulcaprene	4.9
Cellulose acetate (15% DBP)	5.0
Hycar OR 25	6.04
Pliofilm P4	6.2
Perbunan	10.6
Neoprene	11.8
Polyethylene (0.92 g/ml)	20
Buna-S	63.5
Polybutadiene	64.5
Natural rubber	80.8
Ethyl cellulose (plasticized)	84
Gas	G Value
Nitrogen	1.0
Oxygen	3.8
Hydrogen sulfide	21.9
Carbon dioxide	24.2

^a Rogers, C. E., "Permeability and Chemical Resistance," Chap. 9 in *Engineering Design for Plastics*, sponsored by the Society of Plastics, Inc., by Eric Baer, Ed., Reinhold Publishing Corp., 1964.

^b The product FG gives the permeability constant $\times 10^{10}$ in cc (STP)/mm/cm²/sec/cm Hg.

G. Studies on Sterilizable Elastomers

E. Cuddihy and J. Moacanin

The use of sterilizable elastomeric foams has been proposed for solid propellant liner materials (SPS 37-36, Vol. IV). A technique for blowing foams from elastomeric

materials has been developed and was previously described (SPS 37-36, Vol. IV). Since the mechanical strength and sterilizability of an elastomeric foam can be no greater than that of the starting elastomer, the major emphasis of future development will be directed toward the preparation of sterilizable elastomers having high mechanical strength, and which retain adequate mechanical strength after heat sterilization.

It has been shown that copolymers of butadiene and acrylic acid (PBAA) crosslinked to an elastomer by reaction at the carboxyl group with an imine are capable of withstanding a high temperature exposure. In SPS 37-36, Vol. IV, the detailed studies on a PBAA copolymer crosslinked with a commercial triimine, MAPO, were reported. Although this material retained integrity after the high temperature exposure, it suffered a substantial loss in mechanical strength. Additionally, this material, even when optimally cured, was found to have a maximum tensile strength of only 20 psi and an elongation less than 33%, resulting in a weak, highly friable elastomeric foam. For this reason, plus the further loss of mechanical strength after sterilization, this material has been eliminated from further consideration.

Other commercial imines, besides MAPO, are readily available and a screening process was conducted to attempt to find a promising candidate for further more detailed studies. For the screening process, the initial criteria for selection were that quick high-temperature gelation be obtained (a requirement needed for foaming), and the resultant elastomers exhibit improvements

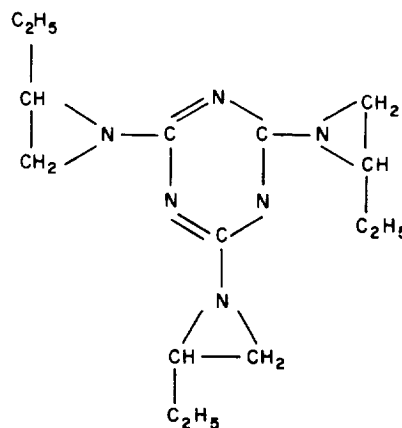


Fig. 17. Chemical structure of HX-874

in mechanical strength over the PBAA-MAPO system. During this process, a triimine obtained from the Minnesota Mining and Manufacturing Corp. satisfied the initial criterion requirements. This material is designated HX-874, and its chemical structure is shown in Fig. 17.

Elastomers prepared from PBAA and four different HX-874 concentration levels (imine/COOH ratios of 1.00:1, 1.05:1, 1.10:1 and 1.15:1) were cured for periods up to 664 hr at temperatures of 40, 70, and 100°C. The extent of cure was followed by means of a Shore A Durometer, and the results are shown in the top half of Table 4.

These results show that optimum cure will probably be achieved at 100°C and at a formulation ratio of

Table 4. Effect on the Shore A hardness of formulation parameter, cure time, cure temperature and sterilization for a PBAA-HX-874 elastomer

Formulation parameters		1.00:1			1.05:1			1.10:1			1.15:1		
Sample number	Cure time, hr	Temperature, °C											
		40	70	100	40	70	100	40	70	100	40	70	100
		Shore A values											
1	16	0	1	4	0	3	6	0	3	7	0	4	10
2	40	0	4	4	0	6	7	0	8	8	0	10	10
3	88	0	5	6	0	7	8	0	8	8	0	10	10
4	160	3	5	7	3	7	8	2	8	10	2	10	10
5	208	3	5	7	3	7	8	4	8	10	5	10	10
6	328	5	6	10	6	7	10	7	9	10	10	10	10
7	400	7	6	10	6	8	10	7	9	10	10	10	10
8	496	5	6	11	9	9	12	11	9	12	12	12	12
9	592	5	6	12	9	9	10	10	9	13	8	11	12
10	664	5	6	12	12	8	12	10	9	13	10	10	12

Table 4. Effect on the Shore A hardness of formulation parameter, cure time, cure temperature and sterilization for a PBAA-HX-874 elastomer (Cont'd)

Formulation parameters		1.00:1			1.05:1			1.10:1			1.15:1		
Sample number	Cycle number	Temperature, °C											
		40	70	100	40	70	100	40	70	100	40	70	100
		Heat sterilization* Shore A values											
4	1	3		10									
	2	6		20									
	3	0		24									
	Inside surface	0		0									
5	1		3		5	3	9		3	6		5	8
	2		3		17	7	13		8	14		12	10
	3		0		19	8	11		9	15		15	12
	Inside surface		0		0	0	0		0	0		0	0
7	1							5				3	
	2							11				18	
	3							14				27	
	Inside surface							0				0	
8	1											11	7
	2											28	15
	3											35	18
	Inside surface											0	0
9	1	3				6							
	2	5				7							
	3	0				7							
	Inside surface	0				0							
10	1		6	12	3		12	12	4	5			15
	2		5	10	10		16	15	10	17			15
	3		0	27	11		15	18	12	23			20
	Inside surface		0	7	0		6	0	0	6			5

* Samples subjected to three consecutive cycles of 40 hr at 295°F under dry N₂. S₁ values were obtained on the exposed surfaces after each cycle. After the third cycle, the samples were cut and a S₁ measurement made on the inside material.

1.10:1, although maximum cure seemingly has not been reached even at 100°C after 664 hr. This is in sharp contrast to the PBAA-MAPO system, which underwent rapid degradation after only 40 to 64 hr at 100°C. The HX-874 materials demonstrate better storage stability for temperatures up to 100°C. At curing temperatures near 140°C the HX-874 materials gelled and cured in less than an hour. The resultant elastomers were significantly

better than the corresponding PBAA-MAPO elastomers cured at the same temperatures.

The effect on these materials of exposure to high temperatures during sterilization was followed by measuring the change in Shore A hardness. The sterilization procedure involved three consecutive 40-hr exposures to 146°C (295°F) under dry N₂. During the sterilization, it

was noted that the surfaces of the materials hardened, whereas the insides became softer. Hence, at the end of the third cycle, the samples were cut in half and a Shore A measurement taken on the exposed inside material. The results of this phase of the study for selected samples are shown in the bottom half of Table 4.

Generally, these materials are characterized by an initial large drop in $S_{.1}$ which then increases in subsequent heating cycles. However, these results reflect only a surface-hardening phenomena; for, in fact, the material below the surfaces was undergoing rapid degradation. This behavior is readily noted by observing the internal $S_{.1}$ values obtained after the third cycle. Except for those cured 664 hr at 100°C, all the samples had a Shore A value of zero for the material below the surface. Elastomers prepared from HX-874 underwent a substantial loss in mechanical strength during sterilization.

Furthermore, tensile curves obtained on unsterilized samples showed that the highest tensile strengths achieved

were about 20 psi. Although this behavior is similar to that for the PBAA-MAPO elastomers, it exhibited a marked improvement in elongation to about 100% extension. This improvement in elongation for the HX-874 materials results in superior tear properties. But the low tensile strength and the poor sterilization behavior of the HX-874 elastomers have eliminated them from further consideration as foam liner candidates.

A survey of the gelation times, mechanical properties, and sterilizability of PBAA elastomers prepared from other imines showed these properties to be so poor as to generalize that the particular PBAA employed in these studies would not yield a high-tensile-strength sterilizable elastomer. Therefore, emphasis was shifted to a carboxyl-terminated polybutadiene designated HC-polymer and obtained from the Thiokol Corp. Initial investigations with this new material were immediately rewarding, for one of the first elastomers prepared from this material had a nominal tensile strength of nearly 60 psi and an elongation of nearly 100%. At this time work is proceeding using the HC-polymer.

References

1. Landel, R. F., and Fedors, R. F., Proceedings of the Fourth International Congress on Rheology, Brown University, August 1963, E. H. Lee, Ed., Interscience Publishers, New York, N. Y., Part 2, p. 543, 1965.
2. Smith, T. L., and Frederick, J. E., *Journal of Applied Physics*, Vol. 36, p. 2996, 1965.
3. Flory, P. J., *Chemical Reviews*, Vol. 35, p. 51, 1944.
4. Berry, J. P., and Watson, W. F., *Journal of Polymer Science*, Vol. 18, p. 201, 1955.
5. Scanlan, J., *Journal of Polymer Science*, Vol. 43, p. 501, 1960.
6. Tobolsky, A. V., Metz, D. J., and Mesrobian, R. B., *Journal of the American Chemical Society*, Vol. 72, p. 1946, 1950.
7. Mullins, L., and Thomas, A. G., *Journal of Polymer Science*, Vol. 43, p. 13, 1960.
8. Mullins, L., *Journal of Applied Polymer Science*, Vol. 2, p. 1, 1959.
9. Kraus, G., *Journal of Applied Polymer Science*, Vol. 7, p. 1257, 1963.
10. Charlesby, A., and Pinner, S. H., *Proceedings of the Royal Society*, Vol. A249, p. 367, 1959.
11. Charlesby, A., *Journal of Polymer Science*, Vol. 11, p. 513, 1953.

References (Cont'd)

12. Novikov, A. S., Galil-Ogly, F. A., Gilinskaya, N. S., and Nudelman, Z. N., *Soviet Rubber Technology*, Vol. 21, p. 5, 1962.
13. Moser, B. G., and Landel, R. F., "The Effect of Surface Modification on the Burning Rate of Composite Solid Propellants," published in preprints of the Western States Combustion Institute Meeting at Santa Barbara, California, October 25, 1965.
14. Rembaum, A., Haack, R., and Hermann, A. M., ACS Meeting, Polymer Preprints, Phoenix, Arizona, January 17, 1966.
15. Maximadshy, Von A., and Dörr, F., *Zeitschrift für Naturforschung*, Vol. 19b, p. 359, 1964.
16. deBoer, E., and Weissman, S. I., *Journal of the American Chemical Society*, Vol. 80, p. 4539, 1958.
17. Rembaum, A., Eisenberg, A., and Haack, R., *Journal of the American Chemical Society*, Vol. 87, p. 2291, 1965.
18. deBoer, E., and Mackor, E. L., *Journal of the Chemical Society*, p. 23, 1963.
19. Atherton, N. M., and Weissman, S. I., *Journal of the American Chemical Society*, Vol. 83, p. 1330, 1961.
20. Crank, J., "The Mathematics of Diffusion," Oxford University Press, 1956.
21. Barrer, R. M., "Diffusion in and Through Solids," Cambridge University Press, 1941.

XV. Liquid Propulsion Systems

A. Advanced Liquid Propulsion Systems

*L. R. Toth, R. S. Weiner, W. H. Tyler, T. A. Groudle,
and R. W. Riebling*

1. Introduction, L. R. Toth

The Advanced Liquid Propulsion Systems (ALPS) program is investigating selected problems generated by spacecraft operational requirements for propulsion systems capable of high inherent reliability, long-term storage in space, multiple start in free fall (zero-gravity), and engine throttling. The solutions proposed to satisfy these requirements are coordinated for practical application in a system.

Periodic reports starting with SPS 37-8, Vol. IV describe the progress of work on the various parts of a specific system. Recent accomplishments are outlined below. These include:

- (1) Continuation of detection of pinholes in aluminum foil and laboratory test results of helium gas migrations.
- (2) Some results of inert fluid flow testing of injector elements formed by liquid sheets.

2. Bladder Development, R. S. Weiner

The lamination of a metal foil into a bladder wall to eliminate gas permeation is one of the methods under

investigation for making propellant expulsion bladders. Current foil production methods do not eliminate the possibility of forming extremely small holes or porous areas during the rolling cycles. Therefore, an effort is being made within the ALPS program to study the

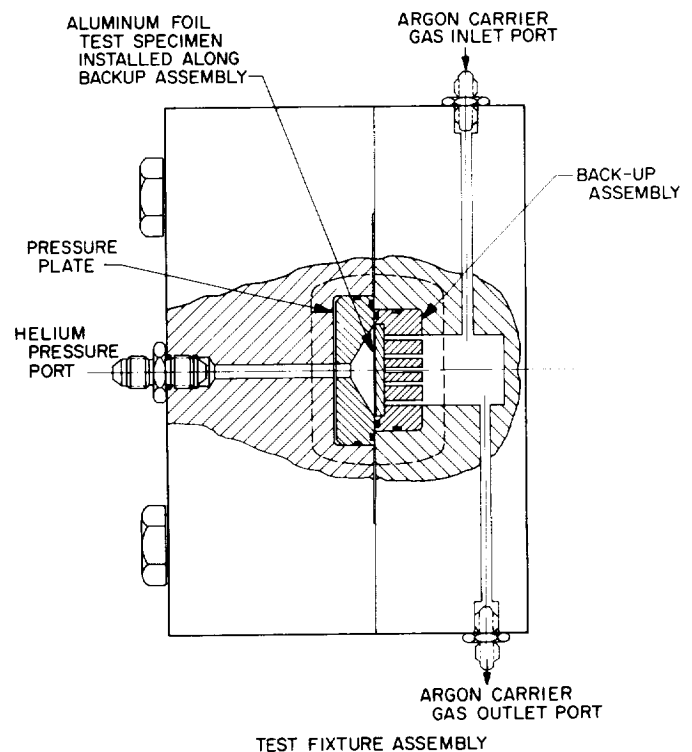


Fig. 1. Fixture for gas migration testing

migration rate of a gas, such as helium, through typical holes that might be found in aluminum foil sheets.

In SPS 37-34, Vol. IV, it was reported that a number of pinholes were detected in the aluminum foil used. The holes were dimensionally checked and the sheets of foil cut up into more convenient sizes for leak testing.

The test philosophy was to attempt to simulate the operational conditions of the bladder; that is, to have a gas (helium, in this case) concentration on one side while maintaining a zero pressure differential across the foil, or test, specimen. The helium migration past the hole is the result of its concentration gradation across the hole. For test purposes, it was decided to substitute argon gas (at a pressure equal to the helium) for propellant and then measure the helium migration rate across the pinhole and into the argon.

The leakage detection instrument was limited to available equipment: either a helium mass spectrometer or a gas chromatograph. The gas chromatograph was selected because of its ability to handle a reasonable flow of the carrier gas. This condition would quickly degrade the mass spectrometer's ionization filament.

The test fixture was designed with helium — the sample gas — supplied to the foil from the top flange and argon — the carrier gas — passed by the foil through the bottom flange (Fig. 1).

The test system was assembled as shown in Fig. 2, using electrical pressure transducers with a counter readout to determine the pressure differential across the pinhole. The sample gas flows from the test fixture through the sampling valve, which is opened and closed

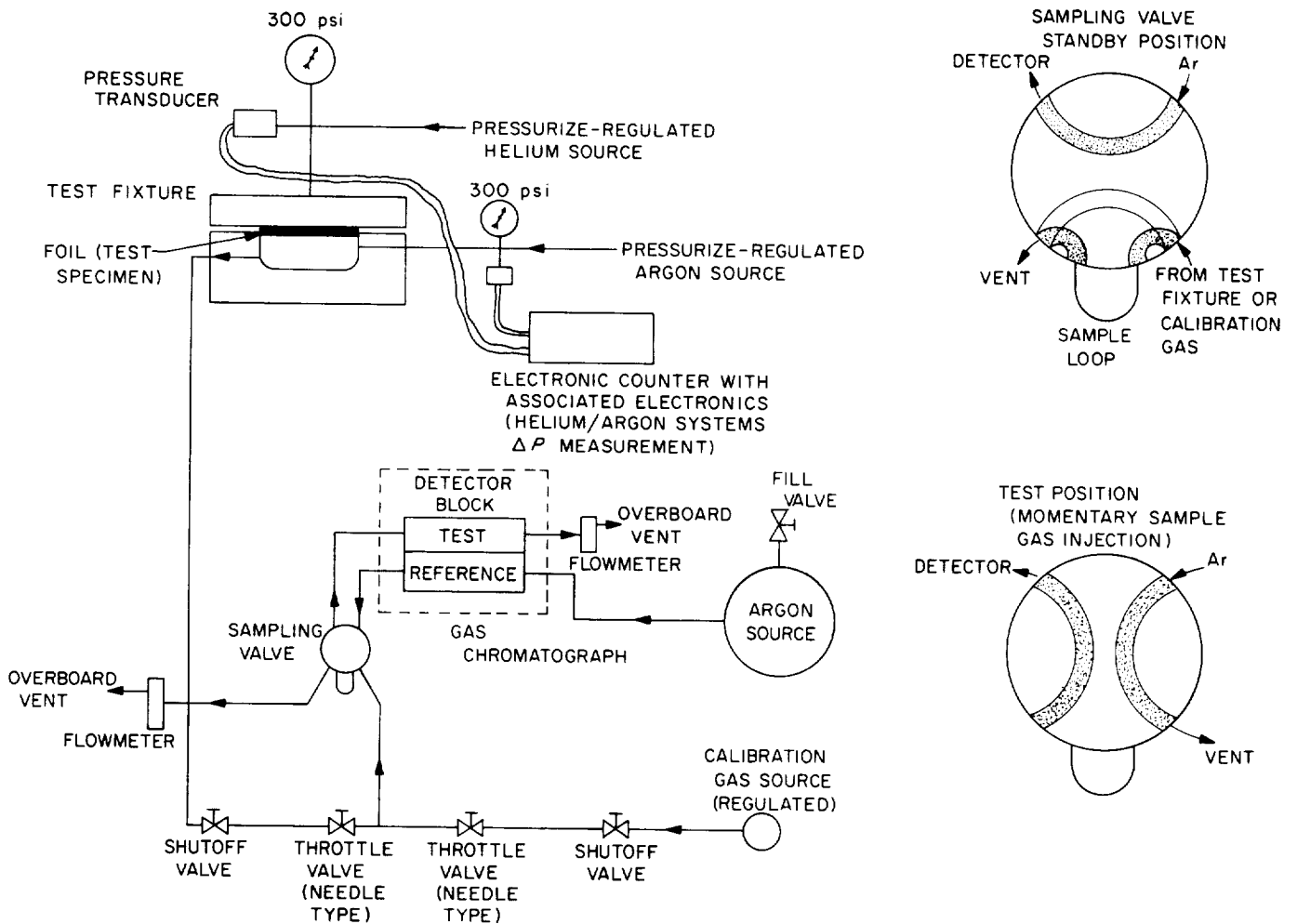


Fig. 2. Gas migration test system

in rapid order to provide the gas chromatograph reaction as a sharp peak readout on a strip-chart recorder. The gas chromatograph is calibrated by means of a premixed reference gas (75% argon and 25% helium) a sample of which was subjected to chemical analysis for mixture mole percent verification.

During actual test conditions the helium and argon systems regulators used were of similar models by the same manufacturer. However, constant hunting of both regulators maintained a cyclic pressure differential across the hole, varying ± 0.5 psi. To date, eight foil test specimens were subjected to the test. Under the conditions stated, the migration of helium through the holes were between 10^{-6} and 10^{-7} (standard) cm^3/sec . The system is being revised to improve the zero pressure differential by eliminating any pressure cycling. The tests will be repeated with the refined system.

3. Refractory Metal Coatings, W. H. Tyler

A refractory metal coatings evaluation test program was recently conducted in support of a NASA Advanced Technology contract. The test program described herein evaluated two new protective coatings for refractory metals. These materials are intended to be used in liquid propellant rocket thrust chambers and were produced by IIT Research Institute (IITRI) under Contract NAS 7-113 and NAS 7-431.

The IITRI-developed materials to be tested were supplied in the form of nozzle throat inserts typical of the type used in small ablative thrust chamber designs. Nozzle insert assemblies were then prepared. These assemblies contain the IITRI test insert with a molded-graphite structural and thermal support which was wedged into two molded pieces of silica fabric and phenolic resin material. These parts were glued together and then overwrapped with fiberglass. This overwrapped assembly was slipped into a steel retainer for mounting against the water-cooled combustion chamber. The test nozzle insert assembly was clamped to a water-cooled chamber section and test injector assembly as shown in Fig. 3.

The injector used in this test program, designated the ALPS Mod. IV, has been characterized in terms of propellant mass, mixture ratio, and chamber wall heat flux distributions. This injector is known to provide a fuel-rich gas at the combustion chamber wall, and has given reproducible test results in firings with pyrolytic graphite and ablative thrust chambers. A description of

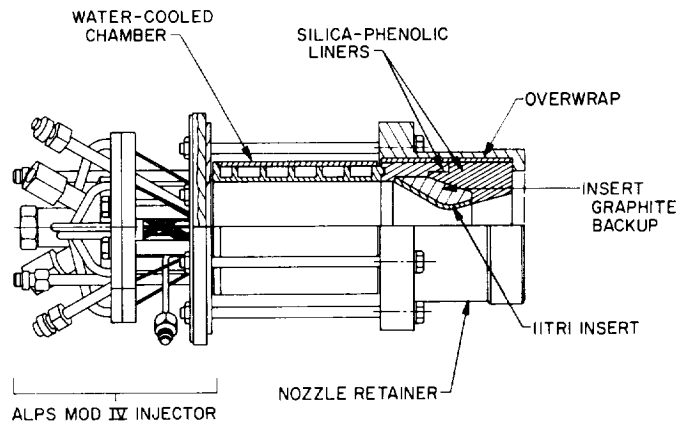


Fig. 3. Engine assembly, IITRI insert test

the injector design, its characteristic data, and the results of previous pyrolytic graphite and ablative thrust chamber firings may be found in Refs. 1 and 2.

Initial insert-evaluation tests were conducted with reduced combustion gas temperatures, followed by increased gas temperature testing of the inserts that successfully passed the lower temperature tests. To obtain the reduced test gas temperature of about 3500°F , the injector was tested with hydrazine and nitrogen tetroxide at a mixture ratio (\dot{w}_o/\dot{w}_f) of 0.8, and with a 15% by weight water diluent added to the fuel. For the increased gas temperature of about 4000°F , the injector was tested with neat hydrazine and nitrogen tetroxide at a mixture ratio of 0.83.

Obtaining an accurate estimate of driving gas temperature, and therefore wall temperature, is exceedingly difficult for these buried-nozzle configurations. Thus an average gas temperature was calculated, based on the assumption that adiabatic flame temperature T_c is proportional to the square of the ratio of the experimental characteristic exhaust velocity to the theoretical characteristic exhaust velocity, i.e.,

$$T_{c, test} = T_{c, theo} \left(\frac{C_{test}^*}{C_{theo}^*} \right)^2$$

A total of 20 tests were conducted. This total includes both heavy-weight molybdenum-nozzle checkout tests, and tests of the two IITRI insert assemblies. One insert was a plasma-sprayed hafnium oxide-graded composite on a tungsten base, and the other was a hafnium-tantalum-clad tungsten-tantalum alloy.

Each of the inserts tested accumulated over 17 min. of firing time at the reduced gas temperature (3500°F) with little or no change of throat diameter. For these

Table 1. Results of firing tests of IITRI nozzle inserts

Type of insert	Test duration, sec	$P_{c, eff}$, psia	\dot{w}_o/\dot{w}_f	c^*_{test} (ft/sec)	$T_{c, test}$ °F
Plasma-sprayed hafnium oxide-graded composite insert	10	116	0.80	4800	3250
	10	116	0.79	4960	3450
	10	116	0.80	4980	3500
	1000	116	0.80	4978	3490
	10	122	0.76	5320	3760
	10	129	0.83	5413	3990
	967	129	0.83	5390	3950
Hafnium-tantalum-clad Tungsten insert	10	123 ^a (estimated)	0.79	—	—
	15	123 ^a (estimated)	0.80	—	—
	1020	123	0.79	5025	3550
	10	134	0.83	5435	4025
	950	139 to 136	0.84	5468	4055

^a Chamber pressure transducer failure.

tests, the chamber pressure records were flat during the run, indicating no erosion had occurred.

The same two inserts were then tested at the higher gas temperatures (4000°F). The plasma-sprayed graded-composite survived two 10-sec tests with little or no adverse effects, but started to erode significantly after 950 sec of a continuous firing, with complete burn-through occurring 17 sec later. The hafnium-tantalum-clad material gave about the same results when it was fired with the 4000°F gas temperature conditions. It was not affected by a 10-sec test, but started to erode slowly after 810 sec of continuous firing with more rapid erosion

starting after 850 sec and insert burn-through occurring after 935 sec of test time.

Results of the test firings are presented in Table 1. Plots of chamber pressure as a function of run time for the long duration, 4000°F gas temperature tests for each insert are shown in Figs. 4 and 5.

Fig. 6 shows the post-test appearance of the hafnium-tantalum-clad insert after the long-duration 4000°F gas temperature test. The view is looking into the insert assembly from the chamber end. The plasma-sprayed hafnium oxide-graded composite insert is shown in Fig. 7

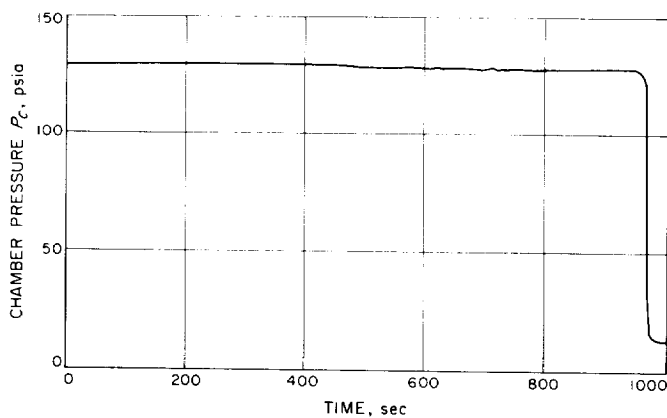


Fig. 4. Chamber pressure during the high-temperature test of the plasma-sprayed graded-composite insert

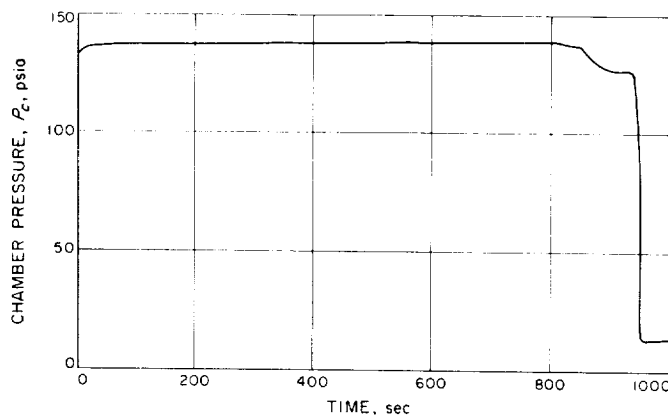


Fig. 5. Chamber pressure during the high-temperature test of the hafnium-tantalum-clad insert

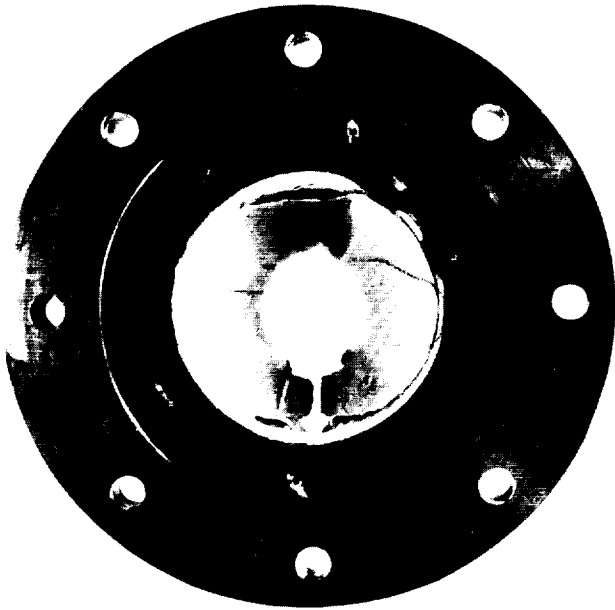


Fig. 6. Nozzle throat after high-temperature test of hafnium-tantalum-clad insert



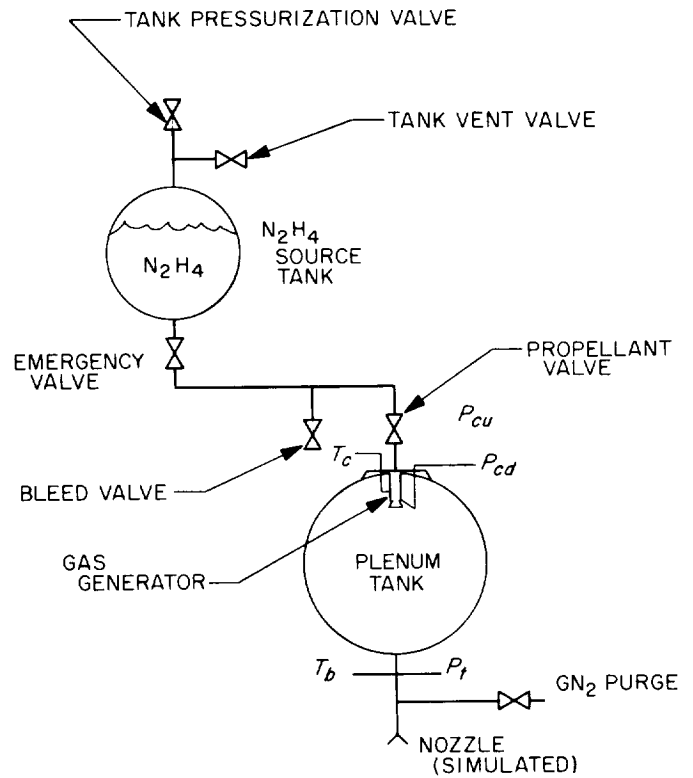
Fig. 7. Nozzle throat after high-temperature test of plasma hafnium-oxide-graded composite

after its long-duration high-temperature test. This test was terminated before the insert backup material had been burned away as badly as the clad insert shown in Fig. 6; however, the insert itself had burned through in several places as shown (Fig. 7).

The inserts have been returned to IITRI for metallurgical examination and analysis of the firing test effects. The results of this work will be published by IITRI in a final report for their NASA contract (NAS 7-113).

4. Reaction Control Gas Supply, T. A. Grouble

During the past several months, a program of development and testing of a gas generator attitude-control system on a breadboard scale has been in progress. A



- T_c GENERATOR CHAMBER TEMPERATURE
- T_g GAS TEMPERATURE
- P_{cd} GENERATOR CHAMBER PRESSURE (DOWNSTREAM)
- P_{cu} GENERATOR CHAMBER PRESSURE (UPSTREAM)
- P_f PLENUM TANK PRESSURE

Fig. 8. Warm gas system schematic

small 0.5-lbf equivalent thrust monopropellant-hydrazine gas generator, with spontaneous catalyst employed for propellant ignition and decomposition, is used as the gas source. The generator is installed in a plenum tank which acts as an accumulator for the gas products (Fig. 8).

The technique of applying gas products as the working fluid for this type of device is not unique. This type system could have a significant advantage for use on large spacecraft for interplanetary exploration. The primary advantage over a more conventional attitude-control system, such as a cold gas system of equal total impulse capability, is the low total system weight. A weight savings of as much as 50% of that of a cold gas system is possible by the use of the energy source stored as a liquid rather than as a gas. Other advantages are: (1) a relatively high specific impulse, if used at gas out-

let temperatures above 100° F, (2) simplicity of design, and (3) a compatible, clean gas at a relatively low temperature.

Fig. 9 illustrates the configuration of the gas generator reactor (Ref. 3). The principal components are: propellant valve,¹ injector head, generator chamber, and nozzle plate. The chamber is filled with Shell 405 catalyst² of 20-mesh size. The generator is installed in a plenum tank of 15-in. D (Fig. 10). The generator-tank mounting plate has fittings attached to permit the two chamber pressures and one chamber temperature to be monitored remotely. The fitting in the outlet of the tank has provisions for the attachment of a temperature probe for measuring gas

¹Eckel Valve Company, Van Nuys, California.

²Shell Development Company, Emeryville, California.

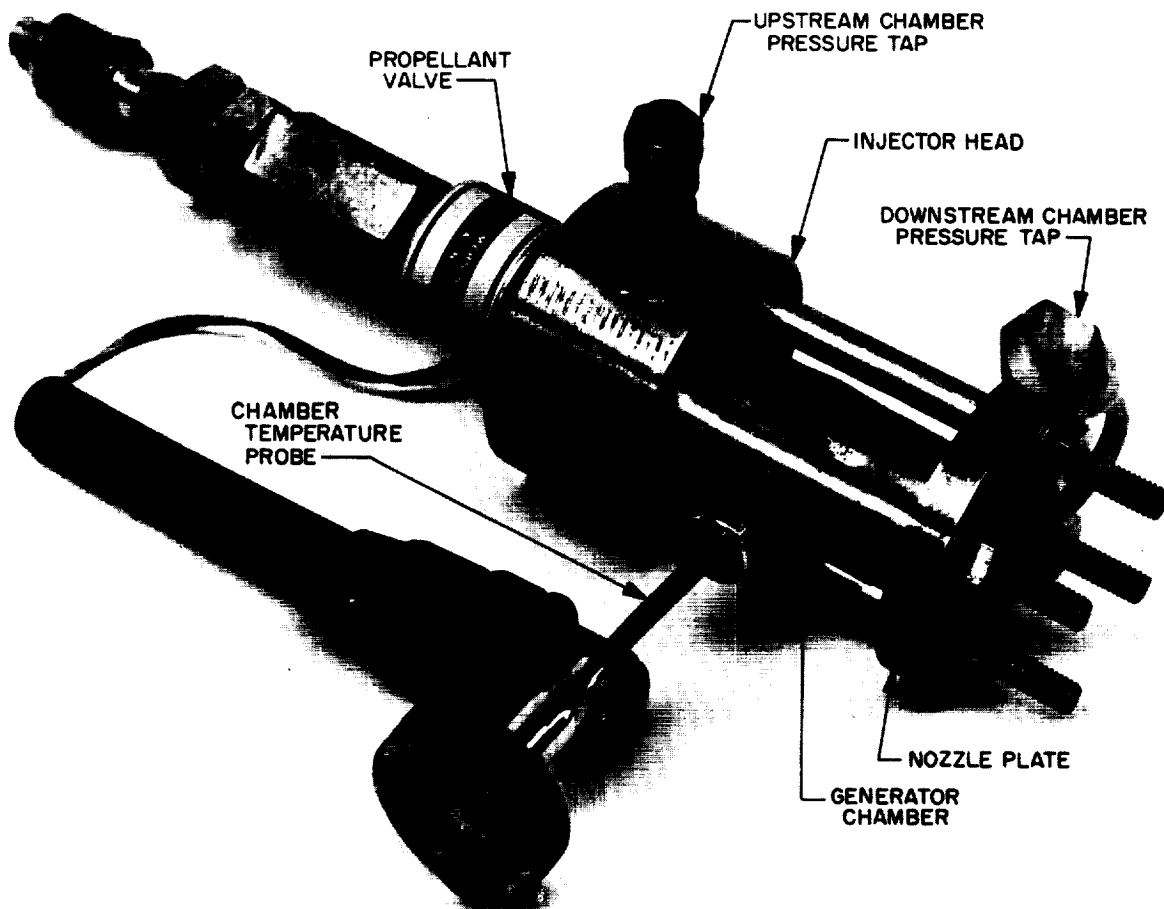


Fig. 9. Gas generator

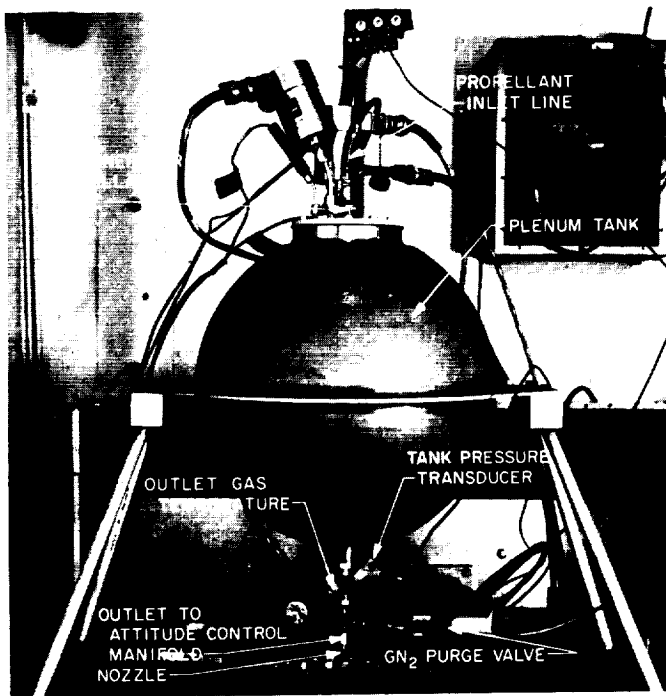


Fig. 10. Warm gas system configuration

outlet temperature, and a pressure transducer which was used as a modified pressure switch to operate the propellant valve. Thus, the gas generator operates intermittently to maintain the pressure in the plenum tank within a preselected bandwidth. A nozzle of 0.028-in. D was attached to the bottom of the fitting on the outlet in order to maintain a flow rate similar to that of an attitude-control nozzle (0.002 lbm/sec).

The sequence of the system operation is as follows (Fig. 8): The plenum tank pressure is initially at 1 atm. Opening of the propellant valve causes fuel to flow, and operation of the gas generator increases the tank pressure to approximately 15 psig. At this time, the modified pressure transducer causes power to be removed from the propellant valve, terminating fuel flow. When the plenum tank pressure decays to approximately 13 psig, the pressure transducer causes power to be applied to the propellant valve, and the gas generator again operates. The cycle is repeated for the desired number of times. The plenum tank was purged with gaseous nitrogen before each test to preclude the formation of a potentially explosive hydrogen-oxygen mixture in the tank during initial gas generator operation. This mixture would have resulted from the presence of air (oxygen) in the tank together with hydrogen, a hydrazine decomposition product. The nitrogen purge pressure is vented to atmospheric pressure just before ignition.

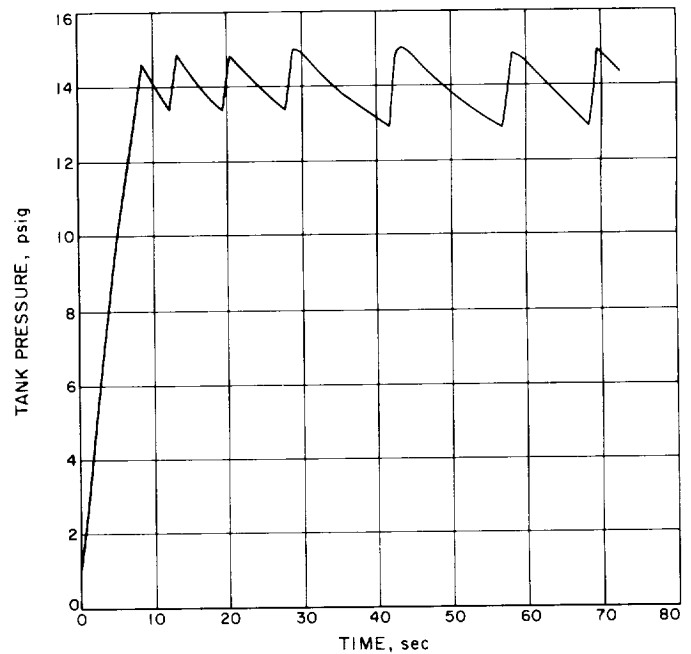


Fig. 11. Plenum tank pressure as a function of time

Several tests of the system configuration described above have been performed and operation of the system has been very good. Fig. 11 is a graph of the plenum tank pressure as a function of time. The set pressure for the modified pressure transducer was 15 psig. It is evident from Fig. 11 that the gas generator responds well to the demand placed upon it. The upper limit was 15.0 psig, and the lower limit was 13.0 psig, resulting in a deadband of 2.0 psi. The gas generator pulse width in this series of tests was approximately 600 msec. Since this system is fundamentally a pulse mode device, the steady-state operation has not been developed to date.

As illustrated in Fig. 12, these tests have shown that the gas outlet temperature is low (less than 100°F) and well within the state-of-the-art attitude-control hardware capability. However, this system had a great deal of thermal mass which would provide a convenient sink for most of the heat in the gas to dissipate to the tank walls and surrounding areas.

After the initial tests of the gas generation system were completed, a *Ranger* Block III attitude-control system valve package was joined to the outlet of the plenum tank. Because of the sensitivity of the attitude-control system to solid particle contamination, a 5- μ filter was installed immediately downstream of the tank outlet in order to deliver a relatively clean gas to the thrusters. As a precautionary measure, a 2- μ filter was installed upstream of the thruster manifold inlet.

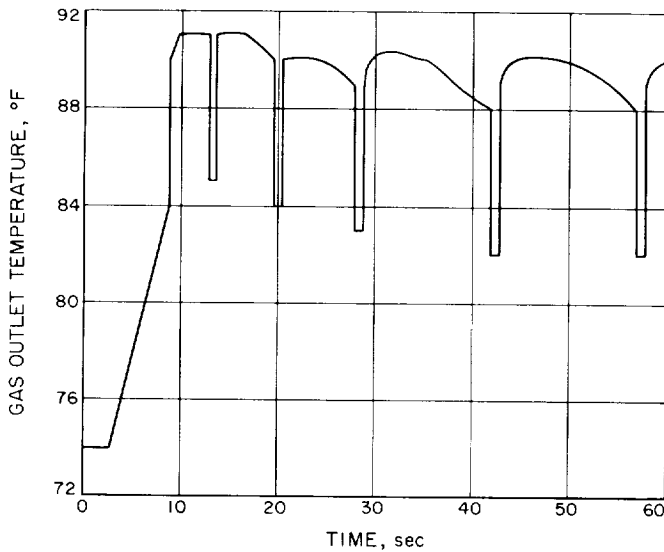


Fig. 12. Plenum tank gas outlet temperature as a function of time

A firing of approximately 4-min duration (28 cycles) was conducted while maintaining two thrusters in the open position. The gas generator cycle pulse widths were of about 600-msec duration. The cold bed ignition delay³ was approximately 350 msec. After this test was completed, the filters were removed and examined. The 5- μ filter was quite dirty with particles up to 250 μ in size being present. Most particles analyzed were found to be catalyst fines from the generator bed. The 2- μ filter was clean, however.

The total system operation was very encouraging. More test firings will be made at various propellant flow rates.

5. Injector Development Program, R. W. Riebling

a. Introduction. Although impinging-jet elements (both like and unlike) have been used for many years in liquid bipropellant rocket engine injectors, they exhibit a number of disadvantages. Precise and reproducible alignment of the impinging-jets is often difficult, and the resultant combustion efficiency may be strongly dependent on the physical size of the elements and the stream energy available for mixing. In addition, for extremely reactive storable propellants such as nitrogen tetroxide (N_2O_4) and hydrazine (N_2H_4), chemical reaction may occur at the liquid interface and disrupt the streams before effective propellant mixing has occurred (Ref. 4). In the light

³Defined as the elapsed time from the propellant valve open to rise of chamber pressure.

of these inherent disadvantages, considerable attention at this Laboratory has recently been devoted to injector designs incorporating flat sheets of propellant, rather than the conventional round jets. In this type of injector element, a thin, flat propellant sheet is formed by directing a jet of liquid from an orifice against a solid, curved deflector surface. One application of these flowing sheets to practical injector design is the so-called "cup-and-plug" injector (SPS 37-31, Vol. IV, p. 203), a concept similar to a showerhead injector, except that the individual propellant streams are flattened into thin sheets to provide increased surface area.

Another application is the impinging-sheet unlike doublet injector (SPS 37-35, Vol. IV, p. 152), one advantage of which is its relative insensitivity to misimpingement due to manufacturing tolerances. The latter injector element is shown schematically in Fig. 13. Both element types also provide a degree of film cooling to the injector face.

Different physical processes govern the magnitude and relative uniformity of propellant mixing, atomization and vaporization (the key spray parameters influencing combustion efficiency) in the cup-and-plug and the unlike impinging-sheet injector. However, intelligent design of either type is predicated upon, although not necessarily limited to, a knowledge of the manner in which three

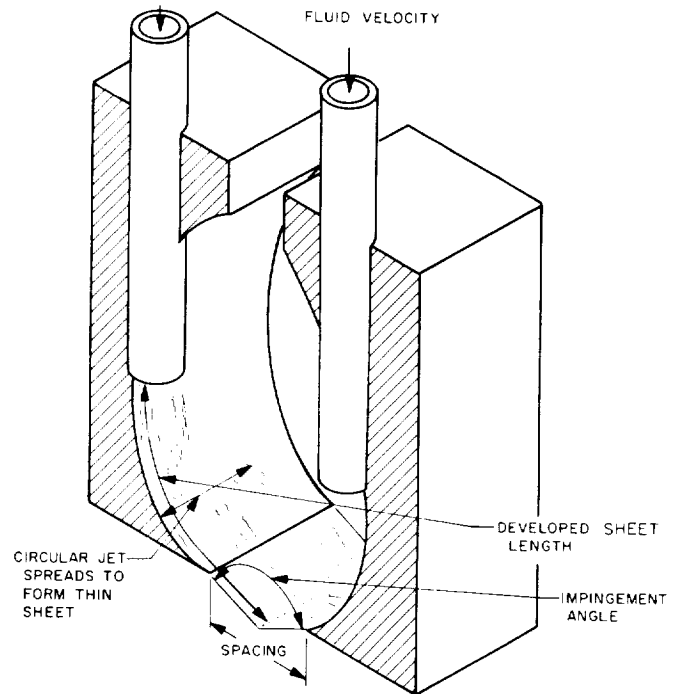


Fig. 13. Unlike-impinging sheet injector element

key sheet parameters vary with deflector geometry, and with the velocity and physical properties of the propellant. These parameters are:

- (1) The dimensions of the free-flowing sheets.
- (2) The spatial orientation of the free sheets with respect to the deflectors.
- (3) The mass flux distribution within a flowing sheet.

Accordingly, a detailed experimental program having as its objective the definition of these effects is currently in progress, and some preliminary results will be presented here. Some very early results appeared in *SPS 37-36*, Vol. II, p. 42.

b. Apparatus and procedures. The experimental apparatus is shown schematically in Fig. 14. Cylindrical deflector surfaces of radius R and included angle θ were machined into aluminum blocks and polished to a high degree of surface finish. Deflector radii ranging between 0.10 and 0.70 in., and deflector angles of 15, 20, 30, and 45 deg were investigated. Jets of water and trichlorethylene (simulating hydrazine and nitrogen tetroxide) were introduced tangentially onto the deflectors through carefully deburred, 0.5 in.-long orifices with diameters d_o of 0.020, 0.030 and 0.040 in. Fluid velocities of 65, 91, and 129 ft/sec for water, and 50, 91, and 124 ft/sec for trichlorethylene, were employed. The corresponding range of Reynolds numbers was from 1.0×10^3 to 7.4×10^3 , based on the orifice diameters.

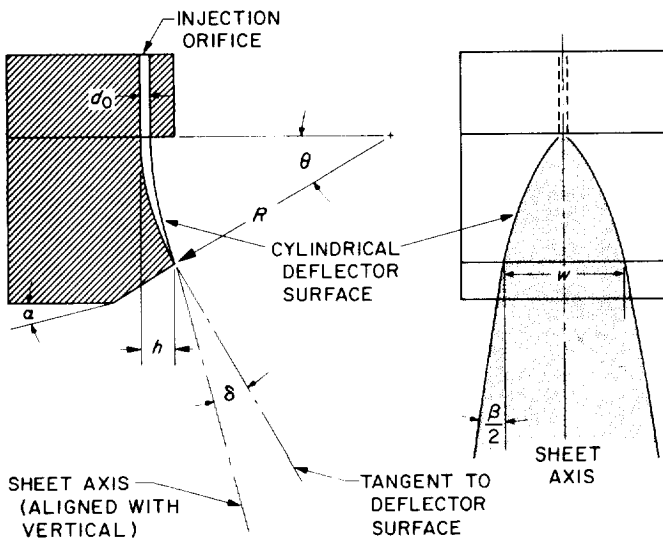


Fig. 14. Experimental apparatus

At these injection velocities (on the order of those employed in typical liquid rocket engine injectors), the jets issuing from the orifices turn on the deflector surface and form a thin liquid sheet of width w (Fig. 14). Upon leaving the deflectors, the free sheets spread through an angle β before finally breaking up into droplets. In general the sheets do not exit tangentially, however. Rather, the axes of the sheets are deflected through the angle δ away from the tangents to the deflector surfaces, as shown schematically in Fig. 14.

The sheet width w and the spreading angle β were measured from high-speed photographs (like those shown on p. 168) made with synchronized-pulse lighting. The lens axis was orthogonal (± 5 deg) to the sheet axis in each case.

The sheet deflection angle δ was measured *in situ* to within about ± 1 deg, as follows. Upon rotation of the entire apparatus, the axis of the flowing sheet (defined as the angle bisector of the sheet as seen edge-on, Fig. 15) was aligned with the vertical by optical techniques. The angle α (Fig. 15) between the bottom surface of the block and the horizontal was then measured, and the deflection angle δ was found from the relation

$$\delta = \theta - \alpha \quad (1)$$

A total of 145 tests have been conducted to date, 97 with water as the working fluid, and 48 with trichlorethylene.

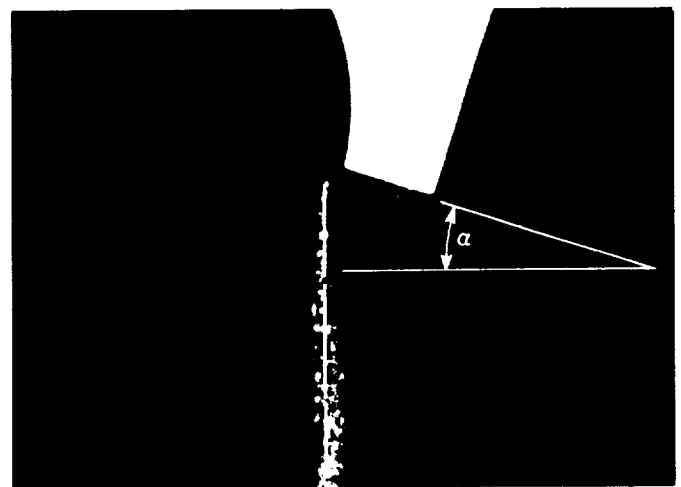


Fig. 15. Typical side view of flowing sheet, showing method of determining the deflection angle. Note nontangential exit of sheet from deflector

c. Preliminary findings. Although data reduction and analysis are still in progress, some preliminary correlations are reported here. These correlations represent convenient ways in which to present the data collected thus far, and are useful for indicating general trends. However, no attempt should be made to scale the data to other geometries, velocities, or fluids, until the results of additional experiments and a more complete analysis are available. It is hoped that these empirical equations may ultimately be related to fluid dynamics theory, in order to present the correlations in terms of the more familiar parameters commonly used in hydraulics practice, such as Reynolds or Weber numbers. Indeed, the use of these and other force ratios in the correlations appears to hold some promise, provided that the proper forces are considered. Meanwhile, the wholly empirical correlations are presented so that those interested may use the experimental data in a convenient form.

d. Sheet dimensions and orientation. The best empirical method for correlating the sheet width data was found to be a plot of w/d_o versus R/d_o on logarithmic coordinates at constant velocity. (Again refer to Fig. 14 for identification of these and following terms.) An example is presented in Fig. 16 for water at $V = 129$ ft/sec. Typically, a family of lines (one line for each value of θ) of slope = $\frac{1}{2}$ resulted at each velocity. The w/d_o intercepts were then plotted against the corresponding values of θ for each fluid and velocity, as shown in Fig.

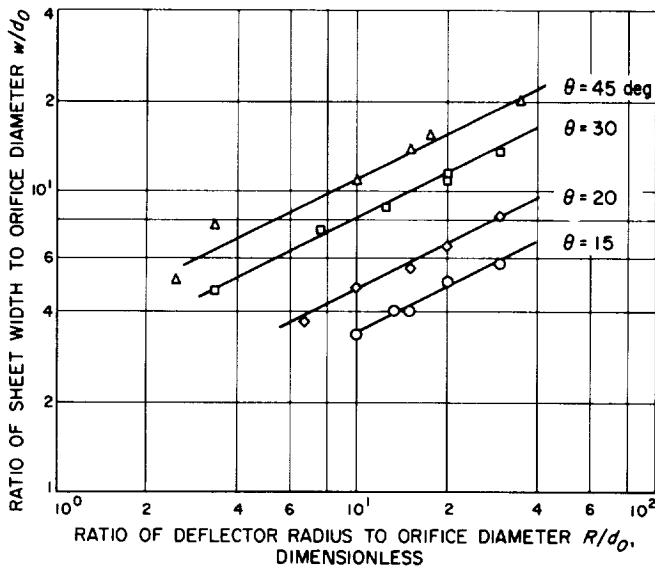


Fig. 16. Variation of dimensionless sheet width parameter with deflector and orifice geometry for water at 129 ft/sec

17 for water. By this procedure, the following correlating equations were determined for water:

$$\frac{w}{d_o} = 0.068\theta \left(\frac{R}{d_o}\right)^{0.5}, \quad V = 65 \text{ ft/sec} \quad (2)$$

$$\frac{w}{d_o} = 0.071\theta \left(\frac{R}{d_o}\right)^{0.5}, \quad V = 91 \text{ ft/sec} \quad (3)$$

$$\frac{w}{d_o} = 0.075\theta \left(\frac{R}{d_o}\right)^{0.5}, \quad V = 129 \text{ ft/sec} \quad (4)$$

From the above three equations, it is seen that w/d_o is directly proportional to the deflector angle θ , the

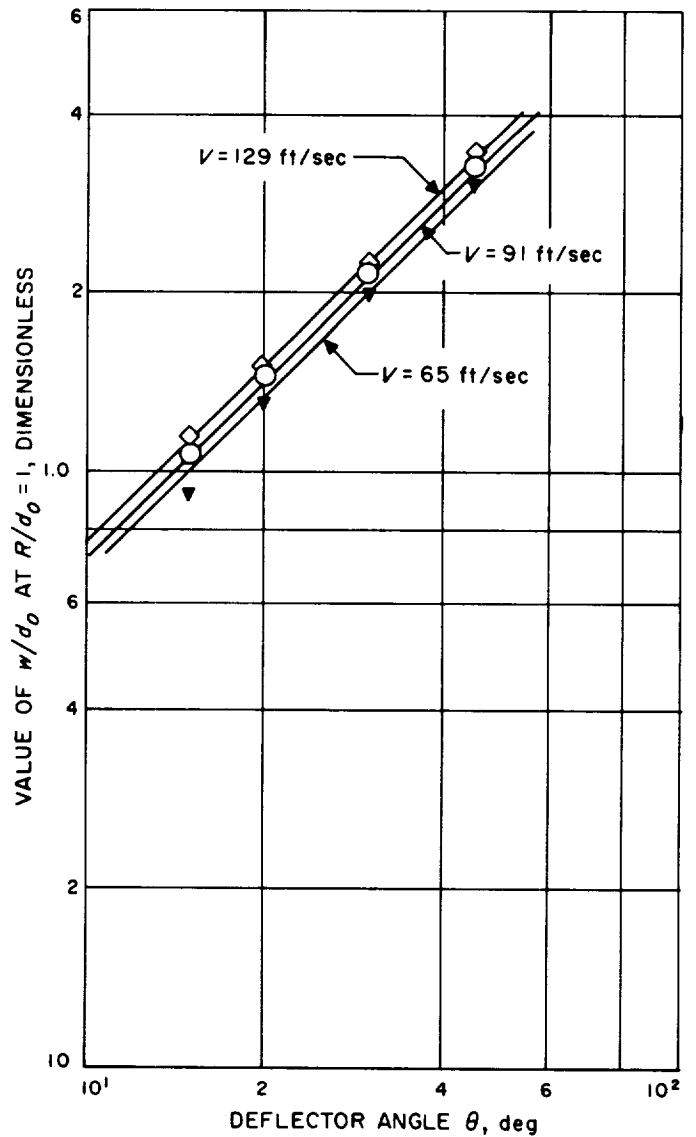


Fig. 17. Effects of deflector angle and injection velocity on width-parameter intercept for water

square root of the ratio R/d_o , and a coefficient which appears to be a weak function of the velocity. Although a single line might well have been drawn through all the data points on Fig. 17, a variation of the coefficient c with velocity V of the form

$$c = a(1 + \epsilon V) \tag{5}$$

was arbitrarily assumed. The final correlating equation was

$$\frac{w}{d_o} = 0.0615 [1 + (1.58 \times 10^{-3})(V)] \theta \left(\frac{R}{d_o}\right)^{0.5} \tag{6}$$

Similarly, for trichlorethylene

$$\frac{w}{d_o} = 0.0375 \theta^{1.172} \left(\frac{R}{d_o}\right)^{0.5}, \quad V = 50 \text{ ft/sec} \tag{7}$$

$$\frac{w}{d_o} = 0.041 \theta^{1.172} \left(\frac{R}{d_o}\right)^{0.5}, \quad V = 91 \text{ ft/sec} \tag{8}$$

$$\frac{w}{d_o} = 0.045 \theta^{1.172} \left(\frac{R}{d_o}\right)^{0.5}, \quad V = 124 \text{ ft/sec} \tag{9}$$

Again, assumption of a relation of the form of Eq. (5) for the variation of the coefficient with velocity resulted in the following general equation for trichlorethylene:

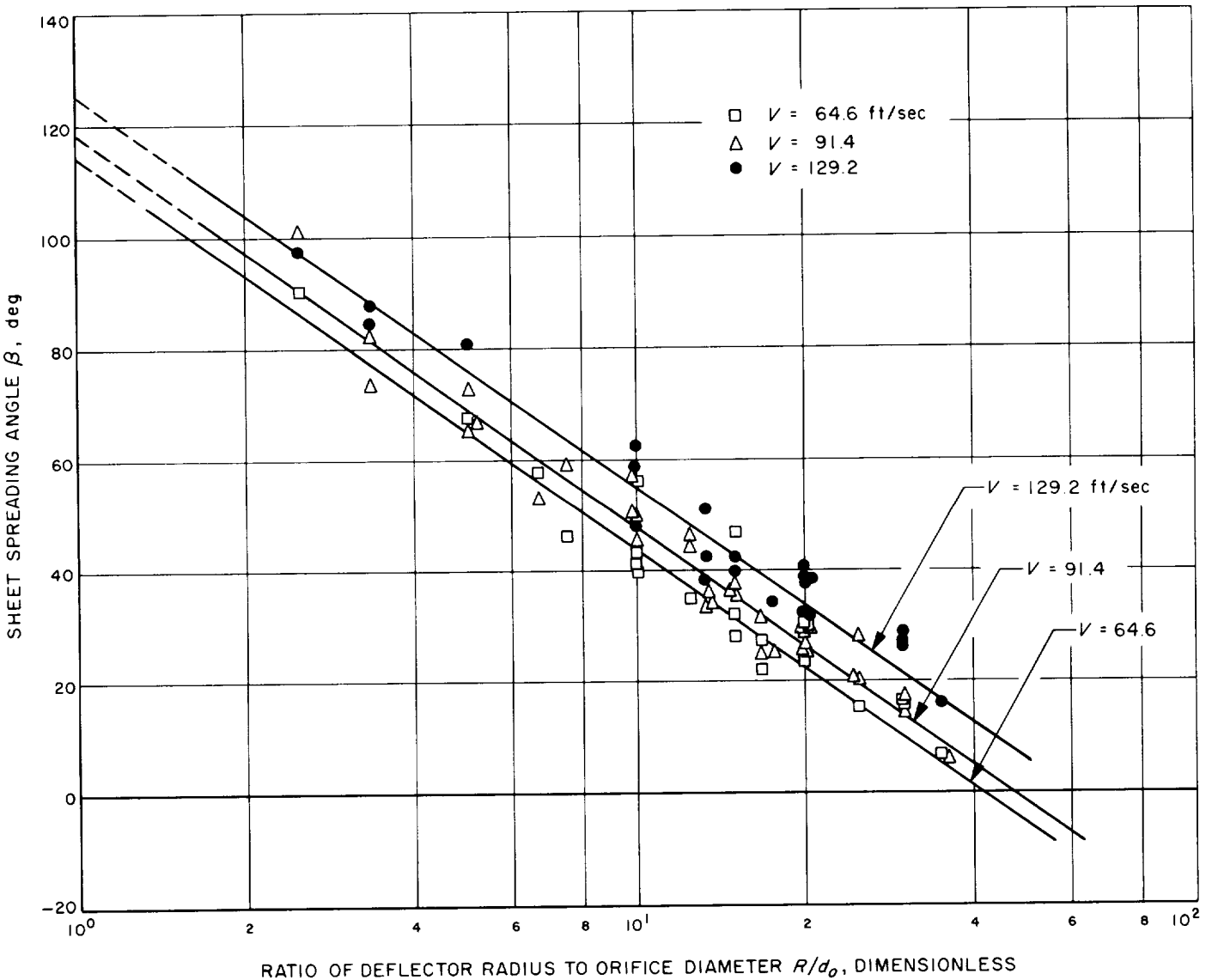


Fig. 18. Effects of deflector geometry and injection velocity on sheet spreading for water

$$\frac{w}{d_o} = 0.0324 [1 + (3.12 \times 10^{-3}) (V)] \theta^{1.172} \left(\frac{R}{d_o}\right)^{0.5} \quad (10)$$

Eqs. (6) and (10) differ in their coefficients and in the exponent of θ . It is quite possible that these may depend upon fluid physical properties. Studies with a third fluid are in progress to define these effects.

The spreading angle β depends upon deflector geometry, injection velocity, and fluid physical properties. The best method of correlating the sheet spreading angle data for each fluid was found to be a plot of β versus $\ln(R/d_o)$ at constant velocity. The results obtained with water and trichlorethylene at several fluid velocities are summarized in Figs. 18 and 19, respectively. The use of a semilogarithmic coordinate system can accommodate negative values of β which may be encountered under certain conditions (which follow). For both fluids the injection velocity apparently exerts a small but not quite negligible effect on the value of β at constant (R/d_o) . There were no nonrandom variations of β with θ or d_o .

The following empirical correlations were found for water:

$$\beta = 125 - 30.7 \ln\left(\frac{R}{d_o}\right), \quad V = 129 \text{ ft/sec} \quad (11)$$

$$\beta = 119 - 30.7 \ln\left(\frac{R}{d_o}\right), \quad V = 91 \text{ ft/sec} \quad (12)$$

$$\beta = 115 - 30.7 \ln\left(\frac{R}{d_o}\right), \quad V = 65 \text{ ft/sec} \quad (13)$$

The three equations above are seen to be of the form

$$\beta = a - b \ln\left(\frac{R}{d_o}\right) \quad (14)$$

where a , the β -intercept, is a weak function of the injection velocity V , and the slope b is constant. For the β -intercept, it was found that

$$a = 105 [1 + (1.49 \times 10^{-3}) V] \quad (15)$$

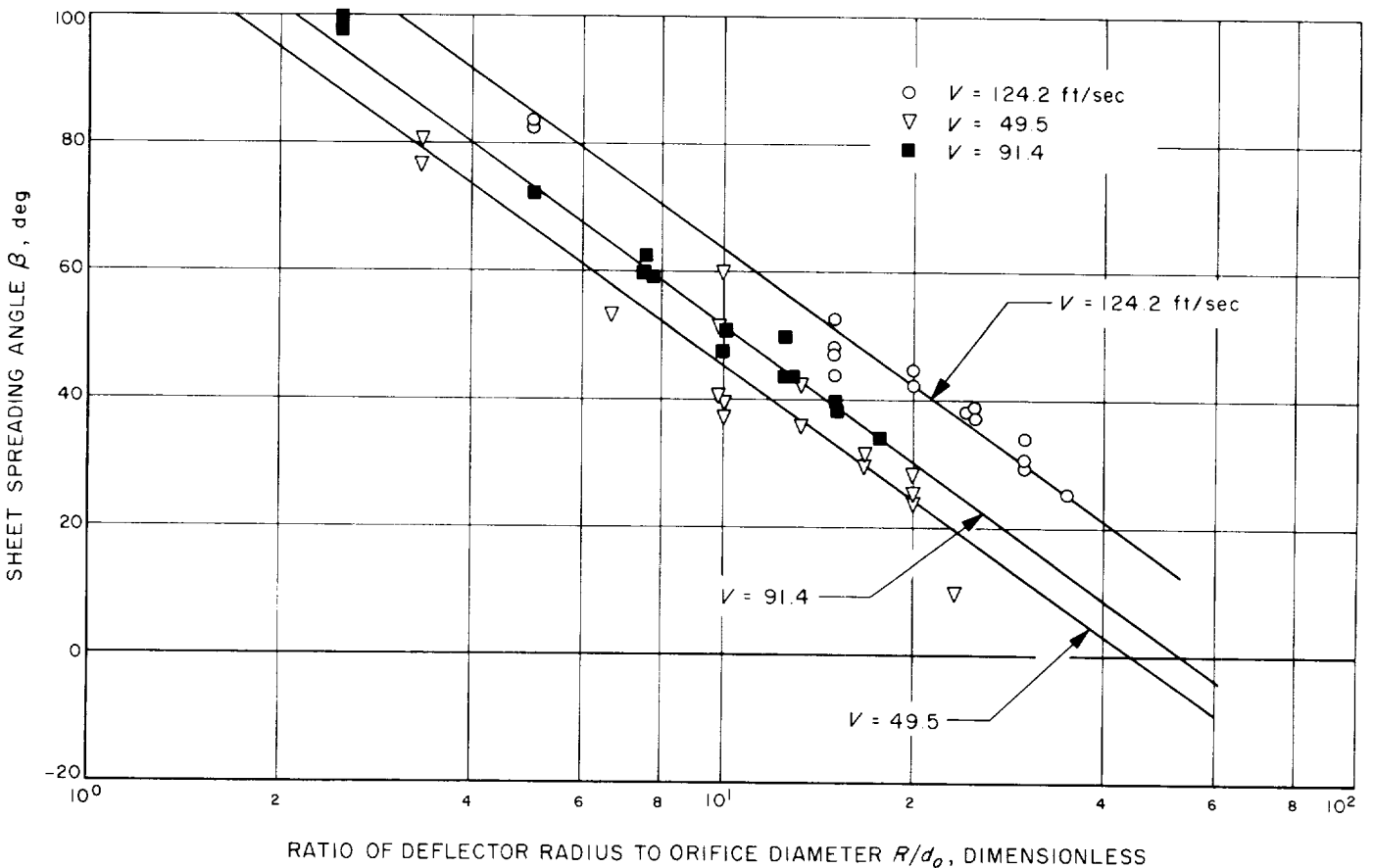


Fig. 19. Effects of deflector geometry and injection velocity on sheet spreading for trichlorethylene

when the units of V are ft/sec. The introduction of Eq. (15) into Eqs. (11), (12), and (13) gives

$$\beta = 105 \left[1 + (1.49 \times 10^{-3}) V \right] - 30.7 \ln \left(\frac{R}{d_o} \right) \quad (16)$$

as a general correlating equation for the water spreading angle.

Similarly, it was found for trichlorethylene that

$$\beta = 134 - 30.7 \ln \left(\frac{R}{d_o} \right), \quad V = 124 \text{ ft/sec} \quad (17)$$

$$\beta = 125 - 30.7 \ln \left(\frac{R}{d_o} \right), \quad V = 91 \text{ ft/sec} \quad (18)$$

$$\beta = 116 - 30.7 \ln \left(\frac{R}{d_o} \right), \quad V = 50 \text{ ft/sec} \quad (19)$$

with the β intercept a being related to velocity by

$$a = 105 \left[1 + (2.34 \times 10^{-3}) V \right] \quad (20)$$

so that

$$\beta = 105 \left[1 + (2.34 \times 10^{-3}) V \right] - 30.7 \ln \left(\frac{R}{d_o} \right) \quad (21)$$

is a general correlating equation for the trichlorethylene spreading angle.

It is immediately apparent that Eqs. (16) and (21) are identical except for the value of ϵ , which is very likely

dependent upon the fluid physical properties. Experiments with a third liquid are presently being conducted in order to define the physical properties effect and yield, if possible, a single, completely generalized equation for β .

No really good correlations have been found for the deflection angle δ , mainly because random data scatter has made it impossible to discern the effects of the principal variables. One of the better methods was a plot of δ versus $(R/d_o)(1 - \cos \theta)$ on logarithmic coordinates. The results are presented in Fig. 20 for water and in Fig. 21 for trichlorethylene. The abscissa is also equal to the so-called "overhang parameter" h/d_o , that is, the lateral distance h (Fig. 14) to which the deflector protrudes into the otherwise undisturbed circular jet, divided by the orifice diameter. No nonrandom velocity effects could be discerned within the limits of experimental precision over the range of values investigated. The equation of a best-fit line for water is:

$$\delta = 2.8 \left[\frac{R}{d_o} (1 - \cos \theta) \right]^{-2.2}, \quad 65 \leq V \leq 129 \text{ ft/sec} \quad (22)$$

As may be seen from Fig. 21, there is considerably more scatter in the trichlorethylene results, so that no correlating equation as such will even be presented here.

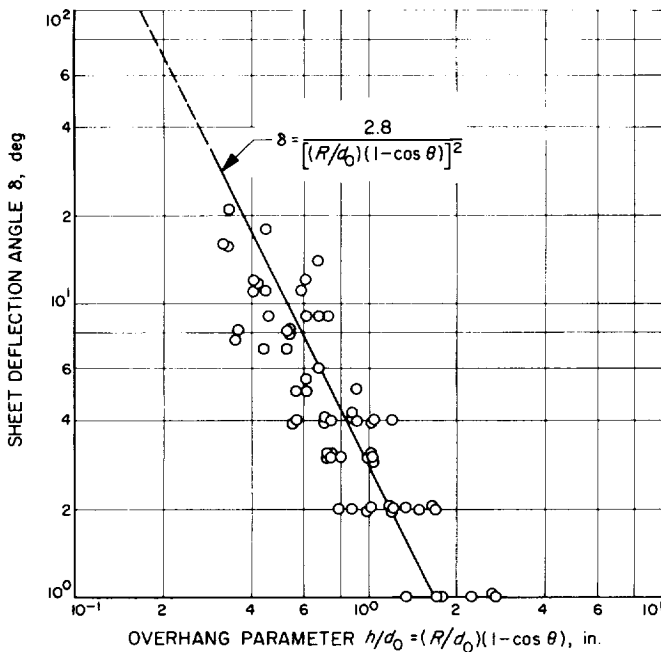


Fig. 20. Sheet deflection angle versus "overhang parameter" for water, $65 < V < 129$ ft/sec

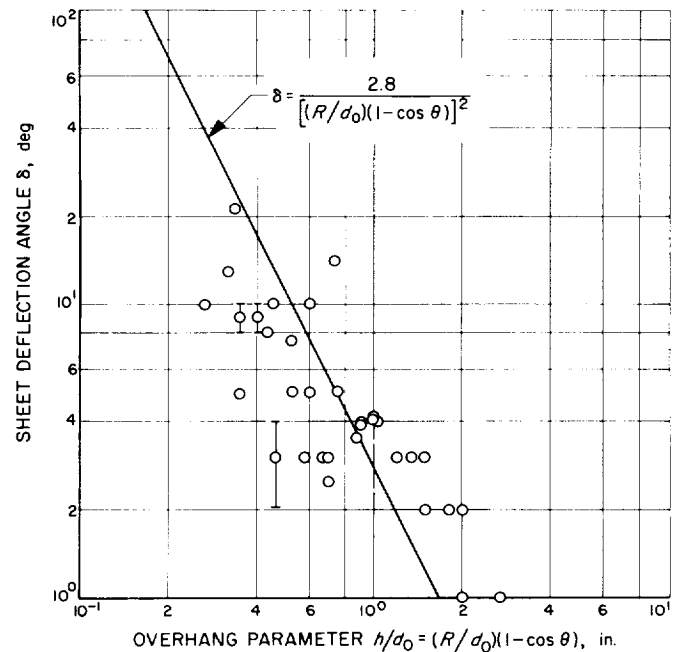


Fig. 21. Sheet deflection angle versus "overhang parameter" for trichlorethylene, $91 < V < 124$ ft/sec

Some general observations are in order, however. First, for both liquids, a distinct trend in the data is noted, and seems to indicate that δ varies mainly with deflector and orifice geometry, e.g., as the inverse square of the overhang. Effects of other variables, such as θ , d_o , V , Re , etc. are not discernible due to the scatter, but are obviously small compared to the influence of the overhang. Second, it is not unlikely that Eq. (22), or one quite similar to it, might also correlate the trichlorethylene data. Finally, it appears that for both liquids the deflection angle δ will be less than 1 deg when the "overhang parameter" h/d_o is greater than about 1.6.

e. Mass distribution within the sheets. That the mass distribution may indeed not be constant across the width of a sheet is indicated by the photographs of Fig. 22, in which are shown the appearances of sheets produced by water at a constant velocity of 65 ft/sec and several values of the ratio of deflector arc length to orifice diameter, L/d_o . (The arc length L is equal to $(\theta\pi R)/180$ when θ is expressed in degrees.) L/d_o has been found to be a convenient geometric parameter in the classification of the flowing sheets in terms of their gross appearance. (Note that the deflectors shown in Fig. 22 do not have identical values of R or θ , however.) Similar results were obtained at other velocities, as well. In general, three distinct flow regimes or regions have been identified. In the first, arbitrarily called region A, the sheet boundaries are not well defined, and the sheet has a ragged or feathered appearance as shown in Fig. 22(a). Mass distribution appears nonuniform, al-

though it is difficult to glean even a qualitative indication of the nature of this distribution from the photographs. Sheets of second or B regime, as in Fig. 22(b), have well-defined, relatively straight boundaries, with an apparently more uniform mass flux distribution, although there does appear to be some mass concentration in the center and in ribs at the edges. In region C, Fig. 22(c), surface tension forces are apparently of roughly the same order of magnitude as inertia and viscous forces, and the sheet boundaries, although still well-defined, may be more sharply curved or, in some cases, pinched in (β may be negative in this case). Most of the mass of the sheet appears to be concentrated in very pronounced ribs at the edges, and holes repeatedly form and propagate in the extremely thin, film-like central portion. An extreme case of region C is shown in Fig. 22(d), where surface tension forces completely dominate all other forces. The sheet breaks up into large ligaments immediately upon leaving the deflector, and large, chunky droplets are produced at the confluence of these ligaments downstream. High negative values of β are typical.

The appearance of trichlorethylene sheets is represented in Fig. 23 at the same values of L/d_o shown in Fig. 22 for water. Figures 22(a) and 23(a) are quite similar. However, Fig. 23(b) does not seem to resemble Fig. 22(b) very strongly, nor does the configuration of Fig. 23(c) correspond too closely to that of Fig. 22(c). Many of the trichlorethylene sheets were seen to shed ligaments, as in Fig. 23(b), an effect not noted with water. Further, although a region C was found for

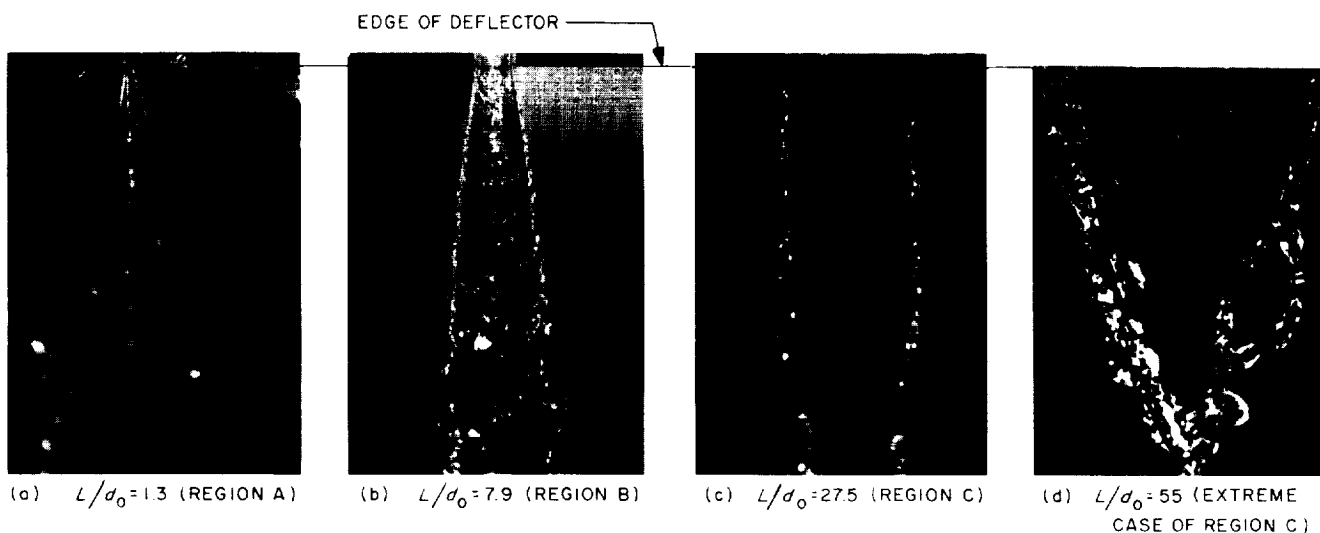


Fig. 22. Variations in sheet configuration with ratio of deflector arc length to orifice diameter for water at a constant velocity of 65 ft/sec

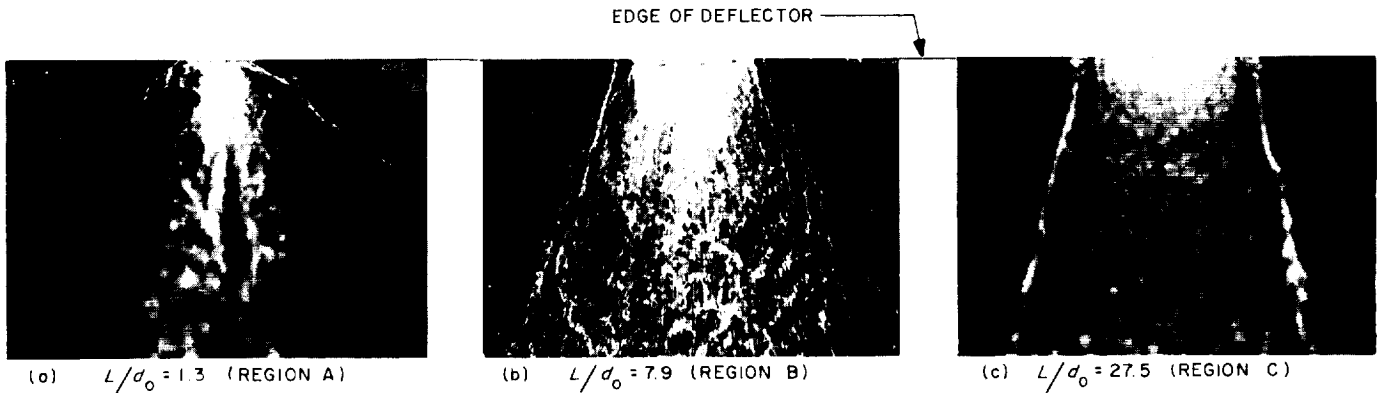


Fig. 23. Variations in sheet configuration with ratio of deflector arc length to orifice diameter for trichlorethylene at a constant velocity of 91 ft/sec

trichlorethylene, it was characterized by the formation of a multiplicity of small holes, giving rise to the lacy appearance shown in Fig. 23(c), as contrasted to the appearance of the region C sheets for water shown in Fig. 22(c). All this suggests that the mass flux distribution within the sheets may well depend upon the particular fluid being used, as well as the geometry and velocities employed.

Although little more can be said about mass distribution in the absence of suitable quantitative measure-

ments, the sheets may be classified into the several categories just described, based on appearance alone.

It is of interest to see the extent of these regions in terms of geometry and fluid velocity. For example, the boundaries of the three regions, based on visual classification of the sheets, are shown for water in Fig. 24 versus L/d_0 and velocity V . The cross-hatched regions indicate those ranges of L/d_0 within which the sheet could be classified into either of the two adjacent regions (i.e., it has some of the characteristic properties

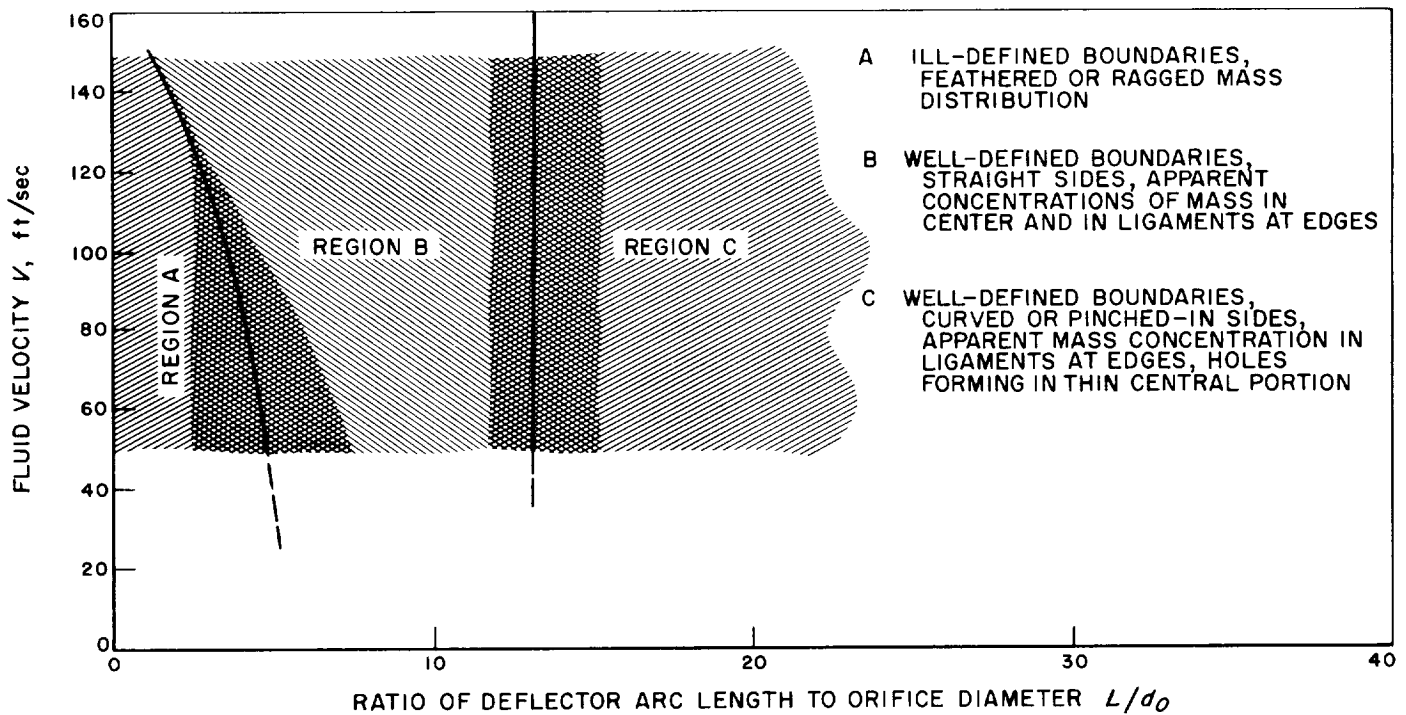


Fig. 24. Effect of fluid velocity and deflector geometry for water, based on photographic observation

of each). Similar regional boundaries were found for trichlorethylene.

By and large, the effect of velocity seems to be small compared to that of L/d_0 , so that L/d_0 alone apparently exerts the major influence on mass distribution. Based

on visual observation of the sheets, it appears as though regions A and C should be avoided in the application of curved deflectors to impinging sheet injector elements. Future work will include quantitative measurements of the mass flux distributions within the flowing sheets for several different liquids.

References

1. Rowley, R. W., and Tyler, W. H., "The Effect of Injector Design on Thrust-Chamber Erosion," Paper No. 65-586, presented at AIAA Propulsion Joint Specialist Conference, U. S. Air Force Academy, Colorado Springs, Colorado, June 14 to 18, 1965.
2. Tyler, W. H., "Thrust Chamber Development," SPS 37-28, Vol. IV, p. 81, Jet Propulsion Laboratory, Pasadena, California, August 31, 1964.
3. Foster, C. R., "Reaction Controls," SPS No. 37-24, Vol. IV, p. 103.
4. Johnson, B. H., "An Experimental Investigation of the Effects of Combustion on the Mixing of Highly Reactive Liquid Propellants," Technical Report No. 32-689, Jet Propulsion Laboratory, Pasadena, California, July 15, 1965.

SPACE SCIENCES DIVISION

XVI. Space Instruments

A. Digitizing TV Data

L. Malling

If a spacecraft sensor is to measure continuous rather than intermittent phenomena, then the output will be a varying DC signal. If, in addition, interest is directed at a space continuum, coordinate sampling must be introduced. Such is the case, for example, with the charge image developed on the surface of a photosensor. Subsequent spacecraft data-handling and ground computations make it generally desirable and convenient to transfer the DC signal into a digital format. If resolution is a critical parameter, as with a TV camera, then onboard digital conversion has particular advantages.

The resolution of a sensor viewed as an analog device is expressible in terms of bandwidth and noise. As noise figures add and bandwidths contract, a complex analog system tends to degrade the signal. On the other hand, the resolution of a digitized sensor signal depends only on the fineness of quantization and the frequency of sampling. With a specified and reasonably high bit-error rate, signal quality is almost independent of the number of serial processes introduced.

This was demonstrated with the pictures obtained from the *Mariner IV* TV camera where the camera signal was digitized directly at the TV camera output. Although followed by potentially high-noise systems that included tape recording with extremely low-speed playback, transmission over a high-noise deep-space link and digitally computed contrast enhancement, the final resolution was almost identical to that achieved directly from the camera itself with Earth-based measurements.

If camera signals are to be digitized, and particularly if, as now proposed, data compression is to be introduced, then the techniques of sampling must receive closer scrutiny.

To permit TV picture synthesis from a small number of samples, the signal may be divided into two groups — slowly varying DC components and fast signal ramps. The DC signal corresponds to average illumination and the ramps to brightness variations created by changes in surface elevation. Such signals may be expressed by polynomials of varying order that require less than an evenly spaced maxima of points to reproduce and are amenable to computer-oriented interpolation techniques.

The ultimate resolution of a TV camera as a systems device is determined by the resultant signal derived from a maximum slope ramp generated by coordinated sampling of the photo-optical image. In the same domain, a maximum resolution ramp is unit impulse contained within Δt , the time scale of a single ΔA picture element. With Nyquist sampling at $2f_c$, where f_c defines the bandwidth, the rise time is thus Δt . The successful transfer of this edge into the encoded digital domain requires adequate fineness of quantization, a minimum of analog noise, and an accurately timed sample.

Assuming that the system capacity or encoding rate is adequate, the quantization may be made as fine as the analog signal-noise will permit, i.e., $\Delta Q = (\bar{e}_n^2)^{1/2}$, where $\Delta Q =$ a single quantized level and \bar{e}_n^2 is the mean squared noise voltage.

The probability that the noise voltage will exceed a voltage v at any given instant

$$P = \frac{1}{\sqrt{2\pi\bar{e}_n^2}} \int_v^\infty e^{-v^2/2\bar{e}_n^2} dv$$

If a ratio r defines the ratio of the instantaneous noise voltage to the rms noise voltage, then $p = 1 - \text{erf } r/\sqrt{2}$, where "erf" is the error function, tabulated in the integral tables as the probability integral. Thus if $r = 1$, $p = 0.3$ so that 30 ΔA elements/100 would have so much additive noise at unity SNR that the digitized resultant would be meaningless. With $r = 1/2$, 60 ΔA elements/100 would be in error. With reduced noise at an SNR of 20 db, 60 ΔA elements would have only a single quantized level inaccuracy, remembering that for this SNR the quantization would be quite coarse. The degradation would be more or less serious, dependent upon the overall contrast ratio. If 6-bit encoding is assumed with $q = 64 \Delta Q$ quantized levels and an SNR = $64/1 = 36$ db, the probability of a ΔA unit being in error by $3\Delta Q$ is $p = 3 \times 10^{-3}$, which means several errors in every line of a 600-line TV picture. If the quantization is allowed to remain at 6 bits but the SNR is improved, the probability of error will decrease accordingly. From this, it would appear that a camera signal of SNR = 40 db, or better, is highly desirable for systems employing data compression. However, even with a greatly improved SNR, because of the finite time required to encode each ΔA element, sampling errors can be introduced that create noise-like disturbances. Typical are the timing errors illustrated in Fig. 1 for a ramp-counter A-D conversion. Clock pulses initiate the count, and the count is terminated when the signal crosses the ramp. When the data is inserted into the digital matrix, the assumption made is that the sampling

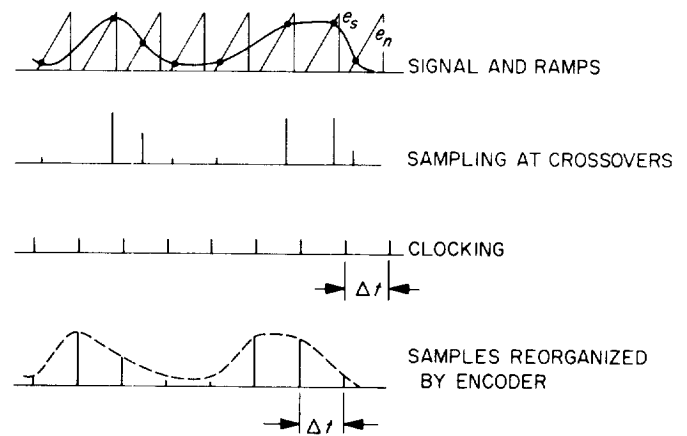


Fig. 1. Sampling errors produced in ramp-counter A-D conversion

intervals are equal. The timing errors are minimized by interposing a sample-and-hold (SH) circuit. The basic SH operation is illustrated in Fig. 2, where the sampling is accomplished with a reed switch that dumps the sampled charge on Capacitor C. A high impedance operational amplifier holds the charge on C and transposes the signal to a high current at low impedance at the output terminals of the amplifier. However, such mechanical switching is much too slow for TV sampling rates.

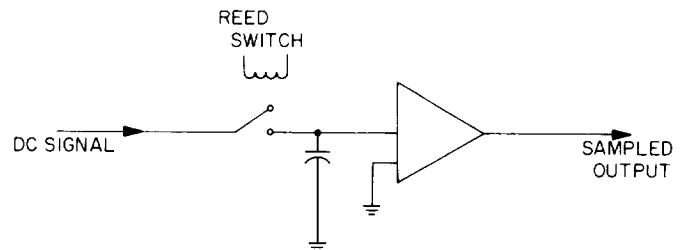


Fig. 2. Sampling using mechanical switch

An SH circuit of particular interest for ΔA sampling is the keyed bilateral bridge (Ref. 1) illustrated in Fig. 3 and sometimes referred to as the diamond circuit (Ref. 2). The bilateral transistor bridge stems from the keyed DC restorer used for television cameras. The input impedance $Z_{in} = (\beta R/2)$, which can be a megohm or more at the sampling instant. The output impedance at the sampling instant is correspondingly low $Z_{out,s} = R/(2\beta)$. During the hold period

$$Z_{out,h} = \frac{E_{cc}}{I_{co1} - I_{co2}}$$

The output impedance on hold may be made extremely high with selected matched transistors. Because of the

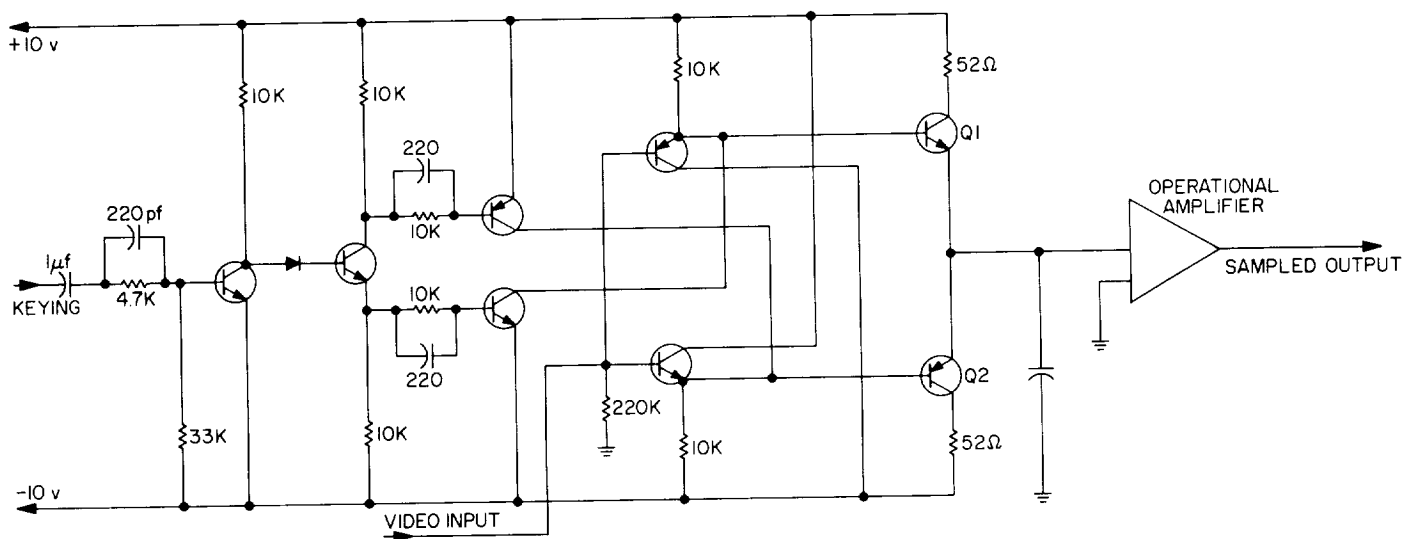


Fig. 3. Bilateral-keyed sampling circuit

complementary transistor symmetry, the bilateral bridge is understandably stable with temperature. Tests have indicated a stability within a few millivolts over a -20 to $+70^\circ$ range with unselected and unmatched transistors and $E_{cc} = \pm 10$ v.

The conclusion is reached that if camera signals are to be digitized and compressed, the SNR at the photo-sensor should be 40 db or better. A sample-and-hold circuit should be interposed between the camera and the encoder.

References

1. Murphy, R. T., "Sample and Hold Circuit with Bilateral Charging," *Electronic Equipment Engineering*, November 1961.
2. "The Diamond Circuit," Technical Report No. 300, Lincoln Laboratory, Massachusetts Institute of Technology, January 1963.

Erratum

In SPS 37-36, Vol. IV, Fig. 4 on p. 198 should be replaced by Fig. 4 on p. 191.

XVII. Bioscience

A. Soil Studies — Desert Microflora. XI. Desert Soil Algae Survival at Extremely Low Temperatures¹

R. E. Cameron and G. B. Blank

1. Algal Versatility

Algae exist in a very wide range of environments on this planet, including some habitats which are restrictive for the survival of many organisms (Ref. 1). Algal habitats include diverse environments, such as salt marshes, salt lakes, seas, rivers, streams, pools, cold and hot fresh and mineral water springs, fumaroles, ice, snow, animals, plants (including other algae and lichens), the upper surface of rocks, the under surface of translucent and transparent materials, dark caves, and surface and subsurface soils. Many hot and cold desert soils contain blue-green and green algae. Some species of algae have a great ability to adapt and survive when introduced into an environment that is dissimilar from their endemic habitat. Depending upon the habitat and various environmental factors, each species can show a wide variation in morphology (Refs. 2, 3, 4).

Blue-green algae, especially the filamentous forms, are the most cosmopolitan phototrophic organisms on this planet. Some species of blue-green algae are obligate phototrophs, but others are capable of chemo-organotrophy (Ref. 5). The fossil record shows that these algae existed early in the Archeozoic Era (Ref. 6). Most of the blue-green algae are tolerant of reducing conditions (Ref. 7), and their pigmentation is particularly efficient in the color and intensity of light which may have existed at the surface of primitive earth conditions (Ref. 5).

In harsh environmental studies, ultraviolet "trained-strains" of blue-green algae have been developed which are able to grow in a medium in which nitrate has been replaced by nitrite (Ref. 8). Powdered and sieved desert soil samples were irradiated with ultraviolet light ($260 \mu\text{W}/\text{cm}^2$ at 2537 \AA and $680 \mu\text{W}/\text{cm}^2$ at 3660 \AA) for 1 to 48 hr. This did not affect the survivable abundance of algae in the samples.² Algae in nonsalty desert soils had the ability to grow in 5% salt solutions of NaCl, MgSO_4 , NaHCO_3 , and CaCl_2 , although growth was delayed and the production of orange pigments (carotenoids) was increased.² A filamentous blue-green alga, *Nostoc commune*, was revived after more than 100 years' desiccation in a herbarium (Ref. 9). Other species of filamentous blue-green algae have been regenerated from soils stored in

¹Algal cultures prepared and temperature measurements made by F. A. Morrelli, JPL Desert Microflora Program.

²Speech presented at the American Microscopical Society, Southern California Branch, April 1964.

the air-dry state for approximately 75 yr.³ When moisture is available in desert soils, filamentous oscillatoroid blue-green algae, e.g., *Microcoleus vaginatus*, *M. chthonoplastes*, and *Schizothrix calcicola*, are rapidly activated, released from their sheaths and are visible as a green algal cover across the desert soil surface (Ref. 10). All of the above factors, as well as others, suggest that algae, especially filamentous blue-green desert soil algae, are microflora which should be studied prior to extraterrestrial investigations for life. These algae, or similar microorganisms, may represent one possible form of life on Mars.

2. Purpose

The present study was undertaken to determine the cold resistance of a mixed population of algae in a desert soil. Information on their ability to survive extreme cold treatments would further enhance their value as a possible Mars life form, or else suggest that they could serve as introduced organisms which might survive under Mars conditions if water were available at some time during the life cycle. No previous studies have been reported for viability of algae in desert soils after subjecting them to extremely low temperatures. However, it has been noted previously that algae can be revived after exposure to a temperature of -80°C , and they can photosynthesize slowly at -30° (Ref. 11). One study has shown that nondesert green algae can survive a 13-hr exposure of -190°C (Ref. 12).

3. Material and Methods

a. Soil characteristics. A sandy desert soil (our No. 1-2), was used for this experiment. This soil had been retained for 5 mo in the air-dry processed state before being used. It is classified as a light-gray Coachella sand and as an entisol derived from ancient, granite beach sand. A high quartz content as well as microcline is evident. Sea shells are also present. The samples consisted of thin, desert algal-lichen soil crusts collected from approximately $\frac{1}{16}$ in. from the surface near Thermal, California, in the Colorado Desert of the greater Sonoran Desert (Figs. 1 and 2). Physically, this soil has a particle size range distribution of 91.7% sand, 5.4% silt, and 2.9% clay. In the field, bulk density was 44.1 g/cc and total voids were 44.2%. Air-dry moisture content was 0.5%. Chemical properties included organic matter, 0.4%, total C, 0.4% and total N, 0.04% with an organic C/organic N ratio of 9.6. Saturated soil paste values showed a *pH* of 7.9, an *Eh* of +375 mv, and an

³JPL Desert Microflora Program, unpublished results.



Fig. 1. Collecting desert soil algal-lichen surface crusts from soil site in Colorado Desert near Thermal, California



Fig. 2. Thin, coherent, desert soil algal-lichen crust dislodged from soil site in Colorado Desert near Thermal, California

electrical conductivity value of 29.6×10^5 mhos/cm at 25°C . A low cation exchange capacity, 6.0 meq/100 g of soil, was primarily occupied by Ca^{++} as CaCO_3 . Microbiological determinations showed the presence of 3.7×10^5 aerobic bacteria + actinomycetes, 300 molds, and between 10^5 to 10^6 algae per gram of soil.

An aliquot of sieved soil (≥ 2 mm) was also powdered with an automatic mortar and pestle for this experiment. The textural classification of the soil was subsequently altered from medium sand to silty clay loam. Mechanical analysis of the powdered soil showed size range separates of 20% very fine sand, 51.8% silt, and 28.2% clay.

b. Experimental. Aliquots of sieved and powdered soils were prepared in 10- and 50-g portions. Samples of

soil (10-g) were placed in 20- × 150-mm pyrex screw cap tubes, sealed with epoxy, and evacuated to a pressure of 55 mm Hg. Samples of soil (50-g) were placed in tightly closed, square bottom screw-cap, pyrex, milk dilution bottles of 150-cc capacity. Several tubes and bottles contained cold-temperature thermocouples (copper-Constantan, 30-gage) which extended beneath the soil surfaces.⁴ Temperatures were recorded primarily during times of sample equilibration. Soil samples (50-g) were subjected to continuous cold in crushed, CO₂ (-79°C) or liquid N₂ (-195°C) for 1 to 48 hr. One set of 10-g soil samples was subjected to diurnal freeze-thaw cycles for periods of 24 to 168 hr with cycling at -79°C for 15 hr and 22°C for 9 hr. A second set of 10-g soil samples was put through a diurnal freeze-thaw cycle for periods of 24 to 144 hr with cycling at -195°C for 15 hr and 22°C for 9 hr.

Following the completion of each designated time period, the soil samples were cultured in serial dilutions of Pochon solution (Ref. 13). This solution consisted of the following salts per liter of distilled H₂O:

Ca(NO ₃) ₂	0.1 g
K ₂ HPO ₄	0.4 g
MgSO ₄	0.3 g
KNO ₃	0.1 g
FeCl ₃	Trace

It also contained a soil extract obtained from autoclaving one part soil to one part water. One part soil extract was used for each 8 parts of salt solution (Ref. 14). All cultures were subsequently incubated at 27 to 30°C under continuous warm white fluorescent lights of 450 to 550 ft-c light intensity (Fig. 3). A check for macroscopic growth of algae was made daily. Microscopic observations were also made intermittently and at the termination of the experiment. Air-dry soils were not subjected to cold treatments, but were maintained at 22°C. Incubations were terminated after 6 mo, following the desiccation of some of the cultures, although nearly all the cultures that showed viability had macroscopic growth within 30 days.

4. Results and Discussion

a. Algal abundance. The results of diurnal freeze-thaw cycles at 24-hr intervals for sieved and powdered samples

⁴Thermocouples were prepared by Kenton MacDavid, Thermocouple Lab., Instrumentation Sect., JPL.

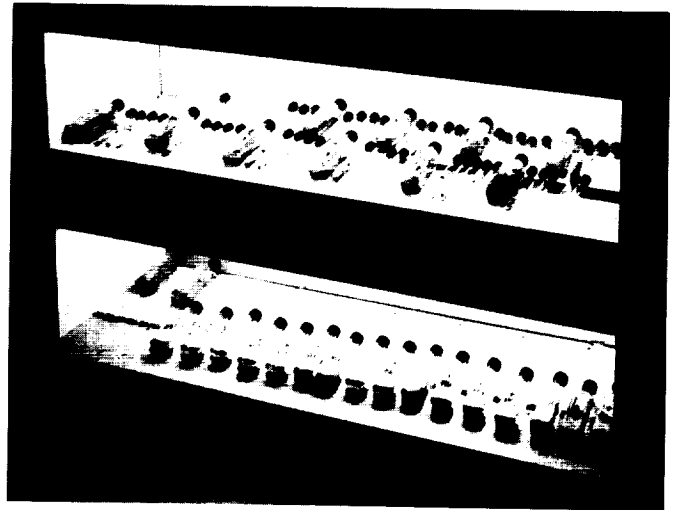


Fig. 3. Incubation of desert soil algae under continuous warm white fluorescent lights of 450 to 550 ft-c light intensity

of soil are shown in Tables 1 through 4. Results of continuous cold treatment are shown in Tables 5 through 8. Algal growth is indicated by the number of days required for macroscopic observation of green pinpoint or spreading colonies which were on the submerged soil surface, attached to the glass surface or floating in culture solution. Soil algae appear to prefer a moist solid substrate rather than an aqueous solution for growth purposes. In

Table 1. Growth of algae in 10 g of sieved soil following diurnal freeze-thaw cycles of -79 to +22°C^a

Time, hr	Dilutions/g soil					
	10	10 ²	10 ³	10 ⁴	10 ⁵	10 ⁶
	Days of incubation before macroscopic appearance of growth					
24	1 ^b	2	3	4	7	°
48	1	3	3	5	6	°
72	1	2	3	3	5	6
96	1	2	3	3	4	4
120	1	2	2	3	3	7
144	1	2	3	3	5	7
168	1	1	2	3	3	4
Average	1.0 ^b	2.0	2.7	3.4	4.7	5.6
Control average	1.0 ^b	1.0 ^b	2.0	2.5	4.5	5.0

^a Average equilibration times: 22°C ← 21.5 min → -79°C
^b 1 day = 24 hr or less.
^c No macroscopic appearance of growth after six months' incubation (April through September, 1964).

Table 2. Growth of algae in 10 g powdered soil following diurnal freeze-thaw cycles of -79 to +22°C^a

Time, hr	Dilutions/g soil					
	10	10 ²	10 ³	10 ⁴	10 ⁵	10 ⁶
	Days of incubation before macroscopic appearance of growth					
24	3	4	5	6	9	^b
48	4	4	4	6	9	^b
72	4	4	5	4	8	14
96	3	3	3	6	21	^b
120	3	3	3	4	4	7
144	3	3	3	4	5	9
168	3	3	3	4	6	6
Average	3.3	3.4	3.7	4.9	8.9	9.0
Control average	3.0	3.0	3.5	4.0	6.0	^b

^a Average equilibration times: 22°C $\xleftrightarrow[36 \text{ min}]{25 \text{ min}}$ -79°C

^b No macroscopic appearance of growth after six months' incubation (April through September, 1964).

Table 4. Growth of algae in 10 g powdered soil following diurnal freeze-thaw cycles of -195 to +22°C^a

Time, hr	Dilutions/g soil					
	10	10 ²	10 ³	10 ⁴	10 ⁵	10 ⁶
	Days of incubation before macroscopic appearance of growth					
24	4	2	2	4	6	14
48	4	3	3	4	7	^b
72	5	4	5	6	8	19
96	4	4	5	6	8	25
120	4	4	12	10	25	^b
144	4	4	5	6	10	^b
Average	4.2	3.5	5.3	6.0	10.7	19.3
Control average	4.0	4.0	5.0	6.0	13.0	^b

^a Average equilibration times: 22°C $\xleftrightarrow[36 \text{ min}]{4 \text{ min}}$ -195°C

^b No macroscopic appearance of growth after six months' incubation (April through September, 1964).

Table 3. Growth of algae in 10 g sieved soil following diurnal freeze-thaw cycles of -195 to +22°C^a

Time, hr	Dilutions/g soil					
	10 ^b	10 ²	10 ³	10 ⁴	10 ⁵	10 ⁶
	Days of incubation before macroscopic appearance of growth					
24	1 ^b	2	3	3	5	^c
48	1	4	4	6	20	^c
72	1	1	2	3	5	12
96	1	4	6	11	^c	^c
120	1	1	4	4	9	16
144	1	2	1	3	4	6
Average	1 ^b	2.3	3.3	5.0	8.6	11.3
Control average	1 ^b	1.5	2.5	5.5	10	24

^a Average equilibration times: 22°C $\xleftrightarrow[35 \text{ min}]{3.5 \text{ min}}$ -195°C

^b 1 day = 24 hr or less.

^c No macroscopic appearance of growth after six months' incubation (April through September, 1964).

Table 5. Growth of algae in 50 g sieved soil following continuous freezing at -79°C^a

Time, hr	Dilutions/g soil					
	10	10 ²	10 ³	10 ⁴	10 ⁵	10 ⁶
	Days of incubation before macroscopic appearance of growth					
1	2	3	4	4	6	14
2	3	4	4	5	7	^c
4	1 ^b	3	3	11	22	^c
8	3	3	3	9	^c	^c
16	3	3	4	5	13	14
24	3	3	4	8	12	^c
48	3	3	6	12	32	^c
Average	2.6	3.1	4.0	7.7	15.3	14.0
Control average	1.0	3.0	3.0	5.0	7.0	^c

^a Average equilibration times: 22°C $\xleftrightarrow[1 \text{ hr, } 16 \text{ min}]{39 \text{ min}}$ -79°C

^b 1 day = 24 hr or less.

^c No macroscopic appearance of growth after six months' incubation (April through September, 1964).

nearly all cases, growth occurred on the surface of submersed soil in the culture solution. Growth also appeared first at the lower dilutions. Growth was sometimes evident in 24 hr or less (Tables 1 and 3), but sometimes took 2 to 4 wk (Tables 5 through 8).

Soil texture may have some influence on the time required for the appearance of growth. Grinding undoubtedly disrupted some cells and dislodged algal aggregates from soil particles. Regardless of the temperature treatments, growth time for algae in powdered

Table 6. Growth of algae in 50 g powdered soil following continuous freezing at -79°C^a

Time, hr	Dilutions/g soil					
	10	10 ²	10 ³	10 ⁴	10 ⁵	10 ⁶
	Days of incubation before macroscopic appearance of growth					
1	4	4	5	5	b	b
2	4	3	4	4	6	b
4	5	6	7	11	28	b
8	5	5	6	9	18	b
16	5	5	6	8	11	b
24	5	4	6	8	9	b
48	5	4	6	9	13	b
Average	4.7	4.4	5.7	7.7	14.2	b
Control average	3.0	3.0	4.0	6.0	19.0	b

48 min
^a Average equilibration times: 22°C ← 1 hr, 16 min → -79°C

^b No macroscopic appearance of growth after six months' incubation (April through September, 1964).

Table 8. Growth of algae in 50 g powdered soil following continuous freezing at -195°C^a

Time, hr	Dilutions/g soil					
	10	10 ²	10 ³	10 ⁴	10 ⁵	10 ⁶
	Days of incubation before macroscopic appearance of growth					
1	6	5	5	7	9	b
2	3	3	5	6	7	b
4	5	7	7	21	b	b
8	5	5	7	12	20	b
16	5	6	6	9	20	b
24	5	5	6	7	12	14
48	4	4	6	7	15	b
Average	4.7	5.0	6.0	9.9	13.8	14
Control average	5.0	5.0	6.0	6.0	7.0	b

28 min
^a Average equilibration times: 22°C ← 1 hr, 35 min → -195°C

^b No macroscopic appearance of growth after six months' incubation (April through September, 1964).

Table 7. Growth of algae in 50 g of sieved soil following continuous freezing at -195°C^a

Time, hr	Dilutions/g soil					
	10	10 ²	10 ³	10 ⁴	10 ⁵	10 ⁶
	Days of incubation before macroscopic appearance of growth					
1	2	2	3	3	6	c
2	1	1	4	5	6	c
4	2	2	6	11	7	13
8	2	3	3	6	9	12
16	3	3	4	6	14	18
24	3	3	5	8	14	18
48	3	3	3	5	28	c
Average	2.3	2.4	4.0	6.3	12.0	15.3
Control average	1.0 ^b	2.0	2.0	6.0	13.0	c

15.5 min
^a Average equilibration times: 22°C ← 1 hr, 41 min → -195°C

^b 1 day = 24 hr or less.
^c No macroscopic appearance of growth after six months' incubation (April through September, 1964).

soils was delayed by 2 to 4 days at lower dilutions. Suspension of soil particles in the culture solution reduced light transmission and probably had an undesirable effect on time to achieve growth. Longer time periods required for temperature equilibration of powdered samples as

compared with sieved samples could also have had a minor effect on the delay in appearance of algal growth.

Soil algae survived after exposure to freeze-thaw cycles as well as continuous freezing. However, interrupted freezing had a greater influence on time of growth. Regardless of sample size or soil texture, the growth was more rapidly obtained for algae subjected to freeze-thaw cycles than for continuous freezing. (Compare Tables 1 through 4 with Tables 5 through 8.) Neither freeze-thaw cycles nor continuous freezing appeared to have a detrimental effect on algal abundance. Following the culturing of these soils, regeneration and growth of algae was approximately as rapid in many cases as for air-dry soils stored continuously at room temperatures.

b. Species viability. All of the indigenous soil algae grew following either alternate freezing and thawing or continuous freezing at -79 or -195°C. The algal species present were common soil forms found in temperate, tropical, or polar soils. These species included the filamentous oscillatorioid blue-green algae *Microcoleus vaginatus*, (Fig. 4), *Microcoleus chthonoplastes* (Fig. 5), and *Schizothrix calcicola* (Fig. 6). Other prominent filamentous blue-green algae included *Nostoc muscorum* (Fig. 7), and *Scytonema hofmannii* (Fig. 8). The only other alga present was the predominate desert soil coccoid green alga, *Protococcus grevillei* (Fig. 9). Cold-temperature treatments did not appear to influence the



Fig. 4. Photomicrograph of active oscillatorioid blue-green alga, *Microcoleus vaginatus*, $\times 1000$

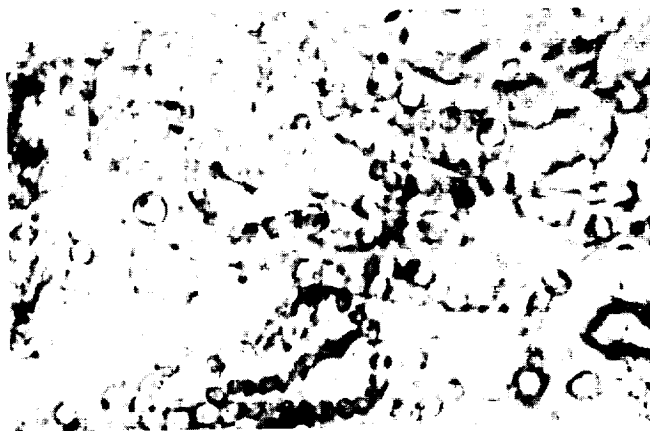


Fig. 7. Photomicrograph of filamentous blue-green alga, *Nostoc muscorum* and trichome of *Schizothrix calcicola*, $\times 1000$

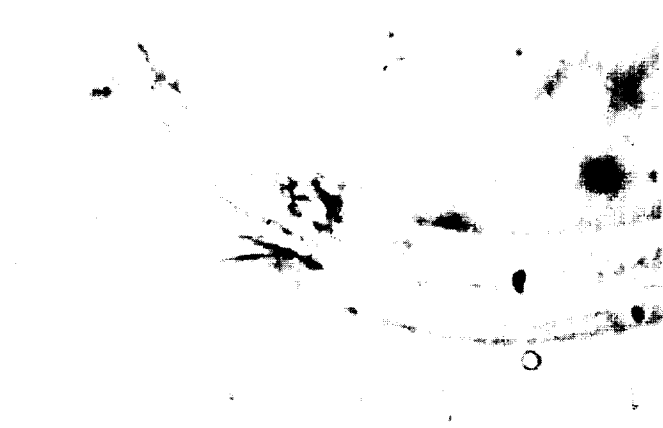


Fig. 5. Photomicrograph of ensheathed oscillatorioid blue-green alga, *Microcoleus chthonoplastes*, $\times 1000$

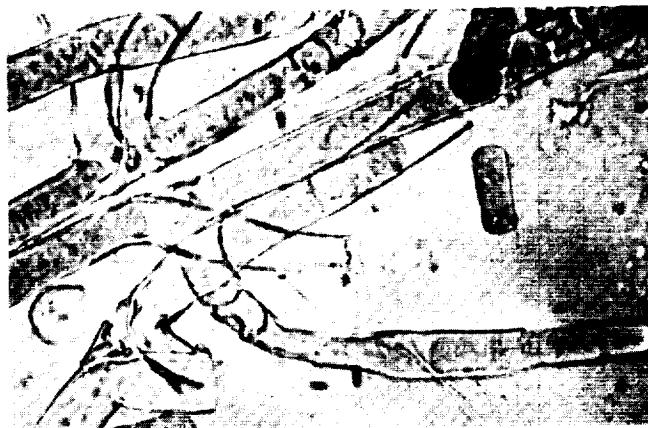


Fig. 8. Photomicrograph of filamentous, branched, blue-green alga, *Scytonema hofmannii*, $\times 1000$



Fig. 6. Photomicrograph of filamentous blue-green alga, *Schizothrix calcicola*, $\times 1000$



Fig. 9. Photomicrograph of coccoid green alga (with zoospores) *Protococcus grevillei*, $\times 1000$

abundance of any particular algal species. *Schizothrix calcicola* was the most abundant alga present in both control and treated soils.

c. *Soil response.* Soil response to cold treatments can be shown as indicated by equilibration times. These times are also given for each set of samples in Tables 1 through 8. All of the samples showed particle fluidity at low temperatures. Insufficient air-dry moisture (0.5%) could account for lack of solidification of the samples at either -79 or -195°C .

Temperature equilibration times were appreciably influenced by sample size, texture, and cold temperature extremes. In nearly all cases, regardless of sample size, equilibration was more rapid for samples which were immediately transferred from $+22$ to -195°C , than for those transferred from $+22$ to -79°C . Equilibration time was also more rapid for samples removed from -195 to $+22^{\circ}\text{C}$, than for those taken from -79 to $+22^{\circ}\text{C}$. Soil texture also had an effect on equilibration times. Regardless of whether the lowest temperature was -79 or -195°C , powdered samples had slower equilibration times than sieved samples subjected to the same temperatures. Freezing of powdered samples was achieved much more rapidly at -195 than at -79°C . Simulated fine-textured soils which have more surface area, more voids, and finer voids evidently have a much slower response to rapid temperature changes and a lower thermal conductivity than a coarse-textured soil. Equilibration time, and therefore the time for a soil to warmup when exposed to heat, or cooldown when exposed to low temperatures, is more rapid when the soil is subjected to -195 than to -79°C .

5. Concluding Remarks

Indigenous identified algae in air-dry sieved and powdered sandy, desert algal-lichen soil crusts have the ability to survive, grow, and reproduce in cultures after subjection to extreme cold treatments. Neither abundance nor individual species were affected by continuous freezing for 1 to 48 hr at -79 and -195°C . Samples evacuated to 55 mm Hg and then subjected to diurnal freeze-thaw cycles (15 hr at 22°C , and 9 hr at either -79 or -195°C) for 24 to 168 hr were also able to grow and reproduce when subsequently cultured in salt plus desert soil extract solution. Growth was obtained more rapidly at low dilutions of soil than at high dilutions; in sieved, rather than powdered, soils; and when subjected to freeze-thaw cycles rather than to continuous freezing.

Simulated fine-textured soil varied in its response to cold treatment as compared to coarse-textured soil. Equilibration times were slower for powdered rather than sieved (≥ 2 mm) soil. Response time for equilibration of soil subjected to -195° was faster than for soils subjected to -79° .

Blue-green algae, especially filamentous, oscillatoroid forms, are cosmopolitan in nature, and occur in widely varying terrestrial habitats, including desert soils and other harsh environments. Desert soil algae or similar algal-like organisms may exist as life forms on Mars, or they might be adaptable to a Mars environment, especially if water were available at some time in the life cycle. Ability of desert soil algae to survive, grow, and reproduce following extreme cold treatments increases their importance as microflora adaptable to harsh environmental habitats.

References

1. Baas Becking, L. G. M., Kaplan, I. R., and Moore, D., "Limits of the Natural Environment in Terms of pH and Oxidation — Reduction Potentials," *The Journal of Geology*, Vol. 68, pp. 243 to 284, 1960.
2. Drouet, F., "Gomont's Ecophenes of the Blue-Green Alga, *Microcoleus vaginatus* (Oscillatoriaceae)," *Proceedings of the Academy of Natural Sciences of Philadelphia*, Vol. 114, pp. 191 to 205, 1962.
3. Drouet, F., "Ecophenes of *Schizothrix calcicola* (Oscillatoriaceae)," *Proceedings of the Academy of Natural Sciences of Philadelphia*, Vol. 115, pp. 261 to 281, 1963.

References (Cont'd)

4. Drouet, F., "Ecophenes of *Microcoleus chthonoplastes*," *Revue Algologique*, Vol. 7, pp. 315 to 324, 1964.
5. Fogg, G. E., "The Comparative Physiology and Biochemistry of the Blue-Green Algae," *Bacteriological Reviews*, Vol. 20, pp. 148 to 165, 1956.
6. Tilden, J. E., "A Classification of the Algae Based on Evolutionary Development, with Special Reference to Pigmentation," *Botanical Gazette*, Vol. 95, pp. 59-77, 1933.
7. Baas Becking, L. G. M., and Wood, E. J. F., "Biological Processes in the Estuarine Environment," *Proceedings of the Academy of Science of Amsterdam, Series B*, Vol. 58, pp. 160 to 181, 1955.
8. Kumar, H. D., "Effects of Radiation on Blue-Green Algae. I. The Production and Characterization of a Strain of *Anacystis nidulans* Resistant to Ultraviolet Radiation," *Annals of Botany, N. S.*, Vol. 27, pp. 723 to 733, 1963.
9. Cameron, R.E., "Species of *Nostoc* Vaucher Occurring in the Sonoran Desert in Arizona," *Transactions of the American Microscopical Society*, Vol. 81, pp. 379 to 384, 1962.
10. Cameron, R. E., "Soil Sampling Parameters for Extraterrestrial Life Detection," in: "Biology of Mars," National Academy of Science, Washington, D.C. (to be published).
11. James, P. F., "The Limits of Life," *Journal of the British Interplanetary Society*, Vol. 14, pp. 265-266, 1955.
12. Kärcher, H., "Über die Kälteresistenz einiger Pilze und Algen," *Planta*, Vol. 14, pp. 515 to 516, 1931.
13. Pochon, J., "Manuel Technique d'Analyse Microbiologique du Sol," *Monographies de l'Institut Pasteur, Masson et Cⁱe*, Editeurs, Paris, VI^e, p. 81, 1954.
14. Cameron, R. E., and Blank, G. B., "Soil Organic Matter," Technical Report No. 32-443, Jet Propulsion Laboratory, Pasadena, California, May 23, 1963.

XVIII. Fluid Physics

A. Rotational Temperature Measurements in the Low-Density Free Jet

H. Ashkenas

The exploitation of the low-density free jet as a test medium for rarefied gas dynamic studies requires a precise knowledge of the jet structure and the parameters affecting that structure. Past free-jet diagnostic studies have relied primarily on Pitot tube investigations of the flow field. At very low densities, Pitot tube measurements lose credibility, due in part to the large viscous corrections which must be applied, and in part to their relative insensitivity to changes in the local temperature and/or local Mach Number.

In an effort to obtain further information on jet structure, a program of rotational temperature measurement by means of a spectrometric analysis of the rotational fine-structure of the band spectra of electron-beam excited nitrogen has been initiated.

The technique which has been applied was first described by E. P. Muntz (Ref. 1). In Ref. 1 Muntz described a model of the excitation and subsequent de-excitation of the N_2 molecule which could be used to interpret rotational spectra in terms of the ground state rotational temperature. The process selected by Muntz was the

$B^2\Sigma_u^+ \rightarrow X^2\Sigma_g^-$ electronic transition of the N_2^+ molecular ion. This transition gives rise to a strong rotation-vibration band in the nitrogen spectrum, with the band head occurring at 3914 Å.

Robben and Talbot (Ref. 2) have summarized the work of Ref. 1 and have refined and simplified the computational tasks involved in the reduction of the spectral data. Robben and Talbot show that

$$\frac{I_{K'}}{P_{K'}} \sim 10^{-(E/T_R)}$$

where $I_{K'}$ represents the spectral line intensity; $P_{K'}$ is a function of the rotational quantum number K' , $E = E(K', T_R)$ and T_R is the rotational temperature. Tabulated values of $P_{K'}$ and $E(K', T_R)$ are furnished in Ref. 2 and the measurement of the rotational temperature is effected by plotting $\log_{10} I_{K'} - \log_{10} P_{K'}$ versus $E(K', T_R)$ and calculating the negative reciprocal of the slope of the resulting straight line.

A schematic view of the experimental setup in the low-density wind tunnel is shown in Fig. 1. The electron beam, collimated by a 0.060-in. ID stainless steel tube, is directed along the axis of the jet; the current collector plate in the stagnation chamber serves as a source for a feedback network which maintains constant beam-current during a spectrum scan. The traversing optical

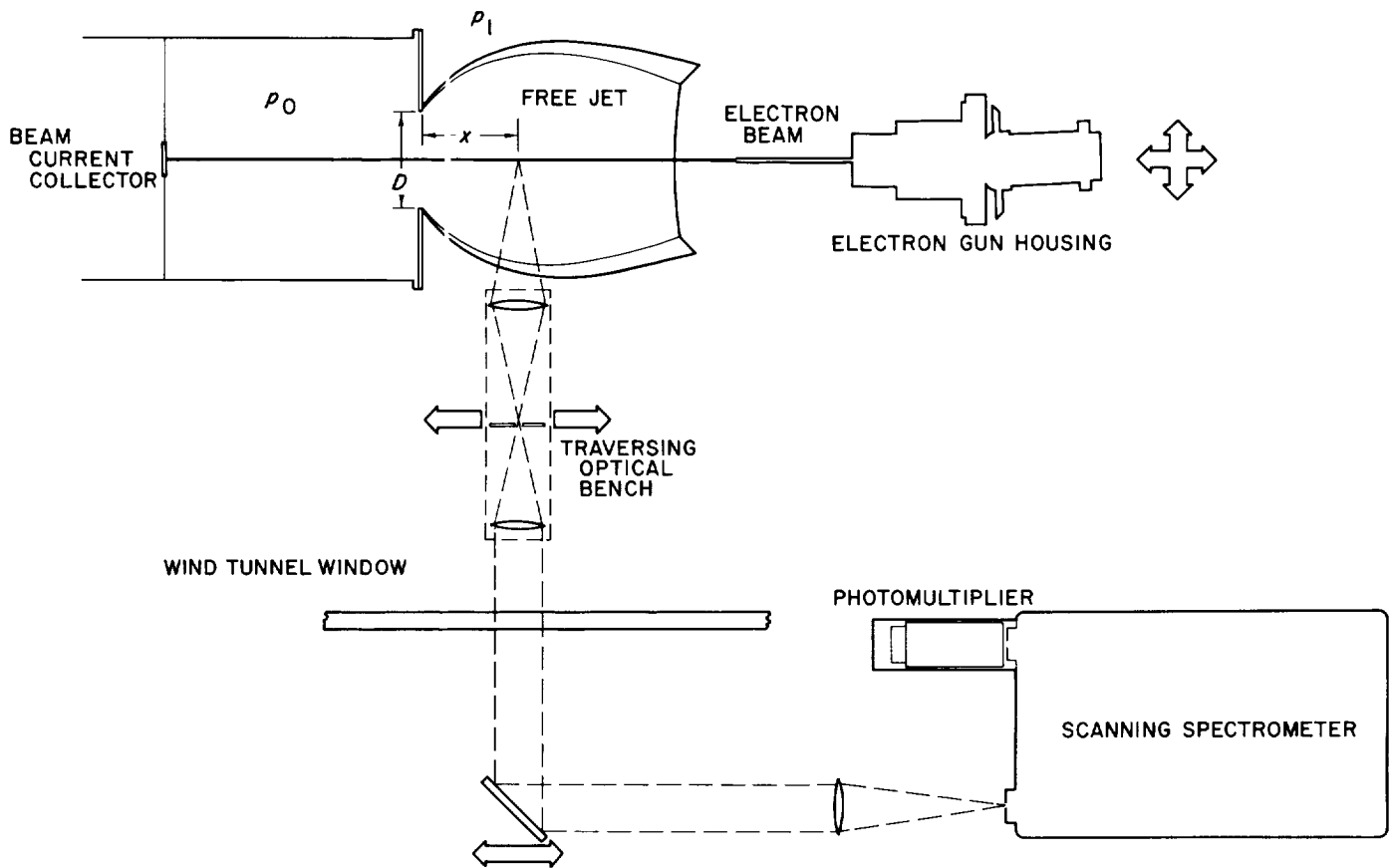


Fig. 1. Experimental setup for rotational temperature measurements in the low-density free jet

bench carries two $f/1$ lenses together with a 0.050-in. wide slit (normal to the electron beam) for defining the point on the jet axis which is being scanned. The external diagonal mirror is traversed in conjunction with the internal optical bench. The output of the spectrometer photomultiplier is amplified and recorded on an $x-y$ plotter. Dry nitrogen (evaporated from liquid N_2) is used as the test gas; stagnation temperature is equal to room temperature; accelerating voltage on the electron gun is 15 kv; gun current is of the order of 100 μ a; the spectrum is scanned at a rate of 2 to 3 $\text{\AA}/\text{min}$; the recording circuit time constant is $\frac{1}{2}$ sec or less; the exit slit of the spectrometer is kept equal to, or larger than, the entrance slit, in order to ensure that the peak of the line intensity is measured.

A sample spectrum, taken in the free jet, is shown in Fig. 2; the evaluation of the spectrum of Fig. 2 is carried out in Fig. 3. A preliminary axial rotational temperature distribution in the free jet is presented in Fig. 4.

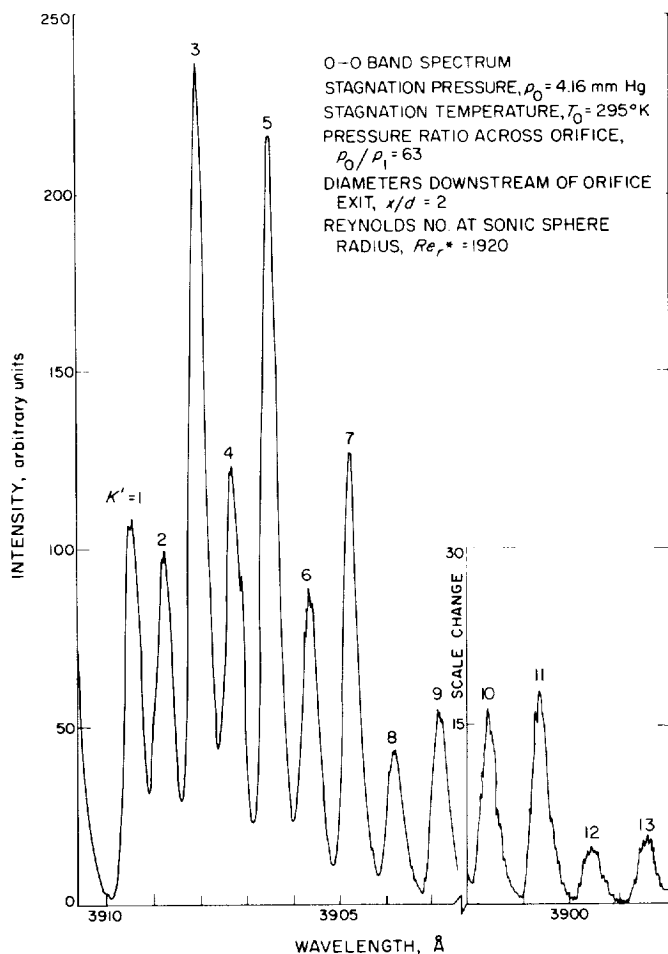


Fig. 2. O-O Band spectrum in the nitrogen free jet

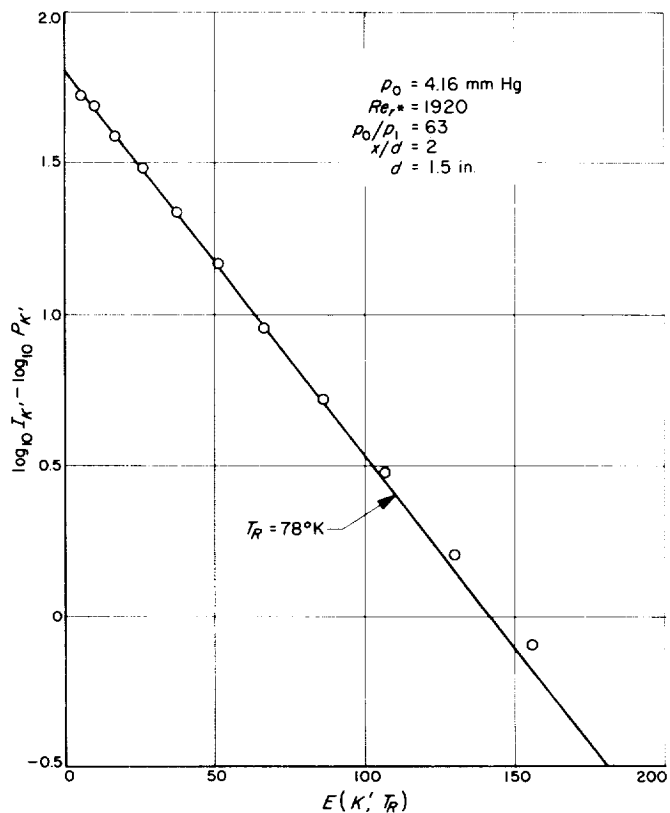


Fig. 3. Rotational temperature determination from the spectrum of Fig. 2

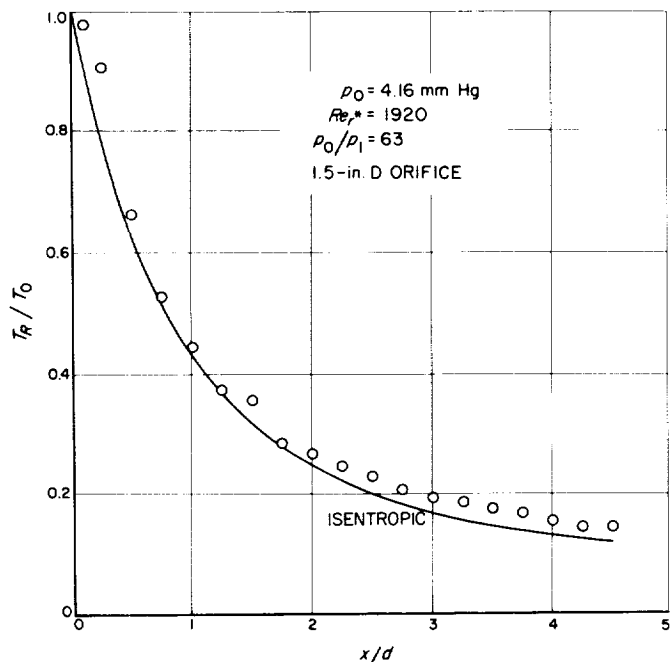


Fig. 4. Axial rotational temperature distribution in the free jet

B. The Neutral Point in a Plasma

A. Bratenahl

The problem of rapid transfer of flux at a magnetic neutral point in a medium of high electrical conductivity has long been the subject of intensive theoretical study, and this problem of "severing and reconnecting line of force" at a neutral point has grown in astrophysical importance with the gradual recognition of a wide class of situations to which it is applicable.

The problem has yielded very reluctantly to this theoretical onslaught, and our double inverse pinch experiment seems to be the first direct laboratory attack. Our attempt, inadequate and incomplete as it is at present, already seems to have supplied a much-needed piece of evidence to consider along with the existing theory. Indeed, it seems to lead us to a remarkably simple hypothesis. Briefly, we find that under the following enumerated conditions, the required energy dissipation will take the form of the production of three distinct classes of particle energy spectra which can nearly completely supplant the usual ohmic j^2/σ dissipation. These conditions are:

- (1) The magnetic pressure of each of the two distinct flux systems that give rise to the neutral point, taken alone, must be greater than the gas pressure at the point.
- (2) Each system, again taken alone, must have a finite radius of curvature at the point. (This implies their equivalent current sources must be reasonably concentrated but separated by a finite distance.)
- (3) Their field strength at the point must be increasing with time.

The process occurring under these circumstances involves a relaxation oscillation which enables the Maxwell stress system to effect a tradeoff favoring direct gas dynamic acceleration in place of the normal ohmic dissipation. The process takes place in discrete steps with a well-defined period that is independent of the conductivity, depending instead on sound speed, the characteristic length, the ratio of gas to magnetic pressure, the polytropic exponent, and the rate of rise of the fields.

At each cycle, a discrete amount of flux $\Delta\phi$, also independent of the conductivity, is transferred through the point in a time short compared to the period; and it is quite astonishing to find that in the limit of very high

conductivity, the rate becomes roughly proportional to the conductivity¹, and the corresponding energy dissipation (gas dynamics in this limit) becomes increasingly violent.

We have reported the experimental evidence for our conclusions relative to the possibility of relaxation oscillations in Ref. 3. We refrain from repeating this discussion here. The fact is, we observe a configurational flip-flop between what might be called a normal neutral point on the one hand, and a sheet pinch in which the neutral point is squashed rather flat, on the other.

Since the pinch still contains the neutral point (in a greatly flattened form), there is, in addition to the normal pinch force, an additional component of the Maxwell stress that is capable of forcibly pumping out or ejecting the gas from in between the pinched lines of force. A considerable amount of gas can thereby receive an acceleration up to the Alfvén speed V_α during a time ΔT . At the conclusion of ΔT , which is the period of the relaxation oscillation, the asymptotic lines rapidly approach a critical state where they become tangent at the point. The current density becomes exceedingly large and concentrated so that, despite a large conductivity, the ohmic electric field (which is equal to $-\dot{\phi}$ by Faraday's Law) becomes large, and hence the flux transfer $\dot{\phi}$ is correspondingly fast. The point is, there exists a critical state which can be reached in a relatively short finite time, ΔT , in which the cross-section of the circuit becomes arbitrarily small. Therefore, even though the conductivity is large, the resistance of the circuit can be arbitrarily large, and the total current that flows in this circuit, which is completely determined by external conditions by requiring $\vec{\nabla} \cdot \vec{j} = 0$, is proportional to the discrete quantity of flux that is gated through the neutral point. During this short gating phase at ΔT , the flash phase (to borrow a term from the physics of solar flares), two distinct additional acceleration processes become operable. Most of the gas that remains in the vicinity of the neutral point will be given a velocity $V_z \sim \dot{\phi}/B$, which can be much greater than V_α . The third acceleration process involves the minute amount of plasma that makes up the concentrated current path. If $\dot{\phi}$ is large enough (this implies that the conductivity is large enough), these particles can enjoy the runaway process, producing a spectrum with an upper limit of energy, $e \dot{\phi} L$ when e is the electronic charge, and L is the length of the concentrated part of the current path. Putting in numbers,

¹At the limit of infinite conductivity, the possibility of flux transfer jumps discontinuously to zero, but this limit has no physical significance for a real plasma.

one finds this last process could account for solar flare-produced cosmic rays. It is interesting to note that under the assumed conditions, we find ΔT and $\Delta\phi$ to have the order of magnitude:

$$\Delta T \sim \frac{a_0}{V_\alpha} \quad \text{and} \quad \Delta\phi \sim B_0 a_0 \omega \frac{a_0}{V_\alpha}$$

where

a_0 = the critical length

$\frac{1}{\omega}$ = rise time of fields

V_α = Alfvén speed

gives time constants in reasonable agreement with the rise time of solar flares, suggesting that the slower but massive acceleration to V_α could account for the brightening of the chromosphere as well as the usually observed surge prominences. But it is particularly interesting that the blast wave and spray surge could be associated with the second acceleration process, occurring as it does at the flash phase. The same is true by associating the cosmic ray production with the third acceleration process.

We take origin at neutral point, x -axis joining the line-current sources, y -axis transverse, z -axis parallel to line-current sources. It can be shown that the first velocity spectrum, produced as it is during the whole time ΔT , with the velocity upper limit given by the Alfvén speed $V_1 = B_0 / \sqrt{\mu_0 \rho}$ represents, very simply, the conservation of momentum, and being independent of σ , has nothing to do with the amount of tradeoff which ultimately substitutes particle acceleration for ohmic dissipation. The amount or degree of tradeoff involves only the other two spectra which develop as the critical state is approached. It is the approach to the critical state that is strongly dependent on σ . However, the spectrum V_1 is directly related to the particular component (y) of the Maxwell stress that is responsible for the tradeoff, i.e., that makes the trading-off possible.

It must be admitted, however, that this theory is still in a very primitive state. We must check many aspects of this, particularly the conservation of momentum and energy. The theory raises as many questions as it answers. Most significant, perhaps, is that now we are able to derive a number of critical tests to perform in the laboratory.

A somewhat more detailed account of this advance in the theory of the neutral point will be presented at the AIAA Meeting, Monterey, California, March 2, 1966.

C. Experimental Investigations of the Base-Flow Problem

III. Pressure-Recovery Distribution

F. R. Hama

In the last report (Ref. 4), the base pressure of a wedge with and without a splitter plate (Fig. 5) were compared. It was noted that the base pressure of the wedge alone was slightly lower than that with the plate.

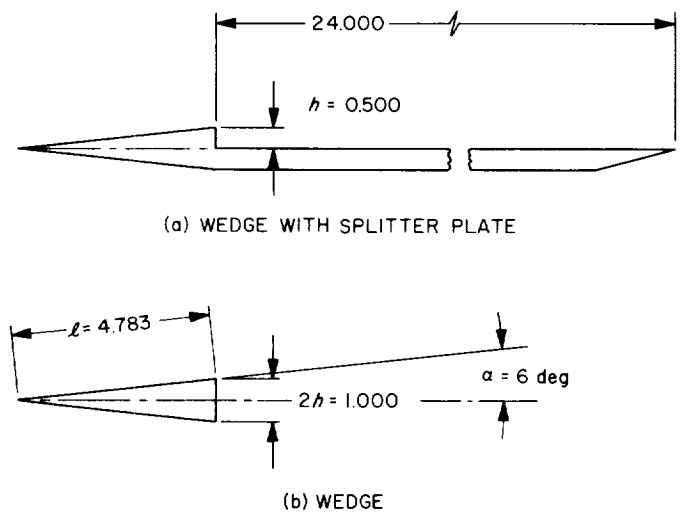


Fig. 5. Experimental configurations

During the period covered in the present report, the static pressure distribution along the centerline of the wake of the wedge alone was measured by a $\frac{1}{16}$ -in. static pressure probe, which pierced the base of the wedge (Fig. 6). The measurements were made for three typical Reynolds numbers at each of the three Mach numbers, $M_1 = 2.61, 3.51,$ and 4.54 . Results are shown in Figs. 7, 8, and 9; p is the static pressure, p_1 the free-stream static pressure, M_1 the free-stream Mach number, and X the distance downstream from the base. They are compared with the pressure distributions for the wedge-plate configuration which were measured previously by a row of static-pressure holes tapped through the plate. In addition, Fig. 10 shows the pressure-recovery distribution with a tripping device (Refs. 5 and 6) mounted on the wedge surfaces. The boundary layer on the wedge surfaces was always laminar without the tripping device in the present experiment. The separated shear layer became turbulent almost immediately after the separation at the largest Reynolds number. At the intermediate

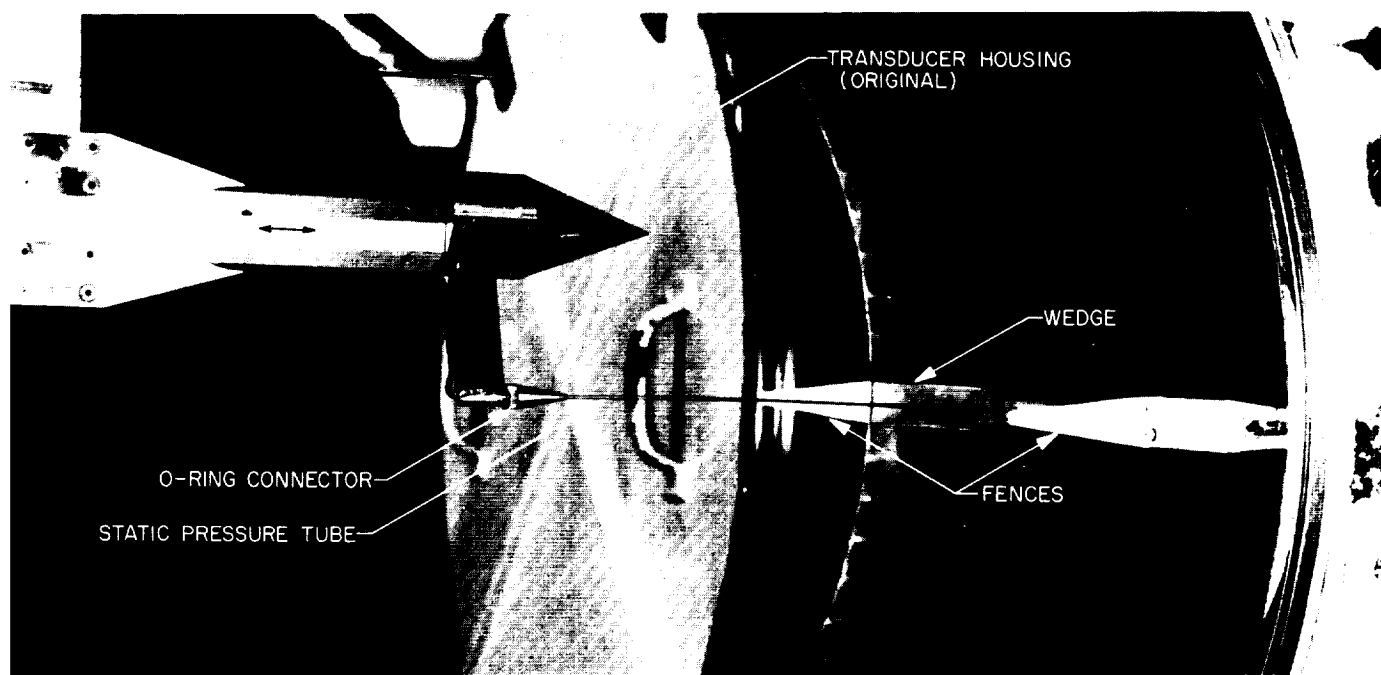


Fig. 6. Static pressure probe

Reynolds number, the transition took place somewhat downstream but still in the free-shear layer, and the reattachment was therefore turbulent. The flow field was entirely laminar at the lowest Reynolds number investigated.

Characteristically, the pressure-recovery distributions for the two different reattachment conditions are not essentially different from each other. This is particularly true for the low Reynolds number cases; the static pressure is monotonically recovered. It seems to be a general tendency that, as the Mach number decreases, the static pressure overshoots the free-stream value. While the reason for it is unknown, the overshoot is generally observed also in the low-speed experiments (Ref. 7) as long as the boundary layer separates more or less parallel to the main flow (Ref. 8). There are, however, minor differences between the two cases. The pressure is recovered slightly more quickly behind the wedge than with the plate, at least in the case of laminar reattachment. This difference must have resulted in part from the difference in the behavior of the dividing streamline near the reattachment; the dividing streamline should bend toward the plane of symmetry to cross it orthogonally at the reattachment point behind the wedge,² whereas

the dividing streamline makes an angle with the plane of a solid boundary (Ref. 9). In addition, the distributed stress in the shear layer might be more quickly released after the reattachment due to the zero-stress condition (instead of the zero-velocity condition) on the centerline in the case of free reattachment behind the wedge, resulting in a quicker readjustment of the pressure. The static pressure also begins to rise somewhat earlier than with the plate. This is accountable not only due to the orthogonality condition described above, which brings the reattachment point closer to the base for a given base pressure, but also due to the free-shear layer direction, which is more sharply tilted toward the centerline because of the lower base pressure at a given Reynolds number. It is not immediately obvious why the base pressure behind the wedge is lower than that with the splitter plate. It is desirable to make a theoretical investigation on this matter.

When the reattachment is turbulent at higher Reynolds numbers, the pressure-recovery distribution displays a more complicated behavior. It shows a hump in the midst of pressure-recovery process at higher Mach numbers and a local peak after the pressure is sufficiently recovered at lower Mach numbers. Such anomalies are particularly pronounced when the wedge-surface boundary layer was made turbulent.

²Kubota, T., private communication.

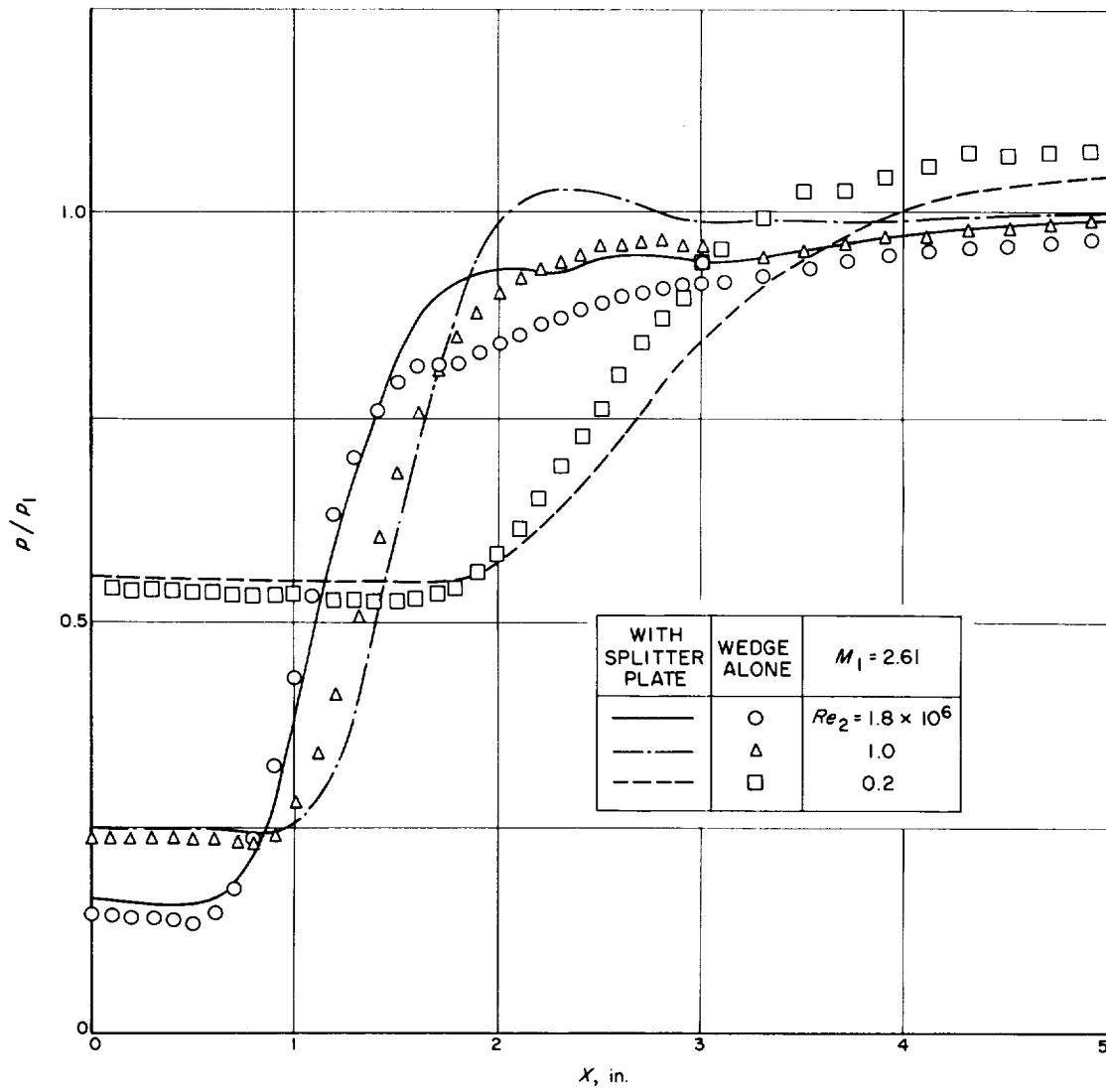


Fig. 7. Pressure-recovery distribution behind a wedge with or without a splitter plate ($M_1 = 2.61$)

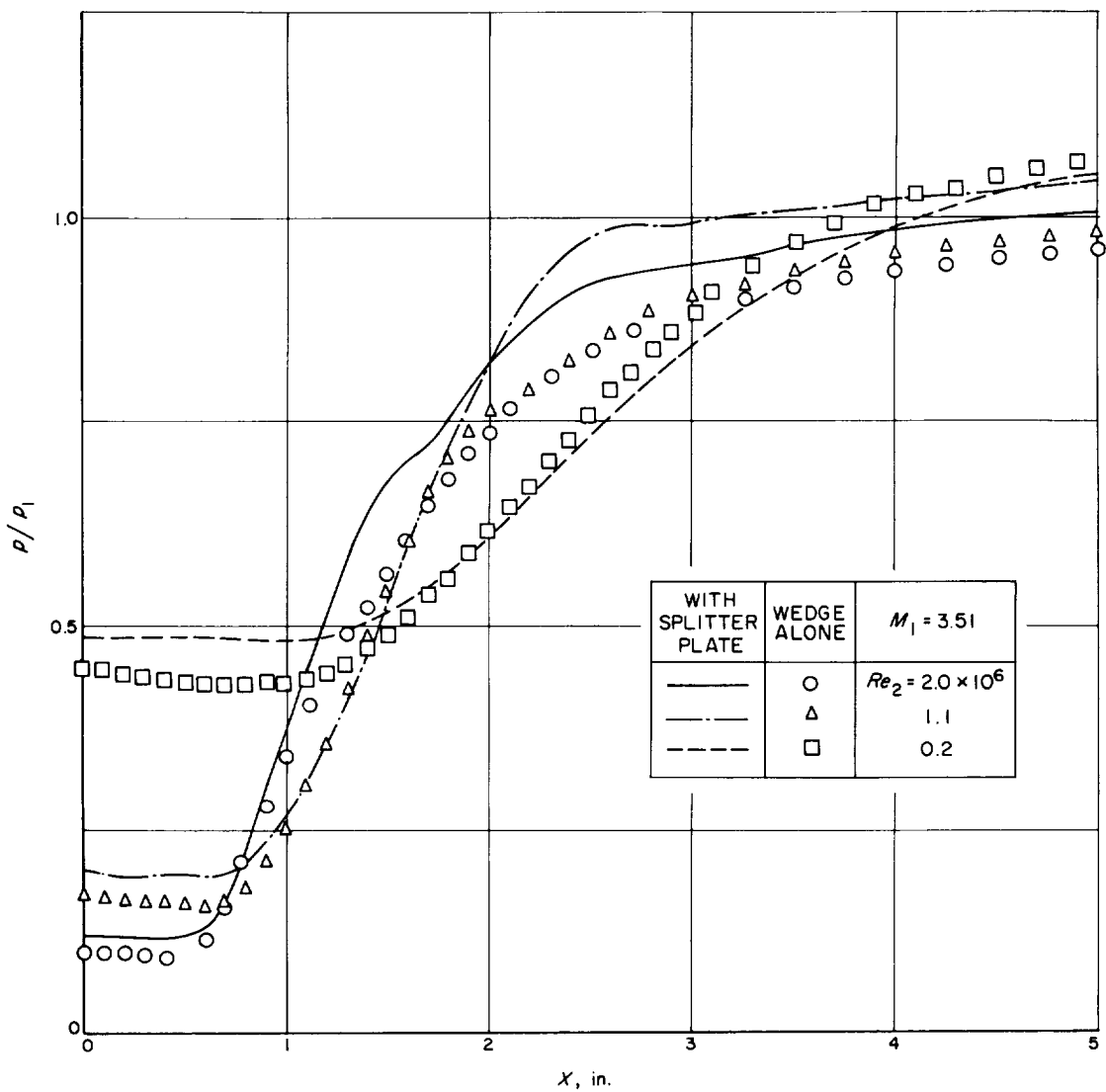


Fig. 8. Pressure-recovery distribution behind a wedge with or without a splitter plate ($M_1 = 3.51$)

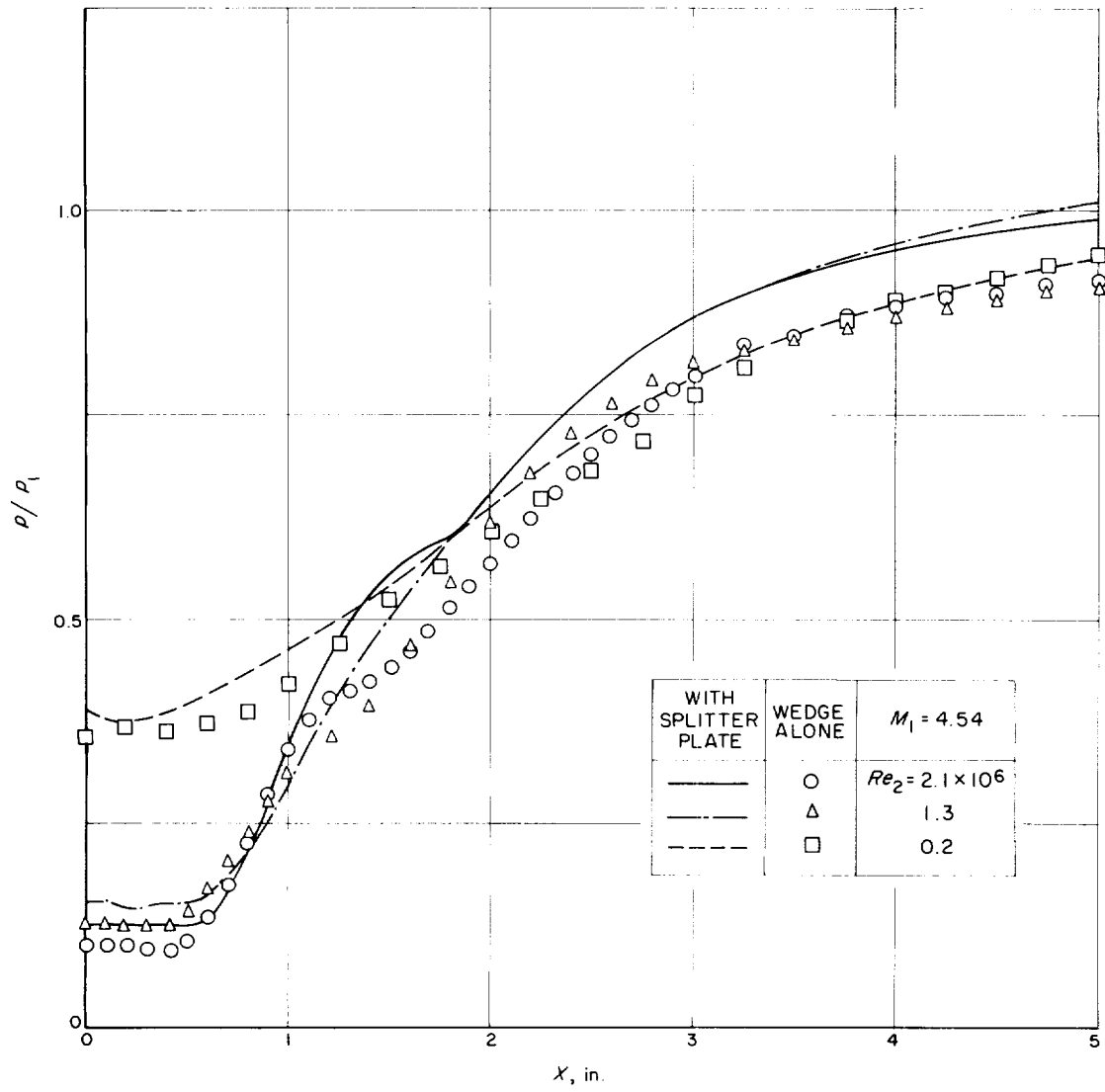


Fig. 9. Pressure-recovery distribution behind a wedge with or without a splitter plate ($M_1 = 4.54$)

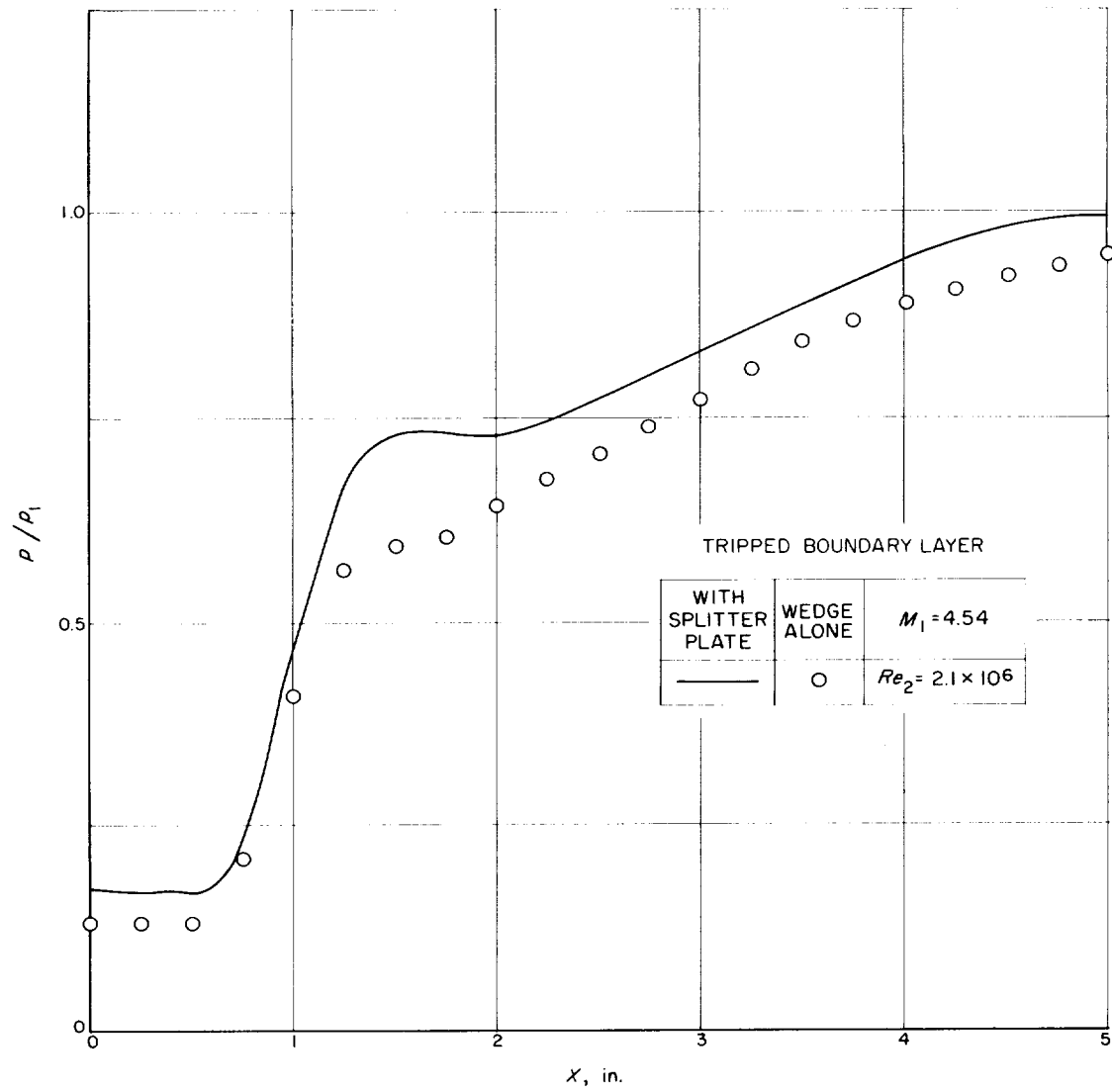


Fig. 10. Pressure-recovery distribution behind a wedge with or without a splitter plate (boundary-layer tripping on wedge surfaces, $M_1 = 4.54$)

These humps and local peaks can be attributed to the interaction of the lip shock, whose strength was found to be substantial (Ref. 10), with the recompression shock. Take, for example, a schematic shock pattern, as in Fig. 11(a), which roughly corresponds to the case, $M_1 = 2.61$, $Re_2 = 1.8 \times 10^6$ in Fig. 7. The flow near the shear layer is expanded first through the expansion fan generated at the separation edge, recompressed by the lip shock to Region 3 where the pressure is approximately equal to the base pressure, and further compressed by the recompression shock to reach Region 4. On the other hand, the flow farther away from the shear layer is recompressed only through the recompression shock. Therefore, the pressure in Region 4 is higher than that in Region 6, and must be readjusted by a weak expansion wave so that the pressure in Region 5 balances that in Region 6, the two regions being separated by a slip stream. Since the pressure in Region 5 or 6 is normally lower than the free-stream static pressure, the pressure must slowly increase to attain the free-stream value eventually. This situation explains the appearance of the pressure peak and the pressure minimum which follows. Numerical estimates of the peak and minimum values agree rather well with the experimental results in this example. Moreover, the location of the pressure minimum is shown to have a good correlation with the location where the lip shock

meets the recompression shock (Fig. 12). The location of the pressure peak, on the other hand, does not necessarily correlate with the lip shock-recompression shock point, because the recompression shock is formed by a convergence of isentropic compression waves which are emanated from the slow turning of the flow near the reattachment point; hence the pressure peak could appear even upstream of the lip shock-recompression shock point and nearer the reattachment point. Indeed, as shown in Fig. 13, the pressure-peak location correlates well with the isentropic reattachment point, which was computed from the base pressure by the use of a flow table.

At higher Mach numbers the same process must equally occur, but the lip shock is now completely imbedded within the free-shear layer, as in Fig. 11(b). This is particularly true for the tripped boundary layer, since the shear layer is already quite thick at the separation. In such cases, the pressure variation due to the lip shock-recompression shock interaction appears as the hump in the midst of the pressure-recovery process of the shear layer, rather than as the distinct local pressure peak after the static pressure is almost completely recovered.

The dependence on the Mach number of the appearance of the hump or the peak should not be looked upon

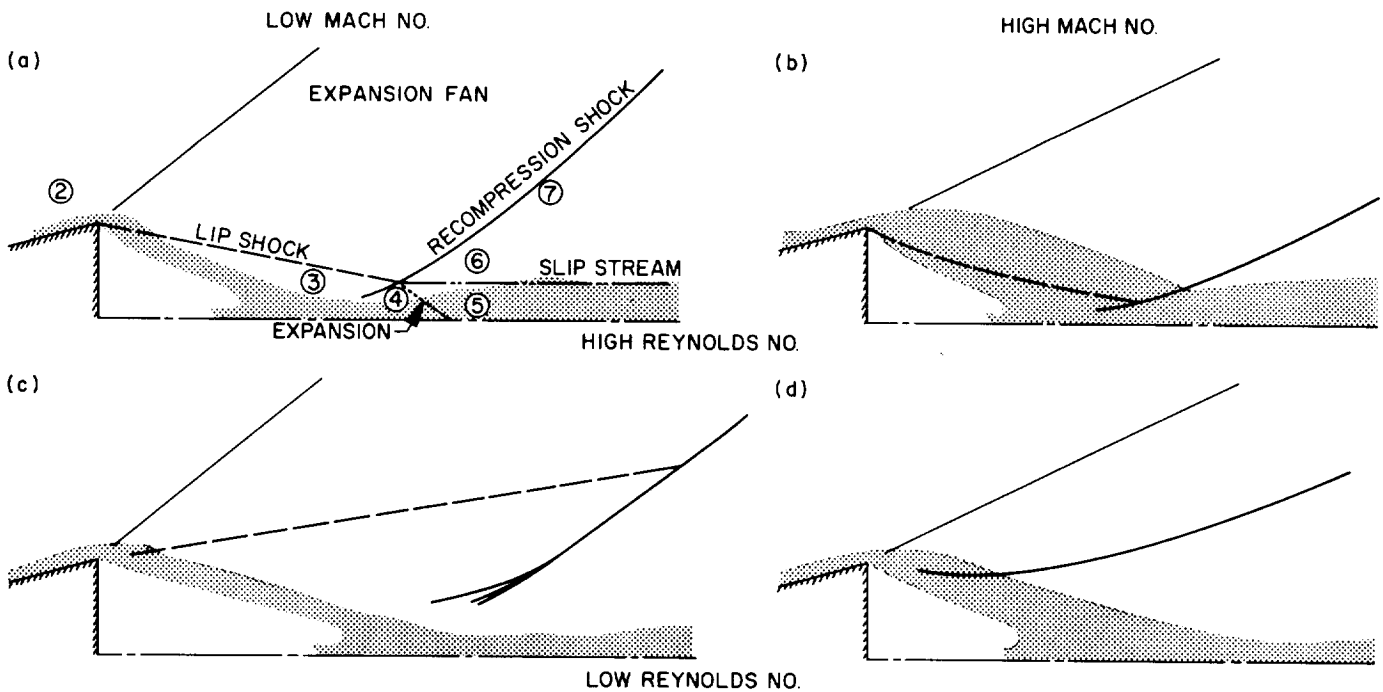


Fig. 11. Schematic representations of shock pattern

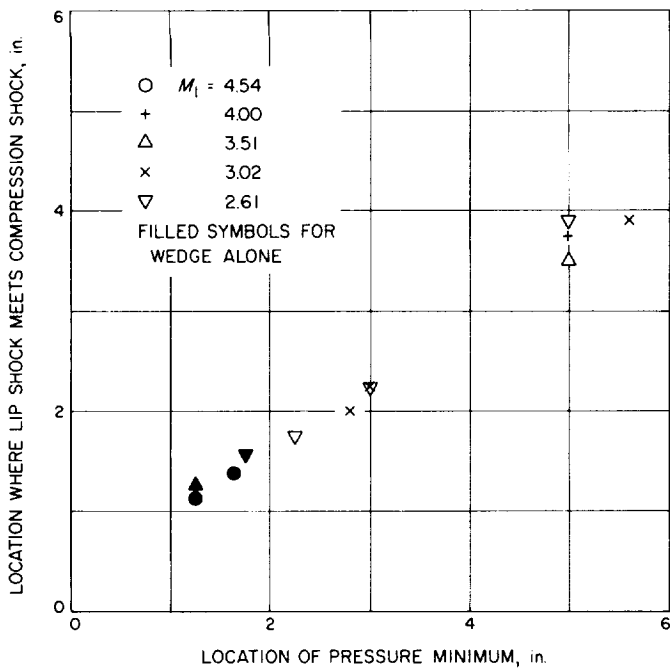


Fig. 12. Correlation between location of pressure minimum and location where lip shock meets recompression shock

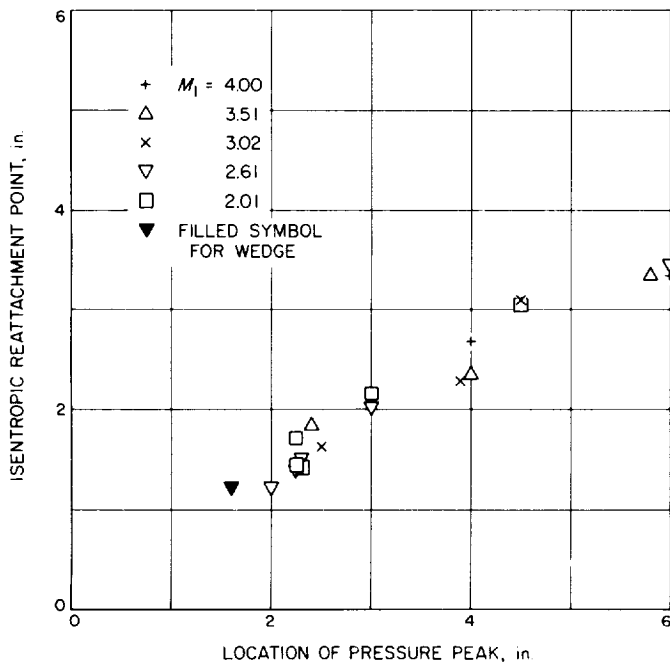


Fig. 13. Correlation between location of pressure peak and isentropic reattachment point

as universal. If the step or the base height is sufficiently large, the flow pattern as shown in Fig. 11(b) should approach that as in (a), even at a fixed Mach number. Consequently, the location of the hump will move toward the end of the pressure-recovery process, and the hump may eventually become the peak. Such a tendency is clearly seen in the pressure distributions measured by Roshko and Thomke for three different step heights (Ref. 11).

The pressure initially recovered in Region 5 or 6 after a relatively steep increase is substantially lower than the free-stream pressure because the recompression shock is quite strong. The higher the Mach number, the initial recovery pressure is indeed the lower, reflecting the stronger recompression shock. The pressure now continues to increase rather slowly. The slow pressure recovery might be attributable to the nonuniform static pressure distribution behind the recompression shock. Since the recompression shock is covered by the expansion fan, the pressure away from the shear layer (Region 7) is higher than that in the near Region 6. As the shear layer grows after the reattachment, its outer edge slowly penetrates into higher and higher pressure regions, resulting in the slow increase in the static pressure along the centerline.

Contrary to the turbulent reattachment, the effect of the lip shock-recompression shock interaction is unlikely to appear in the low Reynolds number laminar reattachment. At lower Mach numbers, the two shocks are well separated as shown in Fig. 11(c). The lip shock, however, is weak and oriented away from the recompression region. The interaction is therefore not only weak, but has little influence on the recompression process. On the other hand, the two shocks are merged to become one continuous shock at higher Mach numbers, as shown in Fig. 11(d). Therefore, the interaction as described above simply does not take place. Nevertheless, the merged shock is not of negligible strength, and the recompression process is slower than that at lower Mach numbers.

In addition to the pressure measurements, shadowgraph and schlieren pictures were taken. Unfortunately, some uncertain misalignments of the wedge existed during the optical observations. Therefore, some of the conclusions, which would have been obtainable from the shock patterns, have to be withheld until more reliable pictures are taken. Nevertheless, preliminary examinations of the shadowgraphs indicate first, that the lip shock is stronger, and second, that the recompression shock appears to be formed more quickly (i.e., nearer the reattachment point) behind the wedge than with the

splitter plate. These observations may account for the generally lower level of the pressure distribution in the case of turbulent reattachment and for the upstream shift of the location of the hump. On the contrary, the recompression shock for the laminar reattachment is formed always well away from the shear-layer region; hence no difference is found in the pressure level.

D. The Inviscid Stability of the Laminar Compressible Boundary Layer for Three-Dimensional Disturbances. Part II

L. M. Mack

The inviscid stability of the two-dimensional insulated-wall boundary layer with three-dimensional disturbances was computed in Ref. 12. In these computations the amplification rate was obtained as a function of the dimensionless frequency αc_r , where α is the dimensionless wave number in the x direction, and c_r is the dimensionless phase velocity in the x direction. For this purpose it was not necessary to know the wave numbers of the neutral disturbances, except as an aid in locating the unstable regions. However, the few neutral wave numbers that were obtained at rather widely spaced wave angles were difficult to fit into any coherent pattern. In order to

clarify the situation, a detailed investigation of the neutral wave numbers as functions of the wave angle has been carried out and is reported here.

The results obtained at a free-stream Mach number M_1 of 4.5 are given in Fig. 14. In this figure $\tilde{\alpha}_{s1}$ and $\tilde{\alpha}_{s2}$, the first and second-mode neutral wave numbers in the direction of the wave normal, are given as functions of the wave angle σ , the angle between the wave normal and the free-stream direction. The effect of increasing the angle σ is to decrease \tilde{M}_1 , the component of the free-stream Mach number in the direction of the wave normal. This Mach number is the only parameter of the external flow that enters the inviscid stability equations. The boundary-layer solution is the same at all component Mach numbers for a given M_1 , and is therefore unstable at all component Mach numbers. The first-mode wave number, as shown in Fig. 14, increases with increasing σ , and, unlike α_{s1} for the two-dimensional disturbances, does not tend to zero as $\tilde{M}_1 \rightarrow 0$ ($\sigma \rightarrow 90$ deg), but approaches a nonzero limiting value.

At $M_1 = 4.5$, the thickness η_1 of the supersonic region in the boundary layer relative to the phase velocity, which controls the second and higher modes, is about 40% of the total boundary-layer thickness. As σ increases from zero, η_1 decreases. It is zero at $\sigma = 58$ deg ($\tilde{M}_1 = 2.4$). Since it is roughly true that the second-mode wave length is proportional to the thickness of the supersonic relative region, $\tilde{\alpha}_{s2}$ must increase with increasing σ and become infinite at $\sigma = 58$ deg. The result shown in Fig. 14 is in accord with these requirements.

Fig. 15 gives the results obtained at $M_1 = 5.8$. At this Mach number, $\tilde{\alpha}_{s2}$ at $\sigma = 0$ is less than $\tilde{\alpha}_{s1}$ at $\sigma = 90$ deg.

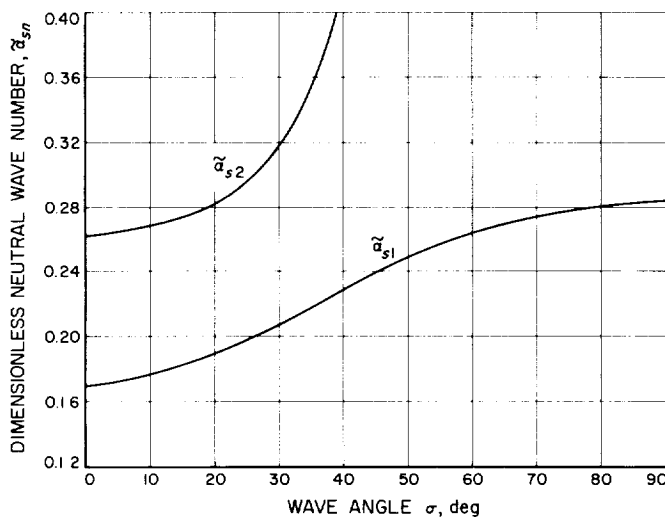


Fig. 14. Effect of wave angle on neutral wave numbers at $M_1 = 4.5$

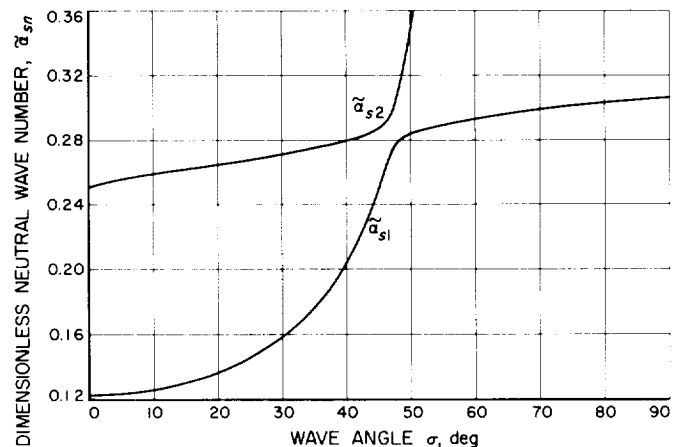


Fig. 15. Effect of wave angle on neutral wave numbers at $M_1 = 5.8$

Near $\sigma = 47$ deg, $\tilde{\alpha}_{s2}$ approaches $\tilde{\alpha}_{s1}$ closely and then increases sharply. The shape of the two curves in Fig. 15 is such as to give the impression that for $\sigma > 47$ deg the curve for $\tilde{\alpha}_{s1}$ is a continuation of the $\tilde{\alpha}_{s2}$ curve from $\sigma < 47$ deg, and the $\tilde{\alpha}_{s2}$ curve for $\sigma > 47$ deg is a continuation of the $\tilde{\alpha}_{s1}$ curve from $\sigma < 47$ deg. This behavior becomes more dramatic at $M_1 = 8$, as shown in Fig. 16. At this Mach number, $\tilde{\alpha}_{s3}$ also enters the picture. The eigenvalues $\tilde{\alpha}_{s3}$ and $\tilde{\alpha}_{s2}$ approach each other closely at $\sigma = 35$ deg, and $\tilde{\alpha}_{s2}$ and $\tilde{\alpha}_{s1}$ approach each other even more closely (to within 1%) at $\sigma = 56.5$ deg. The nearly horizontal line that starts from $\tilde{\alpha}_{s3}$ at $\sigma = 0$ forms a sort of barrier for $\tilde{\alpha}_{s2}$. When the $\tilde{\alpha}_{s2}$ curve reaches this barrier, it turns away from its previous direction to form a continuation of the horizontal line, while the $\tilde{\alpha}_{s3}$ curve forms a continuation of the $\tilde{\alpha}_{s2}$ curve. The same thing happens again when the $\tilde{\alpha}_{s1}$ curve strikes against the barrier formed by the $\tilde{\alpha}_{s2}$ horizontal line. At $M_1 = 10$ (not shown), the first four modes form the same type of pattern. It is the curve starting from $\tilde{\alpha}_{s4}$ at $\sigma = 0$ that is almost horizontal except for brief interruptions at $\sigma = 32$ deg, where it meets $\tilde{\alpha}_{s3}$, at 47.2 deg where it meets $\tilde{\alpha}_{s2}$, and at 60.2 deg where it meets $\tilde{\alpha}_{s1}$. At $\sigma = 60.2$ deg, $\tilde{\alpha}_{s1}$ approaches to within less than 0.1% of $\tilde{\alpha}_{s2}$.

There is no doubt that the identification of the modes is correct as shown in the figures, as it is an easy matter to distinguish the modes by means of the number of

180-deg phase changes across the boundary layer in the fluctuation pressure. Even though the eigenvalues almost coincide at the angles listed above, the solutions do not. The eigenvalues at these angles are nearly degenerate. In some limit, probably $c_s \rightarrow 1$, the eigenvalues will be truly degenerate, i.e., one eigenvalue will correspond to two distinct solutions. The wave-number curves will actually intersect, but the mode identity of a given curve will still change beyond the intersection point. On physical grounds it is necessary for the first-mode curve to always attain a finite value as $\sigma \rightarrow 90$ deg, and for all higher-mode curves to go to infinity with a common asymptote at the angle where the supersonic relative region disappears.

If the wave angles where the eigenvalues are closest together are converted into component Mach numbers, they are, at $M_1 = 5.8$, $\tilde{M}_1 = 3.9$ ($\tilde{\alpha}_{s1}$ and $\tilde{\alpha}_{s2}$); at $M_1 = 8$, $\tilde{M}_1 = 6.5$ ($\tilde{\alpha}_{s2}$ and $\tilde{\alpha}_{s3}$) and 4.4 ($\tilde{\alpha}_{s1}$ and $\tilde{\alpha}_{s2}$); at $M_1 = 10$, $\tilde{M}_1 = 8.5$ ($\tilde{\alpha}_{s3}$ and $\tilde{\alpha}_{s4}$), 6.8 ($\tilde{\alpha}_{s2}$ and $\tilde{\alpha}_{s3}$), and 5.0 ($\tilde{\alpha}_{s1}$ and $\tilde{\alpha}_{s2}$). Or, from a different point of view, for $\tilde{\alpha}_{s1}$ and $\tilde{\alpha}_{s2}$, $3.9 \leq \tilde{M}_1 \leq 5.0$; for $\tilde{\alpha}_{s2}$ and $\tilde{\alpha}_{s3}$, $6.5 \leq \tilde{M}_1 \leq 6.8$; and for $\tilde{\alpha}_{s3}$ and $\tilde{\alpha}_{s4}$, $\tilde{M}_1 = 8.5$. The tendency is clear. As M_1 becomes large, the wave angles, or Mach numbers, of nearest approach take on definite values independent of the free-stream Mach number. It is of interest to recall that this behavior has been encountered previously in the course of this investigation. Fig. 17 shows the neutral wave numbers as functions of the free-stream Mach number for the two-dimensional disturbances. The original version of this figure appeared in Ref. 13, but it

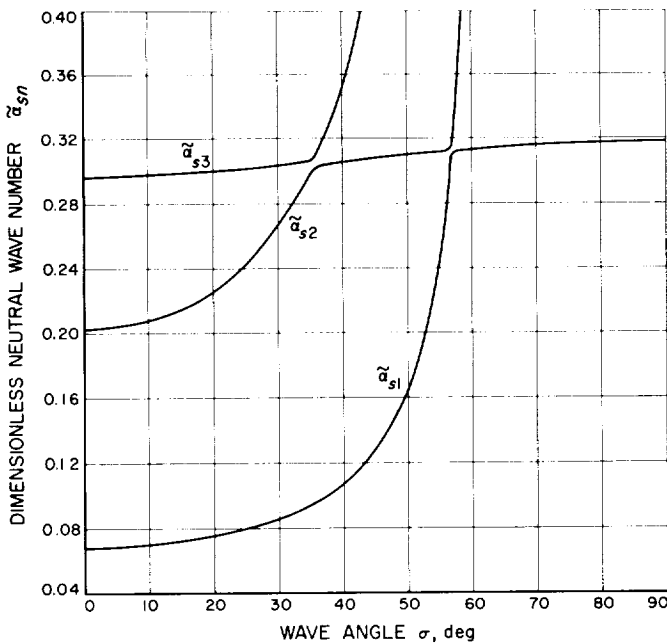


Fig. 16. Effect of wave angle on neutral wave numbers at $M_1 = 8.0$

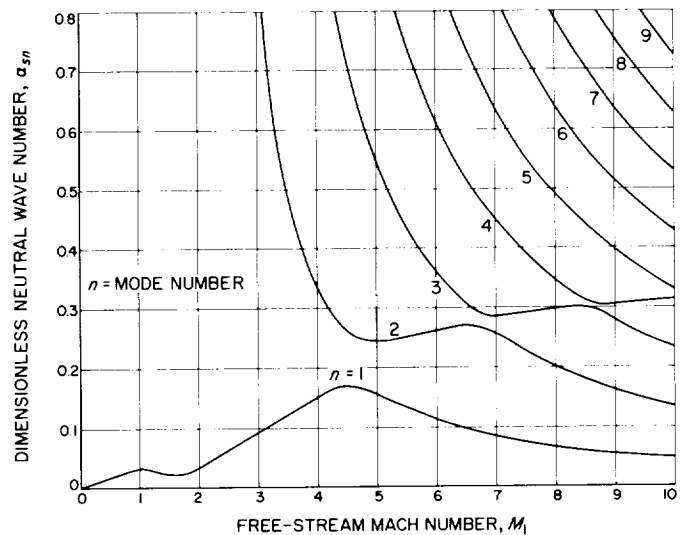


Fig. 17. Effect of free-stream Mach Number on neutral wave numbers of two-dimensional disturbances

has been recomputed more accurately and redrawn for this report. The same phenomenon is observed in Fig. 17 as for the three-dimensional disturbances. The curves for two neighboring modes approach each other and then turn away in such a manner that the curve for one mode appears to be a continuation of the previous curve for the other mode. The Mach numbers of closest approach are 4.7 ($\tilde{\alpha}_{s1}$ and $\tilde{\alpha}_{s2}$), 6.7 ($\tilde{\alpha}_{s2}$ and $\tilde{\alpha}_{s3}$), and 8.6 ($\tilde{\alpha}_{s3}$ and $\tilde{\alpha}_{s4}$). These numbers can be compared with those given above for the three-dimensional disturbances. Obviously the mechanism that gives these results depends almost entirely on the Mach number that enters into the inviscid stability equations and very little on the actual boundary-layer profile.

There are two additional features that distinguish the nearly horizontal lines in Figs. 15, 16, and 17. On these lines, except near the wave angles where the eigenvalues most closely approach each other, the ratio of the pressure-fluctuation amplitude at the wall, $\pi(0)$, to the

amplitude at the edge of the boundary layer, $\pi(\eta\delta)$, is a minimum (of order one) compared to elsewhere on the curves where this ratio can be very large. Further, when the amplified solutions are obtained for a given wave angle, the curve of amplification rate versus frequency, which starts at zero for zero frequency, only returns to zero at the neutral solution of the mode for which $\pi(0)/\pi(\eta\delta)$ is on the minimum portion of the curve. For example, at $M_1 = 8$ and $\sigma = 0$ a single amplification region extends from $\tilde{\alpha} = 0$ to $\tilde{\alpha} = \tilde{\alpha}_{s3}$; at $\sigma = 40$ deg, the same amplification zone extends only to $\tilde{\alpha}_{s2}$; at $\sigma = 60$ deg, it extends to $\tilde{\alpha}_{s1}$. This tendency also exists for the two-dimensional disturbances, but is not clearly defined until a fairly high Mach number, e.g., 7.5, is reached. For instance, at $M_1 = 5.8$, this amplification zone extends not to α_{s2} as one would expect from Fig. 17, but only to α_{s1} . The second-mode amplification zone still exists as a separate, although overlapping, zone. However, at $M_1 = 8$, a combined zone does extend to α_{s3} , and to α_{s4} at $M_1 = 10$, in accord with the interpretation of Fig. 17 given above.

References

1. Muntz, E. P., *Physics of Fluids*, Vol. 5, p. 80, 1962.
2. Robben, F., and Talbot, L., Report No. AS-65-5, University of California, Berkeley, 1965.
3. Bratenahl, A., and Hirsch, W., "Plasma Physics," SPS No. 37-34, Vol. IV, pp. 215-218, Jet Propulsion Laboratory, Pasadena, Calif., August 31, 1965.
4. Hama, F. R., "Experimental Investigations of the Base-Flow Problem, II. Wedge," SPS No. 37-35, Vol. IV, Jet Propulsion Laboratory, Pasadena, California, October 31, 1965.
5. Hama, F. R., "An Efficient Tripping Device," *Journal of the Aeronautical Sciences*, Vol. 24, No. 3, pp. 236-237, March 1957.
6. Hama, F. R., "Boundary-Layer Tripping in Super- and Hyper-sonic Flows," SPS No. 37-29, Vol. IV, Jet Propulsion Laboratory, Pasadena, California, October 31, 1964.
7. Tani, I., "Experimental Investigation of Flow Separation Over a Step," in "Boundary Layer Research, IUTAM Symposium, Freiburg, 1957," H. Goertler, Ed., Springer-Verlag, 1958.
8. Roshko, A., and Lau, J. C., "Some Observations on Transition and Reattachment of a Free Shear Layer in Incompressible Flow," Proceedings of the 1965 Heat Transfer and Fluid Mechanics Institute, Stanford University Press, Stanford, pp. 157-167, 1965.

References (Cont'd)

9. Oswatitsch, K., "Die Abloesungsbedingung von Grenzschichten," in "Boundary Layer Research, IUTAM Symposium, Freiburg, 1957," H. Goertler, Ed., Springer-Verlag, Berlin, 1958.
10. Hama, F. R., "Estimation of the Strength of Lip Shock," *AIAA Journal*, Vol. 4, No. 1, pp. 166-167, January 1966.
11. Roshko, A., and Thomke, G. J., "Observations of Turbulent Reattachment Behind an Axisymmetric Downstream-Facing Step in Supersonic Flow," Douglas Aircraft Co., Report SM-43069, April 1965.
12. Mack, L. M., "The Inviscid Stability of the Laminar Compressible Boundary Layer for Three-Dimensional Disturbances," *SPS No. 37-36*, Vol. IV, pp. 221-223, Jet Propulsion Laboratory, Pasadena, California, December 31, 1965.
13. Mack, L. M., "The Inviscid Stability of the Compressible Laminar Boundary Layer: Part II," *SPS No. 37-36*, Vol. IV, pp. 165-167, Jet Propulsion Laboratory, Pasadena, California, April 30, 1964.

XIX. Physics

A. The Electrostatic Energy per Degree of Freedom of a Two-Temperature Plasma

E. H. Klevans and J. R. Primack

Rostoker (Ref. 1) has computed the electrostatic energy per degree of freedom for a fully ionized two-temperature plasma. He assumed that the electron temperature greatly exceeded the ion temperature and calculated, via resonant integral approximations, the contribution from both electron plasma waves and the weakly damped ion waves. In this note we will consider some features of the calculation not discussed in Ref. 1, and also examine the resonant integral approximation to determine its accuracy.

It is shown in Ref. 1 that the electrostatic energy per degree of freedom for a two-temperature plasma can be written

$$\frac{\theta(k)}{2} = \int \frac{d\omega}{2\pi} W(k, \omega) \tag{1}$$

where

$$W(k, \omega) = \frac{1}{(kL_e)^2} \frac{\pi\theta_e}{k} \frac{f_e^{(0)}\left(\frac{\omega}{k}\right) + f_i^{(0)}\left(\frac{\omega}{k}\right)}{|\epsilon(k, i\omega)|^2} \tag{2}$$

The notation is the same as Rostoker's. Defining $u = \omega/k$, Eq. (1) can be re-expressed in the form

$$\frac{\theta(k)}{2} = \frac{\theta_e}{2} \frac{1}{(kL_e)^2} [K(k) + I(k)] \tag{3}$$

where

$$K(k) = \int_{-\infty}^{\infty} du \frac{f_e^{(0)}(u)}{|\epsilon(k, iku)|^2} \tag{4}$$

$$I(k) = \int_{-\infty}^{\infty} du \frac{f_i^{(0)}(u)}{|\epsilon(k, iku)|^2} \tag{5}$$

Rostoker performed these integrals approximately for two regions of k space. First, when $kL_e < 1$, he neglected the contribution from I , and performed the K integral by integrating over the electron plasma wave resonance. He found

$$\frac{\theta(k)}{2} = \frac{\theta_e}{2} \quad kL_e < 1. \tag{6}$$

Second, for $kL_i < 1$, he evaluated the K and I integrals by integrating over the ion wave resonance. His result is

$$\frac{\theta(k)}{2} = \frac{\theta_r}{2} \frac{(kL_e)^2}{1 + (kL_e)^2} \frac{\sqrt{\frac{m_e}{m_i}} + \sqrt{\frac{\theta_r}{\theta_i}} \exp\left[-\frac{1}{2} \frac{\theta_r}{\theta_i} \frac{1}{1 + (kL_e)^2}\right]}{\sqrt{\frac{m_e}{m_i}} + \left(\frac{\theta_r}{\theta_i}\right)^{3/2} \exp\left[-\frac{1}{2} \frac{\theta_r}{\theta_i} \frac{1}{1 + (kL_e)^2}\right]} \quad (7)$$

It should be emphasized that this is not the complete contribution for $kL_e < 1$, but only the ion wave contribution. This is clearly indicated in Fig. 1 where we have plotted $\tilde{\theta}(k) \equiv \theta(k)/\theta_r$ as a function of kL_e for $\theta_r/\theta_i = 100$. The curves designated as $\tilde{\theta}_P$ and $\tilde{\theta}_R$ are obtained by use of Eqs. (6) and (7). The curve $\tilde{\theta}_E$ will be explained shortly. It is seen from Fig. 1 that for $kL_e < 1$, the plasma wave effect is dominant.

Since the actual behavior of $\theta(k)/\theta_r$ is continuous, the question arises as to what contribution is missing. To find the answer let us examine the behavior of the $K(k)$

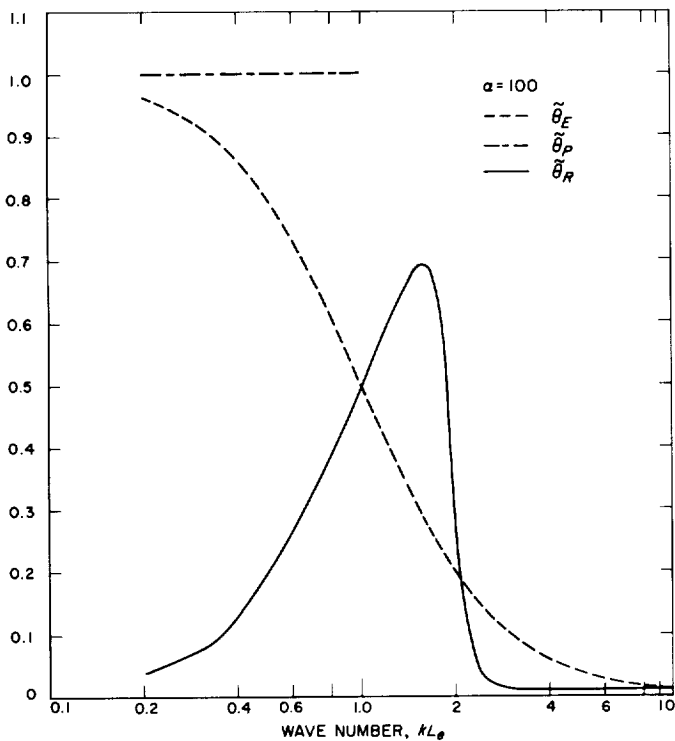


Fig. 1. Comparison of different contributions to the normalized electrostatic energy per degree of freedom. Curves from Eqs. (6), (7), and (11) for $\theta_r/\theta_i = 100$

integral. If $\theta_e \gg \theta_i$ and $kL_e < 1$, then the quantity $|\epsilon(k, iku)|^{-2}$ has a resonance at the ion wave phase velocity

$$u = \left(\frac{\omega_{pi}^2 L_e^2}{1 + (kL_e)^2} \right)^{1/2}, \text{ where } v_e \gg u > v_i.$$

For values of u for which ion waves can exist, $f_e^{(0)}(u) \approx f_e^{(0)}(0)$. On the other hand, when the variable u is sufficiently large that ion waves no longer exist, $\epsilon(k, iku)$ can be approximated by $\rho(k, iku)$, where

$$\rho(k, iku) \equiv 1 + \frac{1}{(kL_e)^2} + \frac{1}{(kL_e)^2} + \int du' \frac{f_e^{(0)}(u')}{u' + u - i\lambda} \quad (8)$$

We are thus able to write

$$K(k) \approx f_e^{(0)} \int_{Res} \frac{du}{|\epsilon(k, iku)|^2} + \int_{-\infty}^{\infty} du \frac{f_e^{(0)}(u)}{|\rho(k, iku)|^2} - \int_{Res} du \frac{f_e^{(0)}(u)}{|\rho(k, iku)|^2} = K_R - K_E - K_{RE} \quad (9)$$

In the term K_E , we are integrating from $-\infty$ to ∞ ; consequently, we have included the term K_{RE} , which cancels the contribution of K_E in the ion wave resonance region. The term K_{RE} is negligible compared with K_R , however, and can therefore be dropped.

The first term, K_R , contains the ion wave contribution. Using the resonant integral approximation (Ref. 2), we obtain

$$K_R = \frac{(kL_e)^4}{1 + (kL_e)^2} \frac{\left(\frac{m_e}{m_i}\right)^{1/2}}{\left(\frac{m_e}{m_i}\right)^{1/2} + \left(\frac{\theta_r}{\theta_i}\right)^{3/2} \exp\left[-\frac{1}{2} \frac{1}{1 + (kL_e)^2}\right]} \quad (10)$$

The term K_E is the electron contribution. It can be evaluated exactly, as shown by Rostoker (Ref. 1), and also in (Ref. 2). The result is

$$K_E = \frac{1}{\rho(0)} = \frac{(kL_e)^2}{1 + (kL_e)^2} \quad (11)$$

If $kL_e > 1$, there is no ion wave resonance, and only the term K_E is important. When $kL_e < 1$, $K_E \rightarrow (kL_e)^2$ and $\theta(k)/\theta_r \rightarrow 1$, the plasma wave result. In Fig. 1, the curve $\tilde{\theta}_E$ represents the electron contribution as obtained from Eq. (11). It is clear that K_E is important over the entire range of kL_e .

Finally, we inquire into the validity of the resonant integral approximation. The discussion is greatly facilitated by the use of Fig. 2. The quantity $\tilde{\theta}$ is defined as $\theta(k)/\theta_e$. On this graph we have plotted four quantities: (1) $\tilde{\theta}_R$, which is obtained by use of Eq. (7); (2) $\tilde{\theta}_{R+E}$ which is found by adding $\tilde{\theta}_E$ to $\tilde{\theta}_R$; (3) $\tilde{\theta}_c$, which is obtained from computer calculation of $\tilde{\theta}$; and (4) $\tilde{\theta}_N$, which is a new approximate evaluation. Although the $\tilde{\theta}_{R+E}$ approximation shows good qualitative agreement with the computer results, there is substantial numerical error for kL_e between 1.8 and 2.5. On the other hand, $\tilde{\theta}_N$ shows good quantitative agreement over the whole range of kL_e . To obtain $\tilde{\theta}_N$ we note that there are two sources of error in $\tilde{\theta}_{R+E}$. First, the resonant approximation for the I integral is not good except for kL_e between 1.9 and 3 (Ref. 2). To improve the approximation we rewrite the $I(k)$ integral (Ref. 2)

$$I(k) = \left(1 + \frac{\theta_i}{\theta_e}\right) \frac{1}{\epsilon(0)} - \frac{\theta_i}{\theta_e} K(k). \quad (12)$$

Then

$$\tilde{\theta}(k) = \frac{1}{(kL_e)^2} \left[\left(1 + \frac{\theta_i}{\theta_e}\right) \frac{1}{\epsilon(0)} + \left(1 - \frac{\theta_i}{\theta_e}\right) K(k) \right]. \quad (13)$$

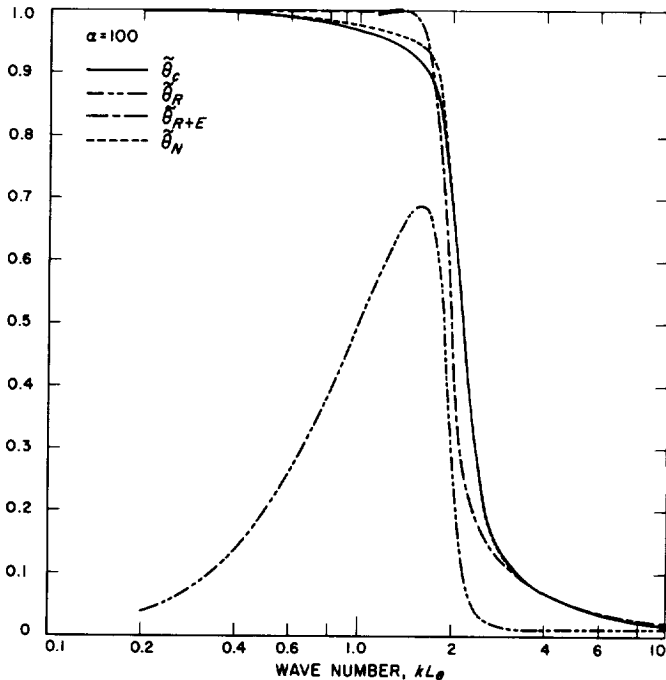


Fig. 2. Normalized electrostatic energy per degree of freedom for $\theta_e/\theta_i = 100$. Curve θ_c obtained by computer calculation; the others by approximate evaluation

If we now substitute $K \simeq K_E + K_R$ into Eq. (13) and use Eq. (9) for K_E , we have

$$\theta(k) = \frac{1}{1 + (kL_e)^2} \left[1 + \frac{(kL_e)^2}{1 + \frac{\theta_e}{\theta_i} + (kL_e)^2} \right] + \frac{1}{(kL_e)^2} \left(1 - \frac{\theta_i}{\theta_e}\right) K_R(k). \quad (14)$$

If Eq. (10) is used for K_R we will find that there is a small improvement over $\tilde{\theta}_{R+E}$ for $(kL_e) < 2$.

A more important error in $\tilde{\theta}_{R+E}$ results from using insufficiently accurate values for the ion wave phase velocity and resonant width in the resonant integral calculation of K_R . More accurate values for these quantities are obtained in Ref. (2). When these values are used, the $K_R(k)$ integral becomes (Ref. 2)

$$K_R(k) = \frac{(kL_e)^4}{1 + (kL_e)^2} \frac{\left[1 + 3 \frac{\theta_i}{\theta_e} (1 + k^2 L_e^2) \right]}{1 + 3/y_i^2} \times \frac{1}{1 + \left(\frac{m_i}{m_e} \frac{\theta_e^2}{\theta_i^3}\right)^{1/2} \exp(-y_i^2)} \quad (15)$$

where

$$y_i^2 = \frac{\theta_e/2\theta_i}{1 + (kL_e)^2} \left[1 + 3 \frac{\theta_i}{\theta_e} (1 + k^2 L_e^2) \right] \quad (16)$$

With this expression, Eq. (14) can be written in the form

$$\tilde{\theta}_N = \frac{1}{1 + (kL_e)^2} \left\{ 1 + \frac{(kL_e)^2}{1 + \frac{\theta_e}{\theta_i} + (kL_e)^2} + \left(1 - \frac{\theta_i}{\theta_e}\right) (kL_e)^2 \times \frac{\left[1 + 3 \frac{\theta_i}{\theta_e} (1 + (kL_e)^2) \right]}{\left(1 + 3/y_i^2\right) \left[1 + \left(\frac{m_i}{m_e} \frac{\theta_e^2}{\theta_i^3}\right)^{1/2} \exp(-y_i^2) \right]} \right\} \quad (17)$$

We have found that Eq. (17) gives excellent agreement with computer calculations over a wide range of temperature ratios.

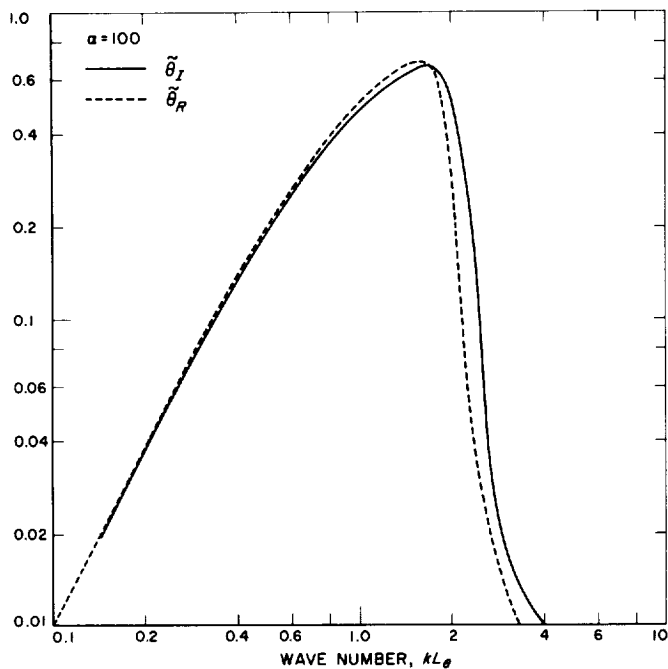


Fig. 3. Comparison of Rostoker's result for the ion wave contribution with the new approximate result, Eq.(18), for $\theta_r/\theta_i = 100$

Finally, in Fig. 3 we compare with $\tilde{\theta}_R$ the improved ion wave contribution $\tilde{\theta}_I$, where

$$\tilde{\theta}_I \equiv \tilde{\theta}_R - \frac{K_E}{(kL_e)^2} \tag{18}$$

Although θ_R and θ_I are qualitatively the same, there is a significant numerical difference for $kL_e > 1.7$.

B. Commutated Analog-to-Digital Converter

L. Lewyn

Measurements of temperature and magnetic field intensity are required in the Spark Chamber Balloon Experiment described in Ref. 3. The temperature-sensor and magnetometer amplifiers have 0-5 v analog outputs which must be measured to an accuracy of 1%. The analog output voltages are commutated to a single-line output by the analog commutator shown in Fig. 4. The commutator

output is fed to an analog-to-digital converter (ADC) shown in Fig. 5.

The analog commutator has eight identical inputs. The first seven inputs are connected to the signals which are to be measured, while the last (reference) input is connected to ground. An input is selected by clamping the input to one of the selection transistor (Q_1-Q_8) base networks to ground. When the base network of one of the selection transistors is clamped to ground it acts as a constant-current source, injecting approximately 1 ma of current into the collector node. This current divides between the diode connected to the output bus and the diode connected to the selected input. The diode connected to the output bus must furnish a constant-current load which is composed of the constant-current source Q_6 , and the current coming from the ADC. The sum of these currents is about $\frac{1}{2}$ ma. Therefore $\frac{1}{2}$ ma is forced into the diode connected to the selected input. The absolute accuracy (neglecting the drop across R_i) is determined by the matching of the characteristics of the input and output diodes and the equality of input and output diode current. The absolute accuracy is not important, since the ADC measures the voltage difference between any two consecutively selected inputs. In normal operation the ADC measures the difference voltage due to first selecting a signal input and then selecting the reference input. Therefore most of the errors associated with changes in supply voltage and temperature-dependent transistor characteristics are removed.

The ADC is a height-to-time device. Capacitor C is first charged to the signal input voltage by the current from the differential amplifier (Q_1-Q_3). Then when the reference command line is clamped to ground, Q_4 is turned on by the constant-current switch (Q_7, Q_8), and C is discharged by the constant-current source Q_6 . When the voltage on C becomes equal to the reference input voltage, the differential amplifier shuts off Q_4 , and the conversion is complete. Q_{10} and Q_{11} drive the peak detector output to +6 while Q_6 is on. The peak-detector output gates a 2-Mc clock into a register which stores the digital result of the conversion. The reference command is synchronized with the clock externally in order to prevent a one-count ambiguity in the digital answer.

Since the ADC measures the difference between two consecutive input voltages, most of the errors associated with supply-voltage variation and temperature-dependent transistor characteristics are removed. Linearity is achieved by operating the differential amplifier at constant load and not switching the constant current source to initiate conversion.

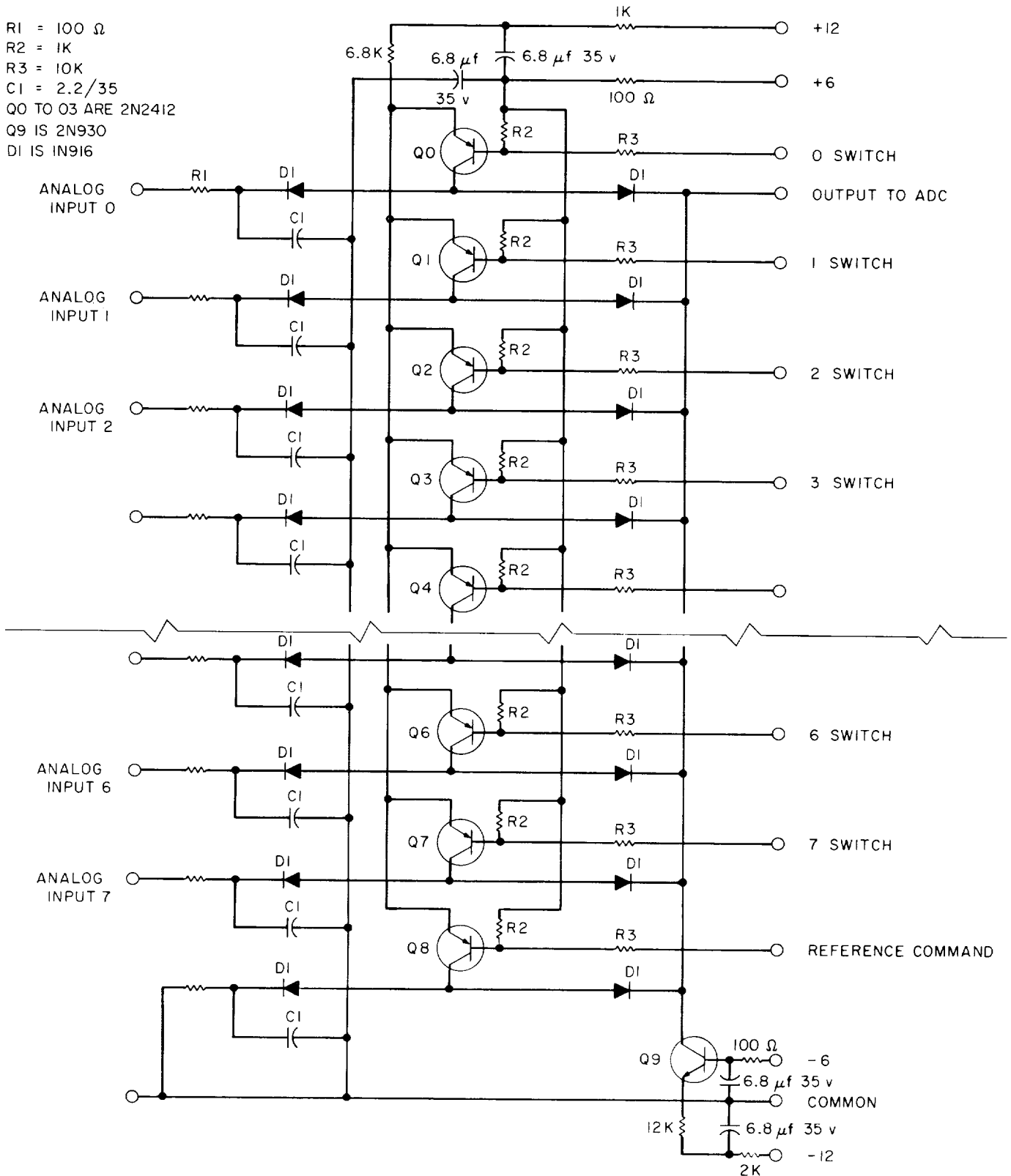


Fig. 4. Analog commutator

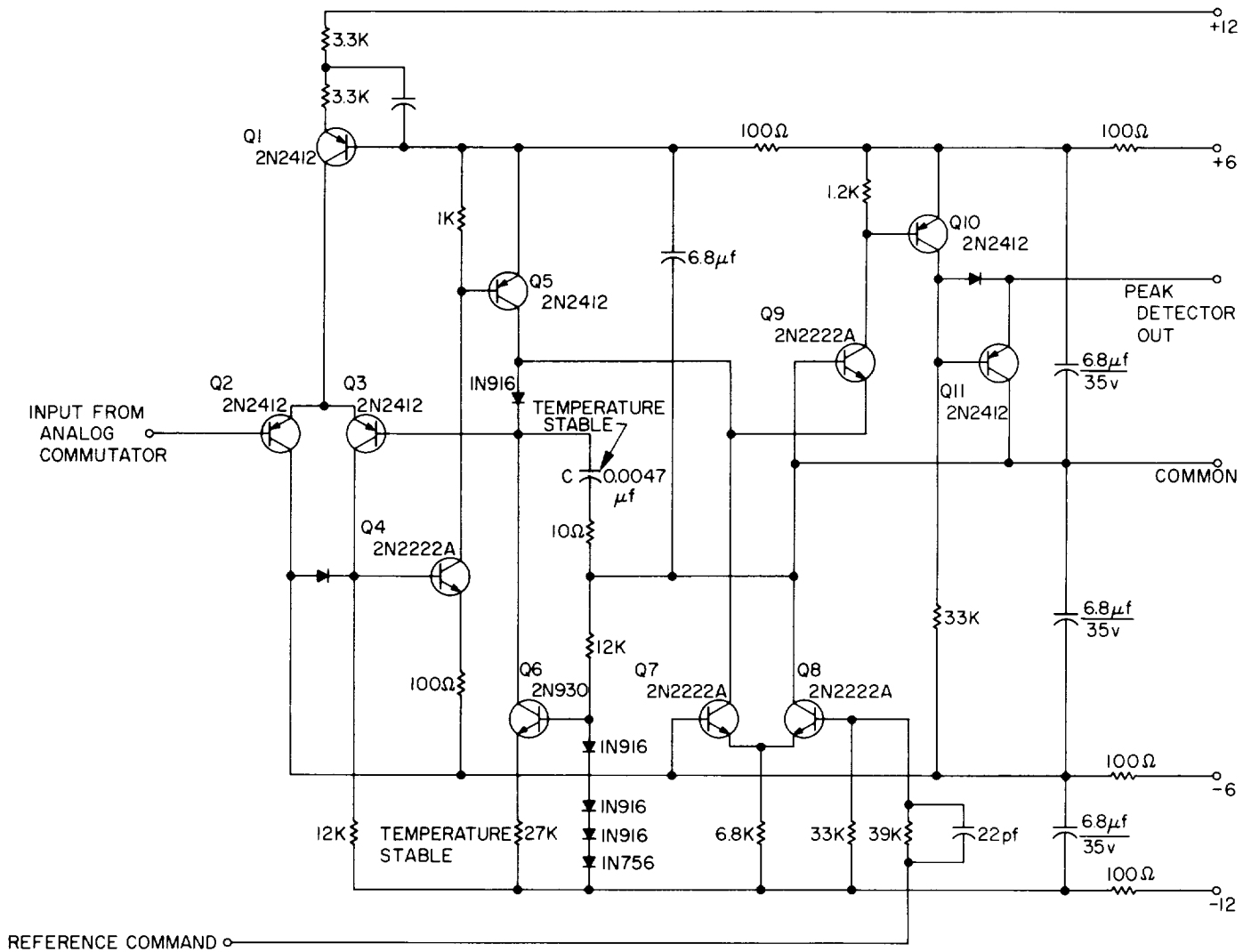


Fig. 5. Analog-to-digital converter

Laboratory tests conducted 10°C beyond the expected limits (0 to +50°C) of the Spark Chamber Balloon Experiment indicated that the system accuracy is better than ±0.5%. The largest source of error is the variation in conversion gain caused by the voltage dependence of the

temperature coefficient of the 1N756 zener diode. The temperature coefficient normally varies from 0.058 to 0.062. Therefore better accuracies may be obtained by using a specially selected zener diode. The integral linearity of the system is better than ±0.1%.

References

1. Rostoker, N., *Nuclear Fusion*, Vol. 1, p. 101, 1961.
2. Klevans, E. H., and Primack, J. R., "Analysis of the Dielectric Constant of a Two-Temperature Plasma and Applications," Technical Report No. 32-888, Jet Propulsion Laboratory, Pasadena, California (to be published).
3. McDonald, W. S., "The JPL Spark Chamber," *SPS 37-35*, Vol. IV, p. 248, Jet Propulsion Laboratory, Pasadena, California, October 31, 1965.

TELECOMMUNICATIONS DIVISION

XX. Communications Elements Research

A. Microwave Electronics

W. H. Higa

1. Hydrogen Maser Frequency Standard

In the measurement of short-term stability of a frequency standard it is convenient to have access to a delay line with a time delay of approximately a microsecond or longer. Such a device would permit autocorrelation measurements to be made. This is a brief report on the possibility of achieving such delays in cryogenically cooled traveling wave structures.

a. Cryogenic delay line. Recent advances in superconductivity have resulted in the use of long coaxial superconducting transmission lines as delay lines; such delay lines depend on dielectric slowing to reduce the group velocity, hence the length of transmission line required is still considerable. An alternative technique is to use resonant slowing, as in a traveling wave maser, to achieve appreciable slowing of wave propagation. Physically, this method utilizes a large number of loosely coupled resonators to provide a transmission line with low group velocity.

For sufficiently high Q in the resonators, it is well known that group velocity v_g equals the energy velocity and is given by

$$v_g = W/P$$

where W = stored energy per unit length and P = transmitted power.

The transmitted power may be related to a loaded Q_e for the resonator in the usual way:

$$Q_e = \omega W/P$$

where ω is 2π times the signal frequency. Thus v_g in terms of Q_e is given by

$$v_g = \omega/Q_e.$$

Experience with traveling wave masers has indicated the possibilities of achieving slowing factors S of the order of 200 to 300 where

$$S = c/v_g$$

here c = velocity of light in free space.

Cryogenic temperatures are desirable to reduce signal attenuation and thermal noise contributions. Comb structures of the type used in traveling wave masers can be fabricated for a total length of approximately a meter and can be readily cooled to 4.2°K. With a slowing of 300, such a delay line would provide a microsecond delay.

To achieve even greater delays it is probably necessary to operate at liquid nitrogen temperatures. An analysis

of the effects of fluctuations in resonator-to-resonator coupling will be made in order to evaluate the limitations of this type of delay line.

B. RF Techniques

W. V. T. Rusch, C. T. Stelzried, T. Otschi, and M. S. Reid

1. 90-Gc Millimeter Wave Work,

W. V. T. Rusch and C. T. Stelzried

a. Summary. The objective of this work is to investigate millimeter wave components and techniques to ascertain the future applicability of this frequency range to space communications and tracking. This involves the development of instrumentation for accurate determination of insertion loss, VSWR, power and equivalent noise temperatures of passive elements. Millimeter wave circuit elements are being evaluated in a radio telescope system consisting of a 60-in. antenna and a superheterodyne radiometer (SPS 37-33, Vol. IV). The radio telescope was used to observe the 90-Gc temperature of the Moon during the December 30, 1963 eclipse (SPS 37-26, Vol. IV, p. 181) and the most recent eclipse, December 18, 1964. These experiments were joint efforts by personnel from JPL and the Electrical Engineering Department, University of Southern California.

b. Nodding subdish. Synchronous switching techniques are generally used to detect weak radio-astronomical signals in the presence of relatively high noise contributions from the atmosphere and the receiver itself. One successful switching technique used in radio astronomy has been to switch the antenna beam from the source to a nearby position in the sky. It appears that this beam-switching may be accomplished by periodically nodding the hyperboloidal subdish in the Cassegrainian feed system between two symmetrical but slightly off-axis positions.

A major problem with the nodding subdish scheme is that of thermal calibration. One contemplated calibration technique is schematically illustrated in Fig. 1 and outlined below:

- (1) Waveguide switch turned to ambient load and ferrite circulator switched synchronously: output = $T_0 - T_0 = 0$.

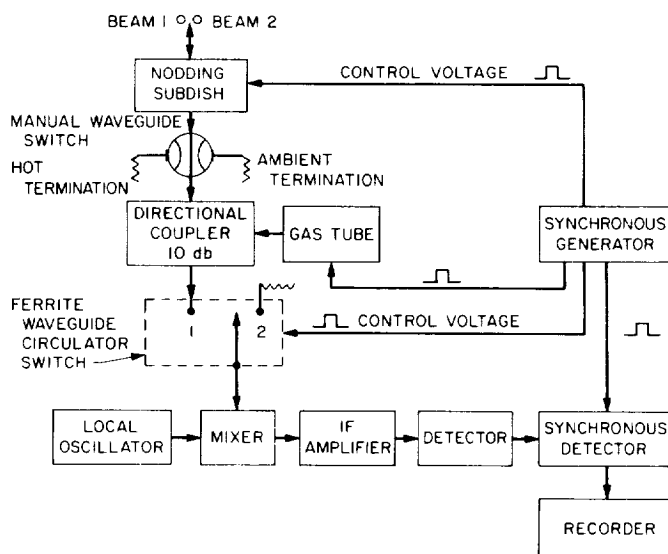


Fig. 1. Schematic of proposed 90-Gc radiometer nodding subdish calibration scheme

- (2) Waveguide switch turned to hot load and ferrite circulator switched synchronously: output = $T_H - T_0$.
- (3) Waveguide switch turned again to ambient load; gas tube fired synchronously: output = $(T_0 + T_{GT}) - T_0 = T_{GT}$.

From (1) and (2) a scale factor is obtained in degrees Kelvin per unit output, which is used to determine the equivalent noise temperature of T_{GT} in degrees Kelvin.

The data-taking technique associated with the above calibration technique proceeds as follows:

- (1) Replace ferrite switch with straight waveguide section.
- (2) Aim away from source and nod subdish synchronously: output = $T_{SKY} - T_{SKY} = 0$.
- (3) Continue aiming away from source; nod subdish synchronously; gas tube fired synchronously when subdish is in Position 1: output = $(T_{SKY} + T_{GT}) - T_{SKY} = T_{GT}$.
- (4) Turn off gas tube; aim one switching lobe at source, one switching lobe at sky:

$$\text{output} = (T_{SOURCE} + T_{SKY}) - T_{SKY} = T_{SOURCE}$$

2. Antenna Temperature Analysis, T. Otoshi

a. Summary. A discussion of the equations for an antenna temperature analysis computer program was presented in *SPS 37-36*, Vol. IV, pp. 262-267. As described, the analysis is restricted to the case of a linearly polarized circularly symmetric antenna containing only $m = 1$ modes.

The computer program has now been generalized to include the circular polarization case and will be useful for determining the antenna gain, zenith antenna temperature, and respective probable errors. The computer inputs required for the program are: (1) raw data from antenna patterns taken in the E and H planes for a linearly polarized antenna or RCP and LCP illuminated antenna patterns for the circularly polarized antenna case, (2) antenna brightness temperature data, and (3) probable errors of the pattern and antenna brightness temperature data.

Writing of the program for the IBM 7094 computer has been completed. Test cases using various probable error values are being run through the computer and results evaluated. Results and discussion of some specific examples will be presented in a future *SPS*.

This report will be restricted to a discussion and presentation of power reflection coefficients and improved ground brightness temperature data which can be used with the computer program.

b. Effective power reflection coefficient. From the referenced *SPS* article, it was shown that for a circularly symmetric antenna, excited by modes with one azimuthal variation ($m = 1$ modes), the complete far field electric field may be expressed as

$$\mathbf{E}_0(R, \phi, \theta) = \frac{|A_1(\theta)|}{R} (\sin \phi) e^{-j[kR - \Phi_{A_1}(\theta)]} \mathbf{a}_\theta + \frac{|B_1(\theta)|}{R} (\cos \phi) e^{-j[kR - \Phi_{B_1}(\theta)]} \mathbf{a}_\phi \quad (1a)$$

where $|A_1(\theta)|/R$ and $|B_1(\theta)|/R$ were defined as the absolute E- and H-plane amplitude patterns, respectively. Definitions of other quantities may be found in the referenced article.

The geometry of a zenith-oriented antenna situated above flat ground infinite in extent may be seen in Fig. 2.

Since $\mathbf{E}_0(R, \phi, \theta)$ is actually the incident wave for this geometry, let

$$\mathbf{E}_i(R, \phi, \theta) = \mathbf{E}_0(R, \phi, \theta) \quad (1b)$$

$$E_{i\theta} = \frac{|A_1(\theta)|}{R} (\sin \phi) e^{-j[kR - \Phi_{A_1}(\theta)]} \quad (2)$$

$$E_{i\phi} = \frac{|B_1(\theta)|}{R} (\cos \phi) e^{-j[kR - \Phi_{B_1}(\theta)]} \quad (3)$$

so that

$$\mathbf{E}_i(R, \phi, \theta) = E_{i\theta} \mathbf{a}_\theta + E_{i\phi} \mathbf{a}_\phi. \quad (4)$$

The term $E_{i\theta}$ represents an incident electric field polarized in the plane of incidence and $E_{i\phi}$ term represents an incident electric field polarized perpendicular to the plane of incidence. Similarly, at the incident point (R, ϕ, θ) on the ground, the expression for the total reflected wave may be written as

$$\mathbf{E}_r(R, \phi, \theta) = E_{r\theta} \mathbf{a}_\theta + E_{r\phi} \mathbf{a}_\phi. \quad (5)$$

At any particular point (R, ϕ, θ) at which \mathbf{E}_i is incident upon the ground, we may by definition, let

$$\begin{aligned} \Gamma_{||}(\theta) &= \text{voltage reflection coefficient of the} \\ &\quad \text{parallel (in-plane) polarized wave} \\ &= \frac{E_{r\theta}}{E_{i\theta}} \quad \frac{\pi}{2} \leq \theta \leq \pi \quad (6) \end{aligned}$$

$$\begin{aligned} \Gamma_{\perp}(\theta) &= \text{voltage reflection coefficient of the} \\ &\quad \text{perpendicular polarized wave} \\ &= \frac{E_{r\phi}}{E_{i\phi}} \quad \frac{\pi}{2} \leq \theta \leq \pi. \quad (7) \end{aligned}$$

Note that $\Gamma_{||}(\theta)$ and $\Gamma_{\perp}(\theta)$ are phasors (complex numbers) so that they possess both magnitude and phase.

The expression for the total reflected wave at the coordinate (R, ϕ, θ) intercept point would be

$$\mathbf{E}_r(R, \phi, \theta) = \Gamma_{||}(\theta) E_{i\theta} \mathbf{a}_\theta + \Gamma_{\perp}(\theta) E_{i\phi} \mathbf{a}_\phi. \quad (8)$$

The generalized expression for the total power reflection coefficient at (R, ϕ, θ) will be defined as

$$|\Gamma_T(\phi, \theta)|^2 = \left[\frac{|\mathbf{E}_r(R, \phi, \theta)|}{|\mathbf{E}_i(R, \phi, \theta)|} \right]^2 \quad \frac{\pi}{2} \leq \theta \leq \pi. \quad (9)$$

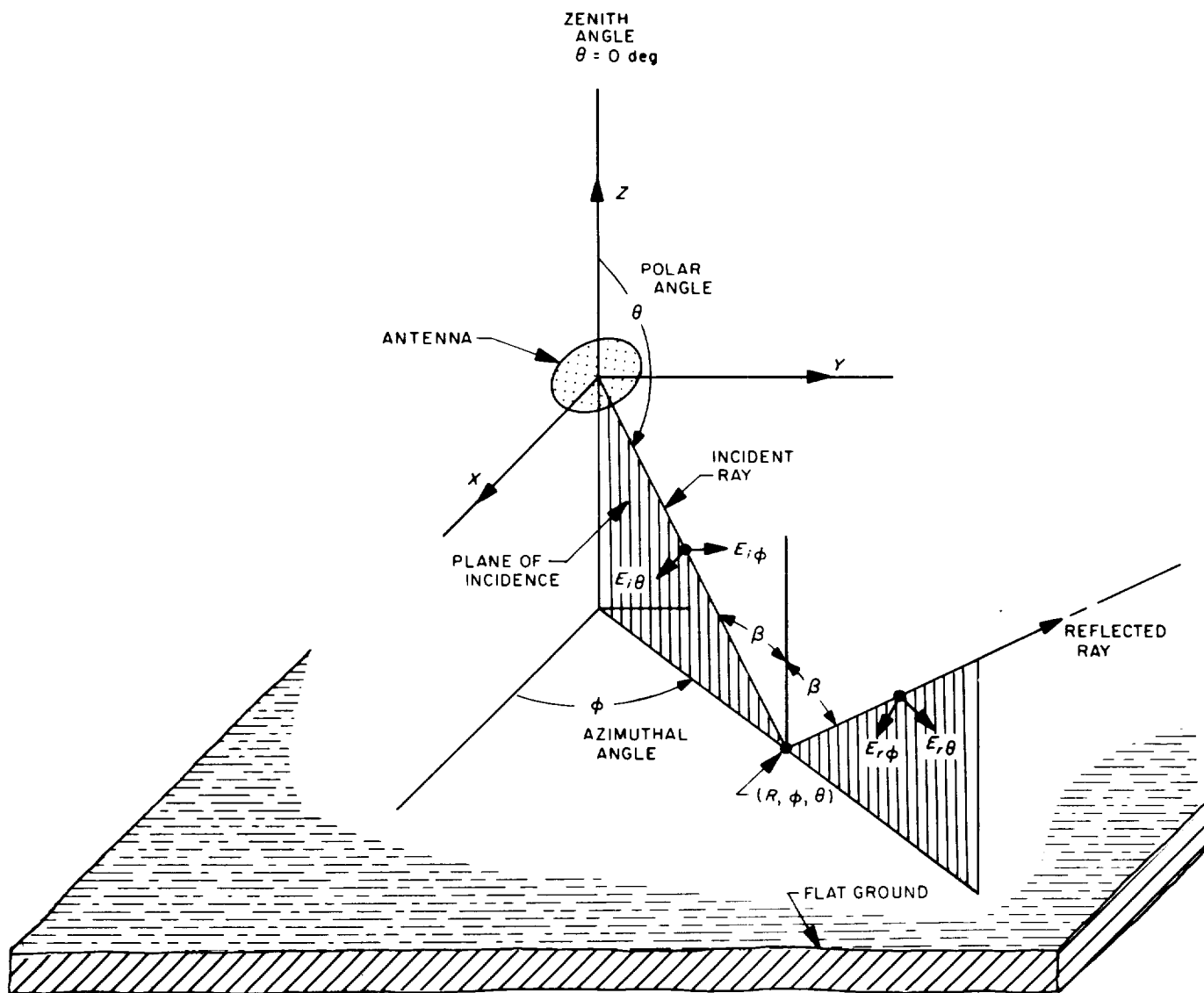


Fig. 2. Antenna situated over flat ground

From Eqs. (8) and (4)

$$|\Gamma_T(\phi, \theta)|^2 = \left[\frac{|\Gamma_{11}(\theta)|^2 |E_{i\theta}|^2 + |\Gamma_{12}(\theta)|^2 |E_{i\phi}|^2}{|E_{i\theta}|^2 + |E_{i\phi}|^2} \right], \quad \frac{\pi}{2} \leq \theta \leq \pi \quad (10)$$

and in terms of E- and H-plane amplitude patterns from Eqs. (2) and (3), we obtain

$$|\Gamma_T(\phi, \theta)|^2 = \left[\frac{|\Gamma_{11}(\theta)|^2 |A_1(\theta)|^2 \sin^2 \phi + |\Gamma_{12}(\theta)|^2 |B_1(\theta)|^2 \cos^2 \phi}{|A_1(\theta)|^2 \sin^2 \phi + |B_1(\theta)|^2 \cos^2 \phi} \right], \quad \frac{\pi}{2} \leq \theta \leq \pi. \quad (11)$$

For zenith antenna temperature calculations, assuming uniform ground properties independent of ϕ , it would be desirable to use an average brightness temperature based on an average or effective power reflection coefficient which is independent of ϕ , and is therefore a function of θ (antenna polar angle) only. Over an annular

solid angle segment, the average or effective power reflection coefficient may be defined as follows:

$$|\Gamma_E(\theta)|^2 = \frac{1}{2\pi} \int_0^{2\pi} |\Gamma_T(\theta, \phi)|^2 d\phi. \quad (12)$$

Special case. For the special case where the amplitude patterns for the E- and H-planes are identical, i.e.,

$$|A_1(\theta)| = |B_1(\theta)|.$$

Substitution into Eq. (11) gives

$$|\Gamma_T(\theta, \phi)|^2 = [|\Gamma_{\parallel}(\theta)|^2 \sin^2 \phi + |\Gamma_{\perp}(\theta)|^2 \cos^2 \phi], \quad \frac{\pi}{2} \leq \theta \leq \pi \quad (13)$$

and from Eq. (12)

$$|\Gamma_E(\theta)|^2 = \left[\frac{|\Gamma_{\parallel}(\theta)|^2 + |\Gamma_{\perp}(\theta)|^2}{2} \right], \quad \frac{\pi}{2} \leq \theta \leq \pi. \quad (14)$$

It may be shown that this effective power reflection coefficient can be used for zenith antenna temperature calculations for the circularly polarized antenna case as well.

The parallel and perpendicular voltage reflection coefficients $\Gamma_{\parallel}(\theta)$ and $\Gamma_{\perp}(\theta)$ for the general case are functions of frequency, incidence angle, dielectric constant, and electrical conductivity of the second media. As derived in Ref. 1 and general electromagnetic theory textbooks, such as Ref. 2, the index of refraction of ground can be determined from the expression

$$n = \frac{\left(\epsilon_{r2} - j \frac{\sigma_2}{\omega \epsilon_0} \right)^{1/2}}{(\epsilon_{r1})^{1/2}} \quad (15)$$

where

ϵ_{r2} = relative dielectric constant of medium 2 (ground in this case)

σ_2 = electrical conductivity of medium 2 (ground), mho-m/m²

ϵ_{r1} = relative dielectric constant of medium 1 (air = 1)

ω = radian frequency in rad/sec

ϵ_0 = dielectric constant of free space = $(1/36\pi) \times 10^{-9}$, h/m

For the case of the electric field polarized normal to the plane of incidence, the phasor expression for voltage reflection coefficient in terms of incidence angle β and n is

$$\Gamma_{\perp}(\beta) = \left[\frac{\cos \beta - (n^2 - \sin^2 \beta)^{1/2}}{\cos \beta + (n^2 - \sin^2 \beta)^{1/2}} \right], \quad 0 \leq \beta \leq \frac{\pi}{2} \quad (16)$$

or in terms of antenna polar angle θ and n ,

$$\Gamma_{\perp}(\theta) = \left[\frac{\cos(\pi - \theta) - [n^2 - \sin^2(\pi - \theta)]^{1/2}}{\cos(\pi - \theta) + [n^2 - \sin^2(\pi - \theta)]^{1/2}} \right], \quad \frac{\pi}{2} \leq \theta \leq \pi. \quad (17)$$

For the case of the electric field polarized parallel to the plane of incidence, the phasor expression of voltage reflection coefficient is

$$\Gamma_{\parallel}(\beta) = \left[\frac{n^2 \cos \beta - (n^2 - \sin^2 \beta)^{1/2}}{n^2 \cos \beta + (n^2 - \sin^2 \beta)^{1/2}} \right], \quad 0 \leq \beta \leq \frac{\pi}{2} \quad (18)$$

or

$$\Gamma_{\parallel}(\theta) = \left[\frac{n^2 \cos(\pi - \theta) - [n^2 - \sin^2(\pi - \theta)]^{1/2}}{n^2 \cos(\pi - \theta) + [n^2 - \sin^2(\pi - \theta)]^{1/2}} \right], \quad \frac{\pi}{2} \leq \theta \leq \pi. \quad (19)$$

c. Antenna brightness temperature. The antenna brightness temperature may be defined as the apparent noise temperature which is seen by the antenna looking along a direct ray. The antenna pattern is assumed to have a delta function of response versus angle and, therefore, subtends an infinitesimal solid angle (Ref. 3).

The relationship of zenith antenna temperature to brightness temperature may be seen from the following. The total effective antenna temperature of a zenith-oriented antenna situated above infinite flat ground can be computed from

$$T_A = \frac{1}{2} \int_0^{\pi/2} T_{sky}(\theta) G(\theta) \sin \theta d\theta + \frac{1}{2} \int_{\pi/2}^{\pi} T_G(\theta) G(\theta) \sin \theta d\theta \quad (20)$$

where

- θ = polar antenna angle, rad
- $T_{sky}(\theta)$ = sky brightness temperature function, °K
- $T_g(\theta)$ = ground brightness temperature function, °K
- $G(\theta)$ = antenna gain function relative to isotropic

The ground brightness temperature function is determined from the expression

$$T_G(\theta) = [1 - |\Gamma_E(\theta)|^2] T_0 + |\Gamma_E(\theta)|^2 T_{sky}(\pi - \theta), \quad \frac{\pi}{2} \leq \theta \leq \pi \quad (21)$$

where

$|\Gamma_E(\theta)|^2$ = effective power reflection coefficient of the ground as previously defined by Eq. (12)

T_0 = physical ground temperature, °K

$T_{sky}(\pi - \theta)$ = sky brightness temperature corresponding to incidence angle β , °K (Fig. 2)

The brightness temperature function of the sky may be obtained by using Hogg's sky data (Ref. 3). For previous JPL computations of antenna temperature and for brightness temperature of the ground, an average value of 240°K (independent of antenna angle) has been assumed for a flat desert ground environment to simplify calculations. With a computer program, it is now feasible to use more accurate values of ground brightness temperature based on Eq. (21) and empirical values of ground dielectric constants and conductivities (Ref. 1). Eq. (21) can also be used to compute brightness temperature function of other media such as sea water by substitution of the proper values of dielectric constants and conductivities.

Special case plot. A sample plot of 2295-Mc brightness temperatures for an antenna situated over flat desert ground may be seen in Fig. 3. For this plot, the brightness temperatures for antenna polar angles $\theta = 0$ to 90 deg are the sky brightness temperatures as obtained from Hogg's curves for the specified frequency.

The brightness temperature values for antenna polar angles $\theta = 90$ to 180 deg are computed with Eq. (21).

The effective power reflection coefficient from Eq. (14) for an antenna with identical E- and H-plane patterns was used. Evaluation of $\Gamma_{\perp}(\theta)$ and $\Gamma_{\parallel}(\theta)$, given by Eqs. (17) and (19), used

$$\epsilon_{rz} = 3.0$$

$$\sigma_z = (1/9) \times 10^{-1} \text{ mho-m/m}^2$$

$$f = 2295 \text{ Mc} = 2.295 \times 10^9 \text{ cps}$$

appropriate for desert ground based on data taken from curves presented in Ref. 1.

Brightness temperatures recalculated for 2388 Mc were found to be essentially the same as for 2295 Mc.

As may be observed in the brightness temperature curve of Fig. 3, a decrease in brightness temperature occurs in the region just beyond the horizon point (90 deg for flat ground). The minimum point appears to be centered at about the antenna polar angle of 93 deg. From the substitutions of the above ground parameters into Eq. (21), it was found that this minimum in brightness temperature occurs very close to the angle at which brightness temperature is contributed equally by the sky and ground environments. To lend support to the fact that a dip could occur in brightness temperature just beyond the horizon, a similar phenomenon has been observed experimentally in a JPL measurement made of antenna temperature versus elevation angle at 960 Mc (SPS 37-10, Vol. IV, p. 71).

3. Error Analysis of Continuous Wave (CW) Signal Power Calibration With Thermal Noise Standards, C. T. Stelzried and M. S. Reid¹

An attempt to improve the accuracy of the calibration of the CW received signal power in the DSN is under way. A convenient measure of a spacecraft-received power level is the receiver AGC voltage which is calibrated for absolute received power, defined at the receiver input, with a calibrated test transmitter. The theory, method of data acquisition, and equipment were discussed in SPS 37-35, Vol. III, p. 58. The Y-factor method utilized consists of accurately measuring the ratio at the output of the receiving system of the CW signal power P_s plus the system noise power P_n , to the system noise power.

¹On leave of absence from National Institute for Telecommunications Research, Johannesburg, South Africa.

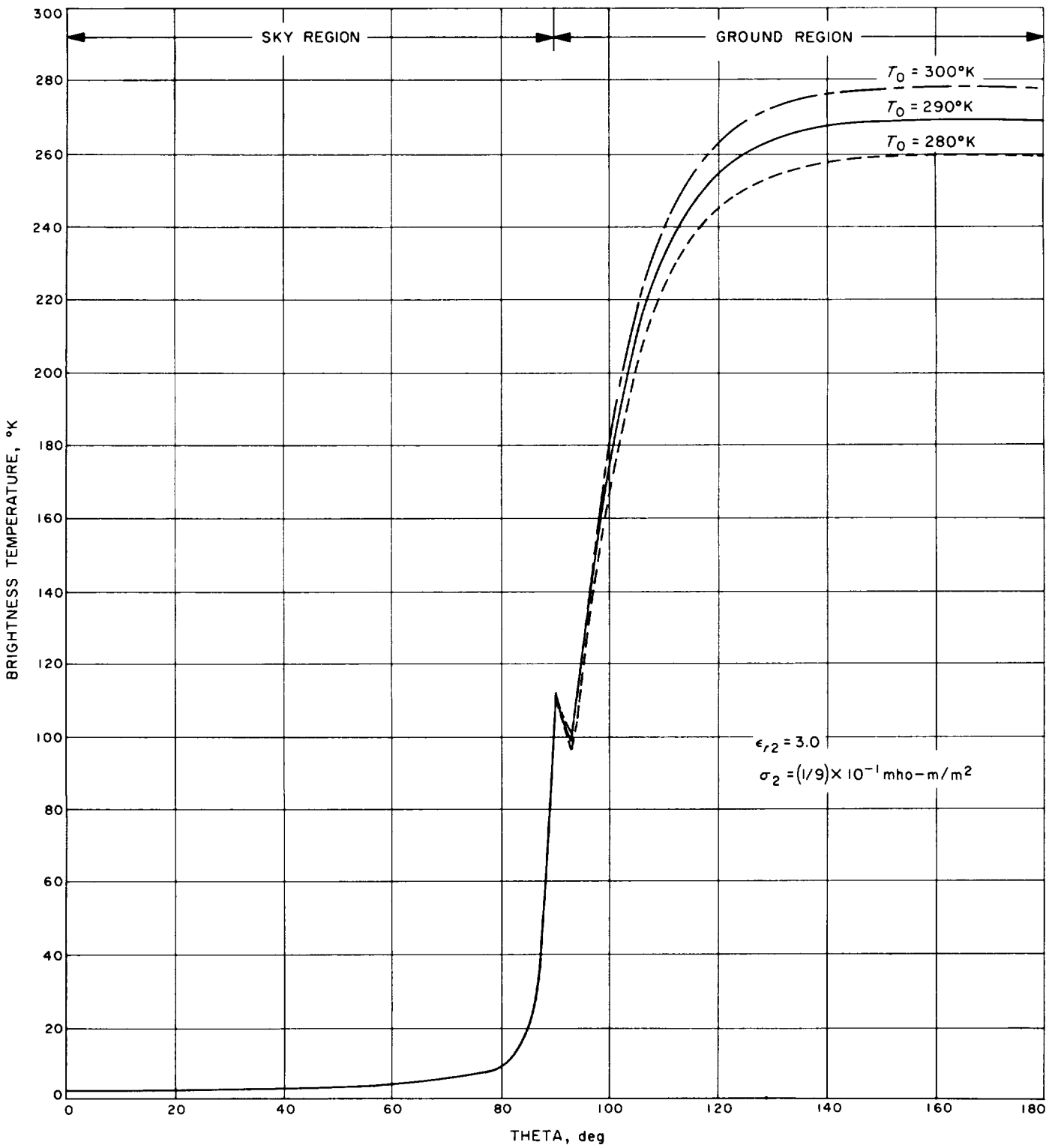


Fig. 3. Brightness temperature curve for antenna over flat desert ground at 2295 Mc

a. Analysis of diode sensitivity to CW and noise signals.
 The detector for the Y-factor measurements was a 1N198 germanium diode used in a circuit whose output is somewhat affected by the signal form factor. As such, the Y-factor method requires an evaluation of the diode's noise or CW power sensitivity.

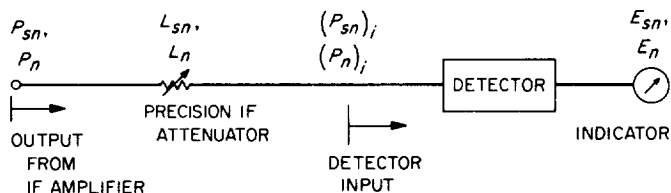


Fig. 4. Detector system used in Y-factor measurements

Fig. 4 is a block diagram of the detector system used in the Y-factor measurements. Assuming unequal output indicator response E_{sn} and E_n due to detector inputs of signal combined with noise $(P_{sn})_i$ and noise power alone $(P_n)_i$ proportional to β'

$$\frac{E_{sn}}{E_n} = \beta' \frac{(P_{sn})_i}{(P_n)_i} \quad (1)$$

When taking Y-factor measurements, the precision IF attenuator is adjusted for attenuations L_{sn} and L_n resulting in a ratio.

$$Y_D = L_{sn}/L_n \quad (2)$$

so that

$$E_{sn}/E_n = 1. \quad (3)$$

The correction factor under these conditions is then

$$\beta = \frac{(P_n)_i}{(P_{sn})_i} \quad (4)$$

The signal plus noise-to-noise ratio before and after the attenuator are related by

$$\frac{(P_{sn})_i}{(P_n)_i} = \frac{1}{Y_D} \frac{P_{sn}}{P_n} \quad (5)$$

so that

$$\frac{P_{sn}}{P_n} = \frac{Y_D}{\beta} \quad (6)$$

β can be related to α [the experimentally determined sensitivity coefficient (SPS 37-36, Vol. III, p. 44)] with

$$Y_D = 1 + \frac{1}{\alpha} \frac{P_s}{P_n} \quad (7)$$

so that

$$\alpha = \frac{P_s/P_n}{\beta(P_s/P_n + 1) - 1} \quad (8)$$

or if $P_s/P_n \gg 1$

$$\alpha \approx 1/\beta \approx \frac{(P_s)_i}{(P_n)_i} \quad (9)$$

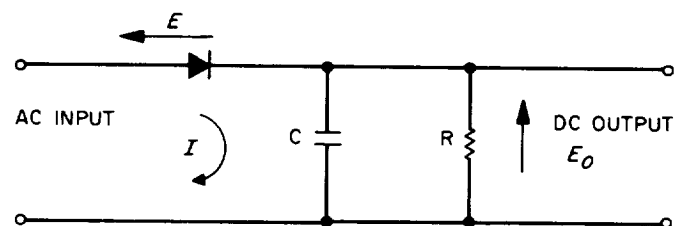


Fig. 5. Representation of diode detector circuit used in Y-factor measurements

The actual detector circuit can be represented as shown in Fig. 5. An analysis of this circuit has been made by Davenport and Root (Ref. 4, p. 304) which considers the dc output with signal and noise applied to the input. The assumptions are: no reverse current, no bias, and v^{th} law diode response as shown in Fig. 6. The no-bias requirement is closely satisfied if the peak input signal level is much greater than the dc output voltage. The dc output with signal and noise is:

$$E_{sn} = \left[\frac{a\Gamma(v+1)}{\Gamma(v/2+1)2^{v/2+1}} \right] (P'_n)^{v/2} {}_1F_1 \left[-v/2; 1; -\frac{(P_s)_i}{(P'_n)_i} \right] \quad (10)$$

and with noise alone

$$E_n = \left[\frac{a\Gamma(v+1)}{\Gamma(v/2+1)2^{v/2+1}} \right] (P'_n)^{v/2} {}_1F_1(-v/2; 1; 0) \quad (11)$$

where

a = proportionality factor

v = detector law

Γ = gamma function

${}_1F_1$ = confluent hypergeometric function

$(P_s)_i/(P'_n)_i$ = CW signal-to-noise power ratio at detector input

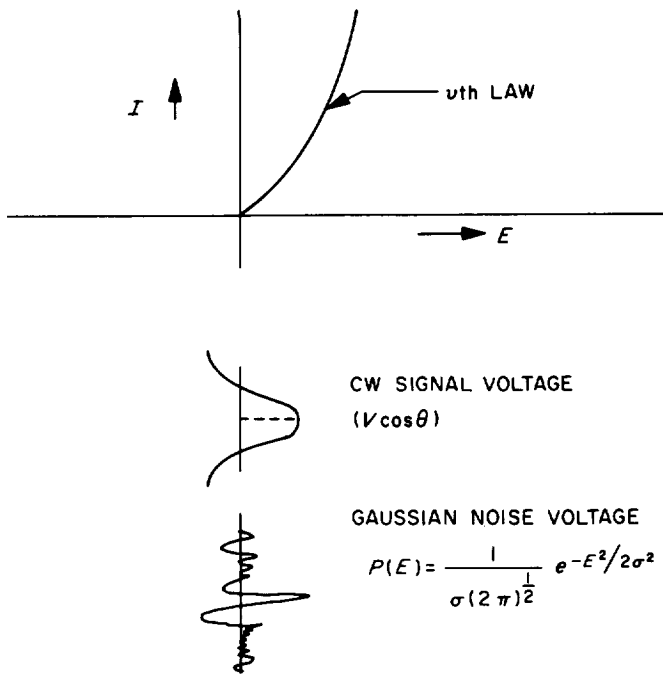


Fig. 6. Representation of ideal ν^{th} law diode characteristics

and

$$(P_{sn})_i = (P'_n)_i + (P_s)_i.$$

Dividing Eq. (10) by (11), since ${}_1F_1(-\nu/2; 1; 0)$ equals 1,

$$\frac{E_{sn}}{E_n} = \left[\frac{(P'_n)_i}{(P_n)_i} \right]^{\nu/2} {}_1F_1 \left[-\nu/2; 1; -\frac{(P_s)_i}{(P'_n)_i} \right]. \quad (12)$$

Manipulating Eqs. (4)-(6) and realizing that

$$\frac{(P'_n)_i}{(P_n)_i} = \frac{1}{Y_D} \quad (13)$$

we have

$$\frac{(P_s)_i}{(P'_n)_i} = \frac{P_s}{P_n} \quad (14)$$

and

$$\frac{(P'_n)_i}{(P_n)_i} = \frac{1}{\beta \left(\frac{P_s}{P_n} + 1 \right)} \quad (15)$$

Using Eqs. (8), (14), and (15) with Eq. (12) and setting $E_{sn}/E_n = 1$,

$$1 = \left(\frac{P_s}{\alpha P_n} + 1 \right)^{-\nu/2} {}_1F_1 \left(-\nu/2; 1; -\frac{P_s}{P_n} \right). \quad (16)$$

The relationship between α and $(P_s)/(P_n)$ is shown by this equation. The confluent hypergeometric function can be expanded in a power series for large signal-to-noise ratios (Ref. 4, p. 307). Eq. (16) has been programmed for the IBM 1620 computer and α determined and plotted for a range of values for ν and for P_s/P_n ratios as shown in Fig. 7. This shows that ideal ν^{th} law detectors with nonlinearities reasonably close to square law have relatively small corrections for the Y-factor.

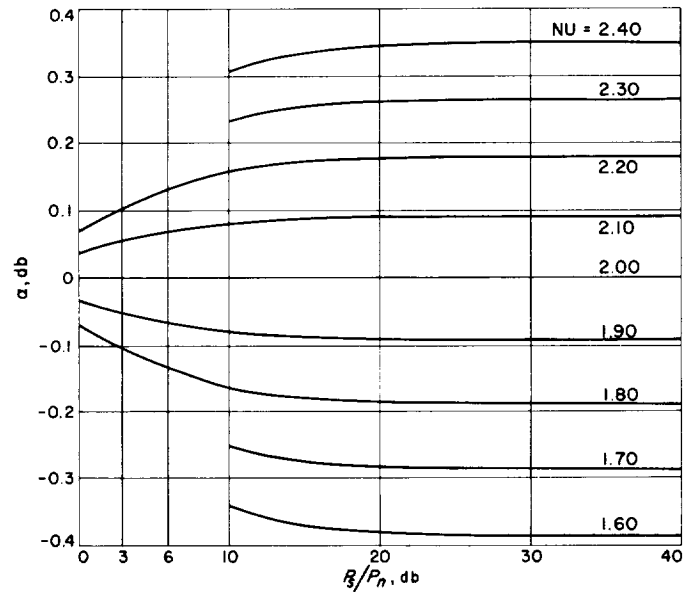


Fig. 7. Plot of α (db) versus P_s/P_n from Eq. (16) for various values of P_s/P_n

The circuit shown in Fig. 5 can be analyzed by a direct method to determine the sensitivity to a CW signal alone, as compared to a noise signal. With the same assumptions as before and with an input signal $V \cos \theta$, the dc output voltage is given by

$$(E_o)_s = R \langle I \rangle_s. \quad (17)$$

Using the relation that $I = aE^\nu$ for $E > 0$,

$$\langle I \rangle_s = \langle aE^\nu \rangle_s = \frac{s}{\pi} \int_0^{\pi/2} (V \cos \theta)^\nu d\theta. \quad (18)$$

Integrating (Ref. 5) and substituting into Eq. (17)

$$(E_o)_s = \frac{aRV^v}{2(\pi)^{1/2}} \frac{\Gamma\left(\frac{v}{2} + \frac{1}{2}\right)}{\Gamma\left(\frac{v}{2} + 1\right)}. \quad (19)$$

Replacing the peak voltage V with an effective rms voltage v where

$$\frac{V^2}{2} = v$$

results in

$$(E_o)_s = \frac{aR(2v^2)^{v/2}}{2(\pi)^{1/2}} \frac{\Gamma\left(\frac{v}{2} + \frac{1}{2}\right)}{\Gamma\left(\frac{v}{2} + 1\right)}. \quad (20)$$

The average dc output voltage due to a noise input voltage is

$$(E_o)_n = R \langle I \rangle_n \quad (21)$$

where (Ref. 6)

$$\langle I \rangle_n = \langle aE^v \rangle_n = a \int_{-\infty}^{\infty} E^v P(E) dE. \quad (22)$$

Assuming a gaussian noise input with an rms noise voltage σ ,

$$P(E) = \frac{1}{\sigma(2\pi)^{1/2}} e^{-E^2/2\sigma^2}$$

so that

$$\langle I \rangle_n = \frac{a}{\sigma(2\pi)^{1/2}} \int_0^{\infty} E^v e^{-E^2/2\sigma^2} dE. \quad (23)$$

Integrating and substituting into Eq. (21)

$$(E_o)_n = \frac{aR(2\sigma^2)^{v/2}}{2(\pi)^{1/2}} \Gamma\left(\frac{v}{2} + \frac{1}{2}\right). \quad (24)$$

Dividing Eq. (20) by (24) and setting equal to 1,

$$1 = \left(\frac{v^2}{\sigma^2}\right)^{v/2} \frac{1}{\Gamma\left(\frac{v}{2} + \frac{1}{2}\right)}. \quad (25)$$

Recognizing (v^2/σ^2) as $[(P_s)_i/(P_n)_i]$,

$$\frac{(P_s)_i}{(P_n)_i} = \left[\Gamma\left(\frac{v}{2} + 1\right) \right]^{2/v} \quad (26)$$

and with Eqs. (4) and (9) for the ideal v^{th} law detector assuming $P_s/P_n \gg 1$,

$$\alpha = \left[\Gamma\left(\frac{v}{2} + 1\right) \right]^{2/v}. \quad (27)$$

Eq. (16) asymptotically approaches Eq. (27) as $P_s/P_n \rightarrow \infty$. Fig. 7 indicates that good accuracy for α can be obtained for signal-to-noise ratios above 10 db which is the range of the measurements used for the spacecraft CW power calibrations (SPS 37-37, Vol. III, pp. 35-38).

The effect of bias can be estimated assuming an ideal square law diode response and $E_o \ll \sigma$ and v , as shown in Fig. 8. This bias is caused by the long time constant

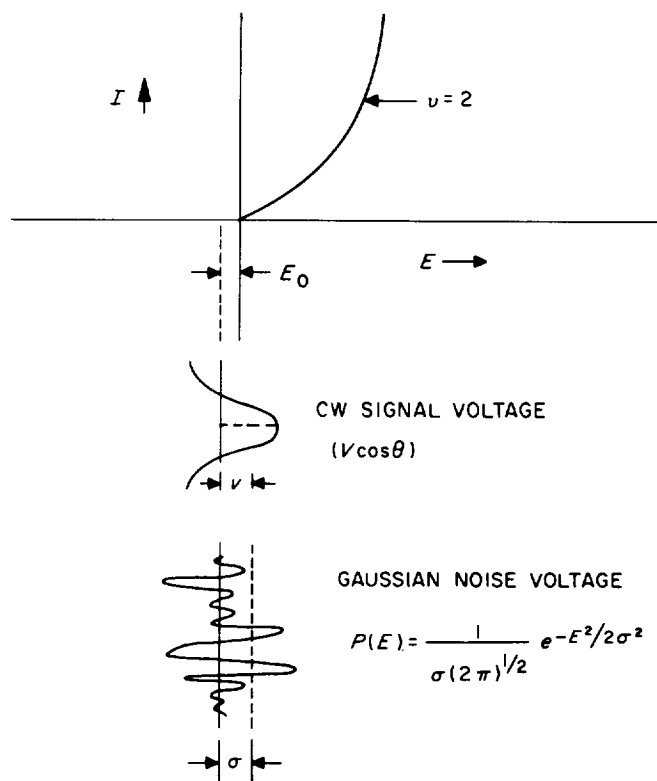


Fig. 8. Representation of square law diode detector characteristics with biased input voltages

compared to the period of R and C shown in Fig. 5. With an input signal $V \cos \theta$, the dc output voltage is given by

$$(E_o)_s = R \langle I \rangle_s. \quad (28)$$

For this example $I = aE^2$ for $E > 0$,

$$\begin{aligned} \langle I \rangle_s &= \langle aE^2 \rangle = \frac{a}{\pi} \int_0^{\theta_1} (V \cos \theta - E_o)^2 d\theta \\ &= \frac{V^2 a}{\pi} \int_0^{\theta_1} \left(\cos \theta - \frac{E_o}{V} \right)^2 d\theta \end{aligned} \quad (29)$$

where

$$\theta_1 = \cos^{-1} \frac{E_o}{V} \approx \frac{\pi}{2} - \frac{E_o}{V},$$

for $E_o/V \ll 1$. Expanding Eq. (29), integrating and retaining the first order correction term,

$$\langle I \rangle_s \approx \frac{V^2 a}{\pi} \left(\frac{\pi}{4} - \frac{2E_o}{V} \right) \quad (30)$$

so that replacing V with $(2)^{1/2} v$ and substituting into Eq. (28),

$$(E_o)_s \approx \frac{Rav^2}{2} \left(1 - \frac{8E_o}{\pi v (2)^{1/2}} \right). \quad (31)$$

The average dc output voltage due to a noise input voltage is

$$(E_o)_n = R \langle I \rangle_n \quad (32)$$

where

$$\langle I \rangle_n = \langle aE^2 \rangle_n = a \int_0^\infty E^2 P(E) dE. \quad (33)$$

Assuming a gaussian noise input with an rms noise voltage σ and a bias $(-E_o)$ (Ref. 6, p. 613),

$$P(E) = \frac{1}{\sigma(2\pi)^{1/2}} e^{-(E+E_o)^2/2\sigma^2}. \quad (34)$$

Then

$$\langle I \rangle_n = \frac{a}{\sigma(2\pi)^{1/2}} \int_0^\infty E^2 e^{-(E+E_o)^2/2\sigma^2} dE. \quad (35)$$

Substituting $x = E + E_o$,

$$\begin{aligned} \langle I \rangle_n &= \frac{a}{\sigma(2\pi)^{1/2}} \int_{E_o}^\infty (X - E_o)^2 e^{-x^2/2\sigma^2} dx \\ &= \frac{a}{\sigma(2\pi)^{1/2}} \left[\int_0^\infty (X - E_o)^2 e^{-x^2/2\sigma^2} dx \right. \\ &\quad \left. - \int_0^\infty (X - E_o)^2 e^{-x^2/2\sigma^2} dx \right] \end{aligned} \quad (36)$$

Expanding the second integrand, integrating both integrals and retaining only first order terms,

$$\langle I \rangle_n \approx \frac{a}{\sigma(2\pi)^{1/2}} \left[(2\pi)^{1/2} \frac{\sigma^3}{2} - 2\sigma^2 E_o \right]. \quad (37)$$

Substituting into Eq. (32)

$$(E_o)_n \approx \frac{Ra\sigma^2}{2} \left(1 - \frac{4E_o}{(2\pi)^{1/2}\sigma} \right) \quad (38)$$

Dividing Eq. (31) by (38) and setting equal to 1

$$1 \approx \left(\frac{v^2}{\sigma^2} \right) \frac{1 - \frac{8E_o}{(2\pi)^{1/2}v}}{1 - \frac{4E_o}{(2\pi)^{1/2}\sigma}} \quad (39)$$

Substituting α for (v^2/σ^2) ,

$$\alpha \approx 1 + \frac{E_o}{v} \frac{4}{(2\pi)^{1/2}} \left(\frac{2}{(\pi)^{1/2}} - 1 \right) + \dots \quad (40)$$

If $E_o/\sigma \approx E_o/v \approx 1/10$ (the approximate operating range of the diode detectors when taking Y-factors), then $\alpha \approx 0.1$ db. This indicates the relative importance of bias effects on the calibrations. Additional studies are being made to correlate theoretical α predications from measured dc diode characteristics with direct experimental α measurements.

b. Antenna efficiency. As discussed in SPS 37-35, Vol. III, p. 62, SPS 37-37, Vol. III, p. 35 and SPS 37-36, Vol. IV, p. 272, the antenna efficiency of each station was measured using radio star tracks over an extended period, typically 3 or 4 wk. A Y-factor method of evaluating radio source temperature was chosen because of the requirement for a simple, quick test which would not interrupt normal station operation to any great extent and which could be carried out by station personnel. Each

station tracked a radio source and the antenna efficiency was derived from the equation

$$\eta = \frac{\text{measured source temperature}}{\text{theoretical source temperature}} = \frac{T_o + T_R}{T_{st}} \left\{ \frac{1}{Y_1} - \frac{1}{Y_2} \right\} \quad (41)$$

where

- η = antenna efficiency
- T_{st} = theoretical source temperature, °K
- T_R = receiver temperature, °K
- T_o = temperature of ambient load, °K
- Y_1 = Y-factor; switching between ambient load and antenna off the radio source (ratio)
- Y_2 = Y-factor; switching between ambient load and antenna off the radio source (ratio)

Two radio sources, Omega and Taurus A,² were chosen and each station tracked them almost nightly for several weeks. The method of taking and recording data was discussed in SPS 37-37, Vol. III, p. 35-37.

Eq. (41) yields antenna efficiency assuming no atmospheric loss. To make valid comparisons of antenna efficiencies between the three stations, atmospheric loss must be taken into account. The zenith angle of a radio source, or atmospheric conditions, may have been different for the various stations and this would lead to invalid comparisons. As insufficient measurements were taken on any one night to evaluate atmospheric loss correctly, an average estimated value was chosen and the data reduced using this number.

If L_o db is the atmospheric loss at zenith, then the measured value of radio source temperature is modified by

$$T = T' (L_o)^{\sec z} \quad (42)$$

where

- T' = measured radio source temperature, °K
- T = actual radio source temperature, °K
- z = zenith angle of radio source, rad

The antenna efficiency then is increased by $(L_o)^{\sec z}$. The Venus Station antenna readout is in terms of azimuth and

elevation. The Pioneer and Echo antenna readouts are in terms of hour angle and declination. The conversions to zenith angle are given by

$$z = \frac{\pi}{2} - El \quad (43)$$

and

$$\cos z = \sin \phi \sin \delta + \cos \phi \cos \delta \cos h, \text{ respectively,} \quad (44)$$

where

- z = zenith angle
- El = radio source elevation
- ϕ = latitude of antenna location
- δ = radio source declination
- h = radio source hour angle

Eqs. (41) to (44) have been programmed for an IBM 1620 computer. Table 1 shows the computer output format for the Venus Station on Omega. The elevations and zenith angles are in degrees. Three columns of data are shown for each of the three assumed values of L_o . $L_o = 0.05$ db is considered the best value; the other two are considered limiting cases. For each assumed value of L_o and for each set of measurement data, an atmospheric loss in db corresponding to the associated zenith angle has been calculated and is shown under the heading L , db. The other two columns, T and Nu , list the measured source temperature (°K) and antenna efficiency (%) for each corresponding zenith angle. The average efficiency, and standard deviation, for each assumed value of L_o have been calculated and are shown at the bottom of Table 1.

Table 2 is a summary of all the data. The average antenna efficiency and standard deviation are shown for each station on each source.

The station latitudes³ used in the computations are

Venus:	35.247 718 889 deg
Echo:	35.299 958 333 deg
Pioneer:	35.389 539 444 deg

²JPL Antenna Acceptance Test, Procedure No. DZM-1074-TP, p. 38, April 29, 1965.

³Private communication from W. R. Bollinger, JPL.

Table 1. Antenna system efficiency measurements for Venus Station on Omega

Over-all antenna system efficiency											
Station: 13			Station latitude: 35.247719 deg								
Source: Omega			Theoretical source temperature: 99.0 deg								
Date, July, 1965	Elevation, deg	Zenith angle, deg	L ₀ = 0 db			L ₀ = 0.05 db			L ₀ = 0.1 db		
			L, db	T, °K	Nu, %	L1, db	T1, °K	Nu1, %	L2, db	T2, °K	Nu2, %
10	31.80	58.200	0.0	44.916	45.36	0.09	45.908	46.37	0.18	46.922	47.39
10	28.00	62.000	0.0	45.471	45.93	0.10	46.600	47.07	0.21	47.757	48.23
10	28.00	62.000	0.0	45.849	46.31	0.10	46.987	47.46	0.21	48.154	48.64
11	34.00	56.000	0.0	45.733	46.19	0.08	46.684	47.15	0.17	47.655	48.13
11	33.10	56.900	0.0	45.336	45.79	0.09	46.302	46.77	0.18	47.288	47.76
12	32.00	58.000	0.0	45.000	45.45	0.09	45.988	46.45	0.18	46.998	47.47
17	35.30	54.700	0.0	45.431	45.89	0.08	46.345	46.81	0.17	47.278	47.75
17	34.33	55.666	0.0	46.561	47.03	0.08	47.521	48.00	0.17	48.501	48.99
17	30.30	59.694	0.0	46.477	46.94	0.09	47.549	48.02	0.19	48.646	49.13
17	28.50	61.500	0.0	45.585	46.04	0.10	46.699	47.17	0.20	47.839	48.32
17	23.90	66.100	0.0	45.876	46.33	0.12	47.198	47.67	0.24	48.559	49.04
17	22.77	67.230	0.0	45.956	46.42	0.12	47.343	47.82	0.25	48.773	49.26
18	16.08	73.920	0.0	46.708	47.18	0.18	48.691	49.18	0.36	50.757	51.27
18	13.09	76.910	0.0	46.561	47.03	0.22	48.989	49.48	0.44	51.543	52.06
19	35.62	54.375	0.0	46.108	46.57	0.08	47.029	47.50	0.17	47.967	48.45
19	34.70	55.293	0.0	46.362	46.83	0.08	47.309	47.78	0.17	48.275	48.76
19	33.68	56.320	0.0	46.420	46.88	0.09	47.394	47.87	0.18	48.388	48.87
19	32.41	57.589	0.0	46.391	46.86	0.09	47.399	47.87	0.18	48.428	48.91
19	29.60	60.400	0.0	46.170	46.63	0.10	47.258	47.73	0.20	48.373	48.86
20	30.34	59.660	0.0	46.533	47.00	0.09	47.606	48.08	0.19	48.704	49.19
20	29.25	60.750	0.0	46.773	47.24	0.10	47.888	48.37	0.20	49.029	49.52
20	27.50	62.500	0.0	46.657	47.12	0.10	47.835	48.31	0.21	49.042	49.53
20	26.00	64.000	0.0	47.176	47.65	0.11	48.432	48.92	0.22	49.720	50.22
20	22.46	67.540	0.0	46.711	47.18	0.13	48.140	48.62	0.26	49.613	50.11
21	24.20	65.800	0.0	46.820	47.29	0.12	48.153	48.64	0.24	49.525	50.02
22	33.90	56.100	0.0	46.567	47.03	0.08	47.539	48.01	0.17	48.530	49.02
25	32.50	57.500	0.0	47.385	47.86	0.09	48.411	48.90	0.18	49.459	49.95
26	31.20	58.800	0.0	47.009	47.48	0.09	48.065	48.55	0.19	49.146	49.64
26	34.10	55.900	0.0	46.265	46.73	0.08	47.225	47.70	0.17	48.205	48.69
Efficiency averages			46.70			47.88			49.08		
Standard deviations			0.6212			0.7723			1.026		

Table 2. Summary of antenna efficiency measurements for Stations 11, 12, and 13

Source	Station	$L_0 = 0 \text{ db}$		$L_0 = 0.05 \text{ db}$		$L_0 = 0.1 \text{ db}$	
		$\eta, \%$	$\sigma, \%$	$\eta, \%$	$\sigma, \%$	$\eta, \%$	$\sigma, \%$
Omega	11	48.93	1.63	50.09	1.59	51.28	1.57
	12	54.21	0.87	55.56	1.07	56.94	1.37
	13	46.70	0.62	47.88	0.77	49.08	1.03
Taurus A	11	49.00	0.65	49.82	0.62	50.66	0.61
	12	58.99	0.59	56.81	0.74	57.65	0.92
	13	45.49	0.63	46.40	0.65	47.33	0.70

Table 3 shows the average efficiencies and a number $\eta_\Omega - \eta_T$, defined as the average efficiency derived from measurements on Omega minus the average efficiency derived from measurements on Taurus A.

$\overline{\Delta\eta}$ is the average of these numbers for each assumed value of L_0 , and $\sigma_{\overline{\Delta\eta}}$ is the standard deviation of this aver-

Table 3. Statistical analysis of antenna efficiency measurement data for Stations 11, 12, and 13

Station	$L_0 = 0 \text{ db}$		$L_0 = 0.05 \text{ db}$		$L_0 = 0.1 \text{ db}$	
	Average efficiency, %	$\eta_\Omega - \eta_T, \%$	Average efficiency, %	$\eta_\Omega - \eta_T, \%$	Average efficiency, %	$\eta_\Omega - \eta_T, \%$
11	48.97	-0.07	49.96	0.27	50.97	0.62
12	55.10	-1.78	56.19	-1.25	57.30	-0.71
13	46.10	1.21	47.14	1.48	48.21	1.75
$\overline{\Delta\eta} (\%)$	-0.21		0.17		0.55	
$\sigma_{\overline{\Delta\eta}} (\%)$	1.22		1.12		1.01	

age. Assuming no error in T_{st} , the theoretical source temperature, then the number $\eta_\Omega - \eta_T$ is zero for the correct value of L_0 . If neither $T_{st(\text{Omega})}$ nor $T_{st(\text{Taurus A})}$ is known exactly, then $\sigma_{\overline{\Delta\eta}}$ will be a minimum for that value of L_0 , which is most nearly correct. It may be seen from Table 3 that $\sigma_{\overline{\Delta\eta}}$ diminishes as the assumed values for L_0 increases and a minimum has not been reached at $L_0 = 0.1 \text{ db}$. More precise measurement would be needed in order to estimate atmospheric losses from this technique.

The best estimate for antenna efficiency is the average of the measurements from Omega and Taurus A for an assumed atmospheric loss at zenith of 0.05 db. The results are:

- Station 11, Pioneer 50.0%
- Station 12, Echo 56.2%
- Station 13, Venus 47.1%

where antenna efficiency is defined at the maser input.

The lower efficiency at the Venus Station is explained by the less efficient feed system configuration. The reason for the large difference between the Pioneer and Echo Stations has not yet been established.

The calibration, with thermal noise standards of CW signal power received from a spacecraft, defines the received power at the maser input. For this reason, antenna efficiency has been measured and defined at the maser input. Thus a common basis for comparison of received power level at the three stations has been established.

References

1. Reed, H. R., and Russell, C. M., "Ultra High Frequency Propagation," pp. 82-97, John Wiley and Sons, Inc., New York, 1953.
2. Ramo, S., and Whinnery, J. R., "Field and Waves in Modern Radio," John Wiley and Sons, Inc., New York, 1953.
3. Hogg, D. C., "Effective Antenna Temperature Due to Oxygen and Water Vapor in the Atmosphere," *Journal of Applied Physics*, Vol. 30, No. 9, pp. 1417-1419, September 1959.

References (Cont'd)

4. Davenport, W. B., and Root, W. L., "An Introduction to the Theory of Random Signals and Noise," McGraw-Hill Book Co., New York, 1958.
5. Pipes, L. A., "Applied Mathematics for Engineers and Physicists," p. 304, McGraw-Hill Book Co., New York, 1946.
6. Bennett, W. R., "Methods of Solving Noise Problems," *Proceedings of the IRE*, p. 614, May 1956.

XXI. Spacecraft Telemetry and Command

A. Low Capacity Dynamic Storage Devices

E. J. Bahm

1. Introduction

Storage of small amounts of digital data is best accomplished with solid-state memories and, at present, the magnetic tape recorder is best suited for large amounts of data. The range of applicability of the two systems is dependent upon many factors and therefore cannot be described in a general manner. Solid-state memories can be used for storage of up to 100,000 bits of information within the constraints of a spacecraft application; however, larger solid-state memories become bulky and complicated. The tape recorder can be used for storage of any volume of information up to approximately 10^9 bits. In contrast to solid-state memories, the complexity of the tape recorder is largely independent of its capacity; only the amount of magnetic tape required is determined by the capacity. This makes the tape recorder an efficient storage device for large amounts of data and an inefficient device for small amounts of data. In the capacity range between 100,000 bits and one million bits, neither solid-state memories nor ordinary tape recorders are suitable storage devices for spacecraft applications, although both are inherently capable of storing the information.

An investigation was conducted of other storage devices better suited for the above-mentioned capacity range. Two devices seem feasible: the magnetic drum and the tape loop recorder. Both have been studied in recent months, and further work is in progress. Results obtained thus far indicate that the magnetic drum, already in use for spacecraft applications, is a highly reliable recording device. Compared with ordinary tape recorders, savings in size and weight cannot be expected; however, increased reliability, longer life, short access time, and better flexibility can be obtained.

2. Magnetic Drum

Several magnetic drums have been developed by the industry for the storage capacity range contemplated. However, only one drum was found to be suitable for a spacecraft application. This drum was developed by the Federal Systems Division of IBM for the *Titan* missile. Some specifications of this drum are:

Total capacity	600,000 bits
Number of tracks	160
Outside diameter of drum	1.85 in.
Weight of mechanical system	2.5 lb
Volume of mechanical system	40 in. ³
Power of mechanical system	3 w @ 3000 rpm

Indications are that this drum is more reliable than any tape recorder can possibly be. It has only one rotating part — the drum itself. It carries the recording media on the outside, while the inside is used as the rotor of the drive motor. Also, the drum is air-floated, and, at continuous operation, life of the whole device is determined only by the electronics. Although the number of start/stop cycles may perhaps limit the lifetime in space, this presents no real problem in the weightlessness of space.

Size and weight of the drum are very close to that of tape recorders. Power consumption is dependent upon the speed of the drum. If the required data rate allows use of very low speed, power for the mechanical portion may be below 1 w. Stable suspension of the drum appears possible at speeds below 1000 rpm. Even lower speed may be achieved by running the drum on an oil film and using the brushless DC motor principle rather than the currently used hysteresis motor principle.

3. Tape Loop Recorder

An alternative to the magnetic drum would be a special endless loop tape recorder. The endless loop of magnetic tape would be so short that it could be stored in a so-called bin or could even be suspended on a series of pulleys. At a recording density of 1000 bits/in. and with five parallel tracks, one million bits of data could be recorded on 17 ft of ¼-in. tape.

Although a tape loop recorder as described would not have any of the problems associated with the tape pack of long endless loops, other problems are encountered. Storage of 100,000 bits would require a tape loop of only 1.7 ft. At a tape speed of 10 in./sec, a complete tape pass would require only 2 sec. Continuous operation of such a recorder over a period of six months would result in 10 million tape passes. The oxide coating of the magnetic tape is subjected to wear when it moves over the recording heads. This results in a progressive deterioration of the coating during long operation of the recorder. No presently available magnetic tape is capable of withstanding 10 million tape passes without serious deterioration.

An endless loop is usually fabricated by splicing the tape at the two ends. Several highly reliable splicing methods have been developed, but none can be considered suitable for 10 million tape passes.

A tape loop recorder can be considered feasible only if the problems of tape wear and tape splicing can be

resolved. Wear of the coated surface can be completely eliminated by placing the recording heads on the uncoated side of the tape and recording through the base material. This results in some spacing between heads and recording surface. Therefore, the magnetic field for writing on tape or reading from tape is not as well focused as if the heads are in contact with the recording surface. This results in reduced recording density, higher recording current, and lower playback signal amplitude.

For a short loop of tape, the splice can also be eliminated. Seamless belts can be fabricated from either Mylar or H-film (Kapton) sheets by cutting out rings of proper dimensions. These rings are plastically formed into belts under application of heat. Seamless magnetic belts can be fabricated either from an already coated web of magnetic tape or from pure Mylar or H-film sheets with subsequent coating or plating of the belts. Both approaches are currently being studied in detail.

4. Plated Mylar Belts

Very short belts are used for the evaluation purposes in order to simplify their handling and the conducting of life tests. Dimensions of the belts are $11 \times 0.25 \times 0.0005$ in. The belts were fabricated from Mylar and then plated with an alloy proprietary to the Cambridge Laboratories that contained mostly cobalt and nickel.

a. Visual inspection. Difficulties were encountered initially with the belt plating. The belts contained tweezer marks and fingerprints and were bent in numerous places. There were small areas with no plating at all. Fig. 1 shows the belt as received. Fig. 2 shows a hole in the plating and some tweezer marks. The same area is further enlarged in Figs. 3 and 4, and it can be seen that the particular hole contains scarcely any cobalt at all. Fig. 5 shows that the plating does not extend to the edge of the belt, and indicates further that the edge of the belt is not straight. This, however, is a peculiarity of seamless belts and improves as soon as the belt is slightly stretched over pulleys. One belt, which was delivered to JPL several weeks later and could not be included in the tests, was inspected under the microscope and found to be of much better quality. No holes—not even microscopically small—were found in the magnetic surface, and wide areas were completely homogenous. The magnetic surface of all belts was very thin and could not be measured with mechanical instruments or a microscope.

b. Magnetic recording. A breadboard tape transport built from a scrapped recorder was used to evaluate the

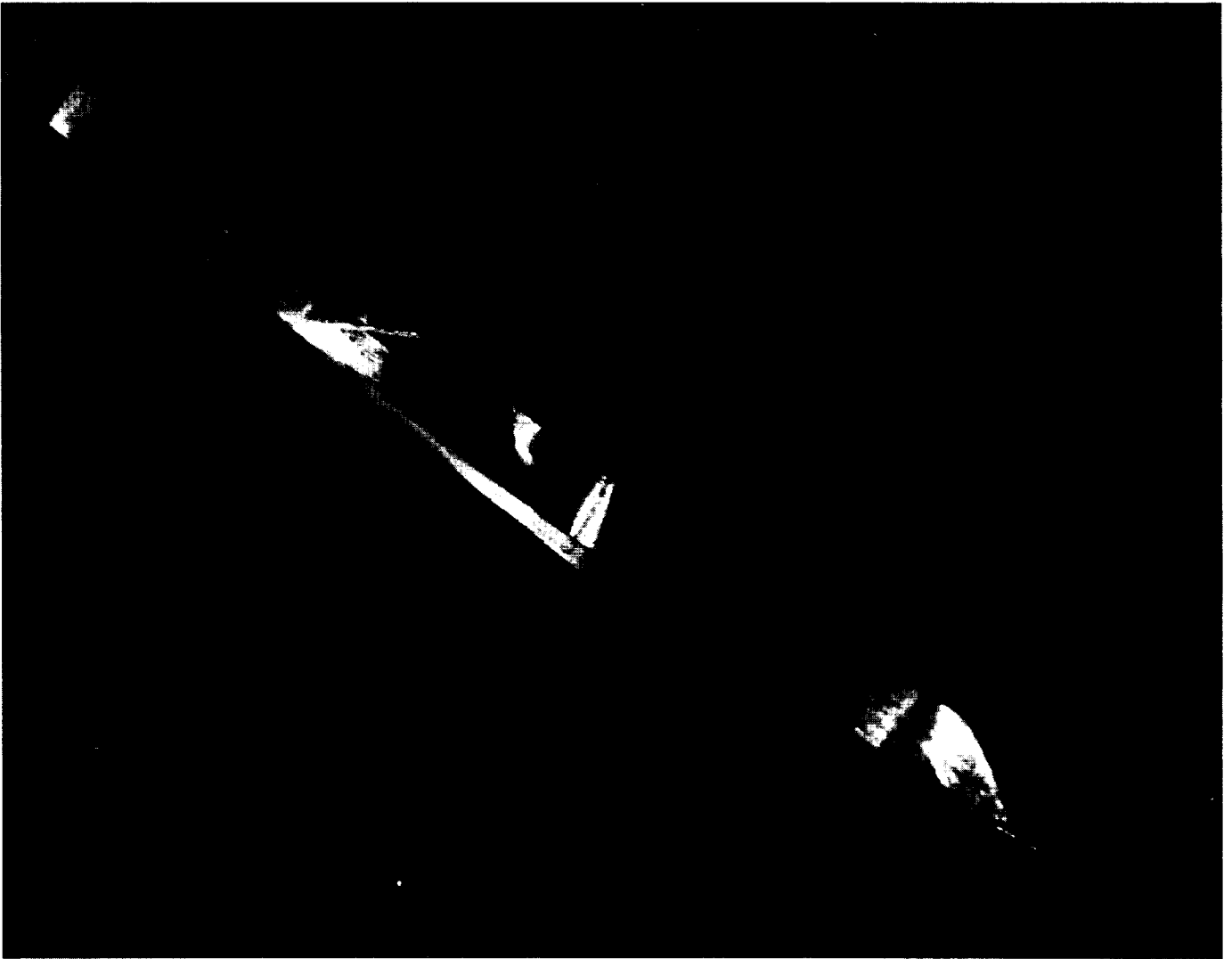


Fig. 1. Cobalt-plated Mylar belt (1.5 times actual size)

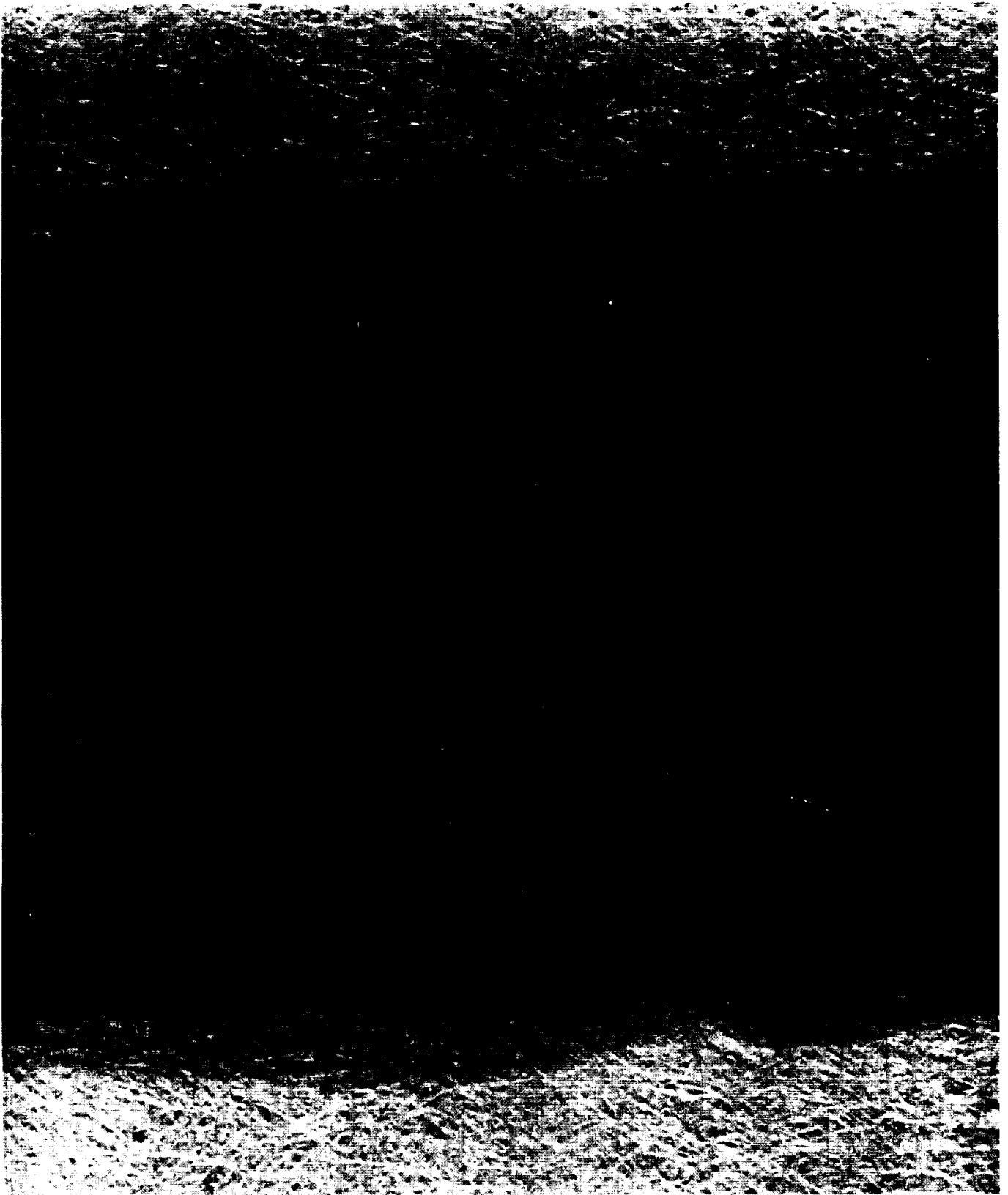


Fig. 2. Faulty area of cobalt-plated Mylar belt (24 times actual size)

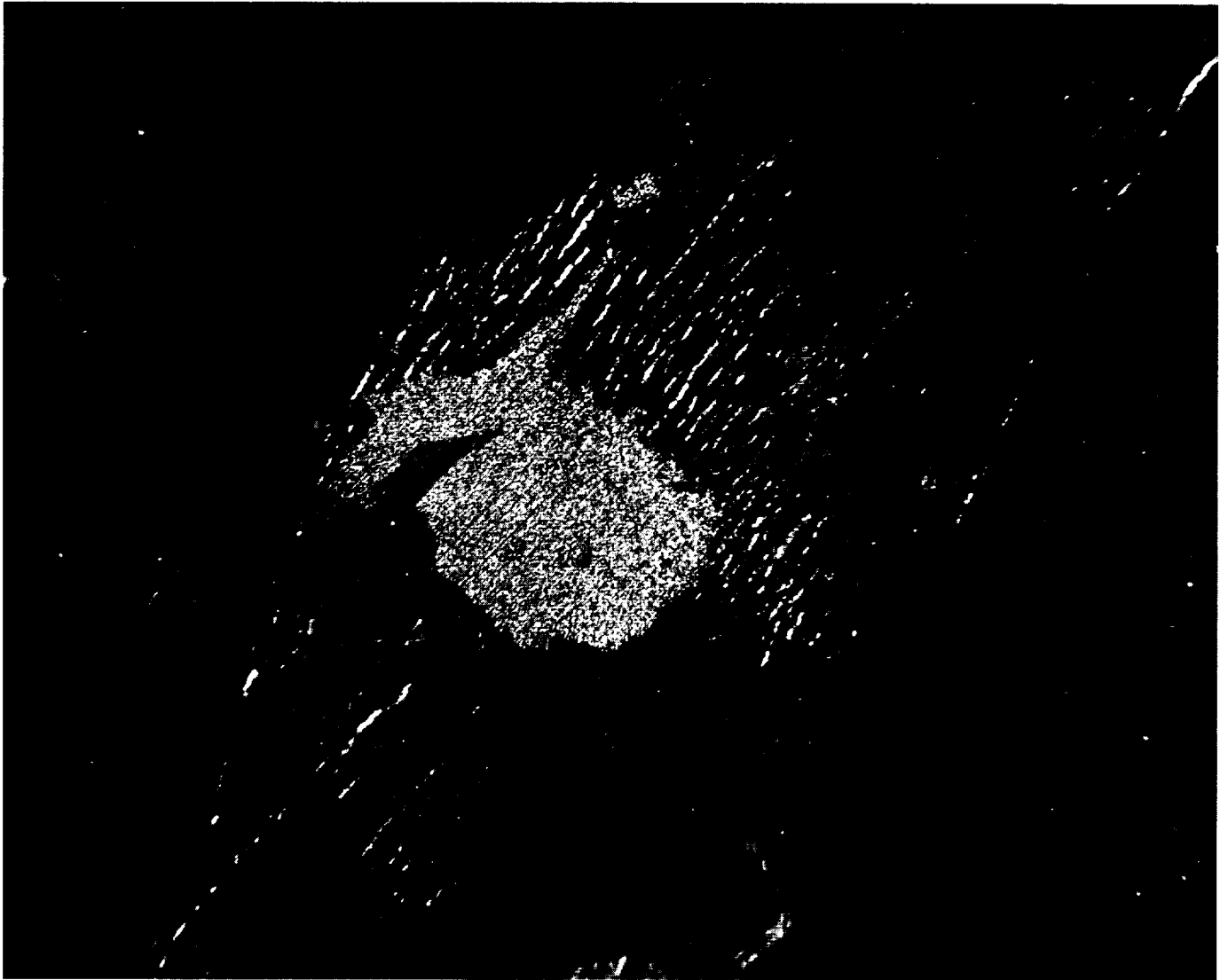


Fig. 3. Faulty area of cobalt-plated Mylar belt (85 times actual size)



Fig. 4. Faulty area of cobalt-plated Mylar belt (340 times actual size)

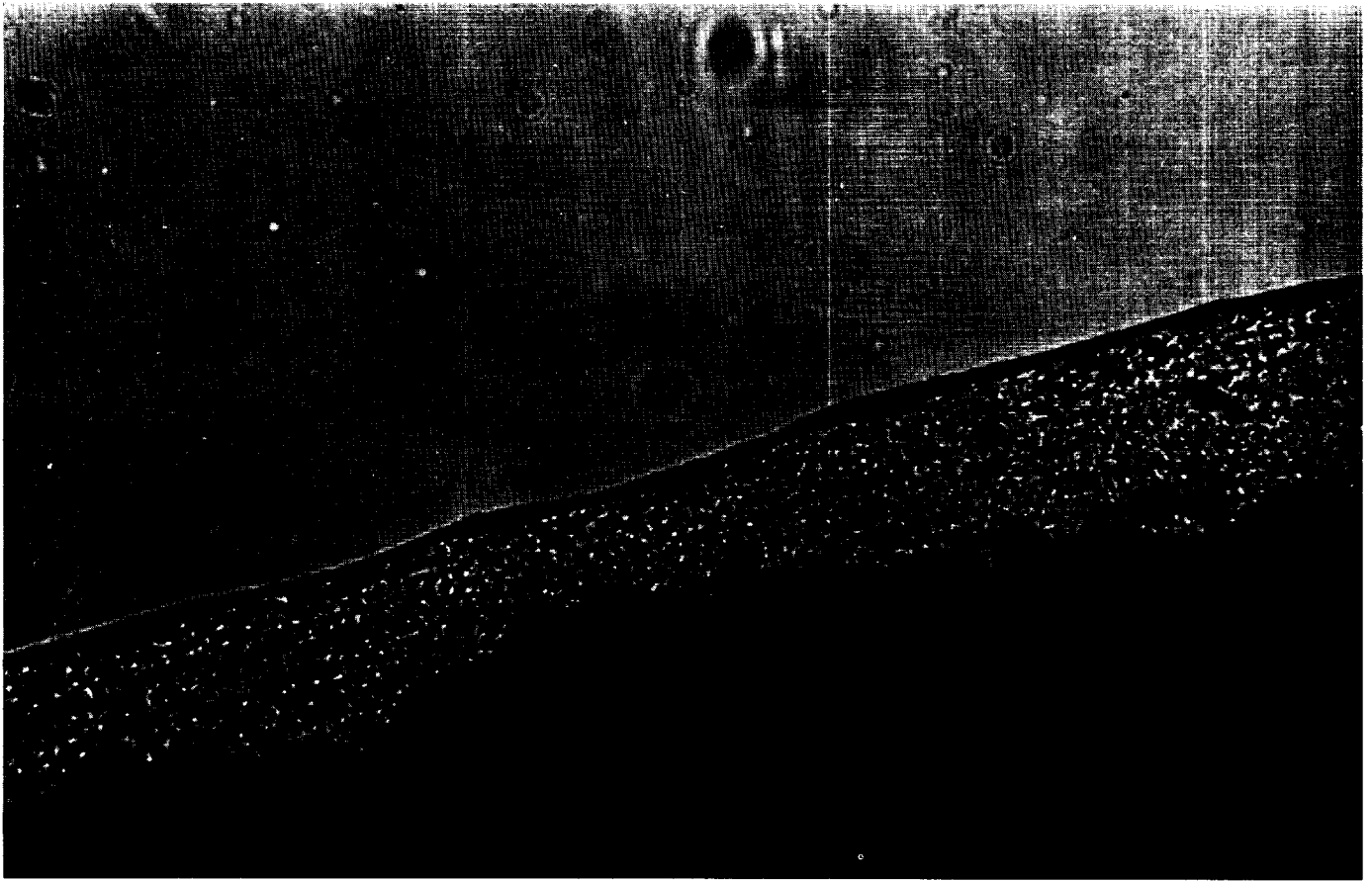


Fig. 5. Edge of cobalt-plated Mylar belt (340 times actual size)

feasibility of actual magnetic recording on these belts. A photograph of the tape transport is shown in Fig. 6. Initial problems encountered with guiding the belt were improved by increasing the tension in the belt, and could

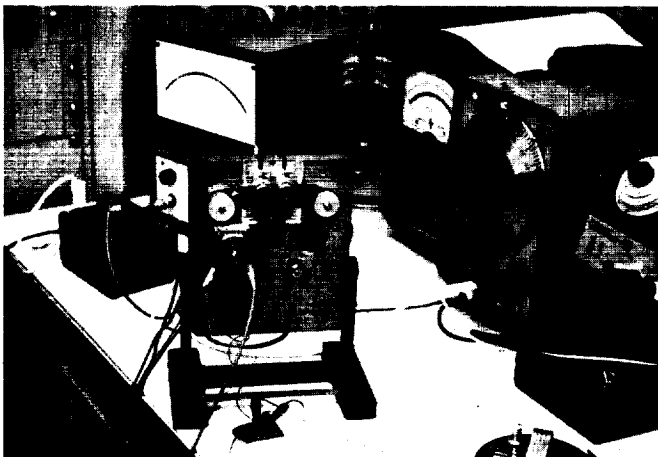


Fig. 6. Breadboard tape transport

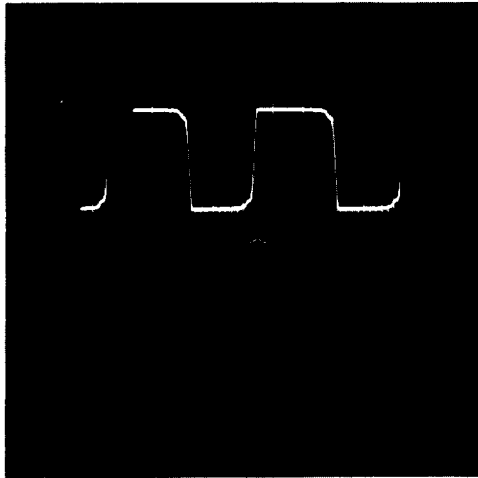
perhaps be further corrected by enhancing the crown on the guiding pulley.

In spite of the poor appearance of the magnetic surface, recording was possible. It must be noted, however, that recording was done on relatively wide tracks. This softened the effects of small holes. During all experiments, a square-wave signal was used for recording. The record and playback signals are shown in Fig. 7, and the same signals are shown at different time scales in Fig. 8. The playback signal on the left oscillogram of Fig. 8 is reasonably good. No dropouts occur from the information recorded on this particular area. The information shown on the right oscillogram was recorded on a particularly poor area of the belt, and most of it must be considered dropouts.

The recording characteristics of these belts were further evaluated by recording of different frequencies and at different tape speeds. The belt was plated on one side only. Recording was first done with the heads in direct contact with the magnetic surface. After measurement

of the playback signal level versus bit density, the belt was reversed. The heads were now in contact with the

Mylar backing, and recording and playing back took place through the half-mil thick belt. Figs. 9 and 10 show the peak-to-peak voltage of the playback signal versus bit density at saturation recording. These curves show the characteristics of the belt as well as those of the



UPPER TRACE: RECORDED SIGNAL 2 v/cm
 LOWER TRACE: PLAYBACK SIGNAL 10 mv/cm
 TAPE SPEED: 52 in./sec
 FREQUENCY: 10 kc (20 μ sec/cm)—BOTH TRACES

Fig. 7. Recording and playback signals

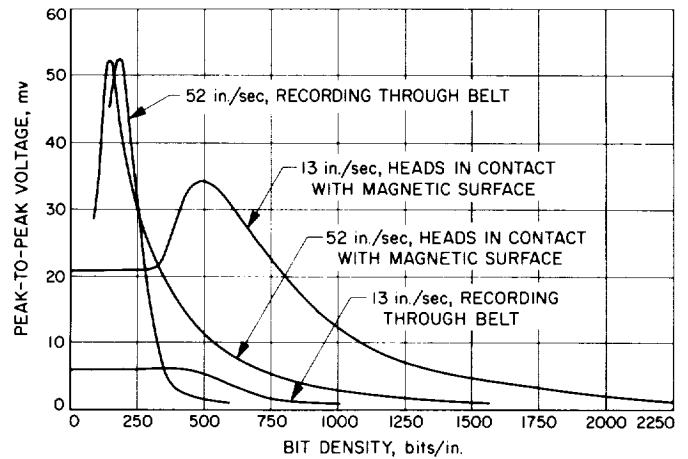
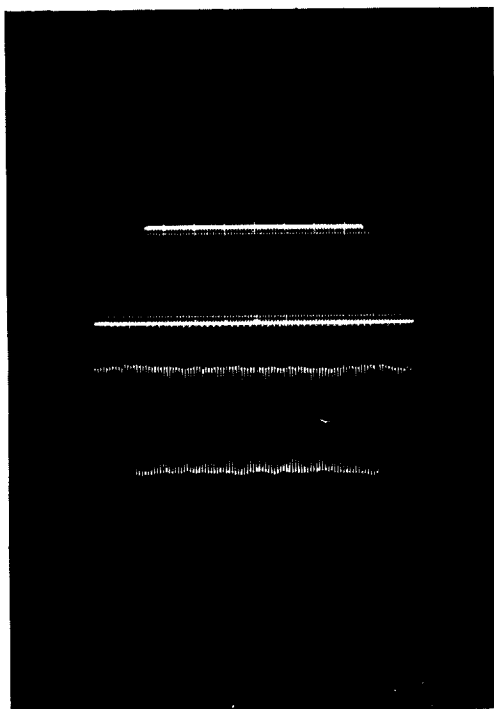
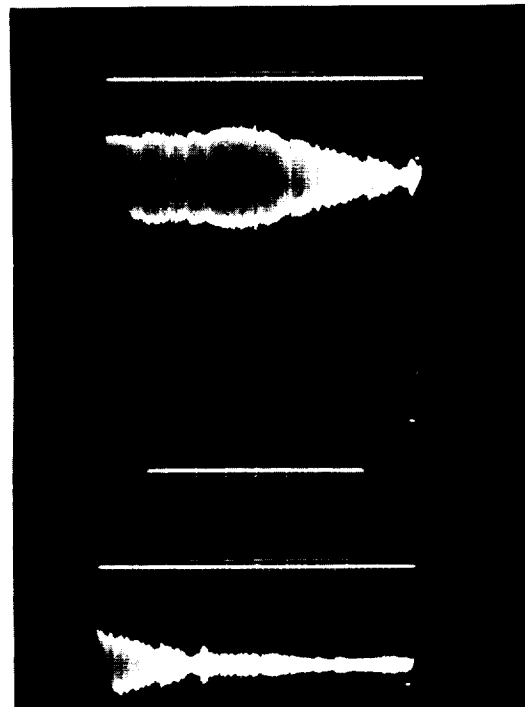


Fig. 9. Amplitude of playback signal at various tape speeds



RECORDING ON A GOOD AREA OF THE BELT
 AT 1 msec/cm



RECORDING ON A PARTICULARLY POOR AREA OF
 THE BELT AT 5 msec/cm

UPPER TRACE: RECORDED SIGNAL 2 v/cm
 LOWER TRACE: PLAYBACK SIGNAL 20 mv/cm
 TAPE SPEED: 52 in./sec
 FREQUENCY: 10 kc

Fig. 8. Recording and playback signals at compressed time scale

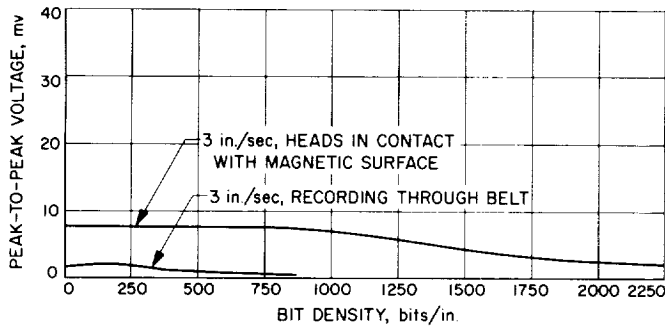


Fig. 10. Amplitude of playback signal at 3 in./sec

whole recording system. The tape transport is a rather crude device and is the limiting factor in many respects. Although the information contained in Figs. 9 and 10 should not be overestimated, it does show that bit densities of 1500 bits/in. are no problem if the head is in contact with the magnetic surface and the tape speed is not too high, and also shows that recording through the Mylar is feasible with bit densities of up to 600 bits/in. The amplitude of the playback signal was surprisingly high, indicating a high residual induction of the plating. Also, the coercivity seems to be higher than with ordinary magnetic tape because of the high record current of approximately 1 amp required for saturation recording (resistance of record head was 5.6Ω). Recording through the belt required approximately 1.5 amp.

Figs. 11-13 contain the same data as given in Figs. 9 and 10, but the form of presentation differs. The reduction of the playback voltage at high bit densities and at

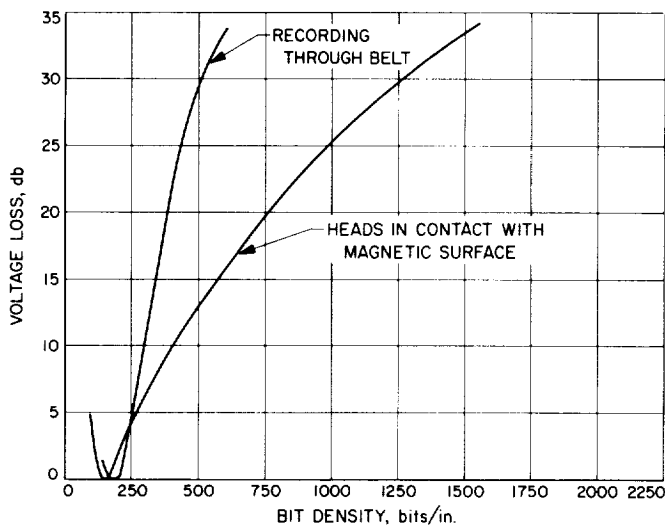


Fig. 11. Comparison of the voltage loss of the playback signal at 52 in./sec tape speed

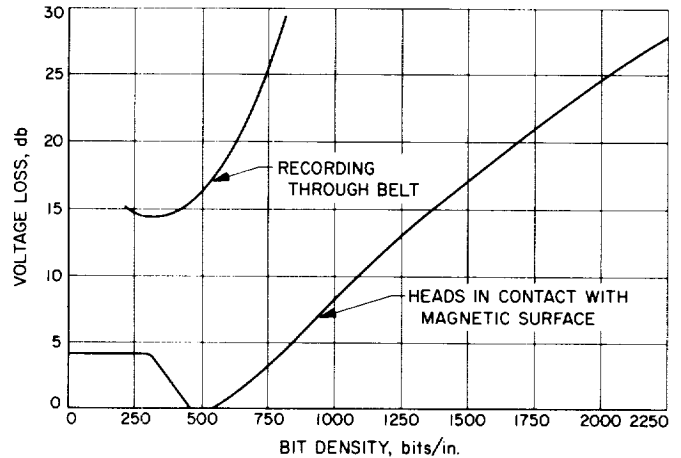


Fig. 12. Comparison of the voltage loss of the playback signal at 13 in./sec tape speed

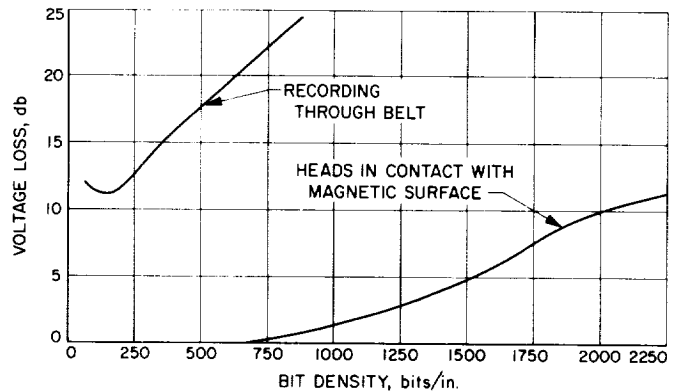


Fig. 13. Comparison of the voltage loss of the playback signal at 3 in./sec tape speed

recording through the belt is shown in decibels. Reference is the maximum playback signal amplitude at the particular tape speed.

c. *Wear test.* A life test was performed with the tape running at 52 in./sec and the heads in contact with the recording surface. It was found that after approximately 200,000 revolutions of the belt, visible shedding of magnetic particles had occurred and definite deterioration of the playback signal could be observed. Many additional holes had been formed in the magnetic surface. After about 500,000 revolutions, meaningful recording was no longer possible. An attempt was then made to remove the plating completely by further running the belt over the heads. However, no additional wear could be detected, and the experiment was terminated after approximately 2,000,000 revolutions.

d. Evaluation and conclusions. The plated belts must be disqualified for spacecraft application at present, because of faulty spots on the plated surface. However, the belt delivered later indicates that this plating process may have some potential, and that lack of experience with this particular task as well as generally poor handling is responsible for the low quality of the plating. Indications are that application of a burnishing process to the new belt is very desirable. The plating is magnetically too hard and requires high power for recording, but does yield a good playback signal. Tape wear is similar to ordinary magnetic tape.

5. Seamless Coated Belts

Seamless belts have been fabricated from already coated H-film sheets. The coating is proprietary to the Lash Laboratories in San Diego, which is marketing magnetic tape under the tradename Pyrotrak. The belts were fabricated by the Kinelologic Corporation in Pasadena, and are the same dimensions as the plated belts except for a thickness of 0.001 in., because this base material is not available in 0.5 mil.

a. Visual inspection. The belts were again inspected under the microscope. A belt as received is shown in Fig. 14, and Fig. 15 shows an enlargement of a particularly ununiform area. The largest of the many small holes which appear in the coating is further magnified in Figs. 16 and 17. The high enlargement of Fig. 17, however, leads to the surmise that perhaps this spot is not a hole in the coating but is possibly an accumulation of some foreign material in the coating which is reflecting the light in a different way. Tiny little cracks of the coating can be seen inside as well as outside of this area. These cracks in the coating have been anticipated and are caused by the belt-forming process. Because the belt is fabricated by plastic deformation of a ring cut out of the sheet material, the coating is also plastically deformed. However, the coating is not as deformable as H-film and therefore will crack. As the inner diameter of the ring must be stretched more than the outer diameter, the belt has more and wider cracks on one edge than on the other. Fig. 18 shows the heavily stretched edge of the belt. The widest of these cracks is approximately 100 μ in., which is still small enough to allow digital recording at medium recording density.

b. Magnetic recording. To afford a basis of comparison, the recording measurements performed earlier on cobalt-plated belts were repeated. Figs. 19 and 20 show

the record and playback signals at two different tape speeds and frequencies. The irregular amplitudes which appear at high tape speed may be attributable to some extent to the transport. At low tape speed, continuity of the playback signal was much better than with cobalt belts, and very few dropouts occurred. Fig. 21 shows the record and playback signals obtained when recording and reproduction were performed through the belt. Larger amplitude variations and, hence, more dropouts occurred under these conditions.

Figs. 22 and 23 show the peak-to-peak voltage of the playback signal versus bit density at saturation recording. To facilitate comparisons, the diagrams are drawn to the same scale as those for cobalt belts. They show that Pyrotrak belts are generally superior to cobalt-plated belts. Signal amplitude at playback was higher and higher recording densities were obtained if the heads had been in contact with the magnetic surface. Recording densities of 4000 cycles/in. could be obtained with the crude breadboard tape transport.

When recording through the base material, inferior performance resulted because of the thickness of the belts (1 mil as compared with the 0.5-mil cobalt-plated belts).

Less current was required for saturation recording of coated belts than for cobalt-plated belts. Record current was only 15 ma at direct recording and 75 ma at recording through the belt.

c. Wear test. The wear characteristics of the Pyrotrak belts are quite different from those of the cobalt-plated belts. With the belt running at 52 in./sec, the amplitude of the playback signal decreased gradually with time. However, the number of dropouts did not increase significantly during the first 200,000 revolutions. The decrease of the playback signal amplitude versus the number of revolutions is shown in Fig. 24. At 1.5×10^6 revolutions, the dropout rate had reached about 2% and the test was terminated. Except for the relatively high dropout rate, a meaningful recording was still possible.

d. Evaluation and conclusions. Because of its inferior quality, the coating is probably not adaptable for many spacecraft applications. Cracks in the coating seem to have only minor effects, but are basically undesirable. A serious shortcoming is the fact that H-film material is presently not available at a thickness below 1 mil. Recording through the belt will therefore require a very low bit density.

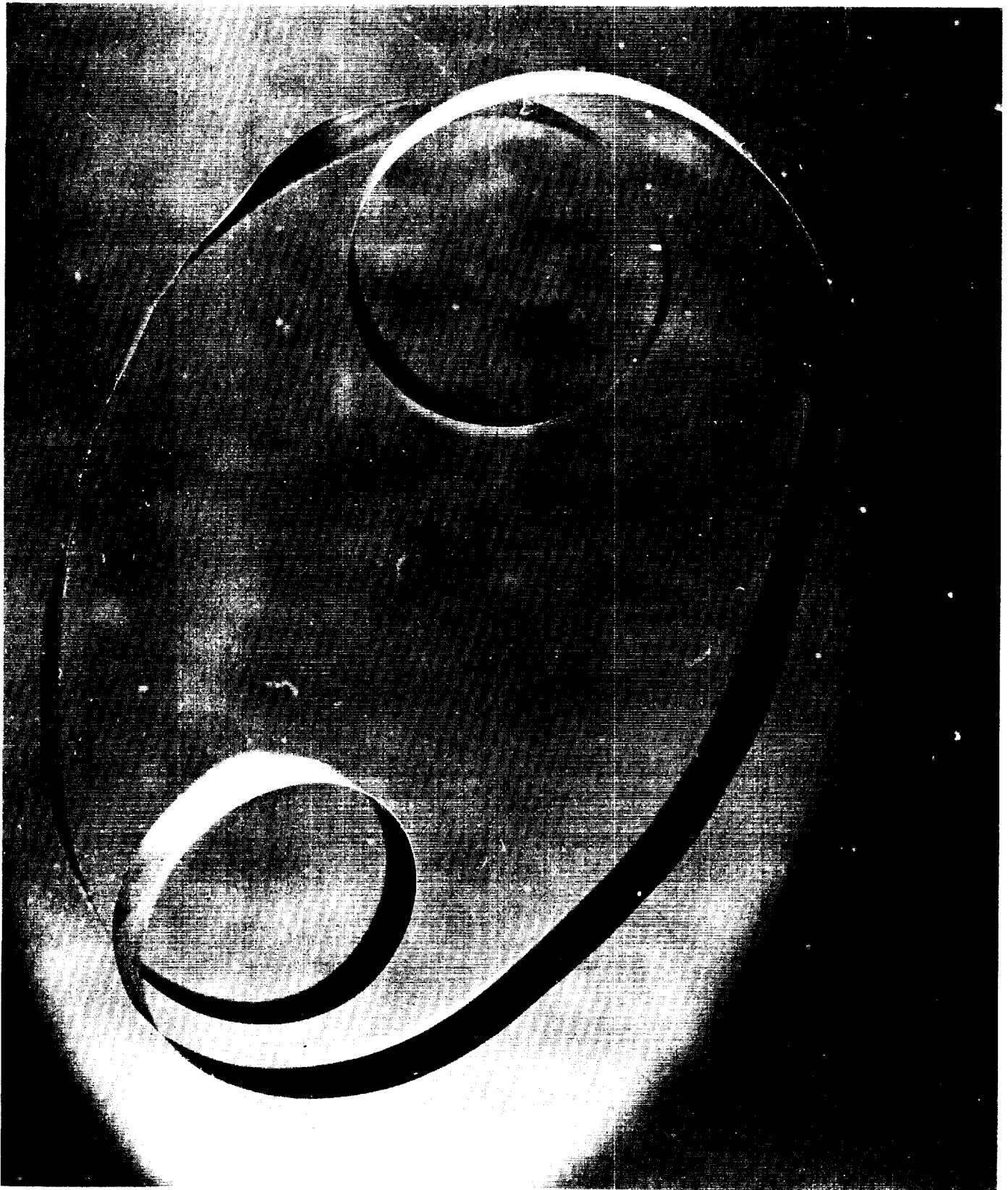


Fig. 14. Seamless belt fabricated from Pyrotrak (two times actual size)

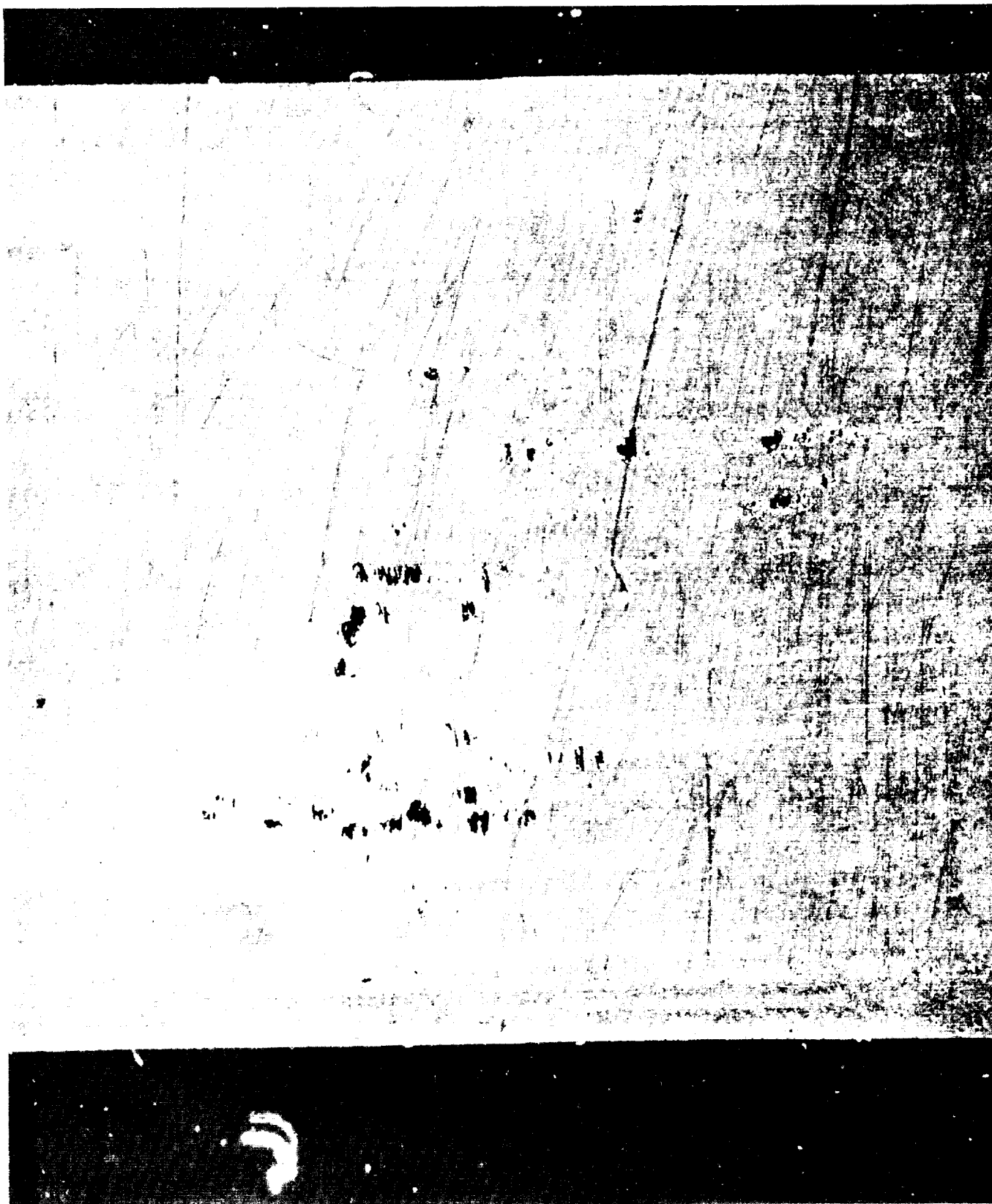


Fig. 15. Ununiform area of Pyrotrak belt (28 times actual size)



Fig. 16. Ununiform area of Pyrotrak belt (85 times actual size)

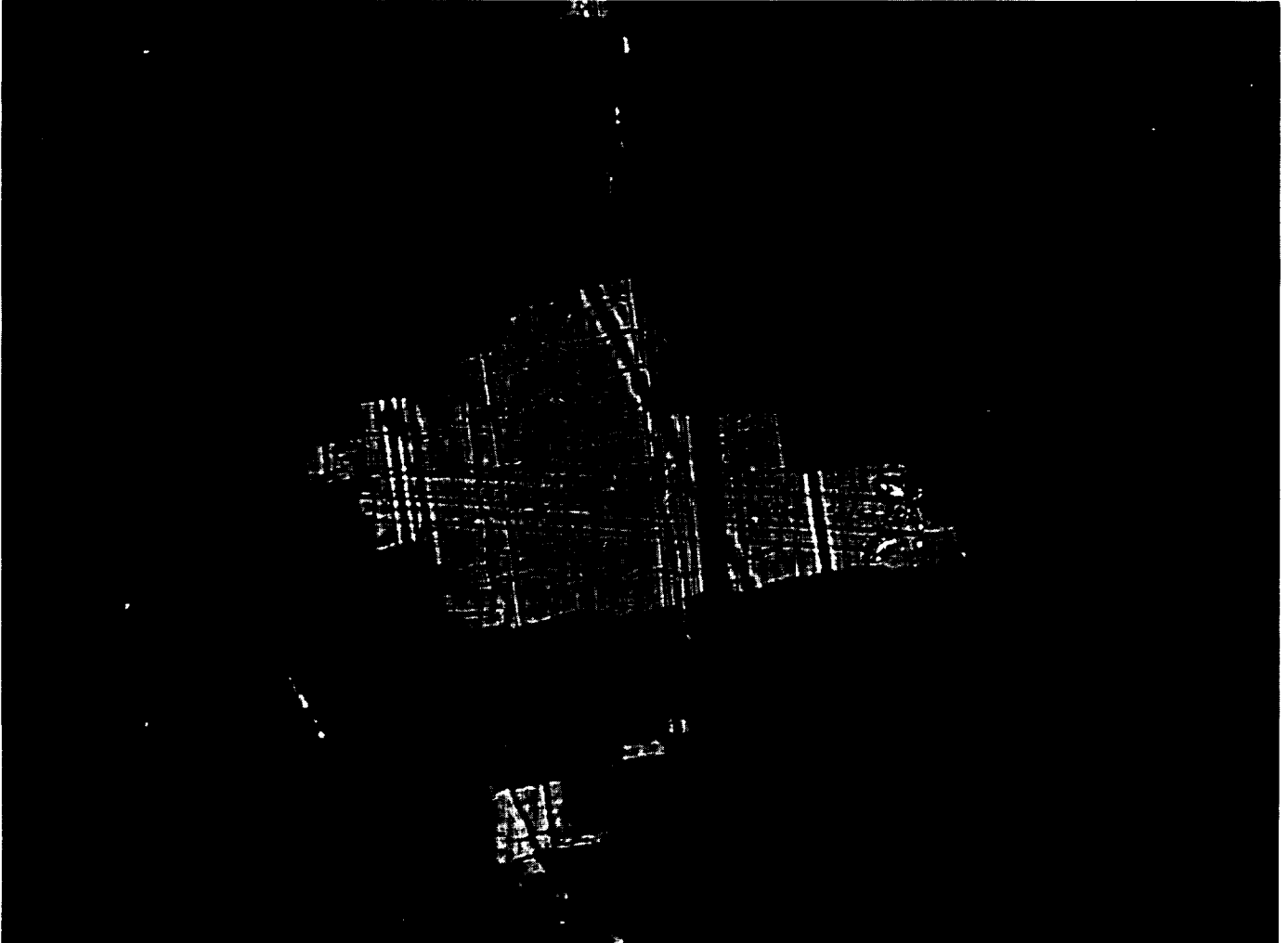
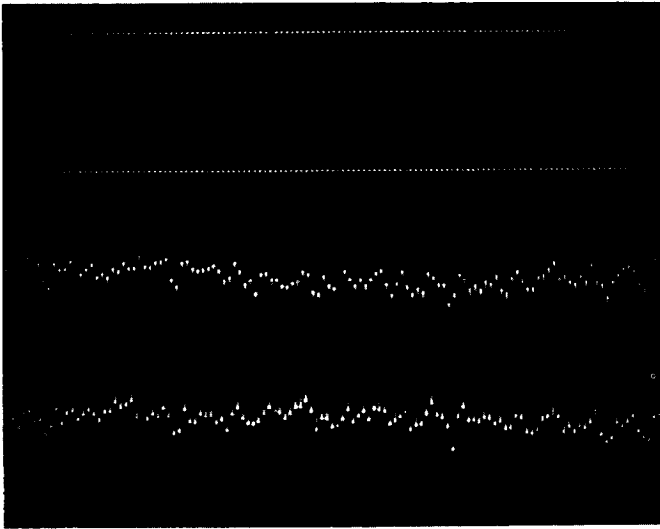


Fig. 17. Ununiform area of Pyrotrak belt (340 times actual size)

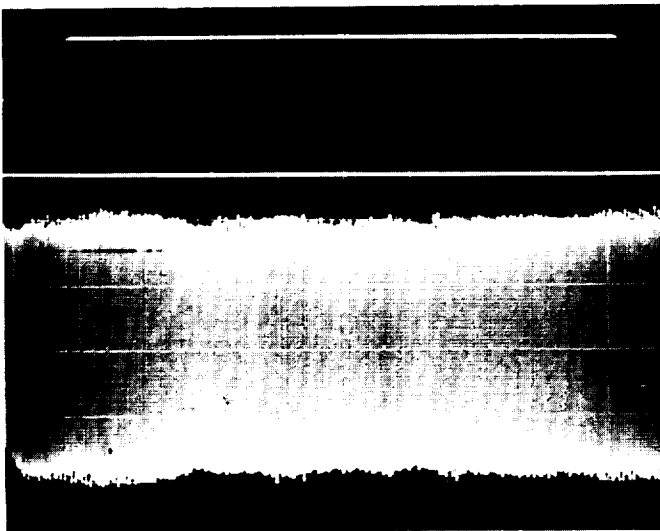


Fig. 18. Heavily stretched edge of Pyrotrak belt (440 times actual size)



UPPER TRACE: RECORDED SIGNAL 5 v/cm
 LOWER TRACE: PLAYBACK SIGNAL 1 mv/cm
 FREQUENCY: 60 kc (0.2 msec/cm)

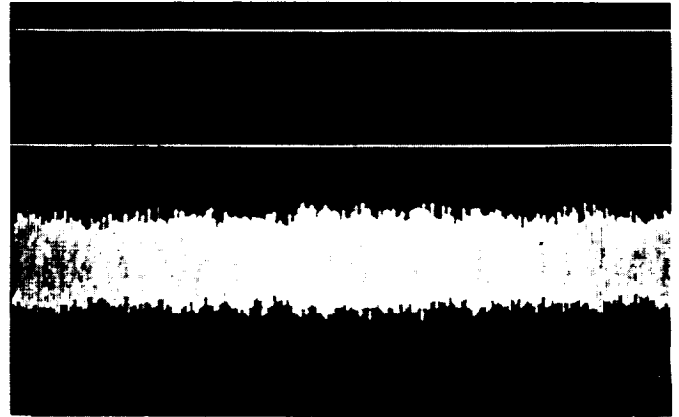
Fig. 19. Recording and playback signal at 52 in./sec—heads in contact with recording surface



UPPER TRACE: RECORDED SIGNAL 5 v/cm
 LOWER TRACE: PLAYBACK SIGNAL 5 mv/cm
 FREQUENCY: 15 kc (2 msec/cm)

Fig. 20. Recording and playback signal at 13 in./sec—heads in contact with recording surface

It must be pointed out, however, that both the coated and the cobalt-plated belts have been fabricated under virtually no quality assurance procedures. All vendors had no previous experience in plating of seamless belts or forming belts from coated sheet materials. This study



UPPER TRACE: RECORDED SIGNAL 5 v/cm
 LOWER TRACE: PLAYBACK SIGNAL 1 mv/cm
 TAPE SPEED: 13 in./sec
 FREQUENCY: 4 kc (5 msec/cm)

Fig. 21. Recording and playback signal at recording through belt

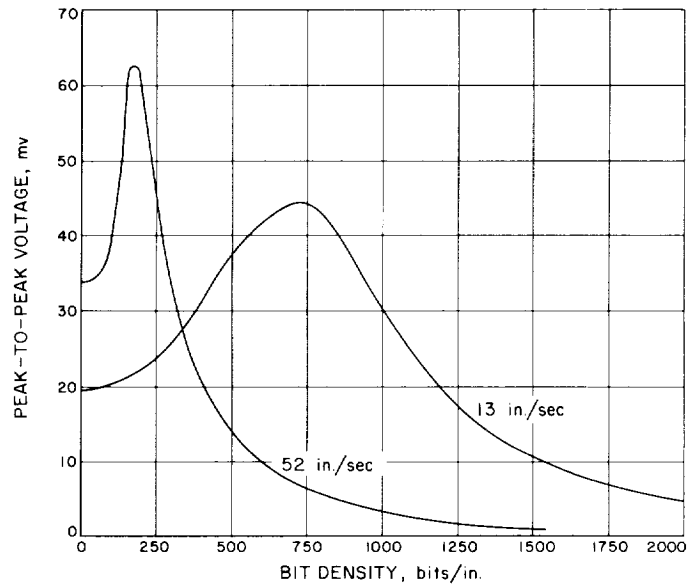


Fig. 22. Amplitude of playback signal at various tape speeds and recording with heads in contact with magnetic surface

shows clearly that seamless magnetic belts for data recording can be fabricated. However, the methods of coating or plating must be somewhat refined and the belt must be handled with more care.

6. Comparison of the Dynamic Storage Devices

Of all known dynamic storage devices, only the magnetic drum and the tapeloop recorder were found suited

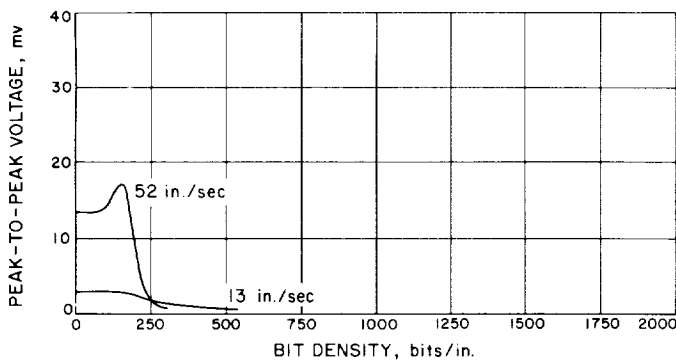


Fig. 23. Amplitude of playback signal at various tape speeds and recording through the belt

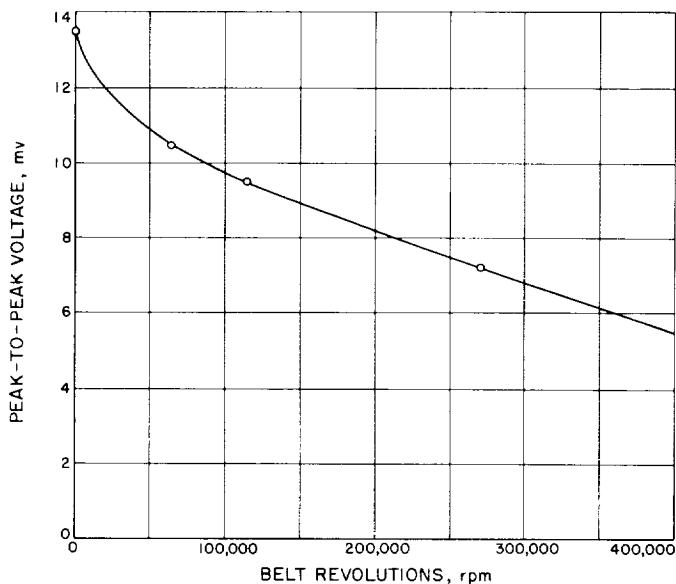


Fig. 24. Reduction of the playback signal amplitude because of tape wear

for spacecraft applications. Both can be built for reliable operation in severe environment over long periods of time. The *Titan* missile drum built by IBM seems to be superior to tape recorders in many respects; long lifetime and reliability are the main assets. In its present configuration, the drum is built for 600,000 bits total storage capacity, but could be further expanded to exceed several million bits. This drum can be built for "no drop-outs" by careful fabrication and inspection. It is expected to remain free of dropouts during its whole lifetime, because the recording surface is never touched.

The fact that the tapeloop recorder can be designed to withstand very high shock pulses and severe vibra-

tions is its main asset. Also, the loop recorder is believed capable of operating in a somewhat wider temperature range than the drum.

B. Magnetic Tape Recorder Sterilization

W. E. Arens

1. Introduction

Data storage is a necessary requirement for a deep-space telecommunications system because of the bandwidth limitations of the communication link. For instance, in numerous cases it is necessary to accept data inputs at comparatively high rates, store, and read out at a rate commensurate with these limitations. For video applications, input data rates are high, and the quantity of data necessary to produce useful information is very large. Therefore, in light of the present status of data storage technology, use of data storage systems with magnetic tape recorders as the primary storage medium appears to be the most feasible approach for such high-capacity applications. In addition, for future data handling systems in which data compression techniques are employed to more efficiently use the available bandwidth, large storage capacity will also be required. In summary, there is little question that magnetic tape recorders will become increasingly important subsystems for future deep-space telecommunications systems.

For deep-space missions involving planetary landers, sterilization will be a requirement to prevent contamination of other planets with living organisms from Earth. Previous experience with tape recorders has indicated that a requirement for heat sterilization could represent a serious problem for numerous components of the transport subsystem. Therefore, work has been formally undertaken in the area of magnetic tape recorder sterilization. The individual task descriptions, work accomplished, and future development plans are presented in detail here.

2. Definition of Program

A program was undertaken in 1963 to define and solve all of the problems associated with the complete sterilization (both dry heat and ethylene oxide) of a typical

spacecraft magnetic tape recorder^a. The endless loop *Mariner IV*-type magnetic tape recorder was chosen as the basis for the transport design because it more closely approached actual flight hardware than any other transport under development at JPL. The program was outlined so that each component to be included in the final transport subsystem would be individually designed and developed for sterilization tests. These tests would serve as the basis for a complete experimental and analytical study to adequately define any degradation affecting the performance or life of the components. An attempt would be made to solve any resulting problems so that a reliable sterilizable component would be available for inclusion into a sterilizable transport subsystem. Since these components would be assembled into a sealed case, the only component requiring ethylene oxide decontamination survival would be the pressure seals. Therefore, the program was defined so that only the seal material would be exposed to ethylene oxide testing prior to transport assembly. When sterilizable components were available, they would be assembled into a complete flightworthy tape-transport subsystem which would be exposed to complete sterilization testing. The performance of this subsystem would be monitored and analyzed before and after sterilization. From these results, any degradation in performance reliability would be detected, and a solution would be sought. Assuming that a sterilizable transport subsystem was achieved, the final phase of the program would be a life test to further determine the effects, if any, of sterilization on life and reliability.

3. Component Evaluation

In 1963, a contract was awarded to Raymond Engineering Laboratory (REL), Middletown, Connecticut, to accomplish the aforementioned program. The initial phase of this contract was concerned with obtaining sterilizable components for a *Mariner IV*-type transport. The individual components considered were (1) magnetic tape, (2) pressure and drive belts, (3) record/playback motors, (4) rotating modules and lubricants, (5) record/reproduce heads, (6) transport plate, (7) preamplifier electronic modules, (8) end-of-tape sensors, and (9) covers and seals.

^aThe NASA sterilization program required that all spacecraft flight subsystems be capable of withstanding a temperature of $135 \pm 1^\circ\text{C}$ in an inert atmosphere for 24 hr (flight acceptance) and that all prototypes survive three 36-hr exposures to a $145 \pm 2^\circ\text{C}$ temperature (type approval). In addition to the aforementioned dry-heat requirement, the equipment must also survive decontamination exposure to an ethylene oxide atmosphere at 35% RH and 40°C for 24 hr.

a. Magnetic tape. Early in the program, an industry-wide search was conducted to determine the availability of a high-temperature magnetic tape capable of surviving the dry-heat sterilization environment with minimum deterioration of performance and reliability. Several tape manufacturers were contacted and their tapes selected and evaluated. A summary of results and conclusions follows.

Minnesota Mining and Manufacturing Company (3M). Two 3M magnetic tapes, LR1220 and LR1353, were selected for evaluation. Both of these tapes have a Mylar backing and are considered to be the best lubricated tapes available from 3M. Tests revealed that the LR1353 tape, recommended for use up to 225°F , was by far the most capable of surviving high temperatures. Following sterilization, samples of LR1353 tape showed no significant deterioration in electrical output. However, mechanical deterioration was evidenced by the excessive shrinkage (approximately 2%) and reduced tensile strength which followed sterilization exposure.

Memorex Corporation. Only standard Mylar-backed tapes rated for temperatures far below the sterilization temperature were available from Memorex. Sample tapes from Memorex were unusable after exposure to the 300°F sterilization testing because of the excessive electrical and mechanical deterioration that resulted.

Remington Rand Corporation (Univac). The only potentially high-temperature tape available from Univac was a Mylar-backed tape called Univac Electroless. A sample of this tape was obtained and exposed to sterilization testing. However, the tape proved completely unusable following sterilization because of the excessive deterioration of the oxide film.

Reeves Soundcraft. Samples of several Mylar-backed tapes were obtained from Reeves Soundcraft and exposed to numerous temperature tests. One of these tapes appeared to retain its stability much better than the others. This tape was lubricated with graphite on one side and had an oxide coating on both sides of the Mylar base. Reeves produced some samples of this double-oxide tape using a high-temperature polyimide backing developed by Dupont (known as H-film) to improve its temperature-resisting capability. Several 6-ft samples were obtained and exposed to sterilization testing. The sterilized samples of H-film tape showed no significant degradation in performance or mechanical characteristics following sterilization tests.

Samples of metal tape were also obtained from Reeves. However, the electrical performance of the metal tape was extremely poor compared with Mylar or H-film-backed tapes. In addition, the tape had a tendency to curl following passage over the small radius of the capstans.

Thin Films, Inc. Several samples of tape with H-film backing were obtained from Thin Films, Inc. This tape exhibited a low output compared with other tapes tested. In addition, it was only available in very short lengths, thereby limiting the degree of testing that could be accomplished.

Arnold Engineering. Several samples of metal-backed tape were obtained from Arnold Engineering. However, as with the Reeves metal tape, electrical and mechanical performance was extremely poor.

From the foregoing evaluation program, it was concluded that H-film represented the most promising backing material for a sterilizable magnetic tape. In addition, the Reeves H-film-backed tape showed the most promise of satisfactory survival of the sterilization environment. Therefore, a contract was awarded to Reeves for the production of a usable reel of H-film-backed tape. Reeves was instructed to use their proprietary oxide binder, which employs oxide coating on both sides of the tape, because of its potentially high temperature stability. From this contract, 6000 ft of H-film tape was produced and sent to REL for evaluation. Preliminary tests indicated an electrical output comparable to good Mylar instrumentation tape.

Initially, a 300-ft pack was made and exposed to sterilization. Inadequate curing of the tape resulted in a test failure. Therefore, a curing process consisting of a 24-hr exposure to 150°C with a dry nitrogen wash over a loose tape pack was incorporated. An ensuing sterilization test of a 300-ft pack of cured tape exposed a new problem: excessive shedding of the graphite lubricant. Therefore, a burnishing machine was constructed to remove the excess lubricant by passing the tape over an abrasive surface.

A 300-ft tape pack of cured and burnished H-film tape was then mounted in a transport case and exposed to complete sterilization testing, with very encouraging results. The pack began normally with no evidence of discontinuities or voids. A total of 310 passes was accumulated on the tape before the amount of lubricant debris collecting about the head and rotating parts was

considered excessive. This is a normal expectation of lubricated tape in an endless loop pack.

Although the Reeves H-film tape survived the sterilization environment with no apparent significant degradation in performance or life, a number of unique characteristics of the tape were determined as a result of the curing and sterilization process. It was noted that during high-temperature exposure the binder system undergoes a modification such that the oxide becomes so affixed to the H-film that it cannot be removed by normal means. Before curing the tape, the oxide coatings are easily removed with ordinary solvents.

Also, there is a definite increase in stiffness of the H-film tape following curing at 150°C, which apparently caused an increase in AM from 10 to 17%. This increase in stiffness is probably a by-product of the aforementioned binder modification.

There is a definite outgassing of the H-film tape during the curing process. Analysis of several tape samples at JPL revealed gas by-products consisting of small traces of polyimide (H-film) and acrylate materials (binders and adhesives). It was necessary to incorporate a nitrogen flow-through during the curing process to allow the removal of these by-products.

In addition, splicing of cured H-film tape requires special consideration. The normal splicing operation requires removal of oxide from the two ends of tape to be spliced. The ends are then bonded together with a separate piece of H-film. However, as mentioned previously, the oxide is extremely difficult to remove from H-film tape. Therefore, the splice must be made over the oxide. Tests of such splices indicate that the splice is adequate. In fact, no failure of oxide interface has ever occurred, because the H-film lap will break before this can happen.

In summary, H-film-backed tape was developed and has survived JPL sterilization testing with no apparent degradation in performance or life of the tape. Since no other known tape has demonstrated this capability, this tape was selected for use in the fabrication of the sterilizable tape transport.

b. Pressure and drive belts. Initial tests of Mylar belts at sterilization temperatures indicated that Mylar would probably be unsatisfactory. Therefore, several belts were fabricated from H-film in the hope that this would provide significant improvement at high temperatures. These

first H-film belts were unsatisfactory because they became wrinkled. It was found that the wrinkles could be prevented by rotating the belts during the curing process. Following the development of a satisfactory curing process, a number of H-film belts were fabricated and exposed to sterilization testing, with extremely encouraging results.

Mylar and H-film belts were mounted to a skeleton transport and comparative sterilization tests were conducted. Test results showed that the tension of the capstan-to-capstan Mylar pressure belt was reduced over 60% by the sterilization environment, making the belt completely unusable. On the other hand, an H-film playback motor-to-first-idler belt and an H-film pressure belt lost 16.5 and 24.5% of their initial tension, respectively. These are usable figures since the belts can be adjusted initially to approximately 20% increased tension to compensate for the decrease in tension during sterilization.

Sterilization testing of unmounted belts also indicated a definite superiority of H-film over Mylar. H-film belts experienced no significant dimensional change, whereas Mylar belts normally suffered a typical reduction in length exceeding 5%, with evidence of actual damage. In addition, Mylar stress characteristics were affected to a much greater extent. As a result of the sterilization process, Mylar showed a typical change in tensile modulus of more than 18%, while the corresponding modulus change of H-film belts was normally 2.5%.

In summary, in the sterilization environment, H-film belts were found to be far superior to Mylar belts. With the initial tension of the H-film belts set approximately 20% above the nominal figure, the belts indicated a capability of surviving the sterilization environment with no significant degradation. Therefore, H-film belts were selected for use in the sterilizable tape transport.

c. Record and playback motors. The record and playback motors required by the transport were designed by H. C. Rotors, Kew Gardens, New York, and fabricated by REL. Both were highly stable AC hysteresis synchronous motors having an efficiency of 25 to 30%. Prior to sterilization of the motors, the laminations were spray-varnished, assembled, bored, and fluidized with an epoxy compound. This process included exposure to several temperature cycles, the most extreme of which was 115°C for 4 hr. This procedure was necessary to drive off any volatiles from the Hysol or varnish used for cementing the laminations together.

The finished record and playback motors were exposed to complete sterilization testing, with very little resulting deterioration. There was a measured reduction of 10% in stall torque in the playback motor at -10°C , and a comparable increase in both synchronization and stall torque of the record motor at room temperature. Similar small changes noted in bearing-running torque were considered insignificant. Experience has shown that bearing-torque tests are generally difficult to repeat within $\pm 10\%$ under ideal conditions. Therefore, to be truly indicative, any effect upon motor bearings brought about by the sterilization process appears dependent upon life testing.

In summary, the motors developed for the sterilizable transport evidenced a capability of surviving the sterilization environment with no deterioration in performance. Therefore, these motors were deemed acceptable for use in the sterilizable tape transport.

d. Rotating modules and lubricants. An investigation of available lubricants was initiated. As a result of discussions with the manufacturer, it was concluded that the Anderson L 245X oil used in the *Mariner IV* transport bearings would probably survive the 145°C sterilization temperature. In addition, a preliminary design study of the rotating modules required by the transport indicated no problems which would necessitate a significant redesign of the *Mariner IV* transport units. On the basis of these results, the following rotating modules were assembled and exposed to sterilization testing: (1) two capstan units, (2) one reel assembly, (3) two pressure-belt modules, and (4) one idler assembly. Five of the six assemblies tested had insignificant changes; however, one of the capstan assemblies experienced an increase in run-out of almost 12 times the initial value. In addition, the coast-down time for this module increased by a factor of 2. An investigation of the cause of failure disclosed a decrease in the module axial preload. A reduction in lubrication was eliminated as a cause because it could account for the increase in coast-down but not run-out time. Although a detailed autopsy of the module was performed, no definitive cause for the failure was determined.

One supposition attributes the excessive run-out to the relaxation in preload combined with an addition of the tolerances of certain mechanical dimensions such as surface flatness, parallelism, and length of separators in a negative fashion. A factor contributing to this effect could be associated with the possible use of material lots having different heat treatment histories for the manufacture of the two capstan assemblies. To substantiate

this possibility, the failed capstan assembly was reworked and resterilized, and demonstrated no apparent effects as a result of exposure to the sterilization environment. Consequently, to obtain a good temperature history, it may be practical to expose a mechanical item to an environment slightly in excess of the required sterilization environment and then rework to account for shifts.

Since all six rotating assemblies had survived sterilization (although one required rework and a second sterilization test), they were designated for use in the assembly of the sterilizable transport.

e. Record and reproduce heads. Preliminary testing indicated that magnetic heads capable of surviving the sterilization environment would require some development. Applied Magnetics Corporation (AMC), Goleta, California, was selected to provide the heads for this program. The initial heads produced by AMC had high curing temperature (400°F) bonding materials, such as Union Carbide R-61 silicone varnish. Three such heads were exposed to and survived sterilization at AMC. However, they had not been mounted nor had the tape pressure been applied to them. Subsequent testing with the heads mounted in a transport resulted in the failure of all three. The primary failure modes were typified by (1) core shifting, (2) changes in gap width, and (3) changes in inductance. Detailed consideration of these failure mechanisms led to the conclusion that a head design stressing a matching of temperature coefficients was necessary. In addition, the possibility of a unique head design incorporating a retaining spring to return the pole pieces to their original position following sterilization was considered worthy of investigation.

To obtain thermal expansion coefficient compatibility, molds were fabricated of RTV rubber, a strip of metal was placed in the bottom of the molds, and epoxy was poured over the metal. Following cure, the end of the metal and epoxy strip was clamped and relative cure vs temperature characteristics were measured by means of a set of rulings at the end of the strip.

The spring arrangement was investigated but rejected because it aggravated the problem of pole-piece "stepping." Although the primary problem in heat sterilizing a head is concerned with gap opening, slight anomalies in head construction can cause significant misalignment of the pole pieces in the plane of the tape. The most successful approach to this problem consisted of a process in which a "poor-match" epoxy was used to fill the back volume of the head. With expansion due to tem-

perature, the back gap tends to open, which in turn causes the front gap to have a tendency to close. This results in an effective fulcrum in the area of the assembly screws. Since the coefficient of expansion and position of the screws were extremely critical, the study resulted in the selection of one screw per head so that one core half is effectively floating (the original head assembly technique used a separate screw for each core half). In addition, a relatively resilient rubber was selected for the fill between the core and shell, rather than all epoxy.

Four sets of heads using these design techniques were produced, with different shell materials used for each set. The four materials used were aluminum, aluminum-bronze, KR Monel, and brass. All four sets were exposed to sterilization testing and remained within the required design tolerances. The superiority of the aluminum head was established on the basis of test results; therefore, it was selected for inclusion in the sterilizable transport.

f. Transport plate. Although sterilization temperature causes expansion of the transport mounting plate, this does not initially appear to be a serious problem, especially when one considers the fact that the plate should return to its original condition following exposure to heat. However, because of this expansion, motor, idler, and capstan shafts will vary in spacing during sterilization. Therefore, when combined with the thermal coefficient of expansion of the associated belts, the expansion causes a net change in belt tension. For the sterilizable tape transport being developed, the plate was made of AZ31B magnesium and the drive and reduction belts were to be made of H-film. Since the coefficient of expansion of magnesium is greater than that of H-film and since the drive belt lengths were equally greater than the pulley centerline distance, the thermal changes very nearly canceled. However, this could not be accomplished with the reduction belts, and there was a 15 to 25% loss of tension. Therefore, the transport-plate design was considered satisfactory for use in the sterilizable transport, with the provision that the reduction belt tensions be first preset to the high side of their original tolerances to compensate for this loss in tension during sterilization.

g. Preamplifier electronics. Since it is desirable to mount the tape recorder playback preamplifiers close to the playback head for minimum noise pickup, the preamplifier electronics package was one of the sterilizable components to be included in the sterilizable transport. The differential preamplifier circuits were packaged in modules consisting of discrete components which were

assembled by a cordwood-construction method. Three such preamplifier modules were assembled into a shielded can identical to that used on the *Mariner IV* flight program. The only change from the *Mariner IV* packaging was the replacement of phenolic circuit boards with epoxy glass boards, because phenolic deteriorated as the result of exposure to a temperature of 145°C.

Sterilization testing of the differential preamplifier assembly resulted in no detectable problems that might affect performance or reliability. Therefore, the preamplifier assembly was deemed acceptable for use in the sterilizable tape transport.

h. End-of-tape sensor. For end-of-tape sensing, the *Mariner IV* transport used metallic fingers to contact a conductive area of the tape; however, the gold-plated Mylar-aluminum laminate used was found to be unsuitable because of a breakdown of the gold edges at sterilization temperatures. An initial approach which consisted of bonding a 0.3-mil gold leaf to the oxide side of the H-film tape was unsuccessful because the gold leaf cracked and did not adhere to the oxide. Another approach which consisted of depositing silver by the Brashear (mirror-silvering) technique met with failure because the Brashear-deposited silver volatilized at sterilization temperature. A third approach, which proved to be most successful, consisted of a spraying process using a silver lacquer. Following sterilization, the silver lacquer remained intact, with a resistivity of approximately 200 mΩ/in.

Although selected for use in the fabrication of the sterilizable transport, the silver-lacquer technique is too noisy at low tape speeds. Therefore, further work is necessary in this area. An optical end-of-tape sensing technique appears most attractive for future applications at this time.

i. Covers and seals. The transport was designed to be contained within a case which is hermetically sealed with Parker Viton rubber gask-o-seals. Considerable work had been accomplished on the *Mariner IV* program to achieve a reliable seal design. Therefore, the *Mariner IV* transport case and covers were sealed using the identical design and were exposed to complete dry-heat sterilization testing. Although the leak rate approximately doubled at a case temperature of 145°C, it returned to normal after cooling to ambient. This added leak rate contributed to a gas-pressure loss of 0.8 psi during the 108-hr sterilization period; however, this was considered insignificant.

Although the covers bulged approximately $\frac{3}{32}$ in., indicating a need for a stronger cover, no degradation of the seal or sealing area was detected.

The seals were also subjected to ethylene oxide (ETO) decontamination testing. The case and covers were assembled and internally pressurized with one atmosphere of a 90/10 nitrogen-helium gas mixture. Leak rates were monitored before and after ETO decontamination cycles. These tests showed no adverse effect on the seal integrity as a result of the ETO exposure. In addition, no evidence of surface corrosion or discoloration was detectable as a result of the ETO tests.

In summary, the basic sealing technique used for *Mariner IV* was considered satisfactory and was therefore selected for use on the sterilizable tape transport.

4. System Evaluation

a. Test procedure. Following qualification of the individual components, the complete transport was assembled and subjected to complete dry-heat sterilization testing (three 36-hr periods at 145°C). After sterilization, the transport started normally, with no indication of sticking or binding. The heat outputs, flutter, and AM were normal. The transport was operated for approximately 25 passes of the tape before the case was opened. The case was then opened and revealed the following:

1. A black stain on the Dow 17 finish adjacent to the Viton seal rubber.
2. Whitish crystals adjacent to the seal toward the inside of the case.
3. A soft gray deposit that soon volatilized, on the reel housing.
4. A surface scale on the beryllium copper clutch spring and capstan "True Arc" (C-clamp), giving the appearance of fine diamond dust.
5. Slight creepage and a crack in the epoxy of the AMC magnetic head (not located in the tape path). However, the gap width had remained constant with no shifting or stepping.
6. An etched or dulled appearance on the brass fly-wheel, the clear anodized aluminum pulleys, and all solder connections.

Photographs of the opened transport following sterilization are shown in Figs. 25 and 26.

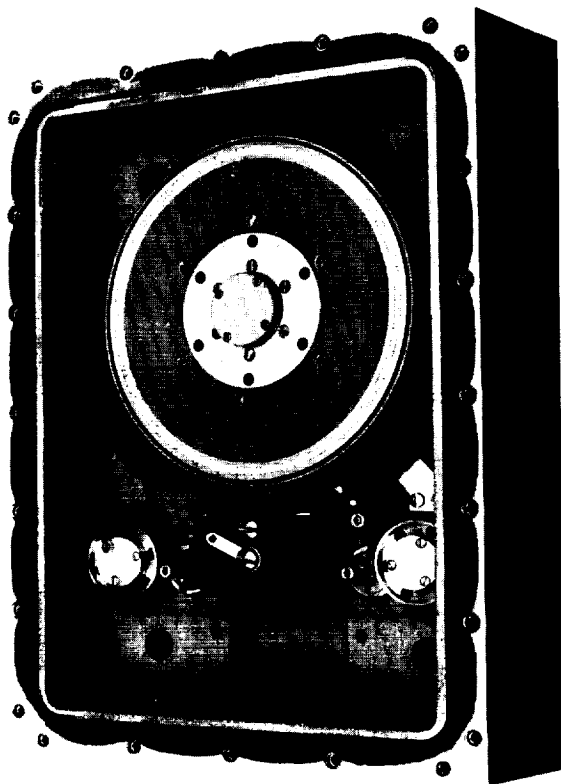


Fig. 25. Sterilized transport—top view

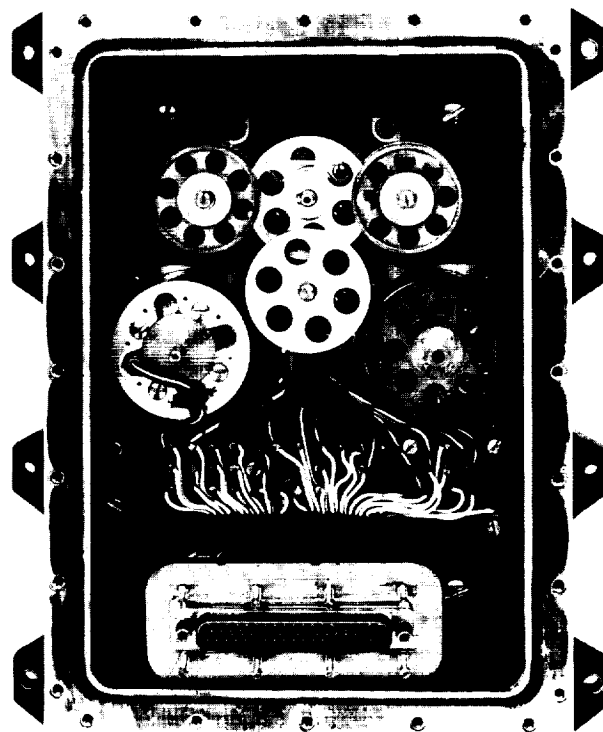


Fig. 26. Sterilized transport—bottom view

Following examination of the assembled transport, a life-test program was undertaken. A program of slow and fast tape velocities (0.01 and 12 in./sec, respectively) was established. After five days of life-testing, a capstan bearing appeared to fail; i.e., it became noisy and caused increased flutter. After 10 days, the flutter again increased, indicating additional bearing failures. At that time, the life-testing was interrupted and preparations for a complete disassembly and analysis of the transport began. The transport was disassembled in the clean room facilities made available at JPL.

b. Transport disassembly and analysis. Following removal of the covers, the first step in the disassembly of the transport was the removal of the head shield. A collection of material thought to be either oxide or tape lubrication was noted inside of the shield. Examination of the heads revealed that the tape was depositing two piles of lubrication or oxide at the head contact area (Fig. 27).

The next step in disassembly consisted of the removal of the tape pack, drive belt, pressure-pad assembly, and

reel collar and shim. The collar showed corrosion, while the drive belt was definitely dirty with vertical scratches. The wiper pad shown in Fig. 28 was loaded with debris. The reel assembly showed a gray-white growth or deposit on the edge of the reel gaps near the tape (Figs. 29 and 30). The tape roller shown in Fig. 30 indicated a large collection of lubricant or oxide deposit. However, it is interesting to note (Fig. 29) that this contaminant varied in degree from roller to roller. In fact, as can be noted from Fig. 30, one tape roller is virtually free of this material. Fig. 30 also shows the tape pack to be stacked unevenly.

At this point, examination of the other side of the transport plate showed a capstan belt to be "riding" approximately $\frac{1}{16}$ in. off the downstream capstan pulley. Further examination showed that the downstream capstan appeared to have radial play. The belt began to center when pressure was applied to align the capstan and the unit was rotated. It was also noted that all visible solder joints on this side of the transport plate were very dull. In addition, the four circuit-board tie-down screws and one from the playback cleat were found to be loose.



Fig. 27. Head deposits

The disassembly continued with the removal of all belts, the motor assemblies, and the first idler. Failure of the first-idler assembly bearings was noted. Although the assembly was not locked up, it was very close. There were two extremely rusty screws at the bearing retainer.

All wires from the transport to the circuit board were clipped and labeled, and the board and connector assembly was removed. The transport plate was then removed from the case. Close examination of the removed

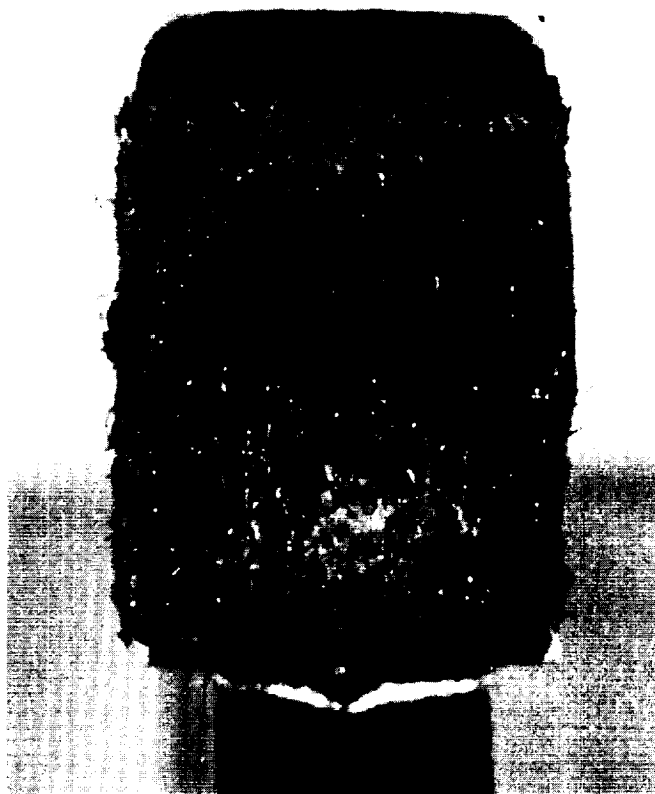


Fig. 28. Pressure pad

transport plate revealed that most of the tie-down screws associated with the capstan and the pressure-belt pulley assemblies were very rusty. Corrosion was also found under all subassembly tie-down cleats. A nut, a washer, and the main tie-down screws of the sense guide assembly were loose. The outer bearing of the right pressure-belt pulley assembly fit the shaft much too tightly, and bearings had failed in both the downstream capstan and the second idler.

The downstream capstan (Fig. 31) was then disassembled, and revealed corrosion of the internal Eaton ring (Figs. 32 and 33). This corrosion had transferred as powder to bearings in the clutch assembly. With preload removed from the downstream capstan shaft bearings, the shaft turned in the ID of both bearings. The dust covers were then removed from both downstream capstan body bearings. Final-stage-type failure reflected in spalling and metal failure and many rust-powder deposits was noted in the bearings (Fig. 34). The bearings of the downstream clutch were found to be in the early stages of "rust"-type failure. Close examination showed the

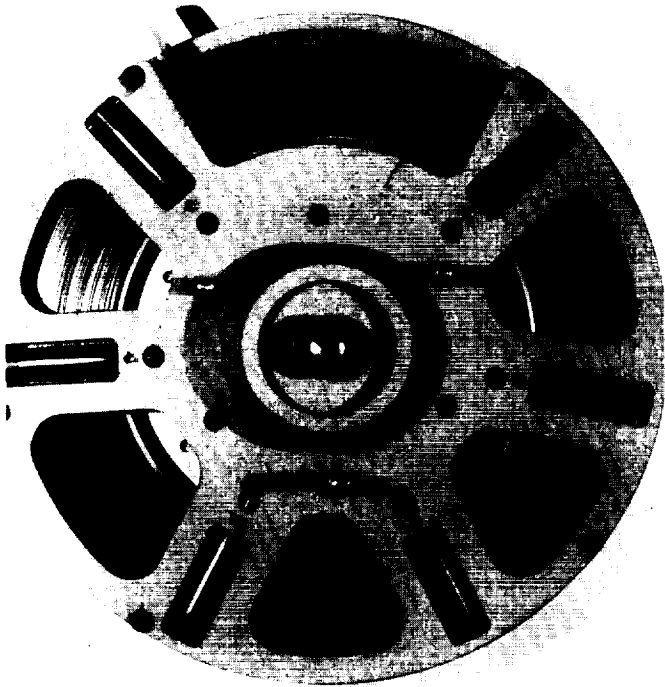


Fig. 29. Reel assembly

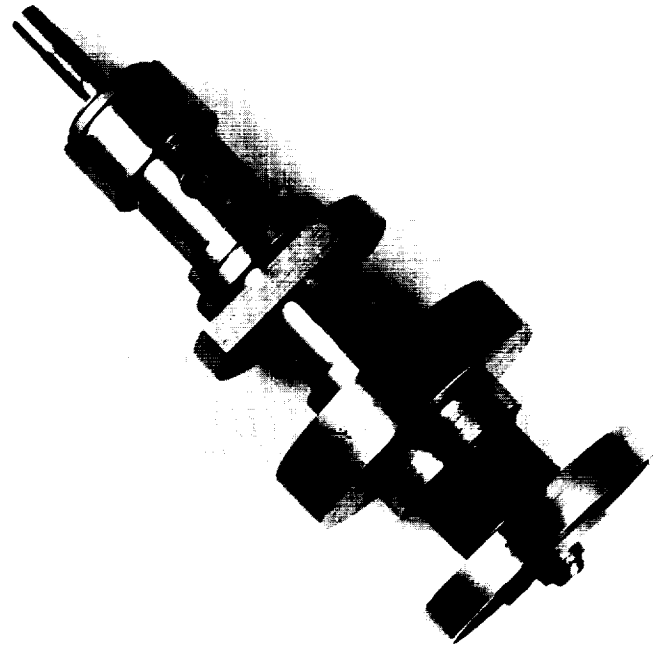


Fig. 31. Capstan assembly

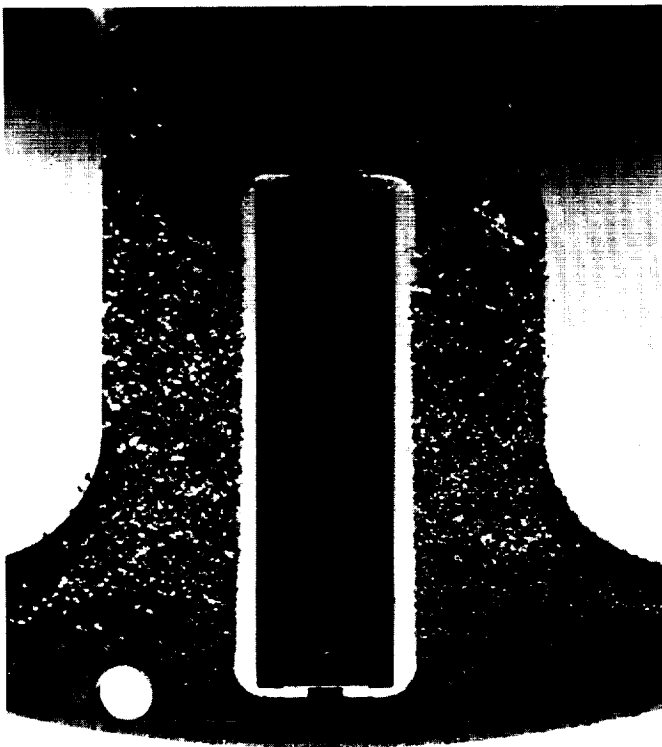


Fig. 30. Tape pack deposits



Fig. 32. Capstan bearing failure

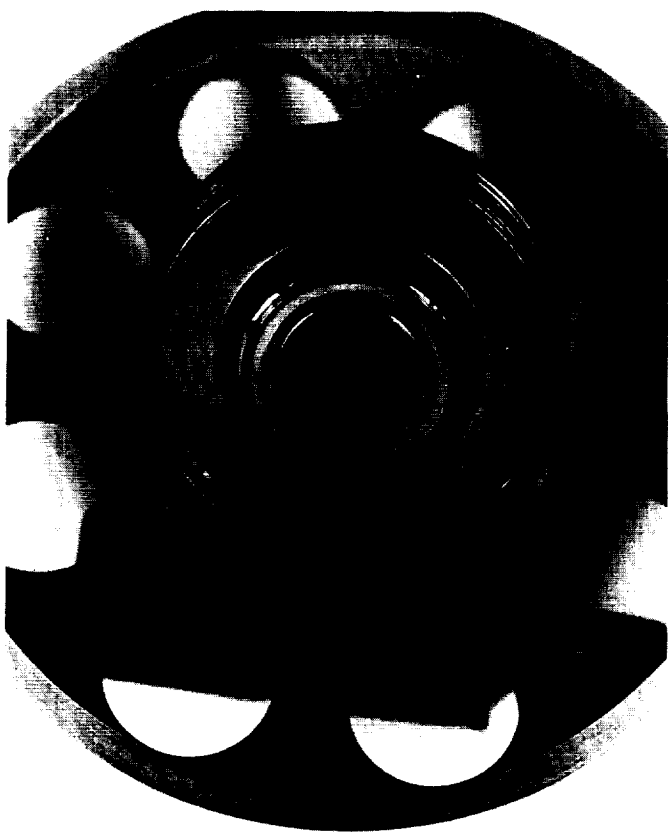


Fig. 33. Capstan pulley corrosion

absence of all lubrication, and there were rust deposits on the contact edges of the ball separator.

The final stage of disassembly involved the tape-pack assembly. The screws were very rusty, and the reel plate showed heavy deposits of material in the roller area where the edge of the tape works. The reel bearings and retainers showed various types of corrosion, some of which were not found elsewhere in the transport. In addition, lubrication was present, but in some cases it had developed a tan, thick, and grain-like appearance.

c. Results of analysis. Following disassembly and examination of the sterilized transport, an extensive chemical analysis program has been undertaken and is presently in progress at JPL to determine the nature and cause of the various degradative contaminants and depositions. Preliminary results of the analysis are given as follows:

1. The material which collected on the heads (Fig. 27) was pressed in a KBr pellet and examined by IR techniques. In addition to oxide, there was an indication of a nitrogen-containing organic compound,



Fig. 34. Ball bearing corrosion

probably due to traces of abraded H-film which is a polyimide.

2. The polyvinyl-polyacetate adhesive used on the H-film tape decomposed during the sterilization exposure, yielding HCl. This produced a chemical reaction with metals throughout the transport, resulting in the formation of metallic chlorides. The corrosion found on the reel assembly (Figs. 29 and 30) represents one specific example.
3. Many bearings were dry and corroded (Fig. 34). None of the lubricants were corrosive. However, the Anderson L 245X oil used in the miniature bearings is an organic aliphatic ester which does volatilize significantly at sterilization temperatures.

4. A gas analysis of a *Mariner IV* TA recorder pressurized and sealed in an identical manner revealed a presence of oxygen ($\approx 7\%$) which was probably due to the air originally present and not completely removed before pressurization with nitrogen. This, combined with the hydrogen gas resulting from the reaction of HCl with the transport metals, accounts for the presence of moisture (H_2O) in the transport. This also accounts for the presence of rust throughout the transport.

5. Summary

The JPL magnetic tape recorder development program has resulted in the development of a magnetic tape recorder transport (similar to that flown in the *Mariner IV* spacecraft) for the purpose of determining and solving all of the associated sterilization problems. Each component developed for and used in the transport was individually exposed to and survived the required sterilization environment prior to transport assembly; consequently, the feasibility of developing individual transport components capable of surviving the sterilization environment was demonstrated. However, the assembled transport, when exposed to the sterilization environment, was affected significantly by the creation and collection of depositions and debris resulting from numerous chemical interactions. Consequently, several transport bearings failed after only a few days of post-sterilization operation. The causes of these chemical interactions and resultant contaminants are presently being investigated and will continue to be investigated until fully analyzed and corrective measures taken to establish adequate reliability and life performance characteristics.

C. A Note on the Probability Distribution of the Phase Error in a Second-Order Phase-Locked Loop

F. J. Charles

1. Introduction

This note is concerned with the probability distribution of the phase error associated with a second-order phase-locked loop (PLL) operating in the presence of noise. The loop filter is of the proportional-plus-integral

control type and corresponds to that generally employed for carrier tracking purposes in the implementation of phase-coherent communication systems. The need for an analytical expression which adequately describes the probability distribution of the phase error is immediately apparent in several situations of considerable practical importance. For example, in predicting the performance of phase-coherent communication systems, a mathematically tractable expression for the phase-error distribution is necessary. When such an expression is available, the deleterious effects of noisy phase references on system performance can be taken into account (Ref. 1). Another situation which is of current practical interest and requires knowledge of the form of the phase-error distribution is that which occurs in the determination of optimum modulation indices or in optimum power allocation analysis (Ref. 2). Aside from these more significant system aspects, the distribution of the phase error is important in its own right. If the phase-error distribution is known, the fundamentals of the loop's nonlinear behavior can be more readily appreciated. Finally, the variance of the distribution as a function of the signal-to-noise ratio (SNR) existing in the bandwidth of the loop plays an important role in the design of PLLs.

The most promising analytical approach used to develop an exact nonlinear theory of PLLs is based on the Fokker-Planck method (Refs. 3, 4, and 5). This particular method leads to an expression for the probability distribution of the nonstationary phase error which, in the steady state, gives an unbounded variance. Of course, this behavior of the variance is a result of the cycle-slipping phenomenon associated with PLLs. However, Viterbi (Ref. 3) and Tikhonov (Refs. 4 and 5) were successful in applying this method to the analysis of the first-order loop by recognizing that the phase-error distribution-reduced modulo 2π is stationary and possesses a bounded variance. The extension of the Fokker-Planck method to the second-order PLL (i.e., where the loop filter is of the proportional-plus-integral control type) represents a formidable problem. However, this method has led to an approximate expression for the phase-error distribution which is valid for very low SNRs and which agrees with the linear theory for high SNRs (Ref. 6). In fact, it has been shown (Ref. 6) that equating the two time constants of the second-order loop filter reduces the approximate expression for the second-order phase-error distribution to a form which corresponds to the first-order result derived by Viterbi (Ref. 3) and Tikhonov (Ref. 4). This suggests consideration of the possibility of approximating the second-order loop phase-error distribution by the more tractable first-order loop distribution. The purpose of this note is to demonstrate

the validity of using the expression for the first-order loop phase-error distribution in describing the statistics of the phase error in a second-order PLL.

2. The Equation of Operation

We now consider the stochastic differential equation which specifies the operation of the loop in the presence of noise. Develet (Ref. 7) and Viterbi (Ref. 3) were among the first to derive the differential equation of operation, although it appears that several Russian authors (e.g., Tikhonov, Refs. 4 and 5) have also derived the result independently.

Fig. 35 illustrates the basic PLL system under consideration. The input signal $s(t)$ to the PLL is assumed to be a sinusoid with average power $P = A^2 w$, a frequency of ω rad/sec, and a phase of $\theta(t) = \theta$ radians. The perturbing noise $n(t)$ is obtained by passing a stationary white Gaussian noise process through the bandpass filter. The random process $n_i(t)$ is assumed to possess a double-sided spectral density of N_0 w/cps. In practice, this filter corresponds to the IF filter which always precedes the PPL.

Performing the multiplication $\epsilon(t) = y(t) \cdot r(t)$, neglecting the double frequency terms, and interpreting the results in terms of the phase error $\phi(t) = \theta(t) - \hat{\theta}(t)$ gives

$$\dot{\phi}(t) = \Omega_0 - KF(p) [A \sin \phi(t) + n'(t)] \quad (1)$$

where $\Omega_0 = \omega - \omega_0$ is the initial detuning and

$$n'(t) = n_1(t) \cos \hat{\theta}(t) - n_2(t) \sin \hat{\theta}(t) \quad (2)$$

as shown in Ref. 3. The low-pass processes $n_1(t)$ and $n_2(t)$ are taken to be statistically independent and Gaussian.

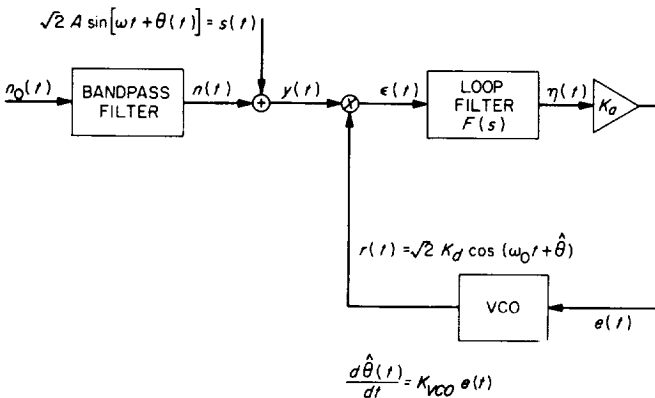


Fig. 35. Phase-locked system

We are concerned here with the behavior of the PLL system of Fig. 35 when the loop filter is of the proportional-plus-integral control type, namely,

$$F(p) = \frac{1 + \tau_2 p}{1 + \tau_1 p} \quad (3)$$

In Eq. (3), p denotes the Heaviside operator. The particular mechanization of the loop filter under study is illustrated in Fig. 36. Substituting Eq. (3) into Eq. (1), we have the equation of operation:

$$\ddot{\phi}(t) + [a + b \cos \phi(t)] \dot{\phi}(t) + c \sin \phi(t) = \Omega_0/\tau_1 + N(t) \quad (4)$$

where

$$a = \frac{1}{\tau_1}, b = \frac{AK\tau_2}{\tau_1}, c = \frac{AK}{\tau_1}$$

and

$$N(t) = -\frac{K}{\tau_1} \cdot \left(1 + \tau_2 \frac{d}{dt}\right) \cdot n'(t) \quad (5)$$

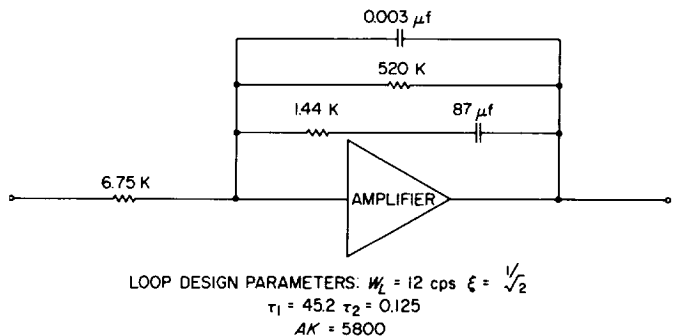


Fig. 36. Loop filter mechanism

3. The Phase-Error Distribution

The "solution" of the nonlinear differential equation [Eq. (4)] is the joint probability distribution $p(\phi, \dot{\phi}, t)$ which satisfies the two-dimensional Fokker-Planck equation. It has been shown (Ref. 6) that the steady state joint distribution $p(\phi, \dot{\phi})$ of interest here is approximated by

$$p(\phi, \dot{\phi}) = K' \exp \left[-\dot{\phi}^2 \left(\frac{\beta_1 + \beta_2 \cos \phi}{2} \right) + \alpha_1 \cos \phi + \alpha_2 \cos 2\phi \right] \quad (6)$$

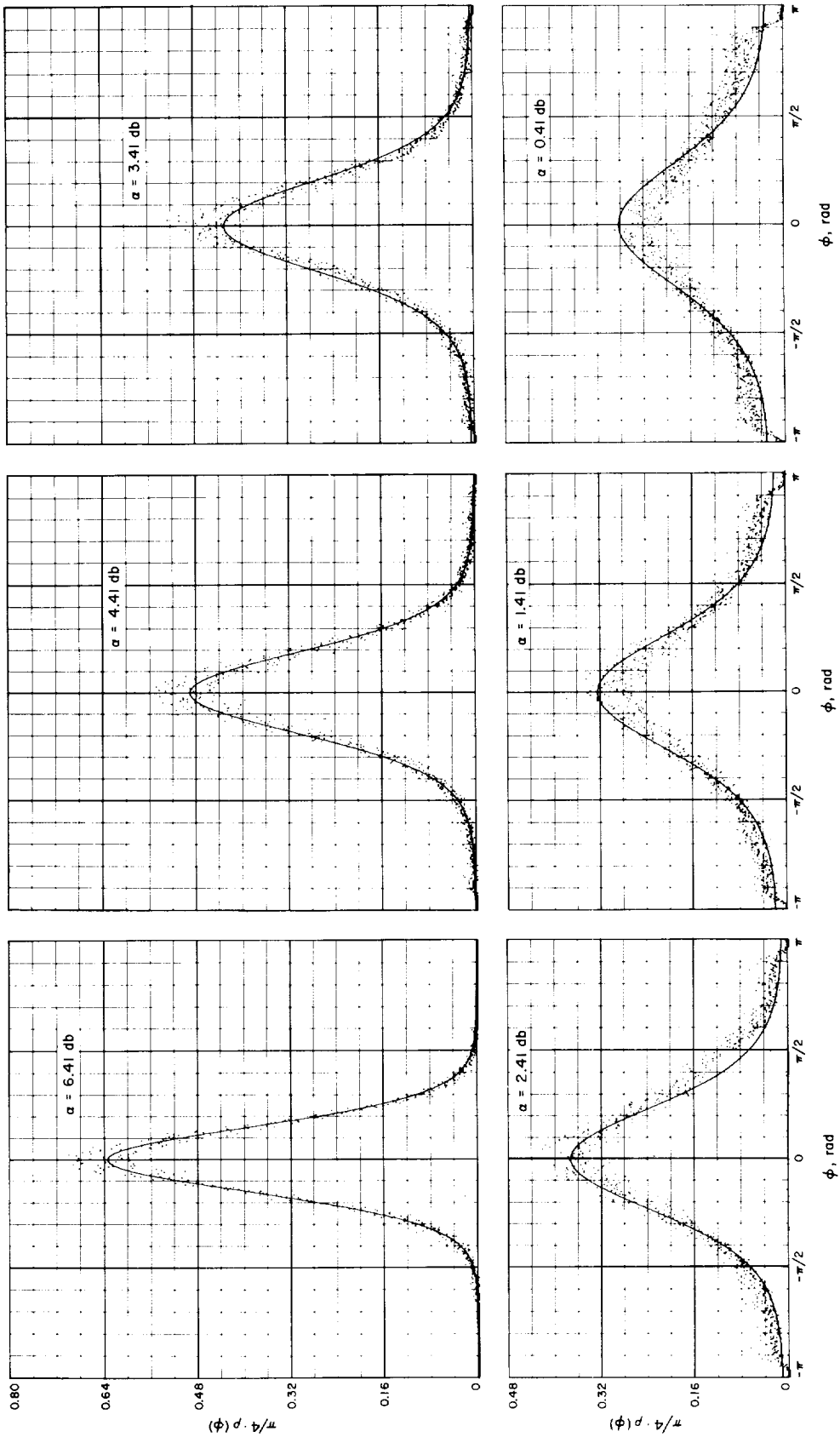


Fig. 37. Phase-error distributions with the first-order loop results imposed

where

$$\alpha_1 = \frac{4A}{KN_0}; \alpha_2 = \frac{A^2\tau_2}{N_0}$$

$$\beta_1 = \frac{4\tau_1}{N_0K^2} = \frac{4A^2\tau_1}{N_0G^2}; \beta_2 = \frac{4A}{N_0K} \cdot \tau_1\tau_2 \quad (7)$$

and K' is a normalizing constant and $G = AK$ is the loop gain. The approximate distribution [Eq. (6)] becomes exact for the special case $\tau_1 = \tau_2 = 0$ (i.e., the first-order loop filter $F(p) = 1$) and, in fact, reduces to the form

$$p(\phi) = \frac{\exp(\alpha_1 \cos \phi)}{2\pi I_0(\alpha_1)}; |\phi| \leq \pi \quad (8)$$

which corresponds to the result obtained by Viterbi (Ref. 3) and Tikhonov (Ref. 4) for the first-order loop. In particular, we note that $\alpha_1 = 4A^2/AKN_0$ is the SNR in the bandwidth of the linearized first-order loop. We now define an equivalent parameter α to be the SNR in the bandwidth of the linearized second-order loop, i.e.,

$$\alpha \triangleq \frac{A^2}{N_0W_L} \quad (9)$$

where

$$W_L = \frac{1}{2\pi j} \int_{-j\infty}^{j\infty} |H(s)|^2 ds$$

and $H(s)$ is the closed-loop transfer function of the linearized second-order loop. Replacing the parameter α_1 in Eq. (8) by α , we obtain

$$p(\phi) = \frac{\exp(\alpha \cos \phi)}{2\pi I_0(\alpha)} \quad (10)$$

As a check on the validity of using Eq. (10) to represent the statistical properties of the phase error in a second-order loop, we compare it graphically with an experimentally derived distribution. The closeness of the approximation of Eq. (10) is clearly evident from Fig. 37, where the analytical distribution (solid curve) is superimposed over the experimental distribution (point plot) for various values of α in the range $6.5 \text{ db} > \alpha > 0 \text{ db}$. The cumulative distributions of the measured phase error are shown in Fig. 38 for the same values of α . From this figure we observe that when $\alpha > 6.41 \text{ db}$, the probability of the loop losing "lock" is extremely small. It is also evident from the cumulative distributions that the phase-

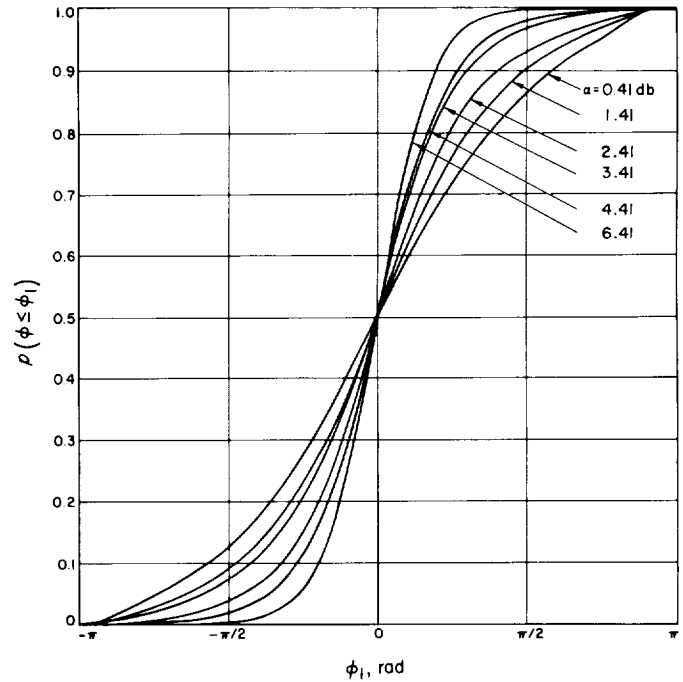


Fig. 38. Cumulative distributions of the measured phase error

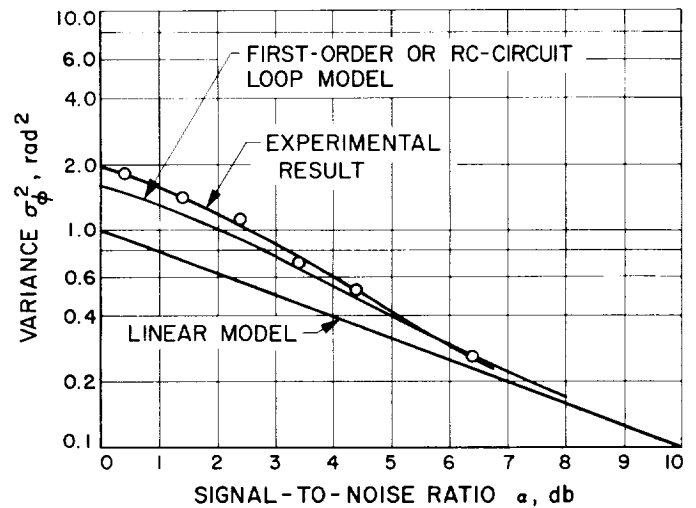


Fig. 39. Experimental and analytical results relative to the variance of the phase error

error distribution tends to become uniform for low SNRs. Finally, in Fig. 39 the variance of the phase error computed from the linear model and from Eq. (10) is compared with the variance of the measured phase error over the range $SNR \ 0 < \alpha < 6.5 \text{ db}$.

D. Some Experimental Results on the Noise Probability Density Function out of a Band-pass Limiter

J. C. Springett

1. Introduction

The filter-limiter-filter, often referred to as a bandpass limiter, is commonly used in many communication systems. A great deal of analysis has been concerned with obtaining input-output signal-to-noise ratio (SNR) relationships for the bandpass limiter. However, little material of either analytical or empirical form has been published relative to the higher order statistics at the output. The nature of the noise voltage probability distribution is of particular interest. As a result, the bandwidth of the device following the limiter is generally taken to be sufficiently narrow relative to the limiter first zone noise bandwidth so that a Gaussian distribution at its output may be assumed. No other approach or assumption currently appears tractable in light of the nearly impossible task of analyzing a random process after nonlinear transformation.

When a problem defies rigorous analysis, empirical evaluation is often pursued. This article describes some experimental results which, in part, answer the questions: (1) What are the statistics of the noise in the limiter first zone? and (2) How much filtering is necessary before the output is nearly Gaussian? A complete interpretation of the experimental results is not attempted; rather, they are allowed to stand as an insight into the magnitude of the total problem, and to perhaps suggest further work, both analytical and empirical, which might be carried on.

2. Observations and Results

The input to the limiter is assumed to be a sine wave plus zero mean, narrow-band Gaussian noise (defined in Ref. 8). The output of the limiter $Z(t)$ may be expressed in terms of the input $y(t)$ by the expression

$$\begin{aligned} Z(t) &= \text{sgn} [y(t)] \\ &= a_1 \cos \omega_0 t + a_3 \cos 3\omega_0 t + a_5 \cos 5\omega_0 t + \dots \\ &\quad + n_1(t) + n_3(t) + n_5(t) + \dots \end{aligned}$$

where a_1, a_3, a_5 are constants depending upon the input SNR (Ref. 8), ω_0 is the first zone center frequency, and

n_1, n_3, n_5 are noise voltages whose spectrum corresponds to the respective zones $\omega_0, 3\omega_0, 5\omega_0$. The first zone is given by

$$Z'(t) = a_1 \cos \omega_0 t + n_1(t).$$

Consider briefly the total limiter output $Z(t)$. The sum of the signal components will have a joint first-order probability distribution which will be limited on the interval $(-a, a)$, $a < \infty$. Since the limiter output is constrained to be $+1$ or -1 , the ensemble of noise voltages n_1, n_3, n_5, \dots will then have a first-order distribution density restricted to the interval $(-1-a, 1+a)$. Further, the ensembles $a_1 \cos \omega_0 t + a_3 \cos 3\omega_0 t + \dots$ and $n_1(t) + n_3(t) + \dots$ are strictly dependent upon each other.

If the first zone is now considered, one might again expect the distribution on $n_1(t)$ to be limited on some interval. There will also be dependence between $a_1 \cos \omega_0 t$ and $n_1(t)$, so that given $p(a_1 \cos \omega_0 t)$ and $p(n_1(t))$, one cannot readily deduce $p(a_1 \cos \omega_0 t, n_1(t))$. However, the direct measurement of $p(n_1(t))$ should provide some understanding of the nonlinear transformation on the input noise, and also an appreciation for the amount of filtering necessary before the output statistics are near-Gaussian.

The experimental setup used to obtain the noise probability distributions in the first zone is shown in Fig. 40. The signal $a_1 \cos \omega_0 t$ was removed (subtracted) from the output of the low-pass filter by accurately calibrating the system in both amplitude and phase for a noiseless input. For noisy inputs, the signal amplifier gain was adjusted below the no-noise gain by a factor $\sqrt{C_{1,0}}$ corresponding to the signal suppression factor (Ref. 8). All probability distributions were obtained using a specially constructed amplitude distribution analyzer. The full-scale vertical axis is divided into 1000 levels, and the horizontal axis into 100 divisions. The nominal time spent in obtaining each data point was 35 sec.

For very high input SNRs, one would expect the output distribution to be very nearly Gaussian, since the predominant noise terms at the output are the input noise (0, 1) and the input noise convolved with the input signal (2, 1) (Ref. 8, Fig. 10, p. 243). This supposition is indeed borne out by the plot shown in Fig. 41, where the input SNR is $+30$ db. A Gaussian plot with the same one-sigma (1σ) value is shown for comparison. (Note that when two plots are shown in the same figure, the reference plot is always made for the same 1σ value as that of the limiter output.) As the input SNR is decreased, the distribution changes quite rapidly away from the

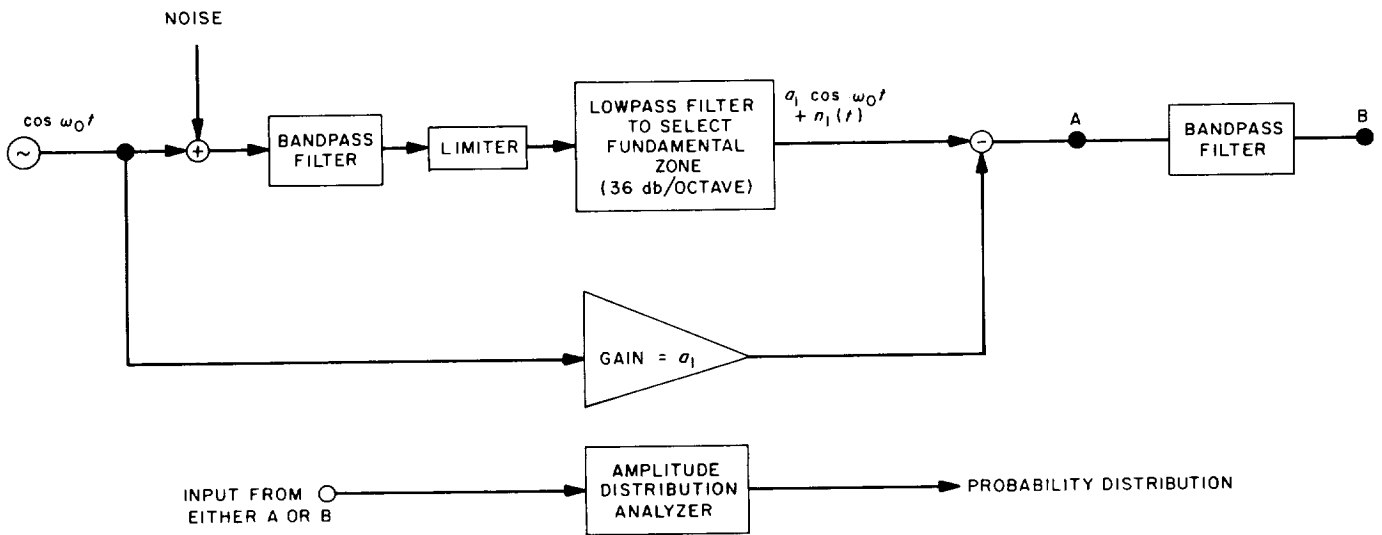


Fig. 40. Experimental setup

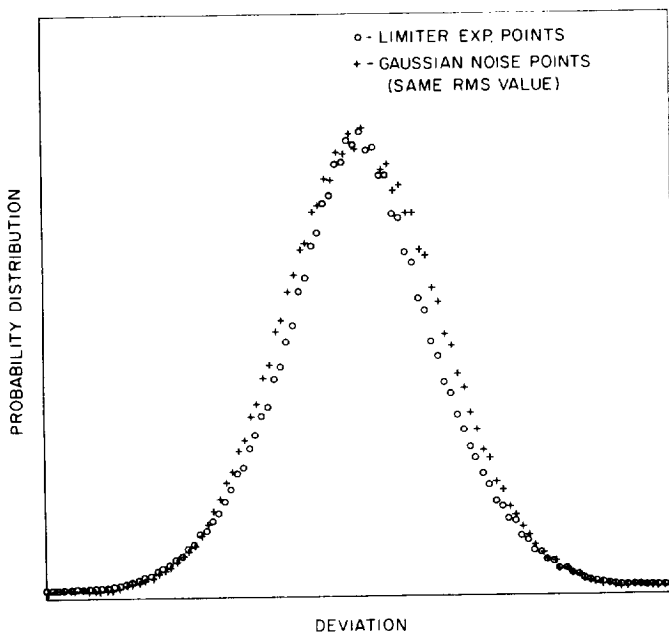


Fig. 41. Limiter first zone probability distribution
(S/N)_i = +30 db

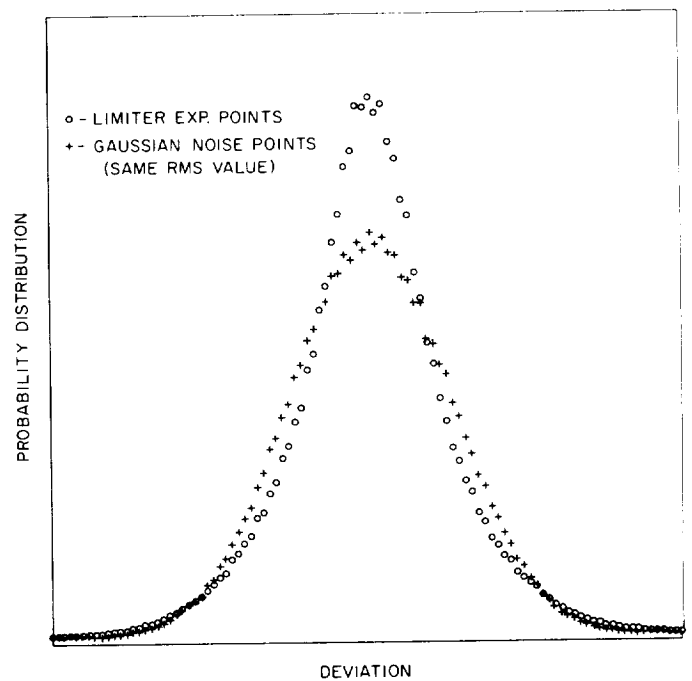


Fig. 42. Limiter first zone probability distribution,
(S/N)_i = +20 db

Gaussian, as indicated in Figs. 42 and 43, for input SNRs of +20 and +10 db, respectively. At 0 db (Fig. 44) the distribution becomes bimodal, and at -10 db (Fig. 45) we can begin to see that the distribution is truly limited on the abscissa. In Figs. 46 and 47 it can be seen that the distribution is approaching something which appears to be sinusoidal; in Fig. 48, for an input SNR of $-\infty$ db, the distribution is barely discernible from that of a sinusoid.

A very similar result has been obtained in Ref. 9 where a random telegraph signal is smoothed by a simple RC filter.

Finally, the distribution out of a bandpass filter following the limiter is investigated. The filter chosen for the experimental plots was a single-pole RLC type. The

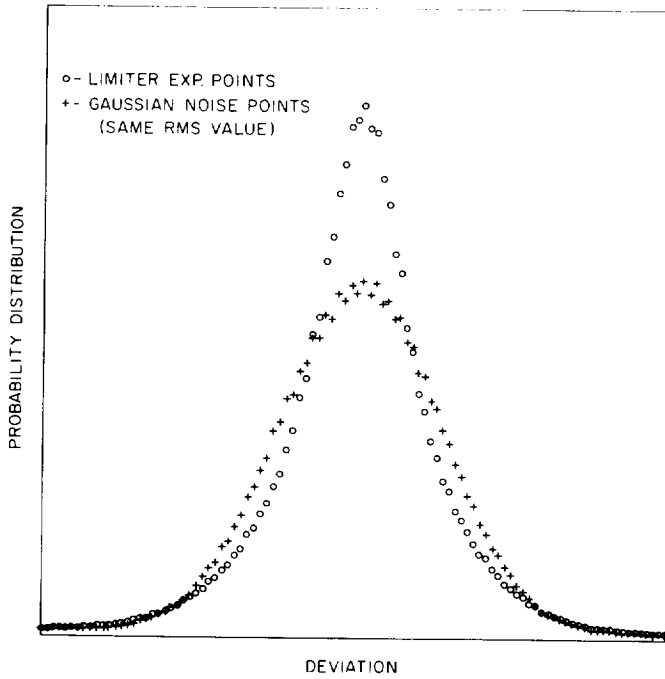


Fig. 43. Limiter first zone probability distribution, $(S/N)_i = +10$ db

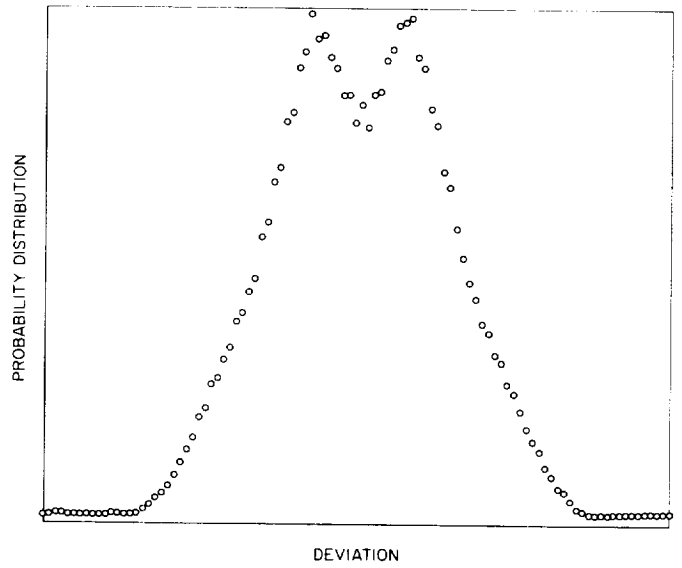


Fig. 45. Limiter first zone probability distribution, $(S/N)_i = -10$ db

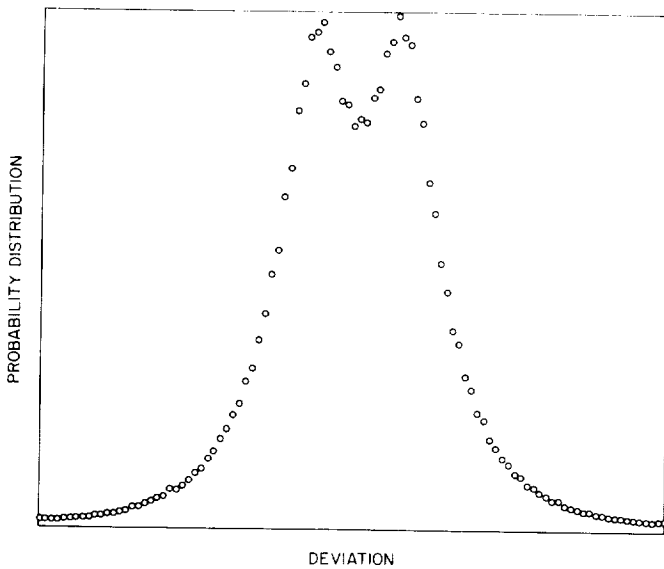


Fig. 44. Limiter first zone probability distribution, $(S/N)_i = 0$ db

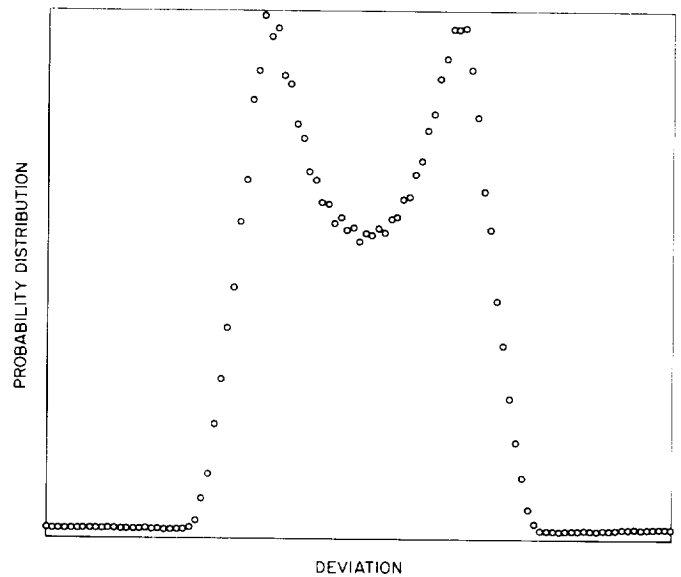


Fig. 46. Limiter first zone probability distribution, $(S/N)_i = -20$ db

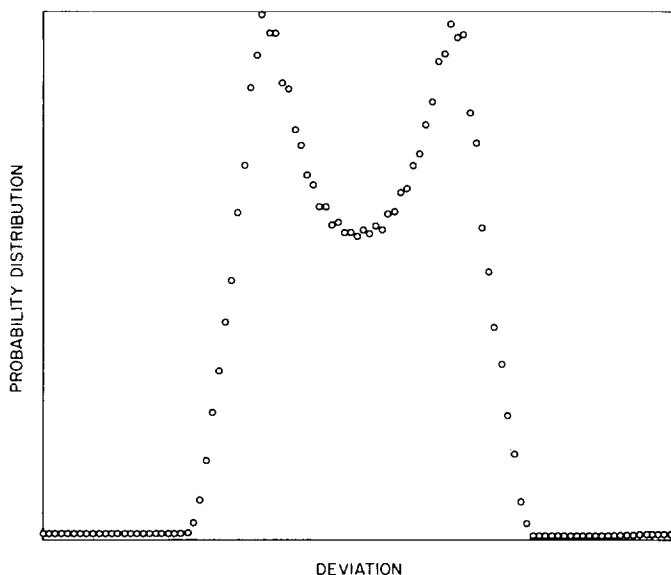


Fig. 47. Limiter first zone probability distribution, $(S/N)_i = -30$ db

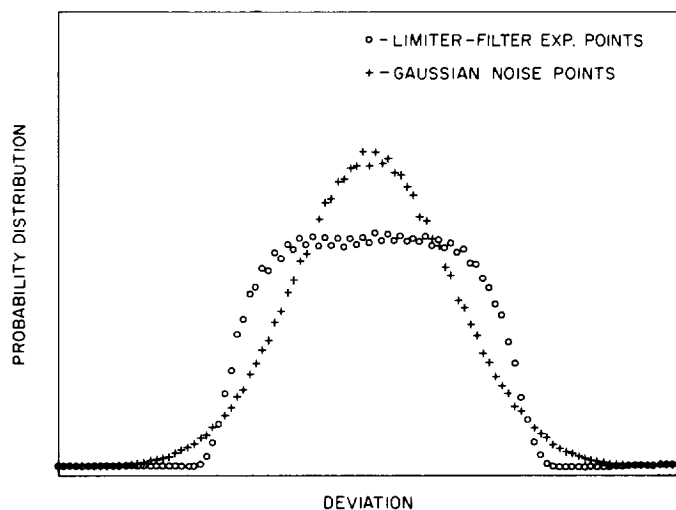


Fig. 49. Limiter-filter probability distribution, $(S/N)_i = -20$ db, $\frac{\text{filter bandwidth}}{\text{zone bandwidth}} = \frac{3}{4}$

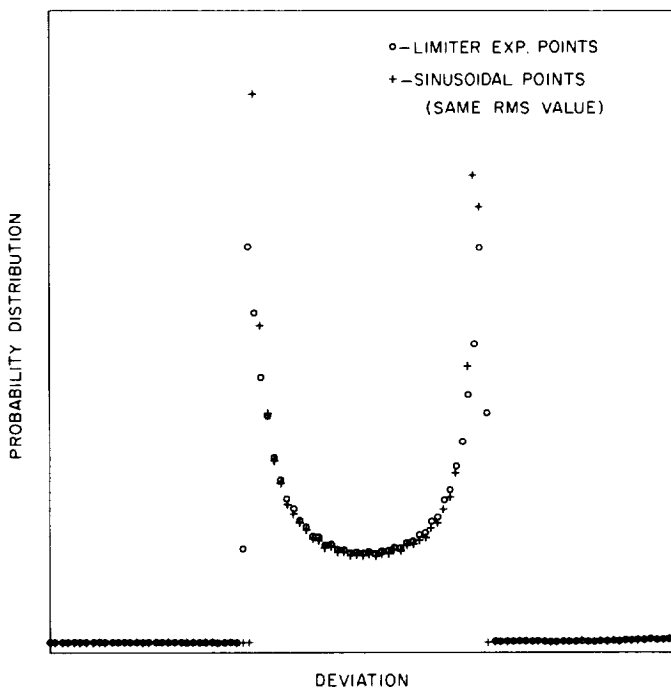


Fig. 48. Limiter first zone probability distribution, $(S/N)_i = -\infty$ db

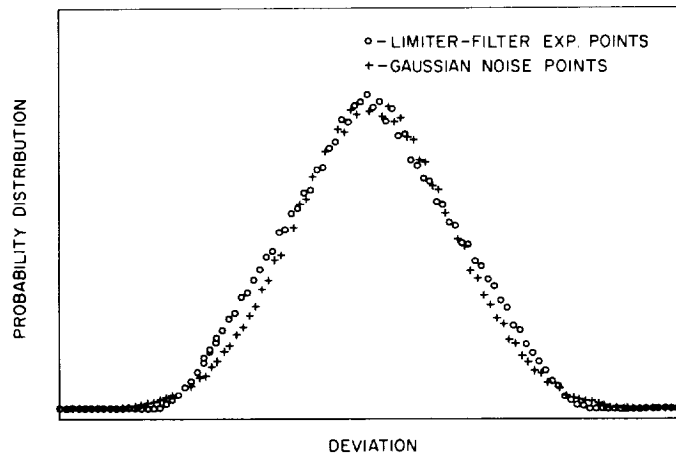


Fig. 50. Limiter-filter probability distribution, $(S/N)_i = -20$ db, $\frac{\text{filter bandwidth}}{\text{zone bandwidth}} = \frac{1}{2}$

bandwidth ratio shown on the plots is equivalent to the ratio of the noise power bandwidths of the filter and the fundamental zone noise. Fig. 49 shows the result for a ratio of 3:4, with a limiter input SNR of -20 db. The output distribution of the filter appears very nearly

trapezoidal compared with its input distribution (Fig. 46) and contrasted with a Gaussian distribution of the same rms value. It is conjectured that with the proper choice of filter bandwidth a uniform distribution could be obtained. In Fig. 50 we see that a nearly triangular distribution is obtained when the bandwidth ratio is 1:2, and in Figs. 51 and 52 the distribution begins to approach the Gaussian. From Fig. 52 it may be summarized that the assumption of Gaussian statistics may be valid only when the output filter bandwidth is less than 1/10 that of the input bandwidth to the filter.

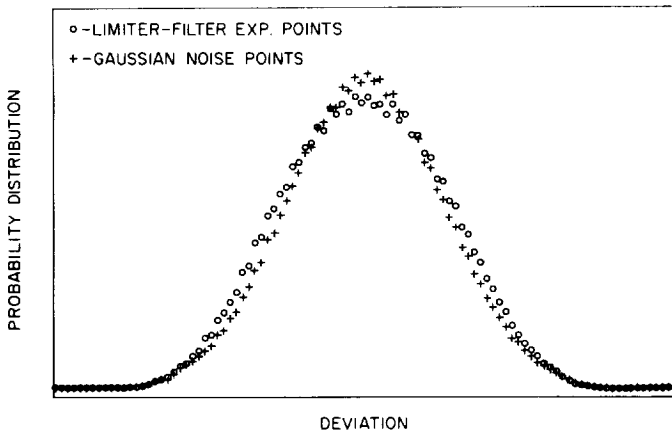


Fig. 51. Limiter-filter probability distribution,
 $(S/N)_i = -20 \text{ db}, \frac{\text{filter bandwidth}}{\text{zone bandwidth}} = \frac{1}{4}$

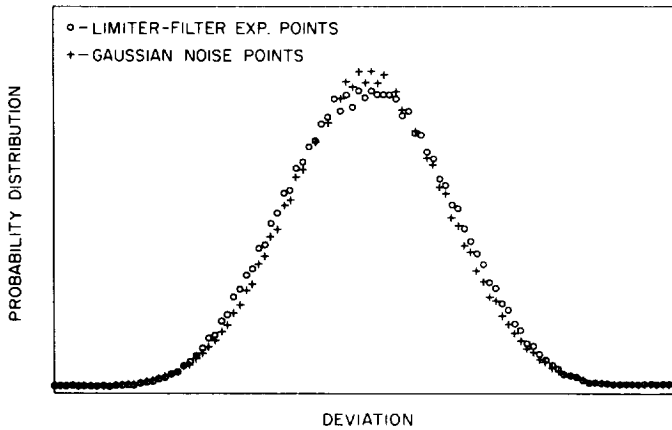


Fig. 52. Limiter-filter probability distribution,
 $(S/N)_i = -20 \text{ db}, \frac{\text{filter bandwidth}}{\text{zone bandwidth}} = \frac{1}{10}$

E. Analog-to-Digital Conversion With Integrated Circuits

J. R. Kinkel

1. System Organization

To minimize power and weight, spacecraft data encoders time-multiplex several sensors before analog-to-digital conversion. With integrated circuits, it now becomes practical to convert sensor response to digital form before multiplexing. There are several important reasons for

providing separate analog-to-digital converters (ADCs); the principal one is reliability. The failure of a single ADC would minimize system degradation by failing to transform only one measurement. In addition, separate ADCs can reduce the sampling time-multiplexing rate dependence. An increase in the number of measurements and the multiplexing rate necessarily decreases the sampling time. This tends to prevent masking high frequency noise by averaging. Analog-to-digital converters for each sensor would also permit multiplexer decentralization and thereby would reduce cabling on a large spacecraft.

2. Analog-to-Digital Converter

The following method for analog-to-digital conversion was suggested by the gate capacitance and large "off" resistance of a metal-oxide-silicon field-effect-transistor (MOS FET). A suitable sample and hold circuit can be derived from the RC product. When the sample voltage E decays past the transistor threshold voltage V_T , the source-drain resistance sharply decreases—typically from 10^{14} to $10^3 \Omega$. The time to reach this threshold voltage is given by

$$t = RC \ln \left(\frac{E - V_B}{V_T - V_B} \right)$$

where V_B is a bias voltage. When two signals, the sample and a reference, decay simultaneously, the difference in times to reach the threshold voltage is given by

$$\begin{aligned} \Delta t &= RC \ln \left(\frac{E - V_B}{V_T - V_B} \right) - RC \ln \left(\frac{0 - V_B}{V_T - V_B} \right) \\ &= RC \ln \left(\frac{V_B - E}{V_B} \right) \end{aligned}$$

The dependence on V_T and its temperature variation are eliminated by measuring the time difference with the assumption that two adjacent transistors on the same substrate share the same threshold voltage. Since

$$\ln(1 + X) = X - \frac{X^2}{2} + \frac{X^3}{3} - \frac{X^4}{4} + \frac{X^5}{5} \dots$$

is an alternating series and V_B is a negative bias, $V_B = -|V_B|$.

$$\Delta t \approx \frac{RCE}{|V_B|} \text{ for } E < |V_B| \text{ with an error } < \frac{(E/V_B)^2}{2}$$

A clock train and a counter are used to measure the interval Δt ; the count is a digital representation of the analog voltage E .

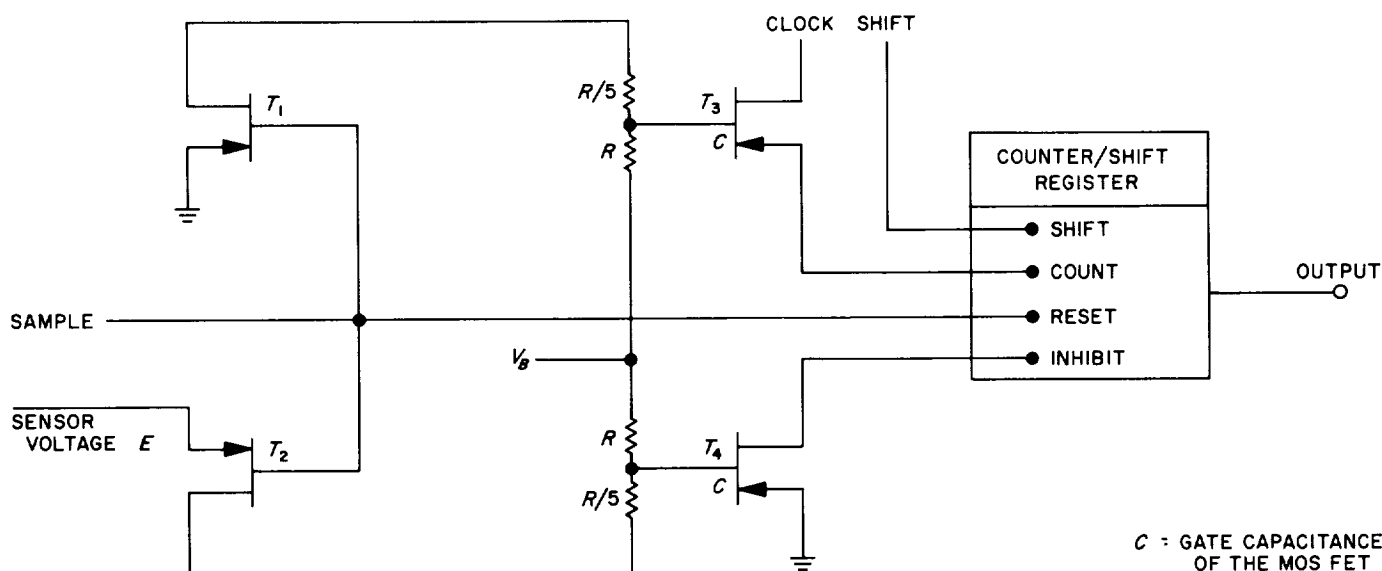


Fig. 53. Analog-to-digital converter

In the circuit of Fig. 53, the transistors T_1 and T_2 gate the reference and sensor voltages to the voltage divider networks. The counter is reset. With T_1 and T_2 off, each gate voltage decays independently to V_B , with a time constant $\tau = RC$. The gate of T_3 will reach the threshold voltage first, and the count will begin to accumulate in the counter. Counting will be inhibited when T_4 reaches V_T and conducts. Minor differences in logic between counters and shift registers permit the contents of the counter to be shifted out upon command. The counter thereby doubles as an extension to memory for any data processing beyond the multiplexer.

The voltage-time transformation is diagrammed in Fig. 54. The following parameter values are selected to illustrate an example and are within the typical ranges for a p -channel enhancement MOS FET.

$$R = 10^{12} \Omega$$

$$C = 10^{-12} \text{ f}$$

$$V_B = -30 \text{ v}$$

A sample voltage $0 \leq E \leq 3$ may be quantized into 2^{10} levels with a sampling error e by a clock whose frequency is f .

$$e < \frac{(E/|V_B|)^2}{2} = \frac{(3/30)^2}{2} = 0.5\%$$

$$f = \frac{2^{10}}{\Delta t} = \frac{1024}{RC \ln \left(\frac{V_B - E}{V_B} \right)} = 10.75 \text{ kc}$$

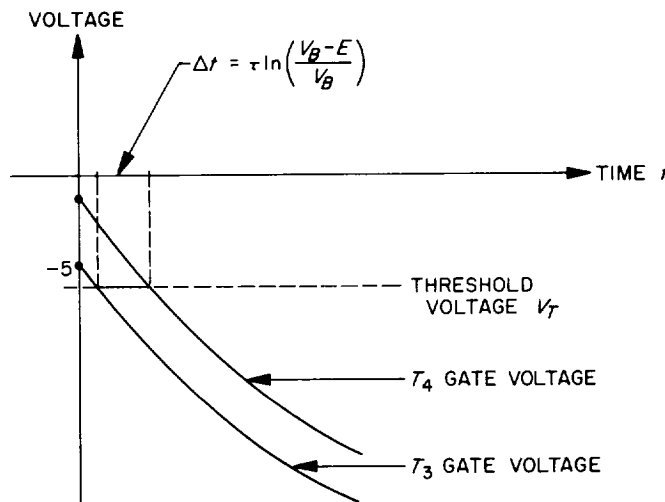


Fig. 54. Voltage-time transformation

3. Implementation

Implementation of this converter with integrated circuits requires further investigation to reduce the manufacturing tolerances of the elements R and C and the temperature dependence of R . The tolerances on MOS equivalents of R and C are not under 10%, due to material and geometry variations. A 20% tolerance on the RC product is too great to mask by external means.

Although the gate capacitance of a MOS FET is stable with temperature, this is not the case for R . Large values

of resistance on integrated circuits are obtained by connecting the gate and drain terminals to obtain a back-biased junction. Current flow across the junction, and therefore the apparent resistance of the element, is very temperature dependent. Hybrid integrated circuits may be a solution to this problem. Thin film resistors and capacitors can provide the desired RC tolerances and temperature stability.

4. Conclusion

The proposed ADC is one possible implementation with integrated circuits; if not one of the most accurate, it is certainly among the simplest. However, the implications for sharply increasing system reliability by failure localization are of principal importance. A failure within

a functional block is usually propagated back through its inputs or ahead as an output. Since the ADC clock, command, and bias inputs may be buffered to minimize loading, only the output is problematical. But because the output by nature assumes one of two discreet states, almost all failures are propagated only with the data. The balance of an electrical net is not subject to imbalance by interaction with other nets at the interface between converter and multiplexer. A failure may lead to a shift register exporting all 0s, all 1s, or some truncated count, but only failures in the last stage of the shift register can degrade the system.

The effect has been to sharply reduce the dependency on the multiplexer in the presence of failure while eliminating the total dependence on a single converter.

References

1. Lindsey, W. C., "The Detection of PSK Signals With a Noisy Phase Reference," *Proceedings of the National Telemetry Conference, Houston, Texas, April 13-15, 1965*, pp. 50-53.
2. Lindsey, W. C., "Optimal Design of One-Way and Two-Way Coherent Communication Links" (to be published in *IEEE Transactions on Communication Technology*).
3. Viterbi, A. J., "Phase-Locked Loop Dynamics in the Presence of Noise by Fokker-Planck Techniques," *Proceedings of the IEEE*, Vol. 51, No. 12, December 1963, pp. 1737-1753.
4. Tikhonov, V. I., "Influence of Noise on Phase-Locked Oscillator Operation," *Akademiia Nauk SSSR, Avtomatika i Telemekhanika*, Vol. 20, September 1959, pp. 1188-1196 (English translation in *Automation and Remote Control*, Vol. 20, September 1959, pp. 1160-1168).
5. Tikhonov, V. I., "Phase-Lock Automatic Frequency Control Operation in the Presence of Noise," *Akademiia Nauk SSSR, Avtomatika i Telemekhanika*, Vol. 21, March 1960, pp. 301-309 (English translation in *Automation and Remote Control*, Vol. 21, March 1960, pp. 209-214).
6. Charles, F. J., and Lindsey, W. C., "Some Analytical and Experimental Phase-Locked Loop Results for Low Signal-to-Noise Ratios" (to be published in *Proceedings of the IEEE*).
7. Develet, J. A., Jr., "A Threshold Criterion for Phase-Lock Demodulation," *Proceedings of the IEEE*, Vol. 51, No. 2, February 1963, pp. 349-356.

References (Cont'd)

8. Springett, J. C., "A Note on Signal-to-Noise and Signal-to-Noise Spectral Density Ratios at the Output of a Filter-Limiter Combination," *Space Programs Summary No. 37-36, Vol. IV, Jet Propulsion Laboratory, Pasadena, Calif., December 31, 1965*, pp. 241-244.
9. Wonham, W. M., and Fuller, A. T., "Probability Densities of the Smoothed 'Random Telegraph Signal'," *Journal of Electronics and Control, Vol. IV, No. 6, June 1958*, pp. 567-576.

XXII. Spacecraft Radio

A. Spacecraft Power Amplifier Development Program

L. J. Derr

A 20- to 100-w S-band electrostatically focused amplifier (ESFA) is being designed as part of the JPL spacecraft power amplifier development program. This work is being performed by the Klystron Department of Eitel-McCullough, Inc., under JPL Contract 951105. This tube incorporates many new circuit concepts and represents a significant advancement in spacecraft transmitter design.

The specifications for this development are as follows:

Power output	20 to 100 w (variable with voltage)
Frequency	2295 ± 5 Mc (tunable at factory)
Efficiency	35% at 20 w, 45% at 100 w
Gain	30 db min.
Bandwidth	± 15 Mc (3 db)
Cooling	60% direct radiation, 40% conduction
Life	20,000-hr continuous operation
Focusing	electrostatic
Beam voltage	3000 v (for 100-w output)
Weight	5 lb max.

Genetically, this is a hybrid design combining helical resonators and extended interaction cavities. It is akin to the Klystron in that amplification is accomplished by standing-wave interaction. The unusual bandwidth is to be attained by the use of broad-band helical circuits and a dual output cavity. The high efficiency is to be reached by phase tapering and collector depression techniques. The beam is focused electrostatically to provide optimum confinement vs velocity characteristics over a 5 to 1 power output range. This focusing system further avoids the problem of magnetic leakage. The energy of the spent beam will be dissipated by direct radiation from the collector electrode.

A pictorial display of the tube is given in Fig. 1. The electron gun is a standard Pierce type, delivering 60 ma/cm², with a perveance of 1.0×10^{-6} and a convergence ratio of 20:1. The helical resonators evolve from the work of Wesselberg at Stanford University. A total of 14 single and bifilar helix designs were evaluated in selecting the optimum circuit for the ESFA. The dual output cavity is operated in the π mode and has a R_{sh}/Q of 300 Ω . Its tuning range is ± 25 Mc.

The focusing electrodes are Einzel lenses. This design is the most widely used and is best understood at present. An experimental assembly of three lenses has yielded 100% beam transmission on the first test. The final tube will use a total of nine lenses.

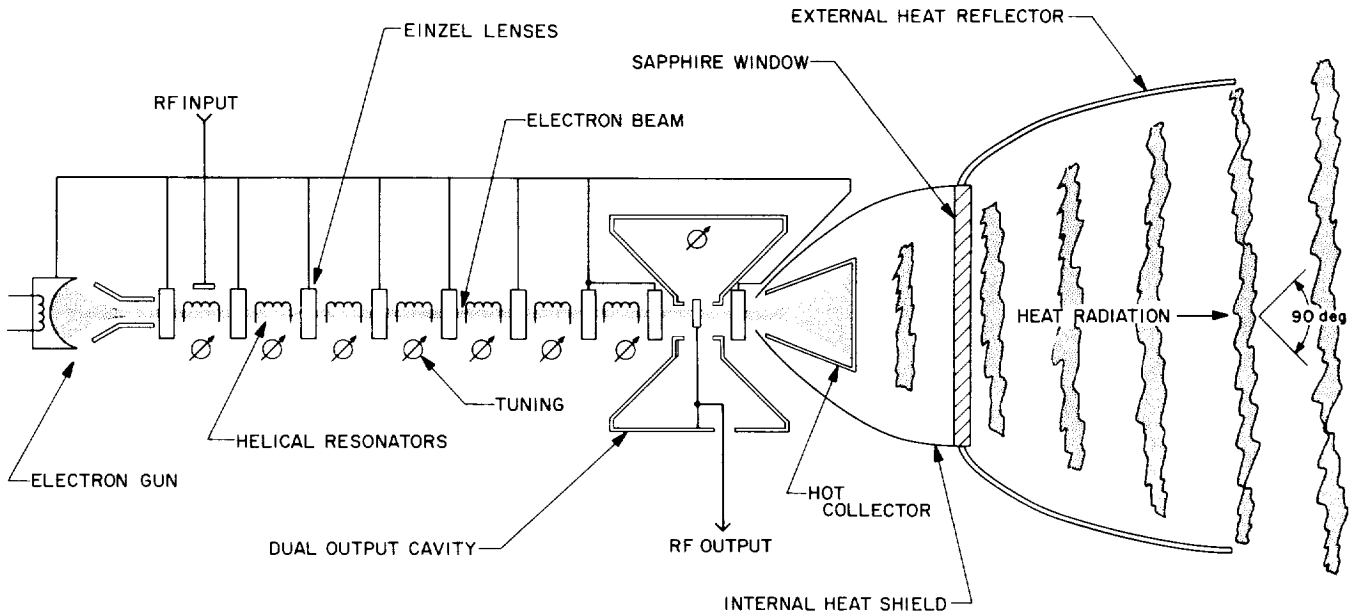


Fig. 1. Schematic of the 20- to 100-w electrostatically focused amplifier

The heat radiating system was conceived at JPL, and a patent application is being prepared for NASA ownership. An experimental assembly has been designed and tested at Eimac. The collector was operated at 1300°C and was observed to radiate 80% of the beam dissipation through the sapphire window which is the optical exit for the radiation. This performance is 20% in excess of the specified requirement.

The individual circuits have been fabricated and tested satisfactorily, and operating tests of the first experimental tube began in January 1966. The first prototype tube is scheduled to be delivered to JPL in July 1966.

B. Signal-to-Noise Ratio Monitoring: Calculation of an Important Probability Density Function

D. W. Boyd

1. Introduction

The desirability of monitoring the performance of communications systems during actual missions has been pointed out by Gilchrist (*SPS 37-27*, Vol. IV, PP. 169-

184), who proposed a simple on-line method of measuring the signal-to-noise ratio (SNR) of a phase shift keyed (PSK) telemetry channel. Since Gilchrist's analysis was performed, further experimental and analytical work has been done. This work has been directed in two general directions:

1. Detailed analysis of the present signal-to-noise ratio estimator (SNORE), with particular emphasis on its practical performance.
2. Consideration of alternate methods of measuring the SNR, with emphasis on developing a scheme which is independent of the modulation technique.

The goal of this research is to develop a standardized piece of hardware which can be used to monitor pertinent SNRs for any mission which might employ the JPL Deep Space Instrumentation Facility (DSIF). In this report an exact expression is found for the probability density function of the estimate made by the SNORE, which was analyzed by Gilchrist. This probability density function can be used to find certain statistical averages which give a direct measure of how well the system performs.

2. Calculation of Probability Density Function of the Estimate

The SNORE measures the SNR at the output of a linear filter that is matched to the telemetry signal. We

assume that the data can be represented by independent samples x_i from a Gaussian density of mean μ and variance σ^2 ; thus the actual SNR, R^2 , is μ^2/σ^2 . The SNORE combines n samples to obtain estimates for μ , σ^2 , and R^2 , where

$$\hat{\mu} = \frac{1}{n} \sum_{i=1}^n x_i \tag{1}$$

$$\hat{\sigma}^2 = \frac{1}{n-1} \sum_{i=1}^n (x_i - \hat{\mu})^2 \tag{2}$$

$$\hat{R}^2 = \frac{\hat{\mu}^2}{\hat{\sigma}^2} \tag{3}$$

We want to derive the probability density function for \hat{R}^2 .

Gilchrist showed that the probability density function of $\hat{R} = \hat{\mu}/\hat{\sigma}$ is given by

$$p(\hat{R}) = \frac{\left(\frac{n}{\pi}\right)^{1/2} (n-1)^{(n-1)/2}}{\Gamma\left(\frac{n-1}{2}\right) [n(\hat{R}^2 + 1) - 1]^{n/2}} e^{-n\mu^2/2\sigma^2} \times \left[\Gamma\left(\frac{n}{2}\right) {}_1F_1\left(\frac{n}{2}, \frac{1}{2}; \frac{\mu^2 n^2 \hat{R}^2}{2\sigma^2 [n(\hat{R}^2 + 1) - 1]}\right) + \frac{\mu}{\sigma} \frac{n\hat{R}(2)^{1/2}}{[n(\hat{R}^2 + 1) - 1]^{1/2}} \Gamma\left(\frac{n+1}{2}\right) \times {}_1F_1\left(\frac{n+1}{2}, \frac{3}{2}; \frac{\mu^2 n^2 \hat{R}^2}{2\sigma^2 [n(\hat{R}^2 + 1) - 1]}\right) \right] \tag{4}$$

We make the transformation $x = \hat{R}^2$ and find the probability density function of x . We first find the probability distribution function in terms of $p_{\hat{R}}(\hat{R})$,

where

$$P(x \leq x_0) = \int_{-\sqrt{x_0}}^{\sqrt{x_0}} p_{\hat{R}}(\hat{R}) d\hat{R} \tag{5}$$

and then differentiate to obtain

$$p_x(x) = \frac{1}{2} \frac{1}{\sqrt{x}} p_{\hat{R}}(\sqrt{x}) + \frac{1}{2} \frac{1}{\sqrt{x}} p_{\hat{R}}(-\sqrt{x}), \quad x \geq 0 \tag{6}$$

Putting Eq. (4) into Eq. (6), for $p_x(x)$ we obtain

$$p_x(x) = \frac{\left(\frac{n}{\pi}\right)^{1/2} (n-1)^{(n-1)/2} \Gamma\left(\frac{n}{2}\right) e^{-n\mu^2/2\sigma^2}}{\Gamma\left(\frac{n-1}{2}\right) [n(x+1) - 1]^{n/2} (x)^{1/2}} {}_1F_1\left[\frac{n}{2}, \frac{1}{2}, \frac{\mu^2 n^2 x}{2\sigma^2 [n(x+1) - 1]}\right] \tag{7}$$

The virtue of this exact solution is that it can be integrated, whereas the approximate solution as given by Gilchrist cannot. Specifically, we find the expected value and variance to be given by

$$E[x] = \frac{n-1}{n-3} \left(\frac{1}{n} + \frac{\mu^2}{\sigma^2}\right), \quad n > 3 \tag{8}$$

$$\text{Var}[x] = \frac{2(n-1)^2}{(n-3)^2(n-5)} \left[\left(\frac{\mu^2}{\sigma^2}\right)^2 + 2\frac{\mu^2}{\sigma^2} \left(1 - \frac{1}{n}\right) + \frac{2}{n} \left(1 - \frac{1}{n}\right) \right], \quad n > 5 \tag{9}$$

From Eqs. (8) and (9) we can make several interesting observations. We see that, in general, x will be a biased estimate of μ^2/σ^2 , but that if $n \gg 1$, x will be asymptotically unbiased and the variance will approach zero, as is desired. We also note that if we had chosen

$$(\hat{\sigma}^2)' = \frac{1}{n-3} \sum_{i=1}^n (x_i - \hat{\mu})^2 \tag{10}$$

as the estimator for σ^2 , we would obtain a better (in the sense of less bias and smaller variance) estimate for x . Since $(\hat{\sigma}^2)' = \frac{n-1}{n-3} \hat{\sigma}^2$, the new mean and variance can immediately be written

$$E[x'] = \left(\frac{1}{n} + \frac{\mu^2}{\sigma^2}\right), \quad n > 3 \tag{11}$$

$$\text{Var}[x'] = \frac{2}{n-5} \left[\left(\frac{\mu^2}{\sigma^2}\right)^2 + 2\frac{\mu^2}{\sigma^2} \left(1 - \frac{1}{n}\right) + \frac{2}{n} \left(1 - \frac{1}{n}\right) \right], \quad n > 5 \tag{12}$$

Comparing Eqs. (8) and (11), we see that the new estimate will have a bias which is

$$10 \log_{10} E[x] - 10 \log_{10} E[x'] = 10 \log_{10} \frac{n-1}{n-3} db$$

smaller than the bias of the old estimate. Similarly, comparing Eqs. (9) and (12), we see that the variance of the new estimate is $(n-3/n-1)^2$ times smaller than the variance of the old estimate. For a small number of samples these differences are important, but at large n they are negligible. For instance, at $n = 10$ the difference in bias

is 1.07 db, while at $n = 1000$ it is less than 0.01 db. Finally, we note that these improvements in the bias and variance are obtained in spite of the fact that $(\hat{\sigma}^2)'$ is a biased estimate of σ^2 .

It is also interesting to note that n must be greater than 5 for the variance of the estimate to exist. This is attributed to a combination of two factors. The first is the fact that one degree of freedom was lost by using the particular estimators chosen. If we are given $(n-1)$ of the x_i 's in Eq. (2), then the n^{th} one is uniquely specified by Eq. (1). Thus, we say that we only have $(n-1)$ degrees

of freedom or that only $(n-1)$ of the x_i are independent in Eq. (2). This lost degree of freedom appears in Eq. (3), which shows that $p_r(x)$ is identically zero for $n = 1$. Secondly, the variance is nonexistent because the form of the density of Eq. (7) requires at least 4 degrees of freedom for the mean square to be finite. This, coupled with the one which was lost, gives 5. Although the probability density function is well defined, any estimate which is made with $1 \leq n < 5$ will have an undefined variance. This restriction is a manifestation of the limitation on the amount of information that can be extracted from a fixed amount of data.

XXIII. Communications Systems Research: Modulation and Detection Theory

A. Error Bounds for M -ary Orthogonal Communication Using Stationary Stochastic Signals

A. J. Viterbi

1. Introduction and Model

We consider the performance of the optimum receiver for an M -ary communication system which transmits over a period of T seconds in the presence of white Gaussian noise one of the signals

$$x_m(t) = A(t) \cos [\omega_m t + \theta(t)], \quad \begin{matrix} 0 \leq t \leq T \\ m = 1, 2, \dots, M \end{matrix} \quad (1)$$

where the frequencies ω_m are known exactly, but $\theta(t)$, and possibly also $A(t)$, are stationary stochastic processes.

The results are applicable in low data-rate telemetry systems where there is considerable oscillator phase jitter over one transmission baud but the amplitude $A(t)$ is constant, while if fading also occurs, $A(t)$ is a stochastic process. We shall consider primarily the case for which $A(t)$ is a Rayleigh process and $\theta(t)$ is flat, so that we may represent the signals as real parts of complex, zero-mean Gaussian processes

$$x_m(t) = \text{Re} [\xi_m(t)] \quad (2)$$

where

$$\xi_m(t) = A(t) e^{i\theta(t)} e^{i\omega_m t} = \xi(t) e^{i\omega_m t}, \quad m = 1, 2, \dots, M$$

and

$$\xi(t) = A(t) e^{i\theta(t)}$$

While this case is most readily analyzed, the results are also applicable to non-Gaussian transmitted signals, provided the product of T and the bandwidth of $x_m(t)$ is sufficiently large, as we shall indicate below.

Let the received signal be

$$y(t) = x_m(t) + n(t) = \text{Re} [\xi(t) e^{i\omega_m t} + v(t)] = \text{Re} [\eta(t)] \quad (3)$$

where $n(t) = \text{Re} [v(t)]$ is white Gaussian noise of one-sided density N_0 w/cps; take as our observables the projections of $y(t)$ onto the eigenfunctions of the complex covariance functions of $\xi_m(t)$ ($m = 1, 2, \dots, M$). Now if $\phi_n(t)$ is a solution of the integral equation

$$\lambda \phi(t) = \int_0^T R_\xi(t-u) \phi(u) du \quad (4)$$

where $R_\xi(t-u) = E [\xi(t) \xi^*(u)]$, then it readily follows that $\phi_n(t) e^{i\omega_m t}$ is a solution of the integral equation

$$\lambda \psi(t) = \int_0^T R_\xi(t-u) e^{i\omega_m(t-u)} \psi(u) du \quad (5)$$

where $R_\xi(t-u)e^{i\omega_k(t-u)}$ is the covariance function of the stationary stochastic process $\xi(t)e^{i\omega_k t}$. Furthermore, the eigenvalue λ_n corresponding to the eigenfunction $\phi_n(t)$ of Eq. (4) is also the eigenvalue corresponding to the eigenfunction $\phi_n(t)e^{i\omega_k t}$ of Eq. (5) for all $k=1,2,\dots,M$.

Thus, for the complex process

$$\eta(t) = \xi(t)e^{i\omega_m t} + \nu(t), \quad 0 \leq t \leq T \quad (6)$$

whose real part is the received waveform, we consider the NM observables

$$\eta_{nk} = \int_0^T \eta(t) \phi_n^*(t) e^{-i\omega_k t} dt, \quad \begin{matrix} n = 1,2,\dots,N \\ k = 1,2,\dots,M \end{matrix} \quad (7)$$

Moreover,

$$\eta_{nk} = \xi_{nk}^{(m)} + \nu_{nk} \quad (8)$$

where

$$\xi_{nk}^{(m)} = \int_0^T \xi(t) \phi_n^*(t) e^{i(\omega_m - \omega_k)t} dt, \quad \begin{matrix} n = 1,2,\dots,N \\ k = 1,2,\dots,M \end{matrix}$$

$$\nu_{nk} = \int_0^T \nu(t) \phi_n^*(t) e^{-i\omega_k t} dt$$

Now let us assume that $(\omega_k - \omega_{k-1}) = \Delta\omega$ for all k and that $\Delta\omega$ is large enough that the covariance functions of all the signals are essentially mutually orthogonal:

$$\int_0^T R_\xi(t-u)e^{i\omega_k(t-u)} R_\xi(u-v)e^{i\omega_l(u-v)} du = 0, \quad k \neq l \quad (9)$$

which implies that the corresponding eigenfunctions are also orthogonal:

$$\int_0^T \phi_n^*(t) e^{-i\omega_k t} \phi_p(t) e^{i\omega_l t} dt = 0 \quad (10)$$

for all n and p when $k \neq l$. This is what we shall mean by orthogonal signals. Consequently,

where we have expanded $R_\xi(t-u)$ in its eigenfunctions according to Mercer's theorem and we have used Eq. (10). Also, since $E[\nu(t)\nu^*(u)] = 2E[n(t)n(u)] = N_0\delta(t-u)$, we have

$$\begin{aligned} E[\nu_{nk}\nu_{pl}^*] &= E \int_0^T \int_0^T \nu(t) \phi_n^*(t) e^{-i\omega_k t} \nu^*(u) \phi_p(u) e^{i\omega_l u} dt du \\ &= N_0 \delta_{np} \delta_{kl} \end{aligned} \quad (12)$$

Similarly, since $E[\xi(t)\xi(u)] = 0 = E[\nu(t)\nu(u)]$,

$$E[\xi_{nk}^{(m)}\xi_{pl}^{(m)}] = 0 = E[\nu_{nk}\nu_{pl}] \quad (13)$$

and consequently, for the observables η_{nk} , when the signal $x_m(t)$ is transmitted, from Eqs. (8), (11), (12), and (13), we have

$$E[\eta_{nk}\eta_{pl}^* | x_m(t)] = (N_0 + \lambda_n \delta_{mk}) \delta_{np} \delta_{kl} \quad (14)$$

$$E[\eta_{nk}\eta_{pl} | x_m(t)] = 0 \quad (15)$$

The means of the η variables are zero since both $\xi(t)$ and $\nu(t)$ are assumed to be zero mean processes.

Now letting

$$\eta_{nk} = \hat{\eta}_{nk} + \tilde{\eta}_{nk} \quad (16)$$

it follows from Eqs. (14) and (15) that

$$\begin{aligned} E[\hat{\eta}_{nk}\hat{\eta}_{pl} | x_m(t)] &= E[\tilde{\eta}_{nk}\tilde{\eta}_{pl} | x_m(t)] \\ &= \frac{1}{2}(N_0 + \lambda_n \delta_{mk}) \delta_{np} \delta_{kl} \end{aligned}$$

$$E[\hat{\eta}_{nk}\tilde{\eta}_{pl} | x_m(t)] = E[\tilde{\eta}_{nk}\hat{\eta}_{pl} | x_m(t)] = 0 \quad (17)$$

$$\begin{aligned} E[\xi_{nk}^{(m)}\xi_{pl}^{*(m)}] &= \int_0^T \int_0^T \xi(t) e^{i\omega_m t} \phi_n^*(t) e^{-i\omega_k t} \xi^*(u) e^{-i\omega_m u} \phi_p(u) e^{i\omega_l u} dt du \\ &= \int_0^T \int_0^T R_\xi(t-u) \phi_n^*(t) e^{i(\omega_m - \omega_k)t} \phi_p(u) e^{i(\omega_l - \omega_m)u} dt du \\ &= \int_0^T \int_0^T \sum_{q=1}^{\infty} \lambda_q \phi_q(t) \phi_n^*(t) e^{i(\omega_m - \omega_k)t} \phi_q^*(u) \phi_p(u) e^{i(\omega_l - \omega_m)u} dt du \\ &= \lambda_n \delta_{np} \delta_{mk} \delta_{ml} = \lambda_n \delta_{np} \delta_{kl} \delta_{mk} \end{aligned} \quad (11)$$

Thus, since the η variables are Gaussian, it follows that all variables are independent and

$$p[\hat{\eta}_{nk}, \tilde{\eta}_{nk} | x_m(t)] = \begin{cases} \frac{1}{\pi N_0} \exp\left(-\frac{\hat{\eta}_{nk}^2 + \tilde{\eta}_{nk}^2}{N_0}\right), & k \neq m \\ \frac{1}{\pi(N_0 + \lambda_n)} \exp\left(-\frac{\hat{\eta}_{nk}^2 + \tilde{\eta}_{nk}^2}{N_0 + \lambda_n}\right), & k = m \end{cases} \quad (18)$$

Also, based on the NM observables corresponding to the first N eigenfunctions of each covariance function, we have the likelihood function

$$\begin{aligned} p(\boldsymbol{\eta} | x_m) &= \prod_{n=1}^N \prod_{k=1}^M p(\hat{\eta}_{nk}, \tilde{\eta}_{nk} | x_m) \\ &= \frac{\exp\left[-\sum_{n=1}^N \left(\sum_{k \neq m}^M \frac{\hat{\eta}_{nk}^2 + \tilde{\eta}_{nk}^2}{N_0} + \frac{\hat{\eta}_{nm}^2 + \tilde{\eta}_{nm}^2}{N_0 + \lambda_n}\right)\right]}{(\pi)^{NM} (N_0)^{N(M-1)} \prod_{n=1}^N (N_0 + \lambda_n)} \end{aligned} \quad (19)$$

On the basis of Eqs. (18) and (19), it has been shown by Price (Ref. 1) and Halstrom (Ref. 2) that the optimum (maximum likelihood) receiver consists of M quadratic operations:

$$z_m = \int_0^T \int_0^T \eta(t) \eta^*(u) h(t, u) e^{i\omega_m(t-u)} dt du, \quad m = 1, 2, \dots, M$$

followed by a decision device, where $h(t, u)$ is the solution of the Wiener-Hopf equation:

$$N_0 h(t, u) + \int_0^T R_\xi(t-v) h(v, u) dv = R_\xi(t-u)$$

Finally, it should be noted that on the basis of this model we may conclude that when the product of T and the bandwidth of $\xi(t)$ is very large this analysis is valid even for non-Gaussian signals, for under this condition, as a consequence of the central limit theorem, the observables $\xi_{nk}^{(m)}$ of Eq. (8) are approximately Gaussian even when $\xi(t)$ is not.

2. Bounds on Error Probability

We now proceed to derive a bound on the error probability of the maximum likelihood receiver by applying a fundamental formula due to Gallager (Ref. 3) for the error probability^a when $x_m(t)$ is sent, P_{Em} , as a function of the likelihood functions:

$$P_{Em} \leq \int_{-\infty}^{\infty} \dots \int_{-\infty}^{\infty} d\boldsymbol{\eta} p(\boldsymbol{\eta} | x_m)^{\frac{1}{1-\rho}} \left[\sum_{m' \neq m}^M p(\boldsymbol{\eta} | x_{m'})^{\frac{1}{1-\rho}} \right]^\rho, \quad \rho \geq 0 \quad (20)$$

Inserting Eq. (19) into Eq. (20), we obtain

$$\begin{aligned} P_{Em} \leq & \int_{-\infty}^{\infty} \dots \int_{-\infty}^{\infty} d\boldsymbol{\eta} \left[\frac{\exp\left(-\sum_{n=1}^N \sum_{k=1}^M \frac{\hat{\eta}_{nk}^2 + \tilde{\eta}_{nk}^2}{N_0}\right)}{(\pi N_0)^{NM}} \right] \\ & \left[\frac{\exp\left(\sum_{n=1}^N \lambda_n \frac{\hat{\eta}_{nm}^2 + \tilde{\eta}_{nm}^2}{N_0(N_0 + \lambda_n)(1 + \rho)}\right)}{\prod_{n=1}^N \left(1 + \frac{\lambda_n}{N_0}\right)^{\frac{1}{1+\rho}}}\right] \\ & \left[\frac{\sum_{m' \neq m}^M \exp\left(\sum_{n=1}^N \frac{\lambda_n (\hat{\eta}_{nm'}^2 + \tilde{\eta}_{nm'}^2)}{N_0(N_0 + \lambda_n)(1 + \rho)}\right)}{\prod_{n=1}^N \left(1 + \frac{\lambda_n}{N_0}\right)^{\frac{1}{1+\rho}}}\right]^\rho \end{aligned} \quad (21)$$

Eq. (21) may be written as

^aJ. Wozencraft and I. M. Jacobs (Ref. 4) have obtained Chernoff bounds for the related problem of slow Rayleigh fading carriers, and H. L. Yudkin (Ref. 5) has applied the Gallager bound to that problem.

$$P_{Em} \leq E \left[\frac{\exp\left(\sum_{n=1}^N \frac{\lambda_n (\hat{\eta}_{nm}^2 + \tilde{\eta}_{nm}^2)}{N_0(N_0 + \lambda_n)(1 + \rho)}\right)}{\prod_{n=1}^N \left(1 + \frac{\lambda_n}{N_0}\right)^{\frac{1}{1+\rho}}}\right] E \left\{ \left[\frac{\sum_{m' \neq m}^M \exp\left(\sum_{n=1}^N \frac{\lambda_n (\hat{\eta}_{nm'}^2 + \tilde{\eta}_{nm'}^2)}{N_0(N_0 + \lambda_n)(1 + \rho)}\right)}{\prod_{n=1}^N \left(1 + \frac{\lambda_n}{N_0}\right)^{\frac{1}{1+\rho}}}\right]^\rho \right\} \quad (22)$$

where the expectations are, with respect to the NM Gaussian variables $\hat{\eta}_{nk}$ and $\tilde{\eta}_{nk}$, each of mean zero and variance $N_0/2$. Now, if we restrict ρ to lie in the unit interval, for the second expectation in Eq. (22) we have

$$E \{ [g(\boldsymbol{\eta}, \rho)]^\rho \} \leq \{ E[g(\boldsymbol{\eta}, \rho)] \}^\rho, \quad 0 \leq \rho \leq 1 \quad (23)$$

by the convexity of the function $f(x) = x^\rho$ for ρ in this interval. Therefore, since the $\hat{\eta}_{nk}$ and $\tilde{\eta}_{nk}$ of Eqs. (21) and (22) are identically distributed, inserting Eq. (23) in Eq. (22) yields

where $h(r, t; u)$ is the solution to the integral equation

$$h(r, t; u) + u \int_0^T R_\xi(t-u) h(s, t; u) ds = R_\xi(r-t) \quad (27)$$

If T is now allowed to become infinite, Eq. (27) can be easily solved. For then we can seek a solution of the form $h_\infty(r, t; u) = h_\infty(r-t; u)$ by first transforming to obtain

$$H_\infty(\omega; u) + u S_\xi(\omega) H_\infty(\omega; u) = S_\xi(\omega) \quad (28)$$

$$\begin{aligned} P_{Em} &\leq (M-1)^\rho \left\{ E \left[\frac{\exp \left(- \sum_{n=1}^N \frac{\lambda_n (\eta_{nm}^2 + \tilde{\eta}_{nm}^2)}{N_0 (N_0 + \lambda_n) (1 + \rho)} \right)}{\prod_{n=1}^N \left(1 + \frac{\lambda_n}{N_0} \right)^{\frac{1}{1+\rho}}} \right] \right\}^{1+\rho} \\ &< \frac{M^\rho \int \cdots \int \exp \left[- \sum_{n=1}^N \frac{\hat{\eta}_{nm}^2 + \tilde{\eta}_{nm}^2}{N_0} \left(1 - \frac{\lambda_n}{N_0 (N_0 + \lambda_n) (1 + \rho)} \right) \right] d\boldsymbol{\eta}}{\prod_{n=1}^N \left(1 + \frac{\lambda_n}{N_0} \right) (\pi N_0)^N} \\ &= M^\rho \prod_{n=1}^N \frac{\left(1 + \frac{\lambda_n}{N_0} \right)^\rho}{\left(1 + \frac{\lambda_n \rho}{N_0 (1 + \rho)} \right)^{1+\rho}} \end{aligned} \quad (24)$$

Since this bound on P_{Em} is independent of m , it is also a bound on the overall error probability P_E .

Also, since one of M equally probable signals may be transmitted in T seconds, the data rate is $R = \ln(M/T)$ nats/sec, and as the number of observables $N \rightarrow \infty$, Eq. (24) becomes

$$P_E < e^{T\rho R} \frac{\left[D \left(\frac{1}{N_0} \right) \right]^\rho}{\left[D \left(\frac{\rho}{N_0 (1 + \rho)} \right) \right]^{1+\rho}} \quad (25)$$

where $D(z) = \prod_{n=1}^\infty (1 + \lambda_n z)$ is known as the Fredholm determinant. It has been shown (Ref. 2) that

$$D(z) = \exp \left[\int_0^z du \int_0^T h(t, t; u) dt \right] \quad (26)$$

where

$$H_\infty(\omega; u) = \int_{-\infty}^\infty h_\infty(r-t; u) e^{i\omega(r-t)} d(r-t)$$

$$S_\xi(\omega) = \int_{-\infty}^\infty R_\xi(t-u) e^{i\omega(t-u)} d(t-u)$$

Then

$$\begin{aligned} \int_0^z du \int_0^T h_\infty(t-t; u) dt &= \int_0^T dt \int_0^z h(0; u) du \\ &= T \int_0^z \int_{-\infty}^\infty H(\omega; u) \frac{d\omega}{2\pi} du \\ &= T \int_{-\infty}^\infty \frac{d\omega}{2\pi} \int_0^z \frac{S_\xi(\omega)}{1 + u S_\xi(\omega)} du \\ &= T \int_{-\infty}^\infty \ln [1 + z S_\xi(\omega)] \frac{d\omega}{2\pi} \end{aligned} \quad (29)$$

Now, when T is finite, let

$$h(t, t; u) = h_\infty(t - t; u) + h_c(t, t, u)$$

where $h_c(\cdot)$ is the correction term, and consequently

$$\lim_{T \rightarrow \infty} h_c(t, t; u) = 0$$

for all t and u . For the case in which $S_\xi(\omega)$ is a rational function, it is now clear from Eq. (27) that $h_c(t, t; u)$ must be of the form

$$h_c(t, t; u) = \sum_i C_i t^{k_i} e^{\alpha_i t} \cos \omega_i t$$

where α_i is a real number and k_i and ω_i are positive real numbers. However, since $h_c(t, t; u)$ must approach zero as $T \rightarrow \infty$, we must have

$$|C_i| \leq e^{-\beta_i T} o\left(\frac{1}{T}\right)$$

where $\alpha_i \leq \beta_i < 0$. Then, for rational spectra,

$$\left| \int_0^T h_c(t, t; u) dt \right| \leq o\left(\frac{1}{T}\right) \quad (30)$$

Thus, from Eqs. (26), (29), and (30), for rational spectra we have

$$D(z) = \exp T \left\{ \int_{-\infty}^{\infty} \ln [1 + z S_\xi(\omega)] \frac{d\omega}{2\pi} + o\left(\frac{1}{T}\right) \right\} \quad (31)$$

Substitution of Eq. (31) in Eq. (25) yields

$$P_E < \exp \left\{ -T \left[E_0(\rho) - \rho R - o\left(\frac{1}{T}\right) \right] \right\}, \quad 0 \leq \rho \leq 1 \quad (32)$$

where

$$E_0(\rho) = (1 + \rho) \int_{-\infty}^{\infty} \ln \left[1 + \frac{\rho}{1 + \rho} \frac{S_\xi(f)}{N_0} \right] df - \rho \int_{-\infty}^{\infty} \ln \left[1 + \frac{S_\xi(f)}{N_0} \right] df \quad (33)$$

To minimize Eq. (32), we must maximize the magnitude of the exponent to obtain

$$P_E < \exp \left\{ -T \left[E(R) - o\left(\frac{1}{T}\right) \right] \right\} \quad (34)$$

where

$$E(R) = \max_{0 \leq \rho \leq 1} [E_0(\rho) - \rho R] \quad (35)$$

It is readily shown by examining Eq. (33) and its first two derivatives that $E(R)$ is maximized when $R = \partial E_0(\rho) / \partial \rho > 0$, and then $E(R) > 0$ for all $R < C$,

where

$$C \triangleq \left. \frac{\partial E_0(\rho)}{\partial \rho} \right|_{\rho=0} = \int_{-\infty}^{\infty} \frac{S_\xi(f)}{N_0} df - \int_{-\infty}^{\infty} \ln \left[1 + \frac{S_\xi(f)}{N_0} \right] df \quad (36)$$

and $d^2 E(R) / dR^2 < 0$ for $R < C$, so that $E(R)$ is a convex function.

We now give a plausibility argument to show that C of Eq. (36) is actually the capacity of the channel under consideration. It is well known that the capacity of an additive white Gaussian channel without bandwidth constraints is the first term of Eq. (36) and that this can be approached asymptotically as $T \rightarrow \infty$ with orthogonal coherent carriers. Now suppose $M = e^{kT}$ coherent orthogonal carriers of unit power were available and were modulated in two ways simultaneously as follows: one of the M carriers is selected, and thus transmits $\ln M = RT$ nats; at the same time, it is amplitude-modulated by a stationary complex Gaussian process whose spectral density is $S_\xi(f)$. Then it is well known that the capacity of the AM system is

$$\int_{-\infty}^{\infty} \ln \left[1 + \frac{S_\xi(f)}{N_0} \right] df$$

while that of the channel is

$$\int_{-\infty}^{\infty} \frac{S_\xi(f)}{N_0} df$$

Consequently, the digital system can transmit no more than

$$\int_{-\infty}^{\infty} \frac{S_\xi(f)}{N_0} df - \int_{-\infty}^{\infty} \ln \left[1 + \frac{S_\xi(f)}{N_0} \right] df \text{ nats/sec,}$$

with arbitrarily low error probability as $T \rightarrow \infty$. The fact that the amplitude modulation is due to instability of the carrier rather than the transmission of information is of no consequence to the performance of the digital system.

We now consider two types of spectra in detail: the flat bandlimited spectral density

$$S_\xi(f) = \begin{cases} \frac{S}{N_0 B}, & -B \leq f \leq B \\ 0, & \text{otherwise} \end{cases} \quad (37)$$

and the Markov spectral density

$$S_{\xi}(f) = \frac{S}{\pi(f^2 + B^2)} \quad (38)$$

Figs. 1 and 2 show $E(R)$ for these two spectra for various values of S/N_0B . Fig. 3 shows $E(0) = E_0(1)$, the zero-rate exponent as a function of S/N_0B for both spectra. Thus it appears that while capacity decreases monotonically with increasing bandwidth, as is shown in Eq. (36), the error exponent for low rates exhibits a maximum for a non-zero bandwidth. (It should be recalled that the zero-bandwidth case corresponds to a carrier of fixed known frequency but constant amplitude, which is a Rayleigh distributed random variable. Consequently, for this case the error

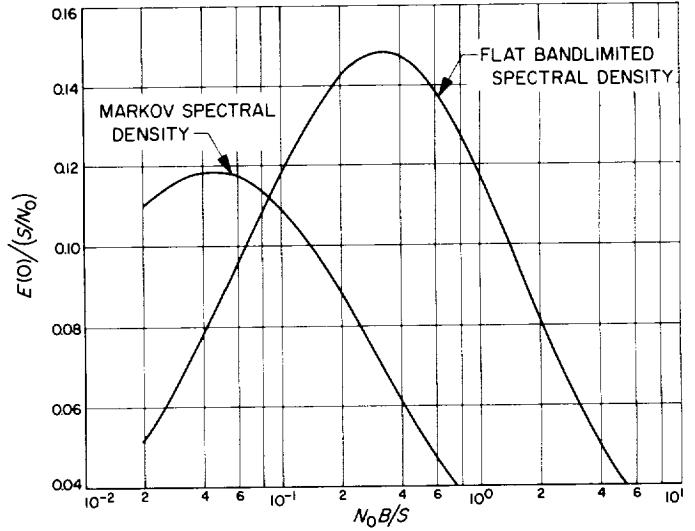


Fig. 3. Zero-rate exponents

probability does not approach zero as $T \rightarrow \infty$.) The bandwidth of the unstable carrier can be increased to achieve the maximum exponent for a given rate either by frequency diversity (dividing the available power among several carriers) or by spatial diversity, for assuming K transmitters and receivers, each with independent carriers of $1/K$ th the total power, we find that Eq. (33) becomes

$$E_0(\rho) = (1 + \rho)K \int_{-\infty}^{\infty} \ln \left[1 + \frac{\rho}{1 + \rho} \frac{S_{\xi}(f)}{N_0K} \right] df - \rho K \int_{-\infty}^{\infty} \ln \left[1 + \frac{S_{\xi}(f)}{N_0K} \right] df$$

which has the same effect as multiplying the bandwidth by K .

We note also that these results should be compared with those for stable orthogonal carriers for which the exponent (Ref. 6) is

$$\frac{E(R)}{C} = \begin{cases} \frac{1}{2} - \frac{R}{C}, & 0 \leq \frac{R}{C} \leq \frac{1}{4} \\ \left(1 - \sqrt{\frac{R}{C}}\right)^2, & \frac{1}{4} \leq \frac{R}{C} < 1 \end{cases} \quad (39)$$

where $C = S/N_0$, so that for flat bandlimited $S_{\xi}(f)$ the exponent at low rates is approximately 0.3 times the exponent with stable carriers.

If the model were modified so that the stochastic carriers had a specular as well as a fading component, this

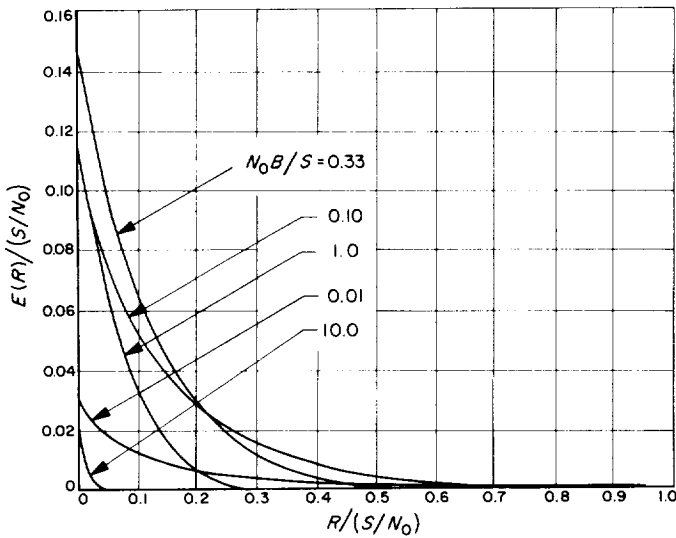


Fig. 1. Error exponents for flat bandlimited spectral densities

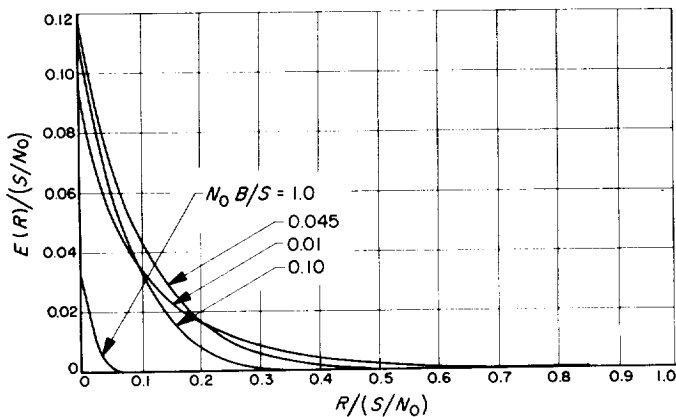


Fig. 2. Error exponents for Markov spectral densities

would give $\xi(t)$ a non-zero complex mean $\mu(t)$ whose projections on the eigenfunctions would be

$$\mu_n = \int \mu(t) \phi_n^*(t) dt = \hat{\mu}_n + i\tilde{\mu}_n$$

This would result in multiplying the error bound (25) by the factor

$$\exp\left(\frac{-\rho}{1+\rho} \sum_{n=1}^{\infty} \frac{\hat{\mu}_n^2 + \tilde{\mu}_n^2}{2N_0 \left[1 + \frac{\lambda_n \rho}{N_0(1+\rho)}\right]}\right)$$

As a result, the exponent would be changed by increasing $E_n(\rho)$ of Eq. (33) by the additive term

$$E_s(\rho) = \frac{\rho}{2N_0(1+\rho)} \int_{-\infty}^{\infty} |\mu_L(f)|^2 \times \left[\frac{1}{1 + \left(\frac{\rho}{1+\rho}\right) \frac{S_{\xi}(f)}{N_0}} \right] df \quad (40)$$

where

$$\mu_L(f) = \lim_{T \rightarrow \infty} \int_0^T \frac{\mu(t) e^{-2\pi i f t}}{T} dt$$

Thus, not only is the exponent increased, but the capacity of the system is increased by

$$C_s = \frac{\partial E_s(\rho)}{\partial \rho} \Big|_{\rho=0} = \frac{\int_{-\infty}^{\infty} |\mu_L(f)|^2 df}{2N_0} \quad (41)$$

Therefore the specular component effectively introduces a parallel channel with transmitting power

$$\frac{1}{2} \int_{-\infty}^{\infty} |\mu_L(f)|^2 df = \lim_{T \rightarrow \infty} \int_0^T \frac{1}{2T} |\mu(t)|^2 dt$$

B. A Comparison of Several Methods of Subcarrier Tracking

J. J. Stiffler

1. Introduction

A number of communication systems (e.g., AM, PAM, binary PSR) transmit information in the form $\sqrt{2} A(t) \sin(\omega_c t + \theta)$. In order to coherently demodulate the received signal, it is necessary to determine, as nearly as

possible, the phase and frequency of the subcarrier, $\sin(\omega_c t + \theta)$. If $A(t)$ contains a dc component, there is an unmodulated subcarrier component in the received signal. This component could be tracked with a phase-locked loop to provide the desired reference signal. On the other hand, the dc component in $A(t)$ represents power which does not convey any information (other than the phase and frequency of the subcarrier) and is essentially wasted since it represents power not available for the information-bearing portion of the received signal.

A number of methods have been proposed for generating a reference subcarrier from the received signal, even in the absence of a dc component in the modulation. Several of these approaches are discussed and compared here. The first of these, the squaring-loop method, has been analyzed in a number of papers (Refs. 7, 8, and 9). The results of these analyses will be reviewed briefly in Section 2. A second method, originally proposed by Costas (Ref. 10), is analyzed in Section 3 and is shown to be equivalent, theoretically, to the squaring loop. A third method (Refs. 8 and 11) involves the following procedure: first, the modulation itself is estimated, and an attempt is then made, by means of this estimate, to eliminate the modulation from the subcarrier, and to leave, as nearly as possible, an unmodulated sinusoid which can be tracked with a phase-locked loop. This method is considered in Section 4.

2. The Squaring-Loop Method

The squaring loop is shown in Fig. 4. The motivation for such an approach rests in the observation that the signal

$$2A^2(t) \cos^2(\omega_c t + \theta) = A^2(t) + A^2(t) \cos(2\omega_c t + 2\theta) \quad (1)$$

must contain an unmodulated sinusoidal component at twice the subcarrier frequency, since $A^2(t)$ must contain a dc component. Tracking this component and halving its frequency should yield an estimate of the subcarrier.

Analyses have shown that the mean-squared jitter of the phase reference is given approximately by

$$\sigma_{\phi}^2 = \frac{1}{Q} \left(\frac{1}{R} + \frac{1}{R^2} \right) \quad (2)$$

Here Q is the ratio of the half-width W of the bandpass filter (assumed ideal rectangular) to the loop bandwidth R_L , $Q = W/R_L$. The term R is twice the signal-to-noise ratio (SNR) at the output of the bandpass

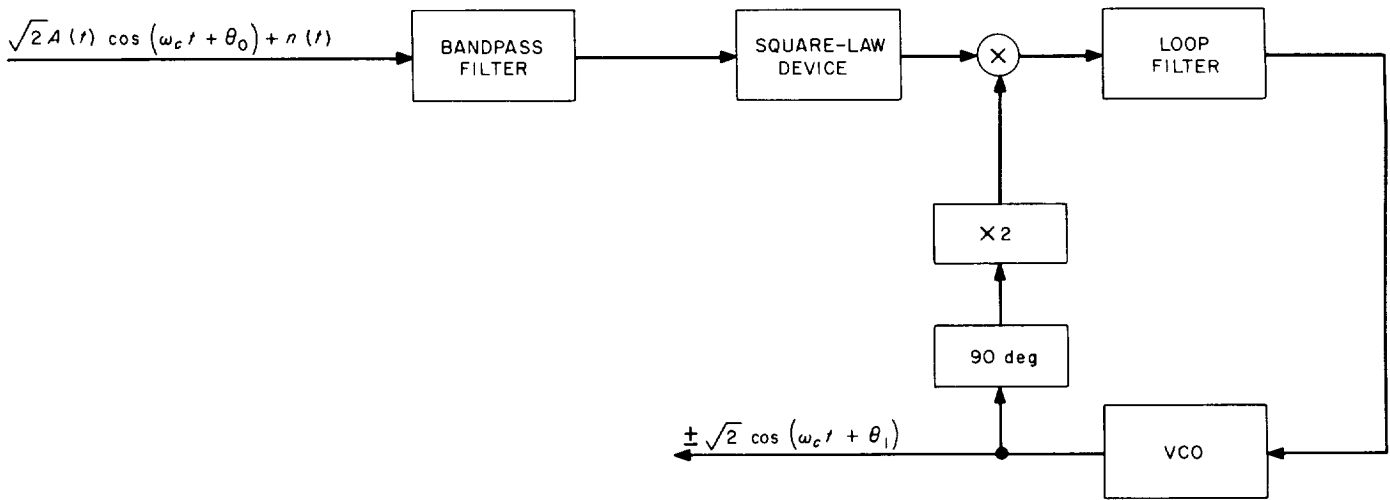


Fig. 4. A squaring loop

filter, $R = P_s/N_nW$, where $P_s = \int_{-W}^W S_{s1}(f) df$, and $S_{s1}(f)$ is the power spectral density of the modulation. The noise is assumed white and Gaussian with the single-sided spectral density N_n . This result can be improved slightly by using a "Weiner-optimum" filter instead of a bandpass filter preceding the square-law device (see Ref. 12). We shall use Eq. (2) as a basis of comparison for the techniques considered in the subsequent sections.

3. The Costas Receiver

A somewhat different device for extracting the carrier from an amplitude-modulated signal is shown in Fig. 5. The signal into the loop filter is $[A_1^2(t)]/2 \sin 2(\theta_1 - \theta_0)$, $A_1(t)$ denoting the filtered version of $A(t)$. Except for the fact that it is centered about zero frequency rather than $2f_c$, the signal spectrum is identical to that produced by the squaring loop. Consequently, the low-pass filters here

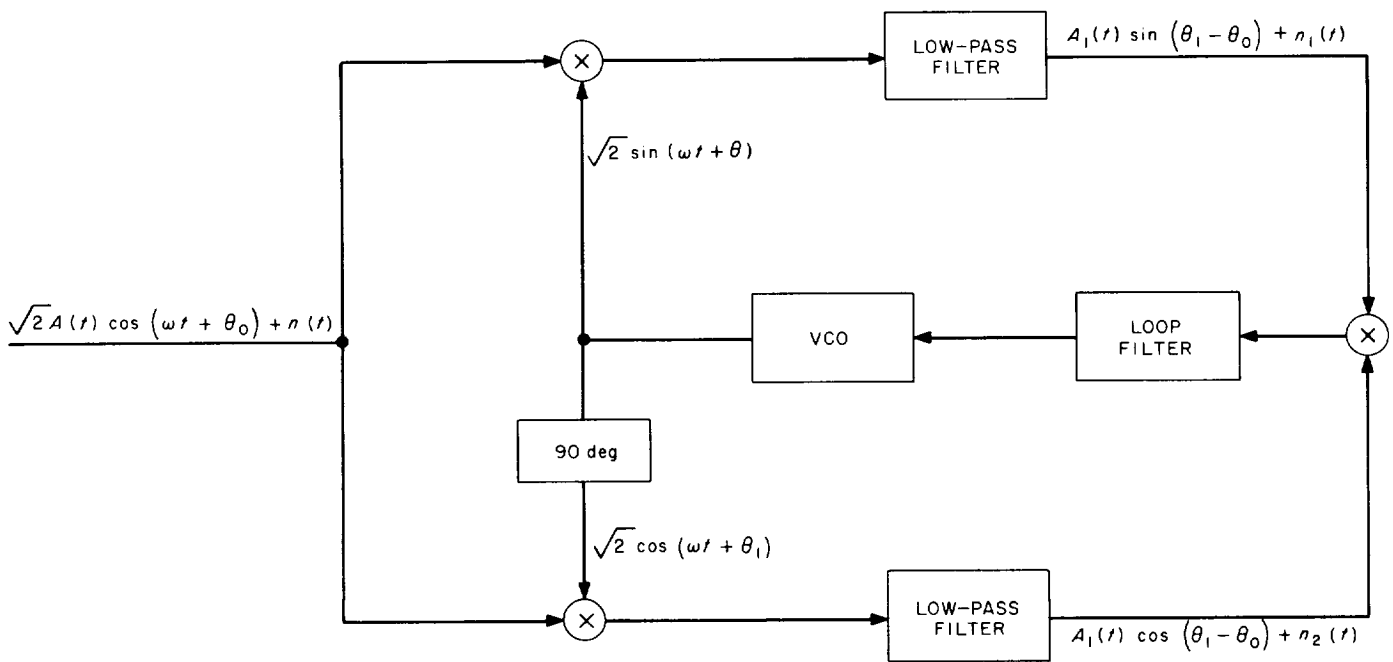


Fig. 5. The Costas receiver

can be obtained by simply translating, by f_c cps, the bandpass filter of the squaring loop. Equivalent filters may therefore be used in the two situations. The noise terms $n_1(t)$ and $n_2(t)$ are just frequency translations of white noise which are then filtered. Their spectral densities are $(N_0/2)/|H(j\omega)|^2$, $H(j\omega)$ denoting the transfer functions of the low-pass filters (assumed identical). Moreover, as is well known, $n_1(t)$ and $n_2(t)$ are independent Gaussian processes (if $n(t)$ is a Gaussian process). As is shown in Ref. 13, $n(t)$ can be written in the form

$$n(t) = n_\alpha(t) \cos(\omega_c t + \theta) + n_\beta(t) \sin(\omega_c t + \theta)$$

where $n_\alpha(t)$ and $n_\beta(t)$ are independent processes. Thus, since

$$n_1(t) = [n(t) \sqrt{2} \sin(\omega_c t + \theta)]_{lf} = \frac{\sqrt{2}}{2} n_\beta(t)$$

and

$$n_2(t) = [n(t) \sqrt{2} \cos(\omega_c t + \theta)]_{lf} = \sqrt{2}/2 n_\alpha(t)$$

$n_1(t)$ and $n_2(t)$ are also independent. (The subscripts *lf* indicate that only the low frequency components are to be considered.)

The autocorrelation function of the noise input to the loop filter has the form

$$E \{ [A_1(t) n_2(t) \sin(\theta_1(t) - \theta_0(t)) + A_1(t) n_1(t) \cos(\theta_1(t) - \theta_0(t)) + n_1(t) n_2(t)] \times [A_1(t + \tau) n_2(t + \tau) \sin(\theta_1(t + \tau) - \theta_0(t + \tau)) + A_1(t + \tau) n_1(t + \tau) \cos(\theta_1(t + \tau) - \theta_0(t + \tau)) + n_1(t + \tau) n_2(t + \tau)] \}$$

and

$$R_{A_1}(\tau) = E [A_1(t) A_1(t + \tau)]$$

Moreover,

$$S_{sxn}(0) = \int_{-\infty}^{\infty} S_{A_1}(f) S_{n'}(-f) df \quad (5a)$$

and

$$S_{nzn}(0) = \int_{-\infty}^{\infty} S_{n'}(f) S_{n'}(-f) df \quad (5b)$$

are their respective spectral densities at the low frequencies. If rectangular filters having bandwidth W are used,

$$S_{sxn}(0) = \frac{N_0}{2} \int_{-W}^W S_{A_1}(f) df = \frac{N_0}{2} P_s \quad (6a)$$

and

$$S_{nzn}(0) = (N_0/2)^2 2W \quad (6b)$$

where P_s , the power in the filtered signal, is as defined in Section 2.

Since the slope of the error signal at the input to the loop filter is $A_1^2(t) \cos 2(\theta_1 - \theta_0) \approx A_1^2(t)$, the effective input signal power is simply the dc power in the squared

$$\begin{aligned} & \doteq R_{A_1}(\tau) R_{n_2}(\tau) E \{ \sin^2(\theta_1(t) - \theta_0(t)) \} + R_{A_1}(\tau) R_{n_1}(\tau) \\ & \times E \{ \cos^2(\theta_1(t) - \theta_0(t)) \} + R_{n_1}(\tau) + R_{n_2}(\tau) \\ & = R_{sxn}(\tau) + R_{nzn}(\tau) \end{aligned} \quad (3)$$

Use has been made of the fact that $\theta_1(t)$ and $\theta_0(t)$ are assumed to be slowly varying functions of time. For those values of τ for which $R_{A_1}(\tau)$, $R_{n_1}(\tau)$, and $R_{n_2}(\tau)$ are not zero, presumably $\theta_0(t) \approx \theta_0(t + \tau)$ and $\theta_1(t) \approx \theta_1(t + \tau)$.

The two noise terms are

$$R_{sxn}(\tau) = R_{n'}(\tau) R_{A_1}(\tau) \quad (4a)$$

and

$$R_{nzn}(\tau) = R_{n'}^2(\tau) \quad (4b)$$

where

$$R_{n'}(\tau) = E [n_1(t) n_1(t + \tau)] = E [n_2(t) n_2(t + \tau)]$$

signal $A_1^2(t)$. It is not difficult to show, as is seen in Ref. 12, that

$$P_{A_1^2}(0) \doteq \left[\int_{-W}^W S_s(f) df \right]^2 \quad (7)$$

The ratio of the signal power to the single-sided low frequency noise spectral density at the input to the loop filter is, therefore,

$$(S/N) = \frac{P_s^2}{P_s N_0 + N_0^2 W} = \frac{W}{\frac{N_0 W}{P_s} + \left(\frac{N_0 W}{P_s} \right)^2} \quad (8)$$

The loop variance is precisely that given by Eq. (2) for the squaring loop. Evidently the two approaches result in identical performances when the filters in the Costas receiver are the low-pass equivalents of the bandpass filter in the squaring loop. The primary advantage, or disadvantage, of the Costas receiver compared with the squaring loop lies in the relative ease with which the corresponding filters can be constructed. The Costas receiver has the slight disadvantage that some method must be devised for ascertaining which of the signals, $\sin(\omega t + \theta_1)$ or $\cos(\omega t + \theta_1)$, is actually in phase with the received carrier; either event represents an in-lock situation. Since one of these references will yield a large signal output while the other results in noise only, the two situations can be easily distinguished. Incidentally, both the Costas and the squaring-loop methods exhibit the usual 180-deg phase ambiguity inherent in all systems which attempt to recover a subcarrier directly from the modulation; i.e., changing the sign of the received signal would leave the sign of the recovered subcarrier unaltered.

Still other variations of this basic approach are possible. An analysis similar to that just presented shows that the system depicted in Fig. 6, for example, also yields

a phase variance as given in Eq. (2). Whether or not this receiver demonstrates any practical advantage *vis-à-vis* the Costas receiver or the squaring loop will depend upon the frequencies involved, the ease of realizing the required filters, etc.

4. The "Optimum" Subcarrier Estimator

Although the method to be considered here is also applicable to any communication system using a signal of the form $\sqrt{2}A(t) \sin(\omega_c t + \theta)$, for the sake of simplicity we shall limit the discussion to the case of binary PSK. Suppose that it is known that the signal is either $\sqrt{2}A \sin(\omega_c t + \theta_0)$ or $-\sqrt{2}A \sin(\omega_c t + \theta_0)$ for every interval of time $iT < t < (i+1)T$. The successive signals are independent and equally likely to have either sign. The time instants iT are assumed known precisely (or, at least with sufficient accuracy to neglect the effect of the uncertainty). The phase θ_0 , however, is a random variable. Presumably, the variation of θ_0 is small in any time interval T . Let us assume, in fact, that θ_0 has remained constant for the last K symbol intervals. Then it is easily verified that the maximum *a posteriori* probability estimate of θ_0 at the time $t = kT$ is that value of $\hat{\theta}_0$ maximizing the expression

$$p(y(t) | (k - K)T < t < kT, \hat{\theta}_0) p(\hat{\theta}_0) = Cp(\hat{\theta}_0) \prod_{l=k-K}^{k-1} \left[\exp\left(2/N_0 \int_{lT}^{(l+1)T} y(t) \sqrt{2} A \cos(\omega_c t + \hat{\theta}_0) dt\right) \exp\left(-2/n_0 \int_{lT}^{(l+1)T} y(t) \sqrt{2} A \cos(\omega_c t + \hat{\theta}_0) dt\right) \right] \quad (9)$$

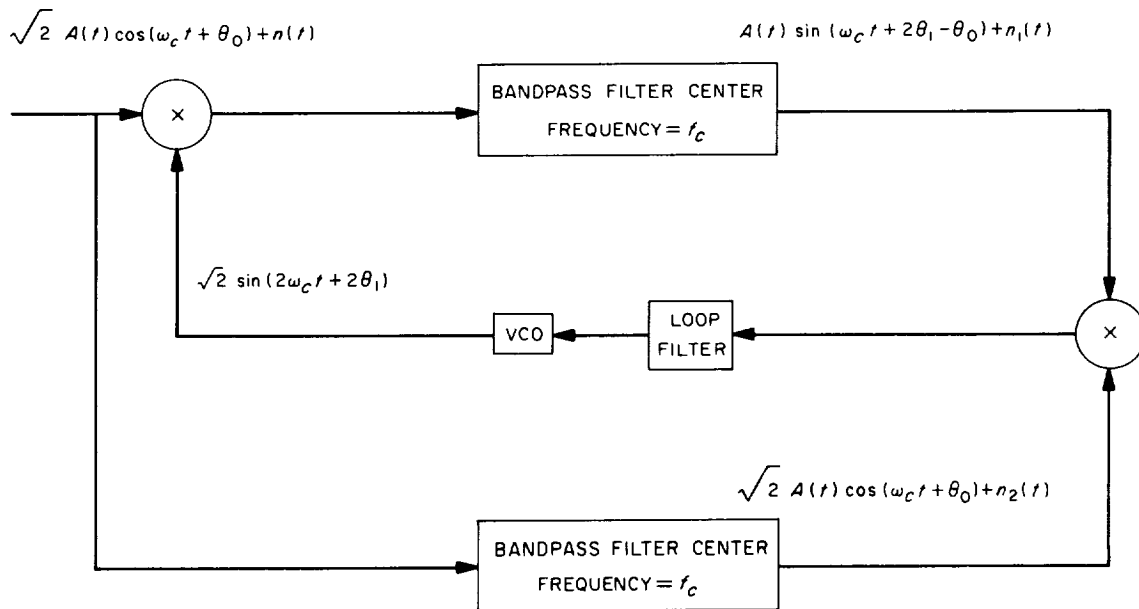


Fig. 6. A variation of the Costas receiver

where C is a constant, independent of $\hat{\theta}_0$, and $p(\hat{\theta}_0)$ is the *a priori* distribution of $\hat{\theta}_0$.

Since we would like $\hat{\theta}_0$ to be such that Eq. (9) attains a maximum, the derivative of this expression must be equal to zero at that value of $\hat{\theta}_0$. This implies that

$$0 = \frac{d}{d\hat{\theta}_0} p(\hat{\theta}_0) + p(\hat{\theta}_0) \sum_{v=k-K}^{k-1} \tanh \left[\frac{2}{N_0} \int_{vT}^{(v+1)T} y(t) \sqrt{2} A \cos(\omega_c t + \hat{\theta}_0) dt \right] \frac{2\sqrt{2} A}{N_0} \int_{vT}^{(v+1)T} y(t) \sin(\omega_c t + \hat{\theta}_0) dt \quad (10)$$

If the *a priori* distribution of θ_0 is flat, the first right-hand term of Eq. (10) is zero. The second term suggests the device shown in Fig. 7.

The box for generating the hyperbolic tangent of its input may be rather difficult to realize in practice. However, when the SNR is small, a good approximation is afforded by replacing the hyperbolic tangent in Eq. (10) with its argument. In this case, the input to the loop filter is

$$z(t) = [A(t) \sin(\theta_0 - \theta_1) + n_1(t)] \int_{iT}^t [A(\xi) \cos(\theta_0 - \theta_1) + n_2(\xi)] d\xi \quad (11)$$

where $n_1(t)$ and $n_2(t)$ are as defined in Section 3.

We observe, first of all, that the average dc signal power at the loop input is

$$\text{error signal} = \frac{1}{T} \int_{iT}^{(i+1)T} A(t) \int_{iT}^t A(\xi) d\xi dt \sin(\theta_0 - \theta_1) \cos(\theta_0 - \theta_1) = \frac{A^2 T}{2} \sin(\theta_0 - \theta_1) \cos(\theta_0 - \theta_1) \quad (12)$$

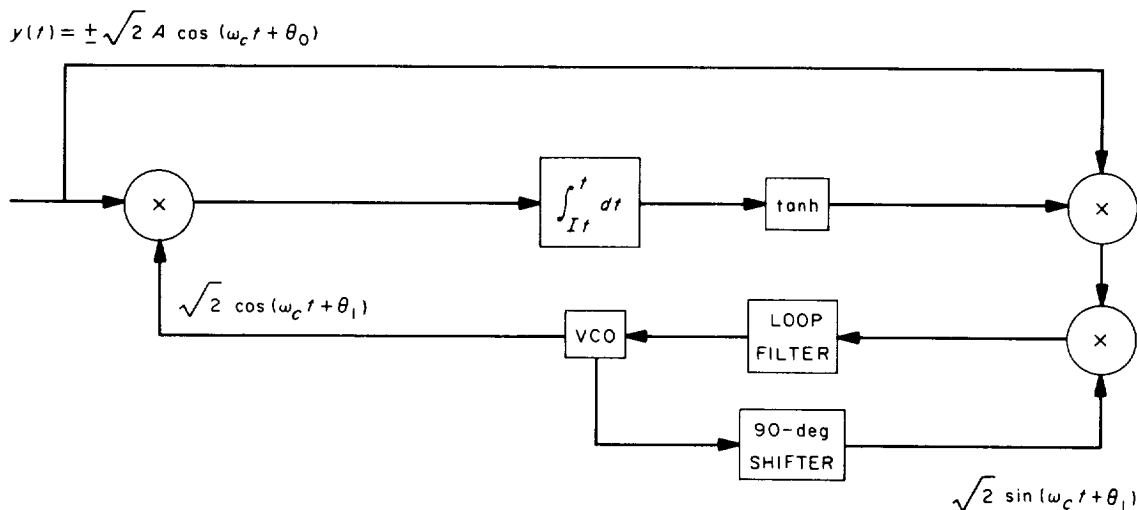


Fig. 7. A decision-variable feedback receiver

implying an effective signal amplitude of

$$\frac{A^2 T}{2} \cos(\theta_0 - \theta_1) \approx \frac{A^2 T}{2}$$

To determine the low-frequency noise spectral density at this point, we must evaluate

$$R_z(\tau) = E[z(t + \eta) z(t + \eta + \tau)] \quad (13)$$

where η is a random variable uniformly distributed over the interval $0 \leq \eta \leq T$. As before, we obtain two noise terms:

$$\begin{aligned} R_{sxn}(\tau) &= E \left\{ \int^{t+\eta} [A(\xi) \cos(\theta_0 - \theta_1) + n_2(\xi)] d\xi \int^{t+\eta+\tau} [A(\xi) \cos(\theta_0 - \theta_1) + n_2(\xi)] \right. \\ &\quad \times d\xi [n(t + \eta) A(t + \tau + \eta) + n(t + \tau + \eta) A(t + \eta)] \left. \right\} \cos(\theta_0 - \theta_1) \\ &= \frac{N_0}{2} E \left[A(t + \eta + \tau) \int^{t+\eta} A(\xi_1) d\xi_1 \right] \cos^2(\theta_0 - \theta_1), \quad \tau > 0 \\ &= \begin{cases} \frac{N_0}{2} A^2 \frac{(T - \tau)^2}{T} \cos^2(\theta_0 - \theta_1), & 0 < \tau < T \\ 0, & T < \tau \end{cases} \quad (14a) \end{aligned}$$

and

$$\begin{aligned} R_{nzn}(\tau) &= E \left\{ n_1(t + \eta) n_1(t + \eta + \tau) \int^{t+\eta} [A(\xi_1) \cos(\theta_0 - \theta_1) + n_2(\xi_1)] d\xi_1 \int^{t+\eta+\tau} [A(\xi_2) \cos(\theta_0 - \theta_1) + n_2(\xi_2)] d\xi_2 \right\} \\ &= \left[\frac{A^2 T^2}{3} + \frac{N_0}{2} T/2 \right] \frac{N_0}{2} \delta(\tau) \quad (14b) \end{aligned}$$

Consequently,

$$S_{sxn}(0) \doteq \frac{A^2 T^2}{3} N_0 \quad (15a)$$

and

$$S_{nzn}(0) \doteq \left[\frac{A^2 T^2}{3} + \frac{N_0}{2} T/2 \right] \frac{N_0}{2} \quad (15b)$$

yielding a phase variance

$$\sigma_\phi^2 = \frac{2B_L S_{sxn}(0) + S_{nzn}(0)}{P_{effective}} \doteq \frac{1}{Q} \left\{ \frac{4}{R} + \frac{1}{R^2} \right\} \quad (16)$$

where R and Q are as previously defined. We note that, at low SNRs, this system yields a phase variance essentially equal to that of the systems analyzed above. At larger values of R , when the approximation to the hyperbolic tangent becomes less valid, this system actually demonstrates a 6-db degradation in performance compared with the previous systems.

At high SNRs, however, a reasonably good approximation to the hyperbolic tangent is just the sign of its argument. In this case, the noise at the loop input is still flat with the density $N_0/2$. The dc signal power is easily seen (Ref. 8) to be simply

$$(1 - 2P_0)^2 A^2 \tag{17}$$

where P_0 is the percentage of time that the sign of the argument of the hyperbolic tangent is in error. But

$$\begin{aligned} P_0 &\approx \frac{1}{2} - \frac{1}{T} \frac{1}{\sqrt{2\pi}} \int_0^T \int_0^x \left(\frac{2Rt}{T}\right)^{1/2} e^{-(x^2/2)/dx} dt \\ &= \frac{1}{2} - \frac{1}{\sqrt{2\pi}} \int_0^{(2R)^{1/2}} \left(1 - \frac{x^2}{2R}\right) e^{-(x^2/2)/dx} \\ &= \frac{1}{2} - \frac{1}{2} \left(1 - \frac{1}{2R}\right) \operatorname{erf}(R^{1/2}) - \frac{1}{2\pi^{1/2} R^{1/2}} e^{-R} \end{aligned} \tag{18}$$

Consequently,

$$\begin{aligned} (1 - 2P_0)^2 &= \left(1 - \frac{1}{2R}\right) \operatorname{erf}(R^{1/2}) + \frac{1}{R^{1/2} \pi^{1/2}} e^{-R} \\ &\approx \begin{cases} 1, & R \gg 1 \\ \frac{16}{9\pi} R, & R \ll 1 \end{cases} \end{aligned} \tag{19}$$

and

$$\begin{aligned} \sigma_\phi^2 &\approx \frac{1}{Q} \left\{ \frac{1}{R(1 - 2P_0)^2} \right\} \\ &= \begin{cases} \frac{1}{QR}, & R \gg 1 \\ \frac{9\pi}{16} \frac{1}{Q} \frac{1}{R^2}, & R \ll 1 \end{cases} \end{aligned} \tag{20}$$

demonstrating a performance equal to the previous systems at high SNRs, but a slight relative degradation at low values of R .

References

1. Price, R., "Optimum Detection of Random Signals in Noise, With Application to Scatter-Multipath Communication," *IRE Transactions on Information Theory*, Vol. IT-2, No. 4, 1956, p. 125.
2. Helstrom, C. W., *Statistical Theory of Signal Detection*, Pergamon Press, London, England, and New York, N. Y., 1960, Chap. 9.
3. Gallager, R. G., "A Simple Derivation of the Coding Theorem and Some Applications," *IEEE Transactions on Information Theory*, Vol. IT-11, No. 1, 1965, pp. 3-18.
4. Wozencraft, J., and Jacobs, I. M., *Principles of Communication Engineering*, John Wiley & Sons, Inc., New York, N. Y., 1965.
5. Yudkin, H. L., *An Error Bound for Gaussian Signals in Gaussian Noise*, MIT-RLE-Quarterly Progress Report No. 73, Massachusetts Institute of Technology, Research Lab. of Electronics, Cambridge, Mass., 1964, pp. 149-155.

References (Cont'd)

6. Fano, R. M., *Transmission of Information*, M.I.T. Press, Cambridge, Mass., 1961, Chap. 6.
7. Van Trees, H., *Optimum Power Division in Coherent Communication Systems*, Technical Report No. 301, Massachusetts Institute of Technology, Lincoln Laboratory, Lexington, Mass., February 1963.
8. Layland, J. W., *Signal Design for Communication with Timing Uncertainties*, Ph.D. Thesis, Carnegie Institute of Technology, Pittsburgh, Pa., June 1965.
9. Stiffler, J. J., "On the Allocation of Power in a Synchronous Binary PSK Communication System," *Proceedings of the 1964 National Telemetry Conference, June 2-4, 1964* (Sponsored by AIAA, IEEE, and ISA).
10. Costas, J. P., "Synchronous Communications," *Proceedings of the IRE*, Vol. 44, December 1956, pp. 1713-1718.
11. Proakis, J. G., Drouilhet, P. R., Jr., and Price, R., "Performance of Coherent Detection Systems Using Decision-Directed Channel Measurement," *IEEE Transactions on Communication Systems*, Vol. CS-12, March 1964, pp. 54-63.
12. Layland, J. W., "An Optimum Squaring-Loop Filter," *SPS 37-37*, Vol. IV, February 28, p. 290.
13. Davenport, W. B., Jr., and Root, W. L., *Random Signals and Noise*, McGraw-Hill Book Co., Inc., New York, N. Y., 1958.

XXIV. COMMUNICATIONS SYSTEMS RESEARCH: INFORMATION PROCESSING

A. Efficiency of the Floating Aperture System of Data Compression

E. C. Posner and H. C. Rumsey, Jr.

1. Summary

The efficiency of the floating aperture system of data compression is found, relative to a theoretically most efficient system obtained from the theory of epsilon-delta entropy. Both systems are compared for the Wiener process (the class of waveforms which form the output of an ideal integrator with a white Gaussian input). It is shown that in this case the efficiency of the floating aperture system is bounded away from zero as the aperture approaches zero.

2. Introduction

The floating aperture system of data compression was introduced in *SPS 37-16*, Vol. IV, pp. 54-55. This system has an "aperture width" 2ϵ . The idea is to report changes in an input waveform only when there is a change from the last reported value of ϵ or more. Then a new aperture of width 2ϵ is put around the new value, and the procedure continues. At each change, the time as well as the direction of change must be reported from the experimental location to the data users on Earth.

The theory of $\epsilon; \delta$ ($\epsilon, \delta > 0$) entropy of probabilistic metric spaces was introduced in *SPS 37-34*, Vol. IV, pp. 292-296, and further studied in *SPS 37-35*, Vol. IV, pp. 328-331. This theory gives estimates for the minimum number of bits $H_{\epsilon; \delta}(X)$ necessary to prescribe at least $1 - \delta$ of the points of a so-called probabilistic metric space X within accuracy ϵ or better.

The probabilistic metric space X of this article is the space of outcomes of the Wiener process (or, alternatively, the process which is the integral of white Gaussian noise) on the interval $[0, 1]$. The metric is the uniform metric on the space of continuous functions of $[0, 1]$:

$$d(f, g) = \sup_{0 \leq x \leq 1} |f(x) - g(x)|.$$

The probability is the Wiener measure on this space of continuous functions; that is, the probability is the measure induced by the Wiener process. It was shown in *SPS 37-34*, Vol. IV, pp. 292-296, that under these definitions, the space X of continuous functions f on the interval $[0, 1]$, such that $f(0) = 0$, is indeed a probabilistic metric space.

Chief interest is in $H_{\epsilon; 0}(X)$, which, in this case, can be defined as the minimum entropy of all $\epsilon; 0$ partitions of X by measurable sets, that is, the infimum over all (disjoint) partitions of all of X , except for a set of measure 0,

by measurable sets of diameter at most ϵ . This article contains hints of proof of the finiteness of $H_{\epsilon;0}(X)$; another proof, using the Karhunen-Loève expansion, can be given.

Now the floating aperture system gives an $\epsilon;0$ partition of X ; the entropy of this partition is of course at least $H_{\epsilon;0}(X)$. In effect, a lower bound for the entropy of the floating aperture $\epsilon;0$ partition will be obtained. The ratio of the floating aperture entropy to $H_{\epsilon;0}(X)$ is then shown to be bounded as the variance of the Wiener process approaches infinity, ϵ fixed, or, equivalently, as the half-aperture width ϵ approaches 0, the variance fixed.

3. Entropy of the Floating Aperture System

To find the entropy of the floating aperture system, observe that at each change by ϵ one bit must be transmitted to indicate whether the change is by $+\epsilon$ or $-\epsilon$. The number of bits cannot be reduced, since given that a change of $+\epsilon$ occurs, both $+\epsilon$ and $-\epsilon$ are equally likely.

Let us for the moment ignore the fact that the time of transition must also be transmitted. Then the expected number of bits needed is the expected number of transitions. As the number of transitions on $[0,1]$ approaches infinity with probability 1, that is, as $\epsilon \rightarrow 0$, the number of transitions approaches, with probability 1, the reciprocal of the expected time for a transition of $\pm\epsilon$. But this expected time is the so-called expected first passage time (Ref. 1) for the Wiener process of unit variance starting at 0 to first exit the interval $[-\epsilon, \epsilon]$. This expected time is found in Ref. 1 to be exactly ϵ^2 . Hence, at least c/ϵ^2 bits are needed in the floating aperture system, where $c = c(\epsilon)$ approaches 1 as $\epsilon \rightarrow 0$.

An outline will be given of an argument which shows that by decreasing ϵ a little, the number of bits necessary to specify the transition times and still keep within ϵ of the sample function is finite. This gives a proof that the $\epsilon;0$ entropy of X is finite.

The idea is that when f changes by $\epsilon/2$, all that is needed to be sure that the function f is known at all times within ϵ is some point in an interval in which the function has changed by $\pm\epsilon/2$ but not by $\pm\epsilon$. Since the distribution of the first passage time has (Ref. 1) an entropy (in the sense of $\int p \log p$, where p is the first passage time density), and since the probability of a jump by more than $\epsilon/2$ in a time interval t approaches 0 very rapidly as $t \rightarrow 0$, it turns out that the time information has finite entropy for fixed ϵ . (In fact, the entropy

of each transition can be shown to be bounded as $\epsilon \rightarrow 0$.) Since the transitions are independent of each other, the number of bits needed in this modified floating aperture system, which works with probability 1, is asymptotic to a positive constant times $(2/\epsilon)^2$, i.e., asymptotic to d/ϵ^2 , $d > 0$. Hence, the number of bits needed by this modified floating aperture system is at most c/ϵ^2 for all $\epsilon > 0$, where c is a positive constant.

4. Efficiency

It has been shown that $H_{\epsilon;0}(X)$ is equal to or greater than c_1/ϵ^2 , for c_1 a positive constant; the proof of this result is deferred to a later SPS. Hence, the efficiency of the system is at least $(c_1/\epsilon^2)/(c/\epsilon^2) = c_1/c$. The conclusion is that the efficiency is greater than the positive constant c_1/c , as $\epsilon \rightarrow 0$. This result proves that the bound $H_{\epsilon;0}(X) \geq c_1/\epsilon^2$ is actually of the right order of magnitude; since, in fact, it is proved that $c_1/\epsilon^2 \leq H_{\epsilon;0}(X) \leq c/\epsilon^2$ for all small $\epsilon > 0$. This is the first time that the $\epsilon;0$ entropy of a Gaussian process has been found up to a positive constant factor.

Note that the floating aperture system transmits bits as the sample comes in, whereas the best system would have to wait for the entire sample function to be observed before starting computations and transmissions. The fact that an arbitrarily large amount is not lost by insisting on this extra requirement is encouraging.

B. The Variance of Spectral Estimates

E. Rodemich

1. Summary

The main result proved here (Theorem 3) is a generalization of a formula of Goldstein's (Ref. 2), who showed that if the estimate $\hat{S}(\omega)$ for the spectral density is computed by the use of the function $y(x) = \text{sgn}(x)$, and the spectrum is flat, then the dominant term in the variance of $\hat{S}(\omega)$ is $\frac{1}{2}\pi^2 K/N$. Theorem 3 evaluates this term for nonflat spectra and for more general functions $y(x)$. No proofs are given here due to their length.

This analysis shows that the loss in accuracy caused by working with $y(x)$ instead of x itself can be decreased

considerably by using for $y(x)$ a step function with more than two values.

2. Introduction

The spectral density $S(\omega)$, $|\omega| \leq \pi$, of a discrete stationary Gaussian process $\{x_k\}$, $-\infty < k < \infty$, of mean zero, can be expressed in terms of the correlations $R_x(k) = E(x_n x_{n+k})$ by

$$S(\omega) = \sum_{k=-\infty}^{\infty} e^{ik\omega} R_x(k) = R_x(0) + 2 \sum_{k=1}^{\infty} \cos k\omega R_x(k).$$

An estimate of $S(\omega)$ can be obtained from observations of $\{x_k\}$ by truncating the series and replacing the quantities $R_x(k)$ by appropriate estimates $\hat{R}_x(k)$. Assume that $R_x(0) = E(x_k^2)$ is known. Then the x_k 's can be normalized so that $R_x(0) = 1$, and the estimate for $S(\omega)$ is

$$\hat{S}(\omega) = 1 + 2 \sum_{k=1}^K \cos k\omega \hat{R}_x(k). \tag{1}$$

A simple choice of $\hat{R}_x(k)$ is

$$\hat{R}_x(k) = \frac{1}{N} \sum_{n=1}^N x_n x_{n+k}, \tag{2}$$

where N is large. Each term in the sum has the expected value $R_x(k)$, and the variance of this expression approaches zero as $N \rightarrow \infty$. Hence, for large N , it is close to $R_x(k)$ with high probability. However, for large N the evaluation of the sum can be quite time consuming.

It has been observed (Ref. 2) that if

$$y_i = \begin{cases} +1, & x_i \geq 0, \\ -1, & x_i < 0, \end{cases}$$

then $R_y(k) = E(y_n y_{n+k})$ satisfies the relation

$$R_x(k) = \sin \left[\frac{\pi}{2} R_y(k) \right].$$

This suggests putting

$$\left. \begin{aligned} \hat{R}_y(k) &= \frac{1}{N} \sum_{n=1}^N y_n y_{n+k}, \\ \hat{R}_x(k) &= \sin \left[\frac{\pi}{2} \hat{R}_y(k) \right]. \end{aligned} \right\} \tag{3}$$

For large N , and K small compared with N , this formula for $\hat{R}_x(k)$ can be evaluated much more rapidly than Eq. (2) (Ref. 2). The problem arises of estimating the mean and variance of $\hat{S}(\omega)$, when evaluated by Eqs. (1) and (3). It is hoped that the mean is close to $S(\omega)$, and the variance is small.

A more general method is considered here. Taking $y_i = y(x_i)$, where $y(x)$ is any odd, bounded, nondecreasing function, normalized so that $E(y_i^2) = 1$ it is shown (Lemma 3) that there is a function $F(t)$ such that

$$R_x(k) = F[R_y(k)].$$

In general, $F(t)$ is not an entire function but is analytic in a region of the complex plane, including the open interval $-1 < t < 1$. For the present purposes, $F(t)$ may be extended in any way to a continuous function on $-\infty < t < \infty$. We take

$$\begin{aligned} \hat{R}_y(k) &= \frac{1}{N} \sum_{n=1}^N y_n y_{n+k}, \\ \hat{R}_x(k) &= F[\hat{R}_y(k)]. \end{aligned}$$

With this definition, it is shown that, except for a term of order $1/N$, $E[\hat{S}(\omega)]$ is

$$S_K(\omega) = 1 + 2 \sum_{k=1}^K \cos k\omega R_x(k),$$

and $E\{\hat{S}(\omega)^2\}$ is approximately $S_K(\omega)^2$, with a leading error term of order K/N , which is given explicitly, and another error term $o(K/N)$, whose exact order depends on the degree of regularity assumed for $S(\omega)$ (Theorem 3). This result is obtained for a large class of summation methods (or windows) in place of Eq. (1), including Césaro sums.

The hypothesis on $S(\omega)$, in Theorem 3, is satisfied if $S(\omega)$ is a periodic function of bounded variation which satisfies a Lipschitz condition of order α , $\alpha > 0$ (Ref. 3, p. 136).

3. Estimates for the Moments of $\hat{R}_y(k)$

Lemma 1. Let $f(z)$, $z = (z_1, \dots, z_n)$ be analytic in a convex region D containing the origin, with $|f(z)| \leq M$. Let $\{\pi_k(z)\}$ be a set of products of the z_j 's such that, in the power series expansion of $f(z)$ at $(0, \dots, 0)$, every

term is divisible by one of the π_k 's. If ζ is a point whose δ -neighborhood

$$|z_j - \zeta_j| < \delta, \quad j = 1, \dots, n,$$

is in D , then

$$|f(\zeta)| \leq 2^n M \sum_k \left(\frac{3}{\delta}\right)^{d_k} |\pi_k(\zeta)|,$$

where d_k is the degree of π_k .

Lemma 2. Let $\{x_i\}$ be a stationary Gaussian process with mean zero and variance 1, and a spectral density $S(\omega)$, $|\omega| \leq \pi$, which is integrable.

Then for any positive m , there is a constant $\mu_m > 0$ such that any $m \times m$ covariance matrix $[R_x(p_j - p_k)]_{j,k=1,\dots,m}$, $p_1 < p_2 < \dots < p_m$, has its eigenvalues $\geq \mu_m$.

Remark. If $S(\omega)$ is bounded below by a positive constant S , we may take $\mu_m = S$ for all m .

Lemma 3. Let $y(x)$ be an odd, monotonic increasing function of x with $y(x) = O(x^n)$, as $x \rightarrow \infty$, for some power n . Let x_1 and x_2 be random variables with mean 0 and variance 1, and a bivariate Gaussian distribution. Let $y_i = y(x_i)$, $i = 1, 2$, and assume $E(y_i^2) = 1$. There is a function $f(z)$ of the complex variable z and an inverse function $F(z)$, depending only on the function $y(x)$, such that $E(y_1 y_2) = f\{E(x_1 x_2)\}$, $E(x_1 x_2) = F\{E(y_1 y_2)\}$. f and F are odd functions, analytic in a region of the complex plane containing the open interval $-1 < z < 1$. $f(\pm 1) = \pm 1$, $F(\pm 1) = \pm 1$, and $f(z)$ and $F(z)$ are continuous, increasing functions of real z on $-1 \leq z \leq 1$.

Hypothesis A. The following hypothesis will be used in several lemmas:

(1) $\{x_i\}$ is a Gaussian process with $E(x_i) = 0$, $E(x_i^2) = 1$ for all i , such that for any set of distinct integers i_1, i_2, \dots, i_m the covariance matrix $[R_x(i_j, i_k)]_{j,k=1,\dots,m}$ is positive definite with its minimum eigenvalue at least μ_m , a positive constant.

(2) $y(x)$ is an odd, bounded, nondecreasing function on $-\infty < x < \infty$ with $E[y(x_i)^2] = 1$. The random process $\{y_i\}$ is defined by $y_i = y(x_i)$.

In some of the lemmas, the full strength of the hypothesis is not necessary. For example, in the next lemma, $y(x)$ may be any bounded measurable function.

Lemma 4. Assume Hypothesis A, with $|y(x)| \leq Y$. Let n_1, \dots, n_p be integers, of which only n_{i_1}, \dots, n_{i_q} are distinct. Then there is an analytic function $F_{n_1 \dots n_p}(\{z_{kj}\}_{1 \leq k < j \leq q})$ of $\frac{1}{2}q(q-1)$ complex variables, such that

$$E(y_{n_1} \dots y_{n_p}) = F_{n_1 \dots n_p}(\{R_x(n_{i_k}, n_{i_j})\}_{1 \leq k < j \leq q}). \quad (4)$$

$F_{n_1 \dots n_p}$ depends only on the function $y(x)$ and the coincidences in the sequence n_1, \dots, n_p . It is analytic in the convex region D_p formed by the union of the regions

$$|z_{kj} - \rho_{kj}| < \mu [(\rho_{mn})]/4p, \quad 1 \leq k < j \leq q, \quad (5)$$

where (ρ_{mn}) is any positive definite symmetric $q \times q$ matrix with 1's along the diagonal, and $\mu [(\rho_{mn})]$ is its minimum eigenvalue. In D_p ,

$$|F_{n_1 \dots n_p}(\{z_{kj}\})| < [(2)^{1/2} Y]^p. \quad (6)$$

In particular, this inequality is valid if

$$|z_{kj} - R_x(n_{i_k}, n_{i_j})| < \mu_p/4p, \quad 1 \leq k < j \leq q.$$

Lemma 5. Assume Hypothesis A. Let p be a fixed positive integer, and let $n_j, m_j, j = 1, \dots, p$ be integers, with $m_j > n_j$. Then

$$E \left\{ \prod_{j=1}^p [y_{n_j} y_{m_j} - E(y_{n_j} y_{m_j})] \right\} = O(\sum |\pi^{(p)}|)$$

where the sum is over all products $\pi^{(p)}$ of correlations $R_x(l_1, l_2)$ with l_1, l_2 taken from $\{n_1, \dots, m_p\}$ and $l_1 \neq l_2$, which have the following properties, and are minimal in this respect:

(1) Each of the $2p$ letters appears an odd number of times.

(2) For each pair (n_j, m_j) , there is an even number of factors, at least two, with exactly one index in the pair (n_j, m_j) .

Lemma 6. Assume Hypothesis A. Let $\{x_i\}$ be stationary, with a spectral density $S(\omega)$, $|\omega| \leq \pi$, which is in L^2 . Let

$$R_y(k) = E(y_n y_{n+k}),$$

$$\hat{R}_y(k) = \frac{1}{N} \sum_{n=1}^N y_n y_{n+k}.$$

Let p be a fixed positive integer. Then for large N and arbitrary positive k_1, \dots, k_p ,

$$E \left\{ \prod_{j=1}^p [\hat{R}_y(k_j) - R_y(k_j)] \right\} = O(N^{-p/2}).$$

Lemma 7. In Lemma 6, if the condition

$$\sum_{-\infty}^{\infty} |R_x(k)| < \infty$$

is added, then

$$E \left\{ \prod_{j=1}^p [\hat{R}_y(k_j) - R_y(k_j)] \right\} = O(N^{-[(p+1)/2]}),$$

where $[(p+1)/2]$ denotes the integral part of $(p+1)/2$.

Theorem 1. Let $G(z_1, \dots, z_m)$ be analytic in a domain of complex m -space, which contains the set

$$-1 < z_j < 1, \quad j = 1, \dots, m,$$

and let $G(z_1, \dots, z_m)$ be defined and bounded when all the z_j 's are real.

Let $\{x_i\}$ be a stationary Gaussian process with mean 0 and variance 1, and a spectral density $S(\omega) \in L^2$. Let $y(x)$ be an odd, bounded, nondecreasing function with $E[y(x_i)^2] = 1$. Put

$$\begin{aligned} y_i &= y(x_i), \\ R_y(k) &= E(y_n y_{n+k}), \\ \hat{R}_y(k) &= \frac{1}{N} \sum_{n=1}^N y_n y_{n+k}. \end{aligned}$$

Then for fixed p , large N , and arbitrary $k_1, \dots, k_m > 0$,

$$\begin{aligned} E \{ G[\hat{R}_y(k_1), \dots, \hat{R}_y(k_m)] \} &= G[R_y(k_1), \dots, R_y(k_m)] \\ &+ \sum_{2 \leq q_1 + \dots + q_m \leq p} a_{q_1 \dots q_m} E \left\{ \prod_{j=1}^m [\hat{R}_y(k_j) - R_y(k_j)]^{q_j} \right\} \\ &+ O(N^{-(p+1)/2}), \end{aligned} \tag{7}$$

where

$$\begin{aligned} a_{q_1 \dots q_m} &= \frac{1}{q_1! \dots q_m!} \left(\frac{\partial}{\partial z_1} \right)^{q_1} \dots \left(\frac{\partial}{\partial z_m} \right)^{q_m} \\ &G(z_1, \dots, z_m) \Big|_{z_j = R_y(k_j), \quad j=1, \dots, m}. \end{aligned}$$

Theorem 1a. If in addition to the hypotheses of Theorem 1,

$$\sum_{-\infty}^{\infty} |R_x(k)| < \infty,$$

the error term in Eq. (7) is $O(N^{-[(p+1)/2]})$.

4. The Main Theorem

Lemma 9. Assume Hypothesis A.

$$\begin{aligned} (1) \quad E(y_{n_1} y_{n_2} y_{n_3} y_{n_4}) &= R_y(n_1, n_2) R_y(n_3, n_4) \\ &+ R_y(n_1, n_3) R_y(n_2, n_4) \\ &+ R_y(n_1, n_4) R_y(n_2, n_3) \\ &+ O(\sum |\pi_3|), \end{aligned}$$

where the sum is over all products π_3 of three distinct correlations $R_x(n_j - n_{j'})$ with $j \neq j'$ such that each index n_1, \dots, n_4 occurs in the product.

(2) Let $v_j = y_{n_j} y_{m_j} - E(y_{n_j} y_{m_j})$, $j = 1, \dots, 4$. Then

$$\begin{aligned} E(v_1 v_2 v_3 v_4) &= E(v_1 v_2) E(v_3 v_4) \\ &+ E(v_1 v_3) E(v_2 v_4) \\ &+ E(v_1 v_4) E(v_2 v_3) \\ &+ O(\sum |\pi_3^*|), \end{aligned}$$

where the sum is over all products π_3^* of three distinct correlations $R_x(q_j, q_{j'})$ with $q_j = n_j$ or m_j , $q_{j'} = n_{j'}$ or $m_{j'}$, such that the three pairs (j, j') include 1, 2, 3 and 4.

Lemma 10. Assume Hypothesis A, with $\{x_i\}$ stationary and

$$\sum_{-\infty}^{\infty} |R_x(k)| < \infty.$$

Let

$$\begin{aligned} R_y(k) &= E(y_n y_{n+k}), \\ \hat{R}_y(k) &= \frac{1}{N} \sum_{n=1}^N y_n y_{n+k}. \end{aligned}$$

Then for arbitrary $N, K > 0$

$$\sum_{k, l=1}^K E \{ [\hat{R}_y(k) - R_y(k)] [\hat{R}_y(l) - R_y(l)] \} = O\left(\frac{K}{N^2} + \frac{K^2}{N^3}\right), \quad (8)$$

for $m = 3$ or 4 and $0 \leq t \leq m$,

$$\sum_{k, l=1}^K (|R_y(k)| + |R_y(l)|) E \{ [\hat{R}_y(k) - R_y(k)]^t [\hat{R}_y(l) - R_y(l)]^{m-t} \} = O\left(\frac{K}{N^2}\right), \quad (9)$$

if $|a_k|, |b_k| \leq 1, k = 1, \dots, K$,

$$\begin{aligned} & \sum_{k, l=1}^K a_k b_l E \{ [\hat{R}_y(k) - R_y(k)] [\hat{R}_y(l) - R_y(l)] \} \\ &= \sum_{k, l=1}^K a_k b_l \frac{1}{N^2} \sum_{n_1, n_2=1}^N [R_y(n_1 - n_2) R_y(n_1 - n_2 + k - l) R_y(n_1 - n_2 + k) R_y(n_1 - n_2 - l)] + O(N^{-1}), \end{aligned} \quad (10)$$

$$\sum_{k, l=1}^K (|R_y(k)| + |R_y(l)|) E \{ [\hat{R}_y(k) - R_y(k)] [\hat{R}_y(l) - R_y(l)] \} = O(N^{-1}), \quad (11)$$

$$\sum_{k, l=1}^K |R_y(k) R_y(l)| E \{ [\hat{R}_y(k) - R_y(k)]^2 \} = O(N^{-1}), \quad (12)$$

Let $\{x_i\}$ be a stationary Gaussian process with mean 0 and variance 1, with

and

$$\sum_{-\infty}^{\infty} |R_x(k)| < \infty.$$

$$\sum_{k=1}^K |R_y(k)| E \{ [\hat{R}_y(k) - R_y(k)]^2 \} = O(N^{-1}). \quad (13)$$

Let $y(x)$ be an odd, bounded, nondecreasing function with $E \{y(x_i)^2\} = 1$. Let

$$y_i = y(x_i),$$

$$R_y(k) = E(y_n y_{n+k}),$$

$$\hat{R}_y(k) = \frac{1}{N} \sum_{n=1}^N y_n y_{n+k}.$$

Theorem 2. Let $G(z)$ and $H(z)$ be odd functions, analytic in a region including the interval $-1 < z < 1$ and defined and bounded for all real z . Let $a_k, b_k, k = 1, 2, \dots$ be numbers of absolute value at most 1.

Then for arbitrary positive integers K, N ,

$$E \left\{ \sum_{k=1}^K a_k G[\hat{R}_y(k)] \right\} = \sum_{k=1}^K a_k G[R_y(k)] + O(N^{-1} + KN^{-2}), \quad (14)$$

$$\begin{aligned} E \left\{ \sum_{k, l=1}^K a_k b_l G[\hat{R}_y(k)] H[\hat{R}_y(l)] \right\} &= \sum_{k, l=1}^K a_k b_l G[R_y(k)] H[R_y(l)] \\ &+ G'(0) H'(0) \sum_{k, l=1}^K a_k b_l \frac{1}{N^2} \sum_{n_1, n_2=1}^N [R_y(n_1 - n_2) R_y(n_1 - n_2 + k - l) \\ &+ R_y(n_1 - n_2 + k) R_y(n_1 - n_2 - l)] + O(N^{-1} + K^2 N^{-3}). \end{aligned} \quad (15)$$

Lemma 11. Let $g(\omega)$, $|\omega| \leq \pi$, have the fourier series

$$g(\omega) = \sum_{k=-\infty}^{\infty} a_k e^{ik\omega}.$$

Let $f(z)$ be analytic in $|z| < \rho$, with $f(0) = f'(0) = f''(0) = 0$. Let b_k , $-\infty < k < \infty$, be such that $b_k = f(a_k)$, if $|a_k| < \rho$. If $g(\omega)$ has bounded variation, and

$$\sum_{-\infty}^{\infty} |a_k| < \infty,$$

then the function

$$h(\omega) = \sum_{k=-\infty}^{\infty} b_k e^{ik\omega}$$

has a continuous second derivative.

Theorem 3. Let $\{x_i\}$ be a stationary Gaussian process with $E(x_i) = 0$, $E(x_i^2) = 1$,

$$\sum_{-\infty}^{\infty} |R_x(k)| < \infty,$$

and a spectral density $S(\omega)$, $|\omega| \leq \pi$, which is a function of bounded variation.

Let $y(x)$ be an odd, bounded, nondecreasing function on $-\infty < x < \infty$, such that $E[y(x_i)^2] = 1$. Define $y_i = y(x_i)$ and

$$\hat{R}_y(k) = \frac{1}{N} \sum_{n=1}^N y_n y_{n+k}.$$

Let $S_y(\omega)$ be the spectral density of $\{y_i\}$.

Let $F(z)$ be the function of Lemma 3, with its definition extended to all real z so that $F(z)$ is bounded for z real.

Let $\{c_k, k = 1, \dots, K\}$ be a nonincreasing sequence of numbers with $c_1 \leq 1, c_K \geq 0$.

Define

$$\hat{S}(\omega) = 1 + 2 \sum_{k=1}^K c_k \cos k\omega F[\hat{R}_y(k)],$$

$$S_K(\omega) = 1 + 2 \sum_{k=1}^K c_k \cos k\omega R_x(k).$$

Then for any positive integers K, N with $K \leq N$,

$$E\{\hat{S}(\omega)\} = S_K(\omega) + O(N^{-1}) \tag{16}$$

and for $0 < \omega < \pi$

$$E\{\hat{S}(\omega)^2\} = S_K(\omega)^2 + \frac{2\gamma K}{N} F'(0)^2 S_y(\omega)^2 + \mathcal{E}, \tag{17}$$

where

$$\gamma = \frac{1}{K} \sum_{k=1}^K c_k^2$$

and \mathcal{E} satisfies the following bounds:

(1) For ω such that

$$S(\omega') = S(\omega) + O(|\omega - \omega'|^\alpha), \tag{18}$$

$0 < \alpha \leq 1$,

$$\mathcal{E} = \begin{cases} O(K^{1-\alpha} N^{-1}), & 0 < \alpha < 1, \\ O([1 + \log K] N^{-1}), & \alpha = 1. \end{cases} \tag{19}$$

(2) If ω is such that the derivative $S'(\omega)$ exists, and

$$S(\omega') = S(\omega) + (\omega' - \omega) S'(\omega) + O(|\omega' - \omega|^{1+\beta}), \tag{20}$$

$\beta > 0$,

$$\mathcal{E} = O(N^{-1}). \tag{22}$$

Remark. The formula for the variance of $S(\omega)$ may be given more explicitly than by Theorem 3 for simple choices of $S(\omega)$. For example, if

$$S(\omega) = 1 + 2R_x(1) \cos \omega,$$

in the terms of order N^{-1} , only the quantities

$$\rho = E(y_1 y_2),$$

$$\sigma = E(y_1 y_2 y_3 y_4),$$

$$v = E(y_1^2 y_2^2),$$

$$\tau = E(y_1 y_2^2 y_3),$$

$$\tau' = E(y_1^2 y_2 y_3)$$

enter. For ordinary partial sums ($c_1, \dots, c_K = 1$),

$$\begin{aligned} \frac{1}{\pi} \int_0^\pi \text{Var} [S(\omega)] d\omega &= \frac{2K}{N} F'(0)^2 \cdot \frac{1}{\pi} \int_0^\pi S_y(\omega)^2 d\omega \\ &- \frac{1}{N} F'(0)^2 [2 + 8\rho + 2v + 4\tau + 8\sigma - 18\rho^2] \\ &- \frac{1}{N} [F'(0)^2 - F'(\rho)^2] [2v + 4\tau + 4\sigma - 10\rho^2] \\ &+ O(KN^{-2}). \end{aligned}$$

For small values of $R_r(1)$, the effect of the terms after the first on the right is to decrease the average variance.

5. The Value of $F'(0)$

If $\hat{S}(\omega)$ is evaluated by the original method of the introduction (using $y(x) = x$), it is easily verified that the conclusion of Theorem 3 applies; e.g., if $S(\omega)$ satisfies hypothesis (2) of Theorem 3,

$$E \{ \hat{S}(\omega)^2 \} = S_K(\omega)^2 + \frac{2\gamma K}{N} S(\omega)^2 + O(N^{-1}),$$

for $0 < \omega < \pi$. The term of order K/N given in Theorem 3 differs from this by the replacement of $S(\omega)^2$ by $S_y(\omega)^2$ and the introduction of the factor $F'(0)^2$.

It can be shown that $S_y(\omega)$ always lies between the same bounds as $S(\omega)$, and has the same average value. Thus, the effect of the factor $S_y(\omega)$ is to increase the variance of $\hat{S}(\omega)$ in some places, and decrease it in others.

The factor $F'(0)^2$ gives a uniform increase in variance for all ω . By differentiating the equation for $f(z)$ in Lemma 3, it can be shown that

$$F'(0) = 1/f'(0) = E \{ xy(x) \}^{-2}.$$

In particular, for $y(x) = x$, $F'(0) = 1$, and for $y(x) = \text{sgn}(x)$, $F'(0) = \pi/2$. It can be shown that for any other choice of $y(x)$, which is an odd nondecreasing function such that $E \{ y(x)^2 \} = 1$, $F'(0)$ lies between these limits.

It is advantageous to pick a function for $y(x)$ such that the computation of $\hat{R}_y(k)$ can be done rapidly, and $F'(0)$ is close to 1. The computation is simple, if $y(x)$ is a step

function taking only a few values. This leads us to consider a function of the type

$$\begin{aligned} y(x) &= a_j, & c_{j-1} < x < c_j, & \quad j = 1, \dots, n, \\ y(-x) &= -y(x), \end{aligned}$$

where $0 = c_0 < c_1 < \dots < c_n = +\infty$, $0 \leq a_1 < \dots < a_n$. For a given value of n , the numbers a_j, c_j may be chosen so as to minimize $F'(0)$, given $E \{ y(x)^2 \} = 1$. This must be done numerically for $n \geq 2$. The best choices for $n = 2, 3$ are:

$$n = 2: \quad a_1 = 0.482,$$

$$a_2 = 1.608,$$

$$c_1 = 0.981, \quad F'(0) = 1.133.$$

$$n = 3: \quad a_1 = 0.327,$$

$$a_2 = 1.030,$$

$$a_3 = 1.951,$$

$$c_1 = 0.659,$$

$$c_2 = 1.447, \quad F'(0) = 1.062.$$

Comparing with the value $F'(0) = 1.571$ when $n = 1$, it is seen that taking $n = 2$ reduces $F'(0)$ most of the way to 1.

In construction of an autocorrelator using such a step function, it is convenient if all nonzero values of $y(x)$ have ratios which are powers of 2. If the function given above for $n = 2$ is modified by making $a_2 = 4a_1$, and then the best value of c_1 is chosen, the function obtained is

$$y(x) = \begin{cases} 1.608, & x > 0.943, \\ 0.402, & 0 < x < 0.943, \\ -y(-x), & x < 0, \end{cases}$$

for which $F'(0) = 1.137$. This is almost the same value as that given above, showing that the value of $F'(0)$ is not very sensitive to small changes in the constants. The function $F(z)$ is plotted for this case in Fig. 1. Note that it is essentially linear until $|z|$ is close to 1.

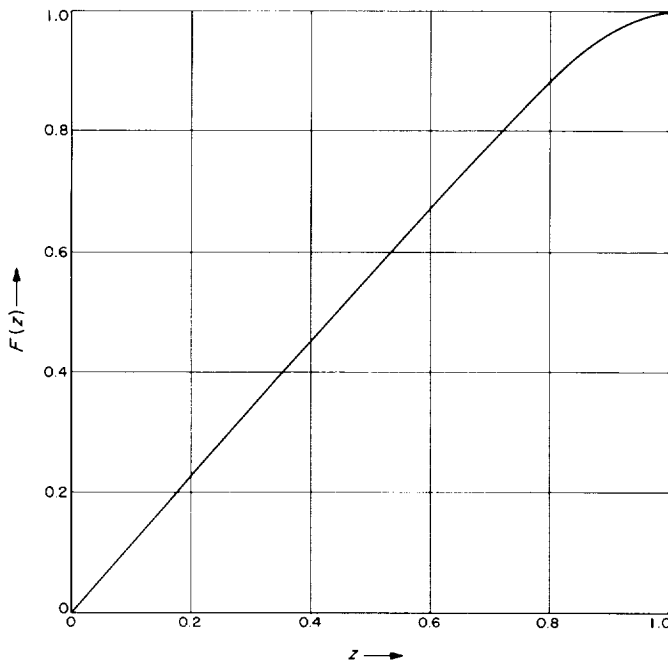


Fig. 1. The function $F(z)$ when $y(x)$ takes four values with a ratio 1:4

Another choice of $y(x)$, which is easier to work with, is given by taking $n = 2, a_1 = 0$. The minimum of $F'(0)$ is 1.232, occurring for the function

$$y(x) = \begin{cases} 1.36, & x > 0.612, \\ 0, & x < 0.612, \\ -1.36, & x < -0.612. \end{cases}$$

For $n = 2, a_2 = 2a_1$, the corresponding values are $a_1 = 0.7095, c_1 = 0.9765, F'(0) = 1.188$.

C. An Easily Encodable and Decodable Code of Constant Weight

H. Fredricksen and G. Solomon

1. Introduction

In SPS 37-35, Vol. IV, p. 347, the (23, 12) Golay code was found to have $56 \cdot 23$ vectors of weight 12 and $56 \cdot 23$ complementary vectors of weight 11. To affect systematic encoding of such a complete nonlinear set of vectors is

impossible. However, 2^n such vectors may be extracted and a nonlinear (24, 9) code systematically encoded with all vectors of weight 12, the distance between each vector being greater than or equal to eight. Such a code may find application in a spacecraft command system, where the property that the words have constant weight approximately half the length is useful to prevent spurious side-band lock.

2. Systematic Encoding

By systematic encoding we mean we may choose k bits arbitrarily and give $(n - k)$ parity checks on these bits by some algebraic rule. To obtain $k = 9$, we stipulate the following rule: Let $f(x)$ be the recursion polynomial degree 12 of the ordinary Golay (23, 12) code

$$f(x) = (x + 1)(x^{11} + x^9 + x^7 + x^6 + x^5 + x + 1) \\ = x^{12} + x^{11} + x^{10} + x^9 + x^8 + x^5 + x^2 + 1.$$

The recursion rule, given $(a_0, a_1, \dots, a_{11})$, is simply

$$a_{n+12} = a_{n+11} + a_{n+10} + a_{n+9} + a_{n+8} + a_{n+5} + a_{n+2} + a_n, \\ n = 0, 1, 2, \dots, 10.$$

We shall allow (a_0, a_1, \dots, a_8) to be chosen arbitrarily and shall choose a_9, a_{10}, a_{11} in such a fashion that when fed into the shift register in the recursion rule, all vectors will have weight 12 or 11. If we further stipulate that another bit a_{23} be added such that

$$a_{23} = \sum_{i=0}^{22} a_i$$

then we have a (24, 9) systematic code, all words of which have weight 12 and have the Golay code error correcting properties; i.e., $d = 8$. This code can correct three errors and detect four or seven errors.

We first construct a (23, 8) systematic code in which all vectors have weight 12. Let $0 \leq \alpha \leq 2^8 - 1$ be written in binary form out to 8 places; i.e., $\alpha = 3$ is written 00000011; $\alpha = 250$ is written 11111010. For any $\alpha = (a_0, a_1, \dots, a_7)$, we would like to adjoin a 3-tuple (a_8, a_9, a_{10}) with the property that the vector (a_0, \dots, a_{22}) generated by $a_0, a_1, a_2, \dots, a_{10}$ has weight 12. For any given 8-tuple there are 2^9 possible 3-tuples we could adjoin, and a computer search has verified that there exists at least one 3-tuple for each 8-tuple having the desired property. (If we were to stipulate 9-bits, we could not ask for and get a 2-tuple that would yield the same results.) Thus, corresponding to every integer from 0 to 255, there is at least one integer from 0 to 7 which, when written in

binary form as $a_8 a_7 a_6 a_5 a_4 a_3 a_2 a_1 a_0$, yields as the resulting Golay vector a word of weight 12.

Since all vectors of weight 11 are obtained by complementing the full 23-bit vector, we obtain 256 words of weight 11 by complementing these. Thus, the rule for integers α , $0 \leq \alpha \leq 511$, is simply to write out α in binary form of 9 bits, with the bit corresponding to 2^8 as the rightmost—i.e., 259 is written 110,000,001. To encode, consider the integer $\alpha - 2^8 a_8$. This is less than 256 and can be encoded via the above-mentioned rule—as a weight-12 vector, μ say. Now examine a_8 . If $a_8 = 0$, send this vector, μ , as is, with a_{23} added on. If $a_8 = 1$, then complement the vector μ , and send it as a weight 11 word, with a_{23} added on. Observe that in the (24, 9) code, a_{23} will always equal a_8 .

3. Decoding

For decoding purposes, after correcting for errors in any fashion that works for the Golay code, the decoder examines a_{23} . If $a_{23} = 0$, it reads the message sent as $a_{23}, a_0^1, a_1^1, \dots, a_7^1$ where $a_0^1, a_1^1, \dots, a_7^1$ are the first eight bits in the decoded word. If $a_{23} = 1$, it reads the information bits as $a_{23}, a_0^1 + 1, a_1^1 + 1, \dots, a_7^1 + 1$. Thus, the (24, 9) systematic code has one additional complication in decoding. This is the table look-up device for integers less than 256, as well as the complementing procedure for integers between 256 and 511.

After decoding, some extra error-detection is still present—the length-23 decoded word must, of course, have weight 12. In fact, merely to error detect on board the spacecraft, a counter on the received word could be used. If other than 12 ones are counted, an error is detected. This is an especially powerful error-detection method for asymmetric channels, such as command channels often are (Ref. 4).

D. Simplified Decoding of the Maximal Length Shift Register Code

G. Solomon

1. Summary

We present a decoding procedure which reduces the decoding of the $(2^k - 1, k)$ shift register codes to two

decoding procedures in the smaller $(2^{k-1} - 1, k - 1)$ maximal length shift register code. Thus, the problem of decoding higher order errors is reduced to the finding of errors of at most half the number. By continuing the procedure, the problem can be reduced to finding single errors in the (7, 3) maximal shift register code.

Let A be a $(2^k - 1, k)$ maximal length shift code. The $(2^k - 1)$ coordinates correspond naturally to the $(2^k - 1)$ roots of unity, the nonzero elements of $GF(2^k)$, and the Galois field of 2^k elements. The usual algebraic decoding procedure (Ref. 5) involves computing the symmetric power sums and the evaluation of $t \times t$ determinants, where t goes from 2 to $2^{k-2} + 1$. To avoid evaluating larger and larger determinants, we reduce the problem to two smaller problems.

Let us consider the set $G = \{\alpha \in GF(2^k): Tr \alpha = 0\}$. The trace $Tr(\alpha)$ is defined to be $Tr(\alpha) = \alpha + \alpha^2 + \alpha^4 + \dots + \alpha^{2^{k-1}}$. One notes that G is an additive group (including 0) of dimension $(k - 1)$. The set

$$G' = \{\alpha: Tr \alpha = 1\}$$

has 2^{k-1} elements of the form $\beta + G$, $\beta \in G'$. It is important to observe that if we examine the code at the positions $\alpha \in G - \{0\}$, we have a $(2^{k-1} - 1, k - 1)$ maximal-length shift register code under a suitable permutation of the coordinates. The code consisting of the points G' is simply a $(2^k, k)$ code which is the cyclic $(2^k - 1, k)$ code, (the $(2^k - 1, k - 1)$ code with the all one vector) plus a parity check on all the $2^k - 1$ bits. Both G and G' correct 2^{k-3} errors under the usual cyclic decoding procedures.

We return to the code A . A code word a is sent and is received with $t \leq 2^{k-2}$ errors. Let us examine a in the positions G and G' ; call these shorter words \bar{a} and \bar{a}' . Clearly, at least \bar{a} or \bar{a}' has been received with $t' < 2^{k-3}$ errors. Decoding \bar{a} and \bar{a}' in G and G' as cyclic codes for $t < 2^{k-3}$ errors, we are able to obtain $(k - 1)$ information bits in G and k information bits in G' .

For the $(k - 1)$ decoded information bits G , we need only decode a k th information bit from one of the coordinates in G' . This can be done by choosing one bit from G' , assuming it to be correct, and generating the complete code word \bar{b} , or assuming this bit to be incorrect and complement it and then generate a complete code word \bar{b}' . From the k information bits obtained by the decoding procedure in G' , we generate the complete code word \bar{b}'' . The final step is to take the minimum of

$d(a, \bar{b})$, $d(a, \bar{b}')$ and $d(a, \bar{b}'')$. Clearly, at least one of the sets G and G' will have $< 2^{k-3}$ errors, and choosing the minimum above will vitiate an error which arises from more than 2^{k-3} errors in either G or G' .

For large k , this method will save computations and time, especially for channels where t errors occur for $2^{k-3} < t < 2^{k-2}$. Clearly, we may continue subdividing, in this fashion, the sets G and G' .

2. Example

Let A be the (15, 4) maximal-length shift-register code ($d = 8$), which corrects three errors. The code is generated

by the recursion $a_{n+1} = a_{n+1} + a_n$. Let three errors be made in the sent vector 10001001101111, in the positions 2, 3, and 9; i.e.; 10111001111111. The set $G = \{0, 1, 2, 4, 8, 5, 10\}$, $G' = \{3, 6, 7, 9, 11, 12, 13, 14\}$. The code word a for the G -positions has one error in the second position. In G' there are 2 errors, so \bar{a}' is incorrectable if only G' is considered.

Thus we solve in G for the error positions and obtain 1001011 as the decoded vector with 100 as a correct set of three bits. Choosing the fourth information bit from position three in G' as 0 or 1, we obtain 1000 or 1001 as the $k = 4$ information bits. A comparison of minimum distances yields 1000 as the correct set of information bits.

References

1. Darling, D. A., and Siegert, A. J. F., "The First Passage Problem for a Continuous Markov Process," *Ann. Math. Statist.*, Vol. 24, pp. 624-639, 1953.
2. Goldstein, R. M., *Radar Exploration of Venus*, Thesis, California Institute of Technology, Pasadena, California, 1962.
3. Zygmund, A., *Trigonometrical Series*, 2nd edition, Chelsea, New York, 1952.
4. Ashlock, J. C., and Posner, E. C., *Application of the Statistical Theory of Extreme Values to Spacecraft Receivers*, Jet Propulsion Laboratory Technical Report No. TR 32-737, Pasadena, California, May, 1965.
5. Peterson, W. W., *Error Correcting Codes*, John Wiley & Sons, New York, 1961.

XXV. Communications Systems Research: Communication and Tracking

A. Optimum Modulation Indices for Single-Channel, One-Way and Two-Way Coherent Communication Links

W. C. Lindsey

1. Introduction

In the design of two-way communication links (SPS 37-31, -32, -33, -34, -35, Vol. IV, pp. 374-379, 284-288, 290-296, 242-247, and 339-341, respectively), it is necessary to know how the total transmitter power should be allocated between the transmitted carrier and one or more subcarriers. Results presented herein permit the ratio of the power in the carrier to the total power transmitted, say m^2 , to be specified so that the system error probability is a minimum. Results are given for both one-way and two-way links.

2. Model

In the following discussion, the notation and results reported in the above issues of the SPS shall be utilized. Briefly, a two-way coherent communication link may be defined as one which radiates a phase-modulated RF carrier from the Earth to the spacecraft; the spacecraft

coherently tracks the noise-corrupted carrier component by means of a phase-locked loop. The phase-locked loop estimate of the frequency and phase of the observed carrier-component is used (after appropriate frequency translation) as a carrier for the transmission of telemetry back to Earth.

Since carrier tracking is noisy, the phase-locked loop estimate of the phase possesses a random perturbation which affects the performance of the ground-based telemetry demodulator. Thus, the observed data on Earth is perturbed by both the uplink and downlink additive noise. Consequently, the modulation index, which minimizes the error probability for the downlink, is generally different from that of the uplink.

It was shown (SPS 37-33) that $P_E(2)$, the bit error probability in an uncoded biphas-modulated telemetry system for the ground system telemetry demodulator, is given by

$$P_E(2) = \frac{1}{\pi} \int_0^\pi \frac{I_0(|\alpha_1 + \alpha_2 \exp(j\phi)|)}{I_0(\alpha_1) I_0(\alpha_2)} d\phi$$

$$\int_{(2R_D)^{1/2} \cos \phi}^\infty \frac{1}{(2\pi)^{1/2}} \exp(-y^2/2) dy \quad (1)$$

where R_D is the signal-to-noise ratio (SNR) in the data; α_1 , the SNR in the spacecraft-carrier tracking loop; α_2 is the SNR in the ground receiver carrier-tracking loop; ϕ is the ground system phase error; and $I_0(x)$ is the imaginary Bessel function of zero order and of argument x . The bit error probability for the command link (uplink) is given by

$$P_E(1) = \lim_{\alpha_1 \rightarrow \infty} P_E(2) \quad (2)$$

More precisely, the basic parameters given in Eq. (1) are:

$$R_{D2} = (1 - m_2^2) P_2 T_{b2} (1 - \lambda_2) / N_{02} = (1 - m_2^2) R_2$$

$$m_2^2 = P_{c2} / P_2 = \frac{\text{power in carrier component}}{\text{total power transmitted}}$$

T_{b2} = duration of downlink's RF phase modulation

λ_2 = signal cross-correlation coefficient
= -1 for biphasic modulation

N_{02} = noise spectral density perturbing the downlink, assumed white and single-sided

$$\alpha_2 = 2m_2^2 P_2 / N_{02} B_{L2} = m_2^2 \delta_2 R_2$$

$$\alpha_1 = \frac{2m_1^2 P_1}{N_{01} B_{L1}} K^1(\beta)$$

P_1 = total power transmitted on up-link

N_{01} = noise spectral density perturbing the uplink, assumed white and single-sided

B_{L1} = bandwidth of the carrier-tracking loop in the spacecraft

B_{L2} = bandwidth of the carrier-tracking loop in the ground receiver

$$\delta_2 = \frac{2 \cdot R_2}{B_{L2} (1 - \lambda_2)} \frac{1}{T_{b2} B_{L2} (1 - \lambda_2)}$$

$$K(\beta) = \frac{2G^2}{3} \beta \left[\frac{(1 + \beta)^2 - \beta + \beta^2/2}{(1 + \beta)^3 - 2\beta(1 + \beta)} \right]; \quad \beta = \frac{B_{L1}}{B_{L2}}$$

$$R_2 = \frac{1}{T_{b2}} = \text{downlink data rate}$$

and G is the static phase gain and is determined by the ratio of the output frequency to the input frequency. In practice $K(\beta)$ is approximately one.

The integrals in Eqs. (1) and (2) may be evaluated; however, the desire to place the result into closed form

seems, at this point, to be unrewarding. In any case, it is possible to show that Eqs. (1) and (2) may be written as

$$P_E(2) = \frac{1}{2} \left\{ 1 - \left(\frac{2R_n [1 - m_n^2]}{\pi} \right)^{1/2} \exp \left[- \frac{R_n}{4} (1 - m_n^2) \right] \times \sum_{k=0}^{\infty} (-1)^k \varepsilon_k b_{2k+1}(n) \frac{I_k \left[\frac{R_n}{4} (1 - m_n^2) \right]}{1 - 4k^2} \right\} \quad (3)$$

$n = 1, 2$

where

$$b_{2k+1}(n) = \prod_{i=1}^n \frac{I_k(\alpha_i)}{I_0(\alpha_i)}$$

and $\varepsilon_k = 1$ if $k = 0$, and $\varepsilon_k = 2$, if $k \neq 0$.

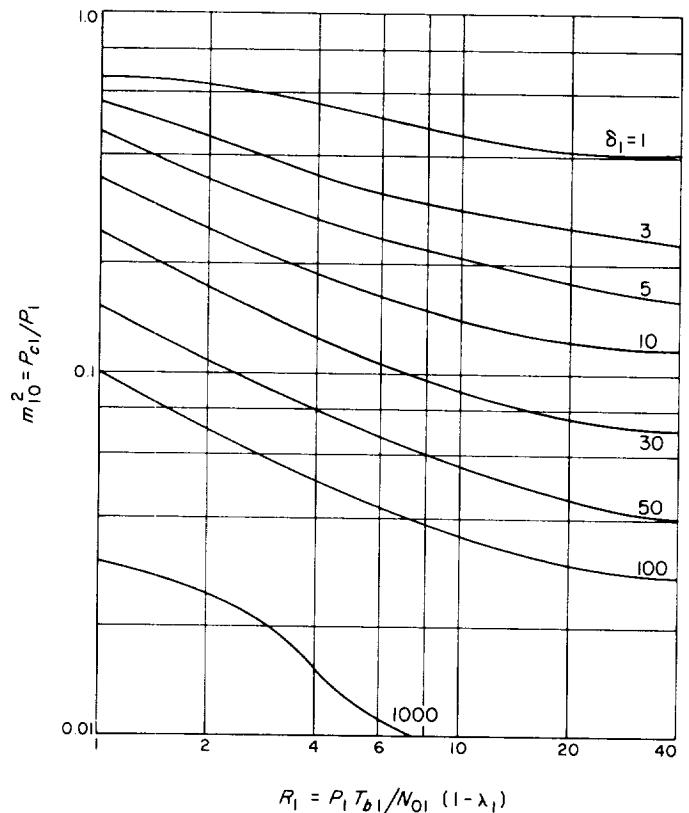


Fig. 1. Optimum modulation index vs R_1 for various values of δ_1

3. Results

It is quite apparent that any attempt to find the value of m_n , which minimizes $P_E(n)$ by the method of differentiation, presents formidable difficulties; however, the surface generated by Eq. (3) has been studied recently on the IBM 7090 Computer.

To illustrate the results graphically, consider the one-way link, i.e., $\alpha_1 = \infty$. Fig. 1 represents a plot of the parameters R_1 and the value of m_1 which minimize, say

$m_{10}^* = P_{c1}/P_1, P_E(1)$ for various values of the parameter $\delta_1 = 2 \cdot R_1 / B_{L1} (1 - \lambda_1)$. These results have been obtained by fixing R_1 and searching, on the IBM 7090 computer, for that value of m_1 which minimizes $P_E(1)$, say $P_{E0}(1)$. The corresponding plot of $P_{E0}(1)$, i.e., minimum error probability, versus R_1 is given in Fig. 2. These two figures may be used in carrying out a particular design.

Fig. 3 represents a plot of the parameters R_2 and m_{20}^* , i.e., the value of m_2 which minimizes $P_E(2)$, say $P_{E0}(2)$. In this case the SNR α_2 , in the vehicle carrier-tracking loop, has been set to 9 db. This corresponds to a "near-threshold" condition in the spacecraft's carrier-tracking loop. The results in Fig. 3 have been obtained by fixing R_2 and α_2 and searching, by means of the IBM 7090 computer, for that value of m_2 , say $m_{20}^* = P_{c2}/P_2$, which minimizes $P_E(2)$, say $P_{E0}(2)$. Finally, Fig. 4 represents a plot of $P_{E0}(2)$ versus R_2 for various values of the parameter $\delta_2 = 2 \cdot R_2 \cdot B_{L2} (1 - \lambda_2)$ and $\alpha_1 = 9$ db. Notice that the behavior of $P_{E0}(2)$ versus m_{20}^* is similar to that obtained for the one-way link. The major difference is that for large R_2 , the $P_{E0}(2)$ versus m_{20}^* characteristic exhibits a bottoming (irreducible error probability) behavior which is due to the presence of additive noise on the uplink. The bottoming behavior can be eliminated by using a "clean" carrier reference in the vehicle or by increasing the up-link SNR α_1 to a point where the phase-jitter in

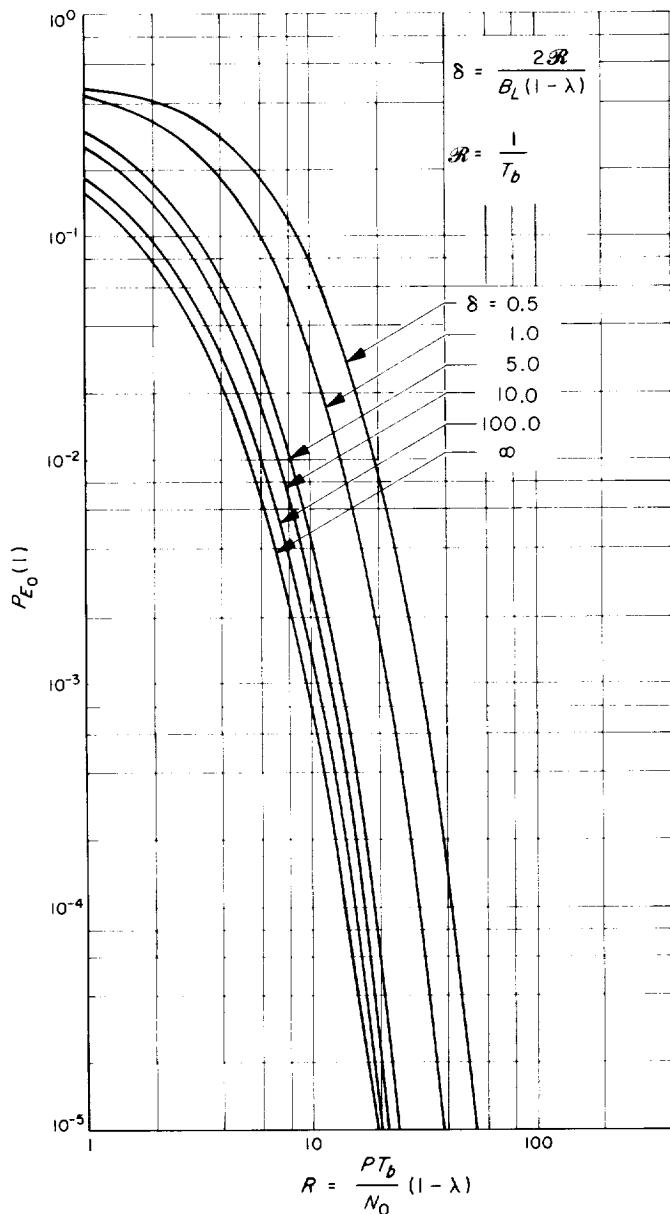


Fig. 2. Error probability $P_{E0}(1)$ vs R_1 for various values of δ_1

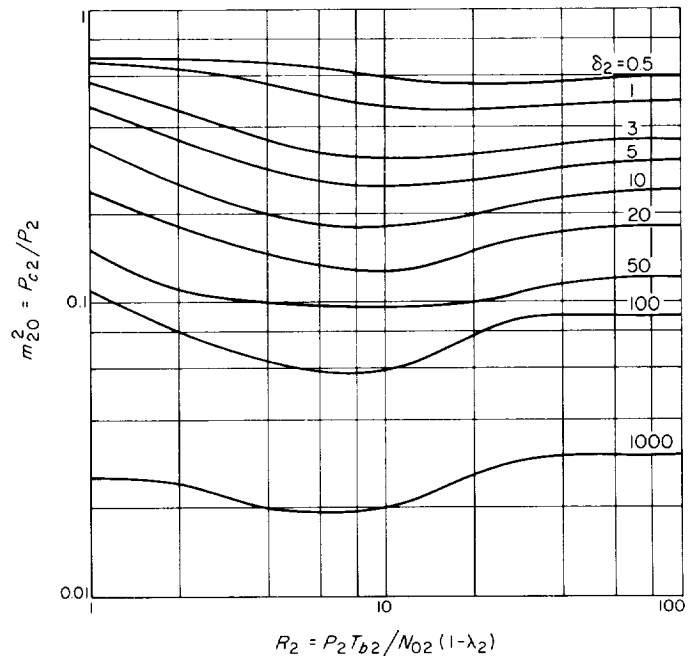


Fig. 3. Optimum modulation index vs R_2 for various values of δ_2 with $\alpha_1 = 9$ db

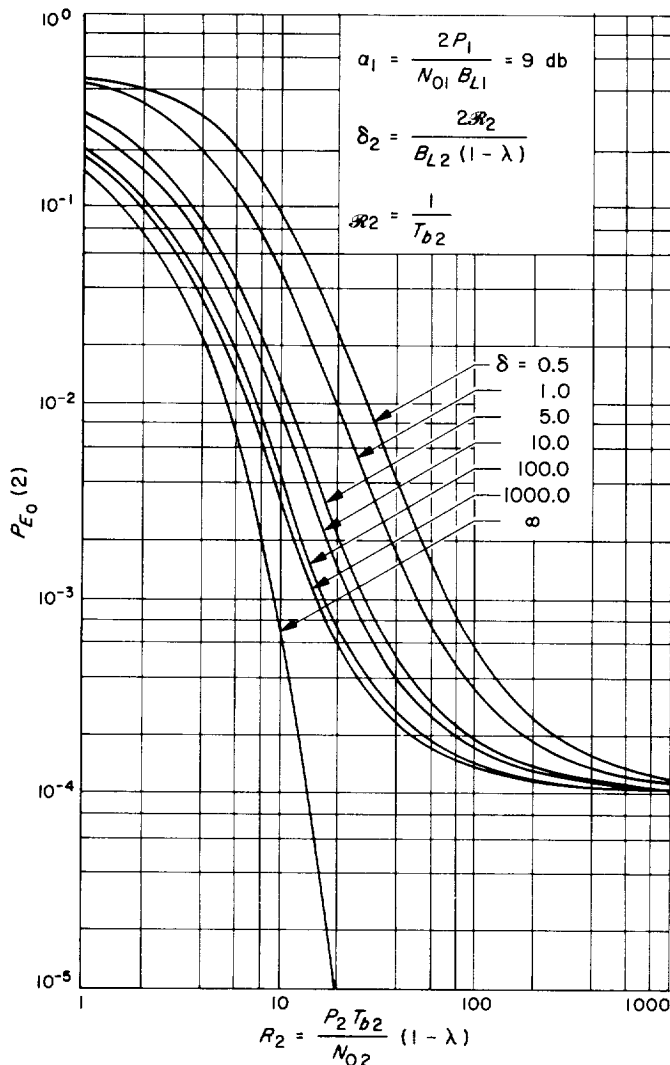


Fig. 4. Error probability $P_{E_0}(2)$ vs R_2 for various values of δ_2 with $\alpha_1 = 9 \text{ db}$

the vehicle's carrier tracking loop becomes negligible. For an error probability $P_E(2) = 10^{-3}$, this occurs for all practical purposes, where $\alpha_1 > 40$ (16 db), SPS 37-35, Vol. IV, pp. 339-341.

The irreducible error probability, say $P_{E_{ir}}(2)$, may be obtained from Eq. (3) by letting R_2 approach infinity. In the limit there is

$$P_{E_{ir}}(2) = \frac{1}{2} \left\{ 1 - \frac{2}{\pi} \sum_{k=0}^{\infty} (-1)^k \epsilon_k \frac{I_k(\alpha_1)}{I_0(\alpha_1)} \frac{1}{1 - 4k^2} \right\} \quad (4)$$

Fig. 5 represents a plot of $P_{E_{ir}}(2)$ versus the SNR $\gamma = 2P_{c1}/N_{01}B_{L1}$ with β as a parameter.

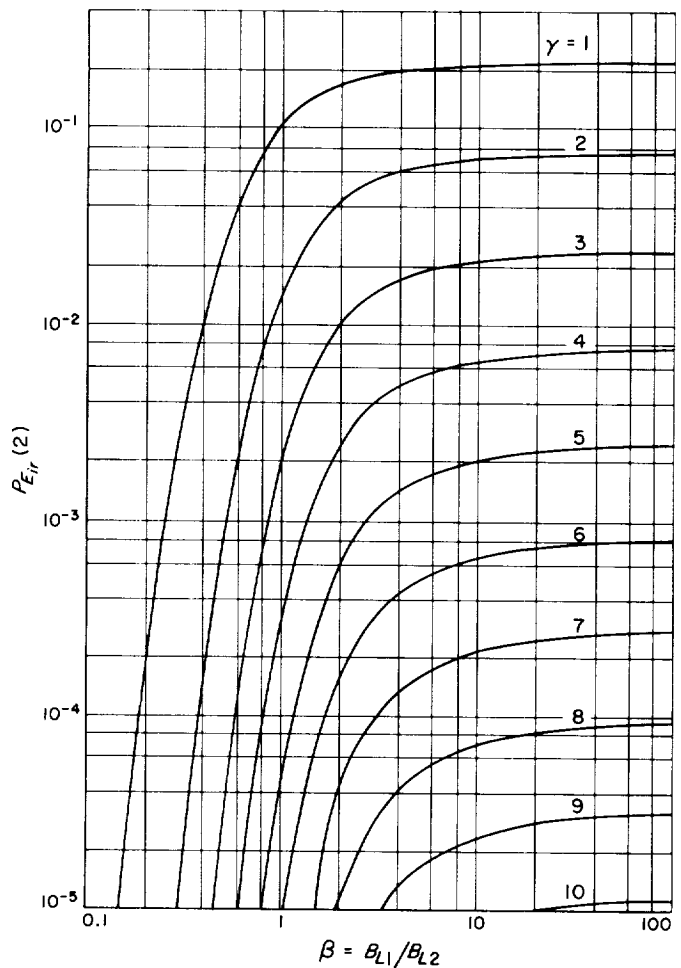


Fig. 5. Irreducible error probability $P_{E_{ir}}(2)$ vs β for various values of $\gamma = 2P_{c1}/N_{01}B_{L1}$

B. An Optimum Squaring Loop Prefilter

J. W. Layland

1. Introduction

Squaring loops have been proposed in the past (Ref. 1) as a means of establishing a coherent carrier reference for 180-deg biphasic PSK Modulation. The received signal is bandpass filtered, squared to remove the modulation, and the resultant double-frequency term is tracked by a conventional phase-lock loop (Ref. 1).

Noise, always present in the received signal, is enhanced by the squaring operation. It is, therefore, natural to ask for the presquaring filter, which maximizes the

signal-to-noise ratio (SNR) at the output of the phase-lock loop. This article develops the optimum prefilter for one important case: when the modulating spectrum is narrow with respect to the carrier frequency.

2. Squaring Loops

Fig. 1 illustrates the system under consideration. $H(s)$ is the prefilter to be optimized. The noise $n(t)$ is assumed to be Gaussian with (one-sided) spectral density N_0 , constant over the frequency region of interest. Since the phase-locked loop behaves like a very narrow band filter centered at $f = 2f_0$, maximizing the SNR of $\hat{\phi}$ is almost identical to maximizing the SNR of the component of $z(t)$ at $f = 2f_0$.

Let the modulating signal $m(t)$ have a low-pass spectrum with no components at or above $f = f_0$, and assume that $H(s)$ is a bandpass filter symmetric about $f = f_0$. Then the component of $z(t)$ at $f = 2f_0$ can be quite simply expressed in terms of a one-sided Fourier Integral representation of $w(t)$. Define $W_c(f)$, $M_c(f)$, $W_s(f)$ and $M_s(f)$ such that

$$w(t) = \int_0^{2f_0} \{ [W_c(f) + M_c(f)] \cos 2\pi ft + [W_s(f) + M_s(f)] \sin 2\pi ft \} df \quad (1)$$

where the W 's denote terms of the spectrum due solely to $x(t)$ and the M 's denote terms due to $n(t)$. Because of the characteristics of $n(t)$,

$$\begin{aligned} E \{ M_c(f) M_c(\nu) \} &= \delta(f - \nu) S_{mm}(f) \\ E \{ M_s(f) M_s(\nu) \} &= \delta(f - \nu) S_{mm}(f) \\ E \{ M_c(f) M_s(\nu) \} &= 0 \\ S_{mm}(f) &= H(2\pi jf) N_0 H^*(2\pi jf) \end{aligned} \quad (2)$$

To develop the component of $z(t)$ at $2f_0$, consider the trigonometric identity

$$\sin(at) \sin(bt) = \frac{1}{2} \cos(a-b)t - \frac{1}{2} \cos(a+b)t \quad (3)$$

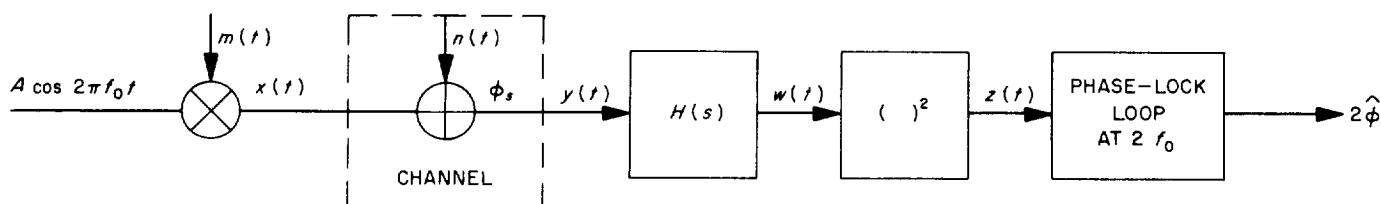


Fig. 6. Squaring loop system

and the two similar identities for $\sin(\cdot) \cdot \cos(\cdot)$ and $\cos(\cdot) \cdot \cos(\cdot)$. Since a and b are bounded in the representation (1), $0 < a, b \leq 2\pi 2f_0$, the components at $f = 2f_0$ come solely from sum-of-frequency terms. The component of $z(t)$ at $f = 2f_0$ can, therefore, be computed to be

$$\begin{aligned} z(t)|_{f=2f_0} &= \frac{1}{2} \cos 4\pi f_0 t \int_0^{2f_0} \{ [W_c(f) + M_c(f)] \\ &\quad \times [W_c(2f_0 - f) + M_c(2f_0 - f)] \\ &\quad - [W_s(f) + M_s(f)] [W_s(2f_0 - f) \\ &\quad + M_s(2f_0 - f)] \} df + \frac{1}{2} \sin 4\pi f_0 t \\ &\quad \int_0^{2f_0} \{ [W_s(f) + M_s(f)] [W_c(2f_0 - f) \\ &\quad + M_c(2f_0 - f)] + [W_c(f) + M_c(f)] \\ &\quad \times [W_s(2f_0 - f) + M_s(2f_0 - f)] \} df \end{aligned} \quad (4)$$

The restrictions upon $m(t)$ and $H(s)$ may be employed to simplify Eq. (4) considerably. Note that if $x(t) = Am(t) \cos 2\pi f_0 t$ were expanded in the Fourier Integral form,

$$\begin{aligned} X_c(f_0 + \nu) &= X_c(f_0 - \nu) \\ X_s(f_0 + \nu) &= -X_s(f_0 - \nu) \end{aligned} \quad (5)$$

Furthermore, if $H(2\pi jf)$ is symmetric about $f = f_0$, the phase-shift induced into a signal component at $f = f_0 + \nu$ is the negative of the phase-shift induced into a signal component at $f = f_0 - \nu$. Such a filter maintains the property of Eq. (5), if it is present in an input signal. Hence,

$$\begin{aligned} W_c(f) &= W_c(2f_0 - f) \\ W_s(f) &= -W_s(2f_0 - f) \end{aligned} \quad (6)$$

The signal portion of $z(t)$ in Eq. (4) is, therefore,

$$z(t) \Big|_{\substack{t=2f_0 \\ \text{signal}}} = \frac{1}{2} \cos(4\pi f_0 t) \int_0^{2f_0} [W_c^2(f) + W_s^2(f)] df \quad (7)$$

which has average power

$$P_s \Big|_{t=2f_0} = \frac{1}{8} \left[\int_0^{2f_0} [W_c^2(f) + W_s^2(f)] df \right]^2 = \frac{1}{2} P_{\text{sig}}^2 \quad (8)$$

The total power in $z(t)$ at $f = 2f_0$ may be determined from Eq. (4) to be

$$\begin{aligned} P \Big|_{t=2f_0} = & \frac{1}{8} E \left\{ \left[\int_0^{2f_0} (W_c^2(f) + W_s^2(f)) \right. \right. \\ & + W_c(f) [M_c(f) + M_c(2f_0 - f)] \\ & + W_s(f) [M_s(f) - M_s(2f_0 - f)] \\ & + M_c(f) M_c(2f_0 - f) \\ & - M_s(f) M_s(2f_0 - f)] df \Big]^2 \\ & + \left[\int_0^{2f_0} (W_s(f) [M_c(2f_0 - f) - M_c(f)] \right. \\ & + W_c(f) [M_s(f) + M_s(2f_0 - f)] \\ & + M_s(f) M_c(2f_0 - f) \\ & \left. \left. + M_c(f) M_s(2f_0 - f) \right) df \right]^2 \Big\} \quad (9) \end{aligned}$$

Under the symmetries of $W_s(f)$ and $W_c(f)$, the integrand of each of the integrals in Eq. (9) is symmetric in f and $2f_0 - f$. Since the integrand is symmetric about the center of the integration range, the value of each integral is twice the value of an integral taken over the first half of the range, or $0 \leq f \leq f_0$. In this reduced range, each of the noise terms are independent with zero mean, and, hence, the expected value of their cross-product is zero. Each of the noise expectations involves only a second-order moment everywhere except at $f = f_0$, where the fourth-order moment enters. Since the noise spectrum is continuous, this infinitesimal amount of fourth-order moment

may be ignored, and Eq. (2) may be used to express Eq. (9) as

$$\begin{aligned} P \Big|_{t=2f_0} = & P_s \Big|_{t=2f_0} \\ & + \frac{1}{2} \int_0^{f_0} \{ W_c^2(f) [S_{mm}(f) + S_{mm}(2f_0 - f)] \\ & + W_s^2(f) [S_{mm}(f) + S_{mm}(2f_0 - f)] \\ & + 2S_{mm}(f) S_{mm}(2f_0 - f) \\ & + W_s^2(f) [S_{mm}(2f_0 - f) + S_{mm}(f)] \\ & + W_c^2(f) [S_{mm}(f) + S_{mm}(2f_0 - f)] \\ & + 2S_{mm}(f) S_{mm}(2f_0 - f) \} df. \quad (10) \end{aligned}$$

Denote the one-sided spectral density of $x(t)$ as $S_{xx}(f)$. Then

$$W_c^2(f) + W_s^2(f) = 2H(2\pi jf) S_{xx}(f) H^*(2\pi jf) \quad (11)$$

and, hence, Eqs. (8) and (10) may be rewritten as

$$P_s \Big|_{t=2f_0} = \frac{1}{2} \left[\int_0^{2f_0} H(2\pi jf) S_{xx}(f) H^*(2\pi jf) df \right]^2 \quad (12)$$

$$\begin{aligned} P \Big|_{t=2f_0} = & P_s \Big|_{t=2f_0} \\ & + \frac{1}{4} \int_0^{2f_0} [H(2\pi jf) \cdot 2S_{xx}(f) H^*(2\pi jf) \\ & \times 4H(2\pi jf) N_0 H^*(2\pi jf) \\ & + 4H^2(2\pi jf) N_0^2 H^{*2}(2\pi jf)] df \quad (13) \end{aligned}$$

The signal-to-noise (SNR) ratio to be maximized is, therefore, given by

$$\text{SNR} = \frac{\frac{1}{4} \left[\int_0^{2f_0} H(2\pi jf) S_{xx}(f) H^*(2\pi jf) df \right]^2}{N_0 \int_0^{2f_0} H^2(2\pi jf) H^{*2}(2\pi jf) \left[S_{xx}(f) + \frac{N_0}{2} \right] df} \quad (14)$$

This SNR is clearly independent of any gain k involved in $H(s)$. SNR may, therefore, be maximized by setting k such that $P_s \Big|_{t=2f_0} = 1/4$ and minimize the noise power subject to this constraint. That is, minimize x , given by

$$\begin{aligned} x = & N_0 \int_0^{2f_0} H^2(2\pi jf) H^{*2}(2\pi jf) \left[S_{xx}(f) + \frac{N_0}{2} \right] df \\ & - \lambda \left[\int_0^{2f_0} H(2\pi jf) S_{xx}(f) H^*(2\pi jf) df - 1 \right] \quad (15) \end{aligned}$$

where λ denotes a conventional Lagrangian multiplier.

In this form, the problem is solvable by a standard calculus-of-variations approach. The result obtained is

$$H(2\pi jf) H^*(2\pi jf) = \frac{\lambda}{2N_0} \frac{S_{xx}(f)}{S_{xx}(f) + \frac{N_0}{2}} \quad (16)$$

The appropriate second-derivative analysis shows that this does indeed result in minimal x as long as $\lambda > 0$. Since the gain-constant of $H(2\pi jf)$ is arbitrary once the restriction upon $P_s|_{f=f_0}$ is removed, λ need not be explicitly evaluated, and the specification becomes

$$|H(2\pi jf)| = k \left(\frac{S_{xx}(f)}{S_{xx}(f) + \frac{N_0}{2}} \right)^{1/2} \quad (17)$$

where k is an arbitrary (positive) constant.

Since only the magnitude of $H(2\pi jf)$ is specified, and $H(2\pi jf)$ has a bounded integral-square, the specification given is physically realizable. The remaining problem is, therefore, one of approximating the ideal physically realizable specification with a practically realizable filter.

The SNR of $\hat{\phi}$, using the optimal prefilter, can be determined readily by substituting the specification Eqs. (16) or (17) into Eq. (14). Thus,

$$\text{SNR} = \int_0^{2f_0} \frac{1}{2} \frac{S_{xx}^2(f)}{2N_0 S_{xx}(f) + N_0^2} df \quad (18)$$

Titsworth (Ref. 2) has determined the spectrum resulting when a sine wave is synchronously modulated by a Markov sequence (± 1) with digit duration t_0 . For $t_0 \gg 1/f_0$, this (one-sided) spectrum is approximately

$$S_{xx}(f) = S t_0 \left(\frac{\sin \pi t_0 (f - f_0)}{\pi t_0 (f - f_0)} \right)^2 \quad (19)$$

where S is the sine-wave power.

With this spectrum, the SNR can be closely approximated (and bounded above) by

$$\begin{aligned} \text{SNR} &\leq \frac{S}{N_0} \frac{S t_0}{N_0} \frac{1}{2} \int_{-\infty}^{\infty} \left(\frac{\sin \pi x}{\pi x} \right)^4 dx \\ &\leq \frac{1}{3} \cdot \frac{S}{N_0} \cdot \frac{S t_0}{N_0} \end{aligned} \quad (20)$$

For a coded system, $(S t_0)/N_0$ is apt to be considerably less than 1, since $t_0 = (k/2^{k-1}) T_b$ for a k -bit biorthogonal code. This may somewhat restrict the usefulness of the squaring loop to uncoded systems, or to coded systems where S/N_0 is large (and, consequently, to high data-rate systems).

C. On the Possibility of Receiving Radar Echoes From the Sun at S-Band

G. A. Morris

A recent paper by Moriyama (Ref. 3) suggests the possibility of detecting radar echoes from the Sun in some frequency range around 1000 Mc. This conclusion is based on an inhomogeneous model of the solar atmosphere in which regions of high density and temperature, covering about 10% of the solar disk, are imbedded in cooler regions covering the rest of the disk. This model predicts that the optical depth to the reflection level may be less than unity between approximately 500 and 2000 Mc.

Moriyama's estimate of doppler spreading takes into account only the orbital and rotational velocities of the Earth and Sun. Radar returns from the Sun at 38 Mc (Ref. 4) show doppler spreading many times greater, due primarily to random mass motions in the solar corona.

Table 1. Design characteristics for the 2388-Mc Sun radar experiment

Transmitter carrier power, dbm	80 (100 kw)
Transmitter antenna gain, db	54
Earth-Sun transmission loss at 149.5 million km, db	- 53
Sun attenuation loss, db	- 9
Sun-Earth transmission loss at 149.5 million km, db ^a	- 263
Receiver antenna gain, db	54
Receiver system temperature, °K	40,000
Receiver predetection bandwidth, mc	4
Receiver threshold, dbm	- 87
Receiver RF carrier, dbm	- 137
Signal to noise ratio, db	- 50
Integration time required, sec ^b	2500

^aInto an isotropic antenna.
^bFor a 0-db output SNR, square-law detection.

An analysis is given in Table 1 for using the Goldstone Venus Station to obtain radar echoes from the Sun at 2388 Mc. Since the radar depth of the Sun is approximately 5 sec, assuming the radar radius may be two optical radii, it is necessary to key the transmitter for relatively long periods such as 1 min on and 1 min off. The return signal is integrated during noise only periods and subtracted from the signal plus noise periods to obtain the signal. Extrapolating the 38-Mc radar returns to 2388 Mc predicts a doppler spreading of from 1 to 4 Mc.

Assuming an optical depth to the reflection level of unity, the attenuation caused by the solar corona is approximately 9 db.

This analysis is worst case since the doppler spreading at 2388 Mc may be much less than that predicted by an extrapolation from the 38-Mc radar data. This decreased doppler spreading might result from the reflection level being deeper in the solar atmosphere, where the random motions may be considerably reduced.

References

1. Stiffler, J. J., "On the Allocation of Power in a Synchronous Binary PSK Communication System," *National Telemetry Conference*, paper No. 5-1, 1964.
2. Titsworth, R. C., *Correlation Properties of Cyclic Sequences*, Technical Report No. 32-388, Jet Propulsion Laboratory, Pasadena, Chapter 1, July 1, 1963.
3. Moriyama, F., "On the Possibility of Receiving Radar Echoes From the Sun at High Frequencies," *Astronomical Society of Japan*, Vol. 16, No. 1, pp. 23-29, 1964.
4. James, J. C., "A 38 Mcps Solar Radar System," *Northeast Electronics Research and Engineering Meeting Record*, pp. 186-187, 1965.

XXVI. COMMUNICATIONS SYSTEMS RESEARCH: COMBINATORIAL COMMUNICATION RESEARCH

A. Computation of Finite Fourier Series

L. R. Welch¹

1. Summary

This article describes an economical algorithm for computing the Fourier series of a function defined on a finite number of points. The method will find use in estimating the frequency of radar returns and of frequency-shift-keyed telemetry signals.

Let N be the number of points of the series required, and let the prime factorization of N be

$$N = p_1^{e_1} p_2^{e_2} \cdots p_n^{e_n}$$

Then the total number of real multiplications required by this method is

$$4N \cdot [e_1(p_1 - 1) + e_2(p_2 - 1) + \cdots + e_n(p_n - 1)]$$

with a similar number of real additions. When the function to be analyzed is real-valued the amount of work is one half of the above number. (In the case $N = 12$,

the method is related to that described in Section 6-5 of Ref. 1.) The method will allow considerable equipment simplification in frequency estimations.

Since the method has general application and is not restricted to standard finite Fourier series, it is described in an abstract setting and then applied to the standard case.

2. Introduction

On any finite abelian group G there are complex valued functions χ_i called characters, with the properties

$$\begin{aligned} |\chi_i(g)| &= 1; & g \in G \\ \chi_i(gh) &= \chi_i(g)\chi_i(h); & g, h \in G \end{aligned} \quad (1)$$

$$\sum_{g \in G} \chi_i(g)\chi_j(g) = \delta_{ij} |G|$$

where $|G|$ is the order of G ; that is, the number of elements of G

The number of such characters is equal to $|G|$. Any complex function f on the group may be expressed as a linear combination of characters

$$f(g) = \frac{1}{|G|} \sum_{i=1}^{|G|} \hat{f}_i \chi_i(g) \quad (2)$$

¹Consultant from the University of Southern California Electrical Engineering Department, Los Angeles, California.

where

$$\hat{f}_i = \sum_{g \in G} f(g) \chi_i(g) \quad (3)$$

In the case where $|G| = N$ and group multiplication is addition modulo N , the characters are merely

$$\chi_i(k) = e^{2\pi i (jk/N)}$$

and the real and imaginary parts of \hat{f}_i are the standard cosine and sine coefficients. Thus, in this case, the representation in Eq. (2) of \hat{f}_i is its Fourier series with N terms.

3. Description of an Algorithm

This section describes an algorithm which, if $|G| = p_1 p_2 \cdots p_n$ (not necessarily distinct primes), then

$$|G| \cdot [(p_1 - 1) + (p_2 - 1) + \cdots + (p_n - 1)]$$

complex multiplications and a like number of complex additions are required to compute f . Since one complex multiplication requires four real multiplications and two real additions, while the complex addition requires two real additions, the total number of computations is

$$4 \cdot |G| \cdot [(p_1 - 1) + \cdots + (p_n - 1)]$$

real multiplications with the same number of additions.

Let G be a finite abelian group. Then there exists a descending sequence of groups,

$$G = G_n > G_{n-1} > \cdots > G_1$$

with

$$\begin{aligned} |G_1| &= p_1 \\ |G_k|/|G_{k-1}| &= p_k; \quad k = 2, \cdots, n \end{aligned}$$

Since p_k is prime, G_k can be represented as a union of p_k cosets of G_{k-1} in the form

$$G_k = G_{k-1} \cup g_k G_{k-1} \cup g_k^2 G_{k-1} \cdots \cup g_k^{p_k-1} G_{k-1}$$

for some element g_k . It follows that the elements of G can all be expressed uniquely in the form

$$g = g_1^{j_1} g_2^{j_2} \cdots g_n^{j_n}$$

where $0 \leq j_k \leq p_k - 1$.

Eq. (3) can now be written

$$\hat{f}_i = \sum_{j_n=0}^{p_n-1} \cdots \sum_{j_1=0}^{p_1-1} \chi_i(g_1^{j_1} \cdots g_n^{j_n}) f(g_1^{j_1} \cdots g_n^{j_n})$$

or [using Eq. (1)]

$$\begin{aligned} \hat{f}_i &= \sum_{j_n=0}^{p_n-1} [\chi_i(g_n)]^{j_n} \cdots \sum_{j_2=0}^{p_2-1} [\chi_i(g_2)]^{j_2} \\ &\quad \sum_{j_1=0}^{p_1-1} [\chi_i(g_1)]^{j_1} f(g_1^{j_1} \cdots g_n^{j_n}) \end{aligned} \quad (4)$$

In the innermost sum, χ_i is evaluated only on the subgroup G_1 . In the next sum χ_i is evaluated only on G_2 , etc. Now χ_i , restricted to G_k , is a character on G_k and, therefore, must be one of the $|G_k|$ such characters. Concluding from this observation, the innermost sum need be evaluated for only p_1 choices of χ_i and $p_2 \cdots p_n$ choices of (j_2, \cdots, j_n) , a total of $N = |G|$ sums. Since $[\chi_i(g_1)]^0 = 1$ only $p_1 - 1$ complex multiplications need be performed with a like number of complex additions. At the k th iterate of summation, the sum must be evaluated for $|G_k| = p_1 \cdots p_k$ choices of character and $p_{k+1} \cdots p_n$ choices of (j_{k+1}, \cdots, j_n) for a total of $|G|$ sums. Again, each sum requires $p_k - 1$ complex multiplications and the same number of additions.

On completion of the n th iterate, \hat{f}_i has been evaluated for all characters χ_i on G with a total of $|G|$.

$$|G| \cdot \left(\sum_{i=1}^n p_i - 1 \right)$$

complex multiplications. The computation may be summarized in the recursion

$$S_0(j_1, \cdots, j_n) = f(g_1^{j_1} g_2^{j_2} \cdots g_n^{j_n}) \quad (5)$$

$$S_k(i, j_{k+1}, \cdots, j_n) = \sum_{j=0}^{p_k-1} [\chi_i^k(g_k)]^j S_{k-1}(i', j, j_{k+1}, \cdots, j_n)$$

where for S_k

$$\begin{aligned} 1 &\leq i \leq |G_k| \\ 0 &\leq j_n \leq p_n - 1 \end{aligned}$$

χ_i^k is a character of G_k and i' is such that χ_i^k restricted to G_{k-1} , is $\chi_{i'}^{k-1}$.

Since the complex conjugate of a character is also a character, if f is a real-valued function, only one of the pair

$$\hat{f}_k \cdot \hat{f}_{\bar{k}}$$

need be computed. The same remark applies to the recursion in Eq. (5). If $|G|$ is odd, this consideration reduces the work by a factor of two.

If $|G|$ is even, then there are characters with $\bar{\chi}(g) = \chi(g)$ for all $g \in G$. χ is real-valued, and its restriction to each subgroup requires only real multiplications and additions.

Concluding from these considerations, the Fourier transform of a real-valued function requires at most

$$2 \cdot |G| \cdot [(p_1 - 1) + \dots + (p_n - 1)]$$

multiplications.

4. Application to Finite Fourier Series

Let $G = \{0, 1, \dots, N - 1\}$ with additional modulo N as group multiplication. The characters are

$$\chi_m(j) = e^{2\pi i (jm/N)}$$

Let $N = p_1 \cdot \dots \cdot p_n$ be a prime factorization of $|G|$ and define $N_k = p_1 \cdot \dots \cdot p_k$. The multiples of N/N_k form a subgroup G_k of order N_k and $G_k > G_{k-1}$.

The recursion in Eq. (5) becomes

$$S_0(j) = f(j)$$

$$S_k(m, j) = \sum_{l=0}^{N_k-1} e^{2\pi i (lm/N_k)} S_{k-1} \left(m \bmod N_{k-1}, j + l \cdot \frac{N}{N_k} \right) \tag{6}$$

where

$$0 \leq m \leq N_k - 1$$

$$0 \leq j \leq \frac{N}{N_k} - 1$$

5. Savings

In practice, N would be a power of 2, say $N = 2^k$, and the function would be real valued. The total number of multiplications is then $2Nk = 2N \log_2 N$. The standard method requires N^2 multiplications. Hence, this method

yields a savings of a factor of $N/(2 \log_2 N)$. For the computation of the Fourier transform of correlation functions, the range at j in Eq. (6) may be replaced by

$$- \left[\frac{N}{2N_k} \right] + 1 \leq j \leq \left[\frac{N}{2N_k} + \frac{1}{2} \right]$$

It can be shown that

$$S_k(m, j) = S_k(N_k - m, -j)$$

and that $S_k(m, j)$ need only be evaluated for $j \geq 0$. If $R(0), \dots, R(L)$ are given, then $N = 2L$; and the work factor is $N \log_2 N = 2L \log_2 2L$, while the standard method has a work factor of L^2 . The savings factor is $L/(2 + 2 \log_2 L)$. For $L = 64$ the savings is $32/7$. For $L = 512$ the savings is $128/5$.

Another way of looking at the savings is that the direct summation method with $L = 64$ takes as much computer time as this method with $L = 256$. Thus, four times as many spectral points could be found in the same time.

It is believed that the algorithm presented here is in a certain sense the fastest, in that no algorithm can use fewer computations.

B. Two Identical Binary Erasure Channels with Feedback are Exponentially Better Than One Channel at Low Rates

E. R. Berlekamp²

1. Introduction

In 1955 Shannon first showed that the capacity of a two-way communication system having separate forward and reverse channels was no greater than the capacity of the forward channel alone, even if the reverse channel was noiseless, delayless, and of unlimited capacity. This raised the question of whether the feedback channel

²Consultant from the University of California Electrical Engineering Department, Berkeley, California.

could be used to reduce the error probability substantially at rates below capacity.

In 1964 it was shown (Ref. 2) that the sphere packing bound on error probability remains valid for all block coding schemes even when used with delayless, noiseless, feedback. (Although this result is conjectured to hold for all discrete memoryless forward channels, it has not yet been proved, except for channels which satisfy certain symmetry conditions, a point not concerned with here). Hence, at least for the reasonably symmetric channels, it is known that the use of noiseless, delayless (Ref. 3) feedback cannot improve the error exponent at rates above $R_{critical}$. For sufficiently low rates, however, it has been shown (Ref. 4) that the error exponent can be improved by the use of noiseless, delayless feedback.

More recent work to account for delayed noiseless feedback has shown that if the feedback is delayed by a fraction of the block length, then the error exponent cannot exceed the linear interpolation between the feedback exponent and the one-way exponent. Furthermore, for certain very simple channels, including the binary erasure channel, this linear variation of exponent with delay is actually attainable.

The purpose of this note is to show that in some cases the feedback link can be used to increase the error exponent at a low rate even if the feedback link is noisy, and, in particular, to refute the conjecture that the error exponent for any feedback system consisting of two identical channels is no greater than for the one-way channel alone.

2. The Coding Scheme

Fig. 1 shows the feedback system considered. Block coding, which shall be used, consists of three separate segments, of lengths AN , BN , and CN , respectively. The feedback channel is used only during the second interval. During the first AN digits, the source sends one of 2^{RN} codewords selected from a very good (i.e., expurgated) nonlinear code of rate R/A and block length AN . During the second interval the source transmits one of 2^{RN} codewords selected from a very good code of rate R/B and block length BN . Meanwhile, the feedback channel is put into operation. At the conclusion of the first AN digits, the sink attempts to decode the message from among these digits. If he is lucky, of course, he will have already received enough information to decipher the message uniquely, and whatever happens subsequently is irrelevant.

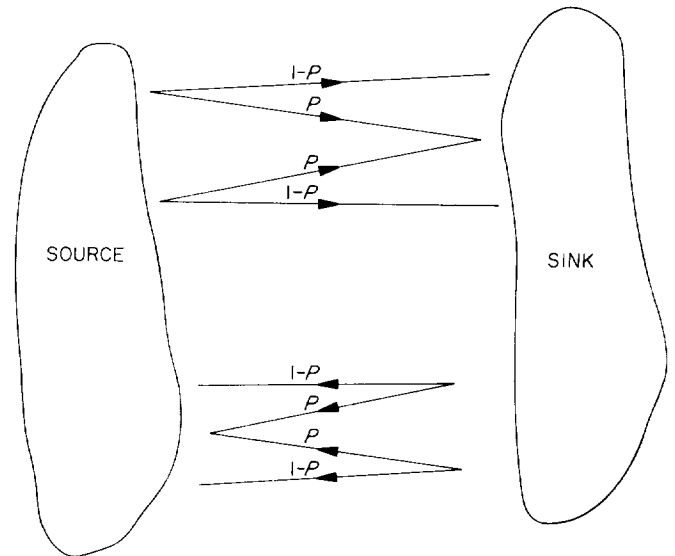


Fig. 1. The channel

However, consider the less fortunate situation in which the sink is not able to decode the entire transmitted message, although he is able to eliminate all but one pair of possible transmitted messages. It is this pair which he transmits back to the source during the second BN digits. If the sink is unable to reduce the possible messages down to a pair (or has already decoded the message completely), he sends a special "panic" codeword. Thus, one of $\binom{M}{2} + 1$ messages are transmitted back across the feedback channel. Since this number is less than M^2 (where $M = 2^{RN}$), the feedback channel transmits one message of a code of rate $2R/B$ and block length RN .

At the conclusion of the second interval, the source attempts to decode the sequence which it received over the feedback channel during the second interval. (It performs this decoding under the assumption that the codewords were selected equiprobably, even though they were not). If the decoding is unsuccessful, then the source proceeds as though the panic message had been sent.

During the third interval, the source transmits a sequence selected from a code containing $2^{RN} + 2$ codewords. This code is to have the property that the 2 auxiliary codewords are complementary (i.e., distance CN), and the code as a whole must satisfy the Gilbert bound. (i.e., D_{min} is almost $CN/2$, if R is very small). If the source were able to decode the sequence he received during the second interval into a pair of candidate messages, then he would send one of the 2 auxiliary codewords, depending upon which of the pair of messages

Table 1. Error probabilities

Interval	Channel	Clock length	No. codewords	Interpretation	Rate	Asymptotic error probabilities if $R \rightarrow 0^2$
1st	for	AN	M	M messages	R/A	List of 1 $p^{1N/2}$
2nd	for	BN	M	M messages	R/B	List of 2 $p^{3AN/4}$
2nd	rev	BN	$M/2 + 1$	pair of messages or panic	2R/B	$p^{BN/2}$
3rd	for	CN	$M + 2$	M messages or 1st of the pair or 2nd of the pair	R/C	$p^{CN/2}$ among all (M + 2) or p^{CN} between the pair

^aRef. 5

is actually correct. If the source were unable to decode the sequence received during the second interval, or if it were decoded into the panic message, then he would send one of the 2^{M+1} sequences corresponding to the original messages.

All four of these various codes are summarized in Table 1 with their probabilities of error.

The sink decodes the final CN digits, if possible. If he cannot decode this sequence he assumes that one of the pair of complementary messages was sent. He is able to decode between these two unless the entire sequence of all CN digits was erased.

3. Performance

An error can occur in only three ways (Table 2), and with the exponents indicated: Exponents if $R \approx 0$ (Note $A + B + C = 1$)

Type 1: $3A/4 + 0 + B/2 + C/2 = 1/2 + A/4$

Type 2: $A/2 + B/2 + B/2 + C/2 = 1/2 + B/2$

Type 3: $A/2 + 0 + B/2 + C = 1/2 + C/2$

Table 2. Decoding possibilities

Error type	1st interval	2nd interval reverse	2nd interval forward	3rd interval
Type 1	Miss the list of 2	Either	Miss	Miss among M + 2
Type 2	Hit list of 2 but miss list of 1	Miss	Miss	Miss among M + 2
Type 3	Hit list of 2 but miss list of 1	Hits	Miss	Miss the pair

To optimize, all three exponents are set equal, obtaining $A = 1/2; B = C = 1/4$. The error exponent for the entire scheme is then 5/8. Since the error exponent for the best zero-rate one-way codes is only 1/2, this proves that the system using the noisy feedback is better.

There are many reasons to believe that this system is far from optimum, and that an even better exponent could be attained by utilizing the feedback channel in a wiser fashion.

C. Coverings by Rook Domains

E. Rodemich

1. Summary

It is shown that a one-dense set in V_n^k must contain at least $n^{k-1}/(k-1)$ points. As a corollary, a conjecture of Golomb and Posner on error-distributing codes is proved. It is also shown that a $(k-2)$ -dense set must contain at least $n^2/(k-1)$ points. Equality is attained if, and only if, $k-1$ divides n , and there are $k-2$ orthogonal latin squares of order $n/(k-1)$.

2. Definitions

V^k is defined to be the set of all k -tuples (j_1, \dots, j_k) of positive integers $\leq n$. This becomes a metric space if the distance between two points is defined to be the number of pairs of corresponding entries which are distinct. The rook domain of a point in V_n^k is defined as the union of the k coordinate lines through the point, i.e., the set of points within distance 1 of the given point.

A one-dense set in V_n^k is a set of points whose rook domains cover V_n^k ; thus, each point is within unit distance of some point of the set. In considering such coverings, it is convenient to adopt the convention that a point is covered k times by its own rook domain, thus taking the basic sets of the covering to be the rows which make up the rook domains.

For any point P covered by a set of rows in V_n^k , if c_j rows in the j th direction cover P , the total number of times P is covered is

$$m(P) = \sum_{j=1}^k c_j = \sum_{c_j > 0} (c_j - 1) + q,$$

if P is covered by rows in q directions. Define

$$\eta_j(P) = \begin{cases} c_j - 1, & c_j > 0, \\ 0, & c_j = 0, \end{cases}$$

for $j = 1, \dots, k$, and for any subset i_1, i_2, \dots, i_l of the integers from 1 to k , define

$$\varepsilon_{i_1 i_2 \dots i_l}(P) = \begin{cases} 1 & \text{if } P \text{ is covered by rows in directions} \\ & i_1, \dots, i_l, \\ 0 & \text{otherwise.} \end{cases}$$

An expression for q is given by

$$q - 1 = \sum_{l=2}^k (-1)^l \sum \varepsilon_{i_1 \dots i_l}(P) = \sum \varepsilon_{i_1 i_2}(P) - \sum \varepsilon_{i_1 i_2 i_3}(P) + \dots + (-1)^k \sum \varepsilon_{i_1 \dots i_k}(P),$$

where $\sum \varepsilon_{i_1 \dots i_l}$ denotes the sum over the $\binom{k}{l}$ distinct functions with l indices. This is true because

$$\sum \varepsilon_{i_1 \dots i_l}(P) = \begin{cases} \binom{q}{l}, & l \leq q, \\ 0, & l > q. \end{cases}$$

Hence, if P is covered

$$m(P) = 1 + \sum \eta_j(P) + \sum_{l=2}^k (-1)^l \sum \varepsilon_{i_1 \dots i_l}(P).$$

Define

$$\eta_j = \sum_{P \in V_n^k} \eta_j(P),$$

$$\varepsilon_{i_1 i_2 \dots i_l} = \sum_{P \in V_n^k} \varepsilon_{i_1 i_2 \dots i_l}(P).$$

Then, for any set of v rook domains in V_n^k , which do not necessarily cover V_n^k , summing the above relation over all covered points yields

$$nk_v = N + \sum \eta_j + \sum_{l=2}^k (-1)^l \sum \varepsilon_{i_1 \dots i_l}, \quad (1)$$

where N is the number of points covered. This is the basic relation which will be used below. η_j/n is the number of points lost when the set S of centers of the rook domains is projected on V_n^{k-1} in the j th direction. $\varepsilon_{i_1 i_2 \dots i_l}$ is the number of points covered by rows in each of the directions i_1, \dots, i_l .

In the proof of the theorem, it is assumed that $k \geq 3$. The result is easy to show for $k = 2$ (and known).

3. Lemmas

a. Lemma 1.

$$\sum \varepsilon_{i_1 i_2} - \sum \varepsilon_{i_1 i_2 i_3} + \dots + (-1)^k \sum \varepsilon_{i_1 \dots i_k} \geq \frac{2}{k} \sum \varepsilon_{i_1 i_2},$$

with equality if, and only if, all points covered by rows in more than one direction are covered by rows in k directions.

Proof. Every point contributes separately to each side of the inequality. It is sufficient to verify it for the contributions of a single point P covered by rows in q directions, $2 \leq q \leq k$. Since

$$\sum \varepsilon_{i_1 \dots i_l}(P) = \begin{cases} \binom{q}{l}, & 2 \leq l \leq q, \\ 0, & l > q, \end{cases}$$

then

$$\begin{aligned} \sum_{l=2}^k (-1)^l \sum \varepsilon_{i_1 \dots i_l}(P) &= q - 1 \\ &= \frac{2}{q} \binom{q}{2} \geq \frac{2}{k} \binom{q}{2} \\ &= \frac{2}{k} \sum \varepsilon_{i_1 i_2}(P), \end{aligned}$$

with equality only if $q = k$.

b. Lemma 2.

$$\varepsilon_{i_1 i_2} \geq \frac{1}{n^{k-2}} \left[v^2 - \frac{v}{n} (\eta_1 + \eta_2) \right] - \frac{1}{4} (\eta_1 + \eta_2) + \frac{1}{4n^k} (\eta_1 + \eta_2)^2$$

Proof. Consider the n^{k-2} planes in the (1,2) direction. In the r th plane, let there be α_r points of S , on a_r rows in direction 1 and b_r rows in direction 2. If

$$\eta_{1r} = \alpha_r - a_r,$$

$$\eta_{2r} = \alpha_r - b_r,$$

then $\sum \eta_{1r} = \eta_1/n$, $\sum \eta_{2r} = \eta_2/n$. Since $0 \leq a_r, b_r \leq n$,

$$|\eta_{1r} - \eta_{2r}| \leq n.$$

By definition,

$$\begin{aligned} \epsilon_{12} &= \sum a_r b_r = \sum (\alpha_r - \eta_{1r})(\alpha_r - \eta_{2r}) \\ &= \sum \left[\left(\alpha_r - \frac{\eta_{1r} + \eta_{2r}}{2} \right)^2 - \left(\frac{\eta_{1r} - \eta_{2r}}{2} \right)^2 \right]. \end{aligned}$$

Applying Schwarz's inequality to the first part of the sum,

$$\epsilon_{12} \geq \frac{1}{n^{k-2}} \left[\sum \left(\alpha_r - \frac{\eta_{1r} + \eta_{2r}}{2} \right) \right]^2 - \frac{n}{2} \sum \frac{\eta_{1r} + \eta_{2r}}{2},$$

which reduces to the given inequality, since

$$\sum \alpha_r = v.$$

c. Lemma 3. Let a covering of V_n^k by rook domains have the property that if any point is covered more than once, it is covered k times—once by a row in each direction. Then the k -covered points form a number of k -cubes at distance ≥ 3 from each other. If the number of rook domains is $n^{k-1}/(k-1)$, there are $(k-1)^{k-2}$ of these cubes, each of side $n/(k-1)$.

Proof. A cube is defined as a set formed from V_n^k by removing an equal number of hyperplanes in each direction.

If two k -covered points are at distance 2, form the coordinate rectangle with these points as opposite vertices. The sides of this rectangle are rows of the covering rook domains. Hence, the other two vertices of the rectangle are also covered k times. It follows easily that if we take the maximal set of k -covered points obtained from one point by repeated addition of points at distance ≤ 2 from the set, this set is a k -dimensional rectangular solid, after permutation of the hyperplanes of V_n^k . Any center of a rook domain which is not in the set is at distance ≥ 3 . Hence, this set is covered by rook domains which are centered in the set. The number of rows in each direction intersecting the set must then be the same, so that the set is a k -cube.

Let S be the set of centers of the covering rook domains. Consider a cube of k -covered points, with m in each row. Since there are m^{k-1} rows through the cube in each direction, this cube contains m^{k-1} points of S . Each row of the cube can contain at most one point of S . Hence, every row contains one point, and any j -dimensional plane in the cube, $1 \leq j \leq k$, contains m^{j-1} points of S .

Let the n^{k-2} planes in the (1,2) direction be numbered by the index r . The r th plane P_r can intersect at most one of the cubes of k -covered points. Let m_r be the length of the side of this cube, if it exists; m_r is zero otherwise. Then there are m_r points of S in P_r , with rook domains covering $n^2 - (n - m_r)^2$ points of P_r . The other points of the cube of side m_r have rook domains covering no additional points of P_r . There are $(k-2)(m_r^2 - m_r)$ of these points at distance 1 from P_r . Every other point of S at distance 1 from P_r has one additional point of P_r in its rook domain, and these points are all distinct. Hence, if v_r is the number of points of S at distance 1 from P_r ,

$$(n - m_r)^2 = v_r - (k - 2)(m_r^2 - m_r),$$

$$\begin{aligned} &\frac{1}{k-1} n^2 - 2nm_r + (k-1)m_r^2 \\ &= -\frac{k-2}{k-1} n^2 + v_r + (k-2)m_r. \end{aligned}$$

Summing over r ,

$$\begin{aligned} (k-1) \sum \left(\frac{n}{k-1} - m_r \right)^2 &= -\frac{k-2}{k-1} n^k \\ &+ \sum [v_r + (k-2)m_r]. \end{aligned}$$

The quantity $v_r + (k-2)m_r$ is the sum of the numbers of elements of S in the $k-2$ three-dimensional planes through P_r . Hence, by symmetry,

$$\sum [v_r + (k-2)m_r] = n(k-2)v,$$

if v is the number of points of S . In particular, if $v = n^{k-1}/(k-1)$,

$$\sum \left(\frac{n}{k-1} - m_r \right)^2 = 0,$$

so that each m_r is $n/(k-1)$. The number of cubes of k -covered points is

$$v/\left(\frac{n}{k-1}\right)^{k-1} = (k-1)^{k-2}.$$

4. One-Dense Set Theorem

a. Theorem. For $k \geq 2$, a one-dense set in V_n^k has at least $n^{k-1}/(k-1)$ elements. This lower bound cannot be attained unless n is divisible by $k-1$.

Proof. It is assumed that $k \geq 3$. The proof is simple for $k=2$. Let S be the 1-dense set, and define η_1, ϵ_{12} , etc., as above. If S contains v elements, Eq. (1) applies, with $N = n^k$. Thus,

$$nk_v = n^k + \sum \eta_j + \sum \epsilon_{12} - \sum \epsilon_{123} + \dots + (-1)^k \epsilon_{12\dots k}.$$

By Lemmas 1 and 2,

$$\begin{aligned} nk_v &\geq n^k + \sum \eta_j + \frac{2}{k} \sum \epsilon_{12} \\ &\geq n^k + \sum \eta_j + \frac{2}{k} \\ &\quad \sum_{(1,2)} \left\{ \frac{1}{n^{k-2}} \left[v^2 - \frac{v}{n} (\eta_1 + \eta_2) \right] - \frac{1}{4} (\eta_1 + \eta_2) \right\}, \end{aligned}$$

with equality only if $\eta_1, \dots, \eta_k = 0$, and all points covered in two directions are covered in k directions.

We have

$$\begin{aligned} \sum_{(1,2)} \frac{v^2}{n^{k-2}} &= \binom{k}{2} \frac{v^2}{n^{k-2}}, \\ \sum_{(1,2)} (\eta_1 + \eta_2) &= (k-1) \sum \eta_j. \end{aligned}$$

Hence,

$$\begin{aligned} nk_v &\geq n^k + \frac{2}{kn^{k-1}} \left[\frac{k+1}{4} n^{k-1} - (k-1)v \right] \\ &\quad \sum \eta_j + (k-1) \frac{v^2}{n^{k-2}}. \end{aligned}$$

For $k \geq 3$,

$$\begin{aligned} kvn^{k-1} - n^{2k-2} - (k-1)v^2 &\geq \frac{2}{nk} [n^{k-1} - (k-1)v] \sum \eta_j, \\ \left(n^{k-1} - v + \frac{2}{nk} \sum \eta_j \right) [(k-1)v - n^{k-1}] &\geq 0. \end{aligned}$$

Hence, if $v < n^{k-1}$, $v \geq n^{k-1}/(k-1)$. If equality holds, $n/(k-1)$ must be an integer, by Lemma 3.

5. Consequences

The function $w(k, n)$ is defined as the maximum number of disjoint one-dense sets in V_n^k (Ref. 6). A simple corollary of the above theorem is:

a. Corollary. $w(k, n) \leq n/(k-1)$. Equality cannot hold unless n is divisible by $k-1$.

Proof. Suppose that a family of j disjoint one-dense sets exists in V_n^k . Each set must contain at least $n^{k-1}/(k-1)$ points. Hence,

$$\begin{aligned} j \cdot \frac{n^{k-1}}{k-1} &\leq n^k, \\ j &\leq n(k-1). \end{aligned}$$

If $j = n/(k-1)$, each of the one-dense sets must contain only $n^{k-1}/(k-1)$ points. Hence, n is divisible by $k-1$. This completes the proof.

This corollary was stated (in a weaker form) as a conjecture in Ref. 6. Using the stronger form, three entries in the table of bounds for $w(k, n)$ given there can be improved, $w(5, 6) \leq 23$, $w(5, 10) \leq 39$, $w(9, 10) \leq 79$.

Another conjecture (Ref. 7) which would imply the above corollary remains unsolved.

6. Generalization

As a generalization of the preceding problem, consider coverings of V_n^k by j -dimensional rook domains, i.e., by sets formed by taking the union of all j -dimensional coordinate planes through a point. If the j -dimensional rook domains of a set of points cover V_n^k , every point of V_n^k is within distance j of at least one of the points of the set: the set is j -dense.

How many points must a j -dense set in V_n^k contain? This number is trivially n^k if $j = 0$, 1 if $j = n$, and it is easy

to show that n points are required if $j = k - 1$. The theorem below gives the lower bound $n^2/(k - 1)$ for a $(k - 2)$ -dense set.

This result is obtained by induction on k . A stronger result must be shown by induction, in which the covering sets include, in addition to rook domains, sets formed by intersecting a rook domain with a cube which does not contain the center of the rook domain.

7. $(k - 2)$ -Dimensional Rook Domain Theorem

a. Definition. An $R_{k,l}^j$ is the set of all j -dimensional coordinate planes in V_n^k which contain any fixed l -dimensional coordinate plane ($0 \leq l \leq j \leq k$). (In particular, a j -dimensional rook domain is an $R_{j,0}^j$.)

b. Theorem. For $k \geq 2$, let V_n^k be covered by a collection C of $(k - 2)$ -dimensional objects consisting of $v_l R_{k,l}^{k-2}$'s, $0 \leq l \leq k - 2$. Then

$$\sum_{l=0}^{k-2} \frac{k-l}{k} v_l \geq \frac{n^2}{k-1}.$$

Equality can be attained if and only if $h = n/(k - 1)$ is an integer, and there are $k - 2$ mutually orthogonal latin squares of order h . If equality holds, the covering consists only of $R_{k,0}^{k-2}$'s.

Proof. (By induction on k .) If $k = 2$, this inequality reduces to $v_0 \geq n^2$, which is clearly true, since the covering objects are points. Hence, it may be assumed that $k \geq 3$, and that the lemma is true for V_n^{k-1} (for all n).

Let i_1, \dots, i_l be any set of $\leq k - 2$ distinct integers from 1 to k . Define μ_{i_1, \dots, i_l} to be the number of objects in the covering which are $R_{k,l}^{k-2}$'s, in which the common l -dimensional plane has every coordinate but the i_1 th, \dots, i_l th fixed. Then

$$v_l = \sum_{(i_1, \dots, i_l)} \mu_{i_1, \dots, i_l},$$

where the sum is over all possible sets of l distinct integers i_1, \dots, i_l from 1 to k .

For $j = 1, \dots, k$, if none of the subscripts i_1, \dots, i_l equals j , μ_{i_1, \dots, i_l} may be decomposed into n quantities

$$\mu_{i_1, \dots, i_l} = \sum_{m=1}^n \mu_{i_1, \dots, i_l}(j, m),$$

where $\mu_{i_1, \dots, i_l}(j, m)$ is the number of $R_{k,l}^{k-2}$'s contributing to μ_{i_1, \dots, i_l} in which the j th coordinate has the value m in the common l -dimensional plane. Define

$$\epsilon_j = \min_{1 \leq m \leq n} \sum_l \sum_j \mu_{i_1, \dots, i_l}(j, m), \tag{2}$$

where the subscript j on the second summation sign indicates that only subscripts i_1, \dots, i_l different from j are to be used.

Let j be fixed, and pick m so that

$$\epsilon_j = \sum_l \sum_j \mu_{i_1, \dots, i_l}(j, m). \tag{3}$$

Denote the hyperplane in which the j th coordinate is m by P . Consider the way in which P is covered by the covering of V^k .

The $R_{k,l}^{k-2}$'s contributing to ϵ_j in (3) intersect P in $R_{k-1,l}^{k-2}$'s. These $R_{k-1,l}^{k-2}$'s are formed by taking the unions of certain $(k - 2)$ -dimensional hyperplanes in P , from a set of hyperplanes which include, at most, ϵ_j in each direction. Permuting the hyperplanes of V_n^k , if necessary, it may be assumed that these hyperplanes in P do not cut the cube

$$1 \leq x_p \leq n - \epsilon_j, \quad p = 1, \dots, k - 1, \tag{4}$$

where x_1, \dots, x_{k-1} are coordinates in P . This cube V' is a $V_{n-\epsilon_j}^{k-1}$ to which the lemma will be applied.

The elements of C which are not counted in Eq. (3) cover V' . Let $\mu'_{i_1, \dots, i_q(j)}$, where the subscript j may be present, or not, and $i_1, \dots, i_q \neq j$, be the number of elements of C which are counted in $\mu_{i_1, \dots, i_q(j)}$, but not in Eq. (3). These sets intersect P in $R_{k-1,q}^{k-3}$'s, but the intersections with V' may be of various types. In each of the $R_{k-1,q}^{k-3}$'s, there is a common q -dimensional plane, in which $k - 1 - q$ of the x_p 's are fixed. Let $\mu_{i_1, \dots, i_q(j)}^{r(r)}$ be the number for which r of the fixed x_p 's takes values $> n - \epsilon_j$. These intersect V' in $R_{k-1,q+r}^{k-3}$'s. Applying the induction hypothesis to V' ,

$$\sum_{q=0}^{k-3} \sum_{i_1, \dots, i_q \neq j} \sum_{r=0}^{k-3-q} \frac{k-1-q-r}{k-1} (\mu_{i_1, \dots, i_q}^{r(r)} + \mu_{i_1, \dots, i_q(j)}^{r(r)}) \geq \frac{(n - \epsilon_j)^2}{k - 2}. \tag{5}$$

If $\mu_{i_1 \dots i_q(j)}^{(r)}$ is defined similarly, but without the omission of those sets which contribute to Eq. (3), this implies that

$$\sum_{q=0}^{k-3} \sum_{i_1, \dots, i_q \neq j} \sum_{r=0}^{k-3-q} \frac{k-1-q-r}{k-1} (\mu_{i_1 \dots i_q}^{(r)} + \mu_{i_1 \dots i_q(j)}^{(r)}) \geq \frac{(n-\epsilon_j)^2}{k-2}. \tag{6}$$

It follows from Eq. (2) that

$$\sum_{\substack{s=1 \\ (s \neq j)}}^k \sum_{m=n-\epsilon_j+1}^n \sum_{i_1 \dots i_l} \mu_{i_1 \dots i_l}(s, m) \geq \epsilon_j \sum_{\substack{s=1 \\ (s \neq j)}}^k \epsilon_s.$$

Each element of C which contributes to $\mu_{i_1 \dots i_q(j)}^{(r)}$ is counted r times on the left in this inequality. Hence,

$$\begin{aligned} & \sum_{q=0}^{k-2} \sum_{i_1, \dots, i_q \neq j} \sum_{r=0}^{k-1-q} r \mu_{i_1 \dots i_q}^{(r)} \\ & + \sum_{q=0}^{k-3} \sum_{i_1, \dots, i_q \neq j} \sum_{r=0}^{k-1-q} r \mu_{i_1 \dots i_q(j)}^{(r)} \\ & \geq \epsilon_j \sum_{\substack{s=1 \\ (s \neq j)}}^k \epsilon_s. \end{aligned}$$

Divide by $k-1$ and add to (6). The result is

$$\begin{aligned} & \sum_{q=0}^{k-2} \sum_{i_1, \dots, i_q \neq j} \sum_{r=0}^{k-3-q} \frac{k-1-q}{k-1} (\mu_{i_1 \dots i_q}^{(r)} + \mu_{i_1 \dots i_q(j)}^{(r)}) \\ & + \sum_{q=0}^{k-2} \sum_{i_1, \dots, i_q \neq j} \sum_{r=k-2-q}^{k-1-q} \frac{r}{k-1} \mu_{i_1 \dots i_q}^{(r)} \\ & + \sum_{q=0}^{k-3} \sum_{i_1, \dots, i_q \neq j} \sum_{r=k-2-q}^{k-1-q} \frac{r}{k-1} \mu_{i_1 \dots i_q(j)}^{(r)} \geq \frac{(n-\epsilon_j)^2}{k-2} \\ & + \frac{1}{k-1} \epsilon_j \sum_{\substack{s=1 \\ (s \neq j)}}^k \epsilon_s. \end{aligned} \tag{7}$$

Increasing the values of some of the coefficients on the left, this becomes

$$\begin{aligned} & \sum_{q=0}^{k-2} \sum_{i_1, \dots, i_q \neq j} \sum_{r=0}^{k-1-q} \frac{k-1-q}{k-1} \mu_{i_1 \dots i_q}^{(r)} \\ & + \sum_{q=0}^{k-3} \sum_{i_1, \dots, i_q \neq j} \sum_{r=0}^{k-1-q} \frac{k-1-q}{k-1} \mu_{i_1 \dots i_q(j)}^{(r)} \\ & \geq \frac{(n-\epsilon_j)^2}{k-2} + \frac{1}{k-1} \epsilon_j \sum_{s \neq j} \epsilon_s. \end{aligned} \tag{8}$$

We have,

$$\sum_{r=0}^{k-1-q} \mu_{i_1 \dots i_q(j)}^{(r)} = \mu_{i_1 \dots i_q(j)}.$$

Hence,

$$\begin{aligned} & \sum_{q=0}^{k-2} \sum_{i_1, \dots, i_q \neq j} \frac{k-1-q}{k-1} \mu_{i_1 \dots i_q} \\ & + \sum_{q=0}^{k-3} \sum_{i_1, \dots, i_q \neq j} \frac{k-1-q}{k-1} \mu_{i_1 \dots i_q(j)} \\ & \geq \frac{(n-\epsilon_j)^2}{k-2} + \frac{1}{k-1} \epsilon_j \sum_{s \neq j} \epsilon_s. \end{aligned}$$

Consider the result of summing this inequality over all values of $j = 1, \dots, k$. The quantity $\mu_{i_1 \dots i_l}$ occurs in $k-l$ of the first sums, with coefficient $(k-1-l)/(k-1)$, and in l of the second sums, with coefficient $(k-l)/(k-1)$. Hence, its coefficient in the resulting inequality is

$$\frac{(k-l)(k-1-l)}{k-1} + \frac{l(k-l)}{k-1} = k-l.$$

Thus,

$$\begin{aligned} & \sum_{l=0}^{k-2} \sum_{i_1, \dots, i_l} (k-l) \mu_{i_1 \dots i_l} \geq \sum_{j=1}^k \left[\frac{(n-\epsilon_j)^2}{k-2} - \frac{\epsilon_j^2}{k-1} \right] \\ & + \frac{1}{k-1} \left(\sum_{s=1}^k \epsilon_s \right)^2, \end{aligned}$$

or

$$\begin{aligned} & \sum_{l=0}^{k-2} (k-l) v_l \geq \sum_{j=1}^k \left[\frac{n^2 - 2n\epsilon_j}{k-2} + \frac{\epsilon_j^2}{(k-1)(k-2)} \right] \\ & + \frac{1}{k-1} \left(\sum_{s=1}^k \epsilon_s \right)^2. \end{aligned} \tag{9}$$

The terms on the right in (9) which are of second degree in the ϵ_j 's form a positive definite quadratic form. Hence, the value of the right side, for unrestricted real values of the ϵ_j 's, is a minimum when all the partial derivatives are zero

$$\frac{\epsilon_j}{(k-1)(k-2)} - \frac{n}{k-2} + \frac{1}{k-1} \sum_{s=1}^k \epsilon_s = 0,$$

$$j = 1, \dots, k.$$

The solution of these equations is $\epsilon_j = n/(k-1)$, $j = 1, \dots, k$. Inserting these values in (9), it follows that

$$\sum_{l=0}^{k-2} (k-l) \nu_l \geq \frac{kn^2}{k-1}, \quad (10)$$

which was to be proved.

If equality holds here, there must be equality in (5)-(8). Assuming the condition for equality for V^{k-1} , it is necessary that

$$\mu_{i_1 \dots i_r(j)}^{(r)} = 0, \quad \text{for } q+r > 0, r \leq k-3-q,$$

and

$$\mu_{i_1 \dots i_q(j)}^{(q)} = 0, \quad \text{if } q \leq k-2. \quad (11)$$

Assume $k \geq 4$. By the first of these conditions, V' is covered only by $R_{k-1,0}^{k-3}$'s, implying that the hyperplanes (4) in V^k , which intersect in V' , are unique; for if not, they may be chosen in a different way so that one of the $R_{k-1,0}^{k-3}$'s becomes an $R_{k-1,r}^{k-3}$ with $r > 0$. Thus the ϵ_j sets counted in Eq. (3) must each contain a $(k-2)$ -dimensional hyperplane in every direction in P

$$\mu_{i_1 \dots i_l(j, m)} = 0, \quad \text{if } l > 0. \quad (12)$$

Eq. (12) holds for each j , for m such that Eq. (3) is valid. For arbitrary m ,

$$\sum_l \sum_j \mu_{i_1 \dots i_l(j, m)} \geq \epsilon_j, \quad (13)$$

which has the value $n/(k-1)$, if equality holds in Eq. (10). If this is true, summing over m and j yields

$$\sum_l (k-l) \nu_l \geq n \sum_{j=1}^k \epsilon_j = \frac{kn^2}{k-1}.$$

Hence, equality in (10) implies equality in (13) for all j, m . For any set of subscripts i_1, \dots, i_l ($l > 0$), pick $j \neq i_1, \dots, i_l$. Then (13) is true for every m . Summing over m , $\mu_{i_1 \dots i_l} = 0$.

Now it is known that equality can hold in (10) only if C consists of $n^2/(k-1)$ $(k-2)$ -dimensional rook domains. $n/(k-1)$ of these domains have their centers in each hyperplane. Any two of the centers have a distance at least $k-1$. For, if not, a hyperplane containing them may be taken to be the plane P above, and the definition of V' would not be unique.

In the projection of the centers of C into P , it follows from (11) that every point lies in one of the two regions,

- (i) $1 \leq x_p \leq n - \epsilon_j, \quad p = 1, \dots, k-1,$
- (ii) $n - \epsilon_j + 1 \leq x_p \leq n, \quad p = 1, \dots, k-1.$

This projection consists of $n^2/(k-1)$ distinct points at distances $\geq k-2$. Hence, the $n^2/(k-1)^2$ centers in the hyperplanes

$$\frac{(k-2)n}{k-1} + 1 \leq x_1 \leq n$$

in V_n^k all project into (ii). It follows that every $(k-3)$ -dimensional plane in (ii) contains exactly one of the projections; hence, the point set obtained in (ii) by the projection of the centers of C is distinguished by the fact that any two points in this set are two members of a sequence of points of the set with successive distances $k-2$.

By considering other hyperplanes of V^k parallel to P , it is easily seen that the set of projections of the centers can be decomposed into $k-1$ sets of this type, each being the projections of the centers in $n/(k-1)$ hyperplanes parallel to P . Hence, by choosing the coordinates x_1, \dots, x_k in V_n^k appropriately, the set of centers of C lies in the union of the $k-1$ disjoint cubes

$$\frac{tn}{k-1} + 1 \leq x_p \leq \frac{(t+1)n}{k-1}, \quad p = 1, \dots, k, \quad (14)$$

for $t = 0, 1, \dots, k-1$. Each cube contains $n^2/(k-1)^2$ points at a distance $\geq k-1$. Hence, in each cube, each $(k-2)$ -dimensional plane contains one center.

Conversely, if a set of $(k-2)$ -dimensional rook domains in V_n^k is distributed in this way, it covers V_n^k . Taking any point of V_n^k of its k coordinates, there must be two which satisfy one of the $k-1$ sets of inequalities (14). Suppose, for example, that $x_1, x_2 \leq n/(k-1)$. Then the $(k-2)$ -dimensional plane through the point in which x_1 and x_2 are fixed intersects the first cube; hence it contains the center of a rook domain. This plane is part of the rook domain, so the given point is covered.

Thus, equality is possible if and only if $n/(k-1) = h$ is an integer, and V_h^k contains h^2 points at distance $\geq k-1$. This condition is known to be equivalent to the existence of $k-2$ pairwise mutually orthogonal latin squares of order h (Ref. 6).

For $k = 3$, the second condition of Eq. (11) implies

$$\mu_{i_1}^{(0)} = 0, \quad \mu_j^{(1)} = 0, \quad \mu^{(1)} = 0.$$

The sets of C consist of v_{11} one-dimensional rook domains and v_1 rows. V' is covered by $\mu^{(0)}$ points. As above, the condition $\mu^{(1)} = 0$ implies that V' is unique, hence Eq. (12)

is true. The rest of the above development for $k \geq 4$ is valid for $k = 3$.

c. Corollary. A $(k-2)$ -dense set in V_n^k has at least $n^2/(k-1)$ elements. This number is possible if and only if $n/(k-1)$ is an integer, and there are $k-2$ orthogonal latin squares of order $n/(k-1)$.

References

1. Hamming, R. W., *Numerical Methods for Scientists and Engineers*, McGraw-Hill Book Co., New York, 1962.
2. Shannon, C. E., Gallager, R. G., and Berlekamp, E. R., "Lower Bounds to the Probability of Error for Discrete Memoryless Channels," forthcoming *Information and Control* paper.
3. Shannon, C. E., "Zero-Error Capacity of Noisy Channels," *PGIT, IT-2*, 8, 1956.
4. Berlekamp, E. R., *Block Coding with Noiseless Feedback*, 1964, MIT PhD thesis (EE), Massachusetts Institute of Technology, Cambridge.
5. Gallager, R. G., private communication, 1965.
6. Golomb, S. W., and Posner, E. C., "Rook Domains, Latin Squares, Affine Planes, and Error-Distributing Codes," *IEEE Transactions of the Professional Technical Group on Information Theory*, Vol. IT-10, No. 3, pp. 196-208, July 1964.
7. Golomb, S. W., and Posner, E. C., "Hypercubes of Non-Negative Integers," Research Problem 10, *Bull. Amer. Math. Soc.*, Vol. 71, p. 587, 1965.